4GLS DARESBURY

4GLS Conceptual Design Report

Light Years Ahead

http://www.4gls.ac.uk/

2006

Published by the CCLRC

This publication can also be accessed in the first instance at:
http://www.4gls.ac.uk

Prof Elaine Seddon
Telephone:+44 (0)1925 603245
Facsimile:+44 (0)1925 603124
E-mail: e.seddon@dl.ac.uk

Foreword

30 years ago the world synchrotron radiation (SR) community numbered only around 100 scientists; today it numbers around 12,000. At that time, staff at the UK's Daresbury Laboratory turned SR from a research curiosity into a tool that could be used by a large worldwide community by their innovative and far-sighted proposal for the SRS – the world's first 2nd generation synchrotron source. Today we find ourselves in the vanguard of a similar watershed in accelerator technology – the development of 4th generation light sources. I am delighted and very proud that once again CCLRC staff are at the forefront of world developments in proposing an innovative and challenging multi-source concept for 4GLS that has a similar potential to transform 4th generation technology into the 21st century light source technology of choice for large communities.

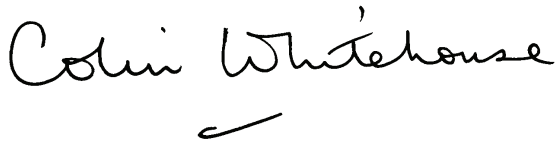

Deputy Chief Executive CCLRC

4GLS Executive Summary

The 4GLS project design takes advantage of the very latest advances in accelerator science and technology incorporated in a unique scheme to provide state-of-the-art research facilities. This will enable a broad range of outstanding science to be undertaken by the UK and international communities.

4GLS will enable the study of real time molecular processes and reactions on timescales down to tens of femtoseconds in short-lived, nano-structured or ultra-dilute systems. The emphasis is on molecular and device function, rather than the largely 'static' structural focus of work on 3rd generation synchrotron radiation sources and X-ray FELs. Key areas where 4GLS will make unique contributions are in:

- understanding the function of single biomolecules in living systems and membrane transport;
- determining reaction pathways in areas as diverse as enzyme processes, reactions contributing to atmospheric pollution or reactions occurring in the interstellar medium;
- studies of electron motion in atoms/molecules and developing 'coherent control' of reactions and intense laser-matter interaction leading to new physics;
- developing new nano-scale devices through understanding electron charge and spin transport; and
- development of new dynamic imaging techniques to improve early diagnosis of conditions such as cancer and prion based diseases.

The major themes of the science case are time-resolved measurements in the life sciences and nanoscience. Particular areas of strength are high resolution pump-probe spectroscopy of atoms, molecules and clusters, including high field dynamics, dynamics at surfaces and interfaces, many-body problems in condensed matter, and studies of the dynamics of biomolecules in 'real' environments.

The science requirement is for an ultra-high brightness facility that allows the use of short pulsed sources in combination, and where the energy range is optimised to allow the extraction of electronic and vibrational information. The 4GLS suite of synchronised sources, operating from the THz to the soft X-ray range is designed to meet this science need.

The 4GLS facility is planned from the outset to be a multi-source, multi-user facility. This is achieved by superconducting radio-frequency (SCRF) accelerator technology, operating using energy recovery, to provide short pulse spontaneous radiation with pulse length variable from ps to < 100 fs. At long wavelengths this allows the condition for coherent synchrotron radiation (CSR) production to be met, with the result that 4GLS will provide enormously bright THz

radiation. The high quality low emittance electron beam provided by the SCRF linacs additionally provides an ideal source with which to operate free electron lasers (FELs). In the 4GLS conceptual design these are embedded within the facility, delivering ultra-high brightness short-pulse radiation in the IR, VUV and XUV energy ranges, with pulse lengths as short as 50 fs FWHM. In world terms, this gives a unique suite of synchrotron radiation (SR) and FEL sources covering the THz to the soft X-ray range. Many of the light pulses originate from the same electron bunch, thus offering levels of internal synchronization as high as tens of femtoseconds. All the 4GLS sources are offered with variable polarization, while the flexibility of SCRF technology allows the repetition rates of the sources to be varied.

The 4GLS accelerator design concept consists of three inter-related accelerator systems. The high average current loop uses energy recovery as an essential element to deliver a 600 MeV electron beam of 77 pC bunches at repetition rates of up to 1.3 GHz. Distributed bunch compression allows for SR pulse lengths from a few ps to approximately 100 fs (RMS) to be delivered according to user requirements. A low Q-cavity VUV-FEL device is incorporated at the end of this loop. The most challenging area of accelerator design for 4GLS is in transporting and accelerating an extremely high quality high-average current (100 mA) beam to this loop, while simultaneously providing extremely high peak current (1.5 kA) at 750 – 950 MeV for the second accelerator system, the XUV-FEL branch. This beam is derived from 1 nC bunches produced by a normal conducting RF photoinjector operating at 1 kHz and it is dumped after traversing a final spontaneous undulator source. The XUV-FEL uses an HHG (high harmonic generation) seed, offering considerable advantages in pulse quality over a SASE (self-amplification of spontaneous emission) design. The third accelerator system is required for the IR-FEL. SCRF linac technology is used to accelerate electrons to 25 – 60 MeV to provide a fully integrated and synchronized IR-FEL facility.

Significant aspects of the 4GLS design have been informed by experience gained on the 4GLS Energy Recovery Linac Prototype (ERLP) currently approaching completion at CCLRC Daresbury Laboratory. In considering detailed 4GLS design decisions considerable attention has been given to ensuring that future upgrade options are not designed out at this early stage. These possibilities include various routes to higher energy operation, increased repetition rate for the XUV-FEL and decreased photon pulse lengths.

4GLS is thus the leading energy recovery proposal in Europe and the most comprehensive in terms of utilisation of combined sources. In terms of multi-user capability it is currently the most advanced energy recovery linac (ERL) proposal in the world. 4GLS is complementary to TESLA XFEL, to table-top lasers and to 3rd generation sources available to the UK research community.

The unique advantages of 4GLS are:

- Combinations of sources. The fully integrated capability to utilize both short pulse SR(ERL) and the FEL sources for pump-probe and two colour dynamics experiments. This results in both experimental flexibility and cost effective delivery.

- Intense, tuneable, variable polarisation FEL sources optimized for spectroscopy and imaging in the frequency ranges of XUV, VUV and IR-THz.

- Energy recovery linac spontaneous light sources available from soft X-ray to THz. This gives short pulse, high repetition rate operation, the capability to 'pulse tailor', and low probability of sample damage.

- Europe's most intense broadband source of coherent THz radiation.

4GLS will be a multi-user facility. Its user community (estimated to be some 920 scientists when fully developed) will evolve from those who have been using the SRS, 3rd generation SR sources and the laser community. The capabilities of 4GLS will ensure that it becomes a major attractor of world class international investigators.

Activities associated with 4GLS offer many diverse opportunities for knowledge transfer and innovation. These span opportunities arising from development and exploitation of both the light sources and the science and technology associated with the accelerator. Knowledge gained on 4GLS, especially in the areas of detector development and beam diagnostics, will be important to the development of other major projects e.g. Diamond and XFEL.

Key international collaborations have been developed with Jefferson Laboratory (ERL technology), Sincrotrone Trieste (FEL science and technology), DESY (FEL and linear collider), Forschungszentrum Rossendorf (ERL component development), Lawrence Berkeley National Laboratory (accelerator science and technology) and Cornell University (superconducting linac and RF technology) and as part of EuroFEL, the European FEL Design Study. 4GLS will underpin the development of key accelerator technologies to support the International Linear Collider Project.

The 4GLS Design Team

John Alexander	CCLRC Daresbury Laboratory
Simon Appleton	CCLRC Daresbury Laboratory
Phil Atkinson	CCLRC Daresbury Laboratory
Alan Austin	CCLRC Daresbury Laboratory
Bob Bate	CCLRC Daresbury Laboratory
Alan Bates	CCLRC Daresbury Laboratory
Peter Bates	CCLRC Daresbury Laboratory
Carl Beard	CCLRC Daresbury Laboratory
Steve Bennett	CCLRC Daresbury Laboratory
Adam Berry	CCLRC Daresbury Laboratory
Paul Birchall	CCLRC Daresbury Laboratory
Stephen Bibby-Trevor	CCLRC Daresbury Laboratory
Neil Bliss	CCLRC Daresbury Laboratory
Marion Bowler	CCLRC Daresbury Laboratory
Stephen Buckley	CCLRC Daresbury Laboratory
Rachael Buckley	CCLRC Daresbury Laboratory
Ian Burrows	CCLRC Daresbury Laboratory
Steve Burrows	CCLRC Daresbury Laboratory
Ryan Cash	CCLRC Daresbury Laboratory
Graham Charnley	CCLRC Daresbury Laboratory
Chris Chorlton	CCLRC Daresbury Laboratory
Jim Clarke	CCLRC Daresbury Laboratory
Mark Colcough	CCLRC Daresbury Laboratory
Dave Coleman	CCLRC Daresbury Laboratory
John Collier	CCLRC Rutherford Appleton Laboratory
Mike Cordwell	CCLRC Daresbury Laboratory
Peter Corlett	CCLRC Daresbury Laboratory
Graham Cox	CCLRC Daresbury Laboratory
Paul Cridland	CCLRC Daresbury Laboratory
Phil Davis	CCLRC Daresbury Laboratory
Steve Davis	CCLRC Daresbury Laboratory
Dave Dawson	CCLRC Daresbury Laboratory
Marta Divall	CCLRC Rutherford Appleton Laboratory
Steve Dobson	CCLRC Daresbury Laboratory
Mike Dufau	CCLRC Daresbury Laboratory
Andy Duggan	CCLRC Daresbury Laboratory
Dave Dunning	CCLRC Daresbury Laboratory
Mike Dykes	CCLRC Daresbury Laboratory
Andy Eales	CCLRC Daresbury Laboratory
Robin Eldridge	CCLRC Daresbury Laboratory

Richard Farrow	CCLRC Daresbury Laboratory
Khal Fayz	CCLRC Daresbury Laboratory
Wendy Flavell	University of Manchester
Leszek Frasinski	University of Reading
Andy Gallagher	CCLRC Daresbury Laboratory
Chris Gerth	Now at DESY
Allan Gillespie	University of Dundee
Keith Gleave	CCLRC Daresbury Laboratory
Andy Goulden	CCLRC Daresbury Laboratory
Eddie Greene	CCLRC Daresbury Laboratory
Steve Griffiths	CCLRC Daresbury Laboratory
Henry Gun-Why	CCLRC Daresbury Laboratory
Fay Hannon	Now at Jefferson Laboratory
Ian Harvey	CCLRC Daresbury Laboratory
Joe Herbert	CCLRC Daresbury Laboratory
Clive Hill	CCLRC Daresbury Laboratory
Paul Hindley	CCLRC Daresbury Laboratory
Graeme Hirst	CCLRC Rutherford Appleton Laboratory
Cheryl Hodgkinson	CCLRC Daresbury Laboratory
Martin Holbourn	CCLRC Daresbury Laboratory
David Holder	CCLRC Daresbury Laboratory
Adrian Hooper	CCLRC Daresbury Laboratory
Peter Huggard	CCLRC Rutherford Appleton Laboratory
Barry Intin	CCLRC Daresbury Laboratory
Steven Jamison	CCLRC Daresbury Laboratory
Paul Johnson	CCLRC Daresbury Laboratory
Lee Jones	CCLRC Daresbury Laboratory
Alex Kalinin	CCLRC Daresbury Laboratory
Tim Kenyon	CCLRC Daresbury Laboratory
Mike Low	CCLRC Daresbury Laboratory
David Laundy	CCLRC Daresbury Laboratory
Terry Lee	CCLRC Daresbury Laboratory
Mike Macdonald	CCLRC Daresbury Laboratory
Oleg Malyshev	CCLRC Daresbury Laboratory
John Manning	CCLRC Daresbury Laboratory
Gary Markey	CCLRC Daresbury Laboratory
Jamie Markey	CCLRC Daresbury Laboratory
Neil Marks	CCLRC Daresbury Laboratory
Marisa Martin-Fernandez	CCLRC Daresbury Laboratory
Brian Martlew	CCLRC Daresbury Laboratory
Pavel Matousek	CCLRC Rutherford Appleton Laboratory
Ian Maxwell	CCLRC Daresbury Laboratory

Peter McIntosh	CCLRC Daresbury Laboratory
Brian McNeil	University of Strathclyde
Keith Middleman	CCLRC Daresbury Laboratory
Sergey Miginsky	Budker Institute, Russia
Boris Militsyn	CCLRC Daresbury Laboratory
Andy Moss	CCLRC Daresbury Laboratory
Alan Muir	CCLRC Daresbury Laboratory
Ian Mullacrane	CCLRC Daresbury Laboratory
Bruno Muratori	CCLRC Daresbury Laboratory
Adrian Oates	CCLRC Daresbury Laboratory
Joe Orrett	CCLRC Daresbury Laboratory
Hywel Owen	CCLRC Daresbury Laboratory
Pete Owens	CCLRC Daresbury Laboratory
Tony Parker	CCLRC Rutherford Appleton Laboratory
Shrikant Pattalwar	CCLRC Daresbury Laboratory
Jonathon Phillips	University of Dundee
Mike Poole	CCLRC Daresbury Laboratory
Alan Quigley	CCLRC Daresbury Laboratory
Frances Quinn	CCLRC Daresbury Laboratory
Paul Quinn	CCLRC Daresbury Laboratory
Peter Rathbone	CCLRC Daresbury Laboratory
Ron Reid	CCLRC Daresbury Laboratory
James Rogers	CCLRC Daresbury Laboratory
Mark Roper	CCLRC Daresbury Laboratory
Ian Ross	CCLRC Rutherford Appleton Laboratory
Ralph Rotheroe	CCLRC Daresbury Laboratory
Harvey Rutt	University of Southampton
Yuri Saveliev	CCLRC Daresbury Laboratory
Duncan Scott	CCLRC Daresbury Laboratory
Elaine Seddon	CCLRC Daresbury Laboratory
Brian Sheehy	Sheehy Scientific Consulting
Ben Shepherd	CCLRC Daresbury Laboratory
Andrew Smith	CCLRC Daresbury Laboratory
Phill Smith	CCLRC Daresbury Laboratory
Rob Smith	CCLRC Daresbury Laboratory
Susan Smith	CCLRC Daresbury Laboratory
Graham Stokes	CCLRC Daresbury Laboratory
John Strachan	CCLRC Daresbury Laboratory
Mark Surman	CCLRC Daresbury Laboratory
Justin Theed	CCLRC Daresbury Laboratory
Neil Thompson	CCLRC Daresbury Laboratory
Brian Todd	CCLRC Daresbury Laboratory

Mike Towrie	CCLRC Rutherford Appleton Laboratory
Jennifer Varley	Formerly CCLRC Daresbury Laboratory
Peter Weightman	University of Liverpool
Greg Westbrook	CCLRC Daresbury Laboratory
Tom Weston	CCLRC Daresbury Laboratory
Chris White	CCLRC Daresbury Laboratory
Paul Whitfield	CCLRC Daresbury Laboratory
Emma Wooldridge	CCLRC Daresbury Laboratory
Naomi Wyles	CCLRC Daresbury Laboratory

Members of the 4GLS design team

Building Consultants

Jacobs Babtie	Architects
Peter Brett Associates	Building Services

4GLS International Advisory Committee

Dr George Neil (Chair)	Jefferson Laboratory, USA
Prof Dr Uwe Becker	Fritz-Haber Institute der Max-Plank, Germany
Prof Ilan Ben Zvi	Collider-Accelerator Department, BNL, USA
Dr Carlo Bocchetta	Sincrotrone Trieste, Italy
Dr Paul Dumas	LURE, France
Dr Mikael Eriksson	MAX-lab, Sweden
Prof Eugene Kennedy	Dublin City University, Eire
Prof Gennady Kulipanov	Deputy Director, Budker Institute of Nuclear Physics, Russia
Prof Ingolf Lindau	MAX-lab, Sweden
Prof Peter Lindley	Director ITQB-UNL, Portugal
Prof Dr Gerd Materlik	CEO, Diamond Light Source Ltd, UK
Dr Jean-Michel Ortega	LURE, France
Prof Hasan Padamsee	Cornell University, USA
Dr Albert Parr	NIST, USA
Prof John Sutherland	East Carolina University, USA
Prof Francois Wuilleumier	LSAI, Universite Paris-Sud, France

The 4GLS International Advisory Committee with some team members

4GLS Steering Committee

Professor Peter Weightman (Chair)	University of Liverpool
Dr George Baxter	NWDA
Prof. Richard Catlow	Royal Institution/University College London
Prof Mike Chesters	University of Nottingham
Professor Martyn Chamberlain	University of Durham
Prof Keith Codling	University of Reading
Professor Mike Dunne	CCLRC
Professor Robert Donovan	University of Edinburgh
Professor Hilary Evans	Liverpool John Moores University
Professor David Fernig	University of Liverpool
Professor Wendy Flavel	University of Manchester
Professor Henry Hutchinson	CCLRC
Prof Dino Jaroszynski	University of Strathclyde
Professor George King	University of Manchester
Professor Colin Latimer	Queens University, Belfast
Professor Jian Lu	University of Manchester
Professor Klaus Muller-Dethlefs	University of Manchester
Professor John McCarthy	University of Manchester
Professor Martin McCoustra	University of Nottingham
Dr Ben Murdin	University of Surrey
Professor Paul O'Shea	University of Nottingham
Professor Mike Poole	CCLRC
Professor Ivan Powis	University of Nottingham
Dr Andrea Russell	University of Southampton
Professor Harvey Rutt	University of Southampton
Progfessor Nigel Scrutton	University of Manchester
Professor Elaine Seddon	CCLRC
Dr Sarah Thompson	University of York
Professor Pankaj Vadgama	Queen Mary College, University of London
Professor John West	CCLRC
Prof Colin Whitehouse	CCLRC
Professor John Wood	CCLRC
Prof Phil Woodruff	University of Warwick

International Collaborations

FZR Rossendorf, Germany
DESY, Germany
FERMI@Elettra, Italy
Cornell University, USA
Jefferson Laboratory, USA
Stanford University, USA
Lawrence Berkeley National Laboratory, USA

EUROFEL, the European FEL Design Study, Partner Institutions:

BESSY, Germany
CCLRC, UK
CEA-SPAM, France
CNRS, France
DESY, Germany
Elettra, Italy
ENEA, Italy
FZR, Germany
INFN, Italy
MAX-lab, Sweden
MBI, Germany
SOLEIL, France
TEMF, Germany
Universität Hamburg, Germany
University of Rome, Italy
University of Strathclyde

Acknowledgements

The 4GLS design has been enhanced by the useful comments and suggestions made by many colleagues from around the world. Their input has been vital to ensuring that the 4GLS design as presented in this report is world class. Their contributions are gratefully acknowledged.

Special thanks are due to the team of international experts who reviewed the technical content of this CDR and also to the proof readers for carefully checking for any typesetting errors.

The 4GLS design studies have been funded by the Department of Trade and Industry and the Council for the Central Laboratory for the Research Councils. The EuroFEL project is funded by the EU Framework 6 and the partner institutions.

Table of Contents

Part A

Part B

Part C

1. Introduction

1.1 Context of the Report

In this volume and its appendices, we present the Conceptual Design Report (CDR) for the UK's Fourth Generation Light Source Project, 4GLS.

The 4GLS proposal arises from the fundamental requirement to understand the *dynamic* behaviour of matter, often in very small (nm) units, on very fast (fs) timescales. 4GLS is a suite of accelerator-based light sources designed to meet this science need. It will provide state-of-the-art FEL and intense *short pulse* synchrotron radiation covering the THz to soft X-ray regime. The 4GLS proposal is the world's first proposal to combine energy recovery linac (ERL) and FEL technology in a multisource, multiuser facility. The facility is uniquely suited to *pump-probe* experiments, probing dynamics on timescales down to 100 fs or better. This is because of the natural synchronization that arises from combining sources that originate from the same electron bunch, and is a significant advantage over 'stand-alone' FEL sources. The emphasis is on providing high quality output (in terms of stability, pulse-to-pulse reproducibility *etc*.) from synchronised multiple sources.

The Science Case for 4GLS was presented by the UK and international scientific community in December 2001, and is available at www.4gls.ac.uk. It passed through Peer Review (organised by EPSRC acting on behalf of RCUK) in April 2002, and was allowed to pass to Gateway 1 (Business Justification stage) of the UK OGC 'Gateway Process' for assessing large scale projects. The substantial body of documentation prepared for the business case assessment is summarised in the 4GLS Business Case, presented in October 2002. Following OGC assessment of the Business Justification in November 2002, the project was given a 'green light' to proceed to the next stages of the Gateway Process. In April 2003, funds were awarded by DTi and CCLRC for the construction of an energy recovery linac prototype source, ERLP. This project is currently underway at CCLRC Daresbury Laboratory. In April 2005, further funds were made available to commence design work for the 4GLS facility.

This document contains the first output of this design process, the CDR. Here we present a conceptual design for the 4GLS facility that can deliver the scientific vision we put forward in the Science Case. In a number of the design areas, rapid technological developments mean that there is no unique solution to the design challenge. In these cases, we have assessed the alternative possibilities, and have presented here the most likely solutions. This outline of the concept will be followed by consultation with our key stakeholders, leading to a detailed Technical Design Report (TDR), planned for March 2007. In the TDR document, we will move on from the concept developed here to an accurately costed proposal that includes experimental details of specimen beamlines, endstations and detector developments. These documents, together with a summary of the impact of 4GLS on the science landscape will form the basis for a bid for full funding of the 4GLS facility in October 2007.

1.2 Structure of the Conceptual Design Report

The report falls naturally into three distinct parts giving a project overview, the body of the technical design work for the accelerator and photon transport and the supporting technical systems, building and services.

Chapter 2 gives an overview of the **science drivers** for the project and the resulting requirements for the facility. **Chapter 3** introduces the energy recovery linac and free electron laser concepts, explaining how they meet these requirements. This is followed by a **summary description of the 4GLS facility**; the accelerator systems, the XUV, VUV and IR free electron lasers and the conventional synchrotron and laser sources. **Chapter 4** discusses the different **source combinations** possible and presents illustrative timing modes.

The conceptual design of the three **injector systems** is covered in **Chapter 5**. The choice of **accelerator technology** is presented in **Chapter 6** and includes the proposed design for the seven 4GLS linacs in the injector systems, the main 590 MeV linac and the XUV-FEL booster linac. This chapter also covers the RF frequency and cryogenic operating temperature choices. **Chapter 7** puts forward the **electron beam transport** design fundamental to delivering bright, intense, sub-picosecond electron bunches. The **fundamental physics underpinning free electron lasers** is presented in **Chapter 8** followed by the design specification and performance of the XUV, VUV and IR FELs. This is followed by the description of the **conventional synchrotron radiation and lasers sources in Chapter 9**, including the expected output from coherent terahertz sources. This chapter also **summarises the photon output from all the 4GLS sources** and compares them to a selection of relevant facilities. The issues important to designing the **photon transport systems** and characterising the radiation are examined in **Chapter 10**. The design philosophy for **timing and synchronisation** is developed in Chapter 11 and is followed by **Chapter 12** which considers the **potential upgrades** that need to be allowed for in the conceptual design.

The final part of the report starts with **Chapter 13**, an overview of the **conventional technical systems** required, focussing on the more challenging systems such as the **cryogenic plant**. **Chapter 14** shows a concept for the **building** and infrastructure together with the significant engineering services. Lastly, **Chapter 15** presents the **health, safety and environment** philosophy, the most critical at this stage of the design process being the estimation of the radiation hazard and control methodology.

The appendices contain a **glossary** of terms and a selection of **key parameter tables** extracted from the body of the report.

2. Science Overview

2.1 The Scientific Impact of 4GLS

4GLS will produce short pulses of light with enormously high brightness. The pulse lengths will be similar to the time taken to make or break a chemical bond. This means that in principle any dynamic process occurring on a timescale as short as this fundamental step (or longer) may be probed. In world terms, the design concept presented in this document will give 4GLS a unique capability in this field. Some examples of the scientific impact of this capability are given below:

- The mechanisms of catalytic reactions in a range of enzyme and chemical processes will be established. It will be possible to monitor reactions occurring in real time on fs and ps timescales, and thus to provide experimental data over timescales that match those of theoretical molecular dynamics techniques.

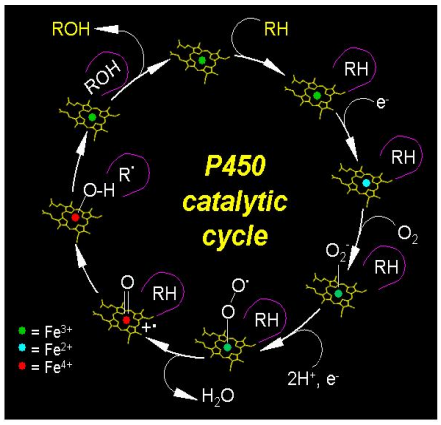

Figure 2.1 The proposed catalytic cycle of cytochrome P450 redox enzyme. RH represents an organic substrate, ROH the product of hydroxylation. Two electrons and two protons are delivered to the P450 haem at strategic points in the cycle. (N Scrutton, University of Manchester, reproduced with permission.)

- Functional dynamic imaging of *live* cells will be possible at 30 – 50 nm resolution allowing mechanisms of cell differentiation, apoptosis, and interaction with pharmaceutical agents to be understood at a sub-cellular level.

- Reactions of transients (such as free radicals and ions) contributing to pollution creation and removal in the biosphere will be understood at a mechanistic level hitherto impossible, allowing the development of strategies for pollution removal and reduction, and improvement in the efficiency of hydrocarbon combustion.

Figure 2.2 Improving the efficiency of hydrocarbon combustion: molecular beam mass spectrometry combined with VUV photoionisation in the study of transient species in flames at the ALS, LBNL (Science 308, 24th June 2005, reproduced with permission of Science and Sandia National Laboratories).

- The dynamics of charge and spin carriers in microdevices will be probed in real time on ps and fs timescales, allowing, for example, fast charge dynamics at critical wide-gap interfaces (such as Si/SiO_2) to be understood in a way not currently possible. This understanding is essential to continued future exploitation of silicon technology.

- A new understanding of the interactions of gas molecules and ions with intense photon fluxes will be obtained that will revolutionise our understanding of stellar coronae, massive star evolution, planetary nebulae, cooling flows in galaxies, active galactic nuclei and the accretion disks around black holes. Fundamental parameters will be provided for theoretical models, allowing direct comparison between calculated astrophysical parameters and data from spectroscopic missions.

The 4GLS Science Case is available at www.4gls.ac.uk.

2.2 The Science Drivers of the 4GLS Design

The scientific need for this facility stems from the fundamental requirement for UK and international scientists to understand the *dynamic* behaviour of matter, often in very small (nm) units, on very fast (fs) timescales.

This requirement is in turn driven by the small lengths and fast timescales governing many 21st century technologies. For example, semiconductor device structures based on silicon are set to become so small that they will operate normally in a non-equilibrium regime which makes *dynamic* carrier distribution measurements essential for their further exploitation. The development of spintronic logic and sensors will require nanoscale characterisation of electron spin distributions of magnetic clusters. Dynamic measurements of protein folding in realistic solutions on fast timescales are necessary to complement the 'static' structure information provided by protein crystallography in the post-genomics world. The ability to manipulate molecules using tailored light pulses is essential for exploitation of the coherent control of reactions, while the ability to follow reaction pathways and pinpoint reaction intermediates is necessary to improve our understanding of all types of industrial catalysis, particularly asymmetric synthesis.

In essence, the UK and international scientific community recognises a need not just to determine *structure* with high precision (as may be done with a 3rd generation SR source), but to understand *how these structures work*.

The extraction of this dynamic information is far from trivial; it will necessitate cutting-edge experiments using multiple pulsed and synchronised sources of ultra-high brightness light. The pulse lengths need to be short enough to study bond breaking and bond making while the energy of the pulses must be low enough to allow very high resolution spectroscopy of the vibrational and electronic motions of these bonds, and to limit damage e.g. to biological material. The need

is thus for an ultra-high brightness *low energy* facility that allows the use of pulsed sources in combination.

In 1993, the Woolfson Report resulting from a review of Synchrotron Radiation in the UK [1] recommended a 'three source scenario' for the UK. High energy X-ray radiation would be provided by the UK's share in the ESRF, the bulk of X-rays for the UK would be provided by a home-based medium energy source (Diamond), and VUV radiation would be provided by a home-based low energy source. The first two recommendations of this report have now been funded, but the provision of *low energy* radiation has not so far been addressed.

Rapid developments in accelerator technology during this period have produced a 'technology pull' that exactly complements the 'science push' described above. This enables us to realise scientific goals that far surpass the original expectations for a low energy source as outlined by Woolfson [1]. Detailed consultation with potential users of low energy photons led in 2001 to the development of a Science Case [2] drawing on contributions from over 200 scientists. In order to deliver this science case, the following were identified at the Business Case assessment of 4GLS in 2002 as key targets for the UK low energy SR and FEL communities [3]:

- Optimised continuous radiation in the IR to XUV region of the spectrum;
- Optimised pulsed sources of radiation in the IR, VUV and XUV regions of the spectrum;
- Multiple, synchronised sources to enable pump-probe and two-colour experiments;
- Both ultra-high brightness and ultra-high flux to enable the study of very dilute or nanoscale samples, and to allow the development of new nanoimaging techniques;
- Pulse lengths which are variable from the ps to the fs regime, with variable pulse spacing for investigation of dynamic processes.

In the four years following the peer-review of the 4GLS Science Case [2], the field has been far from static. Indeed there have been a number of key developments that have led to proposed enhancements in the 4GLS science programme and which impact on the key targets. These are summarised below:

- Increased scientific excitement in exploitation of the THz (far-IR) part of the electromagnetic spectrum in areas as diverse as coherent manipulation of semiconductor qubits, imaging and spectroscopy of biological molecules (particularly of H-bonding), and security applications. This has been coupled with the realisation that linac-based accelerators provide the world's most intense sources of broadband THz radiation [4].

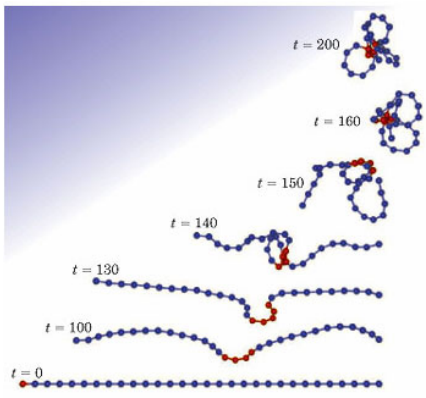

Figure 2.3 A biopolymer chain buckles and folds on itself due to an instability produced by a nonlinear localized mode (see S. F. Mingaleev et al. Europhys. Lett. 59 403 (2002)). These modes can be generated using high field THz light. (Reprinted with permission from Physics Today Jan. 2004 p49, copyright 2004, American Institute of Physics)

- The advent of phase-stabilised few cycle attosecond pulses from table-top lasers [5] has led to increased scientific activity in the use of photons for coherent control of processes in atoms and molecules. There is an increased demand both to combine the advantages of table-top attosecond pulses with the power and energy ranges accessible with FEL sources and to seek progressively to shorten the pulse lengths that are provided by FEL sources.

- An increased demand from the user community for provision of soft X-rays in combination with other 4GLS sources, for example for studies of surface dynamics by soft X-ray absorption and emission initiated by a THz pump and for combined IR/soft X-ray spectroscopy to address environmental problems.

- An appreciation that short pulse broad-bandwidth hard X-rays may be readily produced in modest fluxes by interaction of electron bunches from a linac-based accelerator with pulses from a FEL or table-top laser [6].

2.3 Review of the 4GLS Science Programme and the Resulting Requirements of the Source

2.3.1 Key areas of Scientific Impact

Following the submission of the 4GLS Science Case in 2001, continued close interaction with potential users of the source has led to the identification of five key areas of science where 4GLS will make unique contributions. These are:

- in understanding the function of single biomolecules in living systems and membrane transport. Ultra-high brightness in the IR and THz will enable imaging of sub-cellular structures in *live* cells and will allow development of nonlinear spectroscopic probes capable of studying membranes and their interfaces in real aqueous environments.

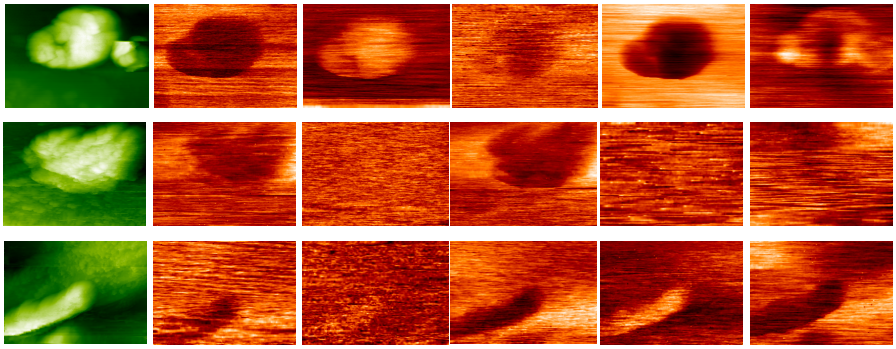

Figure 2.4 Scanning near-field techniques used with the Vanderbilt University IR-FEL source to analyze the distribution of functional groups in a single cell with a resolution well below the diffraction limit. (Antonio Cricenti, ISM-CNR, Roma-ITALY and Vanderbilt University, Nashville, USA, reproduced with permission.)

- determining reaction pathways (in areas as diverse as enzyme processes, reactions contributing to atmospheric pollution or occurring in the interstellar medium). Multiple synchronised sources in the VUV, XUV and THz will allow reaction initiation, the creation of short-lived transients and the study of their evolution on the timescales of bond-breaking and bond-making.

- studies of electron motion in atoms and molecules, developing 'coherent control' of reactions and intense laser-matter interaction leading to new physics. These are enabled by seeded XUV-FEL and VUV-FEL radiation, allowing for pulse shaping, in combination with synchronised variably polarised VUV and XUV spontaneous radiation. High field regimes are accessed with the extremely high EM fields of up to 10^{17} W cm^{-2} generated by the XUV FEL.

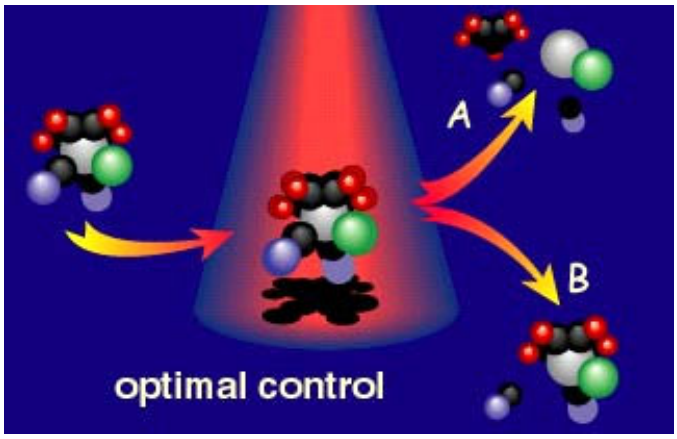

Figure 2.5 Influencing chemical reactions: shaped light pulses may be used to direct the course of a chemical reaction by quantum chemical control. (Gustav Gerber, University of Würzburg)

- developing new nanoscale devices through understanding electron charge and spin transport. High brightness synchronised sources in the IR, VUV and XUV enable pump-probe measurements of electron and spin dynamics and nanoscale dynamic imaging.

- development of new dynamic imaging techniques to improve early diagnosis of conditions such as cancer and prion-based diseases. This is made possible by the ultra-high brightness of the FEL sources and of the spontaneous THz radiation, combined with the ability to generate short-pulsed X-rays by laser-electron beam interaction.

The major themes of the 4GLS science programme are time-resolved measurements and nanoscience. Particular areas of strength are high resolution pump-probe spectroscopy of atoms, molecules and clusters, including high field dynamics, dynamics at surfaces and interfaces, many-body problems in condensed matter, and studies of the dynamics of biomolecules in 'real' environments.

2.3.2 Source Requirements Arising from Analysis of the 4GLS Science Case

2.3.2.1 Source Synchronisation

The 4GLS Science Case [2], which was peer-reviewed in 2002, contains 53 separate science areas. Of these, 19 require simultaneous use of one photon source of 4GLS synchronised with another (and some require synchronisation more than two photon sources). In addition, a significant number also cite the use of a tabletop laser with a 4GLS source. There is a high demand for synchronisation of all the 4GLS FEL sources with undulator radiation, and for synchronisation of the VUV-FEL with both the XUV and IR devices, in the main for pump-probe-type experiments. Thus a primary requirement for the 4GLS facility is the use of FEL and multiple SR sources in combination, with a satisfactory level of synchronisation. This requirement clearly has important implications for the layout of 4GLS and is incorporated into the design from the outset.

Of particular note is a high demand for synchronisation of undulator radiation with VUV-FEL radiation. This is needed to enable a wide range of science including studies of transient free radicals found in the Earth's atmosphere, photon-induced chemistry of ultra-cold ices, leading to an improved understanding of the interstellar medium, and real-time measurements of the dynamics of electrons in microdevices. Another area of especially high demand is in the combined use of synchronised VUV- and IR-FEL radiation. This is important in areas including the development of a number of nonlinear optical techniques allowing the study of the dynamics of molecules at interfaces in real wet environments – for example allowing the real-time study of transport mechanisms across membranes.

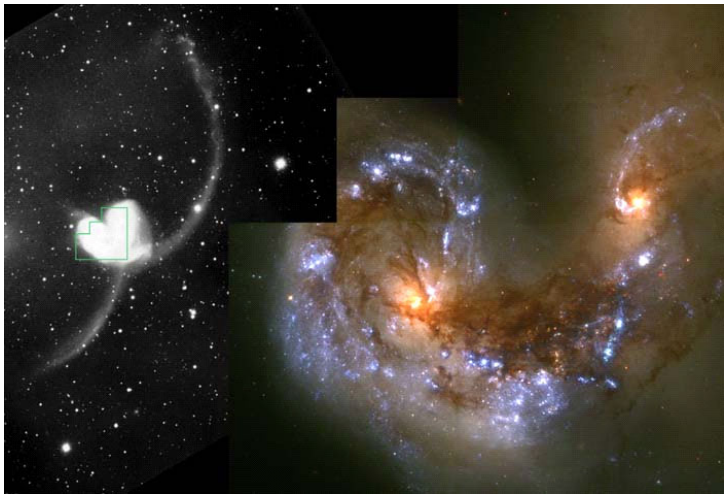

Figure 2.6

***Left panel**: A ground-based telescopic view of the collision between the Antennae galaxies (known formally as NGC 4038/4039) - so named because a pair of long tails of luminous matter, formed by the gravitational tidal forces of their encounter, resembles an insect's antennae. The galaxies are located 63 million light-years away in the southern constellation Corvus.*
***Right panel**: A Hubble Space Telescope image of the galaxy cores. The sweeping spiral-like patterns, traced by bright blue star clusters, shows the result of a firestorm of star birth activity which was triggered by the collision. Much of the oxygen and carbon in the Universe is produced in such regions. The young, massive stars cause the regions to be dominated by highly ionizing far-UV radiation.*

This natural-color image is a composite of four separately filtered images taken with the Wide Field Planetary Camera 2 (WFPC2), on January 20, 1996. Resolution is 15 light-years per pixel (picture element). Credit: Brad Whitmore (STScI), and NASA.

2.3.2.2 Variably Polarised Radiation

Examination of the Science Case also demonstrates a demand for variably polarised (VP) radiation. Eight areas of the science case require variable polarisation; most of these require more than one VP source. The science programme encompasses studies of the conformational dynamics of biomolecules, real-time measurement of the mechanism of enantioselective chemical reactions and studies of electron spin transport in spintronic devices. There is a concentration of demand for VUV VP radiation, both from FEL and undulator sources. The demand for VP radiation in future may reasonably be expected to increase, with increasing focus on issues such as enantioselective synthesis of drug molecules, manipulation of spin qubits, and the homochirality of life. It is clearly more cost-effective to incorporate VP capability from the outset than to modify the 4GLS sources at a later date to produce it.

2.3.2.3 Spontaneous Radiation

An analysis of the 4GLS Science Case reveals a heavy demand for spontaneous radiation. This is required in 26 of the 53 areas of the science case. Except in the IR/THz parts of the spectrum,

this demand is for undulator radiation. There is significant demand in the IR/THz for broadband bending magnet radiation. The demand for spontaneous radiation includes both time-resolved experiments (such as FEL-SR pump-probe spectroscopy which require pulsed sources with pulse lengths typically in the range 100 fs – 1 ps), and non-time-resolved measurements (including high resolution photoemission, CD and RAIRS, where a high brightness CW source is appropriate). The science programme that will use these sources ranges from 2-photon photoemission experiments designed to directly probe the mechanism of high temperature superconductivity to use of the wide tunability in the visible spectrum to visualise multiple fluorophores attached to individual molecules inside single cells. The source must therefore be capable of providing both pulsed and quasi-CW high brightness spontaneous radiation from THz to soft X-ray energies.

2.3.2.4 High Resolution Spectroscopy

Pump-probe experiments are key to the 4GLS Science Case. Many of these experiments are spectroscopic in nature, probing changes electronic and vibrational states on the fundamental timescales of change. However, for any pulse-length, the Uncertainty Principle provides a fundamental limit on the energy resolution that may be attained. If the probe pulse of the experiment is spectroscopic in nature, the attainable energy resolution becomes very important. This may mean that this pulse may ideally be provided by ps spontaneous radiation, even if a shorter FEL pulse is required as the pump pulse (e.g. for reasons of attaining high peak power or field). For spectroscopic experiments that are not time-resolved in nature, again ps spontaneous radiation from an undulator source is ideal. An example is ultra-high resolution photoemission, where energy resolutions of around 1 meV are now almost routinely attainable, and the current experimental drive is to reach resolutions in the μeV range [7].

Table 2.1 The energy broadening given by the Uncertainty Principle for pulse lengths of importance to the 4GLS science programme; this indicates the smallest possible broadening that is in principle attainable in the absence of experimental constraints (e.g. arising from beamline optics).

Pulse length ($\Delta\tau$)	**Energy broadening (ΔE)/ meV**	**Energy broadening (ΔE)/ cm^{-1}**
10 fs	33.3	266
100fs	3.33	26.6
1 ps	0.33	2.66
10 ps	0.03	0.27

In the regime of vibrational spectroscopy, where the required energy resolution is typically around a reciprocal wavenumber (1 cm^{-1}), the pulse length issues become more constraining. As a broad generalisation, Table 2.1 illustrates that in the IR and VUV spectral ranges, there is no requirement for *spectroscopic* probe pulses of shorter than around 1 ps. This in turn reduces the

difficulty of pulse synchronisation in these photon energy regimes. The situation is rather different in the XUV regime, where the requirements on spectral resolution may be less severe, but the drive to reduce pulse length is very much greater (for example, see §2.3.2.5). This in turn suggests that the 4GLS facility must be capable of delivering pulses of varying length from both spontaneous and FEL sources.

2.3.2.5 Time-of-Flight Experiments

Experiments that use time-of-flight detection and/or coincidence techniques have rather different experimental requirements. These experiments include a large number designed to probe atomic and molecular dynamics in the gas phase, including the programme in quantum chemical control. These gas phase experiments require single, reproducible pulses, often of high intensity, with a long interpulse spacing (that may be as long as 10 μs, corresponding to a 100 kHz repetition rate). The pulses required are generally short (fs regime) and in addition there are often stringent requirements for synchronisation to within 10% of the peak width with another 4GLS source or with a tabletop laser. Good photon diagnostics are extremely important, so that each pulse can be characterised. The photon energy range of highest demand for these studies is 8 - 20 eV. In this regime, the source must be capable of delivering pulse trains with relatively low repetition rates, made up of pulses with 100 fs FWHM or better, and which are synchronised to other source components to around 10 fs.

REFERENCES

[1] Woolfson Report on Synchrotron Radiation, 1993.

[2] 4GLS Science Case, 2001, available at www.4gls.ac.uk

[3] 4GLS Business Case, 2002

[4] G. L. Carr, M. C. Martin, W. R. McKinney, K. Jordan, G. L. Neil and G. P. Williams, *Nature*, **420**, 153, (2002).

[5] e.g. A. Baltuska, Th. Udem, M. Uiberacker, M. Hentschel, E. Goulielmakis, Ch. Gohle, R. Holzwarth, V. S. Yakoviev, A. Scrinzi, T. W. Hänsch and F. Krausz, *Nature*, **412**, 611, (2003).

[6] e.g. J. R. Boyce, D. R. Douglas, Hiroyuki Toyokawa, W. J. Brown and F. Hartemann, Proceedings of the 2003 Particle Accelerator Conference, 2003, 938.

[7] e.g. T. Kiss, T. Yokoya, A. Chainani and S. Shin, J. Electron Spectrosc. Rela.t Phenom., 114-116, 635, (2001).

3. Facility Overview

3.1 The 4GLS Concept

The 4GLS project design takes advantage of the very latest advances in accelerator science and technology incorporated in a unique scheme to provide state-of-the-art facilities. This has been made possible by a number of parallel developments at leading international laboratories, including successful demonstrations of technical solutions. The proposed design builds on current world achievements and in some cases extrapolates beyond them. In the most challenging areas an active R&D programme is already underway world-wide and the 4GLS team has augmented this, not least because to do so enhances the necessary skill base for detailed design, construction and operations.

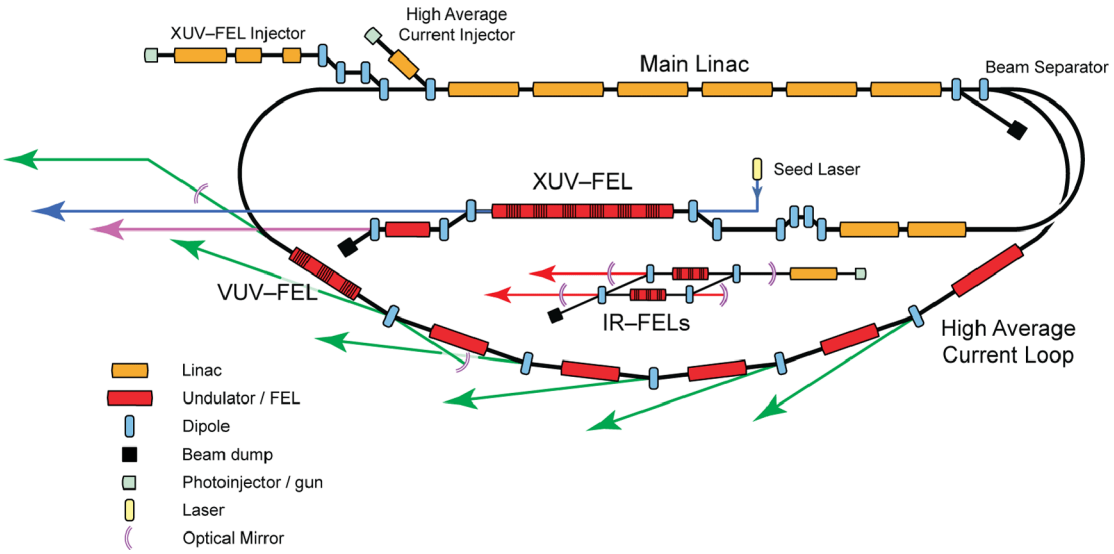

Figure 3.1 Layout of the 4GLS facility

The provision of high intensity electron beams has been revolutionised in the last decade by the successful development of a new variant of accelerator: the Energy Recovery Linac (ERL). Traditionally beam currents in linear accelerators can have high instantaneous values but are restricted to pulses with low repetition rates because the average power dissipation must be kept to manageable levels. For a light source high average flux emission is highly desirable and this output has been possible so far only by the widespread application of the electron storage ring (e.g. Diamond and other 3rd generation sources) that achieves average currents of hundreds of milliamperes by recirculating the same electrons many times (and for many hours). This solution has serious drawbacks, in particular the ring defines the beam properties and they are dominated by the very emission of synchrotron radiation that the ring is built to deliver. If long-term storage of the electron beam can be avoided then greatly superior properties can be provided and this is one of the principal features of the ERL.

The ERL delivers high average currents without beam storage, since electrons are injected, accelerated and circulated only once before the system recovers their energy, dumps them and replaces them with new electrons. This means that if the beam is injected with superior brightness properties it maintains these during its radiation emission phase. The 4GLS project has an ERL at its heart in a generational leap from storage ring sources. Globally, pioneering work on ERLs has been undertaken at the Jefferson Laboratory in the USA where a low energy proof-of-principle ERL has been successfully demonstrated.

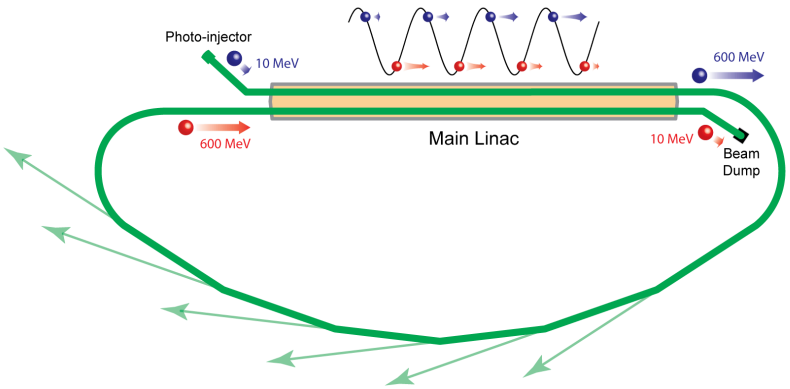

Figure 3.2 Schematic representation of an ERL. Injected electron bunches (blue) are accelerated by the RF field to an energy of 600 MeV. Having passed round the electron transport loop, the returning electrons (red) enter the linac 180° out of phase and give up their energy to the SC cavity and are decelerated to 10 MeV.

The reason why an ERL is now the accelerator of choice is that it has exploited the single greatest advance in modern accelerator technology: the superconducting RF system. Just as earlier developments in superconducting magnets allowed major advances to follow, the more recent, but equivalent, RF solutions are now a central feature of almost all of the leading world accelerator based facilities. Examples include the LHC at CERN, the SNS at Oak Ridge and the new light sources SOLEIL and Diamond that are close to operations. This technology, which is new to the UK, has been incorporated into the ERL Prototype (ERLP) project that is now under construction at Daresbury Laboratory. However the decision to base 4GLS solutions from this technology area on existing development programmes overseas, supported by strong associated collaborations that have been put into place, has already allowed major progress on design refinements to be made.

3.1.1 Linear Accelerators

4GLS is best thought of in terms of three inter-related accelerator systems. The first is the high average current loop (see Figure 3.3).

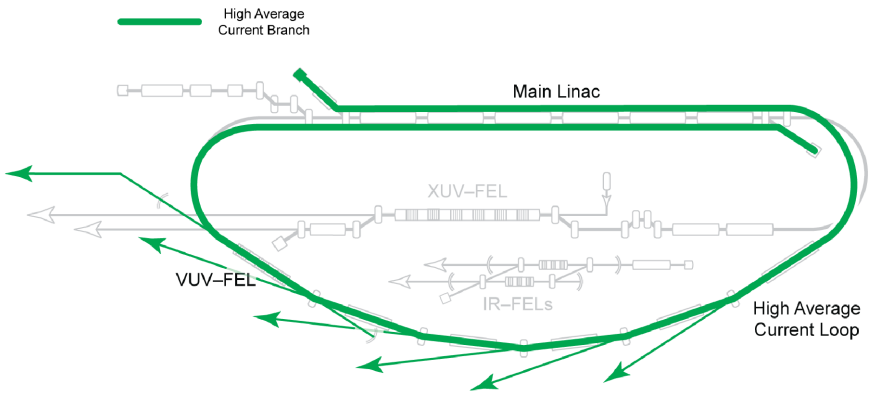

Figure 3.3 The high average current loop of 4GLS

In this a 600 MeV beam of 77 pC bunches is delivered at repetition rates of up to 1.3 GHz and energy recovery is an essential element. Progressive compression of the electron bunches in this loop allows for photon pulse lengths from a few ps to approximately 100 fs (RMS). The VUV-FEL is placed towards the end of the high-average current loop.

The second major accelerator system is the XUV-FEL branch (Figure 3.4). The XUV-FEL requires a peak current of ~ 1.5 kA at beam energies from 750 to 950 MeV. This beam is derived from 1 nC bunches produced by a normal conducting RF photo injector operating at 1 kHz. At this repetition rate the 1 kW of beam can be safely dumped after traversing a final spontaneous undulator source.

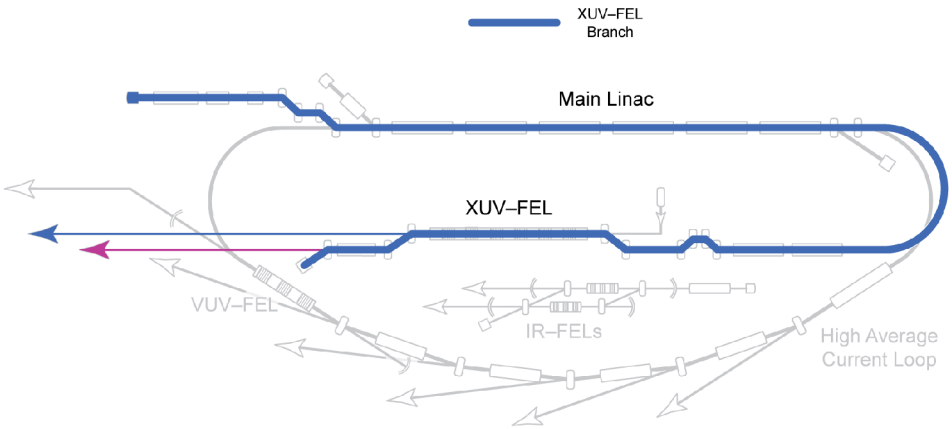

Figure 3.4 The XUV-FEL branch of 4GLS

Although the XUV-FEL beam and the high average-current beam discussed above are derived from separate electron sources after suitable low energy acceleration they are merged and accelerated in a single superconducting linac. The two beams are then separated using magnetic, energy separation for delivery to their respective devices.

The third accelerator system is that required for the IR-FEL (Figure 3.5). The same linac technology is used to accelerate electrons to between 25 and 60 MeV to provide a fully integrated and synchronised IR-FEL facility.

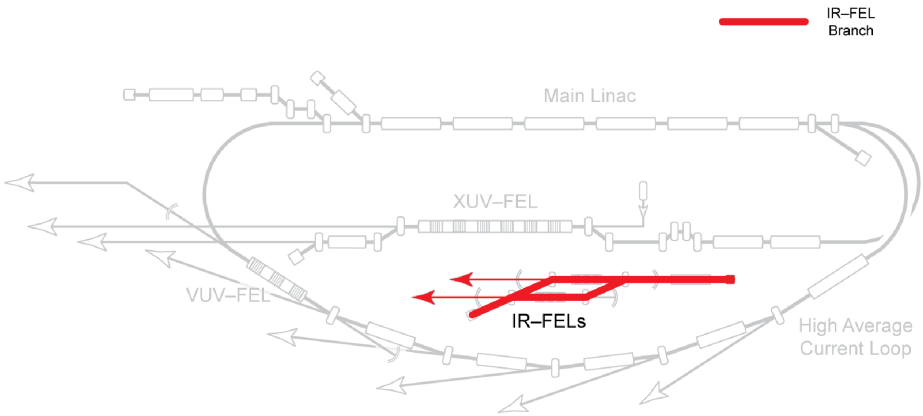

Figure 3.5 The IR FEL accelerator branch of 4GLS

The 4GLS design utilises superconducting linacs to accelerate and manipulate the three beams required to drive the photon sources. The accelerating structures are all based on a fundamental RF frequency of 1.3 GHz and a modified TESLA type cavity design operating at 2 K or below. The chosen RF frequency takes advantage of extensive development and operating experience of such systems (including the fact that industrialisation of the production and processing of such cavities is already well underway in preparation for the international linear collider ILC and superconducting XFEL).

Importantly the 4GLS design team at Daresbury are currently close to completing construction of an energy recovery prototype, ERLP, based on commercially procured Stanford modules incorporating TESLA 9-cell cavities which will provide a valuable test bed for the critical cavity and module developments required to produce linacs capable of operating in CW mode with the high-average beam currents.

For the high average current injector linac the major challenge is the delivery of the beam power required to accelerate a beam of up to 100 mA to 10 MeV without energy recovery. A cavity and coupler scheme similar to the two-cell geometry with symmetric couplers currently being developed at Cornell for the Cornell ERL prototype will be adopted for 4GLS. Two modules consisting of five of these two-cell cavities will suffice to provide the requirements of the ~ 10 MeV high average current injector system.

The main linac will be made up of six cryomodules each containing eight, seven-cell cavities which are currently under development within an international collaboration that includes CCLRC. This development is designed to meet the extreme demands of CW high-average current operation. The choice of six accelerating modules for the main linac is a balance between

capital and operating costs which also provides a reasonable overhead in accelerating voltage. Another five similar accelerating modules are required within the accelerator system, two within the XUX-FEL injector system, two for the XUV-FEL linac to take this beam from 750 MeV to 950 MeV and one to give the 60 MeV requirement for the IR-FEL. Development and verification of this challenging module design will be a major activity during the technical design phase of 4GLS and is envisaged that prototype testing of such a module could be carried out at Daresbury on the ERLP.

3.1.2 Injectors

For linac-based light sources the injectors are an essential element in the delivery of high performance, high quality beams. The requirements for the three injectors proposed for 4GLS come directly from the challenging demands of the FEL and spontaneous sources. Unlike storage rings light sources where the beam properties are essentially decoupled from the properties of the injector beam, the performance of ERL-based sources are directly dependent on the quality of the electron beam as produced by the injector and preserved during transport and acceleration.

The IR-FEL of 4GLS makes relatively modest demands of the injector and the source envisaged requires 200 pC, 1ps electron bunches with a normalised emittance of around 10 mm mrad. This can be delivered in a cost-effective and reliable way by mature thermionic gun technology. In contrast, the proposed injectors for both the high-average current loop and the high brightness XUV-FEL branch are based on developments of existing injectors.

The XUV-FEL injector source is required to deliver 1.5 kA peak current at 1 kHz repetition rate, the normalised emittance required to drive the device is ca. 2 mm mrad. Normal conducting RF photoinjectors today already exceed these bunch charge and emittance requirements and are a proven mature technology but they are typically low duty-cycle systems operating at a few Hz and require development to meet the 4GLS target repetition rate. Development of the Pitz gun is already underway that would increase the demonstrated 0.9 % duty cycle to 2.5 %, a slightly higher duty cycle than that required for 1 kHz operation of the XUV-FEL. Simulations using well developed particle codes have shown that a normalised emittance of 1.7 mm mrads can still be delivered whilst using relatively modest accelerating gradients, producing acceptable thermal loads in a gun engineered to supply additional cooling. This design is an effective starting point for the technical design of the XUV-FEL gun-cavity.

The photoinjector chosen for the high average current loop is required to deliver an unprecedented 100 mA beam with an emittance of 2 mm mrad. With such a high current demand an optimal choice of cathode material is a high quantum efficiency semiconductor which limits the laser power required to reasonable levels. From the experience of the TJNAF DC photo-injector, that has been utilised on the ERLP photo-injector, caesiated gallium arsenide may provide a suitable option for the cathode material. To meet the 4GLS requirements this gun will be driven by a simple stable 160 W, Yb-doped fibre laser operating at 1.3 GHz. Whilst the TJNAF DC and ERLP photo-injector are already designed to achieve the 77 pC bunch current,

the emittance of these guns is limited to around 5 - 10 mm mrads and the maximum, average current achieved at JLAB is only 25 mA. Further development is clearly required to meet the requirements of 4GLS and verification of such performance goes beyond scope and capability of the current ERLP. Evolving from TJNAF DC photoinjector developments, Cornell University is currently building a prototype injector which will produce a 100 mA beam of 77pC bunches. Extensive simulations of this gun based on the use of particle tracking codes predict that the emittance requirements for 4GLS would be fully met by this design.

3.1.3 Diagnostics and Synchronisation

A comprehensive diagnostic system will form a crucial part of 4GLS, with precise beam control and tuning being a high priority necessitating advanced feedback systems. Measuring such high brightness beam dimensions will require specialised developments. A conceptual overview of the major aspects of the diagnostic systems is outlined in this document and R&D programmes are in place to tackle particularly demanding systems such as the realisation of an electro-optical longitudinal profile measurement system. The design of the technical systems within this area will progress throughout the next design phase of 4GLS and the ERLP will be used where appropriate for prototyping testing and evaluation.

3.1.4 Beam Dynamics

The most challenging area of accelerator design for 4GLS is in meeting the requirements of extremely high peak current, (1.5 kA) for the XUV-FEL branch whilst simultaneously transporting and accelerating very high quality high-average current (100 mA) beam to the energy recovery loop. The conceptual solutions to the dynamics challenges for delivering the two most challenging beams are discussed below.

These two beams originate from separate photo-injectors, a high brightness RF photoinjector operating at 1 kHz delivering 2 mm mrad normalised emittance, 1 nC bunches for the XUV-FEL and a low emittance 100 mA, normal conducting DC injector. At relatively low injector energies these high quality beams are susceptible to intense space charge effects. Within the RF gun, the 1 nC beam undergoes rapid acceleration to a few MeV and is then injected into a superconducting linac which quickly boosts the energy to 220 MeV. Rapid acceleration of the 100 mA beam is achieved through the use of a high DC voltage, of around 1 MV followed closely by two superconducting booster modules delivering the ~1 MW power required to accelerate the beam to around 10 MeV.

The bunches within both of these beams have to undergo a significant amount of compression to deliver the required peak currents to drive the XUV- and VUV-FELs and to meet the requirements of the science case for different pulse lengths from undulators in the high-average current loop. An innovative, integrated acceleration and compression scheme is proposed which meets the unique requirements for each of the two beams whilst using the same main superconducting accelerator. By defining appropriate accelerating phases within the linacs, the high compression demands of the XUV-FEL are met using a two-stage compression scheme

including a higher harmonic RF system for flexible non-linear correction, whilst progressive compression through the undulator arc delivers the high peak current in the 77pC bunches required to drive the VUV-FEL. An important part of this design is the optimisation of the scheme to maintain a high quality beam throughout the transport. Wakefield effects in the accelerator are reduced by performing the final compression stage at full energy so that the bunches around the arcs are kept relatively long to control the disruptive effects of coherent synchrotron radiation (CSR) emission which if uncontrolled can produce unacceptable energy loss and emittance growth. Acceleration of a 100 mA beam is very challenging; to accelerate and decelerate such a beam requires that the linac transport design is tailored to give a high threshold for the disruptive beam break-up instability. This is achieved through a combination of techniques including substantial damping of HOMs in an advanced design of RF cavity, tight control of beam focussing throughout the linac and optimisation of coupling and overall transport properties in the energy recovery loop.

For the 4GLS XUV- and VUV-FELs, very high peak current is demanded simultaneously with narrow magnet gaps. These high peak currents are vulnerable to disruption by associated strong wakefields in nearby metallic chamber walls. This wakefield interaction and its undesirable consequences will be controlled through the use of appropriate vacuum materials and an optimisation of the FEL design which maintains vessel apertures that are compatible with delivering the required high quality beam.

3.2 The Photon Sources

3.2.1 Free Electron Lasers

Free electron lasers (FELs) are a maturing development that give huge performance gains on existing, more traditional light sources and there are now many such projects world-wide, ranging from successful infra-red user facilities to adventurous future X-ray ones (LCLS in USA and XFEL in Europe). The characteristics of 4GLS and its central ERL will be optimally exploited by the inclusion of three FELs, each covering a distinct photon energy range matched to the science needs of the UK and each offering unprecedented performance levels. The three designs are all state-of-the-art with key advantages over other designs being proposed elsewhere.

A simple yet robust seeded design for the **XUV-FEL** is proposed to ensure that ultra-high quality, reproducible, tunable radiation is available in the 8 to 100 eV photon range. The output pulses will have selectable polarisation and a pulse repetition rate of 1 kHz is set by the seed laser and the electron beam. Established FEL theory and state-of-the-art simulation codes predict this FEL will generate photon energies at multi giga-watt power levels in pulses of duration 40 - 60 fs FWHM. The pulses will have excellent temporal and spatial coherence with time-bandwidth products close to the Fourier transform limit for a Gaussian pulse. Unlike the self amplified spontaneous emission mode of operation, which effectively self-starts from intrinsic noise, the FEL interaction here is acting as a true amplifier. The high quality spectral properties of the

radiation input seed pulses are maintained by the amplified output radiation pulses. Recent advances in the High Harmonic Generation seed sources mean that the seed requirements for the XUV-FEL already exist and clearly future advances in conventional lasers can be readily harnessed.

The 4GLS design also incorporates an undulator after the XUV-FEL which enables the generation of spontaneous SR light with natural synchronisation to the XUV-FEL radiation.

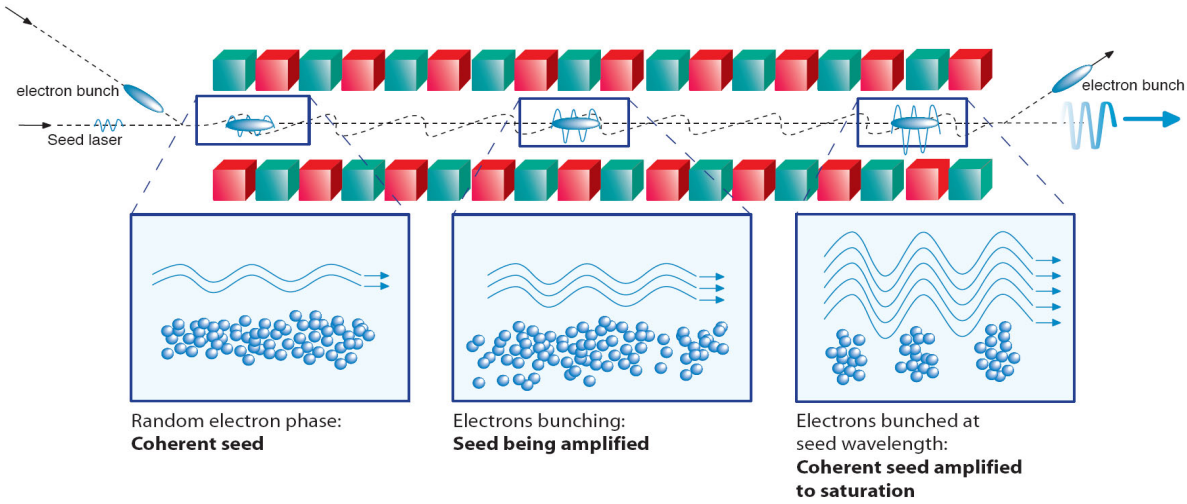

Figure 3.6 A seeded single pass FEL

The **VUV-FEL** offers high repetition rates (multiples of 4.33 MHz) with giga-watt peak power and > 100 W average power. Here advantage is taken of mirrors (with hole out-coupling) that are able to operate over the photon energy range of 3 to 10 eV (see Figure 3.7). Photon pulse lengths of ~ 170 fs (FWHM) will be obtained in standard mode and simulations suggest that pulses as short as ~ 25 fs will be generated in a super-radiant mode. The output pulses will have selectable polarisation and be fully tunable.

By using a pair of mirrors to reflect light emitted by the FEL back to the entrance of the device it becomes, in effect, self-seeding and no external conventional laser system is required. Hence high quality, stable light is ensured through a rather simple optical feedback loop. A particular feature of this FEL when compared with similar designs covering the same wavelength range is the tolerance to low mirror reflectivity. Extensive simulations have shown that mirror reflectivities in the range 40 to 60 % are acceptable for this design.

Detailed modelling has been used to confirm excellent spatial and temporal coherence and a regime has been identified where the performance of the device is relatively insensitive to (and can even be enhanced by) degradation of mirror reflectivity.

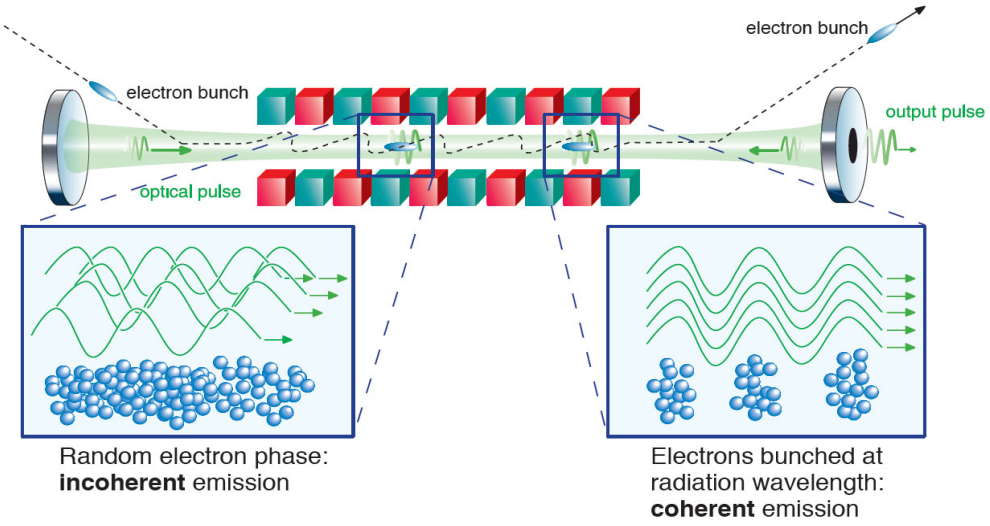

Figure 3.7 A low-Q cavity FEL with hole output coupling

The **IR-FEL** has been designed to produce high intensity, spatially and temporally coherent radiation with variable pulse lengths, flexible output pulse patterns and variable polarisation over the wavelength range 2.5 - 200 μm. The high-Q cavity-based (see Figure 3.8) design employs two undulators and hence offers the potential to satisfy user experiments at two different wavelengths simultaneously. The provision of short electron bunches offers the potential to operate the FEL in super-radiant mode to produce shorter FEL pulses with higher peak intensities than available in normal operation: simulations predict FWHM pulse lengths of only a few optical cycles can be produced in this way. The implementation of a superconducting RF linac with the IR-FEL will offer highly stable operation and also high average powers (> 100 W) though the option of running in modes that reduce the average power for sensitive samples will also be available.

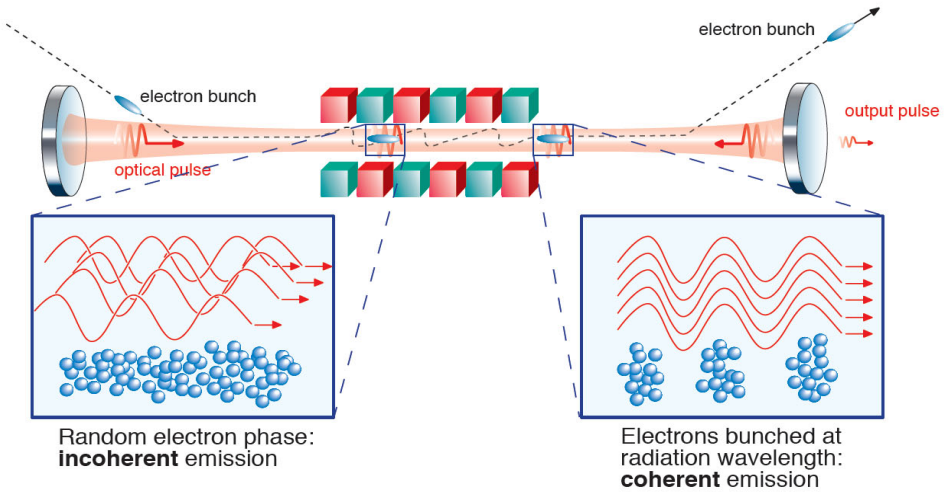

Figure 3.8 A high-Q cavity FEL with transmissive outcoupling

3.2.2 Spontaneous sources

There are six insertion device straights in the high average current loop, one of which is allocated to the VUV-FEL. The remaining five will be used to generate spontaneous radiation. To maximise the potential of the spontaneous sources three different undulator straight lengths have been chosen; two 14 m straights; two 10 m straights and two 8 m straights. Thus the total space available for undulators is ~ 64 m, which exceeds all other existing low energy 3rd generation light sources. More than one insertion device can be placed in each straight with a small corrector magnet between them so as to angularly separate the photon output. Distributed pulse compression will be employed in the high average current loop in order to deliver to users pulse lengths optimised for their experiments ranging from a few ps down to 100 fs (RMS).

Two representative undulators for 4GLS, with 30 and 60 mm period, have been selected for illustrative purposes in Figure 3.9 to Figure 3.14. The peak photon source levels are enhanced by the very short electron bunch lengths that are generated. They are typically a factor of ~ 100 shorter than in 3rd generation light sources such as Diamond and Max III.

It is well known that electrons in a bunch radiate coherently (with a photon intensity proportional to the square of the number of electrons per bunch) at wavelengths of the order of, and longer than, the bunch length. Since 4GLS has very short bunch lengths this so-called Coherent Synchrotron Radiation (CSR) is emitted over a broad wavelength range. Calculations indicate that the onset of the CSR for 4GLS is at around 40 μm and hence it will be an extremely intense source THz radiation.

3.2.3 Summary of 4GLS photon source outputs

Figure 3.9 to Figure 3.14 and Table 3.1 summarise the photon source output of 4GLS in comparison with other planned or operational world sources.

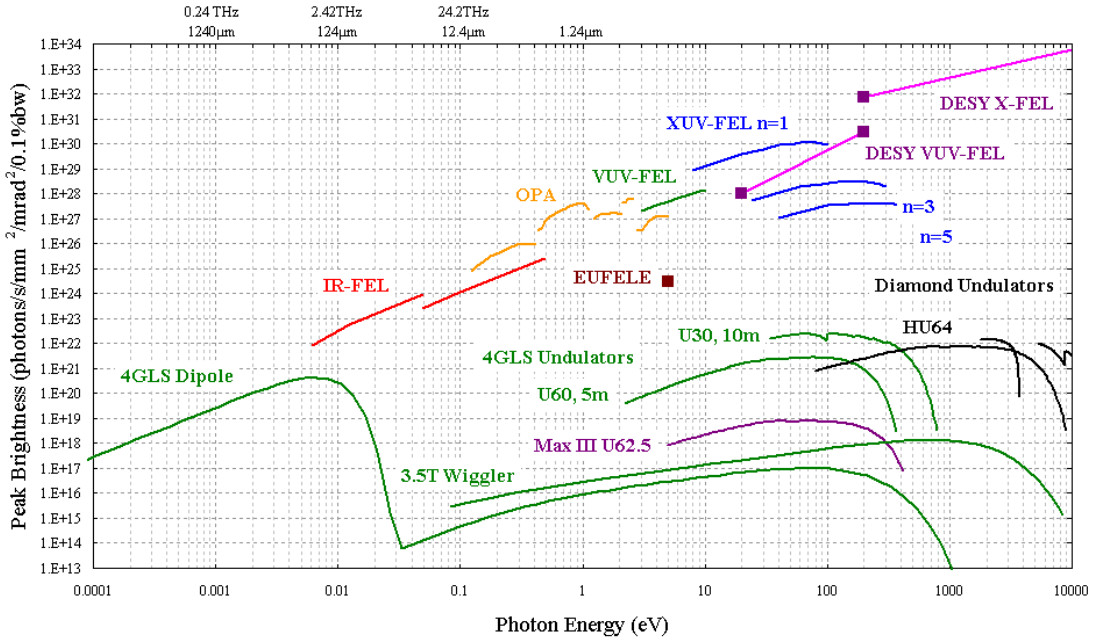

Figure 3.9 Peak brightness for 4GLS FELs, undulators, wiggler, OPA and dipoles compared with EUFELE, X-FEL, Diamond and Max III undulators

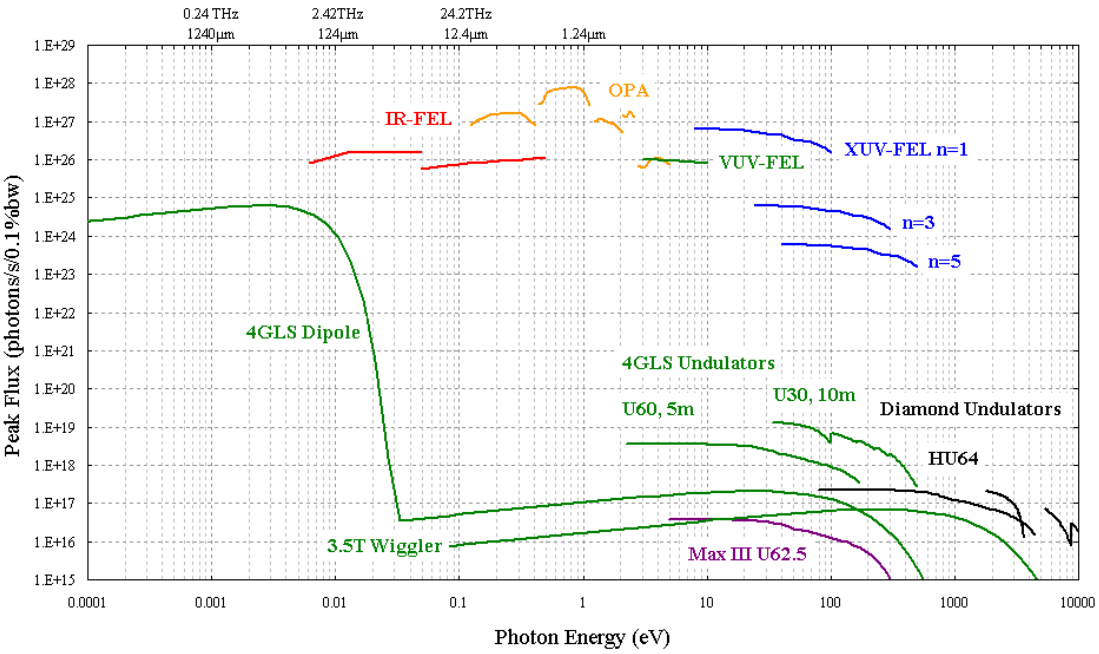

Figure 3.10 Peak flux for 4GLS FELs, undulators, wiggler, OPA and dipoles compared with Diamond and Max III undulators

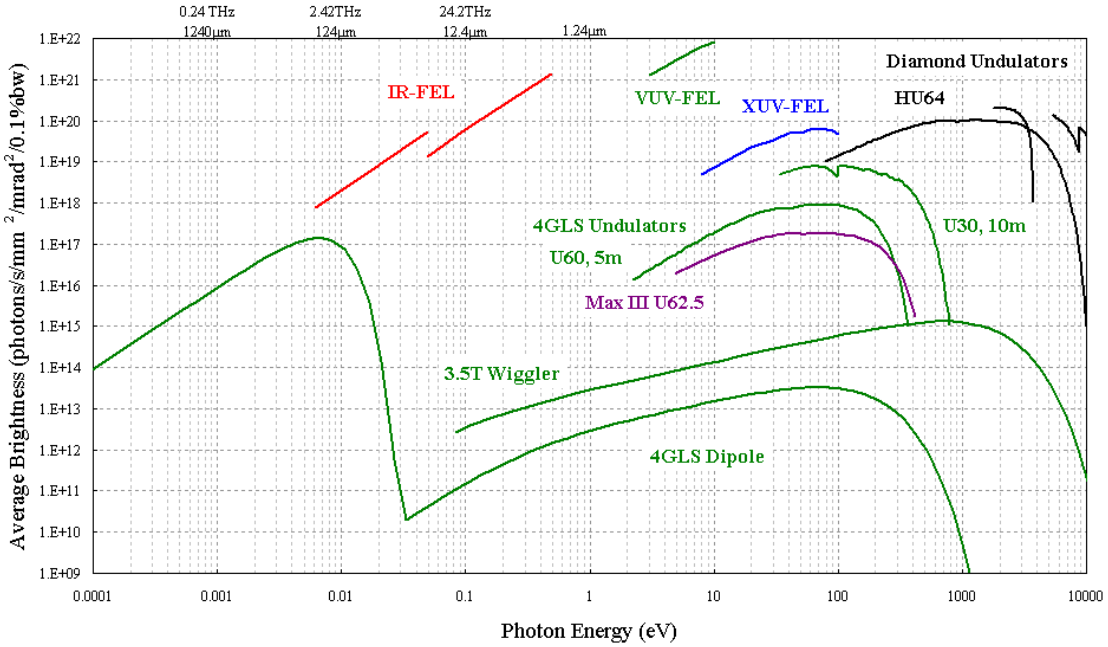

Figure 3.11 Average brightness for 4GLS FELs, undulators, wiggler and dipoles compared with Diamond and MaxIII undulators

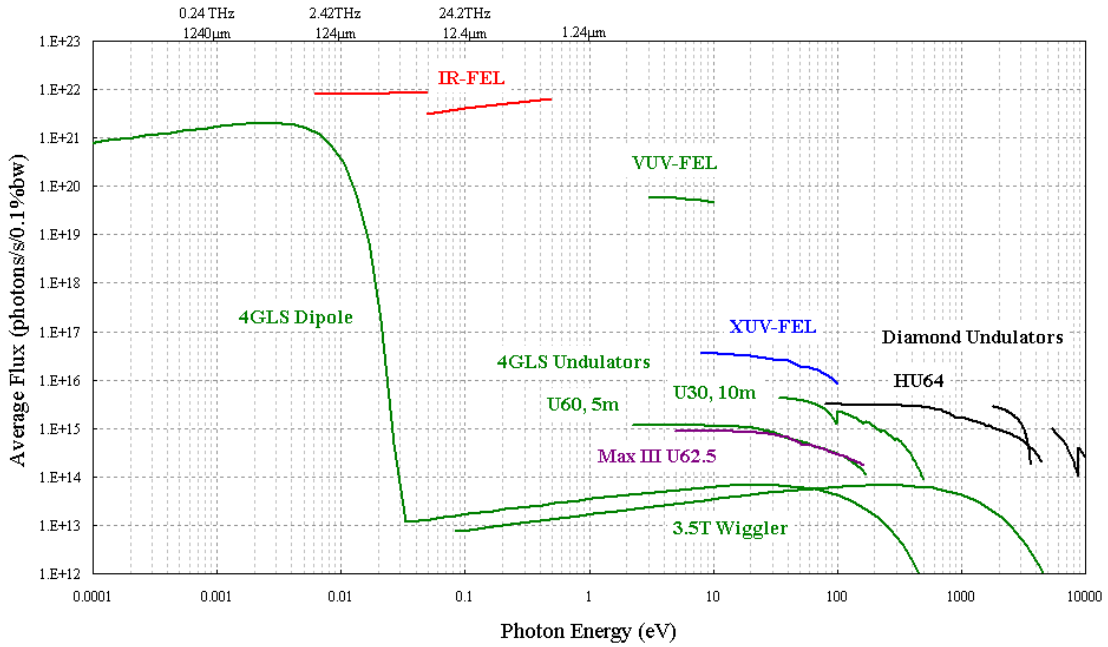

Figure 3.12 Average flux for 4GLS FELs, undulators, wiggler and dipoles compared with Diamond and MaxIII undulators

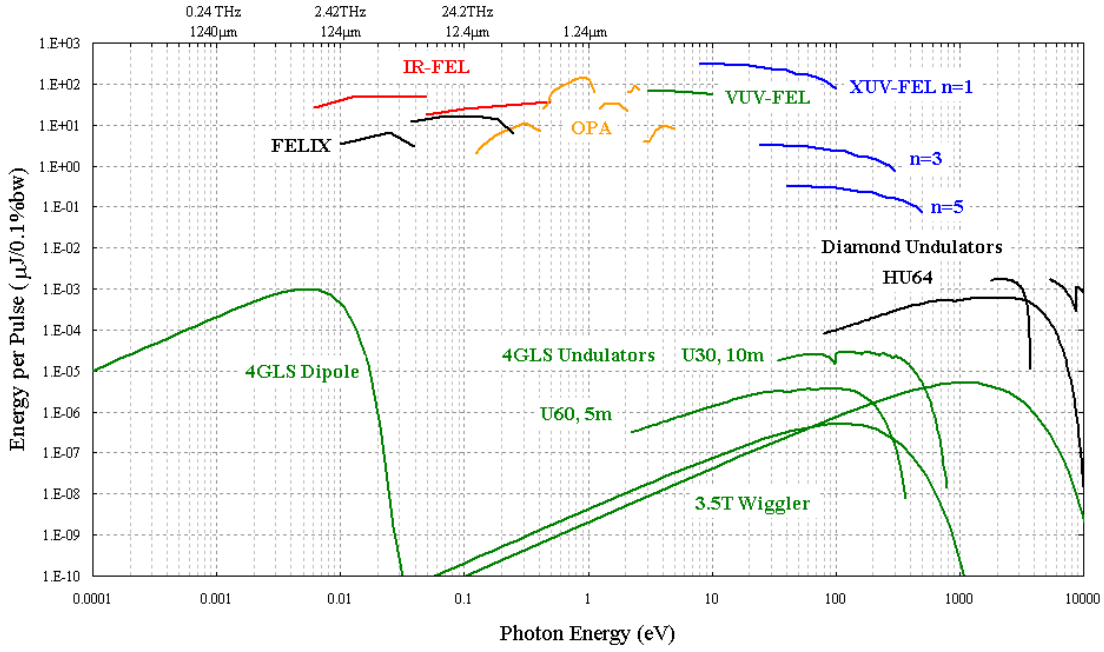

Figure 3.13 Energy per pulse for 4GLS FELs, undulators, wiggler, OPA and dipoles compared with Diamond undulator

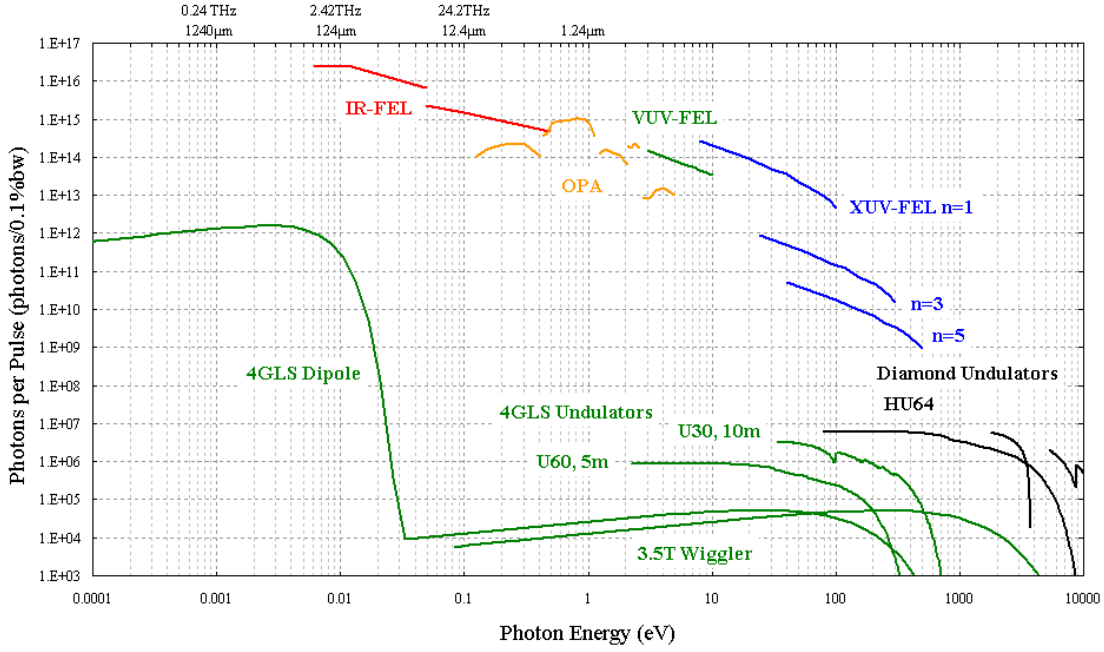

Figure 3.14 Photons per pulse for 4GLS FELs, undulators, wiggler, OPA and dipoles compared with Diamond undulator

Table 3.1 Summary of the photon output from the various sources of 4GLS.

	XUV-FEL	*VUV-FEL*	*IR-FEL*	*U30*	*U60*	*Dipole CSR (HACL)*	*Wiggler*	*OPA Laser*
Harmonic	1	1	1	1 to 9	1 to 9	—	—	—
Photon Energy Range (eV)	8 to 100	3 to 10	0.006 to 0.5	33 to 600	2 to 300	0.0001 to 0.03	1 to 5000	0.1 to 6
Wavelength Range (μm)	0.15 to 0.012	0.4 to 0.12	2.5 to 200	0.04 to 0.002	0.6 to 0.004	10000 to 40	1 to 0.0002	11 to 0.2
Repetition Rate	1 kHz	n x 4.33 MHz	13 MHz	1.3 GHz	1.3 GHz	1.3 GHz	1.3 GHz	1 kHz
FWHM Photon Pulse Length (fs)	50	170	2000 to 10000	300 to 2000	300 to 2000	235	500 to 2000	130
Peak Flux (/s/0.1%)	~5 x10^{26}	~1 x10^{26}	~1 x10^{26}	~1 x10^{19}	~3 x10^{18}	~6 x10^{24}	~6 x10^{16}	~1 x10^{27}
Peak Brightness (/s/mm^2/mrad^2/0.1%)	~1 x10^{30}	~1 x10^{28}	~1 x10^{22} to ~2 x10^{25}	~2 x10^{22}	~2 x10^{21}	~1 x10^{20}	~5 x10^{17}	~1 x10^{27}
Energy per Pulse (μJ/0.1%)	~200	~60	~40	~3 x10^{-5}	~3 x10^{-6}	~1 x10^{-4}	~1 x10^{-6}	~30
Photons per Pulse (/0.1%)	~5 x10^{13}	~1 x10^{14}	~6 x10^{14} to ~2 x10^{16}	~2 x10^{6}	~1 x10^{6}	~1 x10^{12}	~4 x10^{4}	~1 x10^{14}
Average Flux (/s/0.1%)	~3 x10^{16}	~6 x10^{19}	~7 x10^{21}	~3 x10^{15}	~1 x10^{15}	~1 x10^{21}	~5 x10^{13}	~1 x10^{17}
Average Brightness (/s/mm^2/mrad^2/0.1%)	~5 x10^{19}	~5 x10^{21}	~8 x10^{17} to ~1 x10^{21}	~7 x10^{18}	~7 x10^{17}	~1 x10^{16}	~7 x10^{14}	~1 x10^{17}

3.2.4 Complementary tabletop laser facilities

In order to make full use of 4GLS it is important to allow integration of its sources with conventional lasers. Continuous coverage of the visible and near-IR parts of the spectrum is provided by the spontaneous sources as illustrated in Figure 3.9. However, there are currently no plans to provide FEL radiation in the spectral range from 0.5 – 3 eV, as this is covered more cost-effectively by tabletop laser systems. These wavelengths will be made available by using continuously tuneable mid-infrared laser systems, such as mid-infrared OPO (Optical Parametric Oscillators)/OPA {Optical Parametric Amplifier) systems, DFG (Difference Frequency Generators) and diode lasers. Ability to synchronise the additional lasers to within the temporal profile of the 4GLS sources is required. Current synchronisation is achievable to within < 100 fs, and is the subject of a vigorous worldwide research and development programme.

3.3 Summary

Overall, 4GLS has an extraordinarily flexible design that encompasses spontaneous SR and FEL sources that are cutting-edge in their own right and in combination give rise to world-leading capability. The underpinning electron beam technology is extremely challenging, but can be delivered by exploitation of the latest accelerator innovations. The 4GLS specification is unique in the world and will give the UK international leadership in this exciting new area of opportunities.

4. Combining Sources

4GLS has a unique capability to perform multi-photon-beam experiments combining FEL, spontaneous and laser sources into experiment stations. For the visible, IR and THz photon energy ranges, the photon beam can be relatively easily transported over long lengths with high angular deflections. In the UV, XUV and SXR energy ranges, the transport is more restricted, especially when polarisation preservation is considered. For the higher energy sources, multi-beam capability has been designed in from the conceptual stage. The relative positions in the layout of the free-electron lasers and several of the short-period undulators have been chosen to match the requirements of the science case. The specification of the photon beam transport system will include additional elements to enable multi-beam experiments; the precise requirements can be determined in line with the maturing science programme at a later stage, though illustrative worked examples are discussed in Chapter 10. In addition, the building provides sufficient space in the experiment hall to accommodate laser sources close to the experiment stations.

Table 4.1 Some 4GLS multi-beam combinations required to deliver the science programme

Multi-beam stations	*Science/technique area from Science Case*	*Possible 4GLS source combination*	*Same bunch*
XUV-FEL + VUV-FEL	Rydberg wavepacket spectroscopy PES from mass selected clusters	XUV- and VUV-FEL	no
XUV-FEL + XUV short pulse (10-200 eV 100 fs)	Pump-probe, multiply charged molecular ions	XUV-FEL + U30 spent beam undulator	yes
VUV-FEL + VUV short pulse (3-20 eV 100 fs)	Pump-probe, multiply charged molecular ions, free-radical spectroscopy, negative ions, neutrals	VUV-FEL in straight 6+ U60 in straight 4	yes
VUV-FEL and XUV short pulse (10-200 eV, 100 fs)	pump probe, multiply charged molecular ions, photoionisation detection of neutrals	VUV-FEL in straight 6 + U30 in straight 5, pulse-length preserving beamline	yes
VUV-FEL + IR-FEL	SFS, SFG, SFOA	IR-FEL light piped to VUV endstation	no
VUV-FEL + VUV/XUV long pulse (5-350 eV, picosecond)	photoemission, spin-polarised PES, 2PPE, PES of excited states, electron-hole pair dynamics	VUV-FEL in straight 6 + U30 in straight 5, high RP beamline	yes
VUV-FEL + IR (+THz)	RAIRS of ions produced by VUV-FEL - surface astrochemistry	IR light from bending magnet (BM) 5 piped to VUV endstation	yes
IR-FEL + IR/THz BM	pump-probe, bio pump-probe imaging	IR FEL light and IR/THz BM light piped to mezzanine station	yes
X-ray + IR/THz	pump-probe XAS combined XAS + IR	IR from FEL or BM, piped to multi-pole wiggler endstation	Yes (BM) No (FEL)

4.1 Multi-Beam Stations

The required source combinations have been deduced from analysis of the 4GLS Science Case [1] and presented in tables at the 4GLS User Meeting, July 2005 [2]. Table 4.1 shows some of the required multi-beam combinations with their scientific purpose and proposes specific 4GLS sources which fulfil that requirement as closely as possible. Where possible, combinations using adjacent sources are proposed as the light originates from the same electron bunch and their separation is minimised, both factors contributing to optimised synchronisation.

4.1.1 General Layout of Multi-Beam Photon Transport

The layout of the 4GLS facility has positioned the photon sources to enable optimum multi-beam performance and is shown schematically in Figure 4.1.

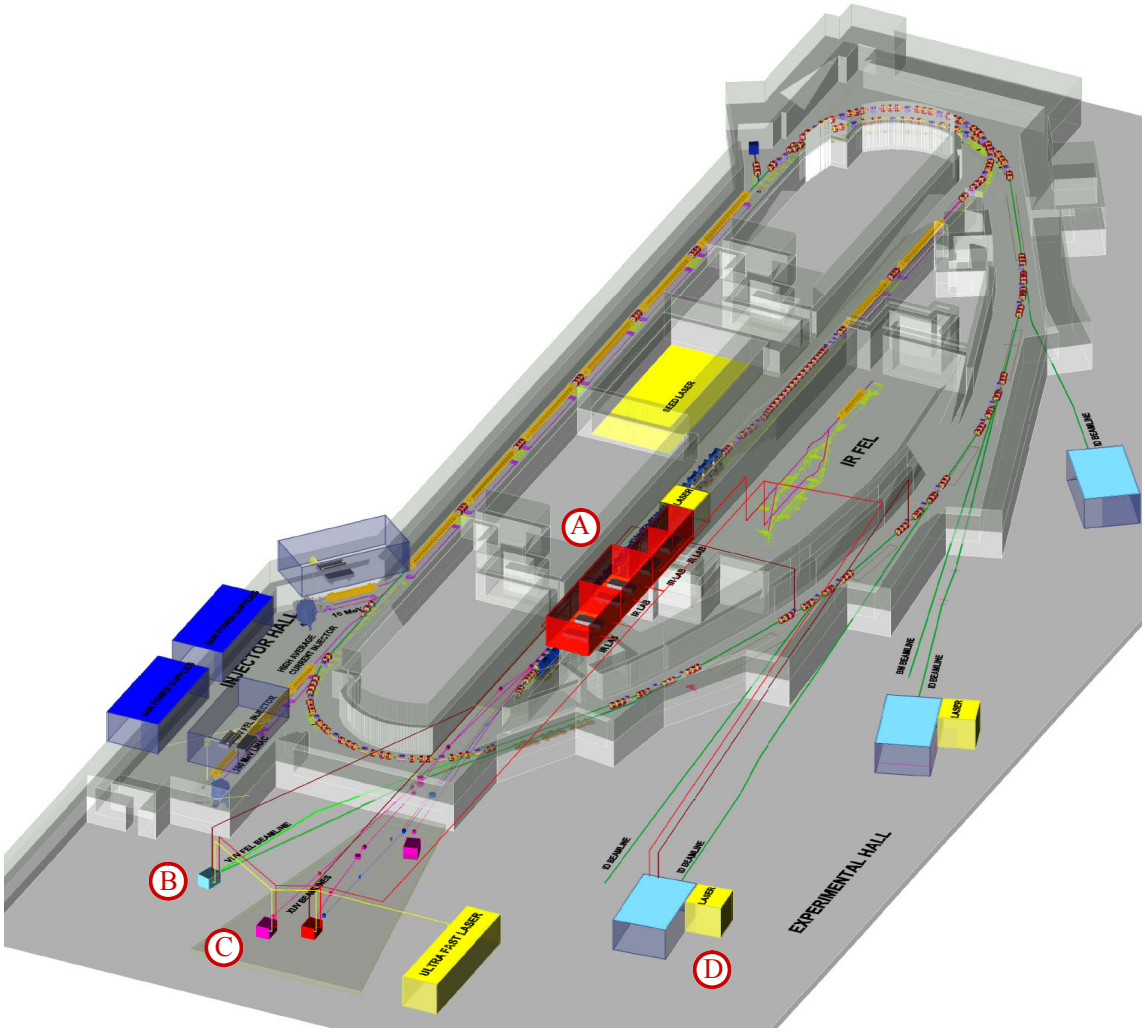

Figure 4.1 A three-dimensional conceptual view of 4GLS showing some of the multi-beam stations possible: A) the IR/THz/laser laboratories, B) the VUV-FEL experiment area, C) the XUV-FEL experiment area showing a worked example combined beam layout for the FEL and the spent beam undulator with a close-in direct beam station, D) a spontaneous beamline taking IR-FEL and THz light.

The key requirements are to enable appropriate combinations of sources, match the total electron and photon path-length for transport to multi-beam stations and allow space for optical delays, beamsplitting/recombining optics and microfocussing. As the facility overview describes in Chapter 3, there are several types of photon source in the facility:

- three FELs;
- five straights in the high average current loop and one in the XUV-FEL branch for insertion devices;
- many bending magnets capable of exploitation for IR to SXR and coherent THz output.

This results in very many possible beamline combinations, only some of which are illustrated in Figure 4.1. Specific beamline conceptual designs for the key combinations will be developed during the technical design phase in collaboration with potential users.

In Figure 4.1, the two key beamline pairs, XUV-FEL with the spent beam undulator and the VUV-FEL with ID beamline 5, have been shown with the VUV-FEL in straight 6 and the spent beam undulator on the straight 6 side of the XUV-FEL branch. As the XUV-FEL branch is ~ 60 cm above the high average current loop, these lines can cross over. The layout will also allow for independent use of all the beamline endstations.

It is clear from this scheme that the experimental area directly in front of the XUV-FEL will be densely packed with challenging optical systems. This area will be designed as a unit, including options for further developments as, once built, it will be very difficult to alter.

Once the layout for the higher energy FELs has been optimised, then the other 4GLS systems can be positioned. For optimised synchronisation, THz from the XUV-FEL branch is taken to the XUV-FEL branch stations. Likewise, THz lines from magnets in the high average current return arc and the IR-FEL system are taken to stations on the corresponding branches. These are transported at high level and will take advantage of the stability of the poured concrete shielding. This also allows ease of transport to several IR/THz/laser experiment laboratories on the mezzanine floor of the facility.

In addition to the normal endstation control space and preparation laboratories, the ground floor experiment area will accommodate synchronised laser systems, allowing space for future developments.

4.1.2 The XUV-FEL Multi-Beam Combinations

The best synchronisation and repetition rate matching with an undulator source is achieved by adding an insertion device between the exit of the XUV-FEL and the electron beam dump. The pulse length of the XUV-FEL photon beam is determined largely by the length of the HHG seed pulse; present simulations show this to be 50 fs FWHM. The electron beam determines the undulator photon beam pulse length and at this stage of the design optimisation this is 626 fs FWHM. Schemes to achieve better matched pulse lengths will be studied in the TDR phase.

This multi-beam system has been used as a worked example to study the underpinning optics design and technology required to combine ultra-fast XUV photon beams and is described in detail in §10.6.3.

For combination with THz, a bending magnet in a final compression stage will deliver high peak field at the XUV-FEL repetition rate due to the high bunch charge of 1 nC.

The IR-FEL light can be relatively easily transported to the XUV-FEL experiment station, though this is derived from a different electron bunch and may be affected by additional sources of temporal jitter.

Due to the twin-branch layout of 4GLS, it has been possible to position the XUV-FEL and VUV-FEL sources so that they can be brought together in a common endstation, though this is not shown on the figures. The detail of the photon transport path layout for the XUV-FEL is shown in Figure 4.2.

Combination with laser sources is also envisaged; space has been allowed in the experiment area layout for location of a laser up to the size of an ultra-fast system in close proximity to the XUV-FEL. The 4GLS synchronisation system will include the designed-in ability to link external lasers into the timing system (see Chapter 11). Exploitation of the XUV-FEL seed laser is also an option.

4.1.3 The VUV-FEL Multi-Beam Combinations

The VUV-FEL is located in the high average current loop and thus gives best synchronisation when used with other sources in this loop. The VUV-FEL is located in straight 6 before the return arc where the electron bunch length is shortest. This position allows combination with several undulator beamlines in adjacent straights.

For combination with THz or IR from the same electron transport branch, a bending magnet in the first cell of the return arc will deliver high average photon power with optimum synchronisation and a matched repetition rate. Again, the IR-FEL light can be relatively easily transported to any of the VUV-FEL multi-beam stations, though this is derived from a different electron bunch and may be affected by additional sources of temporal jitter.

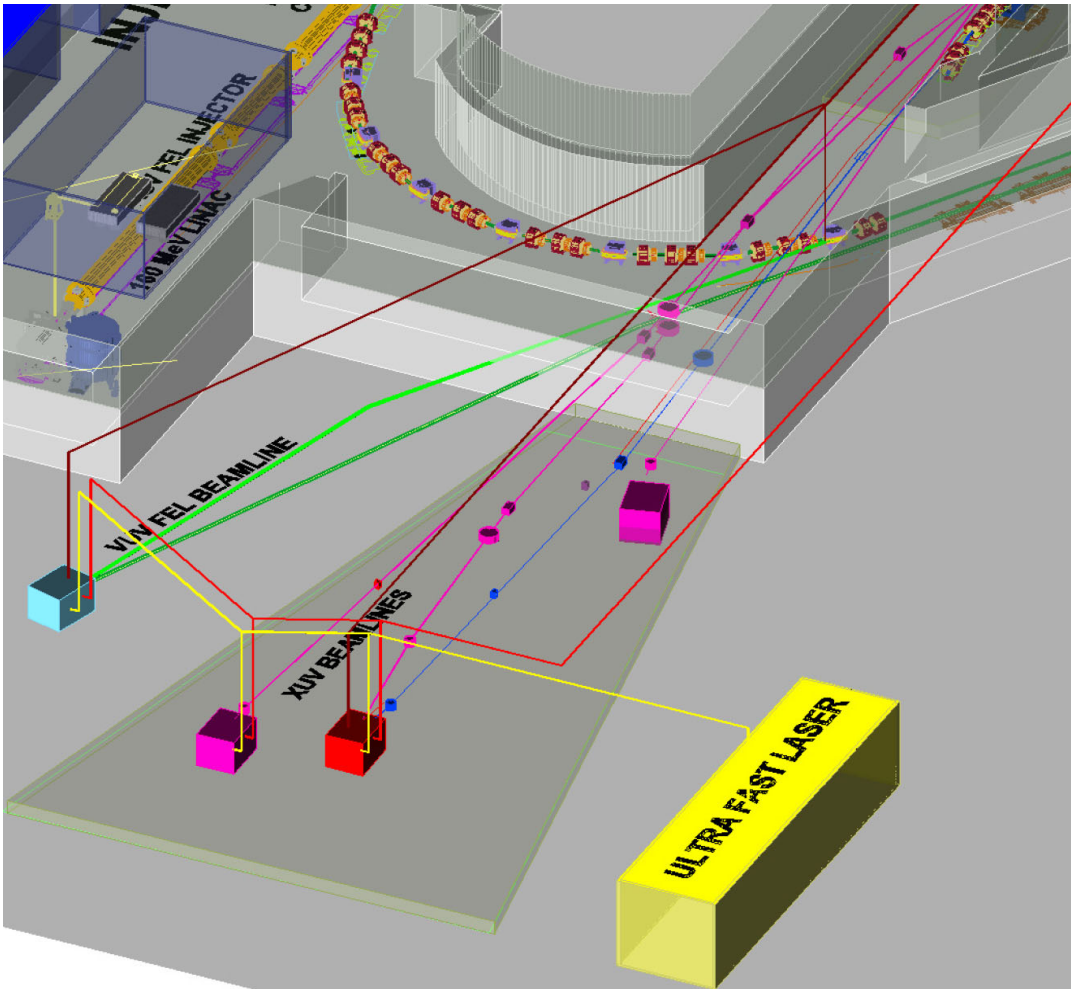

Figure 4.2 Detail of the schematic layout for the XUV-FEL and VUV-FEL experiment area showing the lines for the XUV-FEL beamlines (purple), the spent beam undulator (blue), the VUV-FEL (bright green), a line from an insertion device in straight 5 (dark green), IR-FEL light (red), THz from the XUV-FEL branch and from the high average current loop arc magnet (dark red-brown) and a laser (yellow). Combining the XUV-FEL and VUV-FEL output is envisaged but not shown on this scheme.

Combination with laser sources is also envisaged for the XUV-FEL, and space has been allowed in the experiment area layout for the location of a laser system in close proximity to the VUV-FEL. The detail of the photon transport path layout for the VUV-FEL is also shown in Figure 4.2. As stated above, the VUV-FEL and XUV-FEL outputs can also be combined, though for simplicity, this is not drawn in the figure.

4.1.4 The IR-FEL Multi-Beam Combinations

Taking advantage of the relative ease of transport of highly collimated IR light, the IR-FEL output will be piped to a series of experiment areas on the accelerator tunnel roof where it can be used together with conventional lasers and 4GLS bending magnet THz sources. In addition to combining with the XUV-FEL and VUV-FEL, the IR-FEL output can be transported to any station in the 4GLS facility (see Figure 4.3).

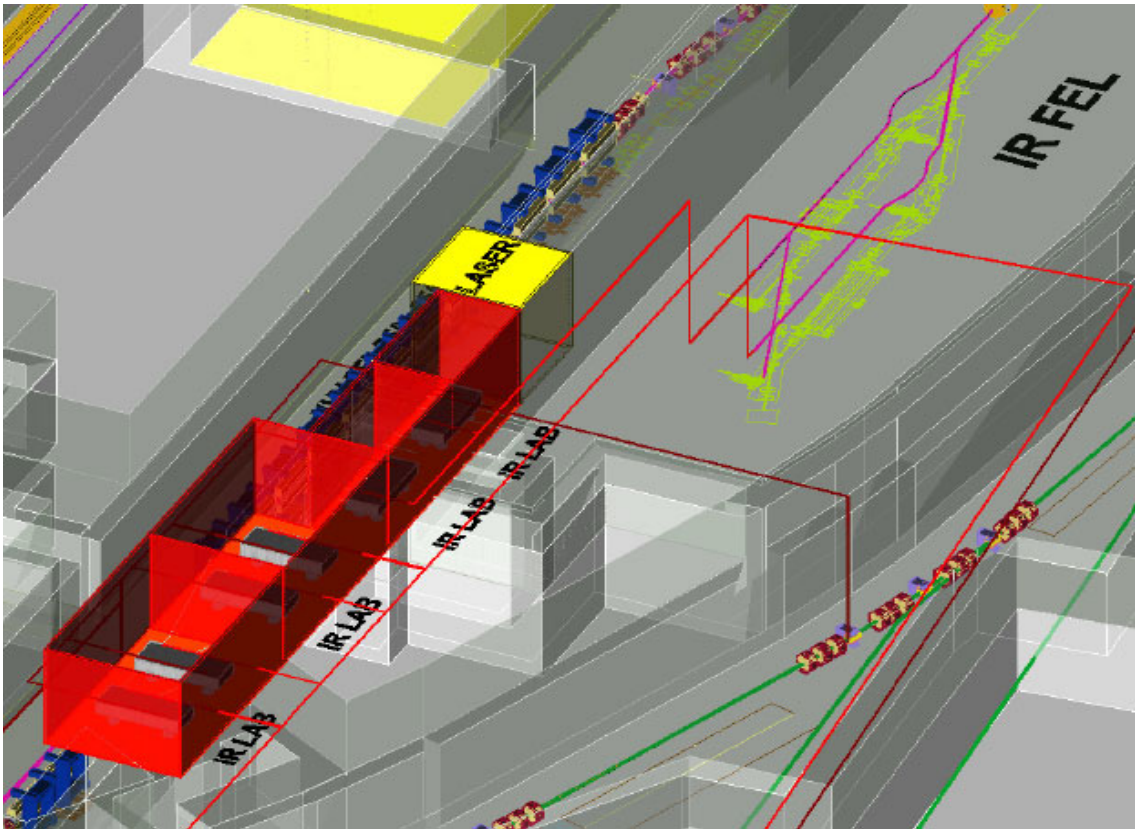

Figure 4.3 Illustrative layout of IR/THz/laser experiment laboratories on the mezzanine level on the accelerator roof. Note that the solid support structure necessary for stability is not shown on this diagram but will be part of the engineering of this system. The figure shows the lines for the IR-FEL radiation (red), THz radiation from a high average current loop bending magnet (dark red-brown) and a conventional laser room (yellow). THz radiation from an XUV-FEL branch bending magnet enters the IR laboratories on the left.

For combination with THz radiation with optimum synchronisation and minimum transport length, a bending magnet in the IR-FEL electron beam system would be best used. However, the wavelength range of coherent emission will depend on the electron bunch length; at this stage of the design of the IR-FEL branch, this is calculated to be 1-10 ps, giving coherent radiation only at frequencies below 0.5 THz. For full coverage of the THz region, use of the bending magnet sources on the XUV-FEL branch (high field) and high average current loop (high average power) is planned.

4.1.5 Spontaneous Source Combinations

The insertion device and bending magnet photon sources in the high average current loop can also be combined in an experiment endstation. This would allow undulator or wiggler radiation to be combined with IR or THz radiation from an adjacent bending magnet. The experiment area floor layout will also provide space for lasers in the endstation area (see Figure 4.4).

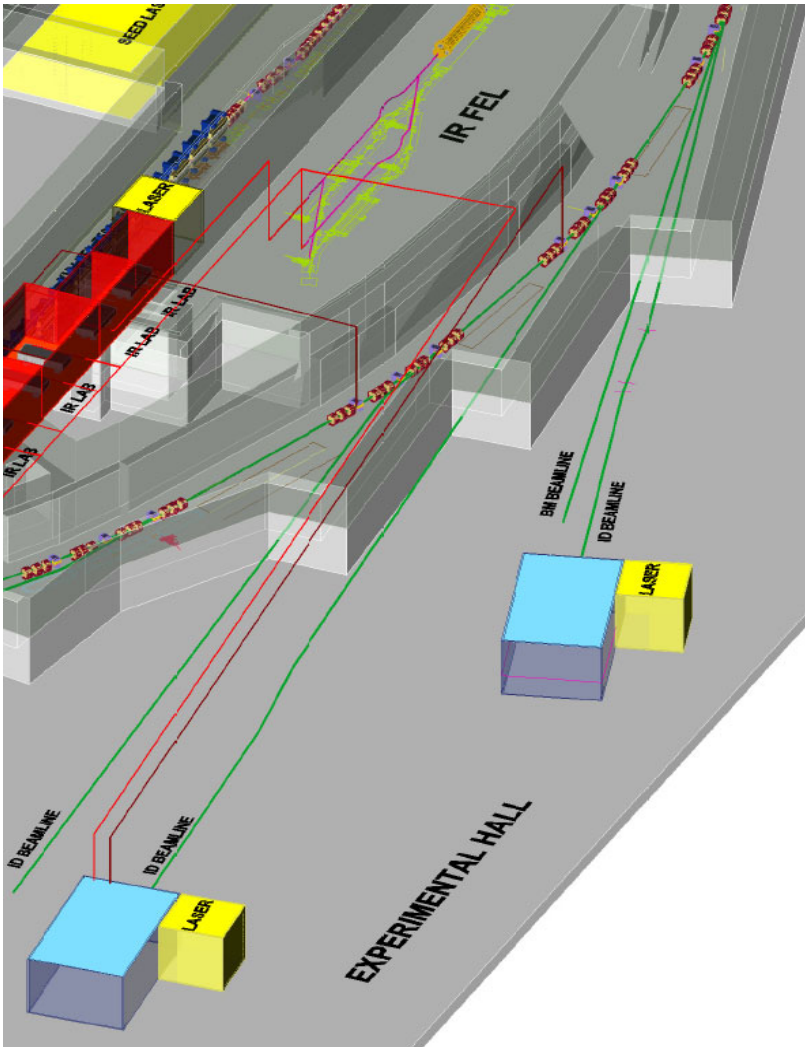

Figure 4.4 Illustrative layout of an experiment area taking light from straight 3 (green),the IR-FEL (red) and a THz bending magnet (dark red-brown) – undulator detail is not shown.

4.1.6 Beam Splitting and Recombining

A further type of multi-beam experiment is to split a single beam, delaying one branch with respect to the other to perform time-resolved experiments. This will be a core capability and is discussed further in §10.6.4.

4.1.7 Designing Optical Systems for Multi-Beam Experiments

Optical systems on storage ring sources of synchrotron radiation tend to lengths of 30 – 50 m with optic sizes of 0.5 – 1.0 m; they are therefore large and not readily reconfigured. Systems for conventional laboratory-based lasers generally occupy one or two optical tables with optic sizes of 25 – 100 mm; they are routinely reconfigured for the needs of individual experiments.

The 4GLS optical systems will merge these philosophies; some systems such those working in the XUV will be large, ~ 100 m, some such as the IR-FEL transport will resemble a laboratory system.

Combining the 4GLS sources into multi-beam stations requires design strategies from both storage ring designs and laboratory-based lasers. Primary components for monochromating the higher energy light sources will be of similar size to storage ring sources, while the components for combining the beams (optical delays, beam splitters) will be more familiar to laser users.

The major difference to both is that the multi-beam combinations must be designed as a whole, including the electron beam sources; this is especially important for the VUV-XUV systems.

The repetition rates proposed for the 4GLS sources (shown in Table 4.2) show that the path length travelled by light in the time between pulses is large enough to build photon transport systems which ensure that the pulses arriving at a multi-beam station derive from the same electron bunch. Time delay ranges for pump-probe up to 10 ns are also within the time window between pulses for repetition rates less than few tens MHz. The XUV-FEL pulse separation of 1 ms allows for pump-probe experiments with detection of slow ions.

Table 4.2 Repetition rates, and pulse separations for 4GLS branches.

Source	Repetition rate	Pulse separation	Equivalent path length
XUV-FEL branch	1 kHz	1 ms	300 km
VUV-FEL & spontaneous sources at low repetition rate	Few MHz	100's ns	10's m
IR-FEL branch	Few 10's MHz	10's ns	Few m
Spontaneous sources at maximum rate	1.3 GHz	100's ps	100's mm

4.2 Time Structure Capability of 4GLS Systems

A key aspect of combining the 4GLS sources is delivery of compatible repetition rates at the experiment.

The ERL concept allows considerable flexibility in the pulse patterns possible and the design of 4GLS is aimed at exploiting this to meet the science programme needs.

There are several contributions to the time structure of the photon pulses, described in Chapters 11 (Timing and Synchronisation), 5 (Injector Systems), 6 (Superconducting Linacs) and 10 (Photon Transport). In summary, these are:

- The RF frequency - the design frequency of 1.3 GHz determines the highest repetition rate. However, not every RF bucket has to be filled so lower rates are readily achievable, with periodic electron bunch patterns giving the optimum synchronisation capability. At low repetition rates, the energy recovery process starts to become inefficient and eventually fails because the RF cavities cannot store the RF power from the previous electron bunch indefinitely. At low enough repetition rates, ~ kilohertz, the electron beam can be dumped without recovery as the beam power is sufficiently low.

- The photo-injector laser system – while there are constraints, the laser system is capable of matching to the facility requirements and will not affect the available time structures.

- The XUV-FEL seed laser – the present design repetition rate is 1 kHz for the HHG seed laser system, with the aim to upgrade to 10 kHz as soon as feasible (see Chapter 12).

- The VUV-FEL and IR-FEL - The VUV-FEL and IR-FEL are based on cavities which store light emitted within the FEL undulator. These impose a fundamental repetition rate determined by the round trip time of the light between the two mirrors. This rate must be a sub-harmonic of the RF frequency so that the stored photon pulses overlap with the electron bunches passing through the cavity. The VUV-FEL cavity is 32 m long giving a fundamental repetition rate of 4.33 MHz. The IR-FEL cavity is designed to give a compatible repetition rate of 13 MHz, three times the VUV-FEL rate. This is the *minimum* output repetition rate of the light. If electron bunches pass through with greater repetition rates than this, then the repetition rate of the FEL will increase. The maximum practical repetition rate will be limited by the ability of the cavity mirrors to withstand the incident photon power density. The IR-FEL can operate with a macro-pulse structure and fast magnetic switching, which will operate at up to 100 Hz, will allow the electron beam to be switched between mid-IR and far-IR branches. The pattern of this switching will be determined on an operational basis dependent on user needs.

- Photon transport systems – the photon pulse repetition rate can be modified in the transport system by mechanical choppers, modulated optics or laser switches. These can

produce macro-pulse trains and the possibility of chopping the 4.33 MHz beam from the VUV-FEL will be assessed for the Technical Design Report (TDR).

The fundamental repetition rates for 4GLS resulting from these contributions are shown diagrammatically in Figure 4.5.

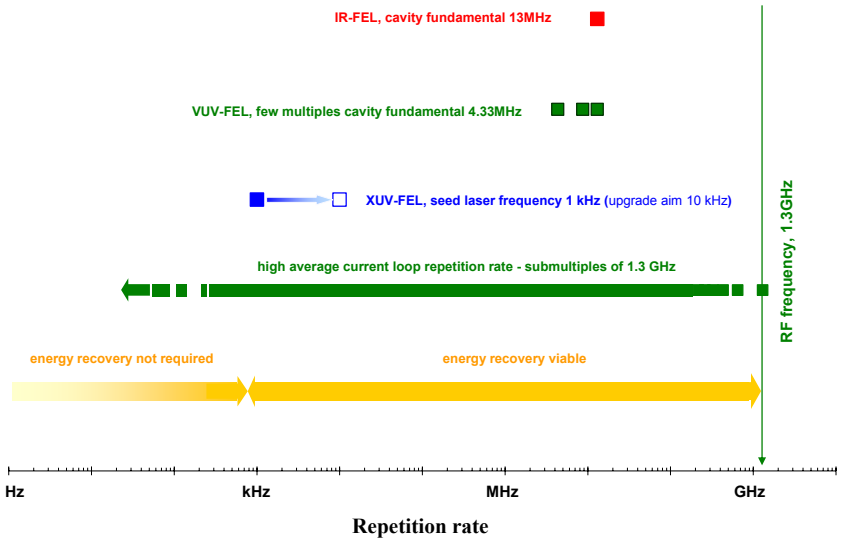

Figure 4.5 Summary of the fundamental repetition rates of the FEL and high average current loop sources. Note that delivered repetition rate at the experiment can be modified by chopping of the photon beams.

Hence, in 4GLS, there is considerable flexibility in choosing the bunch-to-bunch spacing inside the bunch train, the fundamental period of which is given by the 1.3 GHz RF i.e. 770 ps. Figure 4.6 illustrates operation of a continuous bunch train and options for experiments with particular timing requirements.

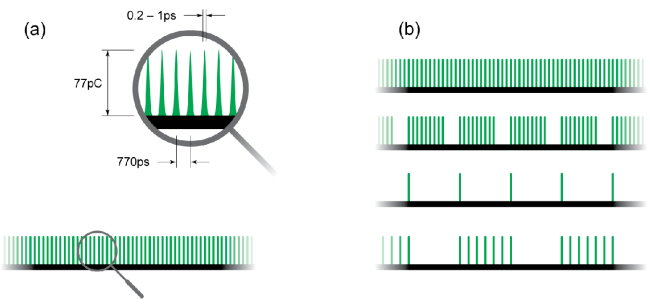

Figure 4.6 (a) A continuous bunch train for the high average current loop: bunch current 77 pc, bunch separation 770 ps (1.3 GHz). (b) Four possible pulse patterns; top to bottom – high regular repetition rate, macro-pulse structure, low repetition rate and a more irregular pattern. Note the flexibility on irregular patterns will be restricted by the need to reduce phase noise for optimum synchronisation – optimum synchronisation will be achieved with regular patterns.

4.3 Illustrative Timing Modes for Multi-beam Experiments

4GLS will provide simultaneous operation of its photon sources to deliver the twin aims of ground breaking multi-beam experiments and multi-user exploitation. As described in the preceding sections, each source will have an optimum repetition rate and it is likely that different facility operating modes will develop. The following section shows illustrative examples of three facility operation modes; high average current, optimum FEL operation and low repetition rate.

It is important to note that the modes described here are illustrative only and are far from being the only modes possible. Actual operating modes will be agreed in response to the needs of the science programme and will exploit the evolution of the technology on which 4GLS is based.

4.3.1 High Average Current

A high current mode would aim to deliver maximum photon output, with a train of 1.3 GHz, 77 pC bunches from the high average current injector system interspersed every millisecond with 1 nC bunches from the XUV-FEL injector. Figure 4.7 shows the timing pattern of these bunches as they are accelerated together in the main linac before separation to give 100 mA in the high average current loop and 1 nC pulses at 1 kHz for the XUV-FEL branch.

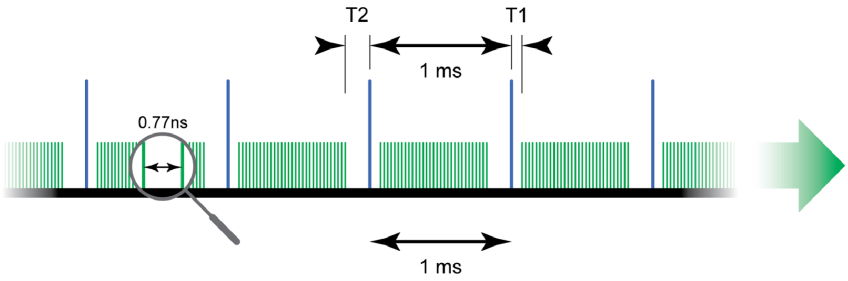

Figure 4.7 Pulse pattern in the main linac for high current operation. T1and T2 are the time separations of the XUV-FEL bunch and the preceding and following high average current loop bunches.

The 1 nC bunches can be injected very close to the 77 pC bunches, even in the same RF bucket giving a time separation T1 ~ 40 ps (see Figure 4.7). Beam loading in the linac following the high charge pulse may effect the acceleration of the following bunches thus requiring a gap T2. A further gap of 1 μs every 100 μs might be needed for ion clearing (§7.7.5).

At this high average current, it is highly unlikely that any cavity mirror material will survive and so the VUV-FEL lasing will be restricted. During the TDR phase, options for running the VUV-FEL with 100 mA in the high average current loop will be explored – for example by using an external laser to seed one in every few hundred electron bunches. The VUV-FEL will deliver high quality undulator radiation when not operated as a FEL. The IR-FEL will operate at its fundamental rate of 13 MHz.

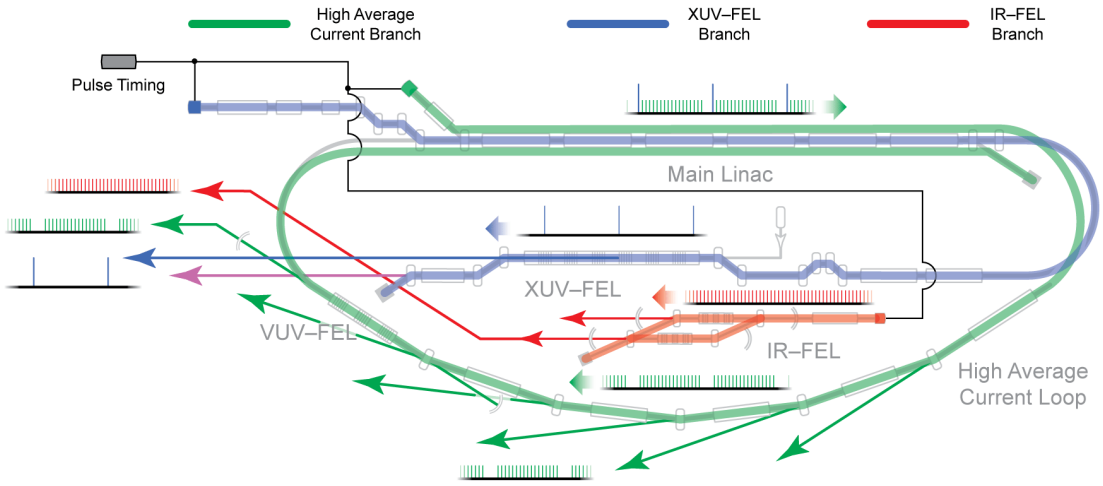

Figure 4.8 Illustration of the pulse patterns in a high average current mode and with all FELs operating. The high average current loop is running at 1.3 GHz (green), the XUV-FEL branch is running at 1 kHz (blue) and the IR-FEL is running at 13 MHz (red).

4.3.2 Lower Repetition Rate Operation

A second possible mode would be to set the high average current photoinjector to deliver the fundamental rate for the VUV-FEL, hence setting the rate for all the high average current loop sources to 4.33 MHz. The 1 kHz XUV-FEL pulses will be interspersed as before, and the IR-FEL along with sources in its branch will also be operated at 13 MHz.

It is also possible to operate the high average current loop sources at a very low rate - indeed virtually any rate from 1.3 GHz to <1 kHz (the lower limit depends on level of synchronisation required). At very low rates, energy recovery is not feasible, but as the average current is small, the beam can be dumped without recovery.

The VUV-FEL will not operate as a cavity FEL at lower repetition rates. The option of using an external laser to seed the VUV-FEL and allow operation at 100 mA would also enable low repetition rates. This will to be explored during the TDR phase.

4.3.3 Pulse Patterning in the Photon Beam Transport

Thus far, the repetition rates and patterns determined by the electron accelerator and free electron lasers have been discussed. It is also possible to adjust the pulse patterns delivered to the experiment by structuring the individual photon beams after they have left the source (see Chapter 11), either to reduce the experiment repetition rate or to provide pulse trains. The choice of method will depend on the photon energy range and power density. At low photon energies, the electro-optic effect and the acousto-optic effect are routinely used.

For photon energies above 5 eV, mechanical systems, though slower than the electro-optic method, are currently the only feasible method. A system based on a rotating disc can have switching times of a few hundred nanoseconds, which is suitable for reducing the megahertz pulse rates typical of cavity FELs to ~ 100 kHz or below. These are optimum rates for applications such as time-of-flight spectrometry. Such mechanical choppers are in regular use on synchrotron sources with a demonstrated jitter of 2 ns (3σ) [3].

Systems based on a rotating mirror deflecting the photon beam across a slit would be slow (~ kilohertz repetition rates), but they do offer the possibility of being one of the fastest mechanical chopping systems available, because of the possibility of using very long lever arms between mirror and slit.

These chopping systems require tightly focused photon beams over a moderate length, requiring them to be designed into the photon transport system from the outset. A mechanical chopper will be implemented for the 4GLS VUV-FEL beamlines. Depending on user needs, chopping systems will also be considered as part of the design for the spontaneous insertion devices on the high average current loop to allow a degree of independent control of the repetition rate at the experiments.

4.4 Conclusions and Further Work

A first iteration of the layout of 4GLS for combined beam experiments has been presented in this chapter. For the TDR phase, a primary aim is to produce conceptual designs for specific multi-beam systems. This will require detailed further discussions with potential users covering a broad range of experiment techniques.

Studies underpinning the ability to combine photon beam from a range of sources will continue, for example, exploring further options for operation of the VUV-FEL and development of photon beam chopper designs.

REFERENCES

[1] 4GLS Science Case, 2001

[2] Summary of estimated science needs, http://www.4gls.ac.uk/Meetings/parameter/4GLStablesv3.doc

[3] M. Gembicky et al., 'A fast mechanical shutter for submicrosecond time-resolved synchrotron experiments', J. Synchr. Rad. 12 (2005) p665.

5. Injector Systems

This chapter states the requirements for the three electron sources for 4GLS, the technical choices that have been made to fulfil these requirements and the justification of how these choices have been made. Before describing the chosen injector solutions, some of the critical technologies and techniques are described, including cathode technology and laser systems. No information is included here on other technical systems required for injector operation (such as radio-frequency power) but it does include an outline of the suite of diagnostics envisaged. This chapter also includes a description of the relevant projects in which CCLRC are presently involved and further work that will be necessary.

5.1 Introduction

4GLS is a synchrotron radiation source consisting of three integrated systems arranged in such a way as to share some critical items of hardware and produce synchronised output for combined-wavelength experiments. A high brightness XUV-FEL injector system (characterised by the requirements for an exceptionally small normalised emittance electron beam, high peak current and a low average current) is required for the XUV-FEL source. A high-average current continuous electron source is required for the high average current loop (which includes the VUV-FEL and from which the subsequent energy gain will be recovered and the beam dumped at near to the injector energy). Finally, the IR-FEL will require its own dedicated electron source. A key requirement is the need to synchronise the output from these three sources.

Start-to-end simulations of the accelerators, which include the user requirements for the photon output, have driven the injector parameters. The three different sets of electron beam parameters that are required lead in turn to the need for three different solutions for the injector. At the heart of these three distinct injector systems are three different electron gun designs. The proposed layout of the injector systems is shown in schematic form in Figure 5.1:

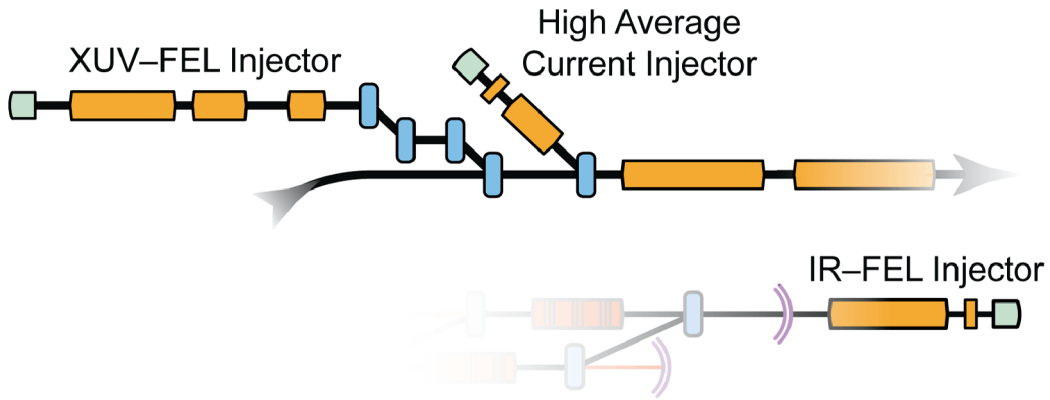

Figure 5.1 Schematic of the 4GLS injectors

Of the three injectors, the XUV-FEL and high average current injector systems will require performance exceeding that yet demonstrated; however there are several promising developments taking place on a timescale compatible with 4GLS. As the success of these developments is highly relevant to 4GLS, reaching its full potential it is important that the project takes a significant role in them. Both these injectors will rely on photoelectron emission arising from a laser pulse hitting a cathode. This allows control of the electron bunch properties via the laser pulse that generated them. For the IR-FEL, a thermionic electron source should be able to produce the electron beam parameters required. However, following more detailed study outside the scope of this report, synchronisation requirements may mean that a photoinjector is also preferred here.

5.2 Common Issues

5.2.1 Electron Sources

In principle, a number of processes can be exploited to generate free electrons, including field emission, ferroelectric phenomena, thermionic emission and photoemission. Of these thermionic and photoemission represent the most mature technologies for linear accelerators. Photoinjectors have emerged as the preferred solution for high-brightness electron beams required by the next generation of light sources for several reasons. They produce bunches of electrons with very low emittance at high peak currents due to the high accelerating gradients applied to the cathode and the ability to shape the bunch in three dimensions with the laser. Photoproduction also offers precise timing and flexibility in pulse train formats not possible with thermionic sources. In some circumstances it is also possible to significantly reduce the thermal emittance via photoemission.

The injector is among the most critical accelerator components because its performance, including that of the drive laser and cathode material properties, largely determines the quality of the electron beam produced. Although the electron beam is accelerated and transported through hundreds of metres, its transport in the first few *millimetres* following the cathode presents the greatest challenge to generating the brightest beams. This is due to space charge effects that rapidly diminish as the beam reaches relativistic energy, scaling as $1/\gamma^2$. Both simulation and analytical work have shown that it is possible to generate a high charge electron beam while preserving a very small phase space volume. These simulations run with distributions that are almost perfectly uniform. Such distributions have proven difficult to generate and measure experimentally. For most injectors realized in practice, the final emittance is dominated by the effects of space charge.

5.2.1.1 Photocathode Characteristics

The properties of the photocathode, together with the drive laser and applied electric field, determine the initial intrinsic emittance. The choice of cathode material is made by optimising a number of parameters against the overall system requirements. Broadly these are as follows:

- **Threshold for photoemission.** The lowest drive-laser photon energy that can be used to generate electrons is determined by the work function in the case of metals and the energy gap and electron affinity in the case of semiconductors. For materials of practical importance this is implies the use of UV drive lasers for metal cathodes while different semiconductors operate over a range of wavelengths, from infrared to UV.

- **Quantum efficiency** (QE). In this context QE is defined as the number of electrons generated per incident (rather than absorbed) photon. It depends upon the cathode material, laser wavelength, accelerating field and vacuum environment and has particular consequences for the specification of the drive laser system. For photoemission in the linear regime, the energy E required per laser pulse of wavelength λ to generate a given bunch charge is related to the quantum efficiency at that wavelength by

$$E_{laserpulse}[\mu J] = \frac{124 x Q[nC]}{\lambda_{laser}[nm] QE[\%]} \qquad (5\text{-}1)$$

In general, the QE of metals is significantly lower than that of semiconductors. For example, under ideal test conditions Srinivasan-Rao et al.[1] report 0.014 % for Cu at 266 nm, while Siggins *et al* [2] obtained 5 % efficiency at 527 nm, under operational conditions, for caesiated gallium arsenide. This difference arises from the high density of conduction electrons in metals, which has a negative impact in two respects. Firstly, the correspondingly high macroscopic reflectivity limits absorption in the first step of the photoemission process. Secondly, electron transport throughout the photon penetration depth is dominated by strongly inelastic electron-electron scattering.

- **Thermal emittance**. The source emittance of a photocathode can be calculated from the following expression [3], where r is the hard-wall radius of the laser beam and $E_{thermal}$ the electron energy at the cathode surface:

$$\varepsilon_{th} = \frac{r}{2}\sqrt{\frac{E_{thermal}}{m_0 c^2}}\frac{1}{\sqrt{3}} \tag{5-2}$$

  For a semiconductor photocathode $E_{thermal}$ depends on the surface band structure, and here a useful distinction between Positive Electron Affinity (PEA) and Negative Electron Affinity (NEA) materials can be made. For PEA photocathodes $E_{thermal}$ is determined by the energy gap and the electron affinity. For NEA photocathodes on the other hand, $E_{thermal}$ is set by the material lattice temperature. Actual values for $E_{thermal}$ range from 34 meV for gallium arsenide (NEA at room temperature) [4] to 550 meV for caesium telluride (PEA) [3].

  It is important to note that although ε_{th} may be decreased by reducing the laser beam footprint, this has consequences for space charge effects at the surface. These should be minimised by ensuring that the surface charge density due to the accelerating field is very much greater than the bunch charge density. A smaller illuminated cathode area for a given charge increases the required cathode field.

- **Cathode lifetime**. This may be regarded as virtually infinite for metal cathodes. Gross contamination may cause variations in quantum efficiency, but RF cavity vacuum levels better than 10^{-8} mbar pose few problems. Semiconductor cathodes, in contrast, are sensitive to operating conditions, both in terms of poisoning from the residual gas and from sputtering of the cathode material by positive ions generated from the gas or desorbed from surfaces. The first process determines the dark lifetime, while the second influences operational lifetime and is often given in terms of delivered charge.

- **Dark current**. A significant benefit of a photocathode as an electron source is the straightforward way in which the drive laser pulse train determines the electron bunch structure. In the ideal case, no electrons are emitted between drive laser pulses or outside of the footprint of the laser beam. In practice, dark current, generated by field emission, limits the purity of the electron bunches used in timing experiments and adds to the desorption of gas from the gun chamber walls. The dark current depends on the surface preparation of the cathode and the applied electric field.

5.2.1.2 Material Options

The requirement for the electron source for energy recovery-based light sources to supply high peak and average current means that any practical solution is likely to be based on a high QE (semiconductor) photocathode. To date, caesiated gallium arsenide (Cs:GaAs) has been the domain of DC guns, while normally conducting and superconducting RF guns have used the PEA materials caesium telluride (Cs_2Te) and potassium caesium antimonide (CsK_2Sb). As the technology develops however, this distinction is likely to blur. In any event, a major challenge in all cases is to deliver a high integrated charge without disruptive intervention to renew the cathode material. The choice of the material depends also on the laser development. As lasers have improved in average power and reduced cost, materials that are more robust, but perhaps with lower quantum efficiency, have become more attractive.

5.2.1.2.1 Caesium Telluride

Caesium telluride is a widely used member of a group of alkali telluride compounds which have shown potential as photocathodes and is commonly formed by reacting caesium vapour with a tellurium film on a heated platinum or molybdenum substrate. The material produced is a positive electron affinity semiconductor, which exhibits a threshold for electron production at 344 nm. At 262 nm the efficiency is >2 % [5]. Although poisoning from residual gas is known to occur, this is not excessive at typical RF cavity vacuum levels and the material has been successfully used in normal conducting RF photoinjectors. The effect of the most serious contaminant - oxygen - appears to be reversible even after quite significant exposures [6].

The specification of the drive laser for Cs_2Te is necessarily more demanding than that for those cathodes with thresholds in the visible spectrum; the total power dissipation within the material will also be higher for the same duty cycle. Nevertheless, the combination of stability and high QE made caesium telluride the chosen material for RF photoinjectors at a number of facilities such as CLIC in CERN, Geneva, PITZ at DESY-Zeuthen, Berlin and FZ Rossendorf, Dresden, albeit at comparatively low duty cycles.

5.2.1.2.2 Potassium Caesium Antimonide

Potassium caesium antimonide is a semiconductor with high quantum efficiency in the visible spectrum (> 5 % at 532 nm), and has a long history of use in photoinjectors [7]. The combination of high efficiency and long wavelength has the advantage of simplifying the drive laser system; however this material is highly sensitive to the vacuum environment.

K_2CsSb has been used at the ELSA linac at Bruyères-Le-Châtel [8] and is the part of the SRF photoinjector R&D programme at BNL, Brookhaven [9]. It is however very sensitive to vacuum conditions and appears to be easily poisoned by the presence of CO_2. Investigations by di Bona [10] showed that RF-related desorption of CO_2 was the major factor limiting lifetime. In a gun operating at 8×10^{-9} mbar the cathode lifetime was ~ 1 hour. Separate dosing measurements showed that a 1/e decay in the quantum efficiency was caused by between two and six Langmuirs (L) of CO_2 (1 L = 1.31×10^{-6} mbar for 1 second). The cathode lifetime was independent of the laser beam, indicating a general poisoning effect rather than a process related to electron production.

However, with the development of superconducting RF guns, the superior operating vacuum has reduced this limitation making the material a realistic option as a high-average current source. As a stoichiometric material, like caesium telluride, it may be also less prone to damage by ion back-bombardment, which is one of the principal limits for the DC injector.

5.2.1.2.3 Caesiated Gallium Arsenide

GaAs itself is not an exceptionally efficient photocathode material, but if a heavily doped p-type wafer (~ 10^{19} Zn atoms per cubic centimetre) is activated with caesium and oxygen (or NF_3) the material can emit with an QE of several percent, at wavelengths up to 800 nm [11]. Heavy p-type doping causes downward band bending near the surface. In addition to this, the electron affinity is reduced by a surface dipole layer formed by the oxidised caesium on the clean gallium arsenide surface. These two effects combine to leave the conduction band minimum at the surface above the vacuum level, creating the negative electron affinity state.

In photoemission, electrons promoted from the valence band to the conduction band thermalise to the conduction band minimum through the dominant electron-phonon energy-exchange process. At the surface, electrons can be reflected back or trapped in surface states, while some tunnel out with energies above E_{vacuum}. Through this mechanism of thermalisation, the mean transverse energy is determined by the lattice temperature, which in turn implies the possibility of using cooling to generate very low thermal emittances compared to PEA materials or thermionic emitters. A further consequence of the electron transport process is that the response time is comparatively long. However, since electron transport is diffusion limited (over a characteristic length of around one micron) the emitted electron bunch length can be shortened by using very thin active layers. A 150 nm epilayer can produce a bunch length of around 10 ps [12]. Reducing the available absorption length also causes a corresponding decrease in the quantum efficiency.

The principal disadvantage of this material is its sensitivity to residual gas molecules. Exceptionally good pumping is needed, generally requiring the use of Non-Evaporable Getter (NEG).

A Cs:GaAs-based gun at the Thomas Jefferson National Accelerator Facility (TJNAF), discussed in more detail in 5.6.1, has revealed the lifetime to be largely limited by ion back-bombardment. Damage occurs around the active emission region through sputtering of the dipole layer by positive ions formed in the beam path and accelerated by the applied gun voltage. This can be offset to some extent by over-caesiating to provide a sacrificial over-layer, directing the drive laser to a point on the cathode off-axis and by periodically moving the drive laser to a new area of the cathode. Hydrogen cleaning, ultra-high vacuum (ideally better than 10^{-10} mbar) and wafer shielding during high-voltage processing were also identified as key factors in maintaining high quantum efficiency and long-lifetime [2].

In operation the 1/e extracted charge lifetime was 618 C, but by reactivating on three occasions the same cathode was used for thirteen months (~ 8500 hrs) and delivered a total charge of 2400. The dark lifetime on the other hand has been estimated at over 2.2×10^4 hours [13].

The development of GaAs-based photoinjectors has been driven particularly by the demand for beams of polarised electrons at high-energy physics facilities. Consequently, a good deal of experience has been accumulated in their preparation and operation in recent years. Following its successful use at the TJNAF IR-FEL, a similar photoinjector is being used on the Daresbury Laboratory Energy Recovery Linac Prototype (ERLP) to take advantage of the current state of the art [14]. This will provide a platform for further improvement in source emittance, QE, dark current and effective lifetime necessary for a fourth-generation user facility.

5.2.1.3 Photoinjector Lasers

The photoinjector drive lasers are among the most important components of the facility because their properties, along with those of the photocathode materials, determine the quality of the electron beams. The laser intensity distribution on the cathode should be very uniform in the transverse and temporal dimensions to minimise adverse space charge non-linearities. This requires pulse shaping to deliver sharp transverse edges and to control rise and fall times with sub-picosecond precision. The drive lasers must also meet stringent timing, stability and reproducibility specifications. They should allow flexibility in the output of different pulse patterns to suit user needs (see chapter 11).

The photoinjector lasers will operate at a wavelength of 1.05 μm. This matches the gain profile of Yb^{3+}, the active medium in both the Ytterbium-Doped Fibre Laser (YDFL) and also in various crystal-based bulk media capable of generating sub-picosecond pulses at significant pulse energies. The advantage of a common wavelength is that all of the lasers can be fed from a single oscillator, ensuring automatic synchronisation.

5.2.1.3.1 Photoinjector Laser System Layout

The laser system architecture is shown in Figure 5.2. The laser oscillator will be synchronised to the 4GLS master clock, which will operate at 40.625 MHz (see chapter 11). This will also be the pulse rate of the oscillator, which will be a YDFL. From the oscillator the beam will enter a time structuring unit which will deliver beams to the individual power amplifiers with the appropriate pulse rates and time structures (a beam for the IR-FEL is shown although it is possible that in that case a thermionic gun will be used). The electron guns are physically separated by many metres. It is proposed to locate the power amplifiers close to the guns to avoid transporting their high power output beams over long distances in free space. The beams from the time structuring unit will be at low enough power that they can travel in optical fibres.

The details of the synchronised laser oscillator and the time structuring unit will be given in the chapter 11. The individual power amplifiers will be discussed in the appropriate sections of this chapter.

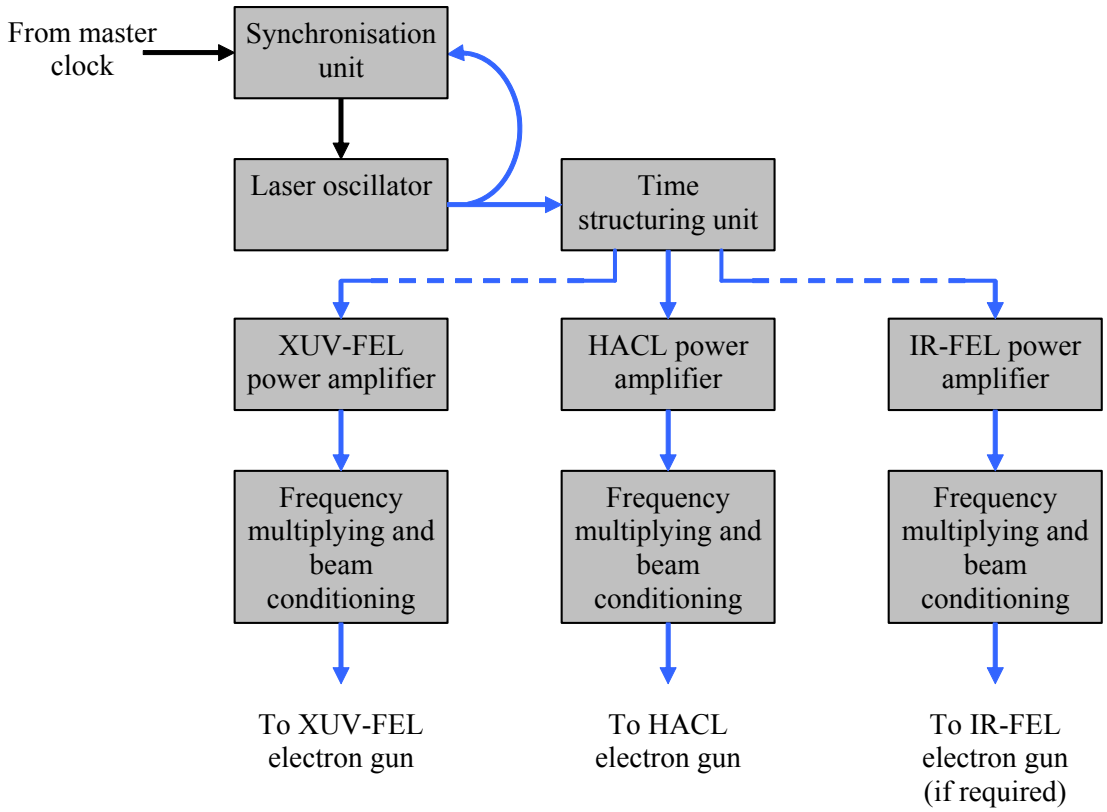

Figure 5.2 Layout of the 4GLS gun synchronisation system

5.2.1.4 Emerging Cathode Developments

It is apparent that there is still considerable scope to further develop photocathode technology. The possibility of reducing the source thermal emittance by cooling a NEA material has already been referred to above. A proposal has recently been made by Ben-Zvi and co-workers [15] at Brookhaven National Laboratory to increase the effective QE by placing a thin diamond window in front of a high-QE material. The diamond acts as secondary electron emitter multiplying the photocurrent by two orders of magnitude. A further advantage is gained by preparing the window with an NEA surface so that the thermal emittance may be minimised. This would allow, for example, the fast response of CsK_2Sb to be combined with the low thermal emittance of an NEA material at very high efficiency. Moreover, the passive diamond surface should also deliver a long cathode lifetime.

Any such cathode developments taking place at other laboratories over the next few years could be incorporated into the 4GLS design if they prove successful. At present, the design will use the well-developed technology described in the appropriate following sections.

5.3 High Average Current Injector System

The high average current injector will provide 100 mA average current for the high average current loop, from which energy is recovered. The chosen injector energy is a compromise between a desire to keep the dump beam energy below 10 – 12 MeV to minimise dump activation while minimising space charge-produced emittance growth. It is intended that this injector will be operated in a continuous mode (every RF cycle will contain electrons). In addition, this injector is required to operate in a mode specifically for the VUV-FEL. This will be at a repetition frequency that is an integer multiple of 4⅓ MHz (see chapter 8).

Arguably, the high average current photoinjector is the most technically demanding of the three 4GLS injectors to design as there are no injectors at present that can fully meet the requirements of 4GLS, however there are a number of different designs being developed elsewhere that are very promising [13]. In addition to continuous-mode operation it is also required that the normalised emittance be less than 2 mm mrad. Indeed, the only photoinjector to operate in a continuous mode is the DC photoinjector used on the IR-FEL facility at TJNAF [16]. A maximum of 9.1 mA has been achieved at TJNAF (although with some degradation of the brightness due to a large transverse emittance). The closest that has been achieved using RF gun technology is the normal-conducting Boeing photoinjector which produced 32 mA average current with a 433 MHz RF gun, operated with 25 % duty factor [17, 18]. Los Alamos National Laboratory (LANL) are presently developing a high-average current RF gun [19]. The 700 MHz normal conducting photoinjector with magnetic emittance compensation should provide 3 nC bunches at a repetition rate of 35 MHz. A 2.5 cell RF cavity will accelerate the beam up to 2.5 MeV with a transverse normalised emittance of less than 7 mm mrad (σ).

5.3.1 Beam Requirements

The specification for the electron beam from the high average current injector, at the entrance to the main linac, is given in Table 5.1.

Table 5.1 Beam requirements for the high average current injector, at the entrance to the main linac

Parameter	**High-average current mode**	**Optimised for VUV-FEL**	
Bunch charge	77	77	pC
Bunch repetition rate	1300	4⅓ N*	MHz
Bunches per train	continuous	1	
Energy	10	10	MeV
Normalised emittance	< 2	< 2	mm mrad
Uncorrelated energy spread	< 0.1	< 0.1	%
Bunch length (σ)	~ 2	~ 2	ps

(*where N is an integer)

The high average current injector beam will be accelerated through the main linac simultaneously with the 1 nC bunches from the XUV-FEL injector. In addition, the energy-recovery beam will also be passing through the linac. At the end of the linac the dump, XUV-FEL and high-average current electron beams will be separated by a DC magnetic separation scheme, described in Chapter 7.

5.3.2 Layout

The high average current injector will comprise an electron gun, solenoid magnets to zero the magnetic field at the cathode surface and to minimise further emittance growth due to space charge and a buncher cavity to control the longitudinal phase space for capture by the subsequent accelerator modules. The layout of the high average current injector is shown in Figure 5.3:

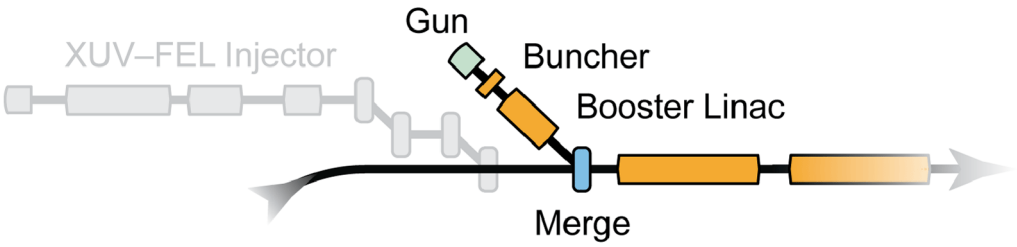

Figure 5.3 Layout of the high average current injector

A 1.3 GHz laser system will produce electrons from a photocathode in high-average current mode; the user requirement is an average current of 100 mA. To achieve this and to minimise space charge effects every 1.3 GHz RF bucket is filled with 77 pC of charge. A normalised emittance of < 2 mm mrad is necessary for high brightness from the spontaneous sources and for good FEL coupling in the VUV-FEL. After the photocathode electron gun there will be a buncher cavity to reduce the bunch length and a linac to accelerate the bunches to relativistic velocities quickly, in order to minimise emittance growth due to space charge.

Due to both the intrinsic properties of the probable cathode material and the low operating voltage of DC guns compared to RF guns, short electron bunches cannot be produced by a DC gun. Typical bunch lengths are of the order of 20 ps (σ). The subsequent acceleration in a linac operated close to an on-crest phase leads to strong non-linearities in the longitudinal phase space due to the sinusoidal shape of the RF. This effect is mitigated by employing a buncher cavity. When operated at zero-crossing RF phase, the head of the bunch is decelerated and the tail is accelerated so that the tail catches up with the head in the subsequent drift space; the net energy gain is nearly zero.

5.3.3 Injector Components in Detail

5.3.3.1 DC Electron Gun

As discussed before, the only photoinjector to operate in a continuous mode is the DC photo-injector used on the IR-FEL facility at TJNAF. This device operates at a DC voltage of 350 kV and produces 135 pC bunches from a laser pulse length of 20 ps with a transverse normalised emittance of 10 mm mrad and an average beam current of nearly 10 mA. The TJNAF gun is shown in Figure 5.4.

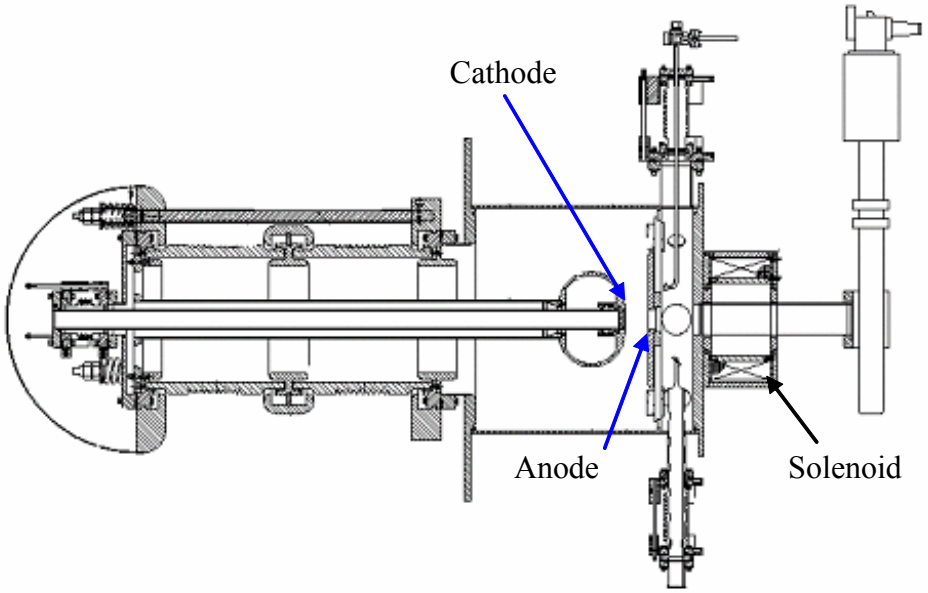

Figure 5.4 Mechanical drawing of the TJNAF gun

This gun design has also been utilised for the ERLP [14]. Daresbury Laboratory is building a state-of-the-art prototype machine to gain experience with the simulation, design, procurement and operation of such a device. It is an obvious choice to develop this technology to meet the requirements of 4GLS. However, the maximum average current that has been achieved so far at TJNAF is less than 10 mA. Thus an order of magnitude increase in the average current is required.

A development of this gun design and technology, such as that at Cornell University, is the most likely solution for 4GLS. At Cornell an ERL-based x-ray source is being planned. The goal is to deliver diffraction-limited x-ray beams at 0.1 nm wavelength. For this application the electron injector is a crucial aspect of the project. Similarly to 4GLS, Cornell are planning to use a CW laser at 1.3 GHz to produce 77 pC bunches with a normalised emittance of < 2 mm mrad, using a DC gun. This gun is now under construction [20].

The Cornell design is based on 1.3 GHz technology, with a cryomodule containing five 2-cell superconducting cavities. The injector uses two solenoids and a normal conducting buncher cavity. The DC gun is based on the TJNAF design, but uses a higher DC gun voltage and a smaller

cathode-anode gap in order to reach higher field gradients at the cathode. Coatings may be required to reduce the possibility of field breakdown.

The baseline Cornell design, modelled with PARMELA, produced a normalised emittance of < 1 mm mrad at 10.6 MeV from the injector, for 77 pC electron bunches, excluding the contribution from thermal emittance. Cornell have further optimised their design by using large scale parallel processing, a genetic optimisation algorithm and the particle tracking code ASTRA [21]. Almost every parameter was permitted to vary within a sensible range and the thermal emittance from the cathode was included in the particle tracking. After optimisation the normalised emittance at 12 MeV for 77 pC bunches was 0.14 mm mrad.

A comparison of the 4GLS injector requirements (in high-average current mode) and the results from [20] is shown in Table 5.2. These show that the design being pursued for this project would also achieve the requirements for 4GLS.

Table 5.2 Comparison of beam parameters required at the exit of the 4GLS high average current injector and the results from [20]

Parameter	**4GLS**	**Cornell ERL**	
Bunch charge	77	80	pC
Bunch repetition rate	1.3	1.3	GHz
Bunches per train	continuous	Continuous	
Energy	10	12.6	MeV
Normalised emittance	< 2	0.14	mm mrad
Uncorrelated energy spread	< 0.1	0.06	%
Bunch length (σ)	2 - 3	2.6	ps

5.3.3.2 Cathode Choice

It is expected that the cathode for the high average current injector will be based on caesiated gallium arsenide, a continuation of the approach taken for the TJNAF DC photoinjector and the ERLP photoinjector. The intrinsically long electron bunch length from this material can be more readily tolerated in this injector, while the high quantum efficiency over a wide spectrum reduces the demand on the drive laser. This is an important factor where high-average currents are required. TJNAF has already demonstrated routine in-situ activation and re-activation of caesiated gallium arsenide, with a single wafer delivering a total charge of 2400 C [2]. This would imply a period of only a few hours of operation before a cathode change would be required for an injector operating at 100 mA average current. In addition, higher average currents would increase the rate of ion back-bombardment, which would reduce the cathode lifetime further. However, results with polarised electron beams at the CEBAF accelerator at TJNAF [13] suggest that this is merely a vacuum problem, which is therefore not insurmountable.

While the average current requirement of 4GLS has not yet been demonstrated with this material, there would appear to be no technological limit as to why it could not be achieved.

5.3.3.3 Laser System

The high average current loop photoinjector laser will need to generate a near-continuous train of 10 ps FWHM pulses at 1.3 GHz. The option of reducing the pulse rate to 4⅓ MHz, or a multiple thereof, to control heat loading effects in the VUV-FEL, is also required. In addition there may be a need for more flexible time structuring.

The laser system has been designed to deliver an electron bunch charge of 77 pC assuming a photocathode quantum efficiency of 1 %. New Cs:GaAs cathodes will have efficiencies much higher than this [2], but the laser specification allows for the gradual efficiency degradation which inevitably occurs. The cathode is sensitive to wavelengths shorter than ~ 0.85 μm so the 1.05 μm laser output will be frequency doubled to 0.52 μm. At this wavelength a laser pulse energy of 18 nJ is required at the cathode. Budgeted beam transport losses of 30 %, conditioning losses of 50 % and a frequency doubling conversion efficiency of 40 % (50 % efficiency was the maximum achieved for the 120 nJ, 7 ps pulses delivered from the commercial Nd:YVO4 laser used in the 4GLS ERLP photoinjector) combine to raise the pulse energy required from the laser itself to 125 nJ. At 1.3 GHz this corresponds to an average power of ~165 W.

Several laser technologies have demonstrated sub-nanosecond pulse durations with more than a hundred watts of beam power. Perhaps the simplest, most efficient and most stable of these is fibre lasing. Since simplicity, efficiency and stability are all very desirable features of photoinjector components a design based around a fibre laser has been chosen for the high average current injector. Its output parameters are listed in Table 5.3, alongside those of a YDFL system which has already been demonstrated [22].

Table 5.3 Parameters of the 4GLS high average current photoinjector laser and a demonstrated fibre laser system

Parameter	Requirement	Value reported in [22]	
Wavelength	1.05	1.06	μm
Pulse frequency	1.3	1	GHz
Average power	160	321	W
Pulse duration (FWHM)	10	20	ps
Peak power	12.5	16	kW
Beam quality	Near diffraction-limited ($M^2 < 1.5$)	$M^2 = 2.4$	
Spectrum	Near transform-limited	~ 4 × transform-limited	
Polarisation ratio	< 1:30	Not reported (1:1 ?)	
Timing jitter (RMS)	~ 100	Timing not stabilised	fs

The major differences between the high average current injector laser requirements and the reported results are:

- The demonstrated laser beam quality was not diffraction-limited. It was only slightly multi-mode ($M^2 = 2.4$) but this might be sufficient to disrupt the frequency doubling, which requires tight focusing for good conversion efficiency and which also tends to increase the

intensity variations which are characteristic of multi-mode beams. These variations translate to non-uniformities in the photocathode electron emission, with consequent degradation of the electron beam emittance. The problem was that the Large Mode Area (LMA) fibre used as the final amplifier in [22] was not truly single-mode. A single-mode system with the LMA needed for high power operation has been demonstrated using photonic crystal fibre [23]. The beam quality was then very close to diffraction limited (M^2 = 1.1) so the use of this fibre is proposed for the high average current injector laser.

- The laser spectrum reported in [22] was not transform-limited. The authors claim that the spectral broadening, caused by Self-Phase Modulation (SPM), would be small enough for it still to be "compatible with frequency doubling". However it seems unlikely that the conversion efficiency would be completely unaffected. Furthermore, like all non-linear processes, SPM will vary disproportionately with any intrinsic shot-to-shot noise and, in the interests of stability, should therefore be avoided. The authors of [23] report no non-linear effects in their photonic crystal fibre, so it may be that adopting this approach will eliminate the problem. On the other hand, unlike many non-linear processes, SPM depends not on intensity but on rate-of-change of intensity. The pulse used in [23] had a smooth spectrum which would have been transformed into a smoothly-varying intensity in the chirping process. The peak power of 20 kW in the fibre might therefore have been reached with a rise time as long as 60 ps (the pulse was chirped to 120 ps duration). This would generate less SPM in a given fibre than a peak power of 12.5 kW rising in 5 ps – the performance needed from the high average current injector laser. Without knowing the SPM coefficient of ytterbium-doped photonic crystal fibre it is not clear whether SPM will be an issue, but if problems were to arise they could always be mitigated by using Chirped-Pulse Amplification (CPA).

- The output of the laser described in [22] appears not to have been polarised. Using unpolarised light would limit the choice of frequency doubling schemes with a likely unacceptable reduction in the conversion efficiency. Fortunately it is possible to deliver highly polarised light from high average power, single-mode fibre lasers, with a polarisation ratio of 1:30 reported in [23] and nearly 1:100 in [24]. It is not clear whether the techniques used in [24] to deliver the very highest polarisation ratios can be extended for use with photonic crystal fibres. If they cannot then it will probably be better to accept limits nearer to 1:30 than to revert to conventional LMA fibre with its need for differential bending-loss designs to ensure single-mode output and CPA to control non-linear effects.

It seems clear that a laser system based on existing ytterbium-doped fibre technology could already be designed to meet the requirements of the high average current photoinjector. Although these are near the limits of what has been demonstrated they do not exceed them. Furthermore, fibre laser development is currently progressing very rapidly and by the time that it is needed the technical risk associated with this laser should have become very low.

5.3.3.4 Diagnostics

The high average current injector will be equipped with a full complement of diagnostics appropriate to measure the electron beam properties and to provide input signals for the machine protection system. It is expected that these diagnostics will be similar to the systems employed on the ERLP and may initially include a dedicated beamline for gun commissioning [25]. A permanent dedicated diagnostic line, with the ability to select a few bunches from the 100 mA average current pulse train, may provide a solution to the problem of measuring the properties of such an electron beam.

A schematic layout of conventional diagnostics for the injector and part of the subsequent beam transport system, is shown in Figure 5.5.

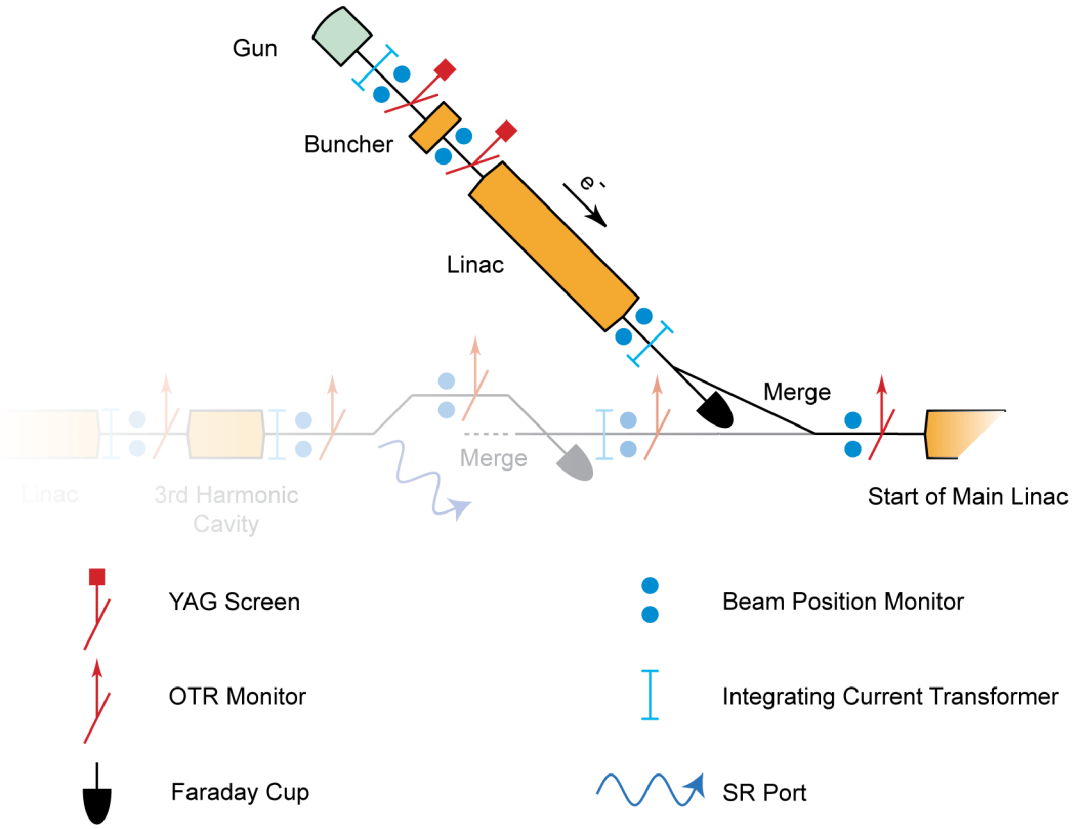

Figure 5.5 Schematic layout of the diagnostics for the high average current injector system

5.4 XUV-FEL Injector System

The XUV-FEL injector will be used to provide electron bunches with low normalised emittance, high-peak current and low energy spread for the XUV-FEL branch. This requires a high-brightness gun for the electron source, advanced diagnostics to measure the beam properties with high resolution, linac modules for acceleration and bunch compression optics. The initial electron beam quality is a crucial component in determining the photon beam characteristics of the XUV-FEL system.

To achieve lasing in shorter wavelength FELs, kiloampere peak currents are typically required from the electron bunches and short bunch lengths are therefore necessary. The design of the XUV-FEL for 4GLS requires the following beam parameters at the FEL: 1 nC electron bunches with < 300 fs (σ) bunch lengths giving ~ 1.5 kA peak current. The normalised emittance must also be ~ 2 mm mrad (see chapter 8), which is limited by the injector and must be preserved as the bunch is transported. The injector alone will not produce these beam parameters directly (particularly the bunch length) so magnetic compression takes place prior to the main linac and the XUV-FEL. A description of this key element of the injector system is given in Chapter 7.

Although not seen as a requirement during the modelling undertaken for this report, the possibility of needing a laser heater prior to the main linac, in order to increase the energy spread and suppress instabilities, cannot be excluded. This issue will be decided upon during the TDR phase.

5.4.1 Beam Requirements

The specification for the XUV-FEL electron beam at the entrance of the main linac is given in Table 5.4*:*

Table 5.4 Beam parameters required at the entrance of the main linac

Parameter	Value	
Bunch charge	1	nC
Fundamental RF frequency	1.3	GHz
Train repetition rate	1	kHz
Energy	160	MeV
Normalised emittance	< 2	mm mrad
Uncorrelated energy spread	~< 0.05	%
Bunch length (σ)	~ 2	ps

The 1 nC bunches from the XUV-FEL injector will be accelerated through the main linac simultaneously with the high average current injector beam. At the end of the main linac, the XUV-FEL and high-average current bunches will be separated by a separator scheme, also described in Chapter 7.

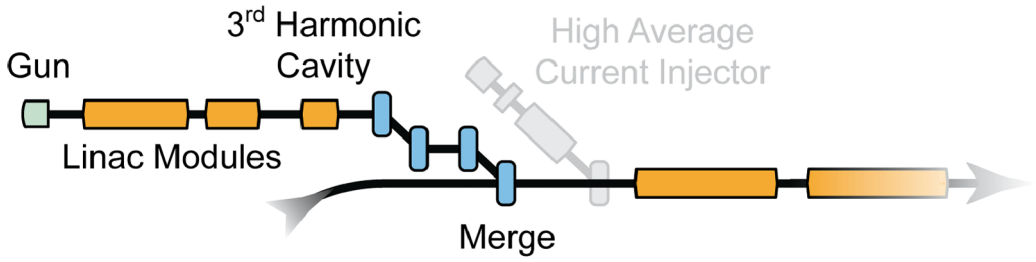

Figure 5.6 Layout of the XUV-FEL injector line

5.4.2 Layout

The layout of the XUV-FEL injector and subsequent components, prior to the main linac, is shown in Figure 5.6.

5.4.3 XUV-FEL Injector Components in Detail

5.4.3.1 Normal-Conducting RF Electron Gun

A normal-conducting RF gun is the chosen technology for the XUV-FEL injector, because it is now sufficiently mature to provide a reliable solution. A DC gun is not an appropriate choice for this gun as it does not provide the rapid acceleration to multi-GeV levels required to control the high space charge forces within a high charge bunch. Normal-conducting RF photoinjectors have been shown to be capable of generating low normalised emittance electron beams with high bunch charges at low repetition rates [26, 27]. Acceleration to several MeV and well understood emittance compensation methods mean that injector normalised emittances of < 1.5 mm mrad are achievable [28]. Superconducting designs, although having many desirable features, are not yet thought to be mature enough.

In a normal-conducting RF gun electron bunches are generated via a photo-emission process from a photocathode situated inside an RF cavity. The laser used to produce the electrons determines the electron bunch dimension, shape and charge density. By placing the cathode at the position of the highest field gradient in the RF cavity the electrons are rapidly accelerated to several million electron volts, thus reducing the effects of space charge. To minimise further emittance growth due to space charge a solenoid magnet is required after the gun, while a second solenoid (bucking coil) is used to zero the magnetic field at the cathode surface.

The most widely used RF gun is the BNL/UCLA/SLAC design for a 1.6 cell photocathode gun operating at 2856 MHz [29]. This gun routinely achieves 100 MV/m at 10 Hz with a 5 MeV exit energy and uses a simple flat copper cathode incorporated into the cavity wall. This design was adapted to 1.3 GHz by a collaboration of DESY/FERMILAB/UCLA/INFN/MBI [30,31] for use at the Tesla Test Facility (TTF). The TTF design replaced the original copper cathode with a high-efficiency Cs_2Te photocathode that is prepared in a dedicated photocathode preparation facility. Further developments of the 1.5 cell normal conducting gun design have been undertaken at the

Photo Injector Test facility in Zeuthen (PITZ), including a coaxial input power coupler that significantly reduced the axial asymmetry of the acceleration field. This gun is presently operating in the TTF-II facility at DESY Hamburg, now known as the VUV-FEL. First results from this gun are reported in [26].

The gun design chosen for the 4GLS XUV-FEL injector is a further refinement of the PITZ gun being undertaken for the BESSY FEL project. The gun is a normal-conducting RF photoinjector which produces electron bunches with properties similar to those required for 4GLS. The gun for the BESSY FEL is currently under construction. CCLRC are involved in the development of phase space tomography systems and modelling of beam dynamics through diagnostic devices for the PITZ collaboration. This is described in more detail in section 5.6.3.

The performance of the original PITZ gun design falls short of the BESSY FEL and 4GLS requirements in one major area, repetition rate. At TTF-II the maximum repetition rate is 10 Hz, limited by cavity cooling; both the BESSY FEL and 4GLS require 1 kHz operation. To increase the maximum repetition rate of this design, developments are underway to improve the cavity cooling capacity [32] and the power transmission through the RF coupler. With the BESSY FEL repetition rate of 1 kHz and a pulse length of 25 μs the duty factor is 2.5 %, significantly more than at TTF-II. The heat load from this increase in duty factor is significant and thermal stability must be guaranteed during operation. Thermal changes will result in drifts of the cavity resonant frequency, causing RF phase and amplitude mismatch. The water cooling system has been improved to cope with the higher heat load. The inlet water temperature can also be adjusted to compensate for cavity detuning, along with the normal tuning mechanisms. The most recent development of this design, in order to meet the duty factor requirements of the BESSY FEL have demonstrated that there should be no problem in meeting the more modest duty factor requirements of 4GLS. In the BESSY FEL design the electrons leave the gun at an energy of 4 MeV.

For comparison, Table 5.5 shows both the 4GLS and the BESSY FEL injector requirements. Note that although the required 4GLS bunch length is less than a third of that for the BESSY FEL, the bunch charge is scaled by a similar amount.

Table 5.5 Comparison of beam parameters required at the exit of the 4GLS XUV-FEL and BESSY FEL injectors

Parameter	4GLS	BESSY FEL	
Bunch charge	1	2.5 to 3	nC
Fundamental RF frequency	1.3	1.3	GHz
Bunches per train	1	3	
Train repetition rate	1	1	kHz
Normalised emittance	< 2	1.5	mm mrad
Duty factor	~ 1.75	2.5	%
Uncorrelated energy spread	< 0.05	0.007	%
Bunch length (σ)	2	9	ps

5.4.3.2 Cathode Choice

The photocathode for the XUV-FEL injector needs to combine high QE with a short response time. At present, it is thought that developments of Cs_2Te, which is a relatively robust material with a QE of several percent (with UV drive lasers), will provide a solution for this gun. Importantly Cs_2Te is sufficiently resistant to contamination from the residual gas to operate within RF cavities [8]. Furthermore, since the material does not rely on a thin dipole layer at the surface to enhance the quantum efficiency, it is less susceptible to the effects of damage by ion back-bombardment. Steps may have to be taken to curb the effects of RF power dissipated in the cavity walls and within the cathode itself. Caesium telluride is already employed in both normal and superconducting RF guns with strategies developed for fast replacement of used photocathodes [33].

5.4.3.3 Laser System

The requirement to deliver a charge of 1 nC from a Cs_2Te cathode means that the laser amplifier design for the XUV-FEL photoinjector will be rather different from that for the high average current loop. The cathode's threshold photon energy is sufficiently high that frequency quadrupling of the laser output will be needed to reach it. Assuming 1 % quantum efficiency, a laser pulse energy of ~ 0.5 μJ will therefore be required at the cathode. Budgeting for 30 % losses in beam transport and 50 % in conditioning raises the energy to ~ 1.4 μJ from the frequency quadrupler. The quadrupling process will be relatively inefficient, particularly if it must preserve enough bandwidth to sustain sub-picosecond rise and fall-times. If 7 % conversion from the infrared can be achieved then the pulse energy required from the laser will be 20 μJ.

To date fibre laser systems have not delivered broad bandwidth pulses with energies as high as 20 μJ. Even using CPA with a photonic crystal fibre the maximum output was approximately an order of magnitude below this [23]. Fortunately, alternative technologies are available. Regenerative amplifiers operate comfortably at a pulse rate of 1 kHz and a conventional diode-pumped ytterbium-based device has already delivered 65 μJ pulses at this rate with bandwidth corresponding to 0.5 ps duration [34]. An amplifier based on thin disc technology has generated similar pulses at rates up to 45 kHz [35] which may be useful if the laser is to be future-proofed against increases in the XUV-FEL pulse rate.

5.4.3.4 Diagnostics

The diagnostics for the XUV-FEL injector are required to fully characterize the electron bunch in all six phase space dimensions. The FEL demands the highest beam possible quality including low emittance, low energy spread and high peak current. The diagnostics must be able to measure each of these quantities and beyond that assist in determining the key parameters that affect the beam quality. These include RF fields that accelerate and focus the beam and the magnetic fields that bend and focus it. The lower repetition rate of this injector compared with the high average current injector allows the use of more diagnostics that are destructive to the beam such as YAG screens and RF deflecting cavities. The diagnostic capabilities required are at or beyond state-of-the-art, making it important to have redundant measurement methods. The proposed diagnostic layout for the injector and the subsequent beam transport system, is shown in Figure 5.7.

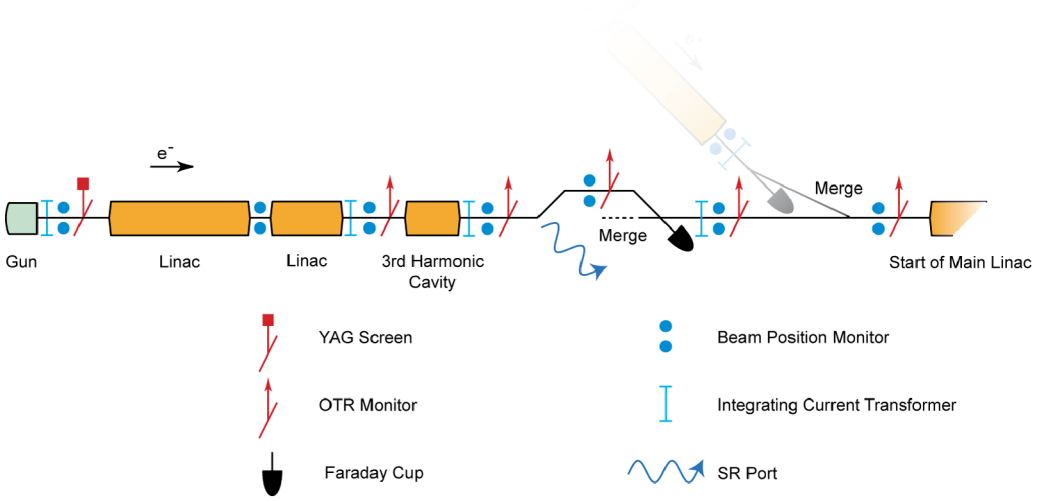

Figure 5.7 Schematic layout of the diagnostics for the XUV-FEL injector system

5.5 IR-FEL Injector System

The IR-FEL injector system is linked to the XUV-FEL and high average current injectors by the requirement to synchronise these electron sources very precisely. If the stability requirements can be met by a thermionic gun, then this is likely to be the chosen technology as it is cost effective, mature and reliable; therefore little study of the possible solutions has been done in this report.

A range of energies between 25 to 60 MeV is required to produce the range of wavelengths required by the users (see Chapter 8). The details of the pulse structure to be supported will be decided following further user consultation during the TDR phase.

5.5.1 Beam Requirements

The specification for the electron beam at the exit of the accelerating module after the IR-FEL injector is given in Table 5.6*:*

Table 5.6 Beam parameters required at the exit of the accelerating module after the IR-FEL injector

Parameter	Value	
Bunch charge	200	pC
Bunch repetition rate	13	MHz
Peak current	8 to 80	A
Energy	25 to 60	MeV
Normalised emittance	< 10	mm mrad
Energy spread (RMS)	< 0.1	%
Bunch length (σ)	1 - 10	ps

5.5.2 Layout

The high average current injector will probably comprise the following major components:

- electron gun;
- solenoids;
- buncher.

The layout of the IR-FEL injector is shown in Figure 5.8.

5.5.3 IR-FEL Injector Components in Detail

The IR-FEL injector system will consist of a thermionic electron gun, which it might be possible to purchase off-the-shelf. However, there is one aspect of the system that has to be comparable with the other injectors; this is the requirement to synchronise this source with all the other photon sources in 4GLS. Following a more detailed study outside the scope of this report, synchronisation requirements may mean that a photoinjector is also preferred here.

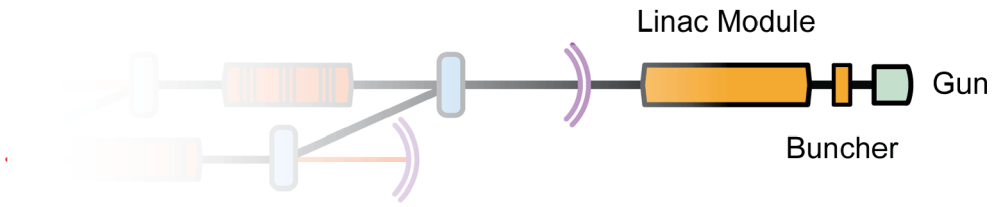

Figure 5.8 Layout of the IR-FEL injector

If a thermionic gun is chosen, it will be followed by a buncher; there will then be one or more linac modules to accelerate the electrons up to a maximum energy of 60 MeV.

5.5.3.1 Gun

Thermionic guns with modulation of the electron beam at megahertz frequencies are widely used in the FEL community. For example, the modulation scheme described in [36] has been used already for several years and produces 350 ps beam pulses with a charge of 240 pC at repetition rate of 25 MHz.

5.5.3.2 Laser System

If a photoinjector is chosen for the IR-FEL, then the gun and associated laser system could be based straightforwardly on the TJNAF design [37]. The pulse energy from this laser has been measured at 300 nJ at a pulse rate of 75 MHz (more than five times the rate required for the 4GLS IR-FEL). Assuming 65 % losses in beam conditioning and transport the pulse energy at the cathode would need to be 100 nJ, which would generate a bunch charge of 430 pC from a 1 % efficient cathode. This exceeds the IR-FEL requirement by more than a factor of two.

5.5.3.3 Diagnostics

The IR-FEL injector will equipped with a full complement of diagnostics appropriate to measure the electron beam properties and to provide input signals for the machine protection system. These will consist of a combination of beam position monitors, integrating current transformers and YAG screens. This is shown in Figure 5.9.

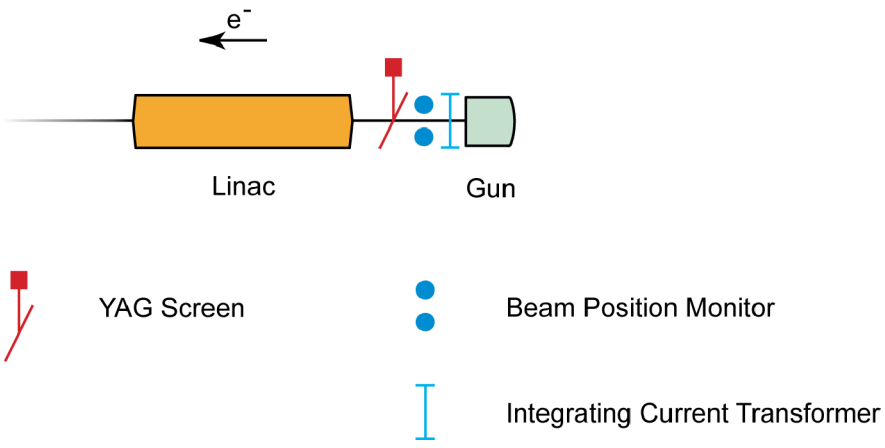

Figure 5.9 Schematic layout of the diagnostics for the IR-FEL injector system

5.6 Existing Relevant Projects

CCLRC are pursuing a number of projects that the design of 4GLS will be built upon. In addition there are many other groups working on similar topics.

The projects that CCLRC are already involved in are:

5.6.1 The Energy Recovery Linac Prototype (ERLP)

The ERLP project at is based on the TJNAF DC photoinjector gun and will operate at a nominal accelerating voltage of 350 kV and bunch charge of 80 pC. Electrons will be generated at a GaAs photocathode by the frequency-doubled light (532 nm) of a mode-locked Nd:YVO_4 laser with an oscillator frequency of 81.25 MHz. Two solenoids will be used for transverse focusing and emittance compensation and a normal-conducting single-cell buncher cavity will be utilised to decrease the bunch length from the GaAs cathode. The buncher cavity will be operated at 1.3 GHz and is based on the buncher design employed at the ELBE facility, FZR. Electrons are accelerated to an energy of 8.35 MeV in the booster linac, which consists of two superconducting 9-cell TESLA-type cavities operated at 1.3 GHz. The cryomodule design is based on the ELBE linac design [38]. A detailed description of the injector design can be found in [14].

The ERLP DC photoinjector will be operated at the maximum bunch repetition rate of 81.25 MHz, i.e. one in every sixteen RF buckets will be filled. Trains of 80 pC bunches, 100 μs long, will be produced at a maximum of 20 Hz, giving an average current of 13 μA.

The transverse properties of the electron bunch at the cathode are partly determined by the cathode laser parameters whereas the longitudinal profile is dominated by the GaAs cathode for short laser pulses due to the rather long response time of GaAs. When modelling the ERLP injector, a longitudinal Gaussian distribution with a length of 20 ps (RMS) was assumed. The transverse distribution was chosen to be Gaussian with a beam size of 1.25 mm (RMS) truncated at +/- 2 sigma. The layout of the ERLP injector and simulation results for the evolution of the RMS values of the beam size, normalised emittance and bunch length are shown in Figure 5.10. The simulations show that an normalised emittance of < 2 mm mrad can be achieved at the end of the injector at an energy of 8.35 MeV and charge of 80 pC.

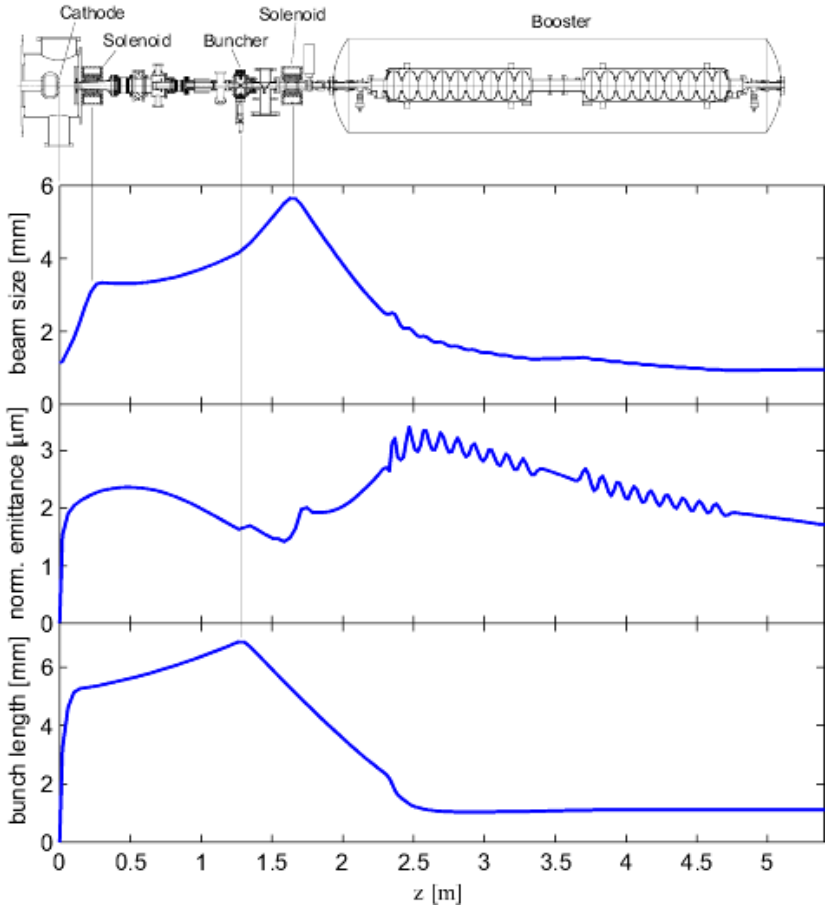

Figure 5.10 ERLP injector layout and electron bunch properties (from simulation)

To determine how the injector performance translates to FEL output, full start-to-end simulations of the ERLP including the FEL interaction were carried out using a suit of accelerator programmes [39]. The beam dynamics in the gun and the superconducting booster were modelled using the particle tracking code ASTRA. After the booster, particles were tracked with the code ELEGANT. The 3D code GENESIS 1.3 was used to model the FEL interaction with the electron beam. The results are illustrated in Figure 5.11. The optimisation and characterisation of the performance of all three injector systems within 4GLS will require extensive simulations using suitable codes and will build on the techniques and experience gained simulating and operating the ERLP.

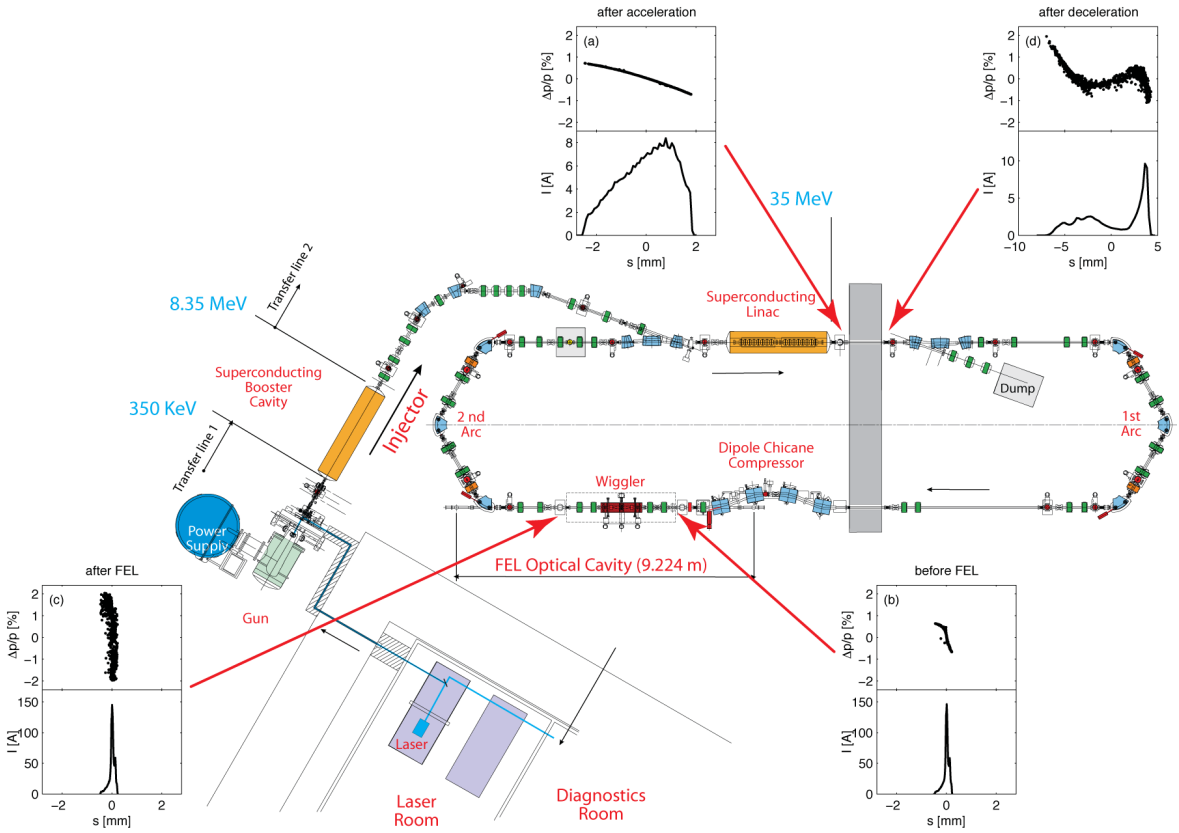

Figure 5.11 Illustrative results from start to end simulations of the ERLP, including both FEL interaction and energy recovery

5.6.2 Gun Developments at Forschungszentrum Rossendorf

CCLRC are participating in the development of superconducting RF guns at Forschungsentrum Rossendorf (FZR) as part of a EU FP6-funded programme called EuroFEL (see http://www.eurofel.org). RF modelling and beam tracking of the ELBE 3.5 cell superconducting gun currently under construction will be undertaken and compared with measurements at the ELBE facility. This gun relies on a novel RF focussing approach for emittance compensation. These results will be used to design further developments of the superconducting gun suitable for high-average current operation. The improved injector design will then re-characterised at ELBE.

5.6.3 The PITZ Collaboration at DESY-Zeuthen

CCLRC are participating in the development of diagnostics for injectors as a member of the PITZ collaboration, also partly funded by EuroFEL. This consists of the design of a module for phase space tomography based on a set of multiple quadrupoles and view screens.

5.7 Conclusion and Further Work

This chapter has identified the three solutions to the requirements for the three injector systems required for 4GLS. These are as follows:

- a high-average current injector based on a development by Cornell of the DC photoinjector used on the IR-FEL facility at TJNAF. The gun will operate at several hundred thousand volts DC and produce 77 pC bunches at 1.3 GHz, giving an average beam current of nearly 100 mA;

- a high-brightness injector for the XUV-FEL based on the development of the PITZ photoinjector for the BESSY FEL. The gun will operate at few million electron volts, producing 1 nC bunches at 1 kHz;

- a thermionic gun for the IR-FEL, producing 200 pC bunches at 13 MHz, which when followed by a buncher and one or more linac modules will give a final energy of 25 to 60 MeV.

All three of these proposals are within a reasonable extension of the present state-of-the-art and therefore are expected to be achievable. Nevertheless there are a number of technical areas that it will be necessary to make progress in:

- 100 mA operation of photoinjectors at < 2 mm mrad emittance;
- cathode efficiency and lifetime with high-average currents;
- diagnostics suitable for use with high-average current beams;
- high-duty factor operation of high-brightness photoinjectors, including the use of superconducting technology.

CCLRC is already taking a role in a number of injector development projects, to assist in achieving progress on these issues. A significant expansion of development work and prototyping is planned for the future.

REFERENCES

[1] T. Srinivasan-Rao, et al., 'Photoemission studies on metal using picosecond ultraviolet laser pulsers' J. Appl. Phys. 69 (1991) 3291.

[2] T. Siggins et al, 'Performance of a DC GaAs photocathode gun for the Jefferson lab FEL', NIM A 475 (2001) 549.

[3] K. Flötmann, 'Note on the thermal emittance of electrons emitted by cesium telluride photocathodes', TESLA-FEL 97-01 (1997).

[4] B. Dunham et al, 'Emittance measurements for the Illinois/CEBAF polarised electron source' 1995 PAC, p1030.

REFERENCES, Continued

[5] I. Boscolo and P. Michelato, 'Photocathodes: the state of the art and some news', NIM A 445 (2000) 389.

[6] P. Michelato et al, 'Characterization of Cs_2Te photoemissive film: formation, spectral responses and pollution', NIM A 393 (1997) 464.

[7] D. H. Dowell, et al., 'First operation of a photocathode radio frequency gun injector at high duty factor', Appl. Phys. 63 (15) (1993) 2035.

[8] J.-G. Marmouget et al, 'Present performance of the low emittance, high bunch charge ELSA photoinjected linac' Proceedings of EPAC 2002, p 1795.

[9] A. Burrill et al, 'BNL superconducting RF guns–technology challenges as ERL sources', NIM. A 557 (2006) 75.

[10] A. di Bona et al, 'Development, operation and analysis of bialkali antimonide photocathodes for high-brightness photo-injectors', NIM A 385 (1997) 385.

[11] K. A. Elamrawi et al., 'Atomic hydrogen-cleaned GaAs(100) negative electron affinity photocathode: Surface studies with reflection high-energy electron diffraction and quantum efficiency', J. Vac. Sci. Technol. A 18(3) (2000) 951.

[12] P.Hartmann et al, 'Picosecond polarized electron bunches from a strained layer GaAsP photocathode', NIM A 379 (1996) 15.

[13] C Sinclair, 'DC photoemission electron guns as ERL sources', NIM A 557 (2006) 69.

[14] C. Gerth, F.E. Hannon: 'Injector Design for the 4GLS Energy Recovery Linac Prototype', EPAC'04, Lucerne, July 2004.

[15] I. Ben-Zvi Collider-Accelerator Department Accelerator Physics Note C-A/AP/149, April 2004.

[16] G. R. Neil et al: 'Sustained Kilowatt Lasing in a Free-Electron Laser with Same-Cell Energy Recovery', Physical Review Letters, 84 (4), 2000, p 662.

[17] D. H. Dowell et al: 'First Operation of a High Duty Factor Photoinjector', PAC, 1993, p 2967.

[18] D. H. Dowell et al: 'First operation of a photocathode radio frequency gun injector at high duty factor', Applied Physics Letters, 63, p. 2035, 1993.

[19] S.S. Kurennoy et al., 'Normal-conducting high current RF photoinjector for high power CW FEL', PAC2005, p 2866.

[20] I. V. Bazarov, C. K. Sinclair: 'High-brightness, high current injector design for the Cornell ERL prototype', PAC, 2003, p2062.

REFERENCES, Continued

[21] I. V. Bazarov, C. K. Sinclair: 'Multivariate optimisation of a high-brightness dc gun photoinjector', Phys Rev STAB 8, 034202, 2005..

[22] P. Dupriez et al, '321 W average power, 1 GHz, 20 ps, 1060 nm pulsed fiber MOPA source', OFC 2005 paper PD3.

[23] F. Röser et al, '131 W, 220 fs fiber laser system', Opt Letts 30 (2005) p.2754.

[24] C. H. Liu et al, 'High-power single-polarization and single-transverse-mode fiber laser with an all-fiber cavity and fiber-grating stabilized spectrum', Opt Letts 31 (2006) p.17.

[25] D.J.Holder et al: 'ERLP Gun Commissioning Beamline Design', LINAC'04, Luebeck, August 2004.

[26] R. Bakker et al: 'First Measurements at the Photo Injector Test Facility at Desy Zeuthen', EPAC 2002, p1813.

[27] K. Batchelor, et al, 'Performance of the Brookhaven Photocathode RF Gun', NIM A, 318, pp372-6, (1992).

[28] S. Schreiber, et al: 'Emittance Measurements at the TFF Photoinjector', PAC 2001, p86.

[29] D.T. Palmer et al., Beam dynamic enhancemet due to acclerating field symmetrization in the BNL/SLAC/UCLA 16-cell S-band photocathode gun, PAC1997, p 2846.

[30] S. Schreiber, First experiments with the RF gun based injector for the tesla test facility linac, PAC, 1999, p 84.

[31] J.-P. Carneiro et al, First Results of the fermilab high-brightness RF photoinjector, PAC1999.

[32] F. Marhauser, Finite Element Analyses for RF Photoinjector Gun Cavities, TESL-FEL Report 2006-02.

[33] I. Ben-Zvi and I. V. Bazarov, 'Summary, Working Group 1: Electron guns and injector designs', NIM A 557 (2006) 337.

[34] H. Liu, J. Nees and G. Mourou, 'Directly diode-pumped Yb:KY(WO4)2 regenerative amplifiers', Opt Letts 27 (2002) p722.

[35] A. Beyertt, D. Nickel and A. Giesen, 'Femtosecond thin disk Yb:KYW regenerative amplifier', Appl Pys B 80 (2005) p655.

[36] B.J.H. Meddens et al. Nucl. Instr. And Meth. A385(1997)195-203

[37] S. Zhang et al, 'Characterization and performance of a high-power solid-state laser for a high-current photo-cathode injector', Proc 27th International Free Electron Laser Conference (2005) p351.

REFERENCES, Continued

[38] A Buchner, A.: 'The ELBE-Project at Dresden- Rossendorf', EPAC'00, Vienna, June 2000.

[39] C. Gerth, M. Bowler, B. Muratori, H.L. Owen, N.R. Thompson, B. Faatz, B.W.J. McNeil, 'Start to End Simulations of the Energy Recovery Linac Prototype FEL', Proceedings of the 2004 FEL Conference, 270-273.

6. 4GLS Superconducting Linacs

The choice of accelerator technology is reviewed in this chapter, identifying superconducting RF (SRF) as being the most appropriate solution for CW or high repetition rate accelerators, particularly those employing Energy Recovery Linac (ERL) techniques, such as that being proposed for 4GLS. The RF frequency choice and operating temperature are reviewed and solutions are proposed. Providing the required acceleration for each linac stage of 4GLS appears to be achievable using predominantly the same cavity/cryomodule configuration, and the fundamental requirements for such an accelerating system are presented. Based on TESLA/TTF technology at 1.3 GHz, cavity/cryomodule modifications are required to sustain CW and/or high repetition rate operation on 4GLS and these modifications are highlighted. For the High Average Current Loop (HACL) injector, substantially more RF power is needed and so an alternative cavity/cryomodule system is proposed based on a solution developed by Cornell University. Effective damping of the higher order modes (HOM) for each of the 4GLS linacs will be critical in maintaining the high degree of beam stability required for optimal lasing at the free electron laser (FEL) insertion devices. Techniques for both delivering the required RF power and damping of the induced HOMs are identified and solutions proposed. Precise low level RF (LLRF) amplitude and phase stability (and subsequent synchronisation) of each linac accelerator must be maintained, requiring sophisticated state-of-the-art digital feedback and feed-forward systems and various techniques are investigated.

6.1 SRF Application for 4GLS

SRF cavities excel in applications requiring continuous wave (CW) or long pulse operation at high accelerating gradients (E_{acc}). Since resistive losses in cavity walls increase as the square of the accelerating voltage, conventional copper cavities become uneconomical when the demand for high CW voltage grows with particle energy requirements. SRF has the major advantage that the surface resistance of a superconductor is five orders of magnitude less than that of copper. The geometry of SRF cavities results in reduced wakefields and therefore reduced collective effects on the beam. Typically, after accounting for the refrigeration power needed to provide the liquid helium, a net gain factor of several hundred remains (in terms of the total AC power) for SRF over conventional normal conducting (NC) copper cavities in providing the required RF power.

The present scheme for 4GLS utilises three electron sources:

1. a high peak current, RF gun feeding a seeded XUV-FEL;
2. a high average current, DC gun feeding a VUV-FEL and a number of spontaneous synchrotron sources;
3. a modest current, thermionic gun feeding a IR-FEL.

Electron beams will be accelerated on 4GLS through superconducting linacs, each operating at 1.3 GHz (see Figure 6.1) so that utilisation can be made of much of the TESLA and TTF development work that has taken place at this frequency [1].

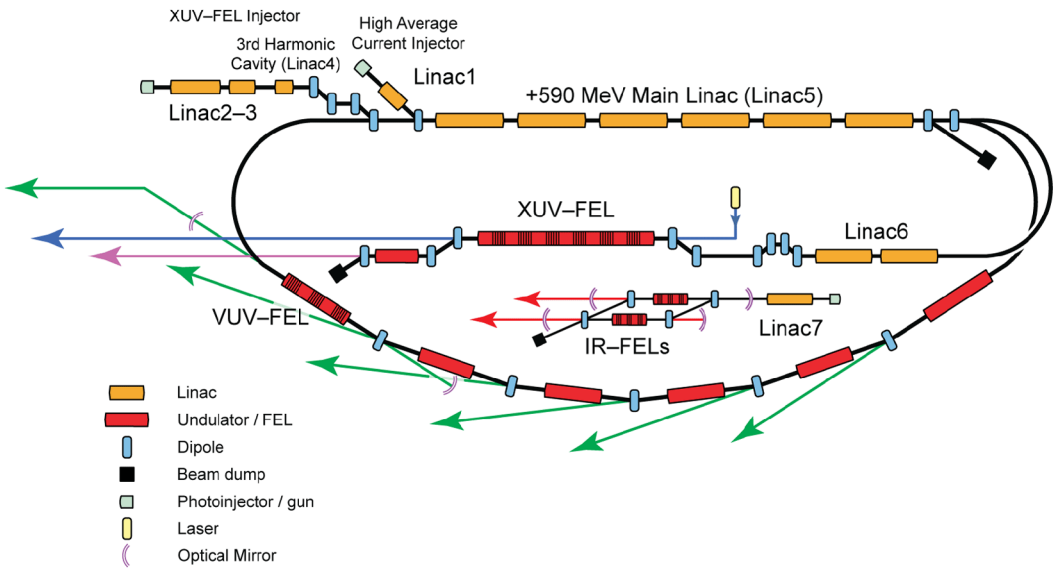

Figure 6.1 4GLS Accelerator conceptual layout and SRF linac conventions

The accelerator system design for 4GLS requires the study of multiple bunches accelerating through a single linac with different charges, and assessments made on the effects of potential beam break-up. There are a total of seven distinct accelerating linacs proposed for the 4GLS accelerator, each having their own RF and beam dynamics requirements. There are issues to be resolved regarding each of these accelerating systems to ensure that not only the 4GLS design requirements are met, but also that a reliability commensurate with a conventional synchrotron light source is achieved and maintained. Preliminary proposals are identified here for RF parameters such as frequency (f_{RF}), E_{acc}, cavity geometry, HOM damping, cryomodule layout, cavity tuning, power coupling and LLRF feedback systems. However a more detailed investigation and subsequent validation/justification will be needed at the technical design stage to refine the chosen solutions for 4GLS. This chapter will not cover details of the cryogenic system as this is detailed more thoroughly in Chapter 14 (Technical Systems – Cryogenics Systems).

6.1.1 The High Average Current Injector Linac1 (CW)

For Linac1, the requirement here is not for high E_{acc} but is to deliver enough RF power to accelerate the high average current beam (100 mA) up to 10 MeV. It is proposed that the cavity scheme to be employed is similar to the ERL injector system developed at Cornell [2]. At an

operating frequency of 1.3 GHz, it utilises a 2-cell cavity geometry with a dual RF input coupler (see Figure 6.2) which is employed to cancel any asymmetric kick that may be imparted to the low energy beam.

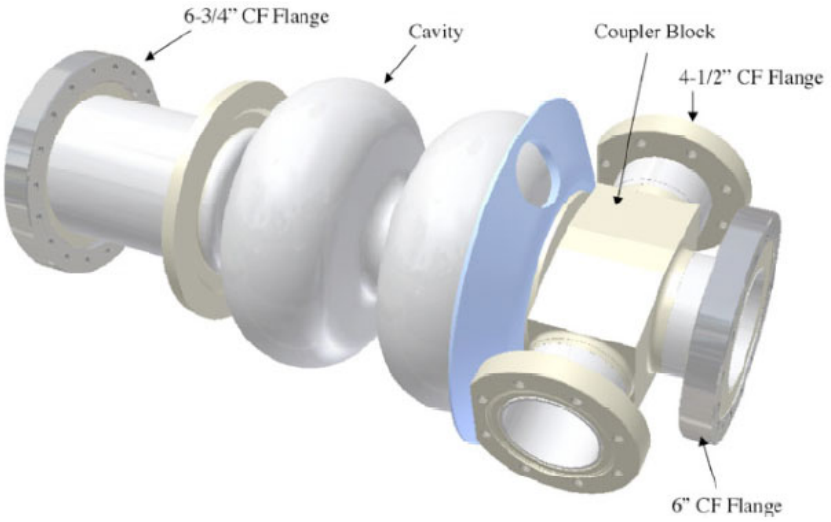

Figure 6.2 Cornell 2-Cell CW injector cavity design (courtesy Cornell University)

Linac1 has the lowest E_{acc}, yet the RF power requirement for this CW Linac is most notably the largest of all the 4GLS linacs. The primary challenge facing the design of this linac, both for the Cornell ERL and 4GLS, is in the development of a suitable RF input coupler capable of delivering the required CW power at 1.3 GHz. The anticipated RF parameters for this linac are shown in Table 6.1.

Table 6.1 Linac1 operating parameters

Bunch Charge (pC)	77
Average Current (mA)	100
Bunch Repetition Rate (MHz)	1300
RF Frequency (GHz)	1.3
Number of cells/cavity	2
Number of Cavities	10
Number of Modules	2
Cavity R/Q (Ω)	218
Q_o	10^{10}
Energy Gain (MeV)	10
E_{acc} (MV/m)	4.3
Q_e	1×10^5
Cavity Filling Time (μs)	12.2
RF Power per Cavity (kW)*	100

** Note that we adopt here the definition of shunt impedance by the relation $R = V^2/P$, where P is the dissipated power and V the peak voltage in the equivalent parallel LCR circuit.*

Coupling RF power into each RF cavity is optimally achieved by choosing an appropriate external Q (Q_e) with regards to the minimum RF power needed to accelerate the beam (Q_e^{beam}) and similarly to generate the cavity accelerating voltage (Q_e^{cavity}). The optimum Q_e^{beam} for a cavity (see Equation 6-1) can be derived from the maximum accelerating voltage (V_{acc}) needed to accelerate an average beam current (I_b) via a cavity with known *R/Q* and operated at some phase with respect to the main RF signal (ϕ_b). This is defined by;

$$Q_e^{beam} = \frac{V_{acc}}{\frac{R}{Q} I_b \cos\phi_b} \tag{6-1}$$

The cavity bandwidth ($\Delta\varpi$) for the accelerating cavity must be chosen such that any susceptibility to microphonic instabilities are minimised wherever possible and so the Q_e^{cavity} can be defined as;

$$Q_e^{cavity} \approx \frac{1}{2}\frac{\varpi_c}{\Delta\varpi} \tag{6-2}$$

The optimum Q_e for the accelerating system must therefore be somewhere between Q_e^{beam} and Q_e^{cavity}. For this heavily beam loaded 4GLS linac, a Q_e of 1 x 10^5 has been chosen as it allows for a large operating bandwidth (6.5 kHz) whilst maintaining the RF power required to an achievable level. Increasing the accelerating voltage further, for example if a single cavity cannot provide its required voltage, will necessitate a re-optimisation of Q_e which is typically performed using impedance transformers, such as 3-stub tuners or E-H tuners in the feeder waveguide system. If beam acceleration is insensitive to cavity microphonics, by means of precise amplitude and phase correction through LLRF controls, then a larger Q_e will minimise the total RF power even further than what has been predicted here. The RF power needed to accelerate the CW-beam is simply a product of V_{acc} and the average beam current I_b, whereby

$$P_{beam} = V_{acc} I_b \tag{6-3}$$

The high average current injector Linac1 requiring a V_{acc} = 10 MV for an I_b = 100 mA gives a total beam power of P_{beam} = 1 MW. There will be ten 2-cell cavities providing the acceleration, giving a beam power/cavity requirement of 100 kW. At the chosen Q_e of 1 x 10^5 the cavity power (P_c) needed to generate the required V_{acc} can be determined from Equation 6-4, which equates to 46 kW/cavity.

$$P_c = \frac{V_{acc}^2}{\frac{R}{Q} Q_e} \tag{6-4}$$

The vast majority of this power will be reflected from each cavity when beam is not being accelerated. When beam arrives at the cavity, it absorbs the full 46 kW/cavity and requires

another 54 kW/cavity (100 kW/cavity in total) to sustain acceleration of the 100 mA of beam current.

6.1.2 The XUV-FEL Injector Linac2 (1 kHz)

Linac2 will be operated at a repetition rate of 1 kHz to accelerate a 1 nC bunch charge up to 95 MeV. As the fill-time for the SRF cavities is long (~ 1.6 ms), the accelerating field within the cavity will be generated in CW-mode, whilst actual beam acceleration will only occur at the 1 kHz repetition rate.

Table 6.2 Linac2 operating parameters

Bunch Charge (pC)	1000
Average Current (mA)	0.001
Bunch Repetition Rate (MHz)	0.001
RF Frequency (GHz)	1.3
Number of cells/cavity	7
Number of Cavities	8
Number of Modules	1
Cavity R/Q (Ω)	805.8
Q_o	10^{10}
Energy Gain (MeV)	95
E_{acc} (MV/m)	14.7
Q_e	1.3×10^7
Cavity Filling Time (ms)	1.6
RF Power per Cavity (kW)	13

The cavity scheme for Linac2 will be an adaptation of the TESLA/TTF 9-cell cavity and is detailed more thoroughly in Section 6.4. Table 6.2 highlights the main RF operating parameters for Linac2. For the 13.9 MV/m gradient and an average accelerated beam current of I_b = 1 μA, the chosen Q_e (as estimated from Equations 6-1 and 6-2) is 1.3 x 10^7. For this injector linac, a bandwidth of 100 Hz has been chosen in order to limit both the RF power needed and its susceptibility to microphonics. The RF power required to accelerate the beam (from Equation 6-3) is only 12 W/cavity. From Equation 6-4, the RF power needed to generate the accelerating voltage for Linac2 is P_c = 13 kW, which subsequently provides the power for beam acceleration.

6.1.3 The XUV-FEL Injector Linac3 (1 kHz)

Linac3 will have exactly the same operating gradient and RF power requirements as that for Linac2, necessitating 12.1 kW/cavity at a $Q_e = 1.3 \times 10^7$ (see Table 6.3).

Table 6.3 Linac3 operating parameters

Bunch Charge (pC)	1000
Average Current (mA)	0.001
Bunch Repetition Rate (MHz)	0.001
RF Frequency (GHz)	1.3
Number of cells/cavity	7
Number of Cavities	8
Number of Modules	1
Cavity R/Q (Ω)	805.8
Q_o	10^{10}
Energy Gain (MeV)	95
E_{acc} (MV/m)	14.7
Q_e	1.3×10^7
Cavity Filling Time (ms)	1.6
RF Power per Cavity (kW)	13

Exiting Linac3 the beam will have an energy of 190 MeV which is then decelerated in Linac4.

6.1.4 The XUV-FEL Injector Harmonic Linac4 (1 kHz)

For the high peak current injector feeding the XUV-FEL, the beam is run off-crest from the peak RF voltage in order to create a particle time versus energy correlation. The correlation is used to compress the bunch when it is run through a subsequent bunch compression chicane. The sine-wave profile of the RF waveform sets the correlation by running the bunch off crest and is non-linear.

Table 6.4 Linac4 operating parameters

Bunch Charge (pC)	1000
Average Current (mA)	0.001
Bunch Repetition Rate (MHz)	0.001
RF Frequency (GHz)	3.9
Number of cells/cavity	9
Number of Cavities	4
Number of Modules	1
Cavity R/Q (Ω)	375
Q_o	10^{10}
Energy Gain (MeV)	-30
E_{acc} (MV/m)	14.5
Q_e	5×10^6
Cavity Filling Time (ms)	0.2
RF Power per Cavity (kW)	13.3

A third harmonic RF accelerating linac, with its higher frequency, has a much steeper RF voltage gradient versus time. The beam is run on the decelerating phase through the harmonic RF waveform (at close to -180^{o}) to remove most of the second order, non-linear part of the correlation, whilst imparting a net deceleration of ~ 30 MeV. It may also be that chromatic correction using sextupole magnets could negate the need for a higher harmonic RF system and compression chicane and investigations are presently ongoing (see Chapter 8, Electron Beam Transport). As yet, a more detailed beam dynamics study needs to be completed to define the RF requirements for Linac4. However, Fermilab have developed a 3.9 GHz accelerating module to be used on TTF [3] for this same application. This would be an attractive solution for 4GLS and Table 6.4 shows some anticipated RF parameters for this 3.9 GHz RF system. A number of FEL-based accelerators have proposed (and are developing) harmonic RF systems to compensate for this non-linear energy distortion, such as LCLS [4], BESSY-FEL [5], Cornell ERL [6] and TTF VUV-FEL [7].

6.1.5 The Main 4GLS Linac5 (CW and 1 kHz)

The main accelerating linac for 4GLS Linac5 is used to simultaneously accelerate both the 10 MeV CW (high average current) beam up to 600 MeV and the 160 MeV, 1 kHz (high peak current) beam up to 750 MeV, whilst also decelerating the energy recovered beam before it is dumped. The injected 1 kHz beam will be accelerated to 160 MeV before entering Linac5 to provide a clear distinction in beam energies, enabling beam separation into two paths within the first bending magnet separator (see Chapter 8, Electron Beam Transport). After Linac5, the HACL electron bunches excite a variety of spontaneous sources before returning back through Linac5 again for energy recovery (ER). When operated in ER-mode, the beam loading imposed on the Linac5 cavities will cancel in the accelerating and decelerating phases. For this reason, the power required to accelerate the beam is orders of magnitude lower compared to the equivalent RF power needed to accelerate in a single pass (~ 1.2 MW/cavity in single pass). In this instance, the generator power required to maintain acceleration is given by:

$$P_g = \frac{V_{acc}^2}{4\frac{R}{Q}Q_e}\left\{1+\left(\frac{2\Delta\omega Q_e}{\omega_c}\right)^2\right\} \qquad (6\text{-}5)$$

Whereby $\Delta\varpi$ is the microphonic tolerance bandwidth and $\varpi_c = 2\pi f_c$. The cavity/cryomodule scheme for this large linac will be identical to that of Linac2 and Linac3, and operated at a nominal accelerating gradient of 15.2 MV/m. If a maximum peak detuning of $\Delta\varpi = 25$ Hz from microphonics is assumed, this gives a $Q_e = 2.6 \times 10^7$ for CW beam acceleration (from Equation 6-2). The RF power needed to generate the required accelerating voltage and subsequently accelerate the beam(s) is $P_c = 3.6$ kW/cavity (from Equation 6-5).

By controlling the cavity microphonics further and with good feedback control, it is believed in the ERL community that a Q_e of up to 10^8 (ω_c ~ 6 Hz) can be sustainable [8], which could reduce P_g even further to ~ 900 W. Cleary the ER efficiency has to be high (> 99 %) to

minimise any additional RF power overhead needed. It has also been assumed that the coherent synchrotron radiation (CSR) losses for Linac5 equate to up to 3 MeV/turn (see Chapter 10, Spontaneous Sources, Lasers and Electrons) which for a maximum CW beam current of 100 mA requires an extra 300 kW of total RF power. Distributing this power over the forty eight Linac5 cavities, increases the total RF power by 6.25 kW/cavity, taking the total RF power needed per cavity up to 9.85 kW (see Table 6.5).

Table 6.5 Linac5 operating parameters

Bunch Charge (pC)	77/1000
Average Current (mA)	100/0.001
Bunch Repetition Rate (MHz)	1300/0.001
RF Frequency (GHz)	1.3
Number of cells/cavity	7
Number of Cavities	48
Number of Modules	6
Cavity R/Q (Ω)	805.8
Q_o	10^{10}
Energy Gain (MeV)	590
E_{acc} (MV/m)	15.2
Q_e	2.6×10^7
Cavity Filling Time (ms)	3.2
RF Power per Cavity (kW)	9.85

6.1.6 The XUV-FEL Booster Linac6 (1 kHz)

Table 6.6 Linac6 operating parameters

Bunch Charge (pC)	1000
Average Current (mA)	0.001
Bunch Repetition Rate (MHz)	0.001
RF Frequency (GHz)	1.3
Number of cells/cavity	7
Number of Cavities	16
Number of Modules	2
Cavity R/Q (Ω)	805.8
Q_o	10^{10}
Energy Gain (MeV)	200
E_{acc} (MV/m)	15.5
Q_e	1.3×10^7
Cavity Filling Time (ms)	1.6
RF Power per Cavity (kW)	14.9

The extracted 750 MeV, high peak current beam is further accelerated up to 950 MeV by a 200 MeV Linac6, having the same cavity configuration as Linac5, before passing through the XUV-FEL. There is no requirement for energy recovery of this ~ 1 kW beam and so it will be dumped at high energy (see Chapter 8, Electron Beam Transport). For an optimum Q_e of 1.3 x 10^7, the RF power needed to generate the 15.5 MV/m gradient will be: P_c = 14.9 kW/cavity of which P_{beam} = 13 W/cavity. Table 6.6 shows the RF operating parameters for Linac6.

6.1.7 The IR-FEL Linac7 (13 MHz)

For the IR-FEL Linac, the average accelerated beam current will be 2.6 mA, based on an electron bunch charge of 200 pC operating at a repetition rate of 13 MHz. Only the photon output from this IR source is anticipated to be utilised in conjunction with photon radiation from other 4GLS sources. The RF operating parameters for Linac7 are shown in Table 6.7, illustrating that although this linac will operate at a relatively conservative E_{acc} of 9.3 MV/m, due to the relatively high average beam current of 2.6 mA, the RF power requirements for this Linac will be considerably more than any of the other 7-cell linacs.

Table 6.7 Linac7 operating parameters

Bunch Charge (pC)	200
Average Current (mA)	2.6
Bunch Repetition Rate (MHz)	13
RF Frequency (GHz)	1.3
Number of cells/cavity	7
Number of Cavities	8
Number of Modules	1
Cavity R/Q (Ω)	805.8
Q_0	10^{10}
Energy Gain (MeV)	60
E_{acc} (MV/m)	9.3
Q_e	1.3 x 10^7
Cavity Filling Time (ms)	1.6
RF Power per Cavity (kW)	19.5

The RF power needed to generate the required E_{acc} will be 5.4 kW/cavity and when the beam is accelerated the total power required will be P_{beam} = 19.5 kW/cavity. Methods for delivering this increased RF power requirement are outlined in Section 6.11. A provisional list of RF parameters for each 4GLS Linac are summarised in Table 6.8.

Table 6.8 Summary of 4GLS linac operating parameters

	Linac1	Linac2	Linac3	Linac4	Linac5	Linac6	Linac7
Number of Cells/Cavity	2	7	7	9	7	7	7
Number of Cavities	10	8	8	4	48	16	8
Number of Modules	2	1	1	1	6	2	1
Energy Gain (MeV)	10	95	95	-30	590	200	60
E_{acc} (MV/m)	4.3	14.7	14.7	14.5	15.2	15.5	9.3
Q_e	1×10^5	1.3×10^7	1.3×10^7	5×10^6	2.6×10^7	1.3×10^7	1.3×10^7
Total RF Power/Cavity (kW)	100	13	13	13.3	9.85*	14.9	19.5

**Includes CSR losses*

6.2 ERL Facilities

Many of the world's accelerator laboratories are now viewing the use of SRF linacs as a viable solution for providing a source for intense synchrotron radiation (SR), whilst utilising the advantages of energy recovery (ER) for the main accelerating linac. On July 21st 2004, the Thomas Jefferson National Accelerator Facility (TJNAF) IR-FEL facility paved the way in successfully proving ERL operation for a user facility, generating average powers in excess of 10 kW in the infrared. SRF technology provides an efficient way to accelerate these intense beams to their required operating energies whilst, more importantly minimising the higher order mode (HOM) wakefield contributions that these multi-cell accelerating structures inherently produce. Subsequently, proposals for new ERL accelerators that provide intense SR by way of Free Electron Laser (FEL) insertion devices are now widespread around the world, a selection of which is highlighted.

6.2.1 ERLP (1.3GHz)

CCLRC Daresbury Laboratory has begun construction of an ERL Prototype (ERLP) [9] to gain expertise in the operation of photoinjector guns, SRF cavities and ER techniques (see Figure 6.3). The ERLP consists of a 350 keV DC photoinjector gun to provide an average beam current of 13 μA with a normalised emittance of 5 mm mrad. The gun is designed to operate at a repetition rate of 81.25 MHz. After leaving the electron gun, the electron bunches pass through a 1.3 GHz normal conducting buncher cavity. Bunching is required to reduce the energy spread in the beam to tolerable levels for the FEL to lase successfully.

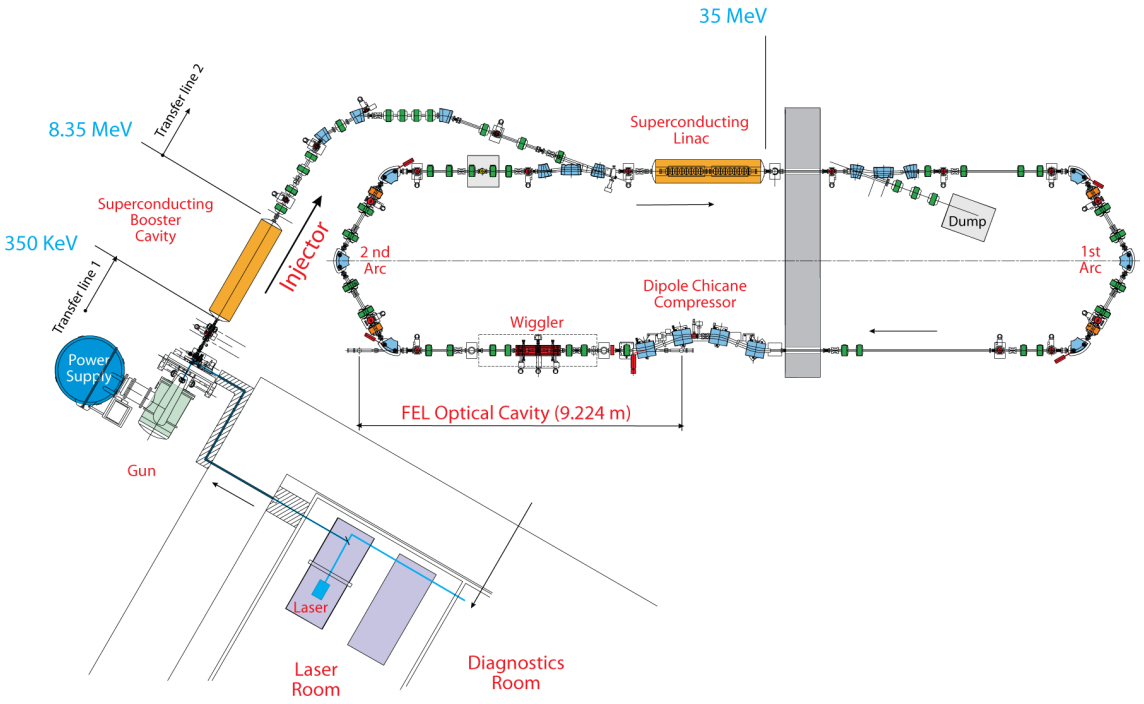

Figure 6.3 ERLP Layout

The beam then passes through the booster SRF module which consists of two TESLA type 1.3 GHz 9-cell cavities operating at ~ 4 MV/m and accelerating the beam to 8.35 MeV. The cavities are powered via a coaxial coupler from two 1.3 GHz inductive output tube (IOT) amplifiers, each providing a peak operating power of 16 kW. Exiting the gun at 350 keV, the electrons are travelling considerably slower than the speed of light when they enter the booster accelerator.

The chosen cavity has not been designed with a reduced cavity length to compensate for the transit time of the non-relativistic beam (the time it takes for the electron bunch to traverse the cell, because $\beta \neq 1$), therefore the phase of the cavity is chosen such that the electrons are initially accelerated off-crest. The beam then passes through the main accelerating module (operating at 13.5 MV/m) where the beam is accelerated to 35 MeV (see Figure 6.4). The beam will then complete one loop of the machine before returning 180^{o} out of phase (with respect to the RF) to the main accelerating module where it is decelerated to 8.35 MeV, after which it is dumped. The energy recovered from this deceleration process is used to accumulate and accelerate the maximum available injected beam current up to 35 MeV.

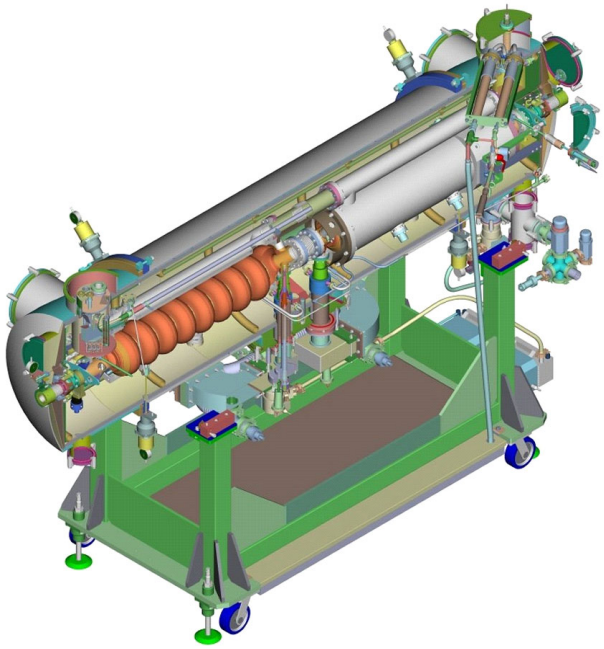

Figure 6.4 ERLP Cavity module layout (courtesy ACCEL Instruments GmbH)

6.2.2 TJNAF ERL Facility (1.5GHz)

The most recent and successful demonstrations of ER was at TJNAF on the IR-Demo FEL (see Figure 6.3). The TJNAF FEL [10] is a sub-picosecond, tuneable light source covering the range from 250 nm in the ultraviolet to 14 μm in the mid-infrared, with pulse energies up to 300 μJ, and at repetition rates up to 75 MHz. Energies in excess of 10 kW average power have been demonstrated in the infrared.

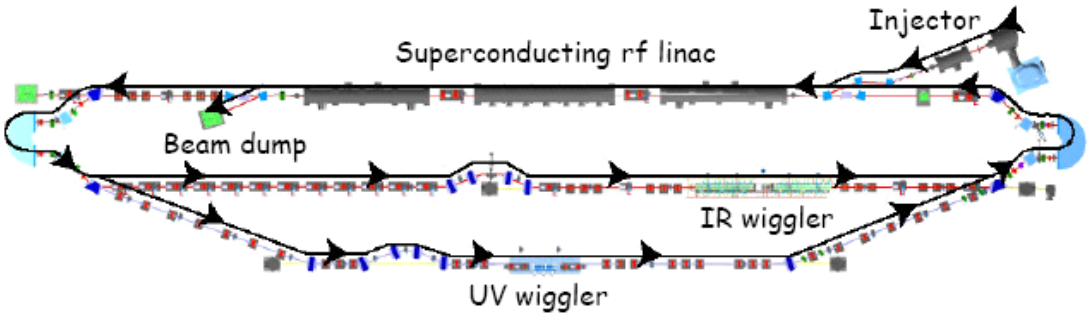

Figure 6.5 JLAB ERL Accelerator complex (courtesy TJNAF)

The electron source is a 350 kV DC photoinjector, followed by a ¼ length module containing two CEBAF 5-cell cavities as an injector module. The cavities operate at 1.5 GHz and use a waveguide coupler as means to introduce power, which are capable of providing up to 50 kW CW RF power. To provide the tuning range required for conditioning of the cavities, 3-stub tuners are employed.

6.2.3 Cornell ERL (1.3GHz, 100mA injector)

Cornell University is exploring the feasibility of an ERL-based light source [2], comprising of a 100 mA, 500 keV DC beam which is bunched in a single 1.3 GHz buncher cavity and then accelerated in five 2-cell SRF cavities to an energy of 5.5 MeV (see Figure 6.6). Up to 500 kW of CW RF power is required to drive the ERL injector, whilst simultaneously removing up to 100 W of beam induced HOMs. At each stage of acceleration, emittance preservation is paramount.

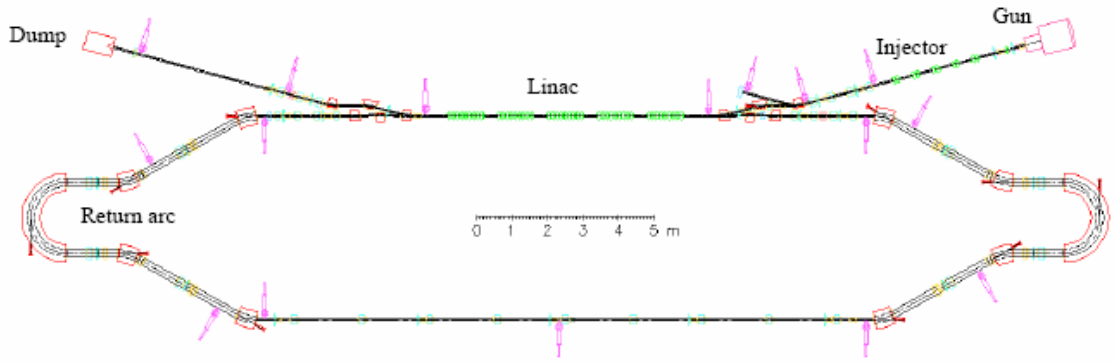

Figure 6.6 Cornell ERL layout (courtesy Cornell University)

The 1.3 GHz cavity design for the Cornell ERL injector cavity is adapted from both the CESR and KEKB cavity design philosophies which operate at ~ 500 MHz [11], whereby one of the beam pipe diameters is opened up to allow HOM propagation to cooled ferrite absorbers housed inside the cryomodule at 80 K (see Figure 6.7). A dual coaxial coupler negates any asymmetric kick imparted to the beam by a conventional single coupler, thereby minimising any emittance growth.

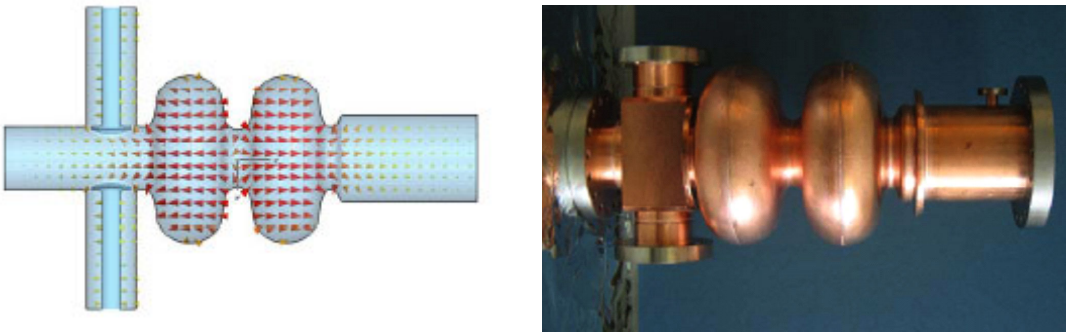

Figure 6.7 Cornell ERL injector cavities (courtesy Cornell University)

The 4GLS high average current Linac1, will adopt this Cornell cavity/cryomodule design in order to achieve the required 10 MeV acceleration for its CW beam. Three different types of absorbing material are used to damp the HOMs to Q's < 1000 for all modes up to 50 GHz, with a maximum power per absorber of 200 W. Parameters for the Cornell ERL prototype accelerator are shown in Table 6.9.

Table 6.9 Cornell ERL operating parameters

	Prototype ERL Injector
Energy (GeV)	0.1
Current (mA)	100
Injection energy (MeV)	5–15
Bunch Repetition Rate (GHz)	1.3
E_{acc} (MV/m)	20
Q_o	10^{10}
Q_{ext}	2.6×10^7
Charge/Bunch (pC)	77
Main Linac Cavities	5

6.2.4 Brookhaven National Laboratory (BNL) ERL Facility (700MHz)

The ERL accelerator at Brookhaven National Laboratory (BNL) is being constructed to demonstrate high current CW operation of an ERL [12] with high ER efficiency (see Figure 6.8).

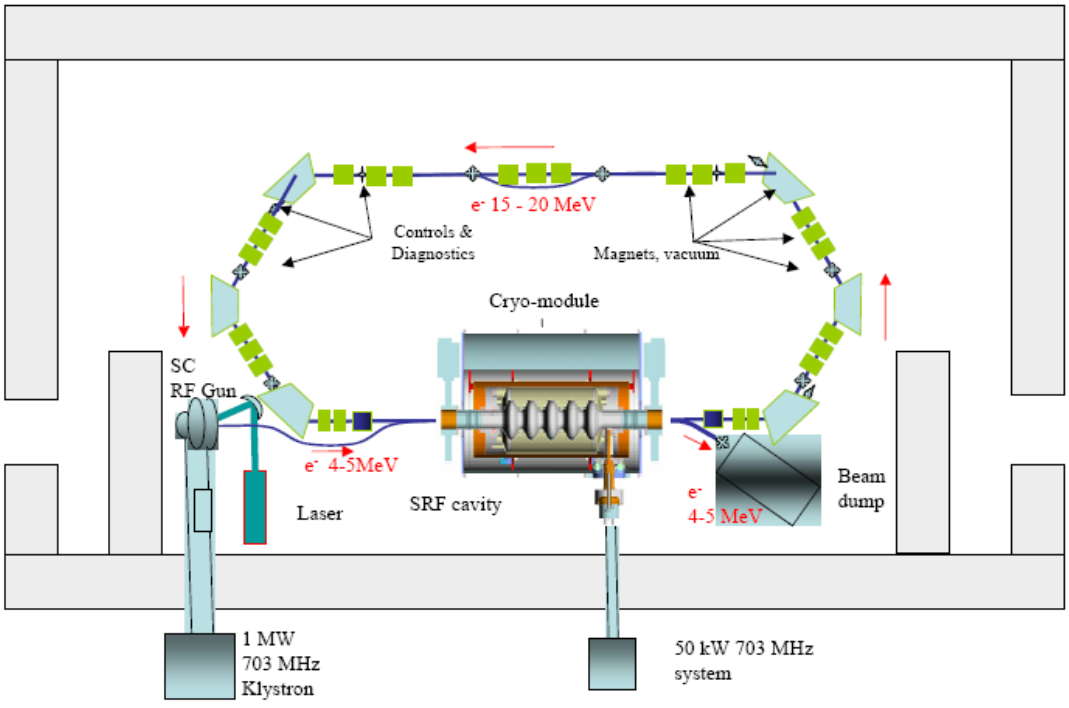

Figure 6.8 BNL ERL accelerator layout (courtesy BNL)

Initially single-pass recovery of up to 500 mA is anticipated, utilising a 5-cell, 703.75 MHz SRF linac with strong HOM damping capability. Successful ER will assist in reaching a ten-fold increase in luminosity for the Relativistic Heavy Ion Collider (RHIC) at BNL [13]. The facility will also allow for testing of feedback systems capable of stabilising intense low energy beams. Developments in 700 MHz RF source technology for APT at LANL have enabled the use of

proven RF power sources to be implemented [14]. Strong HOM damping is achieved in the SRF module by opening the beam pipe diameter so that all HOMs propagate out to external ferrite absorbers, located either side of the cryo-module at room temperature (see Figure 6.9).

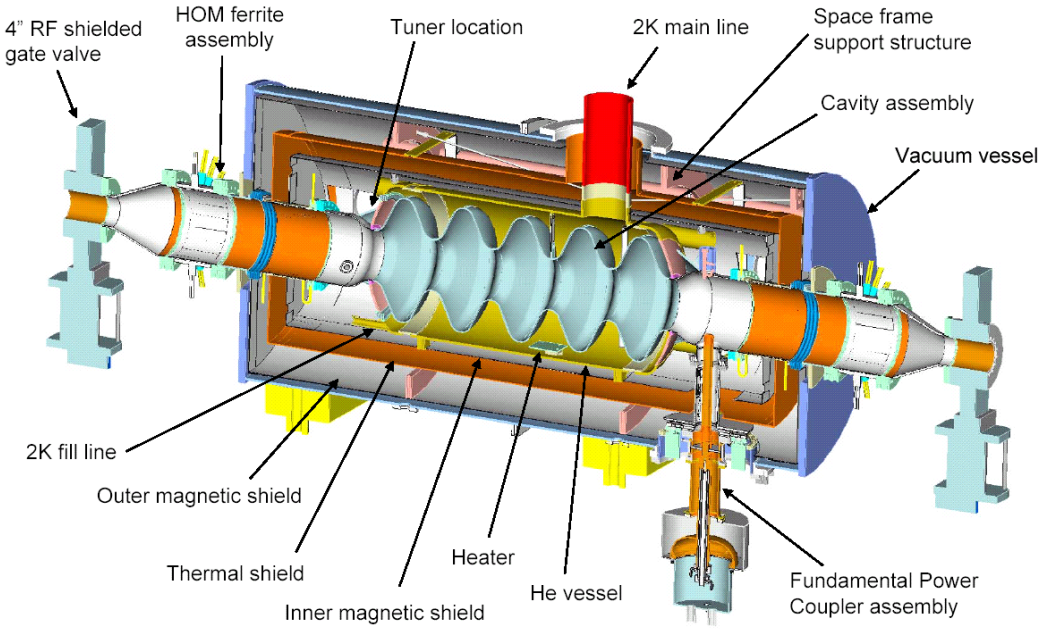

Figure 6.9 BNL Main linac accelerating module (courtesy BNL)

6.2.5 The TTF VUV-FEL (1.3GHz)

The major challenge for the TESLA collaboration was to prove the feasibility and reliability of achieving accelerating gradients well above 20 MV/m i.e. high enough for the 500 GeV linear collider. The TESLA Test Facility (TTF) linac at DESY [15] was constructed to show that the high gradients achieved in these cavities could be maintained during assembly into a linac test string, and then successfully operated with auxiliary systems to accelerate an electron beam to a few hundred MeV. The facility is a testbed for SRF technology, in particular cavity preparation and subsequent integration into full accelerator modules (see Figure 6.10).

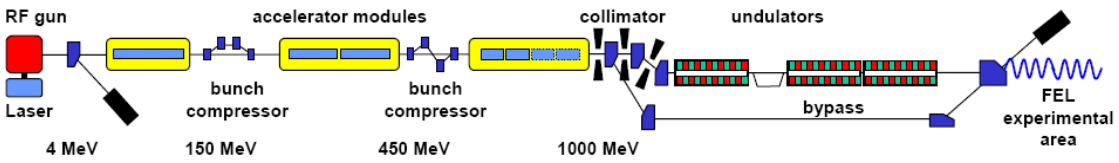

Figure 6.10 TTF VUV-FEL accelerator layout (courtesy TTF VUV-FEL collaboration)

The TTF accelerator consists of an electron source, a superconducting acceleration section and an undulator in which the accelerated electrons are induced to produce X-ray laser light (free-electron laser). Although ER techniques are not employed for the linac systems, the research successes achieved at the test facility are milestones of accelerator technology. SRF accelerator

modules were developed in cooperation with industrial companies and have already achieved accelerating gradients of 25 MV/m - the gradient needed for the 500 GeV linear collider.

Furthermore, an accelerating field of more than 35 MV/m has been reached in several 9-cell TESLA resonators. This gradient would make it possible for TESLA to have operated the at up to 800 GeV collision energy. For the TTF accelerator module, each consists of eight 9-cell TESLA-type cavities plus a focussing quadrupole (see Figure 6.11). The main support for the module is the helium gas return pipe, which supports all the other cryostat components. The cryomodule is designed to maximise the packing factor required for the International Linear Collider. It is primarily designed for a low duty factor regime and so areas such as the HOM damping and subsequent cryomodule helium transfer would have to be re-evaluated to facilitate high power CW application on 4GLS.

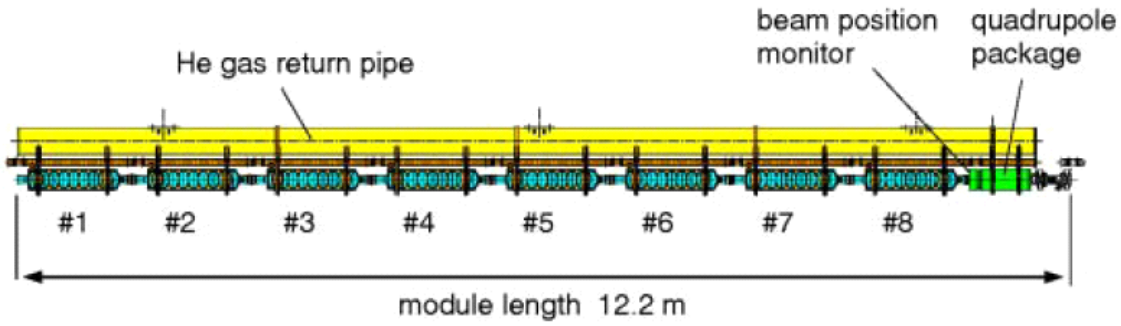

Figure 6.11 VUV-FEL accelerating module layout (courtesy TESLA/TTF collaboration)

6.3 Frequency and Temperature Choice for 4GLS

Niobium (Nb) is the material of choice for the world's SRF accelerating structures owing to its low loss characteristics when high gradients are strived for. The DC surface resistance for Nb material reduces considerably from several hundred nΩ, down to as low as tens of nΩ once its critical temperature is reached (see Figure 6.12).

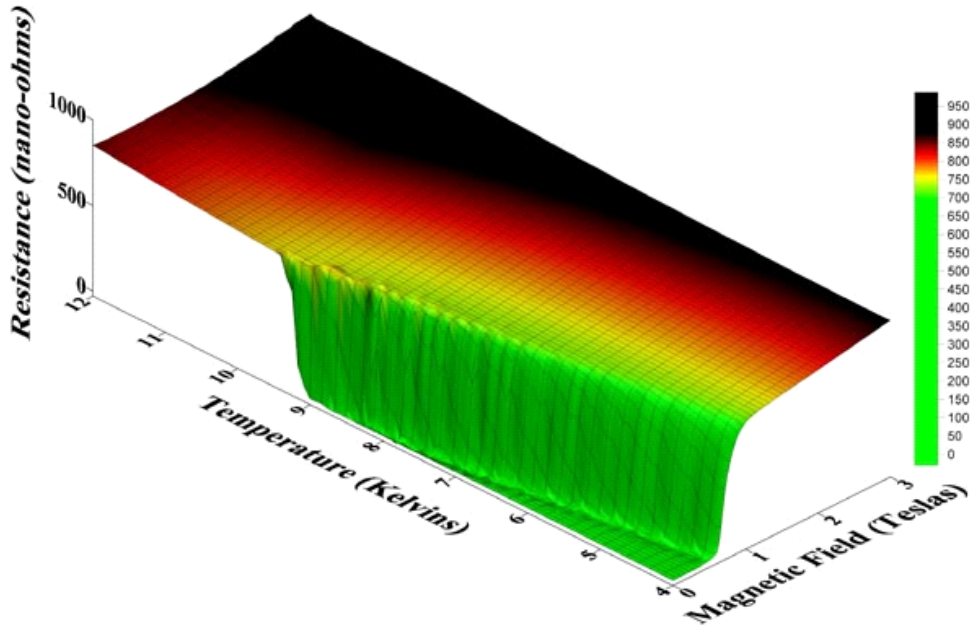

Figure 6.12 Nb Superconductivity[16] (courtesy National Institute of Standards and Technology)

Lowering the temperature further allows for material superconductivity to be maintained in the presence of larger critical magnetic fields (H_{crit}). Applying an alternating electromagnetic field to the same Nb material under these superconducting conditions has the effect of introducing more resistive loss due to magnetic field penetration into the material surface. This skin depth penetration layer has frequency dependence and so directly impacts the cryogenic heat load anticipated. The costing implications on the 4GLS cryogenic system, not only in terms of capital costs but yearly operating costs, varies substantially with the operating frequency chosen. The Bardeen-Cooper-Schrieffer (BCS) theory of superconductivity states that the surface resistance for Nb varies as f^2 and is given by the expression [17]:

$$R_{BCS} \propto \frac{f^2}{T}\exp(-1.76T_c/T) \tag{6-6}$$

where f is the microwave frequency, T is the operating temperature and T_c is the superconducting critical temperature for pure niobium (T_c = 9.2 K). Many laboratories around the world have spent years developing high gradient SRF accelerating structures to achieve the demanding requirements for their respective applications. Clearly the work carried out at DESY for the TESLA/TTF cavity development has enabled gradients in excess of their design goal of

25 MV/m at 1.3 GHz to be reached. In order to attain these high accelerating gradients requires high Q_o cavities, with inherently low conductive losses.

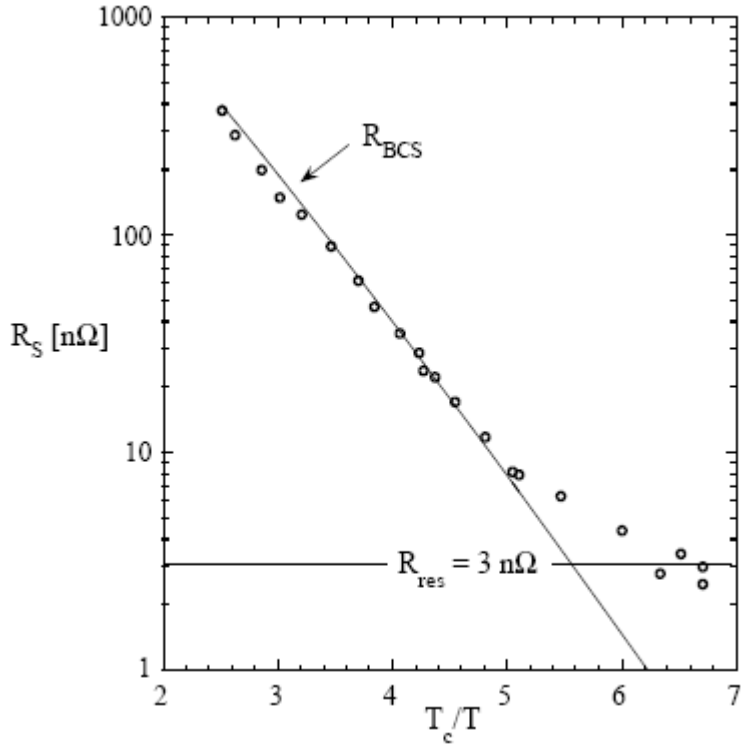

Figure 6.13 The measured surface resistance of a 9-cell TESLA cavity plotted as a function of T_c/T. The residual resistance of 3 nΩ corresponds to a quality factor $Q_o = 10^{11}$ (courtesy TESLA/TTF Collaboration).

At 1.3 GHz for example, the BCS surface resistance for Nb is ~ 800 nΩ at 4.2 K, and drops to 15 nΩ at 2 K (see Figure 6.13), which is a reasonable target for the 4GLS linac cavities to also achieve. Of the SRF cavities that have been developed worldwide, the range of frequencies most suitable for 4GLS are between 352 MHz and 3 GHz. High Q accelerating structures favour lower operating frequencies and Equation 6-5 also shows that low R_{BCS} favours low frequencies, however high gradients favour high frequency cavities. The cavity longitudinal ($W_{//}$) and transverse ($W_{\perp}$) wake potentials scale as f^2 and f^3 respectively, also favouring lower frequencies. The fundamental requirement for the 4GLS SRF linacs is to achieve the required accelerating gradient, whilst operating at a temperature that reduces the cavity losses to a manageable level and therefore a compromise is needed in terms of the chosen operating frequency. For a $R_{BCS} < 20$ nΩ, the maximum frequency becomes limited to ~ 1.8 GHz at a 2 K operating temperature. Conversely, accelerating gradients of up to 20 MV/m have only ever been demonstrated in 1.3 GHz TESLA or TTF accelerating modules.

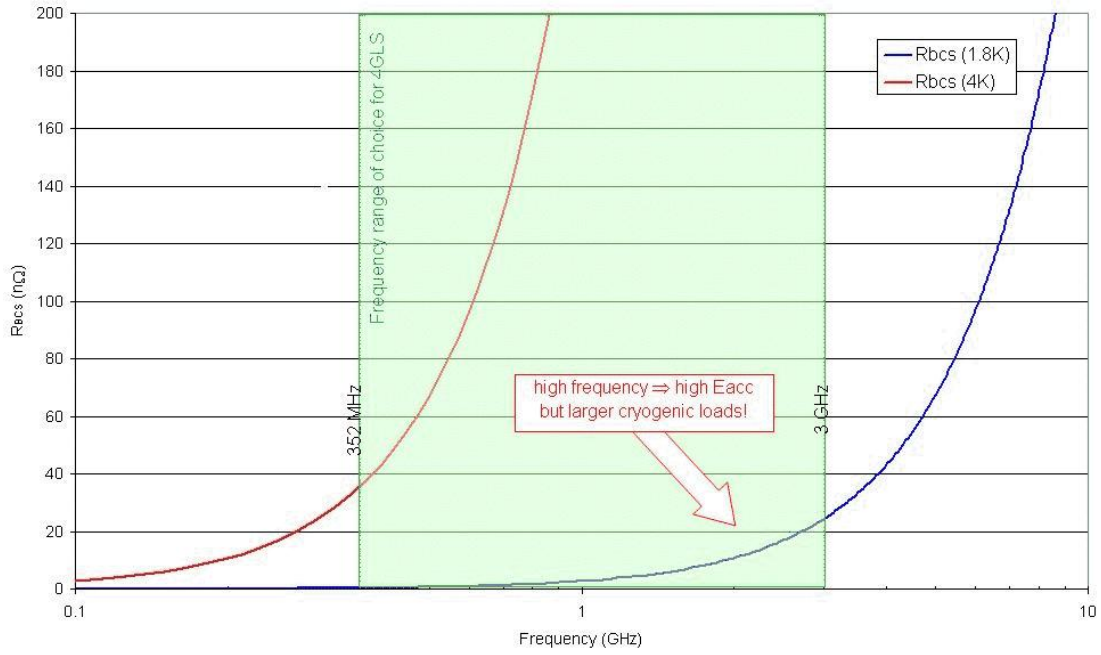

Figure 6.14 BCS resistance as a function of frequency and operating temperature

It is also shown in Figure 6.14 that at 1.3 GHz, operating at 4 K is not appropriate for achieving the required R_{BCS} surface resistance for Nb and that 2 K or below would be the cryogenic requirement for 4GLS. It is therefore proposed that the RF frequency choice for 4GLS be based on 1.3 GHz technology, whereby maximum benefit can be gained from the years of development for the TESLA and TTF accelerators. This frequency choice for TESLA/TTF and subsequently ILC, has provoked worldwide industry to facilitate in the manufacture of high power RF devices and low level RF control systems so that 4GLS is now in a position to reap the rewards.

Clearly a detailed cost evaluation would be required to determine whether it would be more cost effective, in terms of cryogenic system operating costs compared to the cryogenic system capital costs, as to whether operating at 1.8 K would be a more cost effective solution than operating at 2 K. The 4GLS cryogenic system is detailed more thoroughly in Chapter 14 (Technical Systems – Cryogenics Systems).

6.4 Linac Cryomodule Configurations

Assuming a conservative maximum E_{acc} of 20 MV/m for 4GLS, the cavity cryomodule configuration is chosen to provide enough operational flexibility, utilising a manageably sized cryomodule, which is capable of delivering the required RF power and providing the necessary cryogenic cooling. For TESLA/TTF at 1.3 GHz for example, a 9-cell structure was chosen as it provided effective HOM extraction and allowed superior field homogeneity. It is proposed for 4GLS that a modified TESLA cavity configuration be employed, which similarly allows for high gradients whilst providing improved HOM damping capability. Figure 6.15 shows the 9-

cell TESLA cavity configuration, highlighting a single input power coupler and dual HOM couplers at either end of the accelerating cavity.

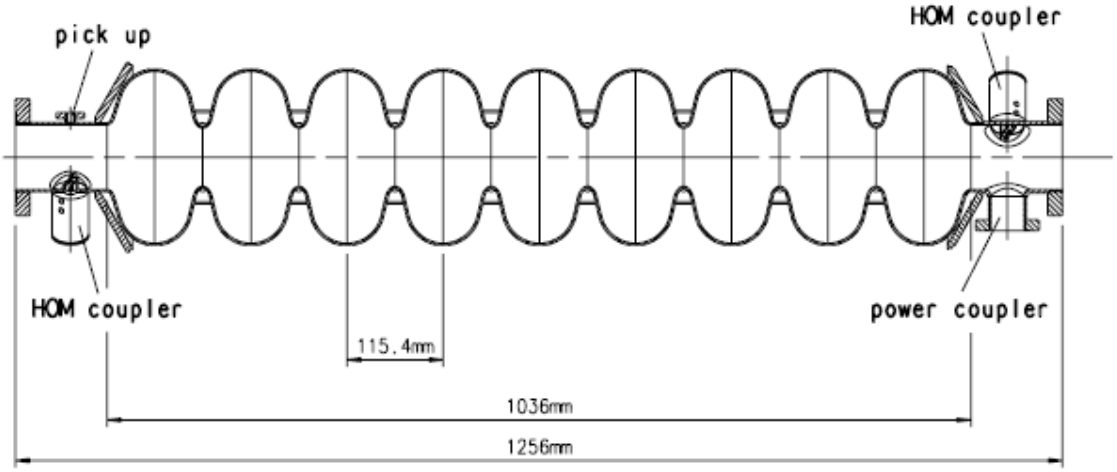

Figure 6.15 TESLA/TTF accelerating cavity layout (courtesy TESLA/TTF Collaboration)

Operating this cavity configuration in CW mode for 4GLS would increase the cryogenic HOM load considerably compared to TESLA/TTF. The present TESLA loop-type HOM couplers are narrow-band and have been designed to operate at low repetition rates, and therefore at relatively low HOM power transmission. This makes them inappropriate for use on 4GLS, and so an alternative HOM damping approach will be required. It is proposed that the TESLA/TTF cavity is reduced from 9-cells to 7-cells and the beam pipes widened (see Figure 6.16), reducing the cavity loss factor and consequently reducing the HOM excitation. With the space that is gained, improved HOM damping can be introduced.

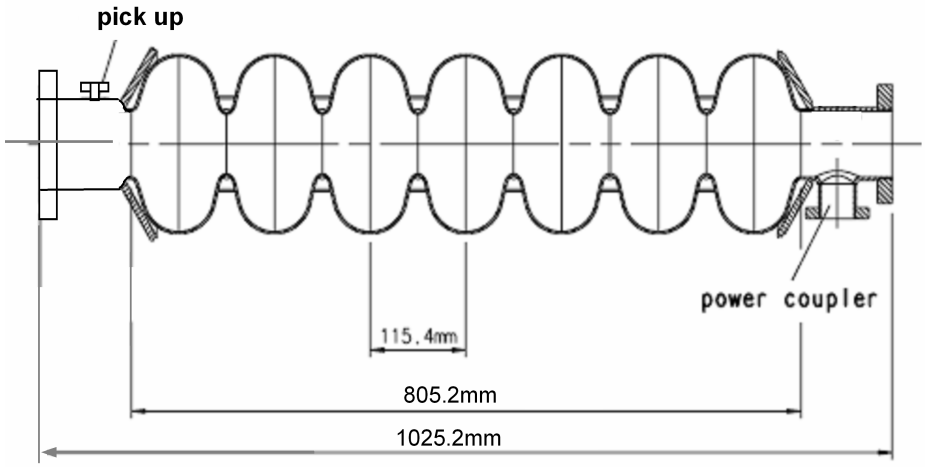

Figure 6.16 Modified TESLA/TTF cavity configuration for 4GLS

A HOM damping scheme for the main 4GLS SRF cavities has not yet been developed and requires more detailed investigation to integrate into a cavity/cryomodule assembly. Detailed configuration solutions for each of the 4GLS linac cryomodules have not yet been performed.

Work is ongoing to refine the cryogenic requirements for such an accelerating system and to then develop a cryomodule layout that meets these requirements whilst maintaining a comfortable operational overhead.

6.4.1 The 2-Cell Cavity Cryomodule

Preliminary investigations have been made by Cornell to develop a cavity/cryomodule layout for their CW injector linac, which is also a suitable application for Linac1 on 4GLS. On 4GLS, ten 2-cell cavities will be required, which will be housed in two cryomodules and cooled at 2 K. Each cryomodule then houses a total of six HOM absorbers which are thermally screened from each cavity and cooled at 80 K (see Figure 6.17). The 2-cell cavity layout requires that each cavity has dual RF input feeds, which complicates the cryomodule design and more importantly will increase the static and dynamic heat loads.

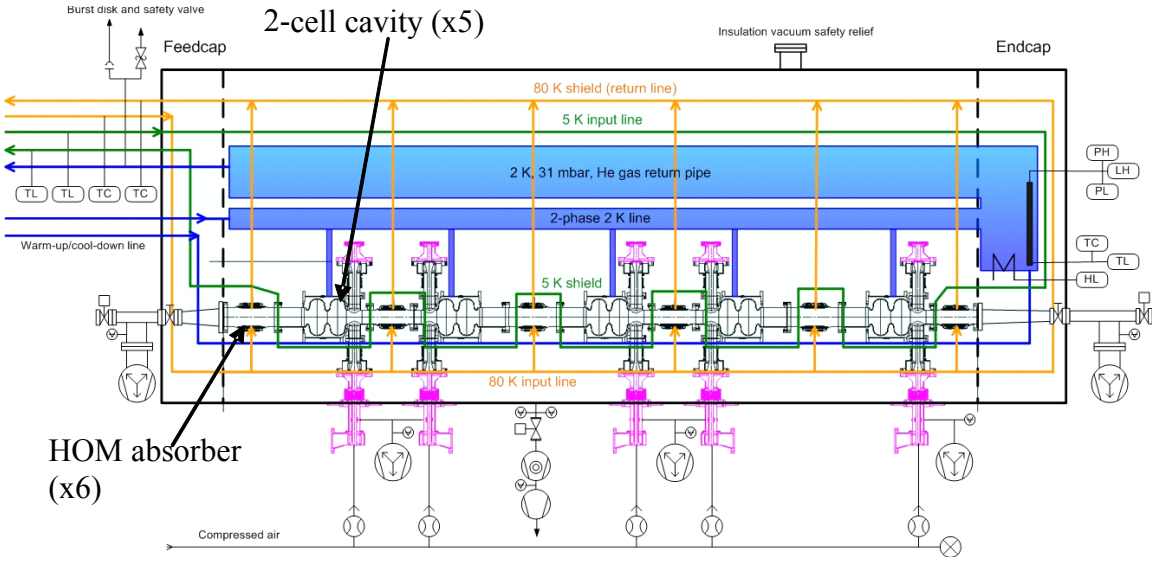

Figure 6.17 Possible cryomodule layout for 4GLS Linac1 (courtesy Cornell University)

6.4.2 The 7-Cell Cavity Cryomodule

The main 4GLS linacs must be capable of delivering their respective energy gain, whilst also ensuring a conservative E_{acc} per module with a cost-effective requirement for cryogenic cooling. Table 6.10 shows (by way of example for Linac5) that for six cryomodules, each containing eight 7-cell cavities to achieve the required energy gain of 590 MeV, an E_{acc} of 15.2 MV/m is needed. The total dynamic RF losses to be accounted for from the cryogenic system at this E_{acc} are then ~ 150 W/module or 900 W in total for a maximum of six cryomodules in Linac5. Alternatively, an additional accelerating module can be included which would lower the total E_{acc} and therefore reduce the dynamic cryogenic heat load. Table 6.11 shows that the E_{acc} would drop to 13.1 MV/m and the total dynamic RF losses reduce to ~ 110 W (or by ~ 13%).

Table 6.10 Six module RF requirements for Linac5

Eacc (MV/m)	E Gain (MeV)	V/Cell (MV)	P/Cell (W)	P/Cavity (W)	P/Module (W)	Total RF Losses (W)	20 Year Lifetime Cost (£M)
1.0	38.8	0.12	0.01	0.08	0.65	3.89	2.34
2.0	77.5	0.23	0.05	0.32	2.59	15.54	2.43
3.0	116.3	0.35	0.10	0.73	5.83	34.98	2.57
4.0	155.1	0.46	0.19	1.30	10.36	62.18	2.77
5.0	193.8	0.58	0.29	2.02	16.19	97.15	3.03
6.0	232.6	0.69	0.42	2.91	23.32	139.90	3.34
7.0	271.4	0.81	0.57	3.97	31.74	190.42	3.71
8.0	310.2	0.92	0.74	5.18	41.45	248.71	4.14
9.0	348.9	1.04	0.94	6.56	52.46	314.78	4.62
10.0	387.7	1.15	1.16	8.10	64.77	388.61	5.16
11.0	426.5	1.27	1.40	9.80	78.37	470.22	5.76
12.0	465.2	1.38	1.67	11.66	93.27	559.60	6.42
13.0	504.0	1.50	1.95	13.68	109.46	656.76	7.13
14.0	542.8	1.62	2.27	15.87	126.95	761.68	7.90
15.0	581.5	1.73	2.60	18.22	145.73	874.38	8.72
15.5	600.0	1.79	2.77	19.39	155.11	930.63	9.13
16.0	620.3	1.85	2.96	20.73	165.81	994.85	9.60
17.0	659.1	1.96	3.34	23.40	187.18	1123.09	10.54
18.0	697.8	2.08	3.75	26.23	209.85	1259.11	11.54
19.0	736.6	2.19	4.18	29.23	233.82	1402.89	12.60
20.0	775.4	2.31	4.63	32.38	259.08	1554.45	13.71

Table 6.11 Seven module RF requirements for Linac5

Eacc (MV/m)	E Gain (MeV)	V/Cell (MV)	P/Cell (W)	P/Cavity (W)	P/Module (W)	Total RF Losses (W)	20 Year Lifetime Cost (£M)
1.0	45.2	0.12	0.01	0.08	0.65	4.53	2.73
2.0	90.5	0.23	0.05	0.32	2.59	18.14	2.83
3.0	135.7	0.35	0.10	0.73	5.83	40.80	3.00
4.0	180.9	0.46	0.19	1.30	10.36	72.54	3.23
5.0	226.2	0.58	0.29	2.02	16.19	113.35	3.53
6.0	271.4	0.69	0.42	2.91	23.32	163.22	3.90
7.0	316.6	0.81	0.57	3.97	31.74	222.16	4.33
8.0	361.8	0.92	0.74	5.18	41.45	290.16	4.83
9.0	407.1	1.04	0.94	6.56	52.46	367.24	5.39
10.0	452.3	1.15	1.16	8.10	64.77	453.38	6.02
11.0	497.5	1.27	1.40	9.80	78.37	548.59	6.72
12.0	542.8	1.38	1.67	11.66	93.27	652.87	7.48
13.0	588.0	1.50	1.95	13.68	109.46	766.22	8.32
13.3	600.0	1.53	2.04	14.25	113.97	797.77	8.55
14.0	633.2	1.62	2.27	15.87	126.95	888.63	9.21
15.0	678.5	1.73	2.60	18.22	145.73	1020.11	10.18
16.0	723.7	1.85	2.96	20.73	165.81	1160.66	11.21
17.0	768.9	1.96	3.34	23.40	187.18	1310.28	12.30
18.0	814.2	2.08	3.75	26.23	209.85	1468.96	13.47
19.0	859.4	2.19	4.18	29.23	233.82	1636.71	14.69
20.0	904.6	2.31	4.63	32.38	259.08	1813.53	15.99

Although the yearly operational running costs (using seven modules) would be lower than for six modules, the capital costs for the additional module are considerable and would outweigh any running cost advantages seen (over a typical twenty five year operating lifetime). A £400k saving can be estimated over twenty five years operation, whereas the capital cost for an 8-cavity cryomodule will most definitely exceed this predicted saving. It is therefore proposed for Linac5, that six modules are employed, each incorporating eight 7-cell cavities. Similar analysis for the other 4GLS linacs is more clear-cut, as the energy gain requirement is much smaller for each.

Operation of each of the 4GLS modules must ensure that optimum acceleration is maintained, and so assessing what might happen if a single module degraded in performance (due to Multipacting, Thermal Breakdown or Field Emission), the remaining modules would have to compensate for this lost energy. Figure 18 shows that for full (100 %) performance degradation in a single Linac5 module (Module 1), the remaining five modules (Modules 2-6) would have to compensate by increasing E_{acc} up to 18.3 MV/m, which is still below the conservative limit imposed (20 MV/m) and so should be readily achievable.

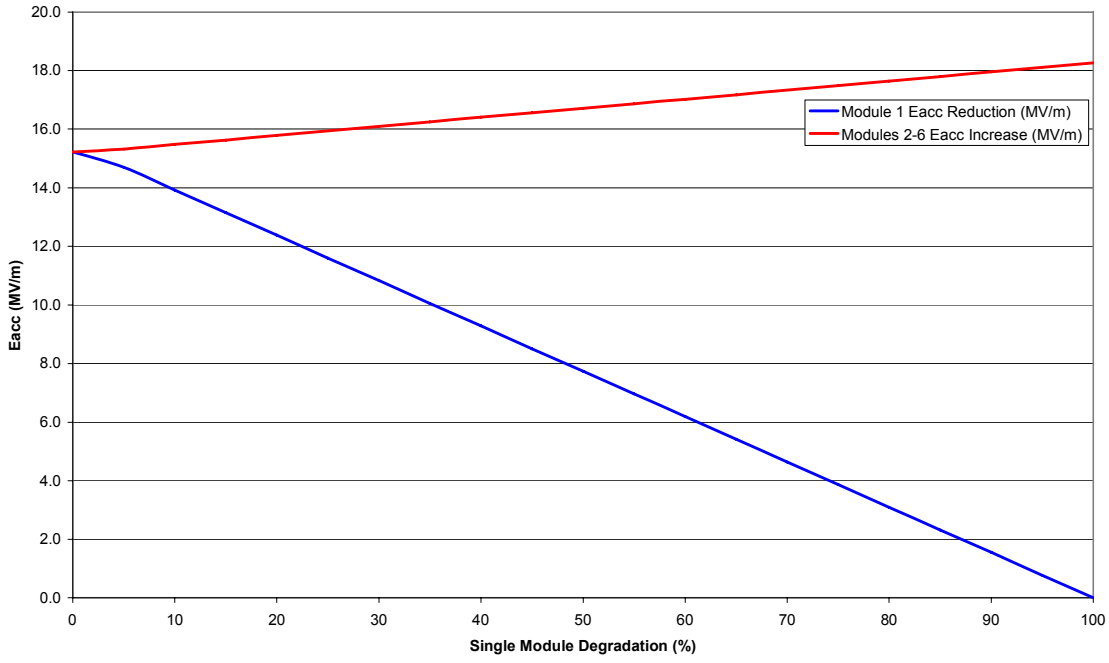

Figure 6.18 Module gradient degradation and subsequent compensation

Linac2, Linac3, Linac6 and Linac7 are of the same cavity/cryomodule configuration and similar operating E_{acc} as Linac5 and it is therefore expected that these will have a similar cryogenic dynamic heat load as outlined in Table 6.10.

6.5 HOM Damping

Higher Order Modes (HOMs) within the accelerating cavities are a possible source of beam loss and a limiting factor on the maximum current that can be accelerated for 4GLS. HOMs are a feature of the cavity design, and in multi-cell cavities are often due to resonances between groups of cells. These resonances can be part of the design or arise from imperfections that make each cell and each cavity different. These resonances will be at different frequencies to the fundamental mode, and since for SRF cavities in particular, any form of HOM damping is likely to be located at the ends of the cavity cells, these electromagnetic resonances are likely to become trapped within the central cells and its HOM power will become difficult to extract. Figure 6.19 illustrates the electric fields inside a TESLA 9-cell cavity for one of the dangerous HOMs that can become trapped.

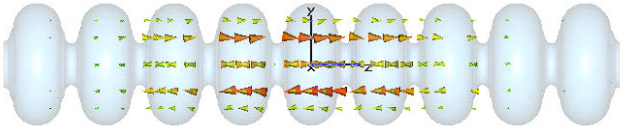

Figure 6.19 Microwave Studio model of mode trapped in middle of a 9-cell TESLA cavity

The use of SRF cavities will reduce the wakefield/HOM effects compared to normal conducting cavities, owing to the naturally lower *R/Q* for both the fundamental mode and associated HOMs. The frequency, loaded Q factor (Q_L) and *R/Q* of the HOMs determine the magnitude of their effect on the beam. The Q_L for each HOM also defines the bandwidth over which the HOM impedance can be excited by the beam. The HOMs closest in frequency to the fundamental are most likely to cause problems. The higher the product of Q_L and *R/Q* the greater the kick the bunch will receive from the HOM. For example, for the TESLA 9-cell cavity there are ten HOMs of concern (see Table 12), all of them transverse dipole modes:

Table 6.12 TESLA 9-cell Cavity HOMs

Frequency (GHz)	Polarisation	*R/Q* (Ω)	Q_L	*R/Q* x Q_L (MΩ)
1.734	x	116.7	3400	0.397
1.734	y	116.7	4500	0.525
1.865	x	42.4	50600	2.145
1.865	y	42.4	26500	1.123
1.874	x	56.8	50200	2.851
1.874	y	56.7	51100	2.897
1.880	x	11.8	95100	1.122
1.880	y	11.8	85500	1.009
1.887	x	1.2	633000	0.759
1.887	y	1.2	251000	0.301

Of these dangerous HOMs, the two modes at 1.874 GHz are of greatest concern. Reducing the number of cells within the cavity to seven will reduce the HOM effective impedance, as the field within the cavity loses stability as the number of cells (N) decreases [18]. A 7-cell cavity has been studied as part of a four 7-cell cavity super-structure for TESLA and simulations [19] have identified HOMs with Q_o values in the range of 1 x 10^5 to 5 x 10^5. Tests have also been carried out on a prototype superstructure [20] where the Q values for all of the HOMs were lowered to ~ 1 x 10^5.

6.5.1 Expected 4GLS HOM Generation

The HOMs for the TESLA 9-cell cavity scale as a function of the single bunch excitation, which for 4GLS gives a loss factor of 11.025 V/pC for a 2 ps bunch length in Linac5. An estimate for the maximum induced longitudinal HOM power ($P_{//}$) can then be determined from:

$$P_{//} = k_{//} Q_{bunch} I_{beam} \tag{6-5}$$

where: Q_{bunch} = bunch charge (pC) = 77 pC

I_{beam} = beam current (A) = 200 mA (2-pass energy recovery)

$k_{//}$ = structure longitudinal loss factor (V/pC) = 11.025 V/pC

If we assume optimum excitation of monopole HOMs, an estimate of ~ 170 W of HOM power per 9-cell cavity is anticipated if this cavity scheme is adopted and operated in CW-mode for 4GLS. The existing TESLA/TTF cryomodule systems are not capable of dealing with this level of CW HOM power, requiring improved liquid helium (LHe) transfer to the conventional HOM coupler assemblies. CCLRC, Cornell, LBNL and FZR Rossendorf are presently collaborating on a 7-cell variation [21] of the TESLA cavity with two cells removed and ferrites added at each end to reduce the Q of the HOMs further. The beam pipe at one end of the cavity has an increased radius to allow more of the trapped HOMs to propagate to the HOM couplers and ferrites. The HOM losses would occur in the cryomodule at liquid nitrogen (LN_2) temperatures of between 40 K and 80 K, and would contribute to a significant cryogenic dynamic heat load. These cavities will be strung together in groups of eight to ten and inserted into a single cryomodule. Although there is no data on the HOMs of this cavity as yet, they should be of a similar frequency but with lower Qs to that of the 9-cell TESLA cavity (see Chapter 8, Electron Beam Transport). This 7-cell cavity configuration is proposed to be used for the 4GLS Linacs 2, 3, 5, 6 and 7. It is hoped that by early 2008, a cavity/cryomodule prototype is available for installation on ERLP at Daresbury for verification as proof of principle for application on 4GLS.

6.5.2 HOM Damping Mechanisms

The beam-induced HOM power, if left to sustain inside the accelerating cells, would overwhelm the 2 K cryogenic system, resulting in a thermal quench of the SRF cavity. It is therefore essential to extract this HOM power as effectively as possible, so that it can be absorbed more

efficiently at higher temperatures. There are typically three different types of HOM damping methods used in the world's SRF accelerators and these are:

- coaxial loop;
- waveguide;
- beam pipe.

Ideally the cavity HOM couplers should be positioned at an optimum location inside the cavity cell itself. For SRF cavities however this would introduce an undesirable field perturbation in the fundamental mode and more importantly, add a potential source for low field multipacting in the presence of large accelerating E-fields. It has therefore become prominent for various HOM couplers to be positioned close to the cavity cell and to then couple out the HOM power via the beam pipe.

Until recently waveguide HOM couplers were more commonly used in high frequency applications (1 – 1.5 GHz) with coaxial HOM couplers being favoured at low frequencies (350 – 500 MHz). The coaxial type coupler has the advantage of being more compact and less intrusive to the cryomodule assembly, whereas the waveguide coupler is a less complex arrangement overall. When relatively large HOM power generation is anticipated i.e. for high current CW applications, then the beam pipe HOM coupler is preferred, as this scheme more optimally couples out the HOM electromagnetic fields.

6.5.2.1 Coaxial Loop Dampers

Loop dampers (or couplers) are typically employed to target specific narrow-band frequencies of concern. Usually multiple couplers are used to cover a sufficiently wide bandwidth in order to damp the HOM impedances to a manageable level. This narrow-band feature of coaxial loop couplers makes them a less attractive option for the 4GLS CW linacs as both waveguide and beam pipe dampers offer a more efficient alternative.

6.5.2.2 Waveguide Dampers

Waveguide HOM absorbers can be fitted to extract the HOMs from the accelerator system, which can be cooled using the helium gas return inside the cryomodule. Unlike coaxial HOM couplers, rectangular waveguide couplers do not need a rejection filter, which is required to avoid damping of the fundamental mode. This is because the waveguide is designed to be below cut-off at the operational frequency. Typically, where both the input waveguide and the two HOM waveguide couplers are used they are angled at 120° to retain symmetry within the system. For damping dipole modes of both polarizations, two rectangular waveguides are used. As the dampers are rotated through 45° to 60° it reduces the longitudinal size and permits coupling to both monopole and dipole modes.

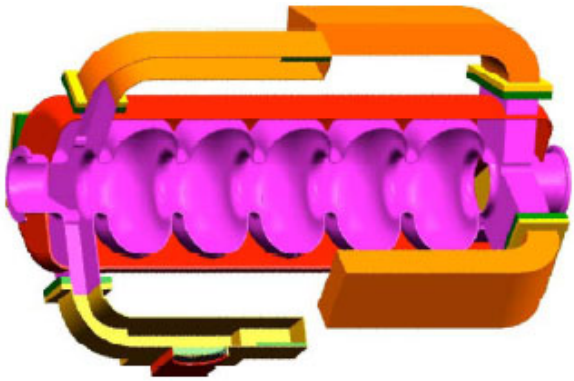

Figure 6.20 TJNAF Renaissance cryomodule waveguide HOM damping scheme (courtesy TJNAF)

TJNAF have designed a system using waveguide dampers for their Renaissance Module (see Figure 6.21), which consists of two sets of waveguide dampers, one on either side of the cavity, each with an angle offset of 120° to optimise the damping of dipole modes [22].

6.5.2.3 Coaxial Loop Dampers

Loop dampers (or couplers) are typically employed to target specific narrow-band frequencies of concern. Usually multiple couplers are used to cover a sufficiently wide bandwidth in order to damp the HOM impedances to a manageable level. This narrow-band feature of coaxial loop couplers makes them a less attractive option for the 4GLS CW linacs as both waveguide and beam pipe dampers offer a more efficient alternative.

6.5.2.4 Beam Pipe Absorbers

Cornell University have designed a HOM absorber (see Figure 6.21) that relies on the widening of the beam pipe to allow the HOMs to propagate out of the cavity and cooled using helium gas at 80 K. This reduces the overall cryogenics cost compared to the LHe cooled coaxial antenna variant.

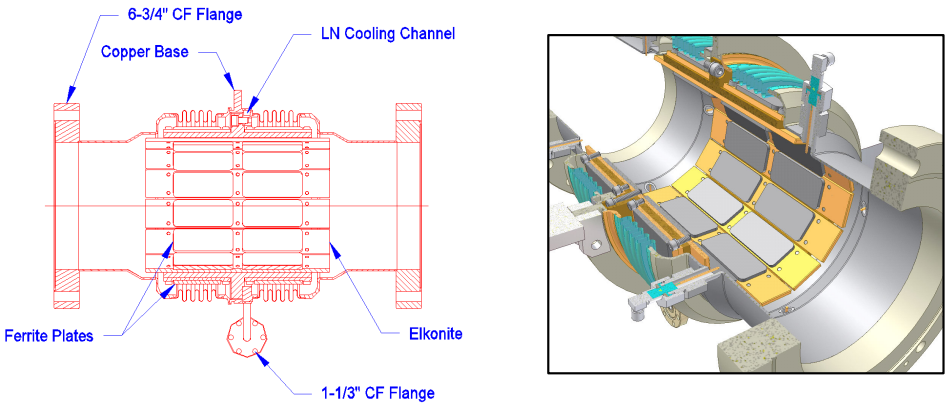

Figure 6.21 Cornell beam pipe HOM absorber (courtesy Cornell University)

The HOM absorbers have been designed using a ferrite and two ceramics in order to broaden the pass band (see Table 6.13). Cooling of the absorbers is carried out with cooling channels to the back of the ferrite plates.

Table 6.13 Cornell HOM beam pipe absorber

Total number of absorbers	3
Average dynamic power per absorber	26 W
Max. power/absorber	200 W
HOM frequency range	1.4 – 50 GHz
Operating temperature	80 K
Coolant	Helium Gas

The bandwidth demonstrated with the ferrite absorber combinations make them suitable from 1.4 GHz to 50 GHz, with a maximum power dissipation of 200 W per absorber. Cornell has used this type of ferrite absorber successfully on the 500 MHz CESR cavities, dissipating up to 5 kW [23].

For each of the 4GLS linacs, HOMs will be of primary concern when operating these accelerator systems in CW-mode. It is anticipated that the most appropriate choice for HOM damping of the TESLA/TTF cavities will be the beam-pipe absorber as its coupling efficiency to the HOMs is somewhat improved over the waveguide damping approach, whilst un-complicating the cryomodule layout due to its less intrusive nature.

6.6 RF Power Coupling

The fundamental power coupler is a device whose primary function is to efficiently transfer RF power from a source to a load. Due to the nature of the device when introduced into the superconducting environment, it presents a number of interdisciplinary design challenges that need to be addressed, since poor performance in these devices can profoundly impact accelerator operations and the overall success of a facility.

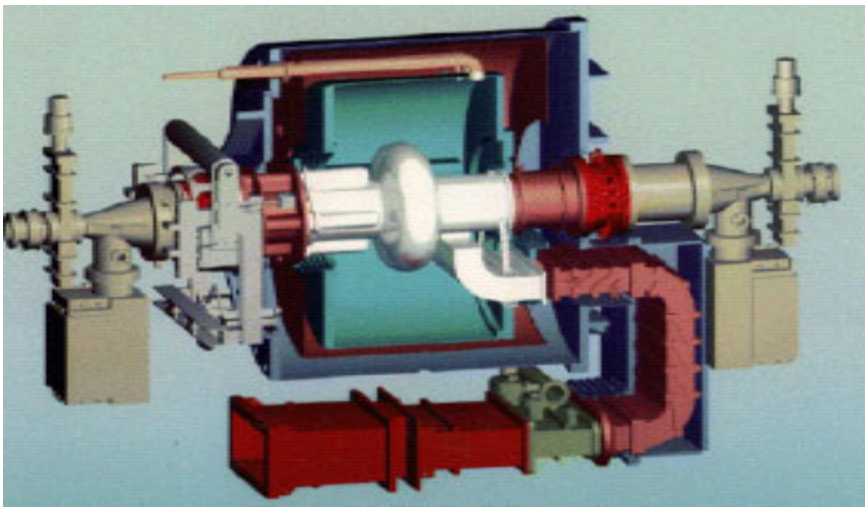

Figure 6.22 Cornell CESR cavity waveguide coupler layout [24] (courtesy Cornell University)

Power couplers can vary considerably depending upon the desired operating parameters. SRF cavities may require tuning of the coupler to allow for *in-situ* RF processing. The range of external Q (Q_e) required for tuning is in the order of approximately one hundred. Waveguide couplers (see Figure 6.22) are typically adjusted through external 3-stub tuners; however these provide additional RF stresses to the RF window ceramic due to the resultant standing waves. The use of 3-stub tuners alone is insufficient, as the tuning range offered is typically only ± 3 times.

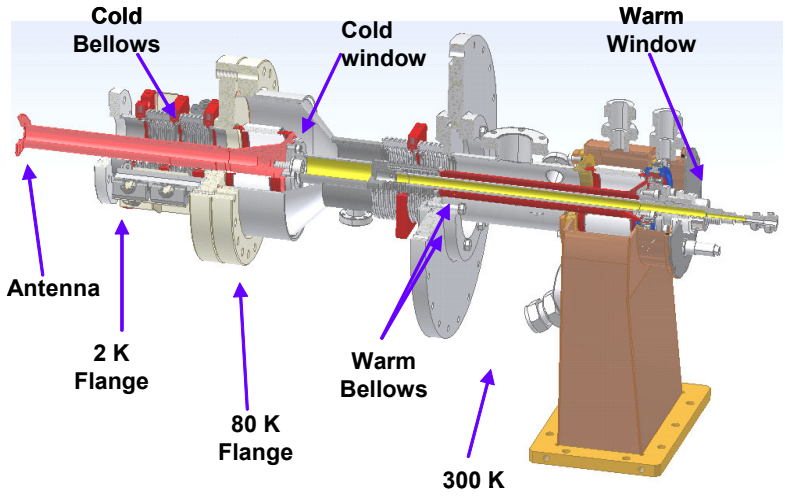

Figure 6.23 TESLA/TTF input coupler (courtesy TESLA/TTF collaboration)

The small tuning range of the 3-stub tuner and the difficulty to adjust the Q_e for waveguide couplers has forced many SRF cavity designs to adopt the coaxial type coupler (see Figure 6.23). There are a number of coupler designs that must be considered for the main 4GLS linacs and a selection of these have been highlighted in Table 6.14.

Table 6.14 Cavity Input Couplers

	Cornell ERL Coupler	CESR	SNS Coupler	APT Power Coupler	KEK-B	ERLP
Type	Coaxial	Waveguide	Coaxial	Coaxial	Coaxial	Coaxial
Frequency	1.3 GHz	500 MHz	805 MHz	700 MHz	508.8 MHz	1.3 GHz
Max power	75 kW	400 kW	48 kW	420 kW	400 kW	10 kW
No. ceramic windows	2	2 (1-ceramic, 1-kapton)	1	2	2 (1-ceramic, 1-teflon)	1
Cold coax line Zo	60 Ω	50 Ω	50 Ω	50 Ω	50 Ω assumed	50 Ω
Q_{ext} range	9.2×10^4 to 8.2×10^5	2×10^5 Fixed	7×10^5	Fixed	Fixed	3×10^6 to 1×10^7

Adjustable coupling is achieved by physically adjusting the length of penetration of the coaxial antenna. To provide this, bellows are introduced to maintain a strong RF seal whilst allowing movement. The bellows are a source of voltage breakdown in high field operation and limit high power operation.

6.6.1 Coupler Design Issues

The coupler acts as a vacuum seal between the waveguide (at room temperature and pressure) to the harsh environments of the SRF cavity (2 K, 10^{-7} mbar). This puts considerable stress on the RF window ceramics particularly when high RF powers are being transmitted and tuning of the coupler is needed. In the event of a coupler window failure, this will allow ambient air or gas into the cavity, contaminating the Nb surface in the cryomodule. Typical failure mechanisms are:

- window rupture;
- window cracking;
- window puncture;
- brazement leaks;
- bellow leaks;
- vacuum seal leaks.

As these are couplers used in SRF applications, the consequences of a potential failure are extremely high. A catastrophic window fault will result in the loss of at least one cavity due to condensed gas and particulate contamination, and perhaps an entire cryomodule of cavities. While the probability of this occurring is decreased due to advances in operational interlocks,

diagnostics and experience, the severity of this possible outcome makes it still a concern. Minor barrier faults due to pinhole leakage are more manageable, but can still erode performance over time. All of the coupler designs that have been considered for 4GLS have included two ceramic windows for additional protection.

6.6.1.1 Transmissive Issues

For the instance when an input coupler maintains vacuum, yet does not transmit RF power, a number of problems may be evident:

- multipacting barriers leading to heating or arcing;
- condensed gas leading to multipacting or arcing over time;
- passband shift due to thermal contraction or expansion;
- Q_e change of match condition due to temperature variations.

Transmissive faults won't generally contaminate and/or compromise a cryomodule, but they can render a cryomodule inoperable. To restore operation, the cryomodule will usually need to be removed from the linac and warmed up. At a minimum for a transmissive fault, the coupler will need to be removed and replaced with a new unit while maintaining clean conditions in the cavity if at all possible. In the case of a contaminated module due to a barrier fault, the entire module would need to be removed and reprocessed in a cleanroom environment.

6.6.2 Dipole Excitation Effects

At low energies, particularly during initial acceleration from the electron source, high charge beams are very sensitive to asymmetric electromagnetic fields. One mechanism for introducing such effects is from the input couplers either in the RF gun itself or the accelerating linac. Figure 6.24 shows the relative E-field that a low energy beam may experience on-axis from a single RF input coupler in the accelerating linac.

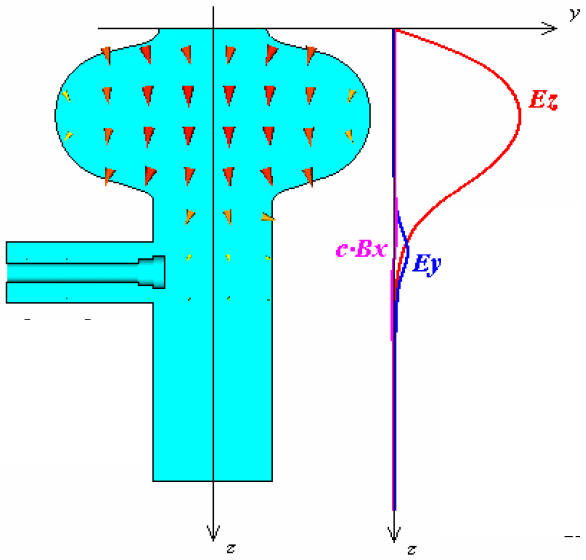

Figure 6.24 Induced E-field kick from single input coupler (courtesy Cornell University)

By introducing a second input coupler opposite to the first, the effect of this asymmetric kick field can be negated, whilst also providing a higher RF input power capability if needed. For 4GLS, the RF power requirements for each linac dictate that a maximum RF power delivery in excess of 50 kW CW will be required for Linac1 and for Linac7 a power in excess of 20 kW will be needed. The Cornell ERL 75 kW coaxial coupler, when proven can clearly provide the power needed for Linac1, however development will be required to provide a cost effective coupler solution for all other 4GLS Linacs.

6.7 Processing Techniques and Systems

Fabricating the SRF cavities for 4GLS will require facilities capable of preparing the niobium (Nb) material to a standard needed to achieve the required Q_o. Typically this entails having Class 10 clean rooms, chemical processing, high pressure water rinsing and vertical testing facilities [25]. Industry is not yet in a position to provide all of these capabilities. The SRF cavity requirement for the XFEL project at DESY, requiring over one thousand 1.3 GHz cavities over the next five years, and looking further ahead to ILC which will require more than ten thousand 1.3 GHz cavities over the next ten years, may make it difficult for industry to deliver cavities in time for 4GLS. Providing as much in-house SRF infrastructure as possible can offset much of the scheduling risk associated with delivering these cryomodules on time. Industry in particular does not have facilities to perform vertical testing of the prepared cavities and so having these facilities available in-house would minimise fabrication delays due to testing and processing.

6.7.1 Buffered Chemical Polishing (BCP) vs Electropolishing (EP)

Chemical etching is used to remove the damaged surface layer obtained from the manufacture of the cavities. The initial etch can remove up to one hundred microns of the surface layer with subsequent etches only removing a further ten microns. An alternative surface preparation method to BCP etching is EP. The material is removed in an acid mixture under the flow of an electric current. Sharp edges or tips are smoothed out and a very glossy surface can be obtained. This is an essential difference to the BCP process which tends to enhance the steps at grain boundaries (see micrographs in Figure 6.25).

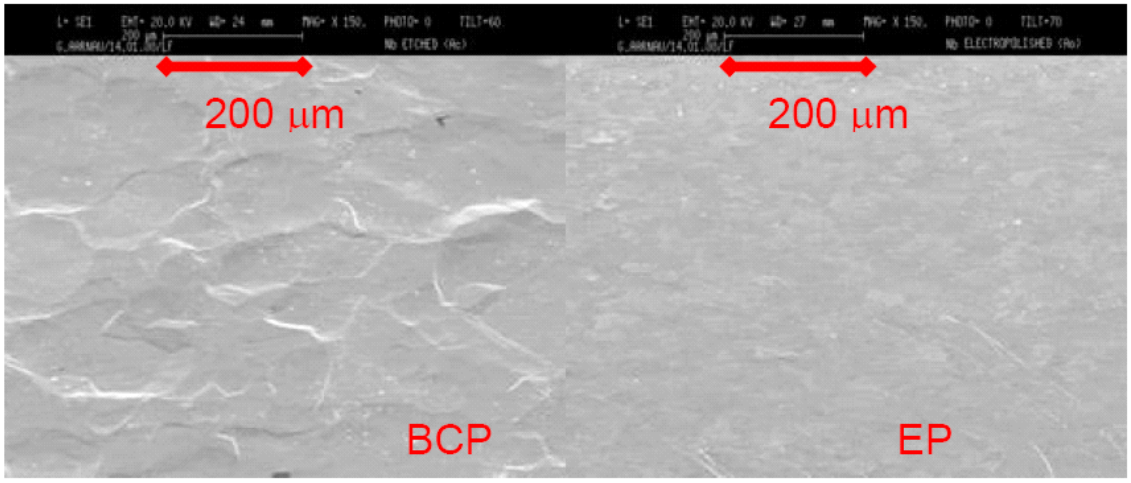

Figure 6.25 Surface micrographs illustrating BCP and EP grain boundaries (courtesy Cornell University)

Using EP, scientists at Cornell and the KEK laboratory in Tsukuba (Japan) have achieved gradients of up to 52 MV/m in single-cell cavities [26]. BCP has been the standard procedure in the preparation of SRF cavities for many years. EP has only recently become a viable solution for SRF applications due to the research and development that has been invested, but there is considerably more data available on the BCP process. Early indications have suggested that it is possible to achieve higher gradients using the EP method; however the spread in cavity performance (see Figure 6.26) suggests that the BCP process is much more understood and reliable. Therefore for the purpose of fabricating the 4GLS RF cavities, the BCP process is anticipated to be sufficient for achieving the required gradients.

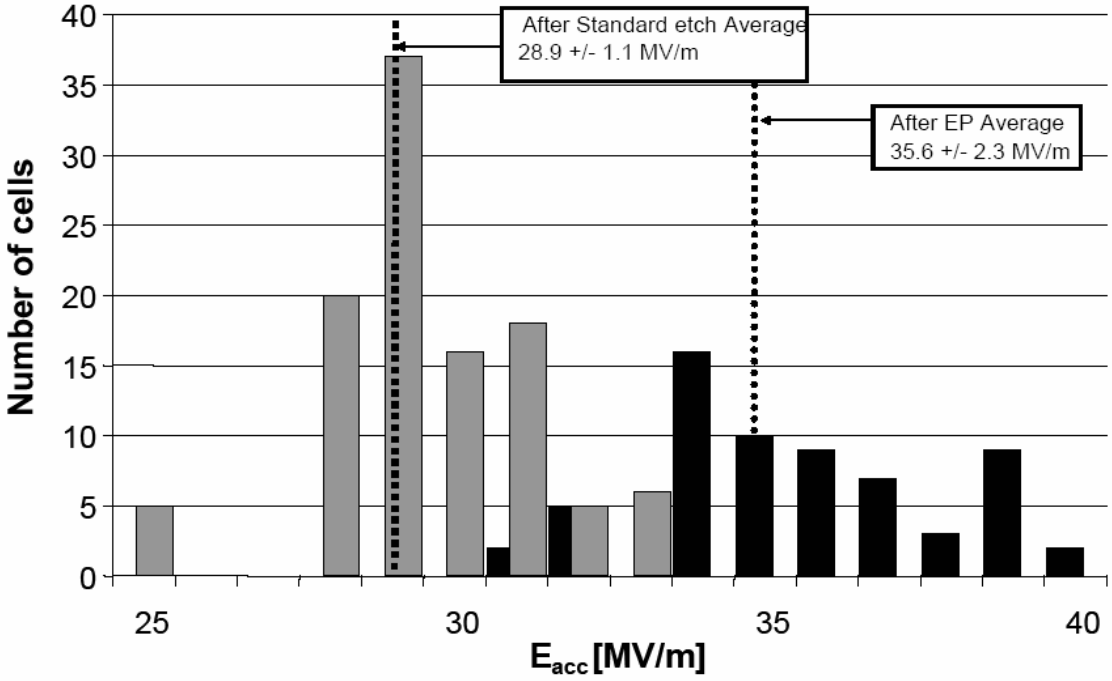

Figure 6.26 TESLA/TTF E_{acc} gains using EP techniques (courtesy TESLA/TTF collaboration)

6.7.2 High Pressure Rinsing (HPR)

Once the cavities have been constructed and polished, the cavities are then tested in a vertical cryostat. Such testing provides an indication of the cavity performance once assembled into the cryomodules [27]. Historically, many cavities tested have been field emission limited. The field emission occurs through the presence of impurities and microparticle contamination on the Nb surface. Once the cavities have been through a HPR process, subsequent testing of the same cavities show better performance in both Q_o and E_{acc}.

Early field emission onset in the vertical tests led to the need to repeat many of the cavity qualification tests. The immediate focus for process improvement was on the HPR system and the deionised water plant that supports it. HPR is the final cleaning step in the assembly process and understanding its effect on cavity performance may indicate avenues for further improvements.

6.7.3 High Pulse Power (HPP) Processing

A 'super-cleanliness' approach to cavity fabrication and assembly can reduce field emission substantially. But in large area structures there is always a possibility of dust falling into the cavity upon installation of power-coupling devices or during the installation of a cavity into the accelerator. There exists a technique to eliminate emitters in-situ, denoted HPP, which has evolved from the observation that application of high fields destroys emitters. The idea is to apply high power RF to raise the surface electric field at the emitter as high as possible, even if for a very short time (say milliseconds). Accordingly, the power level, pulse length, and

coupling need to be varied. An important benefit is that HPP can recover cavities that may be accidentally contaminated, for example in a vacuum mishap.

6.8 Microphonics and Lorentz Force Detuning

Operating SRF cavities at very high loaded Q_L factors and subsequently very narrow bandwidths makes these systems extremely sensitive to mechanical vibrations. These vibrations can be transmitted to the cavity via a number of sources such as support stands, vacuum pumps, beam pipes, cryogenic transfer lines and pressure variations inside the cryomodule itself. The cavity has its own intrinsic response to these fluctuations and the low level RF (LLRF) system must be able to reduce these induced phase and amplitude errors to tolerable levels. Forcing the mechanical resonances to high frequencies minimises coupling to ground motion and/or the cryogenic system. This can typically be done by bracing the cavity cells with stiffeners.

At high accelerating fields, the magnetic fields inside the cavity interact with the surface currents causing a detuning force inside the cavity. This force causes a deformation of the cavity shape, altering the resonant frequency of the cavity, known as Lorentz force detuning [28]. This force is particularly important at high gradients and for pulsed accelerators such as TESLA/TTF. The area of the cavity geometry that experiences the greatest force is the same area that sustains the maximum E-field for acceleration. Therefore, when the Lorenz force oscillates, the cavity resonant frequency oscillates in sympathy. These ponderomotive oscillations result in losing effective coupling to the RF source, causing the fields in the cavity to oscillate. Even if appropriate cell stiffeners are integrated, advanced feedforward techniques may also be required to predict the magnitude of these oscillations to effectively control the cavity amplitude and phase.

6.9 Cavity Frequency Tuning Systems

Due to mechanical tolerances of the cavity geometry and the contracting forces during cool down, especially at very low operating bandwidths (typically < 300 Hz), it is likely that the cavity will be resonating away from the desired accelerator frequency. Tuners are employed to mechanically alter the shape of the cavity to guarantee the required frequency.

Cavity tuners are needed to counter the effects of the Lorentz forces by actively tuning the cavity back to the desired frequency. Controlling the detuning minimizes the power required from the klystron which reduces the operating and capital cost. There are several designs suitable for the cavity tuners for 4GLS, however the main problem associated with the tuners is the location of the stepper motor driver. CEBAF [29] and SNS [30] (both in the US) use externally mounted stepper motors that have been successful in operation. TTF uses stepper motors located inside the cryostat [31]. In the harsh environment of low temperature and pressure, reliability of any moving parts such as bearings and the stepper motors themselves become an issue.

6.9.1 Tuner Choice

There are several different designs currently in use on SRF accelerators. The technology is well developed and the inclusion of piezo-actuators for fast tuning is a requisite for controlling microphonics. Many of the common designs are based on the original Saclay tuner which is a mechanical arm positioned on one end of the cavity. The latest development of this type of tuner is mainly to improve its compact nature and to include piezo actuators.

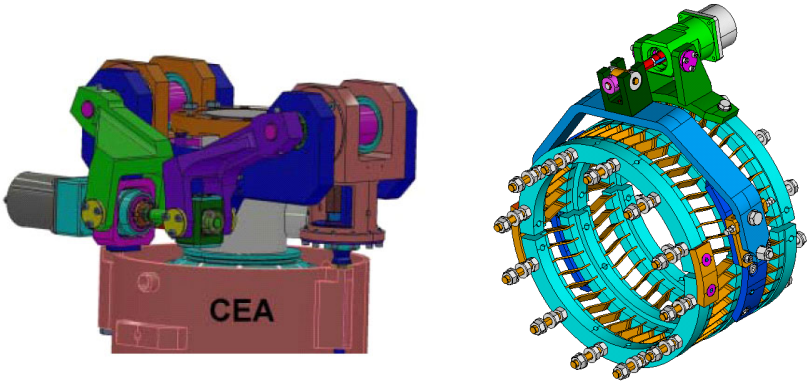

Figure 6.27 CEA Saclay tuner and blade-type tuner assemblies (courtesy TESLA/TTF collaboration)

An alternative is the blade-type tuner developed for the TESLA/TTF superstructure module and is composed of two constituent parts; the movement leverage and the bending rings. Figure 6.27 shows a comparison of these two different tuner types. The leverage system provides amplification of the torque of the stepper motor, considerably reducing the total movement (reducing the required space) and increasing the tuning sensitivity. For the blade-type tuner, the stepper motor is rigidly connected to the helium vessel and produces a rotation of the arm in the centre of the tuner. The movement of the arm induces the rotation of the bending system that changes the cavity length. Table 6.15 shows a comparison of the two different tuner assemblies.

Table 6.15 Tuner options operating parameters

	Lever	**Blade**
Tuning range (mm)	1.9	1.0
Tuning range (kHz)	820	440
Sensitivity (Hz/step)	0.74	0.38
Δf. warm/cold (MHz)	2.3	2.3
ΔF (4.2K/2K) (kHz)	30	70

For CW application of the TESLA-type cavity/cryomodule design, such as for 4GLS, enlargement of the beam pipes to allow HOMs to propagate is a requirement. The blade-tuner is the most appropriate solution for application in the 4GLS cryomodules as it also takes up

minimal longitudinal space, allowing more room for improved HOM damping devices, whilst efficiently utilising the space available within the cryomodule envelope.

6.9.2 Fast Tune Control

SRF cavities exhibit a high susceptibility to mechanical vibrations due to their narrow bandwidth of operation. Fast actuators are required to provide adequate tuning response capability for these microphonic and Lorentz forces. At present, two technologies are available that have been demonstrated on SRF modules; a fast mechanical tuner based on piezoelectric actuators, or magnetostrictive actuators which operates by a micrometric deformation of the cavity geometry. With modern control theory and high speed digital signal processors (DSP) and field programmable gate arrays (FPGA) it is now possible to design complex controllers which allow high gain up to several hundred hertz. Since microphonics are induced by mechanical vibrations, a natural solution to the problems appears to be a fast mechanical actuator which is driven in such a way that the detuning caused by microphonics is perfectly compensated.

6.9.3 Piezo Actuation

Piezo devices are especially well suited for applications where magnetic fields cannot be tolerated. For the operation of SRF cavities it is essential to minimise all stray magnetic fields, therefore the piezoelectric devices are the preferred option. Figure 6.28 shows the likely configuration of the actuator in the lever-type tuner frame.

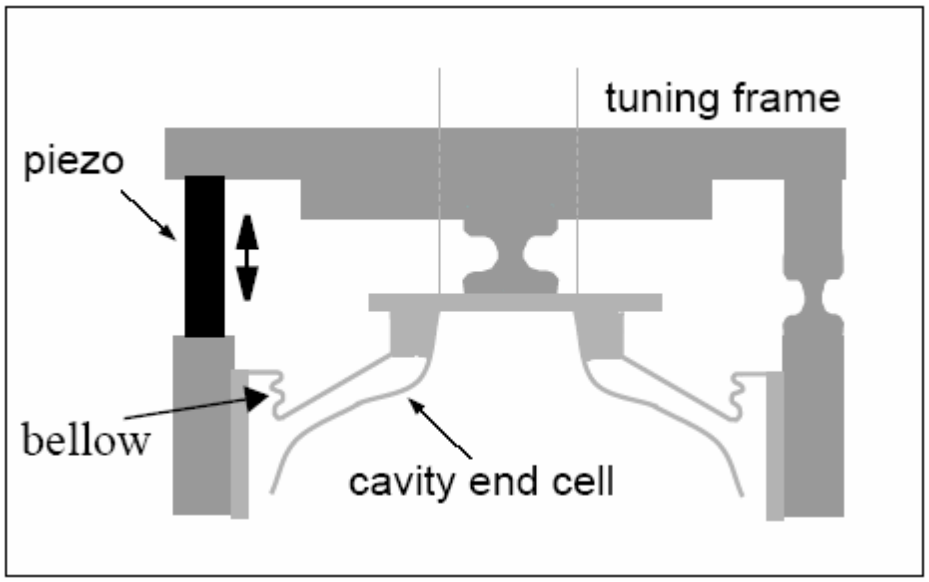

Figure 6.28 Typical piezo tuning actuator schematic for a SRF cavity (courtesy TESLA/TTF Collaboration)

6.9.4 Magneto Control

Magnetostrictors elongate when exposed to a small magnetic field. This extension is reversible and repeatable enabling a wide range of applications. The tuner consists of a high force linear actuator that elongates the cavity along its axis thereby changing its resonant frequency. This mechanism has a motion range that provides a tuning range of up to 6.4 kHz. Since magnetostrictors rely on magnetic fields it is not recommended to utilise these for active tuning. Should this type of tuner be employed on 4GLS, the heat load generated would need to be assessed and compensated for by the cryogenics system.

6.10 Low Level RF Control Systems

6.10.1 Frequency Reference

4GLS needs an extremely stable source of RF as its reference, frequency drift of better than 1 Hz/year at 1.3 GHz will be required as the bandwidth of the accelerating cavity is very small (< 100 Hz). The close in phase noise of the RF reference (< 1 kHz) is especially important, as this is directly responsible for causing energy spread and jitter in the electron beam. The frequency reference will need to be amplified and transmitted along the length of the RF system to each accelerating structure preserving its high quality noise characteristics.

6.10.2 Coaxial Transmission

It is possible to transmit the raw 1.3 GHz reference signal over long distances, however temperature effects become an issue for phase stability and transmission loss of the cable (0.02^{o}/meter/^{o}C at 1.3 GHz typically). The longer the cable run, the more sensitive the distribution system is to ambient temperature variations. Transmitting a lower base frequency, say at 10 MHz, alleviates some of these issues as the lower the frequency, the less the phase change per unit length. The 10 MHz can then be converted back to 1.3 GHz locally at each RF station using frequency conversion techniques (see Figure 6.29).

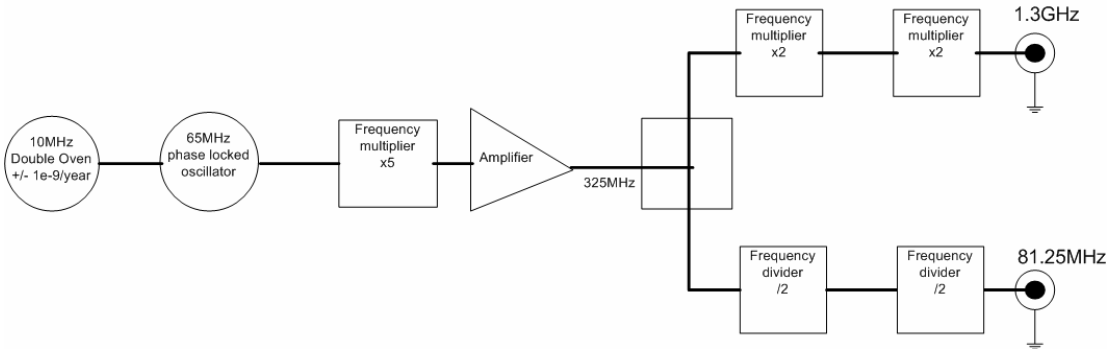

Figure 6.29 High stability multiplied oscillator

6.10.3 Fibre Optic Systems

Lasers are currently being tested for use as long distance femtosecond synchronisation sources of RF. The fibre laser is mode locked to the low noise RF source and encoded with the 1.3 GHz. This signal is transmitted over the distance required and demodulated as necessary (see Figure 6.30).

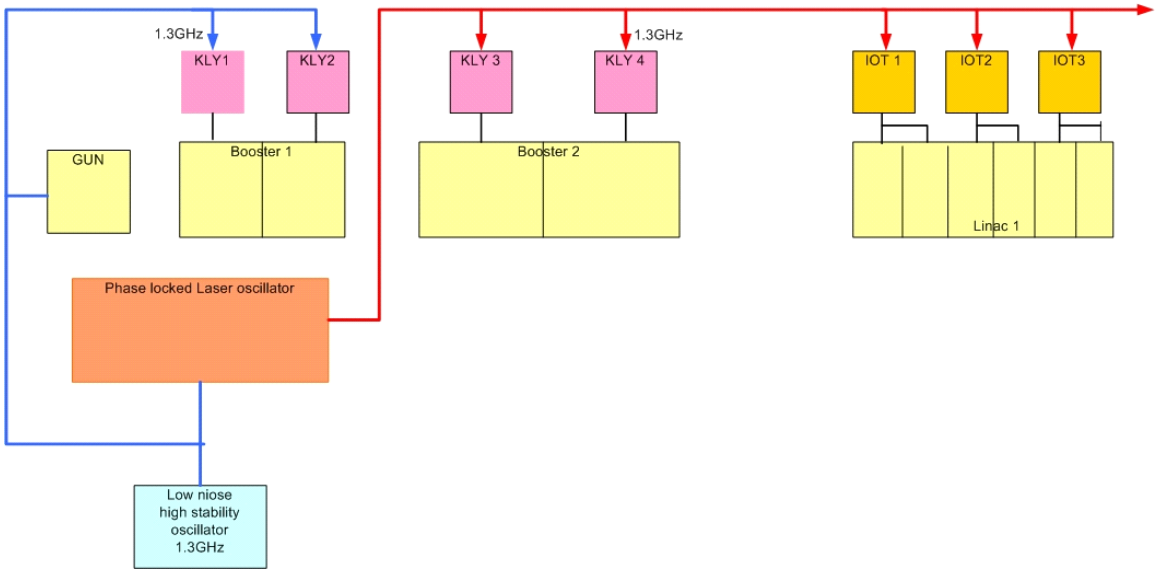

Figure 6.30 High stability laser RF distribution system

Long lengths of optic fibre are also susceptible to phase shift due to temperature but this can be compensated by using optical line stretchers coupled to feedback systems. Many accelerator groups are pursuing this technology at the moment, including TESLA [32], XFEL and MIT. These systems will provide stabilised timing signals to tens of femtoseconds. Fibre optic systems cannot be located in high radiation areas, so if this type of system is used it must be located outside the accelerator tunnel.

6.10.4 Phase and Amplitude Stability

In the photoinjector and linac sections for 4GLS, the phase stability of the RF field will need to be kept to 0.01^{o} (~ 21 fs at 1.3 GHz) and to 10^{-4} for amplitude due the electron bunch acceleration being off-crest. Errors in phase and amplitude at this point will produce energy modulation and hence timing jitter of the pulse to pulse structure of the beam. This level of phase control has been shown at TJNAF using the Cornell LLRF control system [33]. In the main linacs the beam will be accelerated almost on-crest, reducing the required phase stability to 0.1^{o} (or ~ 0.1 ps at 1.3 GHz) and 10^{-3} for amplitude. However as the same RF control system will be used for all the cavity feedback loops, the $0.01\ ^{o}$ and to 10^{-4} amplitude control should still be available to all linacs.

6.10.5 Feedback Systems

The 4GLS feedback system will comprise a phase comparator and regulation loop to maintain a phase error of < 0.01° where needed with reference to the desired working point for each RF station. The amplitude loop will consist of a proportional integral controller taking inputs from the cavity probe and amplitude set point for that acceleration structure and controlling the drive level to the RF amplifier using vector modulation techniques.

4GLS will set high demands on the LLRF control system. For the ERLP, the LLRF control will be an analogue electronic system based on the system developed at FZR Rossendorf for the ELBE facility [34]. This has the advantage of low cost and extremely fast operation due to low latency. For 4GLS the dynamic range of the controller will need to be higher and less susceptible to noise and environmental effects. These criteria point towards a digital feedback system, an example of which is shown in Figure 6.31. The current state of the art, FPGA-based digital feedback systems can stabilise the RF to enable 10 mA to circulate in an ERL. The same LLRF system will enable mechanical tuning of the SRF module for slow field changes to allow both setting and control of the required accelerating field.

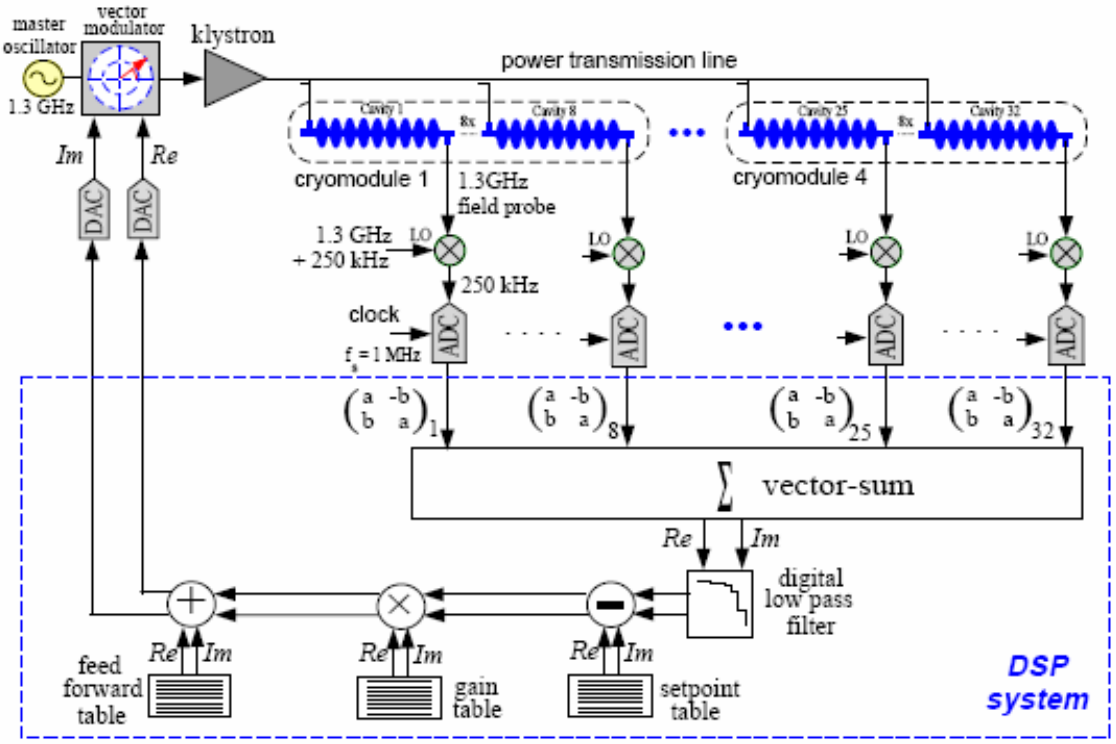

Figure 6.31 Example of a digital based LLRF feedback system for 4GLS (courtesy TESLA/TTF Collaboration)

6.10.6 Feed Forward Systems

In addition to feedback controls, should microphonic compensation be required for 4GLS, an adaptive feed-forward approach can be implemented in the LLRF system [35]. This will consist

of a data table for each individual cavity that corrects and modifies the action of the LLRF control loop prior to the application of the control function.

6.10.7 Operating Q (Q_e)

The amount of RF power needed to support acceleration in each 4GLS module will be several kilowatts at a Q_e of approximately 10^7. Using the LLRF control system it should be possible to operate the cavities at a higher Q_e in the 10^8 range, therefore reducing the amount of RF power needed to support acceleration. In order to control cavity microphonics, a system bandwidth which encompasses the cavity mechanical modes, determines the Q_e for the cavity system and is matched at the maximum operating current of the machine. The Q_e is therefore dependant on the performance of the LLRF control system holding the phase and amplitude to the required level in combating microphonics and detuning effects. These can move the cavity operating point many bandwidths away from the optimum resonance of the cavity and under these conditions, a reserve of RF power will be needed to bring the cavity back on tune [36].

6.10.8 Synchronisation

The 4GLS accelerator will be driven from one RF source that can be multiplied and divided to any required frequency. This will be achieved using low noise passive devices. Where an exact division ratio is unavailable, a phase locked loop will be used to provide a phase-referenced signal. A high temperature stability and low ageing rate oscillator will form the basis of the RF system for 4GLS, this will be phase locked into the laser synchronisation system. Chapter 12, Timing and Synchronisation, details more thoroughly how the 4GLS RF, drive laser and FEL sources are appropriately phase locked.

6.11 RF Power Sources

Vacuum tubes suitable for modern particle accelerators are triodes, IOTs and klystrons. Klystrons and triodes have been the traditional power source for particle accelerators because they produce high power RF and offer high gain (50 dB) with efficiencies > 50%.

Table 6.16 RF Power sources available from industry

Type / Device	**IOT**	**IOT**	**IOT**	**Klystron**	**Klystron**
Manufacturer	CPI	e2v	Thales	e2v	Thales
Frequency (GHz)	1.3	1.3	1.3	1.3	2.45
Beam Voltage (kV)	34	25	28.5	45	49
Beam Current (A)	1.58	1.13	0.88	5.5	3.2
Output Power CW (kW)	29.5	14	16	120	50
Gain (dB)	22.5	20.9	20	45	48
Efficiency (%)	54.9	63	59	51	59

Triodes are limited to below 300 MHz [37], and therefore are not considered for 4GLS. IOTs have recently become available at L-band frequencies with efficiencies up to 65 % with gains in excess of 20 dB. The low gain feature of IOTs requires more RF drive than is required for klystrons. The use of IOTs is being demonstrated on the ERLP. Table 6.16 lists the operating parameters and outputs of suitable RF power sources for 4GLS. Current designs are limited to tens of kilowatts of power, for this reason they are unsuitable sources for the high current ERL injectors. IOTs capable of operating at 100 kW CW are being developed suitable for high current ERL type applications. The principle obstruction envisaged for operating IOTs at hundreds of kilowatts would be the increased RF drive power needed due to the low gain of such devices.

6.11.1 DC Power Sources

There are two options being considered for supplying HV to the RF amplifiers for 4GLS. These are a common high power converter supplying multiple IOTs, for example one converter for each cryomodule, housing nine amplifier tubes; or separate lower power high voltage converters, one for each of the amplifier tubes. The power converter topology will almost certainly be switched mode, since these are physically smaller and have low stored energy thereby reducing the sensitivity requirements of the crowbar protection circuit. Careful attention must be paid to the noise spectrum below 60 kHz as this could contribute to noise on the RF signal to the cavities. Each IOT will require a power converter rated at 25 – 35 kV/ 1.5 A, which can protect the tube in the event of an internal arc by removing HT and guarantee an energy transfer into a fault of less than twenty joules.

The preferred solution for 4GLS would be to use a multiple lower power converter for each amplifier and its associated cavity, providing optimum versatility in adjusting the amplifiers performance. A loss of supply due to converter failure or IOT protection activation would only switch off one amplifier tube with limited effect on accelerator efficiency. A locally installed lower power converter spare could be made available for rapid replacement at low cost. Additionally the electrical isolation and safety issues would be simplified.

6.12 RF Distribution Schemes

The RF distribution system consists of RF amplifiers and transmission systems, each connecting to accelerating structures in the machine. Amplifiers could consist of solid state designs, klystron or IOT tubes depending on the power required. The output from these devices will be coaxial cable in lower power applications and waveguide in high power lines to the linac structures. A control loop for phase and amplitude will provide feedback around each structure acting on the cavity tuners and modifying the input to the amplifier device (see Figure 6.32).

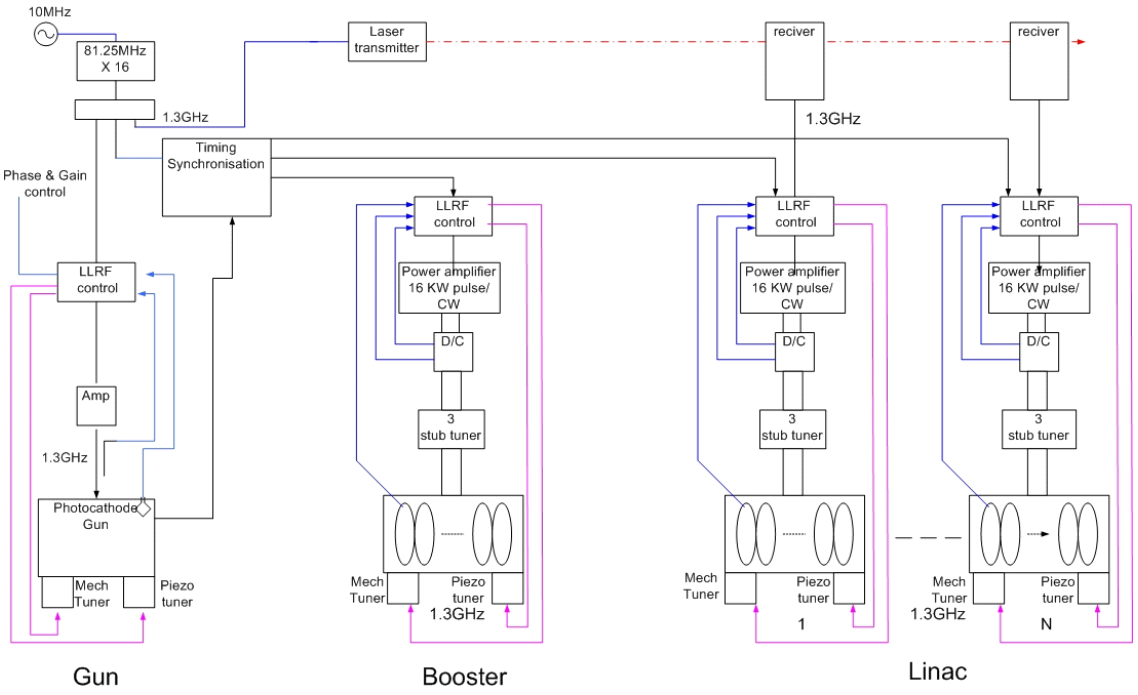

Figure 6.32 4GLS LLRF schematic layout

The RF power input to the cryomodules will be WR650 rectangular waveguide. Therefore the amplifiers will need a transition to this transmission format or provide it as the main output from the device. The amplifiers should be mounted adjacent to, but not in, the accelerator hall where access can be gained for monitoring and adjustment while systems are operating (see Figure 6.33).

Figure 6.33 RF Waveguides coupling into TTF module couplers

Between the amplifier system and the cavity, various waveguide components will need to be installed including circulators, phase shifters, directional couplers and 3-stub tuners. The waveguide will end with a 90° bend followed by a flexible joint ready for connection to the warm window transition of the cavity RF feedthrough. Mounted on the 90° bends will be a thermal imaging camera, arc detector electronics and a photomultiplier tube head. These diagnostics will indicate possible problems with the window and shut off the RF system once a fault is detected (see Figure 6.34).

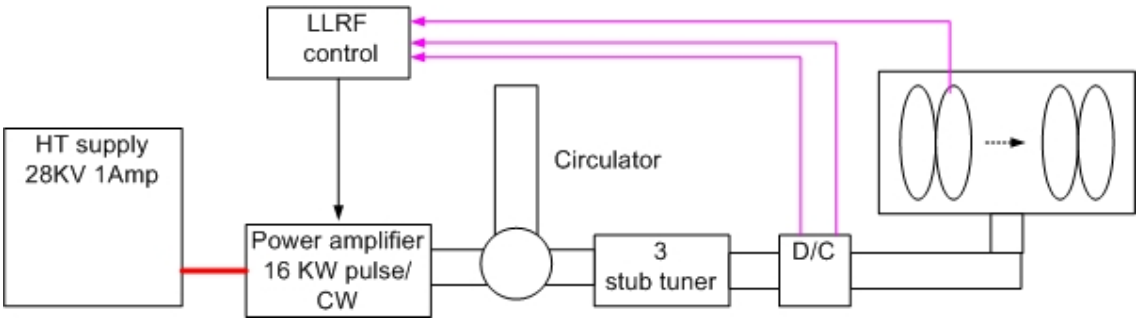

Figure 6.34 Layout of the 4GLS RF system

6.13 Conclusions and Recommendations

The fundamental requirement for each of the 4GLS accelerating linacs is the ability to operate at high CW gradients, whilst demanding an RF system that is both commercially available from industry and practically manageable in terms of its capacity. SRF technology enables these high gradients to be achieved, whilst the choice of beam current and repetition rates for the various 4GLS linacs enables each of them to operate in CW-mode and provide acceleration when beam is available, thereby simplifying the RF power delivery for each linac. RF power sources at the chosen RF frequency of 1.3 GHz are either already available commercially from industry or otherwise are very close to being available, to deliver the power levels needed for 4GLS. The development availability of ERLP at Daresbury will assist greatly in evaluating suitable LLRF control systems capable of providing the required stability for the 4GLS linacs. Along with collaborative developments over the next few years, many (if not all) of the outstanding RF technical risks for 4GLS will be addressed, providing a sound basis for system procurement and integration when funding is approved and released.

REFERENCES

[1] TESLA - The Superconducting Electron-Positron Linear Collider with an Integrated X-Ray Laser Laboratory, Technical Design Report, DESY, March 2001.

[2] 'Phase 1 Energy Recovery Linac at Cornell University', M Tigner et al, Intl. Proc. EPAC02, Paris, 2002, pp 644-646.

[3] 'Development of the Superconducting 3.9 GHz Accelerating Cavity at FermiLab', N Solyak et al, Intl. Proc. PAC04, Knoxville, 2005, pp 3825-3827.

[4] 'LCLS Conceptual Design Report', SLAC-R-593, April 2002.

[5] 'The BESSY Soft X-Ray Free Electron Laser, Technical Design Report', March 2004.

[6] 'Study for a proposed Phase I ERL Synchrotron Light Source at Cornell University', S. Gruner, M. Tigner, CHESS Tech. Memo 01-003, JLAB-ACT-01-04, July 2001.

[7] 'The Conceptual Design Report for the TESLA Test Facility', March 1995.

[8] 'Pushing QL', M Liepe, Presented in working group 3 at the ERL workshop 2005.

[9] '4GLS and the Prototype Energy Recovery Linac Project at Daresbury', M Poole et al, Intl. Proc. EPAC04, Lucerne, 2004, pp 455-457.

[10] 'A 10 KW IRFEL Design for Jefferson Lab', D Douglas et al, Intl. Proc. PAC01, Chicago, 2001, pp 249-252.

REFERENCES, Continued

[11] 'HOM Absorbers of Superconducting Cavities for KEKB', T. Tajima et al, Int. Proc. EPAC'96, Sitges, 1996, pp 2127-2129.

[12] 'High Current Energy Recovery Linac at BNL', V Litvinenko et al, Int. Proc. PAC05, Knoxville, 2005, pp 2242-2244.

[13] 'eRHIC, A Future Electron-Ion Collider at BNL', V. Ptitsyn et al, Intl. Proc. EPAC04, Lucerne, 2004, pp 923-925.

[14] 'The RF System for the Accelerator Production of Tritium (APT) Low Energy Demonstration Accelerator (LEDA) at Los Alamos', M Lynch et al, Intl. Proc. LINAC96, Geneva, 1996, pp 692-694.

[15] 'RF Control System for the DESY VUV-FEL Linac', V Ayvazyan et al, Intl. Proc. PAC05, Knoxville, 2005, pp 2899-2901.

[16] National Institute of Standards and Technology, web reference: http://www.boulder.nist.gov/div818/81803/2004/StandardsForSuperconCharacter/

[17] 'Theory of Superconductivity', J. Bardeen, L. N. Cooper, and J. R. Schrieffer, Phys. Rev. 108 (5), 1175 (1957).

[18] J. Sekutowicz et al, Phys. Rev. ST Accel. Beams, Volume 2, 062001 (1999)

[19] 'HOM Damping Requirements for the TESLA Superstructures, N. Baboi et al, Intl. Proc EPAC00, Vienna, 2000, pp 2016-2018.

[20] 'Analysis of the HOM Damping With Modulated Beam in the First Prototype of Superstructure, P. Castro et al, Intl. Proc. PAC03, Portland, 2003, pp 1086-1088.

[21] 'Challenges for Future Light Sources ERL and FEL, M. Liepe, Presented at SRF 2003, Travemünde, Germany, 2003.

[22] 'Concepts for the JLAB Ampere-Class CW Cryomodule', R Rimmer et al, Intl. Proc. PAC05, Knoxville, 2005, pp 3588-3590.

[23] 'Design and Fabrication of a Ferrite-lined HOM Load for CESR-B', D. Moffat et al, Intl. Proc. PAC93, Washington DC, 1993, pp 977-979.

[24] 'Accelerating Cavity Development for the Cornell B-Factory, CESR-B', H. Padamsee et al, Intl. Proc. PAC91, San Francisco, 1991, pp 786-788.

[25] 'Status of the Production Electropolishing System at JLAB', J Mammosser et al, Intl. Proc. PAC03, Portland, 2003, pp 2860-2862.

REFERENCES, Continued

[26] 'State of the Art SRF Cavity Performance', L.Lilje, Proceedings of LINAC '04, Lübeck, Germany pg 518.

[27] 'Investigation into the effects of the JLab High Pressure Rinsing System', J.Mammosser et al, Proceedings PAC'03, Portland, Oregon, USA (2003), pg 1386

[28] 'RF Superconductivity for Accelerators' H. Padamsee et al. Wiley Series in Beam Physics and Accelerator Technology, 1998.

[29] 'Improved Prototype Cryomodule for the CEBAF 12 GeV Upgrade', E. F. Daly et al, Intl. Proc. PAC'05, Knoxville, pp 1377-1379.

[30] 'Testing of the New Tuner Design for the CEBAF 12 GEV Upgrade SRF Cavities', E. F. Daly et al, Intl. Proc. PAC'05, Knoxville, pp 3910-3912.

[31] 'TESLA Test Facility Linac – Design Report', TESLA-Collaboration, D.A. Edwards, DESY, March 1995, TESLA 95-01.

[32] 'First Generation of Optical Fiber Phase Reference Distribution System for TESLA', Krzysztof Czuba et al. TESLA Report 2005-08.

[33] 'High-precision Optical Synchronization Systems for X-Ray Free Electron Lasers', Axel Winter et al. Presented at FEL 05, FROA002.

[34] 'Noise Measurements at the RF System of the ELBE Superconducting Accelerator', F. Gabriel et al, Intl. Proc. EPAC02, Paris, 2002, pp 2214-2216.

[35] 'Adaptive Feed Forward for the Digital RF Control System at the TESLA Test Facility', M. Liepe et al, Intl. Proc. EPAC98, Stockholm, 1998, pp 1735-1737.

[36] 'Pushing QL', M Liepe, Presented in working group 3 at the ERL workshop 2005.

[37] 'Review of Available Power Sources' C. Beard, Presented in working group 3 at the ERL workshop 2005

7. Electron Beam Transport Systems

To operate the free electron lasers and to deliver a suite of spontaneous sources requires high-quality electron beams with small transverse and longitudinal emittance. The operation of the XUV-FEL at photon energies of 10 to 100 eV, requires a peak current of ~ 1.5 kA at beam energies from 750 to 950 MeV. The spontaneous sources in the high average current loop (HACL) will exploit the unique output achievable from the 600 MeV, 100 mA beam of sub-picosecond electron bunches. VUV-FEL output is also achieved towards the end of this loop through progressive compression of the electron bunches down to bunch lengths of approximately 100 fs (RMS). The IR-FEL utilises superconducting linac technology to deliver continuous trains of bunches at a high repetition rate of 13 MHz; the required electron beam properties in the IR-FEL are modest compared to those for the XUV-FEL and the HACL arc. Similar electron beam properties are already routinely delivered at user facilities today, e.g. at FELIX [1] and Thomas Jefferson National Accelerator Facility (TJNAF) [2], and those that are planned in the ERLP accelerator [3].

In this chapter, issues that drive the overall topology of the layout are discussed and we present a design for the most challenging aspect of the beam transport – the common accelerator transport of the XUV-FEL branch and high average current loop. A topology is presented which efficiently merges the injected high average current and XUV-FEL bunches, with high average current bunches being returned for energy-recovery in a common superconducting linac. After the Main Linac, the lower-power energy-recovered beam is safely dumped while the two high-energy beams are separated and then independently transported and compressed before passing through their respective photon output devices. An outline of the scheme for compression is presented which meets the differing demands of the two bunch types. A two-stage magnetic chicane system is used to compress the XUV-FEL bunches, with a 3rd harmonic RF cavity to linearise the system; this delivers the required 1.5 kA peak current at the XUV-FEL. To avoid the complexity of integrating magnetic compression elements within the Main Linac, a single-stage, progressive compression scheme has been chosen for the high average current bunches. In this case the chosen scheme utilises the natural longitudinal dispersion of the HACL outward arc (after the Main Linac) and progressive compression through the spontaneous sources to achieve the bunch lengths required in those sources and a sufficient peak current at the VUV-FEL. Simulations indicate that 300 A peak current at the VUV-FEL is feasible using only sextupoles within the outward arc for linearisation.

A graded-gradient scheme for the Main Linac is proposed and an initial estimate of the linac wakefield effects of the XUV-FEL bunches on the adjacent high average current bunches shows little disruption to the energy spread, with linac accelerating phases chosen to be compatible with the compression scheme.

A system of chicanes and spectrometers is proposed to merge and separate the various bunch energies in the accelerator system. This is straightforward where the energy ratio is large;

however, a dual-aperture dipole is required in the spreader after the linac that separates the high average current and XUV-FEL bunches which are similar in energy, whilst still preserving the required longitudinal phase space properties of both beams. After separation the requirements for the transport of the XUV-FEL branch and the high average current loop are considered separately. The major components in both lines are identified, outline designs for some of the components are presented, and future developments are discussed. In addition to these two interlinked beam transport systems, an outline of the electron beam transport scheme for the IR-FEL component of the overall scheme is also given.

Some of the potential sources of disruption, such as wakefields, coherent synchrotron radiation (CSR) emission, ions and beam break-up (BBU) have been studied to gauge their potential effects during the transport, acceleration and compression of the high quality beams. These estimates are at a relatively early stage but have already given confidence that the design goals can be met with the accelerator concept that has been proposed.

Although the diagnostic requirements are not a high-risk part of the design, to ensure that the overall concept for the transport system incorporates the cost and space requirements of this instrumentation, an indicative suite of diagnostics is presented for each area of the accelerator. An exception to this is the requirement for longitudinal profiling of the electron bunches at important locations in the accelerator transport, principally at the FELs and spontaneous source points. Because of the importance of accurately measuring the longitudinal bunch profile a detailed discussion is given toward the end of the chapter of how electro-optic techniques may be used to do this, including reference to studies performed in part for the ERLP design.

Future work to develop the concept of the electron transport system is outlined together with the plans for extensive start-to-end simulations, using an integrated suite of simulation methods and codes that the 4GLS team is developing in partnership with international collaborators.

7.1 Introduction

4GLS is a challenging design from an accelerator point of view. To satisfy the user needs to provide multiple synchronised sources the accelerator complex is required to deliver three types of electron beams to a variety of undulator, wiggler and FEL sources. These are:

- 750-950 MeV, 1 nC bunches with peak current >1.5 kA driving an XUV-FEL at 1 kHz, with RMS bunch lengths less than 270 fs;
- 600 MeV, 77 pC bunches with short bunch lengths down to ~100 fs RMS, operating at 1.3 GHz for a suite of spontaneous sources or operating at some multiple, n, of 4.33 MHz for a VUV-FEL. The peak current at the VUV-FEL must be over 300 A (see Chapter 8);
- 25-60 MeV, 200 pC bunches for an IR-FEL, delivered at 13 MHz with RMS bunch lengths between 1 and 10 ps.

The first two of these — the 750-950 MeV and 600 MeV beams — are combined into a single accelerator system, whilst the output photons from the third are available for delivery with good synchronisation to a wide variety of pump-probe experiments. An overall accelerator specification has evolved in an iterative manner to deliver electron beams which are capable of driving sources designed to meet the science requirements. Electron beam parameters for the different accelerator sections and operating modes are summarised in Table 7.1 to Table 7.3.

Table 7.1 XUV-FEL electron beam parameters

XUV-FEL Bunch Parameter	
Energy at XUV-FEL, E	750 to 950 MeV
Normalised Emittance at XUV-FEL, ε	2 mm mrad
RMS Projected Energy Spread at XUV-FEL	0.1%
RMS Bunch Length at XUV-FEL	< 270 fs
Bunch Charge	1 nC
Bunch Repetition Rate	1 kHz
Electron Beam Average Power at XUV-FEL	1 kW
Energy at start of Main Linac (Linac5)	160 MeV

Table 7.2 HACL electron beam parameters

HACL Bunch Parameter	*100 mA Operation*	*VUV-FEL Operation*
Energy at VUV-FEL, E	600 MeV	600 MeV
Normalised Emittance at 600 MeV, ε	2 mm mrad	2 mm mrad
RMS Projected Energy Spread	0.1 %	0.1 %
RMS Bunch Length at Device	100-900 fs in six straights	100 fs
Bunch Charge	77 pC	77 pC
Bunch Repetition Rate	1.3 GHz	$n \times 4.33$ MHz
Electron Beam Average Power at 600 MeV	60 MW	$n \times 200$ kW
Injector Energy	10 MeV	10 MeV
Dump Energy	~ 10 MeV	~ 10 MeV

Table 7.3 IR-FEL electron beam parameters

IR-FEL Bunch Parameter	
Energy at IR-FELs, E	25-60 MeV
Normalised Emittance at 60 MeV, ε	10 mm mrad
RMS Projected Energy Spread at 60 MeV	0.1%
RMS Bunch Length	1 to 10 ps (variable)
Bunch Charge	200 pC
Bunch Repetition Rate	13 MHz
Electron Beam Average Power at 60 MeV	156 kW

The simultaneous provision of three bunch sources – IR-FEL, HACL and XUV-FEL – allows a number of multi-wavelength experiments to be performed. Several operating modes for the HACL and XUV-FEL common branches are possible; some modes will be required to manage ions, optics heat loads etc. The full range of operating modes will be developed in the project technical phase. However, two operating modes are presented here:

- *Spontaneous/XUV-FEL operation*. In this mode, the full 100 mA current is circulated through the HACL branch with 1.3 GHz spacing simultaneously with the 1 kHz XUV-FEL bunches. Gaps will be left in the HACL bunch train to clear ions (see Section 7.7.5). However, the resulting heat load on the VUV-FEL optics will be too high to allow lasing at this bunch frequency. Energy recovery is required in the HACL to manage the beam power;

- *VUV-FEL operation*. A lower HACL bunch repetition rate of at least 4.33 MHz is used (see Chapter 8); higher repetition rates are possible but will be limited by the heat load on the VUV-FEL optics. Gaps are unlikely to be needed for ion clearing, and XUV-FEL operation can take place simultaneously. Energy recovery is assumed but may not be needed at lower repetition rates (see Table 7.2).

7.2 Overview of Design

The 4GLS design is shown schematically in Figure 7.1. It involves the simultaneous acceleration of the 1 nC, XUV-FEL bunches and 77 pC high average current bunches in a common superconducting linac: these two bunch types are then separated and independently transported and compressed before passing through their respective photon output devices. The nature and degree of disruption of the high average current bunches as they pass through the spontaneous output devices, and then through the VUV-FEL, is such that the energy may still be recovered. This is carried out by returning the bunches via a second arc to the Main Linac, which decelerates them and recovers most of the 60 MW of beam power to be used to accelerate fresh bunches. The average beam power carried by the XUV-FEL bunches is relatively modest — 1 kW — compared to the power carried by the HACL beam, so after the spent-beam undulator these bunches are delivered to a beam dump.

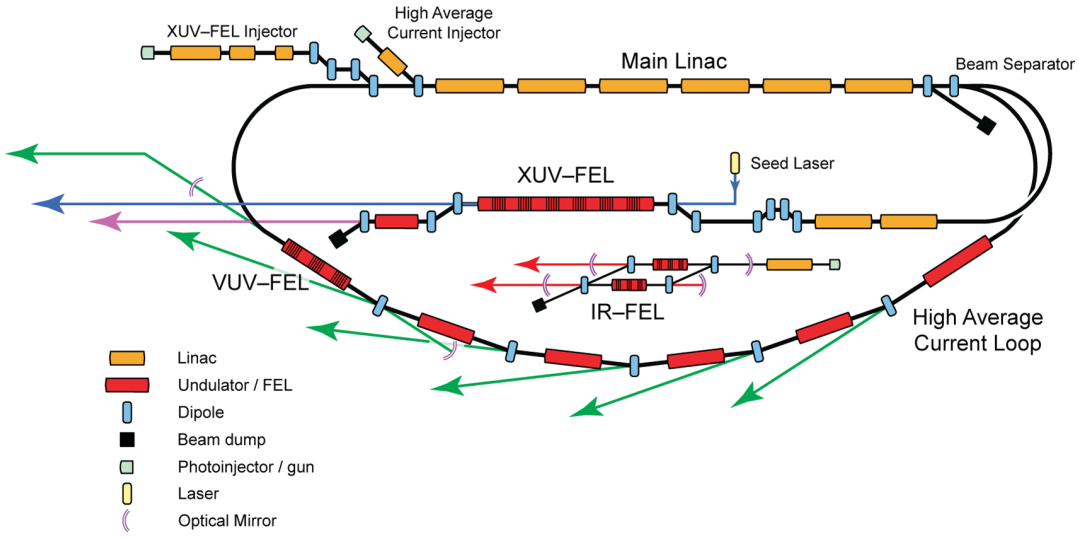

Figure 7.1 Schematic of the 4GLS design

The chosen layout has the benefit that the three FELs and all the spontaneous undulator sources deliver their output towards the same end of the facility, thereby minimising the optical path lengths to experiments that require the interaction of more than one source. The additional requirement for energy recovery of the HACL beam naturally then leads to a requirement to transport both the XUV-FEL and high-current bunches through approximately 180° bending systems before their delivery to the FELs. As the bunches of electrons travel through these arcs they emit incoherent synchrotron radiation which has a negligible effect on the electrons (see Chapter 9). However, the small bunch lengths and large bunch charge required for the XUV-

FEL mean that these bunches emit significant quantities of CSR, which may cause significant disruption to the emittance and energy spread of the beam. Studies of the CSR emission have indicated that if the bunch lengths are kept relatively long through the arc (~ 2 ps) then the CSR effects can be tolerated. The compression scheme to achieve this is outlined in Section 7.3.1 and a more detailed description of the effects of CSR is given in Section 7.7.3.

A beam energy at the dump of 10 MeV has been chosen for the high average current loop to keep the discarded electrons below the neutron production threshold for the likely dump materials and thus significantly reduce the radiation hazard.

In the Main Linac the 10 MeV injected beam is accelerated to 600 MeV and after the sources is returned to the Main Linac to be decelerated from 600 MeV back to 10 MeV by co-propagating the return beam with the accelerating bunches with a 180° phase difference. A topology showing the paths of the co-propagating HACL and XUV-FEL bunches is given in Figure 7.2. There is thus a factor of sixty difference in the beam energies that need to be simultaneously focused in the Main Linac. Preliminary estimates of BBU thresholds have shown that by using the graded-gradient scheme suggested by Douglas [4], satisfactory control of the focussing of the two beams within the linac can be obtained (see Section 7.7.8).

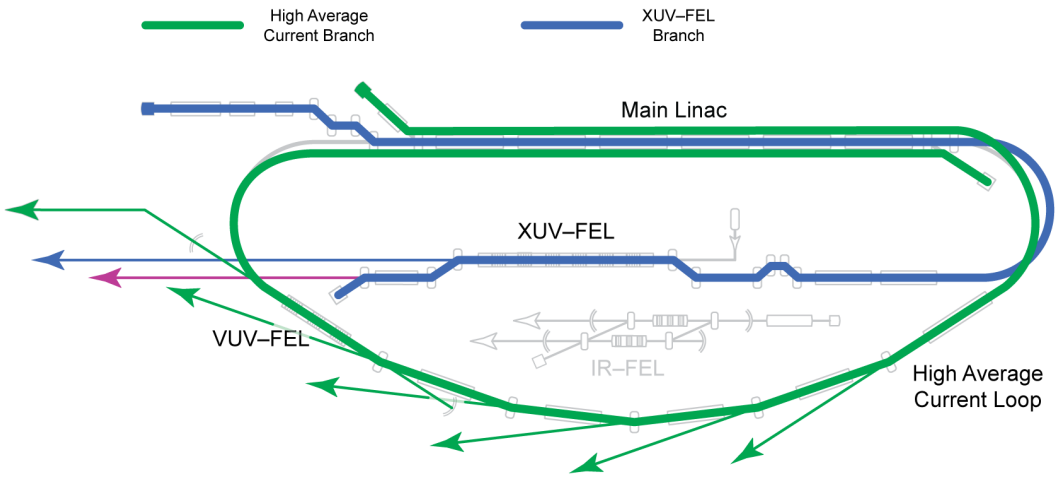

Figure 7.2 Paths taken by the HACL (green) and XUV-FEL (blue) bunches

An alternative scheme which would reduce the energy ratio of the beams that are co-propagating is to split the main acceleration into 2 loop stages, as depicted in Figure 7.3. This would decrease the energy ratio in the linac at any one point and could also allow injection (and hence beam dump) at a lower energy.

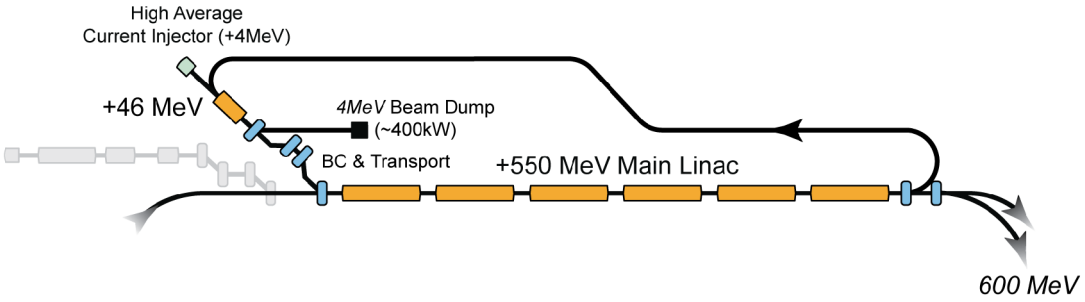

Figure 7.3 Schematic of a postulated cascaded injection system for the High Average Current Loop. This scheme is not part of the present 4GLS design.

There are three reasons for adopting such a scheme:

- Improve the focusing in the linac, thus decreasing the effect of BBU and increasing the possible current in the linac;
- Reducing the dump energy/power;
- Increasing the efficiency of energy recovery.

The BBU threshold is not a strong concern for this machine: using the graded-gradient scheme thresholds of the order of 50 mA have been estimated for a linac using TESLA cavities with standard higher-order mode (HOM) damping. It is envisaged that these currents may be dramatically increased by improved HOM damping and by manipulating the transport matrices in the recirculation optics (see Section 7.7.8). In particular it is possible to rotate the betatron planes by 90° so that any displacement in the second pass of the linac is orthogonal to the original displacement; simulations at TJNAF show a large increase in threshold current using such a rotation scheme, yielding a threshold of around 200 mA for skewed HOMs. [5].

The lower dump energy would imply equally low injection energy, but the injection energy cannot be decreased much below 10 MeV as longitudinal space charge (LSC) effects become much larger. The extra transport paths required between the linacs in the cascade system will introduce extra LSC effects which may be significant if the RMS bunch length is less than about 2 ps, and will certainly increase if there were a requirement to go to higher bunch charges in the high average current loop. The spent beam returning from the HACL devices will be far from ideal, and will have a larger energy spread after being subjected to energy losses in the output devices and to collective effects, and will have to be transported round an additional arc at 50 MeV if a two-loop system is adopted.

The problems of a two-loop scheme, in particular the increased transverse and longitudinal space charge, outweigh the difficulties of producing an adequate focusing scheme for BBU control. For this reason, a single-loop system is proposed in 4GLS.

7.3 Common Systems

7.3.1 Bunch Compression

At the heart of the 4GLS science case is the synchronised provision of short pulse radiation from the FELs and spontaneous undulators. The operation of the XUV-FEL requires a high peak current, low emittance beam with small energy spread. The VUV-FEL demands a more modest peak current but this must be produced using a much smaller bunch charge. The compression of the lower charge (77 pC) bunch is therefore equally demanding, as not only have the VUV-FEL requirements to be met, but also the science case requires different bunch lengths at different undulators in the HACL branch. The small magnet gaps required in the spontaneous devices can give strong wakefield effects: to control these, whilst providing different bunch lengths in the undulators, an elegant solution is proposed which makes use of the natural compression afforded by the bending cells between each undulator.

The IR-FEL is more conventional in that similar bunch properties have been achieved in working facilities [1,2,3]. In particular, the required emittance and bunch lengths are larger, and so a similar scheme to these existing designs may be adopted with confidence. The design of the IR-FEL transport is outlined in Section 7.6.

This section describes the principles of bunch compression, lists the issues considered during this phase of the design and outlines the chosen schemes for the 4GLS design. The important processes that impact on the compression such as wakefields and CSR are described in Sections 7.3.2.2 and 7.7.3. The preliminary simulation work which gauges the performance of the chosen scheme is described in Section 7.7.4.

7.3.1.1 Principles of Bunch Compression

Bunch compression is achieved using two processes. First, a correlated energy spread – or 'chirp' – is imprinted onto the bunch by passing it through an RF cavity off the voltage crest so that the front of the bunch sees a different gradient than the back. The beam then passes through a dispersive magnetic system which gives a path length dependence on energy. Figure 7.4 is a schematic illustrating this process ignoring non-linear effects. Note that the sign of the longitudinal dispersion R_{56} is not consistently defined in the literature or in simulation codes. In the following, we define magnetic chicanes to have positive R_{56}, which means that arc sections with positive dispersion have negative R_{56}. Note that sign conventions also differ over whether a particle at the front of a bunch has a positive or negative displacement compared to the centre; we adopt the convention that a positive chirp is compressed when passing through a magnetic system with positive R_{56}.

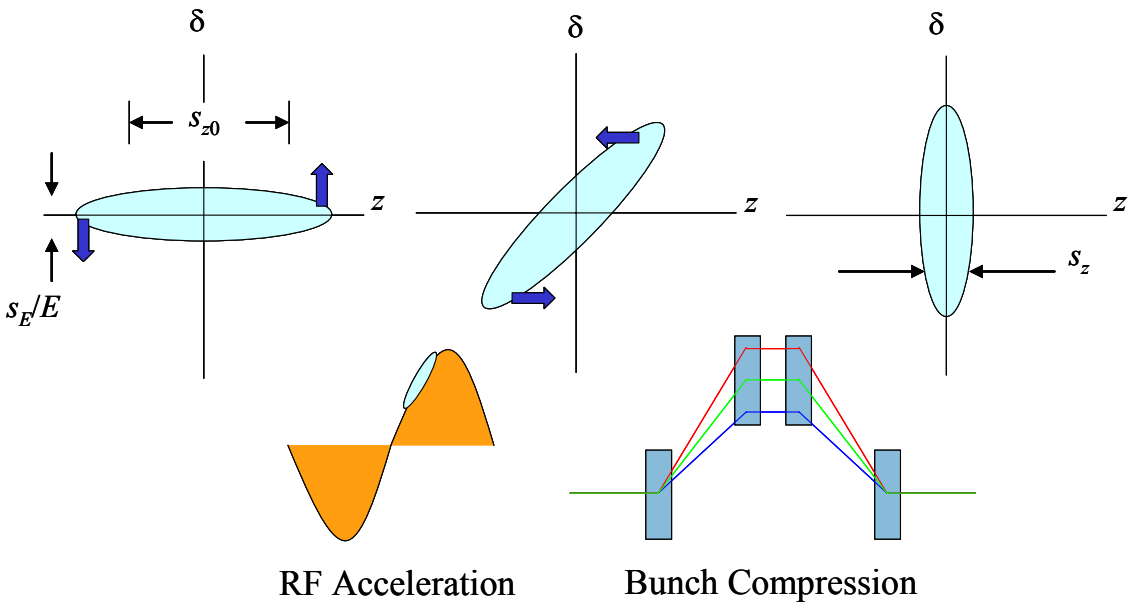

Figure 7.4 Schematic of bunch compression. After chirping of the bunch by an RF cavity, the higher-energy particles (blue) take a shorter path through a magnetic chicane downstream of the cavity, resulting in a shorter bunch with a larger (projected) energy spread.

In terms of the conventional longitudinal beam coordinates z and δ the acceleration/chirp may be described as:

$$z_1 = z_0$$

$$\delta_1 = \frac{(1+\delta_0)E_0 + eV_0\cos(\phi_0 - k_0 z_0)}{E_0 + \Delta E} - 1 \qquad (7\text{-}1)$$

where (z_0, δ_0) and (z_1, δ_1) are the longitudinal particle coordinates before and after acceleration. ϕ_0 is the shift in phase from on-crest acceleration, k_0 is the wavenumber of the accelerating field of amplitude V_0, and ΔE is the change in energy from the initial energy E_0.

The magnetic stage of compression gives resulting coordinates (z_2, δ_2) of:

$$\begin{aligned} z_2 &= z_1 + R_{56}\delta_1 + T_{566}\delta_1^2 + U_{5666}\delta_1^3 + O(\delta_1^4) \\ \delta_2 &= \delta_1 \end{aligned} \qquad (7\text{-}2)$$

where R_{56} is the linear (5,6) element in the transfer matrix for the system that couples the longitudinal coordinates. With the appropriate sign of R_{56} and chirp a longitudinal compression may be achieved. T_{566} and U_{5666} are the higher-order matrix terms that couple z to δ. For complete compression in a single stage the required R_{56} value is:

$$R_{56} = -\frac{\lambda_0}{2\pi \tan(\phi_0)} \frac{E_0 + \Delta E}{\Delta E} \tag{7-3}$$

A non-zero R_{56} is produced naturally by most magnetic systems with bends. In many single-pass systems for high-charge applications, a positive R_{56} (higher energy particles advance with respect to lower energy particles) is generated using a 4-dipole chicane. This has the twin advantage of simplicity and of cancelling out higher-order terms within the compressor However, in certain instances a simple chicane is not appropriate or even possible.

Both equations (7-1) and (7-2) are non-linear. All RF acceleration is inherently non-linear due to the sinusoidal form of the RF accelerating voltage. Higher-order terms are also inherent in the magnetic transport, and together with the RF non-linearity give a limitation in the compression that may be achieved. An illustration of this effect is shown in Figure 7.5.

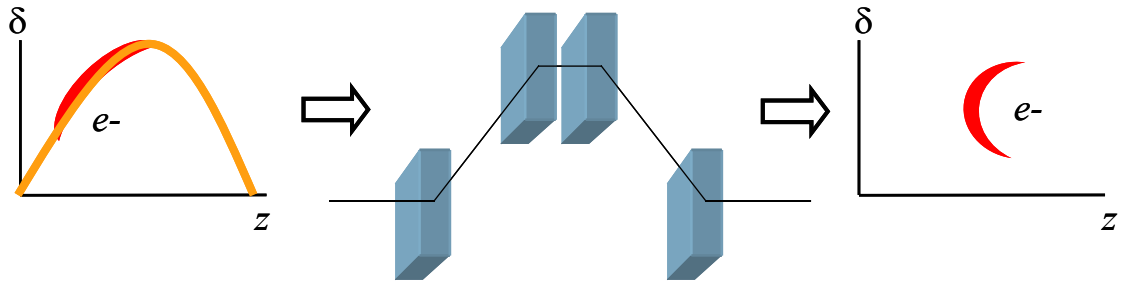

Figure 7.5 A schematic showing how the (non-linear) curvature of the RF limits the final bunch length after compression

RF curvature also produces spikes in the current distribution (see for example results obtained at the TESLA TTF-FEL [6]), due to the way the curvature in phase space is translated into longitudinal density after compression. Linearisation of the curvature produced both by the acceleration chirp and by the magnetic compression can be carried out with higher-harmonic cavities and/or higher-order magnetic correction. A higher-harmonic system is an attractive system as it is simpler to optimise and operate – non-linearities are corrected by adjusting a single voltage rather than a more complex magnetic correction using sextupoles. There are proposals to implement this method in several high charge, linac-based FEL projects, e.g. DESY VUVFEL [7,8], LCLS [9] and BESSY-FEL [10]. The alternative method of sextupole correction is discussed in [11].

Higher-harmonic RF linearisation requires the bunch to be decelerated to provide the correcting curvature. The total accelerating voltage is:

$$V_{rf} = V_0 \cos\left(\omega_0 t + \phi_0\right) + V_h \cos\left(\omega_h t + \phi_h\right), \tag{7-4}$$

where $\omega_h = h\omega_0$ is the harmonic frequency. Compensation of the quadratic term in the main RF is achieved with a harmonic voltage of

$$V_h = -\frac{V_0}{h^2}\frac{\cos\phi_0}{\cos\phi_h} \quad (7\text{-}5)$$

3rd harmonic correction is illustrated in Figure 7.6:

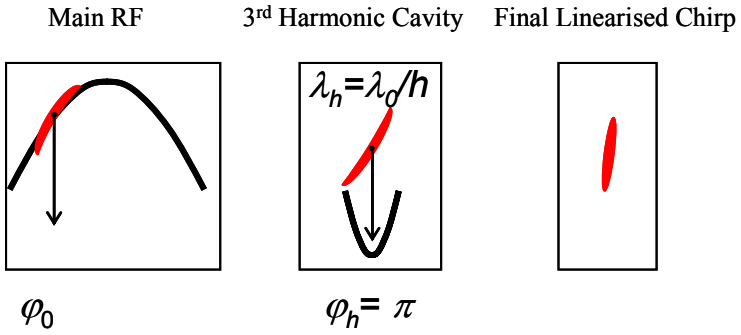

Figure 7.6 Schematic showing linearisation of curvature using deceleration with higher harmonic RF

Higher-order magnetic linearisation can be achieved by using families of appropriately placed sextupoles in dispersive sections of the magnetic system which then modify the higher-order longitudinal transport terms to cancel out the unwanted curvature. Use of this magnetic method is planned for ERLP [3] and has been successfully implemented in existing ERL based FELs such as at TJNAF [2,11]. Although this system is probably more cost-effective as it avoids the installation of costly additional RF systems, the tuning can be complex because of the cross-talk with the rest of the optics.

The above arguments suggest that in principle full compression can always be achieved in a single step. However, in reality there are many non-linear and collective effects that make detailed consideration more complicated. These are outlined in the following section.

7.3.1.2 Design considerations for the 4GLS Compression Scheme

There were many issues that influenced the design of the compression scheme for 4GLS and the scheme has evolved in an iterative manner together with the design of the arcs, merger and separator. Some of the issues which drove this evolution are listed below:

- Bunch lengths should be kept as large as possible for as long as possible to minimise the disruption to the bunch distributions from collective effects (space charge, wakefields, CSR) which scale approximately as the inverse of the bunch length. This is particularly important at low energy where the effects of space charge and wakefields are greater;

- The above requirement needs to be balanced by keeping the bunches short enough so that non-linear terms in the transport matrix do not become important, especially in regions where the projected energy spread is large, such as after RF chirping;

- The inclusion of sextupoles in dispersive regions and/or a third order harmonic RF cavity can be used to compensate for much of the non-linearity in the energy-time correlation along the bunch;

- Compression at an intermediate energy part way through the Main Linac would be complex; the accelerating/decelerating HACL bunches and the XUV-FEL beam would all have to be transported through the device;

- All non-isochronous transport elements have to be designed into the overall compression schemes, for example the mergers and separators.

In particular for the high charge XUV-FEL branch, which is more susceptible to collective effects, the following points are noted:

- The bunch should be kept reasonably long at all positions through the Main Linac and the outward arc to reduce space charge, CSR and longitudinal wakefield effects. Over compression must be avoided and the final compression kept as near as possible to the XUV-FEL to avoid degradation of the beam quality;

- The chirp introduced by the longitudinal cavity wakefields tends to cancel the RF curvature if a chicane-type compression scheme is used. The stronger wakefields acting on the 1 nC XUV-FEL bunches mean that chicane-type compression is preferred;

- Pre-acceleration of the beam provides an opportunity to compress the relatively long high peak current bunch to an intermediate value before the Main Linac, thus decreasing the non-linear energy chirp acquired in the linacs and allowing linearisation using a 3rd harmonic RF system with modest power requirements;

- A two stage compression scheme may also reduce timing and charge jitter on a highly compressed beam [7].

For the high average current loop, the following points need to be taken into account:

- Compression of the 10 MeV bunches before the main accelerator is undesirable because of space charge blow-up;

- Progressive compression through the HACL Insertion Device (ID) Arc is required;

- Acceleration with a negative chirp would allow magnetic compression through the outward arc and easily provide final progressive compression through the HACL ID arc; the varying bunch lengths in the spontaneous devices make it easier to handle resistive-wall wakefields and thereby to allow smaller magnetic gaps.

7.3.1.3 Design of the High Average Current Loop

A schematic for the high average current loop is shown in Figure 7.7. In this case the bunches are accelerated on the negative side of the RF wave, which allows the HACL outward arc (Arc-1) to be used to achieve compression progressively through to the first spontaneous insertion device. Wakefield effects will be smaller in the lower charge 77 pC bunches, although the bunches must still be transported through the six insertion device straights with bunch lengths generally much less than 1 ps.

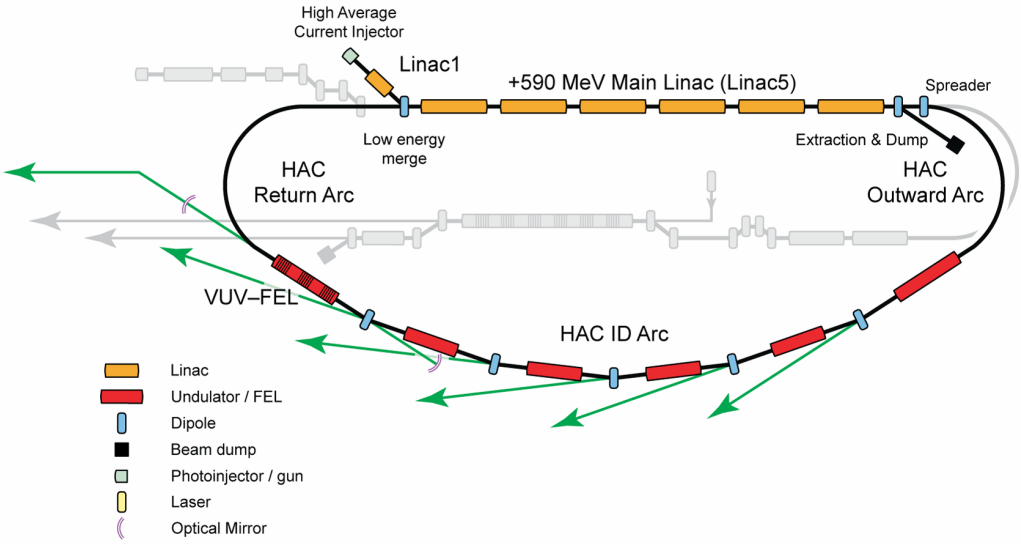

Figure 7.7 Schematic layout of the High Average Current Loop

Progressive compression is continued through the ID arc to balance the bunch length required in each insertion device with the effects from resistive wall wakefields (see section 7.7.6). The HACL return arc is adjusted to give the smallest possible longitudinal dispersion, and is followed by a strong positive compression in the merger section with the XUV-FEL branch injection to give an overall zero R_{56} prior to bunch deceleration: $R_{56} = 0$ is required from the HACL optics to minimise the final decelerated energy spread in the extracted and dumped bunches [4]. Compensation of the RF curvature by use of a 3rd harmonic cavity is not possible within the Main Linac (Linac5), and so it is proposed to linearise the curvature by using sextupoles in the outward arc. Such a scheme has been adopted, and the resulting bunch lengths achieved are described in Section 7.7.4.

7.3.1.4 Design of the XUV-FEL Branch

In common with other linac-based designs, the XUV-FEL branch is operated using a positive chirp and positive (chicane) bunch compressors. A schematic layout of the branch is given in Figure 7.8. Initial simulations [12] show that a single stage scheme would require a 3rd harmonic voltage of over 93 MV for the XUV-FEL branch for acceleration up to 750 MeV, as predicted

by equation (7-5). However, the voltage required is predicted to be of the order of 30 MV for a two-stage scheme with an intermediate energy of 160 MeV. The compression will therefore be carried out in two magnetic bunch compressors (denoted BC1 and BC2) to compress positively, and operating the XUV-FEL injector linacs (Linac2/Linac3) off-crest to provide the energy chirp for BC1. BC1 provides the dual function of bunch compression and merging of the beam with the High Average Current Loop. Third-harmonic linearisation is provided mostly by the 3rd harmonic cavities (Linac4) and by sextupoles in the XUV-FEL Arc.

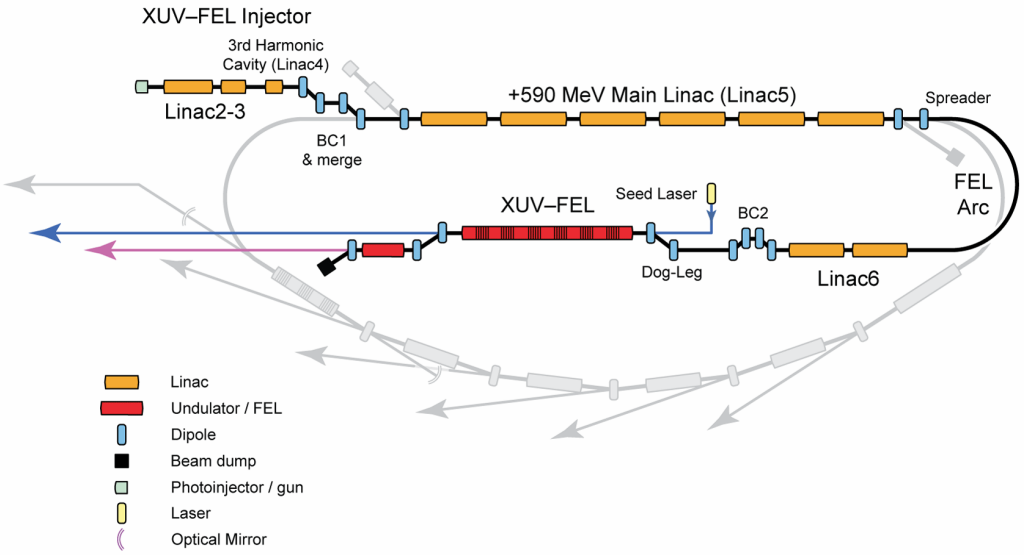

Figure 7.8 Schematic layout of the XUV-FEL branch

The bunches are then accelerated in the Main Linac, nearly on-crest to minimise chromatic effects in the transport and to avoid over-compression in the Spreader. The spreader/arc combination is made nearly isochronous, with a final positive chirp being carried out in XUV-FEL linac (Linac6). Final compression is provided by BC2 and the dog-leg. This scheme allows the wakefield chirp to be compensated to some extent and minimises the distance over which the fully-compressed bunch has to be transported before passing through the FEL; both of these help to minimise emittance degradation from wakefields and CSR. Sextupoles will be used to control higher-order terms in the transport; a preliminary sextupole scheme has been included to control higher-order transport terms.

7.3.2 Acceleration

4GLS is unusual in that we need to transport and compress two different bunch charges and deliver them to two different sets of user devices, with the bulk of the acceleration being carried out in a common linac.

7.3.2.1 Phase of Acceleration and Deceleration

The effective compression of each bunch type in the two branches requires quite different transport optics and linearisation, with compression of the two bunch types having opposite phases and polarities. Figure 7.9 shows a schematic of the acceleration and deceleration phases in the common Main Linac. In addition to allowing for opposite phase compression in each branch, there are two other benefits from accelerating the 1 nC and 77 pC on opposite sides of the RF crest. Firstly, the 1 nC and neighbouring 77 pC bunches are longitudinally separated, which prevents any mutual space charge problems. Secondly, the separation reduces the effect of the trailing wakefield from the 1 nC bunch that acts upon the following HACL bunches. The phases shown in Figure 7.9 will change when each branch is tuned, but the separation between the two bunch types will be of the order of tens of picoseconds. Mutual space charge could also be avoided by leaving 1-bunch gaps – or 'holes' – in the HACL bunch train that the 1 nC bunch could sit in, but this may give troublesome beam loading effects in the linacs that accelerate the HACL bunches.

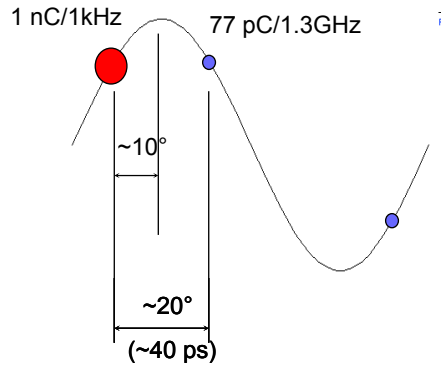

Figure 7.9 Illustration of acceleration and deceleration in the Main Linac

7.3.2.2 Longitudinal Wakefields

The longitudinal effect of the trailing wakefield from the 1 nC XUV-FEL bunch has been estimated using the existing nine-cell cavity TESLA design; the longitudinal delta-wake potential of an 8-cavity module is shown in Figure 7.10 [13,14]. Assuming six such modules the energy change imparted to the following HACL bunch 40 ps from the XUV-FEL bunch driving the wakefield will therefore be around 50-60 keV, or $\sim 10^{-4}$ in relative energy. This is much less than the final projected energy spread of 10^{-3} required at the spontaneous devices, and so will not cause a significant shift in the output of these devices. Bunches following the first 77 pC bunch will see progressively less deceleration.

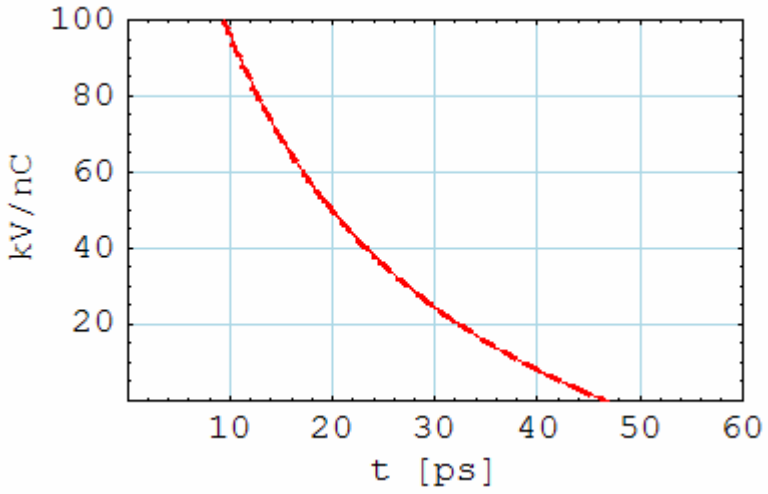

Figure 7.10 Delta-wake potential for 1 TESLA-type module consisting of eight nine-cell cavities

7.3.2.3 Linac Focusing Scheme

The focusing scheme in the Main Linac is primarily dictated by the requirement to provide for a sufficiently large beam break-up threshold; this is discussed more fully below (see 7.7.8). However, the phase advance from module to module must be compatible with emittance measurement and other diagnostics in this section. Studies for the Technical Design Report will determine the best phase advance choice to balance the requirements of BBU and diagnostic needs. At this stage, a graded-gradient scheme is being considered which, for flexibility, utilises a triplet of quadrupoles between each accelerating module, as shown schematically in Figure 7.11. Twiss values below ~50 m are readily obtained in both planes without much perturbation of the transfer matrices that are required to obtain a large BBU threshold. This will be explored further in the future.

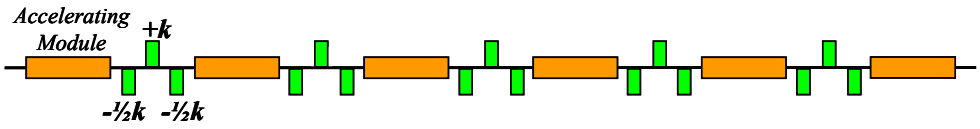

Figure 7.11 Schematic of the graded-gradient focusing scheme; each module is separated by a triplet of quadrupoles powered as $-\frac{1}{2}k, k, -\frac{1}{2}k$.

7.3.3 Merge Sections

The HACL beam from the injector must be merged with the returning HACL bunches from the return arc, and with the 160 MeV bunches from the XUV-FEL injector. The large energy ratio between each of the 10, 160 and 600 MeV bunches means that it is appropriate to have two merger sections:

1. A 160/600 MeV merger to combine the XUV-FEL injector and returning HACL bunches. The 4:1 energy ratio makes this merger rather straightforward, and it is most appropriate to achieve this using a combination of a 4-dipole chicane and a 4-dipole slide;

2. A 10 MeV/high energy merger to combine the high energy XUV-FEL/HACL bunches with the 10 MeV injector beam. The energy ratio is over 10:1, so we can consider the action of this merger section as a small perturbation to the higher energy (160/600) MeV bunches.

7.3.3.1 The 160/600 MeV Merger

The 160/600 MeV merger is shown schematically in Figure 7.12. This merger conveniently performs three tasks:

- Merge of 160 MeV injected XUV-FEL bunches and 600 MeV return HACL bunches
- First stage compression of XUV-FEL bunches
- Final application of R_{56} to return HACL bunches to allow efficient deceleration and energy recovery

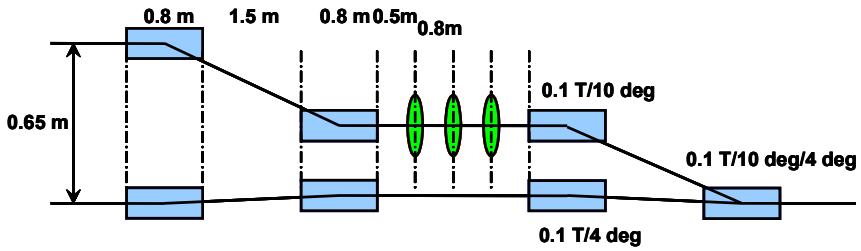

Figure 7.12 Schematic of 160/600 MeV merger; the 160 MeV beam passes through the four-dipole slide whilst the 600 MeV passes through the four-dipole chicane.

Table 7.4 Parameters of first XUV-FEL bunch compressor/merge BC1

Parameter		*Unit*
Energy E	160	MeV
1st-order momentum compaction R_{56}	113	mm
2nd-order momentum compaction T_{566}	506	mm
Dipole Length	0.8	m
Dipole Bend Field	0.1	T
Quadrupole Length	0.3	m
Quadrupole Strength	1.8	T/m

7.3.3.2 The 10 MeV/High Energy Merger

A schematic of the merger is shown in Figure 7.13. The aim of such a merger is to divert the rather low energy high average current, injected beam into the main accelerator transport system without significant emittance degradation; this is generally done using an emittance compensation scheme.

In our case we require a significant bend angle to displace the HACL injector from the other accelerator items in this congested region. We have examined a two-dipole achromatic transfer line using an optimisation code that takes space charge oscillations into account [15]. Three quadrupoles are used within the achromat, plus five more to match from the upstream HACL injector and into the main superconducting linac.

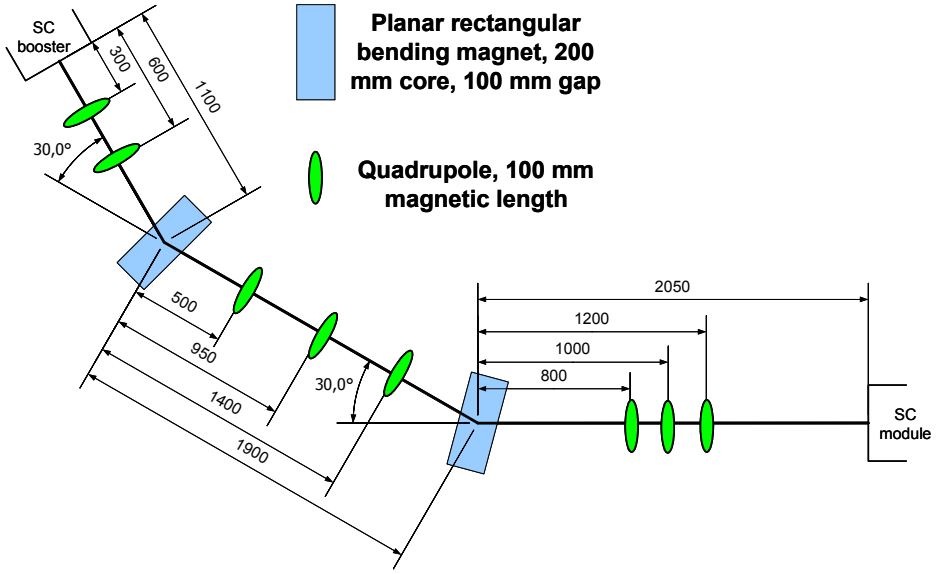

Figure 7.13 Schematic of the 10 MeV/high energy merge

Table 7.5 Parameters of HACL/high energy merge

Parameter		*Unit*
Energy E	10	MeV
Dipole Length	200	mm
Dipole Bend Field	0.06	T
Quadrupole Length	100	mm

7.3.4 Beam Separation

7.3.4.1 Low Energy Dump Separator

Similar to the considerations for beam merging (see section 7.3.3), it is appropriate to separate the low-energy recovered 10 MeV bunches from the accelerated HACL and XUV-FEL beams in a dedicated extraction chicane. A design for such a separator is shown in Figure 7.14; this separator acts as a perturbation on the higher energy 600 MeV and 750 MeV beams. The first 0.2 m long dipole (shown in blue) extracts the low energy beam whilst the following three identical dipoles create a chicane for the high-energy beams that close their dispersion; this chicane is a weak perturbation on the optics of the high energy beams. Matching quadrupoles (in green) and the spectrometer spreader dipole are also shown.

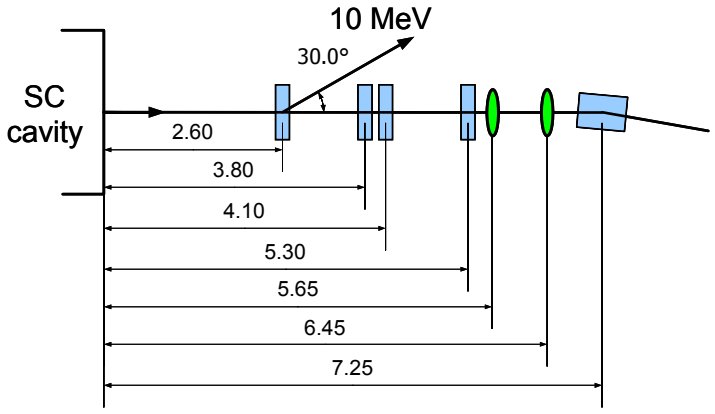

Figure 7.14 Low energy dump separator for the energy-recovered HACL bunches. Distances from the last accelerating module are shown in meters.

7.3.4.2 High Energy Separation

The separation of the XUV-FEL and HACL bunches is challenging because of the required beam energies and the high 1.3 GHz repetition rate of the HACL bunches. A single 180° arc transporting both the 600 MeV and 750 MeV bunch types was rejected partly because of the large acceptance this would require. More importantly a single arc would imply using a pulsed deflector or RF separator capable of selecting bunches at 1.3 GHz to deliver them to the different source points; it is considered that such a system would be far too complex and insufficiently stable to satisfy the requirements of 4GLS [16]. A DC magnetic separation scheme is therefore an appropriate choice, but is complicated by the narrow separation of the beam energies.

The beam spreader must separate the 600 MeV and 750 MeV bunches sufficiently to allow feasible magnetic elements and a large enough aperture to control both wakefields and beam loss. To minimise the R_{56} imparted to the beam by the spreader, a modular slide spreader is considered unsuitable, and instead a spectrometer-based spreader is proposed. This scheme is shown in Figure 7.15, and is intended to separate the 600 MeV and 750 MeV beams in as short

a distance as possible. The spreader consists of a dipole magnet followed by a spreader magnet with opposing fields; a possible realisation of the spreader magnet is shown in Figure 7.16. The dipole magnet is rectangular and has a magnetic length of 700 mm. It bends the 600 MeV beam by 9.2° and the 750 MeV one by 8° if its field is 0.5 T. One metre downstream from its centre the distance between the beams is ~ 35 mm, which allows for a relatively small aperture but keeps the spreader close to the spectrometer dipole. After the spread the angle between the beams is 9.2°, which allows the first quadrupoles to be placed close to the spreader and therefore constrains the growth of dispersion and R_{56} in the 750 MeV bunches. Note that the 750 MeV XUV-FEL branch beam exits outside the 600 MeV beam in this design, which dictates that one arc must incorporate a vertical offset to allow the beams to cross; this is needed to place the XUV-FEL within the HACL to avoid beamline clashes. The rather small aperture in the spreader dipole means that care may be needed to protect it against radiation damage from beam halo generated upstream in the injectors and Main Linac. This issue will be considered in the future.

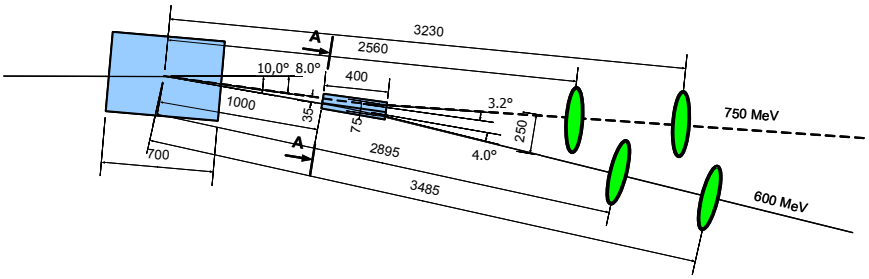

Figure 7.15 Schematic of spectrometer-based spreader proposed for the 4GLS design, consisting of a dipole spectrometer (shown in blue on the left) with a spreader magnet (centre blue). Section A-A at the entrance to the spreader dipole is shown in Figure 7.16. Because the beam dispersion is not corrected by the spreader the design must be integrated with the following arc design – this is indicated by the downstream quadrupoles shown on the right in green.

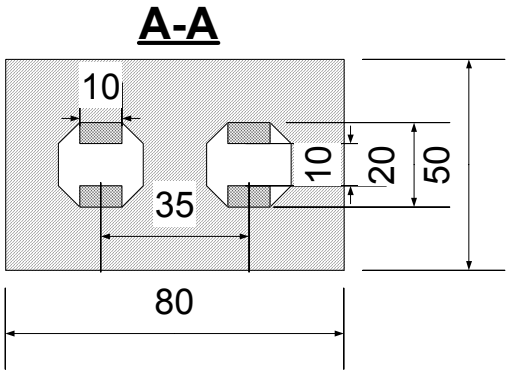

Figure 7.16 A possible realization of a spreader magnet giving two apertures with opposing dipole fields using permanent magnet technology. A-A is a section through the spreader as shown in Figure 7.15. The beam aperture must be rather small, ~10 mm. The overall length of dipole in this scheme is 400 mm, with a field in each aperture of 0.35 T.

7.4 The High Average Current Loop

7.4.1 Introduction

This section describes the general lattice design philosophy developed to provide the loop arc and ID arcs for the High Average Current Loop. The overall electron transport system is shown schematically in Figure 7.7. The description below outlines the chosen concept in terms of lattice type and approximate lattice functions. Although further development will have to be performed in the future, this design is sufficient to illustrate the general properties of the chosen lattice types for 4GLS.

The ID arc was chosen to be 60° to allow a 10° separation of six ID beamlines and this then set the two outer arcs to 150° , with the assumption that they are to be of the same arc design. An initial design for the loop arcs proposed the use of triple-bend achromats [17], but this design was found to be too inflexible to give the large longitudinal dispersion required for progressive compression. To overcome the size and inflexibility of the initial solution, a more compact design was chosen which uses FODO cells and integrates the beam spreader with the arcs. The beam spreader section is described above in section 7.3.4.2, and is followed by three arc sections – the outward arc, the ID arc, and the return arc. The HACL outward and and return arcs are each composed of seven 20° cells; the magnet parameters are given in Table 7.6. Each dipole forms a regular cell with three quadrupoles as shown in Figure 7.17. The longitudinal dispersion R_{56} can be controlled in the range of +20 to +100 mm by adjustment of the quadrupoles, which is the requirement envisaged for the HACL transport.

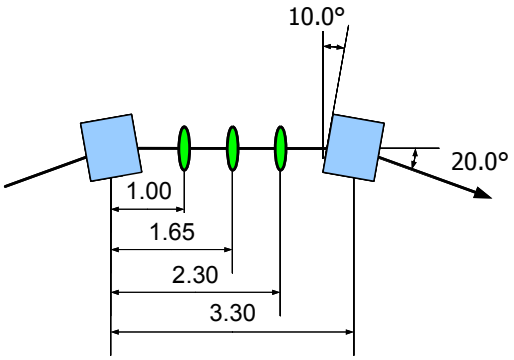

Figure 7.17 Regular cell of the HACL outward and return arcs

As an example of the tuning and matching of this arc, the results of an optimisation are given which set the gradients to +2.4, +7.7, and -7.0 T/m (+ indicating horizontal focusing). The resultant R_{56} is approximately +48 mm, and is obtained with relatively small Twiss parameters and dispersion. The lattice functions within the cell are illustrated in Figure 7.18. The figure shows a section between the centers of the dipoles. The OPTI code [18] was used to simulate and optimise the cells and their matching to the HACL ID Arc.

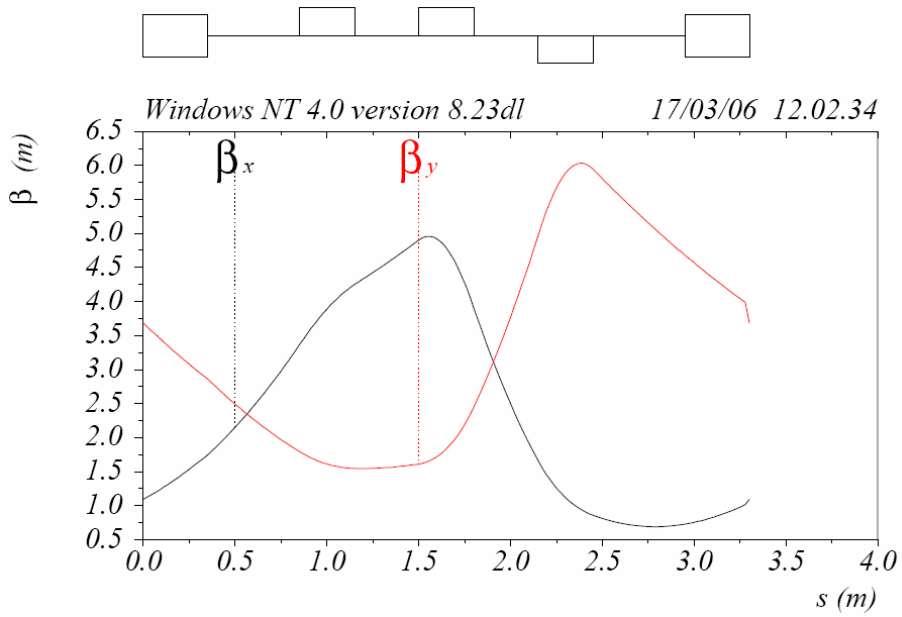

Figure 7.18 Lattice functions in the regular cells of the HACL outward and return arcs

.

Table 7.6 Magnet parameters in the HACL outward and return arcs

Parameter		*Unit*
Bunch Energy	600	MeV
Dipole Length	700	Mm
Dipole Bend Field	1.00	T
Quadrupole Length	300	Mm
Quadrupole Max Gradient	8	T/m

Consideration has been given to the engineering of the components that will have to be incorporated into the HACL arc design. These components will add approximately 1 m to the length of each cell shown in Figure 7.18 [19], but no significant change in the optical properties or collective effects are expected; the layouts shown elsewhere in this report (for instance, Figure 7.1) take account of this increase.

7.4.2 Matching the Beam Parameters

The two quadrupoles in the extraction and entry section from the Main Linac (see Figure 7.14) are not sufficient to match all the required beam parameters of both the XUV-FEL and HACL beams; this includes the dispersion which is not cancelled within the spreader itself. The first few cells in both the HACL outward arc and the XUV-FEL arc are non-symmetric to achieve the correct matching condition. The entrance to HACL outward arc is shown in Figure 7.19; the

entrance consists of the spreader magnet, four quadrupoles and a cell geometrically identical to the regular one. However, the strengths of the quadrupoles obviously differ from the ones in the regular cell to match into the periodic optical functions in the rest of the arc cells. A schematic of the complete arc is shown in Figure 7.20 with associated optical functions in Figure 7.21. The final cell and matching section into the first insertion device straight are also non-symmetric; this is discussed in the following section.

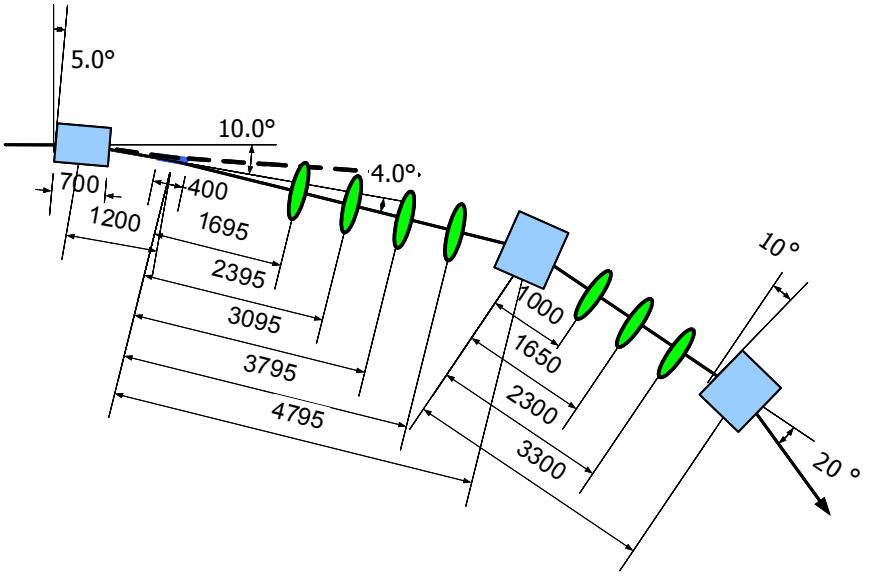

Figure 7.19 Entrance and first non-symmetric cell of HACL outward arc. Dimensions are shown in mm unless otherwise indicated.

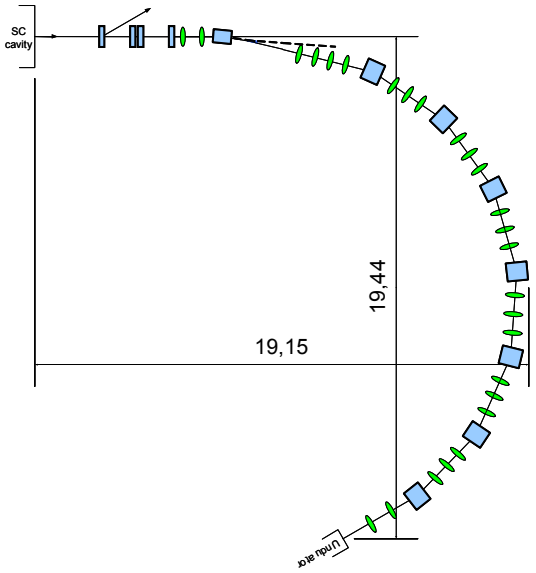

Figure 7.20 Overview schematic of the HACL outward arc. Dimensions are shown in meters.

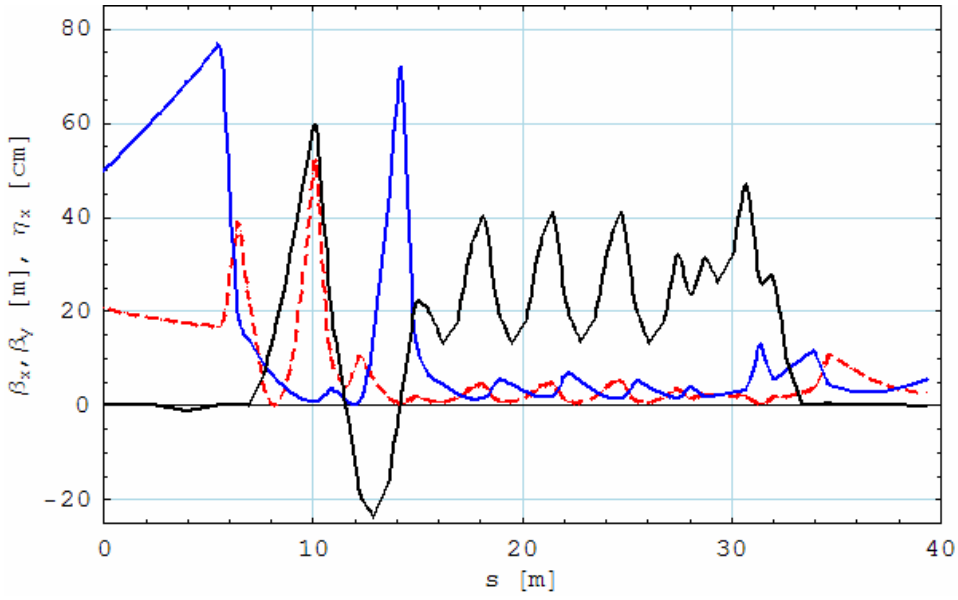

Figure 7.21 Optical functions in the complete HACL outward arc; β_x is shown in red, β_y in blue, and dispersion η_x in black.

7.4.3 ID Arc Design

7.4.3.1 Cell Design

The cell design has been performed using a custom program written in MLC (the Mathematica Lattice Code) [20] using an adapted parameterisation of an isochronous TBA by Guignard [21,22]. The design procedure allows for straightforward modifications of the input parameters (e.g. number of cells, total arc angles, bending fields) and a semi-automated optimisation of the cell parameters. The result is that for each set of chosen input parameters the important cell

properties – total cell length, quadrupole strengths (which determine chromatic aberrations) and betatron envelope sizes – are well-optimised.

In the design of the HACL ID arc cell, the following parameters were chosen:

- Total ID Arc bend angle 60°;
- Varying straight length for insertion devices, as demanded by the user case and layout constraints;
- In each straight, an allocation of 0.5 m has been made at each end for correctors, transitions, instrumentation, pumping, flanges etc;
- Quadrupole length 0.3 m for cell compactness whilst minimising quadrupole gradient;
- Minimum element to element separation of 0.2 m to allow for coil overhang etc;
- Maximum quadrupole gradient of 12 T/m to reduce chromatic aberration;
- Dipole length of 0.3 m, which is long enough to allow a sensible magnet design, but short enough to give a reasonable dipole field of 0.33 Tesla at 600 MeV (given the other specifications above);
- The design is optimised to give a small negative R_{56} of ~ 10 mm per cell, to give the required variation of bunch length from straight to straight whilst at the same time minimising the disruption from resistive wakefields.

7.4.3.2 Arc Design

Five cells with a modular layout give six insertion device straights, as shown in Figure 7.1. The HACL outward arc and return arc provide matched conditions into and out of the first and last straight respectively (see Figure 7.22). A close-up of the engineering layout in Figure 7.23 shows one of the modular TBA arcs. The TBA cell consists of this arc and two halves of the adjacent ID straight. This cell matched with symmetrical Twiss values is shown in Figure 7.24 – matching into the different straights gives a modulation of these values, shown in Figure 7.25. Future work will match the present model to the engineering straight layout, and will allow the Twiss functions to be set to the values required by the user devices. The associated longitudinal dispersion for this layout is shown in Figure 7.26, which shows how a small progressive compression may be achieved from straight to straight. Note that the present illustrative solution may be varied to give the smaller Twiss values down to $\beta \sim 2$ m in each plane at the straight centres, as required by the user devices (see Chapter 9). The exact requirements will be integrated into later designs.

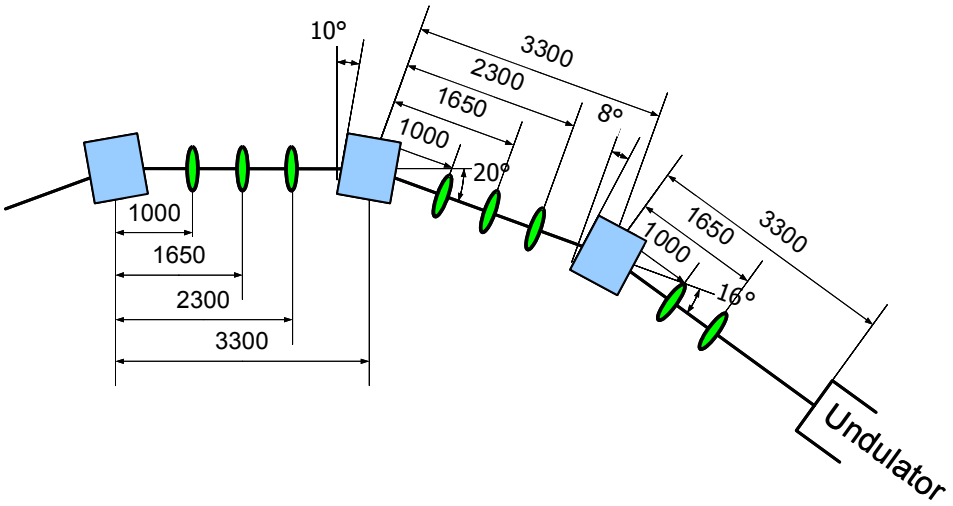

Figure 7.22 End of the HACL outward arc. The final two cells have a non-symmetric quadrupole configuration to match the bunches correctly into the first insertion device straight. The reverse happens at the entrance to HACL return arc. Dimensions are shown in mm unless otherwise indicated.

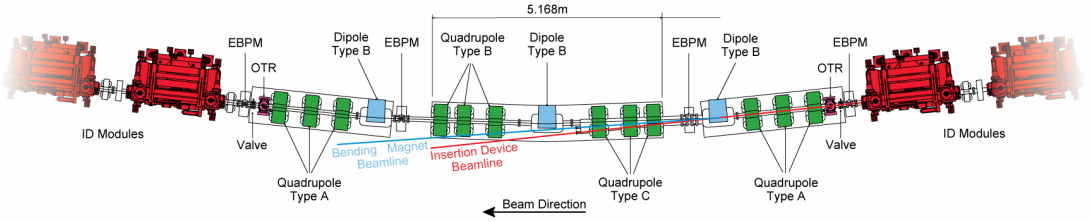

Figure 7.23 Engineering layout of a typical HACL ID TBA arc. The IDs are situated in the straight sections adjacent to this TBA arc.

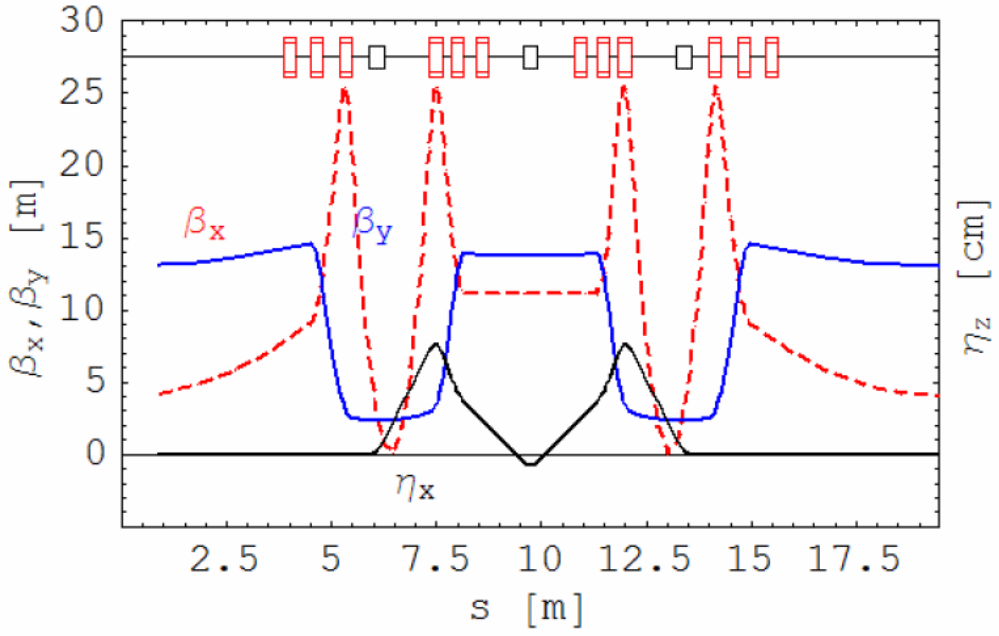

Figure 7.24 The basic unit of ID Arc design is this TBA cell. Three quadrupoles each side of the centre dipole allow a small variation of the longitudinal dispersion R_{56}, and the outer quadrupole triplets allows matching to a variable length straight with some control over the optical Twiss values at the ID straight centre.

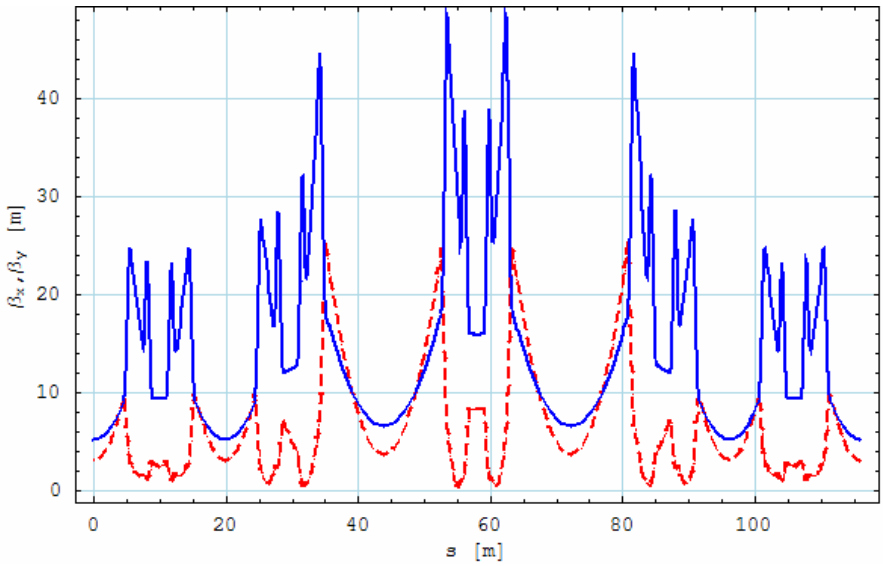

Figure 7.25 Example optical functions for the HACL ID arc

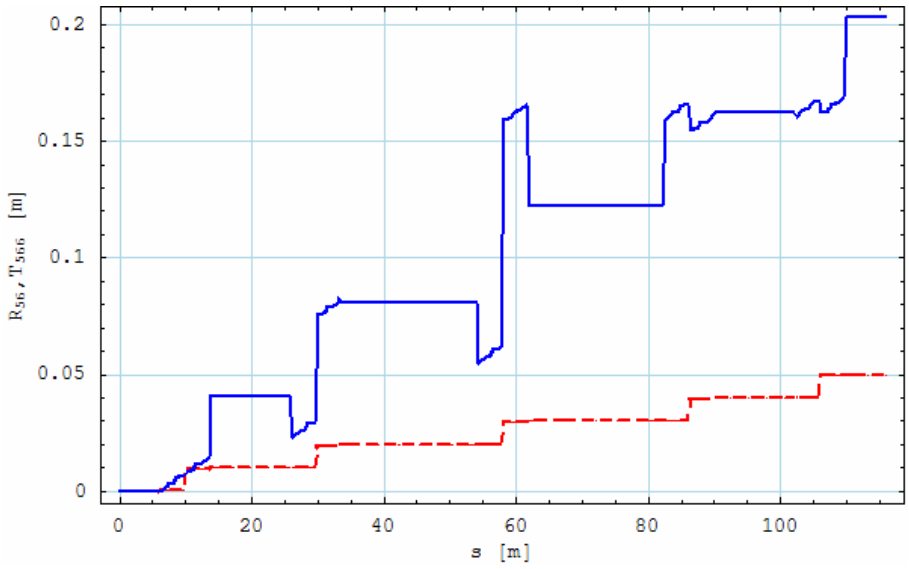

Figure 7.26 Development of the first- and second-order longitudinal dispersion R_{56} (red dashed line) and T_{566} (blue solid line) for the straight arrangement of Figure 7.25. The small compression of ~10 mm per cell is readily apparent.

7.4.4 Return Path Topology

To correctly chirp the bunches for energy recovery, the R_{56} from the Main Linac exit to the Main Linac re-entry must be approximately zero – this gives a cancellation of the chirp from acceleration during deceleration to manage the final energy spread [23]. However, the three arcs in the HACL transport – The outward, ID and return arcs - all contribute to the R_{56} with the same sign. The R_{56} from the return arc may be reduced compared to the outward arc, but as it is composed of FODO cells (to make it optically and geometrically similar to the outward arc) it cannot be made opposite in sign. To accomplish this, it is envisaged to use one or more dipole chicanes to produce an R_{56} of opposite sign to cancel the accumulated R_{56} from the three arcs; the positive R_{56} from the BC1 merge (see Figure 7.12) helps in part. It is also envisaged that this chicane section will allow adjustment of the path length which – together with small path length adjustment in the arcs – will give the variation necessary to give the correct phase for deceleration. The alternative scheme used on ERLP (and on other ERLs such as the JAERI ERL [24]) - namely to mechanically move the arcs to provide phase adjustment - is not considered to be appropriate due to the large size and geometry of the arcs. A design for the path-length adjusting chicane has not yet been made, and will be a subject for future study.

7.4.5 High Average Current Loop Beam Dump

7.4.5.1 Requirements

The High Average Current Loop transports 60 MW of quasi-continuous beam power; even when the bunches are decelerated to 10 MeV to recover most of this power back into the Main Linac, there remains a nominal 1 MW beam to be transported safely and dumped. The overall power handling requirement will depend on the efficiency with which energy recovery has been

performed, and so some safety margin over and above 1 MW is needed. Also, as will be discussed below, there may be some requirements on the recovered beam energy to optimise the dump design.

Disposing of 1 MW of power is not difficult given sufficient cooling, and for example klystron collectors have been built which accomplish this [25]. Particle beam dumps which handle 1 MW of incident beam power have also been constructed, and for example have been operated for over 30 years at SLAC [26,27], albeit with some technical issues. Beam dumps of 10 MW and greater have been considered for TESLA [28] and now are being considered for the International Linear Collider (ILC) [29]. However, a low energy, high power beam dump presents important design issues which are particular to 4GLS and other ERL projects [25].

There are three issues that determine the design of a high power beam dump:

- How the beam power is to be spread volumetrically to lower the power density per unit volume. This may be achieved either by spreading the beam transversely [25,29] or tailoring the material to spread the deposition longitudinally [25-29]. There are some basic physics limitations which are important that are dealt with below.

- The incident average power may be pulsed in a very short time - say over 1 ms or less - which increases local heating problems during the pulse; or it may be quasi-continuous, which reduces the ability of certain designs to remove the generated heat.

- Activation of the dump material.

7.4.5.2 Comparison with High Energy Dump Designs

Linear collider projects such as those at SLAC [26,27] and now TESLA and ILC [28, 29] have dump power requirements of 1-10 MW which at first glance are similar to those for 4GLS. This is not true: the difference lies in the incident beam energy. Dumping electrons of 10 GeV [26] or greater has the advantage that the dE/dx energy loss occurs over a much larger depth of target material than with electrons in the ~ 10 MeV range. For example, a 400 GeV electron beam is stopped over ~ 5 m of copper (including developed showers) [29] whereas a 10 MeV electron beam is stopped in only 8 mm of copper [25]. With unexpanded transverse beam sizes typical for a collider of up to (say) ~1 mm the local heating from several MW of incident power is still too great to allow a conduction-based solid dump design to work effectively, i.e. one that relies on heat conduction through a solid material and then into a system of water-cooled channels. Even at 400 GeV the heat load must be spread over some transverse area by sweeping the beam. In the case of the 1 MW SLAC dump [26,27] this problem led to their rejection of a solid dump, in this case a copper-based one, in favour of using a water-based dump.

7.4.5.3 Low Energy Dump Design

It can be seen that high energy beam dumps accommodating several megawatts of beam power pose significant design difficulties; it is perhaps counter-intuitive to realise that low-energy dumps can be even more difficult. The problem at low energy (for example 10 MeV) is that the absorption shower is developed over a much shorter range, which results in solid or liquid materials having to withstand much greater volumetric power densities than is the case at higher energies. In terms of practical designs [25] this has two consequences:

- The small absorption depth means the beam *must* be spread out transversely, resulting in a very wide, flat dump.

- Water-based dumps are essentially not feasible. If the beam is not spread out transversely then the power deposition per unit volume is too high; if the beam is spread transversely then the vacuum/water window is not feasible. The window itself will absorb much more effectively than the water (as it has a higher density) and therefore must be much thinner than for a high-energy beam, i.e. << 1 mm. For example, a 100 mA, 13 MeV beam will deposit ~ 7.5 kW into a 250 μm Beryllium window. This is not a sensible option.

A Cornell study [25] has considered several solid materials, and concluded that dumps based on either copper (Cu) or aluminium (Al) are most promising. In each case, the concept is to deposit the energy onto an array of extruded cooled bars which have internal water cooling, with the side of the bar facing the incident beam of the correct thickness for full absorption. For example, a 13 MeV incident electron requires 8.25 mm of Cu or 27 mm of Al. Conceptual designs of such extrusions are shown in Figure 7.27.

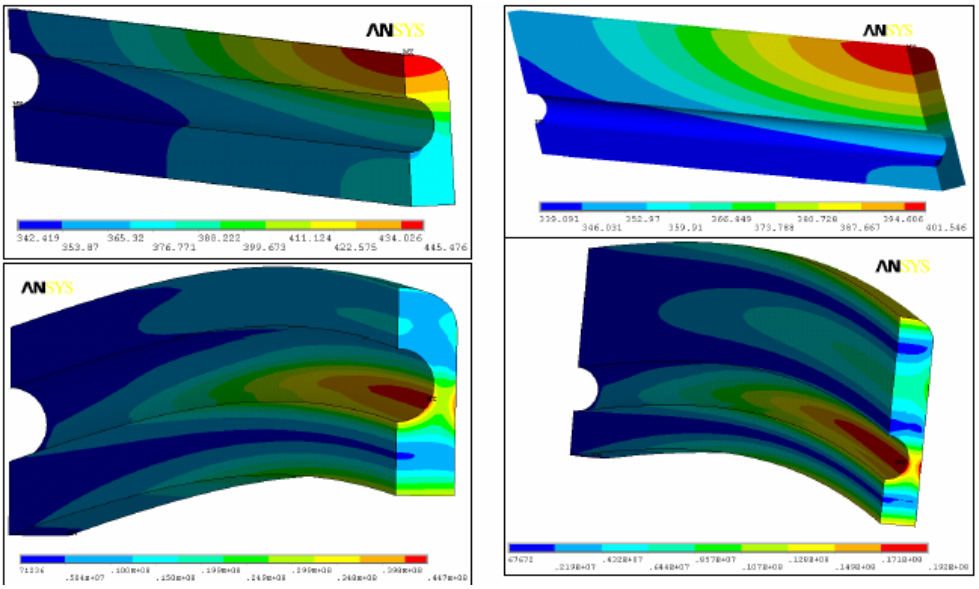

Figure 7.27. Temperature (K) and Von-Mises stress (MPa) of Cu-based (left, Glidcop) and Al-based extrusion dumps (taken from [26] with kind permission of Cornell University); dumps are shown in cross-section. The upper edges face the incident electrons, as can be seen by the thicker side of the Al extrusion.

In the Cornell design the temperature rise and deflection of the dump are kept within realistic limits (although the deflection is still over 6 mm) by spreading the incident power over a wide area of ~1 m [25]. Since no window can be used (see above) the entire dump must be placed in vacuum with the associated engineering complications.

It can be seen that whilst this design is feasible in principle there are many important issues that will require consideration in the next phase of the design:

- A robust optical scheme which is tolerant to position errors, and perhaps a feedback system with diagnostics to maintain a large beam size is required to expand the beam in a reliable way after deceleration. There are possible issues with varying 'hot-spots' in the beam distribution which may vary from bunch to bunch.

- Machine protection issues will lead to regular and repeated beam interruptions. This will result in significant thermal cycling and rapid temperature and stress changes in the dump. It is likely that the dump will have to survive as many as 10^6 thermal cycles [25], which requires careful engineering consideration.

- The material choice should be considered in the light of neutron activation [25]. For example, Al has a threshold of 13.3 MeV versus Cu of 9.9 MeV. Thus the material choice will be influenced by the choice of recovered energy.

- The Cornell design utilises extrusions which face the incident beam perpendicularly. Photon absorbers on 3rd-generation storage rings – particularly crotch absorbers (e.g. on SLS and DIAMOND) – have utilised oblique incidence to help with cooling. This

should be examined as a way to reduce the required transverse expansion of the electron beam.

Although not yet considered for low energy applications, the use of gas-based dumps could be considered for 4GLS. Similar to designs considered for the ILC beam dump [29], a noble gas may be used to spread the power deposition longitudinally, and then to absorb the power in a metal surround. The great advantage at low energy is that the overall length is much reduced (this is to be determined), and can be tailored by varying the gas pressure. However, the principal disadvantage is that any window between the gas and the upstream vacuum system (which contains cold superconducting surfaces in the linac) must be very thin. The alternative is to use a conductance, which may not be possible from a vacuum point of view. In either case this will limit the pressures that are possible in the absorber. However, a gas-based dump would not require beam expansion, which may give significant advantages in design, operation, and magnet and diagnostic design in the dump region.

The considerations above show that a low energy beam dump can be more difficult than a high energy dump that handles the same power, due to the smaller absorption depth. Material limitations almost certainly exclude the use of a liquid (e.g. water) based dump, or a solid dump separated from the accelerator vacuum system by a window. The most promising solution is a wide, thin solid dump composed of many water-cooled extrusions [25], but this requires the beam to be greatly expanded transversely. Alternative concepts such as a gas-based dump should also be considered to avoid design and operational complications that may arise from this. In either case, the engineering and physics design is very challenging, and prototyping may well be required.

7.5 The XUV-FEL Branch

The XUV-FEL branch consists of the following components:

- A FODO arc which provides a 180° net bend and vertical offset to bring the transport within the High Average Current Loop;
- A third linac stage, XUV-FEL linac to allow energy tuning for the XUV-FEL (see Figure 7.1) from 750 MeV to 950 MeV;
- The second bunch compressor BC2, which compresses the chirped beam to towards the short bunch length required at the XUV-FEL;
- A diagnostic section for emittance measurement and optical tuning;
- A final dog-leg to offset the electron bunches and allow the XUV-FEL laser seed pulses to enter. The dog-leg also provides for energy measurements and longitudinal collimation (see Section 7.8.1.2), and performs the final compression before the FEL;
- After the XUV-FEL modules, a further offset to transport the electron bunches into a spent beam undulator. The photon pulses from the undulator will then be naturally synchronised to those from the XUV-FEL, making it ideal for pump-probe experiments;
- An extraction and dump section to safely contain the 1 kW power XUV-FEL electron beam. A triplet of quadrupoles is used to suitably defocus the beam before entering the dump;

These components are described in the following sections.

7.5.1 XUV-FEL Branch Arc and Linac

The regular cell of the 750 MeV XUV-FEL branch arc (see Figure 7.28) is similar in design to the 600 MeV HACL arc cells, except that it is shortened and adjusted to give the minimum longitudinal dispersion R_{56} of 19.4 mm per cell that is possible from the compact FODO design. Magnet parameters are summarized in Table 7.7. The arc uses two solenoids to produce the vertical displacement necessary for the XUV-FEL branch arc to pass under and within the path of the HACL Arc-1. The solenoids each rotate the principal planes of the beam motion by 2°, one at the start of the arc and one at the end after 180° of bending. This allows the plane of the XUV-FEL arc to be tilted without inducing coupling between the horizontal and vertical axes of motion of the beam. Since the beam spreader delivers a beam 4.8° from the axis of the Main Linac, a small final 4.8° dipole is placed after the final solenoid to bring the exit beam direction anti-parallel to the ERL linac.

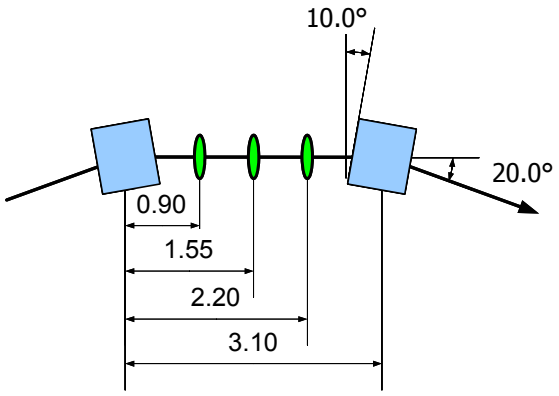

Figure 7.28 Regular cell of 750 MeV XUV-FEL branch arc. Dipoles are shown in blue, quadrupoles in green. Dimensions are given in metres unless otherwise indicated.

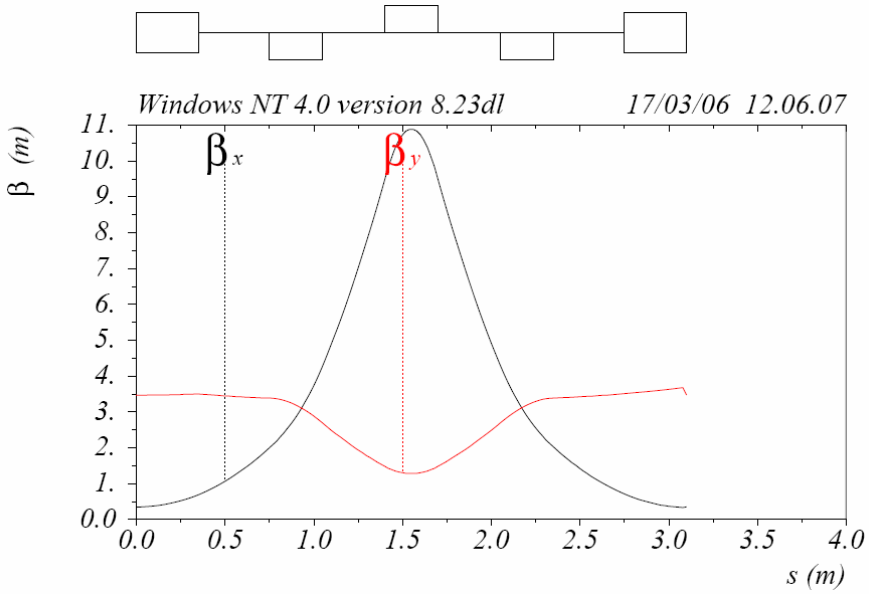

Figure 7.29 Optical functions in the 750 MeV XUV-FEL branch arc regular cell

Table 7.7 Magnet parameters in the XUV-FEL branch arc

Parameter		*Unit*
Energy E	750	MeV
Dipole Length	800	mm
Dipole Bend Field	0.55	T
Quadrupole Length	300	mm
Quadrupole Max Gradient	15	T/m
Solenoid Length	500	mm
Solenoid Field	0.35	T

An overview schematic of the two arcs (HACL and XUV-FEL branch) is shown in Figure 7.30. The vertical offset at the end of the XUV-FEL arc is approximately 600 mm in the design but may be increased if necessary by changing the XUV-FEL arc tilt.

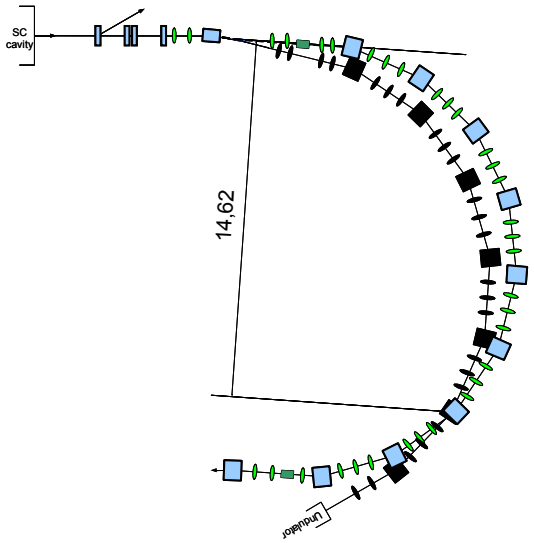

Figure 7.30 Layout of the 600 MeV (HACL) and 750 MeV (XUV-FEL) arcs

At the exit of the XUV-FEL branch arc are two quadrupoles whose purpose is to match the beam into the linac. The linac has two modules each of eight seven-cell TESLA cavities. Triplet focusing similar to the Main Linac is used, using a (-1/2k, k, -1/2k) pattern to control the Twiss parameters in this section.

7.5.2 XUV-FEL Branch Bunch Compressor

Simulations reported later in this chapter show that the required bunch lengths for the XUV-FEL can be achieved using a standard 4-dipole chicane compressor for BC2. The model for the compressor has not been optimised and can be shortened; however for reference the parameters used in the simulation are given in Table 7.8. In the later design phases the overall compression scheme will be optimised to produce the required compression within the geometrical constraints of the facility.

Table 7.8 Parameters of the XUV-FEL compressor

Parameter		*Unit*
Dipole Length	1.03	m
Dipole Bend Field	0.61	T
Drift length	4.0	m

7.5.3 XUV-FEL Branch Diagnostics Section

The intent of the diagnostics section is to fully characterise the beam parameters - emittance and longitudinal bunch profile - not just for a train of bunches but also to monitor a single bunch within a bunch train. Four quadrupoles are used to match into the diagnostics section. The diagnostics section consists of two transverse deflecting cavities (one for each plane), eight optical transition radiation (OTR) monitors and eight wire scanners, and fourteen quadrupoles (seven 'OFODO' cells with the middle drift space twice the length of the outer ones); the design is similar to the proposed XFEL design [30].

The two transverse deflecting cavities (TDCs) both operate in the TEM110 mode and the incoming electrons will be at zero crossing of the RF field (i.e. 90° off-crest). Because of the finite bunch length the head of a bunch will be deflected upwards whereas the tail is deflected downwards. This means that if an OTR screen is placed at 90° phase advance the bunch length may be derived from the projected profile. Further, if a kicker magnet is placed after the cavity, this measurement may be performed off-axis and one can look at just a few bunches. However, the kickers introduce dispersion so the bunch profile can only be measured in the plane perpendicular to the kick hence the need for eight screens — four for the *x* plane and four for the *y* plane [31]. After the diagnostic section the separated bunches are dumped in an absorber downstream. Measurement without streak gives the transverse beam profile, which allows a precise reconstruction of phase space via tomographic methods. Measurement with streak gives the slice emittance measurement, with one dimension on the screen corresponding to time whilst the other gives the emittance of a slice of the bunch in time. This is much more important than just seeking the ordinary RMS emittance because due to space charge and CSR the beam profiles should not be expected to be Gaussian and, in the case of incorrect emittance compensation in the injector, the electron bunches will have significant tails. This results in the RMS emittance not being representative of the beam, thus only slice emittance allows us to properly look at the part of the bunch which takes part in the lasing process.

The first OTR screen is the start of the seven OFODO cell section with 22.5° phase advance per cell; this is not the only choice and other phase advances may also be used, for example 30°, 45°, 60° and 67.5° [30,32,33]. The most convenient is decided by the trade-off between the need for relatively large β functions for the TDCs to increase their resolution ($\beta \approx 15$ m) and the small β-function requirements for a good resolution at the OTR screens ($\beta \approx 2$ m) to keep the mismatch due to space charge small [31]. The total number of OTR screens and wire scanners, as well as their position, is still to be determined and will be the subject of later technical work. The TDCs kick the beam transversely and therefore the bunch undergoes a transverse oscillation. For slice emittance measurements the optimum positions for OTR screens, whilst still keeping the required phase advance per cell, is where the amplitude of this oscillation is largest so as to achieve good parameter resolution. From an error point of view the more measurements that are done the better, since the resulting emittance error scales with the square root of the total number of measurements. A proposed schematic for the main part of the

diagnostic section is shown in Figure 7.31 below; the quadrupole strength and length requirements are given in Table 7.9.

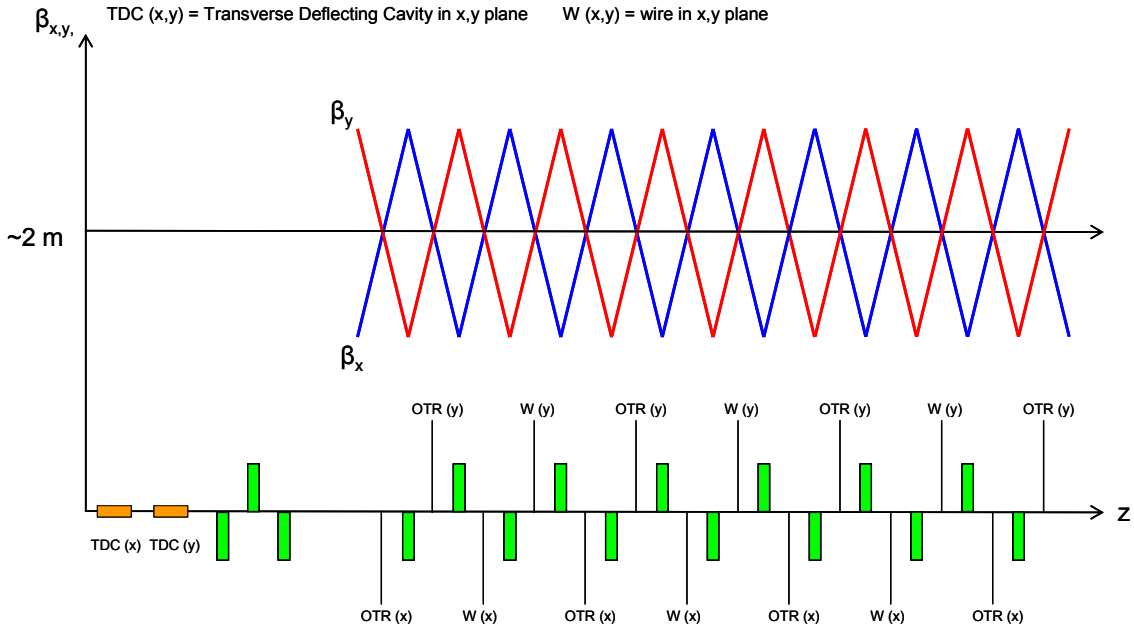

Figure 7.31 Possible layout of the diagnostics section for the XUV-FEL

Table 7.9 Parameters of the XUV-FEL diagnostic section

Parameter		Unit
Quadrupole Length	300	mm
Quadrupole Strength	< 20	T/m

7.5.4 XUV-FEL Collimation Dog-Leg

Collimators are designed to remove undesired electrons in a bunch, that is, electrons, which have deviated far from the core of the bunch. This beam halo can arise from dark currents originating as far back as the injector, a mismatched beam, or just the high bunch charge and short bunch length leading to strong space charge forces which give rise to long bunch tails. As a result, electrons far from the core of the bunch may be lost on the accelerator vacuum walls and thereby irradiate downstream undulators, resulting in demagnetisation of the magnet blocks [34]. Investigations into the irradiation tolerance of the magnets at TTF [35] show significant magnet damage even for small losses of ~ 0.1 % of the beam current. The removal of these electrons causes no loss in the FEL process as only electrons in the core of the bunch contribute to lasing. Moreover, it has been noticed [35] that the beam halo distribution is very unstable and changes frequently, making it difficult to control through accelerator tuning. Collimation of the high charge beam is therefore considered to be mandatory.

For transverse collimation, it is possible to add a section to the diagnostics section described earlier with two collimator apertures together with a 90° phase advance between them as this would naturally limit the transverse phase space [36]. Downstream of the transverse diagnostics section and before the XUV-FEL is a dog-leg which will provide the required offset to allow the seed laser pulse to be brought into the FEL; the dog-leg will also serve as an energy collimator. This means that all particles outside a chosen volume of longitudinal phase space are removed so they are not lost in the XUV-FEL undulator magnets. This dog-leg is made up of three quadrupoles, the outer two to cancel dispersion through the dog-leg and a third to control the Twiss parameters. Two collimators will be placed at the locations of high dispersion just before the first and third quadrupoles, and will be accompanied by sextupoles immediately after the quadrupoles as shown in Figure 7.32 below. The function of the sextupoles — which also have to be located in a region of high dispersion and have to be placed downstream of the collimators — is to reduce the orbit deviations of the particles which have not been collimated. A summary of the required magnets for the dog-leg is given in Table 7.10 below.

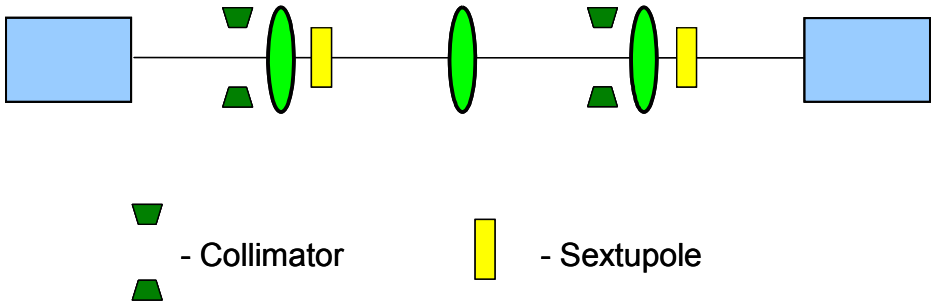

Figure 7.32 Schematic of the XUV-FEL branch dog-leg

Table 7.10 Magnet parameters of the XUV-FEL dog-leg

Parameter		Unit
Dipole Length	1.03	m
Dipole Bend Field	0.61	T
Quadrupole Length	0.3	m
Quadrupole Strength	< 20	T/m
Sextupole Length	0.2	m

7.5.5 XUV-FEL Spent-Beam

After the XUV-FEL the spent beam is transported through another chicane, to a spent-beam undulator. This design provides a spontaneous undulator source which will be highly synchronised to the XUV-FEL output. The average beam power carried by the beam is a relatively modest 1 kW, so after the spent-beam undulator these bunches are delivered to a beam dump.

7.6 IR-FEL Transport

7.6.1 Introduction and Overview of Requirements

The IR-FEL will deliver intense pulses of tuneable coherent radiation with FWHM pulse lengths varying from less than 1 ps to 10 ps over the wavelength range 2.5-200 μm. The wavelength range will be covered by two separate undulators in dedicated branches notated A-Branch and B-Branch. The undulator in A-Branch will operate in the mid infrared from 2.5 μm to 25 μm, and the undulator in B-Branch will operate in the far-infrared from 20 μm to 200 μm. To cover these wavelength ranges the electron beam energy must be varied from 25 MeV to 60 MeV. To satisfy the FEL output pulse length requirements the bunch charge of the driving electron beam must be 200 pC and the bunch length longer than the required optical pulse lengths: the RMS length (assuming a Gaussian longitudinal current profile) must vary from 1 ps to 10 ps.

For satisfactory FEL performance the normalised emittance must satisfy $\varepsilon < 10$ mm mrad in the A-Branch whereas the requirement at the longer wavelength B-Branch is less stringent. The RMS relative energy spread must be less than 0.1% for both branches. To ensure synchronism with other sources and to provide a suitable cavity length, the electron bunch repetition rate provided by the injector is 13 MHz. The required electron beam parameters to enable the IR-FEL to satisfy its output requirements are summarised in Table 7.11.

Table 7.11 Summary of electron beam parameters

Parameter		
Normalised emittance ε	< 10 mm mrad	
Relative RMS energy spread	< 0.1 %	
Bunch charge Q	200 pC	
Repetition rate f	13 MHz	
CW Beam power (at 60 MeV)	156 kW	
Electron bunch length σ_t	1 ps - 10 ps	
Twiss parameters at FEL (planar mode)	**A-Branch**	**B-Branch**
α_x	1.75	1.75 – 2.6
β_x	3.0 m	6.0 m
α_y	0.0	0.0
β_y	0.35 - 1.7 m	0.5 - 1.7 m

7.6.2 Chosen Layout

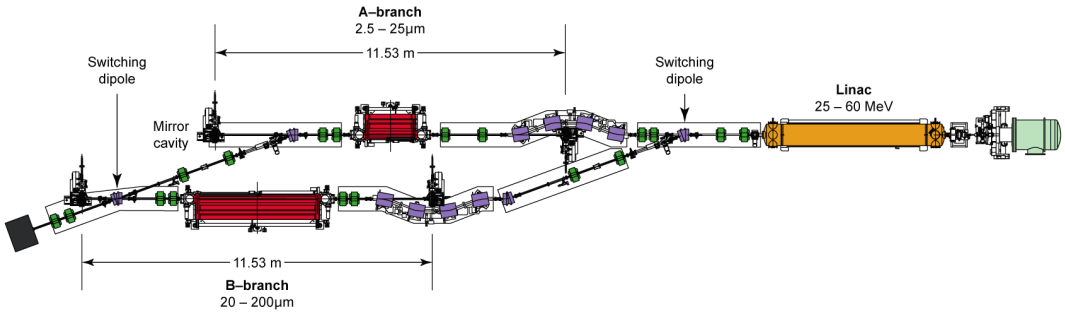

Figure 7.33 Conceptual layout of the 4GLS IR-FEL. Two dipole chicanes and switching magnets are shown in blue; matching quadrupoles are shown in red.

The chosen layout is shown in Figure 7.33; the positions, lengths and numbers of quadrupole magnets are provisional at this stage.

At the exit of the linac the electron beam energy will be between 25 MeV and 60 MeV depending on the required wavelength of the FEL output. A fast switching dipole, operating at up to ~100 Hz, will allow the electron beam to be switched between A-Branch and B-Branch. The pattern of this switching will be determined on an operational basis dependent on user needs. The maximum frequency of the switching dipole will be determined after further feasibility studies.

The electron beam straight ahead path leads into a four-dipole chicane compressor, used in combination with suitable selection of the RF accelerating phase in the linac to provide RMS bunch lengths from 1 ps to 10 ps to the A-Branch undulator. The compressor also provides a suitable location for the FEL upstream cavity mirror chamber. After the compressor a quadrupole triplet will be used to provide the required Twiss parameters at the entrance to the A-Branch undulator. The Twiss parameters depend upon both the operating wavelength of the FEL and the polarisation mode of the undulator, so independent control in both planes is required. The optimum Twiss parameters for planar mode are given as examples in Table 7.11. The downstream FEL cavity mirror is placed after the dipole which deflects the electron beam through large aperture defocusing quadrupoles into the dump.

The alternate beam path is used for the longer wavelength B-Branch, which apart from the dog-leg has a similar layout. The dog-leg path has been chosen for B-Branch because this undulator operates at a longer wavelength than the one in A-Branch and is therefore less affected by emittance growth in the beam transport. The cavity mirrors for B-Branch have a large diameter (180 mm) and appropriately large apertures will be required. The four-dipole compressor will then be specified so that the internal apertures are sufficiently large and that adequate space is

allowed to house the upstream mirror cavity. After the undulator another fast switching dipole will be used to divert the electron beam into the dump. An assessment will be made of the economics and practicalities of providing this second switching dipole rather than providing separate beam dumps for each branch (see discussion in Section 7.10.6).

The requirement that the compression chicanes house the mirror cavities places a lower limit on the R_{56} of the chicanes. This means that compression is achieved in combination with adjustment of the accelerating phase. The corollary to this is that this design does not allow independent compression at the undulators in A-Branch and B-Branch. The advantages and disadvantages of alternative independent compression schemes exploiting the R_{56} in the dog-leg, and of siting the mirror cavities outside the outer dipoles, will be explored in future work.

7.7 Collective and Radiative Processes

7.7.1 Transverse Space Charge

Transverse space charge was considered earlier in the design of the HACL injector merger section (see Section 7.3.3.2), and of course will be studied and optimised during the detailed design of the all three 4GLS injectors. Transverse space charge has some effect at higher energies above 150 MeV, but for the emittances and bunch lengths considered for 4GLS the effect is not considered to be significant compared to the other issues of longitudinal space charge (LSC), coherent synchrotron radiation (CSR) and other effects such as wakefields; this is based on scaling estimates made for ERLP [80]. During the project technical design phase estimates of the transverse space charge growth will be made.

7.7.2 Longitudinal Space Charge

The main effect of longitudinal space charge (LSC) — the electron-electron repulsion in the bunch in the direction of motion — is to introduce an energy chirp along the bunch as the head of the bunch is pushed forward and the tail decelerated; this has been seen for example in the IR-FEL at TJNAF [37]. It can also cause micro-bunching as any density modulation in the bunch, for example from the photoinjector, can induce an energy modulation through LSC and is thought to be the mechanism responsible for micro-bunching observed in the DUV-FEL [38].

7.7.2.1 Initial Estimates of the Effect of LSC

The effect of LSC increases with decreasing electron energy and increasing charge density. The sections in 4GLS most susceptible to LSC will therefore be in the XUV-FEL branch where the bunch charges are higher, particularly where the beam is fully compressed adjacent to the XUV-FEL, as well as in the injection lines which have not been studied in detail at this stage of the concept design

In order to assess the importance of LSC prior to the full design being available, the machine was split up into various sections as shown in Table 7.12. A recent version of the tracking code ELEGANT [39] contains a model of LSC in linacs and drifts and was used to track Gaussian bunches of the appropriate length, energy spread and energy along drift spaces equivalent to the lengths of the different sections. The emittances were derived assuming a normalised emittance of 2 mm mrad, and the uncorrelated energy spreads were set by the value needed to achieve the desired compression at the XUV-FEL, which was found to be 0.02% at the final energy. The effect of varying the drift and bunch lengths in the key region after BC2 was also investigated. The results are given in Table 7.13, where the importance of LSC can be measured by the increase in relative energy spread.

Table 7.12 Approximate lengths of the different sections of the XUV-FEL branch of 4GLS up to the FEL, showing beam parameters obtained from simulation.

Machine Section	*Length (m)*	*Energy (MeV)*	*Emittance (nm rad)*	*RMS Bunch Length (μm)/(ps)*	*RMS Slice Energy Spread*
Up to BC1	40	160	6.4	1800/6	< 0.1 %
BC1 to Main Linac	5	160	6.4	600/2	
Main Linac	70	160-750		600/2	
Prior to compression in BC2	100	750	1.4	600/2	< 0.02 %
After BC2	25	750	1.4	85/0.285	< 0.02 %

The bunch length of 0.285 ps after compression was obtained by requiring a peak current of 1.5 kA with a Gaussian charge distribution. The momentum distribution of such a bunch after a 25 m drift is shown in Figure 7.34. An energy chirp can be seen, however the overall increase in energy spread of less than 10% should not pose a problem for the performance of the FEL. The energy chirp due to LSC round the XUV-FEL branch can be compensated for in part by adjusting the phase of the linacs.

The pulse length of the FEL is determined largely by the seed laser pulse length; given sufficient peak current it is not necessary to provide a electron bunch length as short as the required photon pulse length of 50 fs FWHM (see Chapter 8). However, if short pulses were required at the Spent-Beam Undulator in the XUV-FEL branch, the last two rows of Table 7.13 show that LSC could become a problem for RMS bunch lengths less than 0.1 ps.

Table 7.13 Initial and final bunch properties from tracking with ELEGANT including LSC

Machine Section	*Energy (MeV)*	*Drift Length (m)*	*Initial RMS Length (ps)*	*Initial RMS Energy Spread*	*RMS Bunch Length (ps)*	*RMS Slice Energy Spread*
BC1 to Main Linac	160	10	2	0.05 %	2	0.0501 %
Main Linac to BC2	750	100	2	0.01 %	2	0.0100 %
After BC2	750	25	0.285	0.01 %	0.285	0.0108%
After BC2 (short length case)	750	10	0.1	0.01 %	0.1	0.016%
After BC2 (short length case)	750	10	0.05	0.01 %	0.05	0.044%

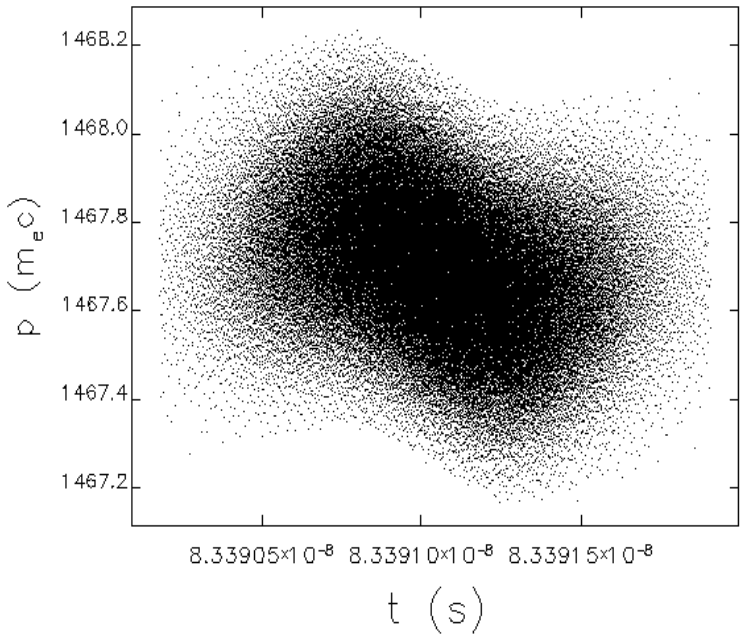

Figure 7.34 Momentum distribution through the bunch at the end of a 25 m straight, for an initial bunch of energy 750 MeV, uncorrelated energy spread of 0.01% RMS and bunch length of 285 ps

7.7.2.2 Micro-bunching due to LSC

Shaftan and Huang [38] have carried out an analytic treatment for LSC induced micro-bunching, and derived a formula relating the amplitude of the input density modulation to the output energy modulation

$$R_{amp} = \sqrt{\gamma \frac{I_o}{I_A} \frac{2\lambda Z_\lambda}{Z_0}} \sin(\frac{\Omega_{sc} L}{c}) \tag{7-6}$$

where λ is the wavelength of the modulation, I_A is the Alfven current, I_0 is the peak current, Z_0 is the free-space impedance, L is a drift length, Z_λ is the LSC impedance per unit length, given by

$$Z_\lambda = i \frac{Z_0 \lambda}{2\pi^2 r_b^2} \left[1 - \frac{2\pi r_b}{\gamma\lambda} K_1(\frac{2\pi r_b}{\gamma\lambda}) \right] \tag{7-7}$$

and Ω_{sc} is the space charge oscillation frequency

$$\Omega_{sc} = c \sqrt{\frac{8\pi^2 I_0 |Z_\lambda|}{\gamma^3 I_A \lambda Z_0}} \tag{7-8}$$

where r_b is the beam radius and K_1 is the modified Bessel function of the second kind [40].

The transverse sizes of the bunch at the XUV-FEL were estimated assuming the emittance values given in Table 7.12 and $\beta_{x,y} = 2$ m. The values of R_{amp} as a function of modulation wavelength for the 0.285 ps bunch along a 25 m drift section are given in Figure 7.35. Increasing the beam cross-section decreases the amplitude ratio and increases the wavelength of the peak amplitude. The amplitude of density variations from the photocathode are typically of the order of 3% [38], which would lead to the amplitude of the energy fluctuations of 0.035% at a modulation wavelength of about 1 μm. This is within the intrinsic uncorrelated energy spread of 0.1 % assumed at the XUV-FEL for modelling purposes but is not negligible; the effect on FEL output will be investigated further in future start-to-end simulations

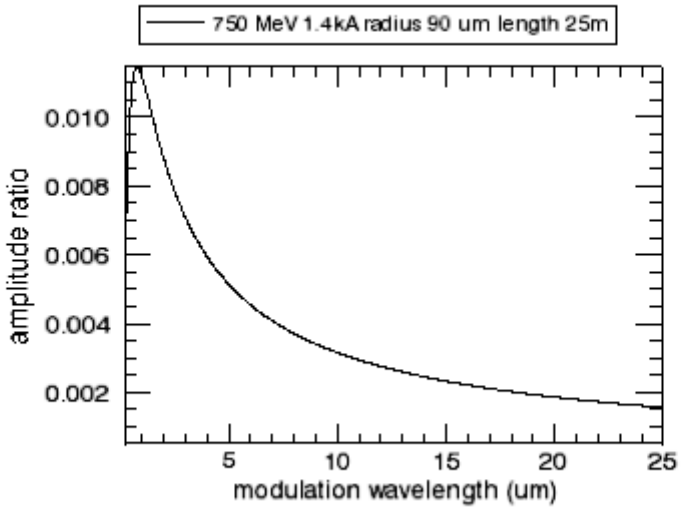

Figure 7.35 Amplitude ratio R_{amp} of density modulation for a 0.285 ps bunch before the XUV-FEL

Results obtained at the DUV-FEL indicate that the observed energy modulation occurs at a wavelength near the peak of the amplitude ratio curve. ELEGANT calculations were performed with the bunch density modulated with a sinusoid of relative amplitude of 3 % and wavelength of 0.8 μm. Only very slight micro-bunching was observed: it may be that at these short wavelengths numerical effects in the code were obscuring the micro-bunching, or else smoothing is occurring due to energy spread. The simulations were repeated for a modulation wavelength of 3.3 μm. The modulation is now clearly visible (Figure 7.36) but does not increase the overall energy spread significantly. The amplitude of the energy modulation is about 0.024 %, i.e. about 8.10^{-3} times the initial density modulation. This is consistent with the calculated amplitude ratio.

From Figure 7.35, as the wavelength of the disturbance increases, the amplitude decreases, and so the performance of the FEL should not be affected by any micro-bunching.

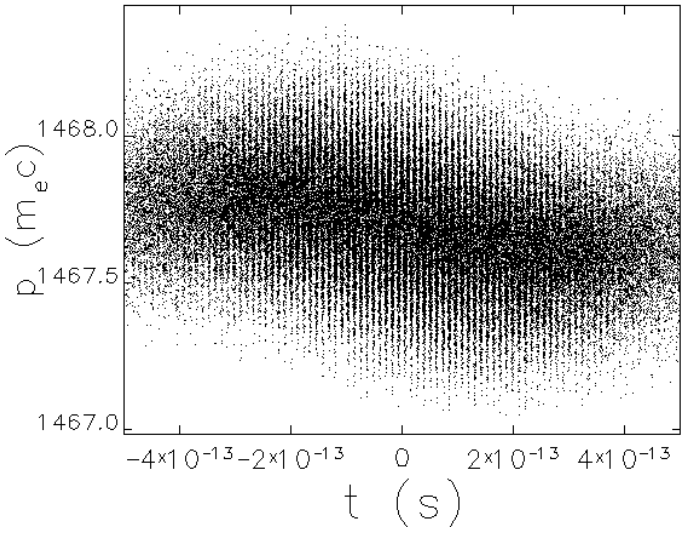

Figure 7.36 Momentum distribution in the central part of a 750 MeV bunch of RMS length 285 fs, intrinsic energy spread 0.01 % after tracking along a 25 m drift. The initial density was modulated by a sinusoid of length 3.3 μm with relative amplitude of 3 %.

7.7.2.3 LSC in Linacs

ELEGANT simulations of transport through the Main Linac were performed for both the HACL and XUV-FEL bunches. In simulations of the 77 pC HACL bunches being accelerated from 10 MeV to 600 MeV, a small shift was found in the energy distribution due to the inclusion of LSC in the linac, as seen in Figure 7.37 . In simulations of the 1 nC XUV-FEL bunches being accelerated from 160 MeV to 750 MeV, no significant difference could be detected in the bunch distributions obtained with and without LSC.

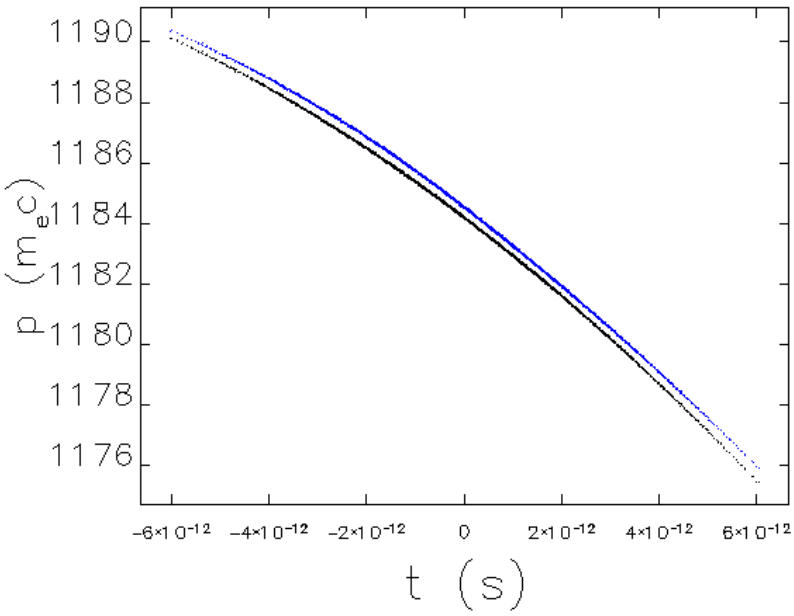

Figure 7.37 Momentum distribution for the HACL bunches after the Main Linac – black without LSC, blue with LSC included in the linac model.

7.7.2.4 Summary of LSC

From these initial studies, it can be seen that while the effects of LSC will not be negligible in the electron beam transport system, especially for the fully compressed bunch in the XUV-FEL branch, they are not expected to impinge on the desired performance of the machine, except perhaps if very short bunches (of the order of 100 fs) are required after the XUV-FEL. The main effect of adding an energy chirp to the bunch can in part be compensated by altering the phase of the linacs. The effects of LSC will be studied further in start-to-end simulations of the complete transport paths.

7.7.3 Coherent Synchrotron Radiation

The electrons in the bunch radiate coherently at wavelengths comparable to and longer than the bunch length. The intensity of this coherent synchrotron radiation (CSR) is proportional to N_e^2 where N_e is the number of electrons in the bunch. The CSR emitted at the tail of a bunch can 'catch up' with the head of the bunch as it travels round a bending magnet, and the intense coherent radiation fields interact with the electrons inducing a variation of energy loss across the bunch and in some cases micro-bunching [41]. For the energies of relevance to 4GLS, CSR is independent of energy. Incoherent synchrotron radiation is of course also emitted, but its effect upon the transverse emittance is expected to be small (see Chapter 9).

CSR is obviously most relevant for the high charge bunches required for the XUV-FEL, and will not be a major problem for the lower charged bunches in the HACL branch, where the effect will be about two orders of magnitude less. In order to minimise the disruption to the electron bunches, they are kept as long as possible round the XUV-FEL transport arc and are

finally compressed as near the FEL as possible. An RMS bunch length of 2–2.5 ps in the outward arc was found to be a suitable trade-off between keeping the bunches short enough so that non-linear transport terms were not important, but long enough to reduce collective effects.

The electron tracking code ELEGANT [42] includes the one-dimensional model of CSR due to Saldin et al [43] and has been used to assess the importance of CSR. A comparison of CSR codes has been made [44] and it is expected that the one-dimensional model used in ELEGANT will give a reasonable estimate of the effect of CSR. To investigate the effect of micro-bunching, many macroparticles (> 1 million) need to be included in the simulations, and at present this is only feasible with a one-dimensional model.

The target peak current at the XUV-FEL is 1.5 kA. Simulations were performed to confirm that the CSR disruption arising from passage through a 180° arc and bunch compressor will not prevent the achievement of the target peak current or energy spread; these simulations were performed using ELEGANT using Gaussian bunch distributions in all planes, albeit with a linear time-energy chirp imposed. The compression scheme achieves compression at the XUV-FEL with a projected energy spread of 0.1 %, and requires the slice energy spread to be less than 0.02 %. The normalised emittance was set to 2 mm mrad, and the initial RMS bunch length was 2 ps (600 μm). In this initial study, two trial triple-bend achromat (TBA) lattices were used for the arc, one with five TBA cells and 0.5 T bending magnets and the other with four TBA cells and 1.0 T magnets. A standard four-dipole chicane was used as the compressor, with dipole strengths of 0.66 T. This is not the present lattice design, but has sufficiently similar parameters that the simulation results are applicable.

Table 7.14 gives the bunch lengths, peak current and total percentage energy loss at the end of the bunch compressor, for the two lattice designs and for two different uncorrelated energy spreads. It can be seen that the required peak current was achieved when the initial uncorrelated energy spread is 0.01 %. Over half the energy was lost in the bunch compressor, and it is expected that these results can be improved with an optimised design for the compressor. Figure 7.38 shows the momentum distribution at the end of the arc, where the variation of energy loss due to CSR can be seen in the deviation from a straight line. The charge density along the bunch at the end of the bunch compressor is given in Figure 7.39 (using one million macroparticles), and shows little evidence of micro-bunching due to CSR. It must be emphasised that the actual bunch profiles may be significantly different as the real distributions will not be Gaussian, and no attempt has been made so far to achieve the best bunch profile; this is a topic for future work when injector design is progressed.

Simulations were performed for different bunch charges, and it was found that the peak current increased from 1.2 kA for a 0.5 nC bunch to 1.4 kA for a 1.0 nC bunch, then decreased very slightly for a 1.2 nC bunch. The increase in CSR which would be expected from the higher magnetic fields in a 1.0 T arc design is compensated by a decrease in bending magnet length and there is very little difference in the results for the two arcs.

Table 7.14 Final bunch lengths, peak currents and total energy loss for a 1 nC bunch of RMS length 2 ps transported round an arc and bunch compressor.

Lattice	*σ (δ) uncorr*	*σ (z) μm*	*σ (z) fs*	*Peak current (kA)*	*Energy Loss*
0.5 T	0.02 %	126	420	1.0	0.12 %
	0.01 %	118	390	1.3	0.13 %
1.0 T	0.02 %	107	360	1.05	0.13 %
	0.01 %	99	330	1.5	0.15 %

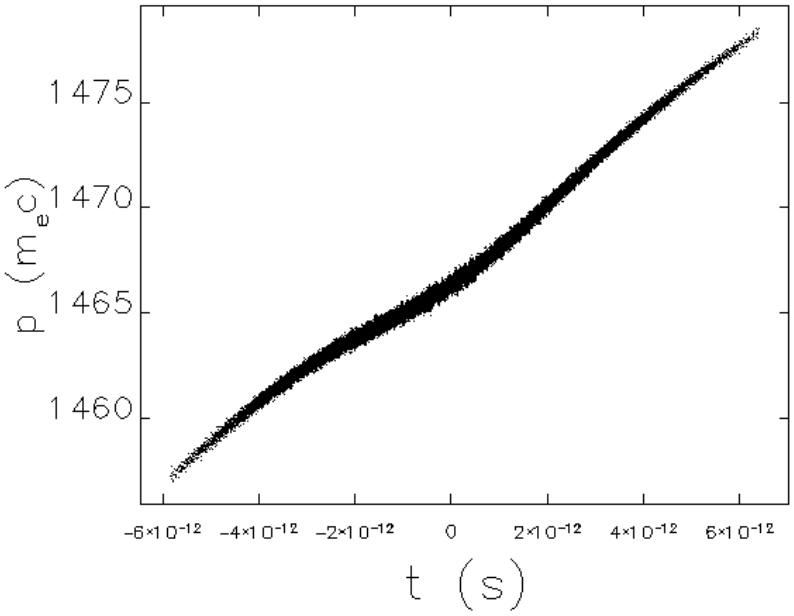

Figure 7.38 Momentum distribution along the bunch at the end of the arc, showing the effect of CSR on the energy distribution, for the case of a 1.0 T arc, 0.01% initial uncorrelated energy spread, 1 nC bunch charge.

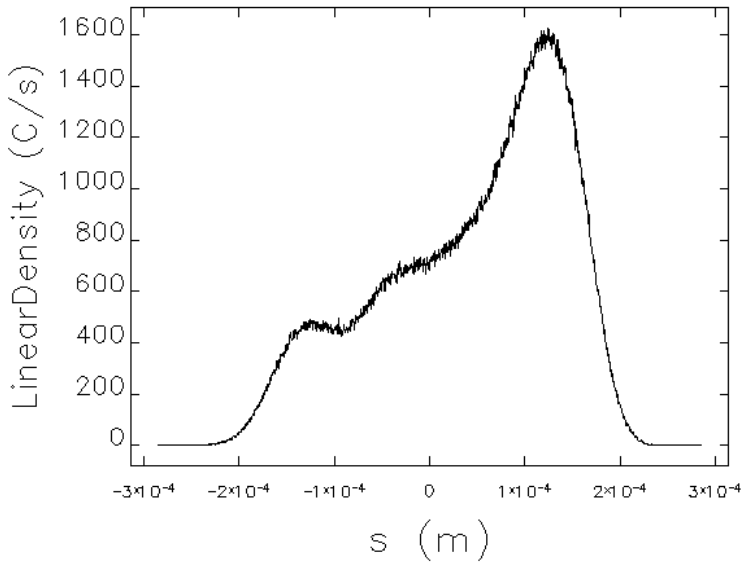

Figure 7.39 Bunch profile at the end of the compressor, for a 1 nC bunch, initial uncorrelated energy spread 0.01 %, using the 1.0 T TBA lattice.

The conclusion from these preliminary studies is that the effect of CSR in the transport of a 1 nC bunch through a 180° arc and bunch compressor will not be large enough to prevent the bunch from being adequately compressed.

7.7.4 Start to End Simulations

Much of the initial design of the lattice has been carried out with linear optics. In order to fully study the non-linear effects induced by wakefields, collective effects as well as higher-order terms in the transport matrix, numerical simulations need to be carried out. These simulations are also useful to study effects such as misalignment, and errors in power supplies and other components.

Simulations for ERLP are the first start-to-end simulations to be performed which include both FEL lasing and energy recovery [3,45]. The electron bunch distribution from the gun was produced using the ASTRA code, and this code was also used for the low-energy propagation of the electrons (where space charge effects are most important). After the acceleration of the electrons to 35 MeV, ELEGANT was used to track the bunch to the FEL, where GENESIS 1.3 was used to follow the evolution of the bunch through the FEL. The GENESIS 1.3 output was then converted back to ELEGANT to track the bunches through their energy recovery in the linac and onward to the beam dump.

Similar full start-to-end simulations will be carried out for 4GLS. Simulations of parts of the accelerator system have already been performed to investigate specific issues: for example,

ELEGANT has been used to track bunches from the start of the Main Linac to the FELs for both the XUV-FEL branch and HACL to verify that the required peak currents can be achieved. Nine-cell RF cavities were used in the linac simulations, but the use of seven-cell cavities should not significantly change the results that have been obtained to date. Of more importance is the approximation of using Gaussian distributions for the bunches, and complete start-to-end simulations will be performed during the project technical phase using bunch distributions obtained from models of the guns. Results obtained so far are discussed below. It is important to note that even starting with Gaussian bunches, complex bunch profiles are obtained at the FELs. Numerical simulations need to be carried out to predict the FEL performance with such bunch distributions.

7.7.4.1 High Average Current Loop.

A 10 MeV Gaussian bunch of RMS length 2 ps and uncorrelated energy spread of 0.1% was tracked through the Main Linac, spreader, HACL outward arc and ID Arc. Excluding collective effects, the RMS bunch length at the last straight in the ID arc was 135 fs, with a peak current of 750 A. The addition of the sextupoles in the outward arc cells reduced the bunch length to 100 fs (RMS), increasing the peak current to 860 A. Note that the peak current relevant to lasing depends upon the longitudinal particle distribution, and so thus the *effective* peak current may be somewhat smaller than this (see discussion of longitudinal phase space below).

In order to check the effect of CSR, a one–million-particle simulation was carried out including the effect of CSR in the bends and into the drift spaces immediately following the dipoles. There was no sign of micro-bunching. The extra energy chirp induced by CSR required that the linac phase was decreased from 97.3° to 97.0° to obtain maximum compression at the end of the ID arc.

To check the effect of LSC, simulations were carried out including the effect of LSC in the linac and drifts, but in this case CSR was not included. A small adjustment to the linac phase is again needed to account for the energy chirp in the bunch, but the final bunch profile is very similar to the case without LSC.

Figure 7.40 shows the progressive compression along the ID arc; the RMS bunch length decreases from 120 μm (400 fs) in the first straight to 24 μm (80 fs) in Straight 6.

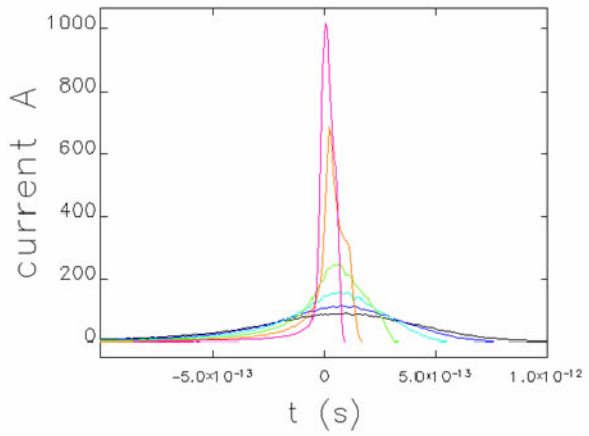

Figure 7.40 Bunch profiles at the HACL ID straight centres, starting from the first straight (black) through to the FEL straight (pink). Model includes CSR but excludes LSC.

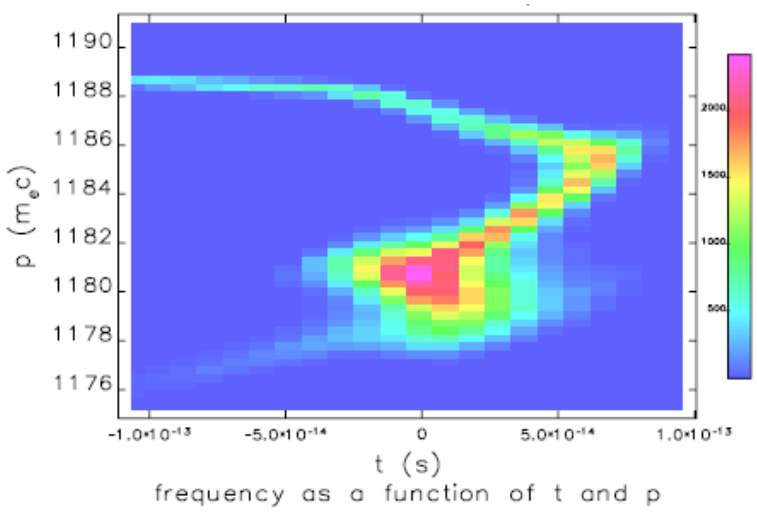

Figure 7.41 Electron bunch longitudinal phase space just upstream of the VUV-FEL

The RMS energy spread over the bunch is somewhat larger than the 0.1 % that has been specified for VUV-FEL operation. However, as shown in Figure 7.41, the expected longitudinal phase indicates that there will be enough charge contained within the required bandwidth of time and energy to provide lasing. This result gives confidence that, once start-to-end simulations have been performed with a full injector design, adequate beam properties at the VUV-FEL may be obtained.

7.7.4.2 XUV-FEL Branch

A 160 MeV bunch of RMS length 2 ps was tracked through the Main Linac, extraction chicane, bunch spreader and arc for the XUV-FEL branch. A typical 4-dipole chicane bunch compressor

was added after the arc to check that the non-linear effects were not too large to prevent adequate bunch compression, followed by a 20 m drift to allow for the diagnostic section. The effects of CSR, LSC in the linacs and straights and wakefields in the linac were included. Note that the phase of the linac had to be changed to allow mainly for the change in energy chirp due to the wakefield and LSC. Even without any linearisation from 3rd harmonic cavity or sextupoles included, a peak current of 1.4 kA was obtained, just short of the 1.5 kA target. Further simulations using a more realistic input bunch distribution will be performed in future design work.

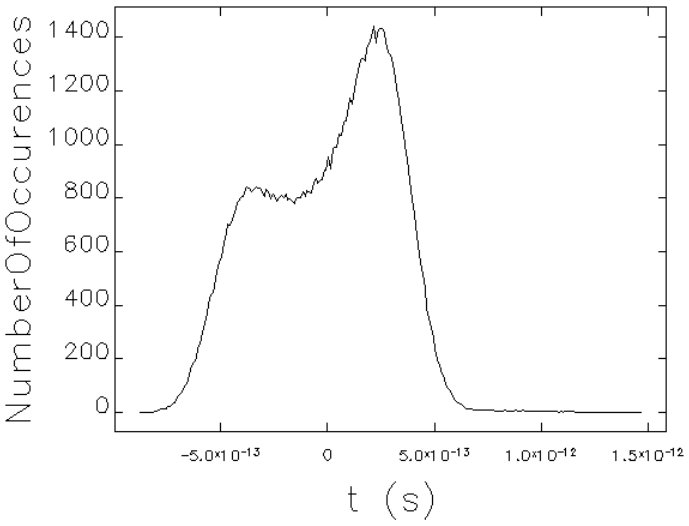

Figure 7.42 Bunch profile at the end of the 20 m drift section. Simulations include LSC and CSR.

7.7.5 Ion Trapping

The train of High Average Current Loop bunches produces a strong periodic space charge potential into which (positive) residual gas ions may be attracted, and under certain conditions these ions may be trapped onto the beam axis. The HACL bunches will then scatter from these trapped ions leading to emittance growth, and the potential from the trapped ions can cause a strong focal change in the HACL optical transport, and thus change the beam waist position and phase advance through the HACL. These effects have been observed at 3rd-generation storage rings and 4GLS is in a similar parameter regime. Preliminary estimates suggest that gaps in the bunch train will be required to promote clearing of trapped ions, similar to the ion clearing gaps that are used on 3rd-generation storage rings. The other possible solution is to have strong electrostatic potentials at various locations in the transport to draw trapped ions longitudinally to locations where they are no longer stable [48].

We first consider a continuous train of 80 pC bunches passing some location; the periodic potential produced when these bunches pass some particular point in the accelerator may be given by:

$$M = \begin{bmatrix} 1 & t \\ 0 & 1 \end{bmatrix} \cdot \begin{bmatrix} 1 & 0 \\ d_i & 1 \end{bmatrix} \cdot \begin{bmatrix} 1 & 0 \\ -d & 1 \end{bmatrix} = \begin{bmatrix} 1 + t(d_i - d) & t \\ d_i - d & 1 \end{bmatrix} \tag{7-9}$$

where $t = 0.77$ ns is the bunch spacing at 1.3 GHz, and d is given (in CGS units) as

$$d = \frac{2 r_p N_e c}{a^2 A} \tag{7-10}$$

r_p is the classical proton radius, N_e is the number of electrons in an 80 pC bunch, a is the electron bunch radius (which varies widely through the transport), and A is the molecular weight of the residual ion under consideration. Note that the form of equation (7-9) is not unique. As will be seen below, the choice of 80 pC is also not unique, but the conclusions below are still valid for the differing bunch charges that may be requested in 4GLS (including the nominal 77 pC case). The molecular weights of residual ions will depend upon the vacuum conditions, but may typically vary between two for hydrogen and forty-four for carbon dioxide. d_i is the space charge kick from the trapped ions themselves, which will vary as the ions are trapped and de-trapped. Ion focusing is stable (i.e. ions will be trapped), if

$$-2 \le Tr(M) \le 2 \tag{7-11}$$

Neutralisation occurs when the defocusing from the ions matches that from the electron bunches, i.e. when $d_i = d$. This means that the maximum number of trapped ions will be approximately the same as the number of electrons in the beam. Applying the stability condition (7-11) for a typical beam radius of $250\ \mu$m we find that all ions with masses greater than

$$A \ge \frac{r_p N_e c t}{2 a^2} = 1.4 \cdot 10^{-3} \tag{7-12}$$

will be trapped. This means that in virtually all locations in the HACL transport we expect all ion species to be trapped.

The 1 nC bunches pass through some regions of the HACL at 1 kHz, for example in the beam spreader. The combined focusing effect, assuming for example that the 1 nC bunches are followed by some gap T, may be described as

$$M_{tot} = \begin{bmatrix} 1 - T \cdot D & T \\ -D & 1 \end{bmatrix} \cdot \begin{bmatrix} 1 - t \cdot d & 0 \\ -d & 1 \end{bmatrix}^N \tag{7-13}$$

where D is the focusing term given by

$$D = \frac{2 r_p \overline{N}_e c}{a^2 A} \tag{7-14}$$

$\bar{N}_e$ is the number of electrons in the 1 nC bunch. This focusing is shown schematically in Figure 7.43. It can be shown for smooth harmonic oscillations of the ions that [46] trapping is unlikely if the condition

$$\left|Tr(M_{tot})\right| = \sqrt{(2 - T \cdot D)^2 + (\omega T + D/\omega)^2} >> 2 \qquad (7\text{-}15)$$

is satisfied. It may also be shown that the effect of the 1 nC bunches is small [46]; the corollary of this is that from the perspective of ion trapping it does not matter where the 1 nC bunch occurs within the 80 pC bunch train (it does not have to occur at the end, for instance). Figure 7.43 illustrates one possible bunch structure.

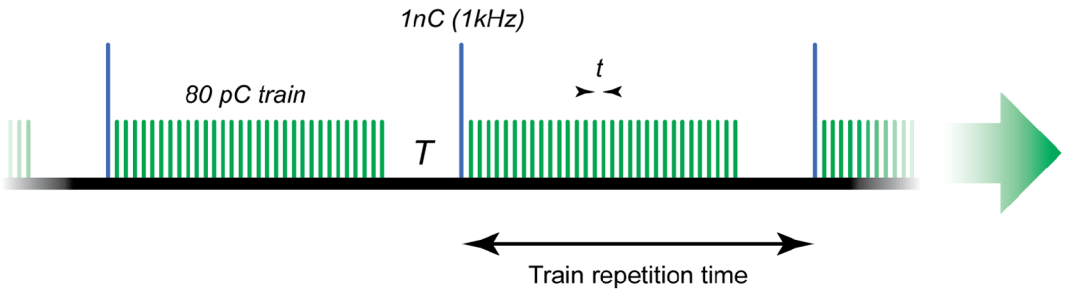

Figure 7.43 One possible bunch time structure for 4GLS, studied in this section

Figure 7.44 shows how $\left[Tr(M_{tot})\right]$ varies with ion mass. Applying the requirement of equation (7-15) we see that a gap of $T = 1000t$ should be maintained to keep $\left[Tr(M_{tot})\right]$ sufficiently above 2 to avoid trapping. The parameters for one possible bunch structure are given in Table 7.15. It is important to realise that this bunch pattern requirement will depend on both the residual gas that is present and on the focusing mode of the accelerator transport. Some flexibility in the control system will be required to provide different bunch patterns to control particular trapping conditions; this may also place some restriction on the bunch patterns that may be provided to users.

Table 7.15 Possible HACL bunch structure configuration to avoid ion trapping

Parameter		*Unit*
Train Length	100	μs
Gap Length	1	μs

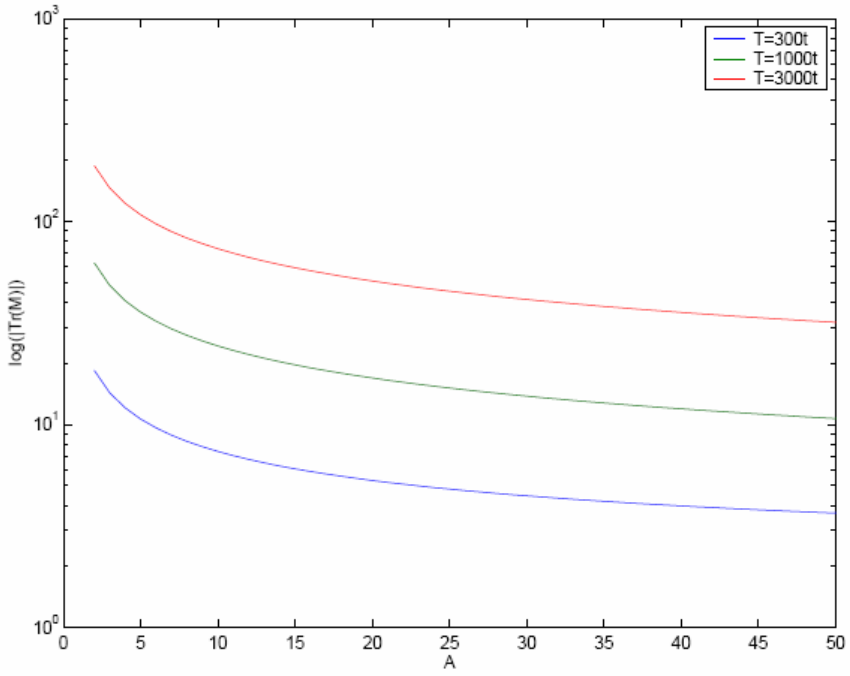

Figure 7.44 $\left[Tr(M_{tot})\right]$ *versus ion mass A for a range of gap sizes T, assuming that the 80 pC bunch train is* $100\ \mu s$ *long*

Leaving gaps in the bunch train to control ion trapping can possibly cause beam loading problems in the linacs, both in the HACL injector and in the Main Linac. In some parameter regimes it may be possible to cancel the beam loading by arranging for the gaps in the bunch train to overlap in the Main Linac [47], but in the case of 4GLS the required gap is similar in size to the revolution time so this technique is not possible. Beam loading may result in a requirement to ramp the bunch current up or down at the start and end of each bunch train [48]; if this cannot be done then it may be possible to introduce strong clearing electrodes into the transport system to draw ions longitudinally along the beam path from regions where they are trapped to regions where they are not, where they will then be cleared. Further work on this topic to look at the ion clearing alternatives is planned for the technical design of the 4GLS project.

7.7.6 Resistive Wall Wakefield Effects of the Undulator Vessel Walls

The electromagnetic fields generated by a moving charged bunch exert forces on the particles in that bunch or following bunches due to the impedance of the surrounding vacuum vessel. The general formalism which describes these effects on the trajectories of the particles is given by the concepts of wake functions and impedances. The wake function is the effect at a given distance of a point-like driving charge in a structure, whereas the wake potential is the effect of a whole bunch with a given charge distribution. The beam dynamics and wakefield effects presented here are discussed in detail in [49].

Longitudinal and transverse wakefield effects have been examined for various bunch length and charges for cylindrically symmetric 'round pipes' with a non-zero resistance. The longitudinal wakefields will affect the total energy and energy spread of the beam whereas the transverse wakes kick the beam and can cause an orbit-dependent emittance growth.

We require that wakefield effects should not produce an energy spread that is greater than the natural energy spread of the beam. The mean energy lost by the beam will inform the level of tapering required, if any, from one undulator module to the next. The transverse kicks should be small enough to not significantly dilate the beam emittance.

Extruded aluminium vessels will be used for the narrow gap vessels. Aluminium has been chosen because its conductivity is significantly higher than stainless steel and it is easier to manufacture into the required shape than copper. If further wakefield studies indicate a problem arising from using aluminium, for example studies of surface roughness effects, then a copper coating may be specified to reduce the wakefield effects. All the calculations are based on a round vessel formalism; if an elliptical vessel is used then all the effects on the beam are expected to be less.

The results discussed in the following sections show that the magnetic gap for all eight of the XUV-FEL planar undulator sections can be 10 mm. For the five XUV-FEL APPLE-II undulators a magnetic gap of 8 mm — as required for the 6 to 100 eV option — is acceptable. For the five VUV-FEL APPLE-II undulators a magnetic gap of 10 mm can be used.

7.7.6.1 Longitudinal Wake

The longitudinal monopole wake for a delta-function impulse, $\tilde{w}_{\parallel}^{\delta}$, of a round-pipe resistive wall of conductivity σ_c is [50]:

$$\tilde{w}_{\parallel}^{\delta}(s) = -\frac{4}{\pi\varepsilon_0 b^2}\left\{\frac{1}{3}e^{-\frac{s}{s_0}}\cos\left(\sqrt{3}\frac{s}{s_0}\right) - \frac{\sqrt{2}}{\pi}\int_0^{\infty}\frac{x^2}{x^6+8}e^{-x^2\frac{s}{s_0}}dx\right\},\ \text{for } s>0$$

$$\tilde{w}_{\parallel}^{\delta}(s) = \frac{\tilde{w}_{\parallel}^{\delta}(0_-)}{2} = -\frac{1}{2\pi\varepsilon_0 b^2},\ \text{for } s=0, \tag{7-16}$$

$$\tilde{w}_{\parallel}^{\delta}(s) = 0,\ \text{for } s<0.$$

s_0 is the characteristic distance of the vessel,

$$s_0 = \sqrt[3]{\frac{2cb^2\varepsilon_0}{\sigma_c}}, \tag{7-17}$$

b is the vessel radius.

The wake potential for an electron bunch is obtained by the convolution of the wake function with the longitudinal charge distribution, $\rho(s)$. For a Gaussian bunch with an RMS length of σ the wake potential, $\tilde{w}_{\parallel}^{gauss}$ is:

$$\tilde{w}_{\parallel}^{gauss}(s) = \frac{1}{\sqrt{2\pi}\sigma}\int_0^{\infty} \tilde{w}_{\parallel}^{\delta}(s') e^{-\frac{(s-s')^2}{2\sigma^2}} ds' \tag{7-18}$$

The longitudinal loss factor, $k_{\parallel}$, is given by:

$$k_{\parallel} = -\int_{-\infty}^{\infty} \rho(s)\tilde{w}_{\parallel}^{gauss}(s) ds, \tag{7-19}$$

from which the induced RMS energy spread of the bunch, σ_{ε}, can be calculated:

$$\sigma_{\varepsilon} = eN\left|\int_{-\infty}^{\infty}\left(\rho(s)\tilde{w}_{\parallel}^{gauss}(s)^2 - k_{\parallel}^2\right)ds\right|^{1/2}. \tag{7-20}$$

The energy lost by the source charge, ΔE, is the work done by the longitudinal electromagnetic force along the structure. This is related to the loss factor by the relation:

$$\Delta E = q_e^2 N k_{\parallel}, \tag{7-21}$$

where N is the number of particles of charge q_e.

7.7.6.2 Transverse Wake

The dipole order wake function, $\tilde{w}_{\perp}^{\delta}$, per unit length, r, in the resistive 'round-pipe' is [51]:

$$\tilde{w}_{\perp}^{\delta}(s) = \frac{2s_0 r}{3\pi\varepsilon_0 b^4}\left\{e^{-\frac{s}{s_0}}\left[\sqrt{3}\sin\left(\frac{s\sqrt{3}}{s_0}\right) - \cos\left(\frac{s\sqrt{3}}{s_0}\right)\right] + \frac{12\sqrt{2}}{\pi}\int_0^{\infty}\frac{e^{-x^2\frac{s}{s_0}}}{x^6+8}dx\right\}. \tag{7-22}$$

The wake potential is then found via a convolution with the bunch charge distribution, as before. A change of variables is required to evaluate the integral, where $s'/\sigma \to s'$ and $s/\sigma \to s$. This gives the integral normalised to σ:

$$\tilde{w}_{\perp}^{gauss}(s) = \frac{1}{\sigma\sqrt{2\pi}}\int_0^{\infty}\tilde{w}_{\perp}^{\delta}(s')e^{-\frac{(s-s')^2}{2\sigma^2}}ds' = \frac{1}{\sqrt{2\pi}}\int_0^{\infty}\tilde{w}_{\perp}^{\delta}(s')e^{-\frac{(s-s')^2}{2}}ds'. \tag{7-23}$$

A transverse loss factor, $k_{\perp}$, sometimes called the kick factor, can then be defined as:

$$k_{\perp} = \frac{1}{r}\frac{1}{\sqrt{2\pi}}\int_{-\infty}^{\infty}\tilde{w}_{\perp}(s')e^{-\frac{s'^2}{2}}ds' \tag{7-24}$$

7.7.6.3 Relevant Parameters for the 4GLS FELs

To achieve the highest on-axis field in the FEL undulators the smallest magnet gap, and hence smallest vacuum vessel diameter, should be used. However wakes from smaller radius vessels have a much greater effect on the beam energy and energy spread. The wakes are inversely proportional to the radius raised to some power, depending upon which effect is being considered. In Figure 7.45 to Figure 7.50 this dependence on an inverse power of the radius can be seen. There is also a dependence on the bunch length and charge. Table 7.16 gives the bunch lengths and charges considered.

Table 7.16 Bunch lengths, charges and energy ranges considered

Parameter	*Unit*	*VUV-FEL*	*XUV-FEL*
Bunch Charge	C	$77\ 10^{-12}$	10^{-9}
RMS Bunch Length	fs	50	250
Energy Range	MeV	600	750-950

Copper, aluminium and stainless steel vessel materials were also considered; Table 7.17 gives their bulk conductivities. The large difference in the conductivity between stainless steel and copper means that the wakefield effects for stainless steel will be worse.

Table 7.17 Bulk conductivities of vessel materials considered

Material	*Unit*	*Value*
Copper (Cu)	$\Omega^{-1}\ m^{-1}$	$5.88\ 10^{7}$
Aluminium (Al)	$\Omega^{-1}\ m^{-1}$	$3.62\ 10^{7}$
Stainless Steel (SS)	$\Omega^{-1}\ m^{-1}$	$1.7\ 10^{6}$

7.7.6.4 Results for Longitudinal Wakes

Figure 7.45 shows an example calculation of the longitudinal wakes for copper vessels. The profile of the wake can be seen against the Gaussian charge distribution, with RMS length of 50 fs. The longitudinal wake is seen to decrease as the vessel radius increases.

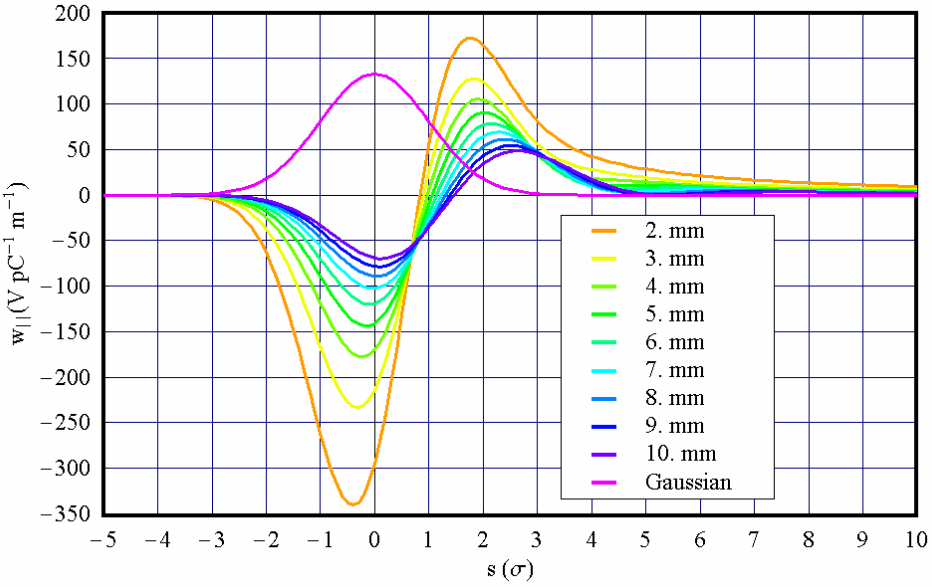

Figure 7.45 Gaussian bunch profile (purple) and longitudinal wake potentials for a 1 nC, 50 fs bunch for different copper vessel internal radii

Figure 7.46 shows the energy lost per metre per bunch, for the different parameters given in Table 7.16 and Table 7.17 as a function of vessel radius. The induced energy spread per metre per bunch as a function of vessel radius is shown in Figure 7.47. A dependence on an inverse power of the radius can be seen as well as the worsening effect of using a stainless steel vessel.

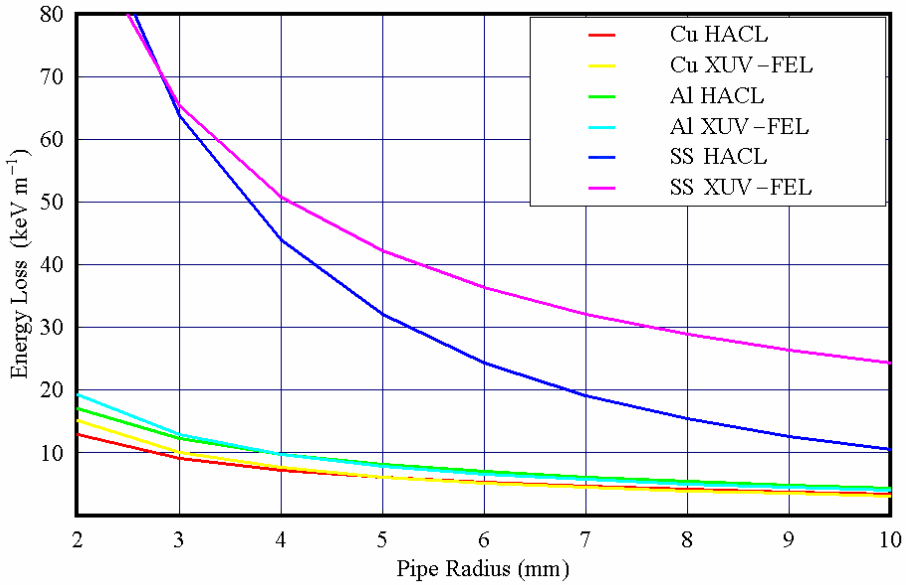

Figure 7.46 Energy lost per metre per bunch versus vessel radius for different bunch charges, lengths and vessel materials

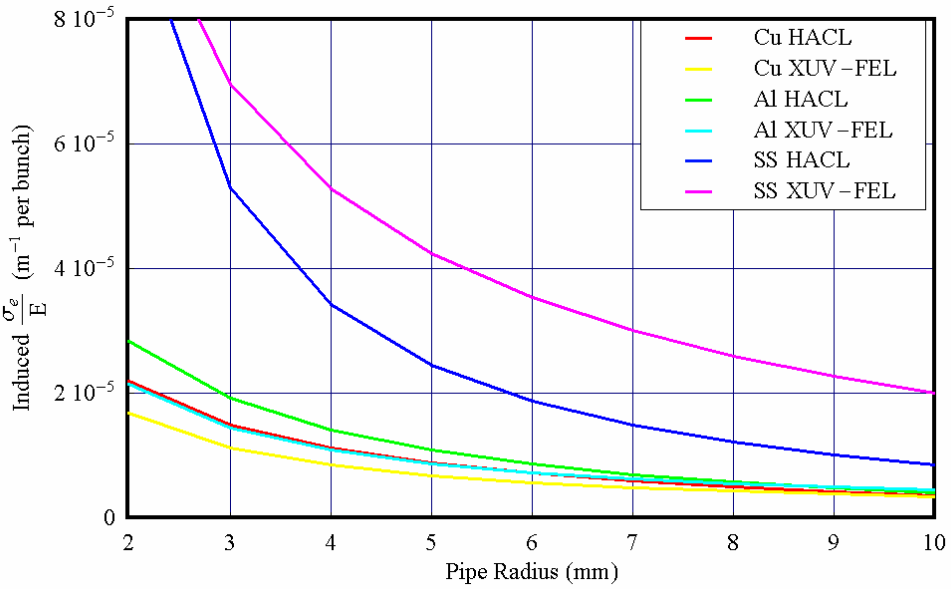

Figure 7.47 Induced relative energy spread per metre per bunch versus vessel radius for different bunch charges, lengths and vessel materials

7.7.6.5 Results for Transverse Wakes

Figure 7.48 shows an example calculation of the transverse wakes for copper vessels. The profile of the wake can be seen against a Gaussian charge distribution, with RMS length of 50 fs and 1 nC charge. The transverse wake can also be seen to decrease as the vessel radius increases. The transverse kick per mm offset from the axis of the vessel, for the different parameters given in Table 7.16 and Table 7.17, are shown in Figure 7.49.

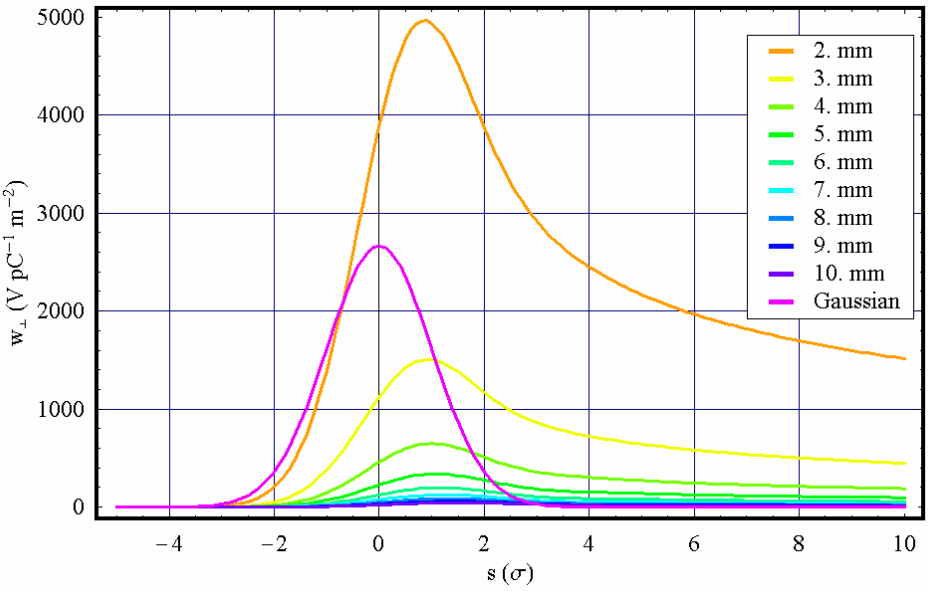

Figure 7.48 Gaussian bunch profile (purple) and transverse wakes potentials for a 1 nC, 50 fs bunch for different copper vessel radii

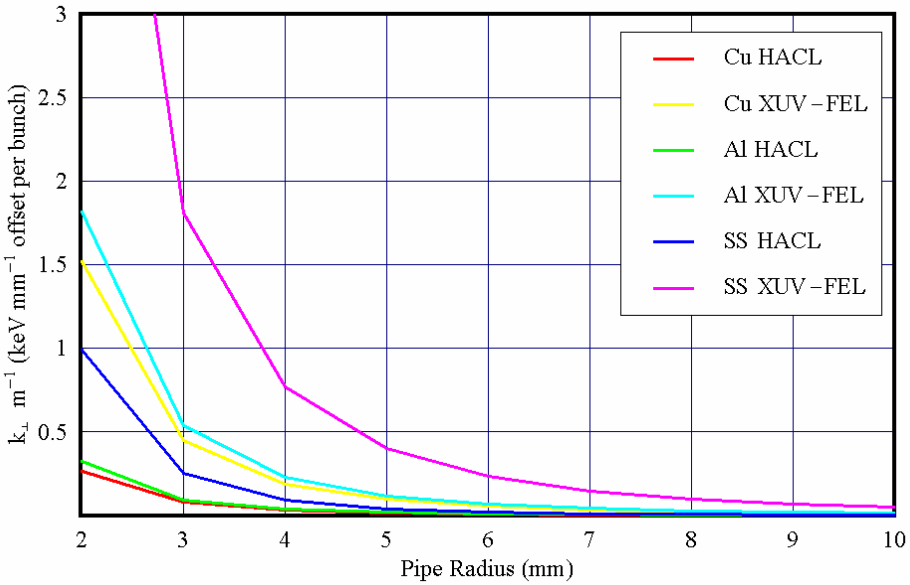

Figure 7.49 Transverse kick factors for different bunch charges lengths and vessel materials versus vessel radius

7.7.6.6 XUV-FEL

The XUV-FEL comprises ~ 16 m of planar undulator with a minimum magnetic gap of 10 mm and ~ 10 m of APPLE-II undulator with a minimum magnetic gap of 8 mm (for the option which requires the smallest magnetic gap – see Chapter 8). These magnetic gaps are required to provide the desired photon energy range from the FEL. Allowing for 1 mm thick vessel walls and 0.5 mm clearance above and below the vessel this sets the minimum internal vessel diameter to 7 mm for the planar undulators and 5 mm for the APPLE-II undulators. Each

module is ~ 2 m long. Table 7.18 shows the longitudinal and transverse resistive wake effects of the XUV-FEL undulator vessels on the beam. In fact, this is a worst-case since the XUV-FEL will utilise a tapered vessel (see Chapter 8), and the minimum gap quoted here will only be present in the APPLE-II modules and in a small section of the planar undulator vessel.

Table 7.18 Resistive wake effects of the XUV-FEL undulator vessels on 1 nC, 250 fs bunches

Parameter	*Unit*	*Value*					
Vessel Material		Cu		Al		SS	
Transverse Kick	keV mm^{-1}	13		16		52	
Total Energy Lost	keV	260		333.67		1683	
Beam Energy	GeV	0.75	0.95	0.75	0.95	0.75	0.95
Relative Energy Lost	10^{-5}	35	27	45	35.1232	224	177
Induced Relative Energy Spread	10^{-4}	1.4	1.1	1.7	1.4	8.3	6.6

The transverse kick the beam receives can lead to an increase in the emittance. The tolerance on the steering of the beam is at most of the order of 100 μm and so the expected transverse kicks are of the order of 1 keV from the entire length of the XUV-FEL undulator vessels.

The total energy lost effects the magnet gap of the undulator. As the beam loses energy the undulator magnetic field will have to be slightly increased to keep the output radiation at the resonant energy. This effect is discussed further in discussing undulator tolerances (Section 9.3.4) and does not present a problem in the current design.

The induced energy spread of stainless steel vessels is of the order of the natural energy spread of the beam and so a pure stainless steel vessel should not be used. A copper-coated vessel could be used providing the copper coating is thick enough. For aluminium the induced energy spread is about a tenth of the natural energy spread of the beam, after the beam has passed through the entire FEL. Typically vessels are made of aluminium or stainless steel and so aluminium will be used due to the significantly lower wakefield effects.

7.7.6.7 VUV-FEL

To cover the required photon energy range a variety of magnetic gaps and undulator periods can be chosen. The length of undulator will be ~10 m and the wakefield effects for internal vessel diameters of 7 mm and 12 mm have been considered, corresponding to 10 mm and 15 mm magnet gaps respectively.

Table 7.19 Resistive wake effects of the VUV-FEL undulator vessels on 77 pC, 50 fs bunches

Parameter	*Unit*	*Value*					
Vessel Material		Cu		Al		SS	
Vessel ID	mm	7	12	7	12	7	12
Total Energy Lost	keV	81	53	108	70	524	244
Relative Energy Lost	10^{-5}	13	8.8	18	12	87	41
Induced Relative Energy Spread	10^{-6}	9.6	5.7	12	7.3	60	35
Transverse Kick	keV mm^{-1}	0.21	0.045	0.25	0.054	0.84	0.19

The bunch length in the VUV-FEL may change, but any increases in bunch length will reduce the effects on the electron beam. Figure 7.50 shows how the energy lost and induced relative energy spread change as a function of changes in bunch lengths; aluminium vessels with internal diameters of 7 mm and 12 mm have been considered. The wakefield effects for the VUV-FEL are approximately an order of magnitude less than for the XUV-FEL. Therefore a magnetic gap of 10 mm is acceptable.

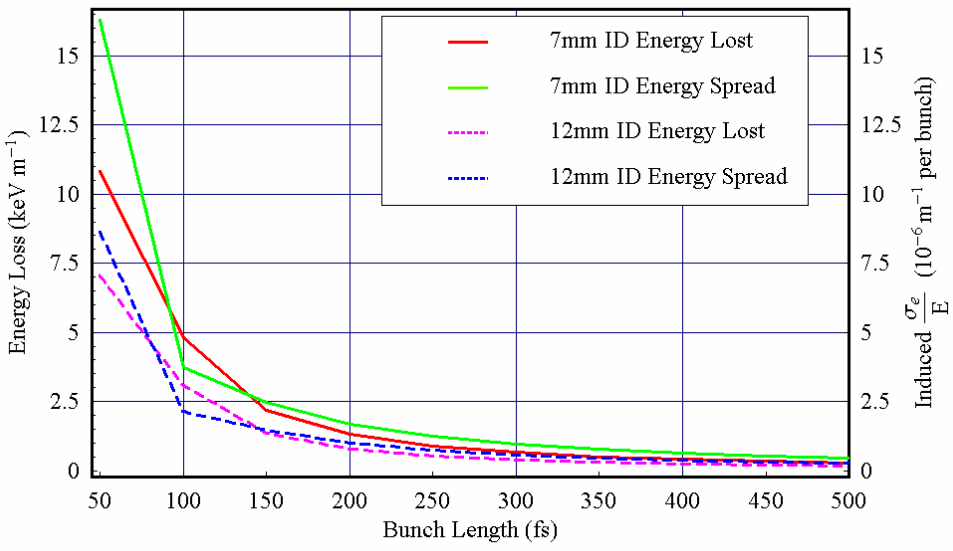

Figure 7.50 Energy lost and induced energy spread for different RMS bunch lengths for 7 mm and 12 mm ID aluminium vessels

7.7.6.8 Further Work

All the results in this section have been based on the static conductivity of the vessel walls. For AC fields the conductivity is frequency dependant [52] and this influences the resulting wakes. AC conductivity effects will be more rigorously studied when a realistic charge distribution has been produced (see discussion of start-to-end simulations in Section 7.7.4 above). If higher

frequency components exist then the anomalous skin effect will also be considered. This effect occurs when the mean free path of the electrons in the conductor becomes large when compared to the classical skin depth [53]. Currently, for a 50 fs Gaussian bunch, the skin depth is ~ 37 nm and the room temperature mean free path of electrons in aluminium is ~ 16 nm.

Although not a resistive effect, further work will study the surface roughness wakefields of the vessel in more detail. Using the best quality commercial finish vessels an RMS height of the roughness of 100 nm can be achieved [54]. This is presently assumed to be good enough for 4GLS. The macroscopic simulations that have been discussed in this chapter — i.e. the effect on the overall bunch modulation and energy spread — indicate that wakefield effects are not likely to significantly affect FEL performance. However, further analysis and simulation will investigate how the distribution of induced energy spread and its modulation are relevant for the FEL.

The analysis presented here has looked at the effect of resistive wall wakefields on the macroscopic bunch properties of mean energy and energy spread. This has been done for worst-case scenarios: a round vacuum vessel (where in fact the vessel could be elliptical) and a constant minimum aperture through all of the XUV-FEL undulator modules (where the proposal is to use a step-tapered vessel as discussed in Chapter 8). It has nevertheless been found that the effect on the beam energy is small and that the effect of this energy change on the resonance between the electron beam and FEL radiation could easily be corrected with small module-to-module gap adjustments. The induced energy spread is found to be well within the natural energy spread of the electron beam so that the effect on the FEL performance will be small. However, it is recognised that the effect on the FEL interaction also depends on the distribution of energy loss and induced energy spread along the bunch. Future design work will include start-to-end simulations with realistic phase space distributions which will allow these factors to be modeled explicitly.

7.7.7 Other Scattering Effects

4GLS is not a storage ring and as such the vacuum requirements are far less stringent that for 3rd generation storage rings: this is because lifetime per se is not an issue as bunches are continually re-injected. A vacuum pressure of around 10^{-7} mbar should be adequate to provide a reasonable environment for the beam. At this pressure the scattering rate from the beam will be low; the main concern will be bremsstrahlung radiation from the long straights.

Single and multiple coulomb scatterings in the beam will not be a significant issue as the beam is renewed every turn and the time the beam is in the machine is approximately 1 μs. This is insufficient time for these scattering events to lead either to significant beam loss or to a noticeable increase of the emittance in the case of multiple scattering.

7.7.8 Beam Break-Up

Beam break-up is an instability whereby higher-order modes (HOMs) interact with the beam causing it to be kicked either longitudinally or transversely. Higher-order modes are resonant modes, other than the fundamental accelerating mode, which are trapped within the cavity. Within a multi-celled cavity of the type considered for 4GLS the majority of the trapped modes will be contained in only some of the cells, most likely the central cells as these are furthest from the HOM couplers or dampers. These HOMs can be created as part of the cavity designs or from imperfections in manufacture that are smaller than specified tolerances. They are fed from the wakefields of the bunches passing through the cavities. The most damaging modes with regard to BBU are the dipole modes which can give the beam a kick in either the x or y plane. When a bunch crosses the cavity off-axis it transfers energy to any HOM of approximately opposite phase, and receives energy, in the form of a kick in either the longitudinal or transverse direction, from those of similar phase. Those HOMs which have gained energy can then in turn kick subsequent bunches with greater force; this growth in the kick is exponential and leads to the beam breaking up. If the kicks received by the bunches are damped the beam will remain stable. For each of the HOMs there will be a value for the beam current below which the beam will remain stable but above which it will break up. This value is a function of the properties of the HOM and of the optics of the accelerator transport. In the single cavity case, the threshold for each HOM m may be given as:

$$I_{th} = \frac{-2p_r}{e\left(\frac{R}{Q}\right)_m Q_m k_m R_{ij} \sin(\omega_m t_r)}; \tag{7-25}$$

p_r is the momentum of the particle, t_r is the revolution time from cavity back to cavity, and $\left(R/Q\right)_m$ is a cavity geometry parameter for the particular HOM. The threshold for the BBU instability is then just the lowest threshold of any of the HOMs. Q_m is the quality factor of the HOM and k_m is the wave number of the mode (given by $k_m = \omega_m / c$, where ω_m is the frequency of the mode). R_{ij} is the (i, j) component of the transport matrix for a complete recirculation from a cavity round a loop and back to the cavity and is either (1,2), (3,4) or (5,6). When $(i, j) = (1, 2)$ or $(i, j) = (3, 4)$ then this equation applies to transverse BBU; when $(i, j) = (5, 6)$ then the equation applies to longitudinal BBU. To obtain a complete overview of the BBU within the machine this equation must be applied to every HOM within the frequency range of interest.

There are multiple methods by which the BBU instability can occur, of which two are of concern in this kind of machine; these are explained in greater detail below.

7.7.8.1 Single Bunch and Single Pass Effects

Single bunch and single pass effects arise from short range wakefields. The single bunch effect occurs when a beam enters a cavity off-axis or enters a misaligned cavity, and therefore the head or tail is accelerated more than the other part of the bunch thereby forcing the head or tail

to undergo transverse betatron oscillations about the beam axis. This can be cured by Balakin-Novokhatski-Smirnov (BNS) damping [55,56] where the tail of the bunch is more strongly focussed than the head to compensate for the wakefields produced by the head of the bunch. This effect is similar to the regenerative case explained in greater detail below, but within a single pass of the cavity/module. The threshold in this case is proportional to the energy of the beam and inversely proportional to the loaded Q and length of the cavity. Therefore this is of greater concern in the booster before the Main Linac when the beam is at particularly low energy.

7.7.8.2 Regenerative Multibunch Instability

This type of instability comes in both transverse and longitudinal forms although the transverse form is usually only considered for this type of machine; the longitudinal form is far more sensitive to frequency and generally has a slower growth rate [57] and therefore can be corrected by bunch-by-bunch feedback systems if necessary. The transverse regenerative instability occurs within a single multi-celled structure with strong electromagnetic coupling between the cells. As the bunches enter the cavity off-axis they are fed and are kicked by the HOMs contained within the cells; after the bunches have been round the ERL transport they pass through the linac again to be decelerated where they are kicked again by the same HOMs. This continues with each bunch until either a stable equilibrium is reached, where the same amount of power is coupled in and out of the HOMs but no kick is great enough to lose the beam or the HOM kicks to the beam grow exponentially until the beam is lost.

There is an effect where the instability is driven between separate cavities by the coupling of the HOMs to be beam, known as cumulative multibunch BBU. It is of less concern to this type of machine as it is believed to have thresholds far higher than the 100 mA required in the Main Linac.

7.7.8.3 Simulations

Equation (7-25) above gives a threshold current for each individual HOM for a single cavity. It is seen as somewhat a worst-case scenario but it does not include coupling between the HOMs which can lower or raise the threshold. There are several codes available to calculate the threshold for a system of many HOMs and many cavities. Two of these — BI and ERLBBU [58,59] — have been used for preliminary investigations into the threshold currents for 4GLS. These codes calculate the regenerative transverse threshold by passing a number of bunches through the machine and calculating their interaction with the higher-order modes in each of the cavities.

The preliminary investigations of the threshold have assumed nine-cell TESLA-type cavities with the HOMs given in Table 6.12. This cavity was chosen as it is similar to the seven-cell cavity proposed for 4GLS, and has HOMs that are well categorised. As discussed in Chapter 6, HOMs from the seven-cell cavity should have lower quality factors and therefore cause less disruption to the beam than the nine-cell TESLA cavities. This has led to a conservative

threshold from the modelling as the HOMs couplers of the nine-cell TESLA cavity are not as efficient as the HOM dampers of the seven-cell cavity in removing the HOM power.

A graded-gradient scheme has been used for the quadrupole focusing through the Main Linac. This matches the strength of each quadrupole triplet to the lowest energy beam at that point. Hence through the first half of the linac the quadrupoles are matched to the accelerating beam, whilst in the second they are matched to the decelerating beam.

Initial simulations of 4GLS, using five modules each containing eight nine-cell TESLA cavities, have obtained a threshold current of around 30 mA. This is without optimising the graded-gradient focusing scheme or the recirculation. By including optics as described in [60] a threshold increase of two orders of magnitude has been observed: these methods involve reflecting or rotating the beam so it enters the linac for the second pass either reflected in the x or y plane or rotated by 90°. The effectiveness of these methods depends on the orientation of the HOMs: if the modes are only in the x and y plane then simulations suggest the reflection method may increase the threshold by a factor of one hundred and the rotation method by a factor of 300. If the HOMs are skewed through the cavity the increase in the threshold is smaller, perhaps up to a factor of six for the reflected optics set-up and one hundred for the rotated optical setup.

7.7.8.4 Summary

Initial simulations suggest a threshold for 4GLS of at least 30 mA. Although it is below the target 4GLS HACL current, optimisation of the linac focusing and recirculation, including the methods described above, and use of the seven-cell HOM-damped cavity design should lead to a threshold in excess of the required 100 mA. These simulations are analogous to those performed for the proposed Cornell light source, where such considerations have predicted a threshold current of 205 mA [61]. The Cornell simulations give some confidence that a sufficient current threshold may also be achieved in the 4GLS design.

7.8 Common Issues

7.8.1 Beam Loss and Halo

Beam loss is a significant issue in the 4GLS design not only in the HACL, but also in the lower average current XUV-FEL branch. The HACL carries 60 MW CW beam power, so beam loss must be very carefully controlled, to avoid heating of the vacuum vessels and other accelerator components and to control irradiation both inside and outside the accelerator facility. To put these losses in context, the ERLP design specified a local loss limit of 3 W/m of accelerator transport to keep radiation and heat loads within acceptable limits; a larger point loss limit of 15 W is being considered for the warm sections of 4GLS to avoid component damage (see Section 15.2), but this will still require up to 3 m of concrete shielding.

A loss of 15 W from a total beam power of 60 MW is very small ($0.25\ 10^{-6}$) and is much smaller than can be measured either from changes in the overall charge or from loss in the efficiency of energy recovery. Instead, sensitive monitors that measure the number of lost particles will be necessary: these are presently assumed to be long ionisation chambers which have been successfully used at the ELBE facility at Rossendorf [62] and are planned to be used for the ERLP project (see Section 13.7.6.2).

The very large beam power in the HACL will also necessitate passive protection in case of mis-tuning, steering errors, energy errors from the linac and other problems such as magnet faults. This passive protection must protect the accelerator components from errors and faults until the loss monitors can respond by activating an interlock in the machine protection system (see Chapter 13). It is envisaged that a system of collimators will be placed at regular locations through the HACL to provide effective protection from focusing, steering and energy errors. These collimators will also provide protection against beam halo. Simulations of the likely losses on these collimators will be performed during the technical phase of the design.

7.8.1.1 Halo Production and Collimation in the HACL

Beam loss may occur from the particles surrounding the dense beam core — the beam halo. This beam loss must be minimised for both health physics and machine protection reasons, limiting exposure to both personnel and equipment. It is important to know the causes of the halo production in order to minimise it either at the design stage or by damping the instabilities that cause it. The majority of these causes are resonances either due to the design of the machine or from the space charge potential [63,64].

The space-charge potential requires no further perturbation from the machine to grow and produce a halo. There are multiple ways in which the space-charge resonance can form. These include:

- *The collectively coupled resonance.* This occurs when the space-charge potential driving the instability resonates with a harmonic of the lattice periodicity. In a linac

where the x and y betatron tunes can be very different there can be many asymmetric resonances to consider;

- *Intrinsic incoherent resonances.* This is the dominant form of halo generation in linacs. These are resonances between single particles and the beam's collective oscillations; they are dominated by the phase advance but still have a weak dependence on the space-charge effect.

Machine resonances may be driven by the lattice and can be avoided in many cases by an appropriate choice of parameters. Errors can occur in magnetic fields which can induce this resonance, which is then worsened by the effects of space-charge. Non-lattice generation methods include gas scattering and collective instabilities. In ERLs there are further effects to consider. High current photoinjectors for ERLs work in extreme space-charge regimes with non-linear space-charge. There are the effects of space charge and dispersion in the arcs, as well as longitudinal space charge and CSR. The fast acceleration of the beam means that the beam very quickly moves into the region where halo production is dominated by the emittance.

The physics of halo production is a complex and evolving field [65], and the degree of halo that is expected is difficult to predict. We presently propose in the HACL to use a system of collimators that effectively collimate in transverse phase space and in energy to passively protect against heat load and radiation induced by beam halo. It is envisaged that a system of collimators will be placed throughout the HACL outward and return arcs to remove halo that may be progressively generated in the transport. Details of the placement and design of this collimation system will be performed during the technical design phase of the project, and may influence the design and layout of the arcs. The design of this system will depend greatly upon the nature of the machine protection system, radiation protection issues, the type of collimators that are to be used, and the chosen vacuum aperture in the HACL. Similar problems have been encountered in other designs [66], and their experience will be used to develop the 4GLS solution.

Beamlines from the spontaneous sources and VUV-FEL in the High Average Current ID Arc are susceptible to showers from electron loss within the insertion device vacuum vessels, and from bremsstrahlung from residual gas in those same vessels. The beam power is much higher per milliampere of circulating current than in a traditional storage ring, and there is no stored beam in an ERL which could self-limit a radiation dose in case of loss. It is not possible to collimate for these phenomena as they are produced by electrons co-axial with the normal transport through the insertion devices. In consequence, the machine protection system must try to collimate those halo particles which are most likely to be lost in the insertion device regions, and the beamlines themselves must separate out the output photons from the path of any possible radiation of this nature. Possible beamline layouts which achieve this are discussed more fully in the Technical Systems Chapter (Chapter 13).

7.8.1.2 Beam Loss in the XUV-FEL Branch

The average beam power carried by the XUV-FEL bunches is much lower (a maximum of around 1 kW), and so machine protection is not as onerous as in the HACL transport. However, similar operating facilities such as the VUV-FEL have needed to be careful of beam loss [67]; operational experience during TTF-II commissioning has indicated that it is difficult to diagnose beam halo loss from core beam measurements. Similarly to the high power HACL transport, residual gas bremsstrahlung and loss on the vacuum vessel walls must be controlled to minimise ionising radiation passing down the user beamlines, and the beamline design will take this into account (see Section 15.2.7). To control beam loss, it is proposed in 4GLS to use a similar collimation strategy to that considered for the BESSY-FEL [36], which is itself modelled on the system used at TTF-II/VUVFEL. This collimation system dictates the layout of a significant part of the XUV-FEL branch, and has been considered in Section 7.5.4.

7.9 Diagnostics and Tuning

Preliminary consideration has been made of the diagnostic requirements for the HACL transport and XUV-FEL branch bunches, principally to identify studies that must be performed during the technical phase of the project, but also to approximately determine space and cost requirements. Significant experience has been gained from similar facilities and proposed projects, particularly the Cornell ERL, the DESY TTF-II/VUVFEL, the IR-FEL ERL facilities at TJNAF, the proposed BESSY FEL project, and the Daresbury ERLP which is presently under construction. The diagnostic systems proposed below are based on work done for these projects.

7.9.1 Overview of Diagnostics

The diagnostic systems must allow the HACL and XUV-FEL bunch properties to be tuned to:

- Provide the required transverse and longitudinal properties at the spontaneous sources, the VUV-FEL and the XUV-FEL;
- Diagnose and thereby minimise beam loss and halo;
- Achieve and control energy recovery in the HACL return arc and then dispose of the waste HACL beam.

As well as providing information for tuning purposes, the bunch properties at the various source points must also be measured accurately to provide information that in particular will be vital to understanding the FEL lasing process. This includes measurement of the slice emittance and energy spread properties of the electron beam prior to its entry into the XUV-FEL, and the measurement of the bunch longitudinal shape and timing properties at each of the XUV-FEL, VUV-FEL and spontaneous source points.

Because of its significant influence on the layout of the XUV-FEL branch transport, the XUV-FEL diagnostic section is described in Section 7.5.3. The diagnostic needs in other parts of the facility are dealt with in the sections below.

7.9.2 Integrated Diagnostics

The measurements detailed in the following sections are needed throughout the 4GLS facility.

7.9.2.1 Beam Position Monitors

Several types of beam position monitor (BPM) will be used, including striplines and button-type pickups. The primary purpose of these will be for alignment and steering of the beam centroid, for which they need an accuracy at the source points of approximately 1/10 th the beam size both at full current operation and during tune-up of the FELs. This typically means sub-micron accuracy, which has been achieved at several facilities.

A large dynamic range is required from a subset of the BPMs so that they may be used during tune-up of the HACL and XUV-FEL bunches at low current. Less accuracy is required during tune-up, and the requirements will be quantified during the technical phase of the project.

As well as providing beam centroid position information, the BPMs will be used as part of the machine protection system, and sum signal measurements will give basic but fast information on beam loss during tune-up. Some BPMs in dispersive regions will additionally be used for energy measurements in conjunction with variations in the linac gradients.

For measurement of the 1 nC bunch trajectory with the required resolution of 1 μm, a novel BPM has been designed for 4GLS. For 1 kHz bunch repetition rate it is possible to store on-line the position readings of a full set of the BPMs for some large number of subsequent bunches. Either button or strip line pickups can be used. The latter are preferable as they provide a higher signal to noise ratio. For best accuracy and performance, the signals from a pair of opposite pickups are processed in same channel. For this, one of the signals is delayed by (say) 20 ns and combined with another one on the channel input.

In the basic BPM configuration, the output signal is also a pair of pulses spaced in time by the same delay. The pulses will be measured subsequently by a fourteen-bit 100 MHz analogue-to-digital converter (ADC). To realise full resolution of the ADC the pulses are made with a flat top. A proof test of the basic configuration has been done at the KEK ATF [68].

Another configuration is possible where the output pulses are de-combined and their sum and difference is obtained in some additional analogue circuit. The sum and difference are measured by two ADCs. In this case, the requirements on the resolution and speed of the ADCs can be relaxed.

To achieve good absolute position information the BPM units should have geodesic survey fiducials. Beam-based centre offset measurements of a set of units can be done on a test bench

which is being set up for use for ERLP. A full test of the BPMs, including beam-based resolution measurement, may also be performed on the same bench.

The XUV-FEL and HACL bunches co-propagate in the Main Linac and the merger/separators at either end of it. It is envisaged that the tune-up of this section will be performed as follows:

- Tune-up of a low-current HACL beam to determine the correct focal and steering conditions separately for this beam;
- Tune-up of the XUV-FEL beam to match it to the linac setup for the HACL beam;
- Iteration between HACL and XUV-FEL beams to increase the current of both;
- Full-current operation of both beams; the diagnostic instrumentation will only see the HACL bunches, which are most important to monitor and control beam halo and loss.

7.9.2.2 Charge Measurement

Charge measurement will be made using a variety of detectors. Faraday cups will give a slow but absolute measurement, and will be used to calibrate both the BPMs and integrating current transformers (ICTs). The three types of detector will in particular be used in the XUV-FEL branch to provide beam loss information.

Charge measurement will need to provide good information from the pulsed charge trains, and to gate measurements to measure charge transmission of different parts of the bunch train. A system of this nature has been developed for TTF-I and TTF-II, and a similar technique will be explored for 4GLS [69].

7.9.2.3 Long Ionisation Chambers

Long ionisation chambers have been developed at ELBE to sensitively measure showers from lost particles with good position localisation [62], and this technique will be used both on 4GLS and at ELRP to measure beam loss in the HACL transport. These monitors will be used in conjunction with the passive collimation system (see Section 7.8.1 above) to protect the vacuum vessels in the HACL from damage and to prevent irradiation of beamlines, accelerator equipment and personnel.

7.9.2.4 Beam Profile, Emittance and Energy Spread

Beam profiles will be measured using YAG and optical transition radiation (OTR) screens [70], and by using wire scanners. YAG screens are appropriate for lower energy regions such as the injectors, and at the dump. OTRs have a large opening angle at low energy [71] which precludes their use in this low energy regime, but are useful for high energy, lower current measurements of pulsed beams such as in the XUV-FEL branch, and during tune-up of the HACL; OTR screens are preferred at higher current because of their better linearity. Higher current

measurements will be performed using wire-scanners, although power absorption into the wires may be a problem. This will be explored during the technical phase of the project.

Emittance measurement will be performed in the XUV-FEL branch in a dedicated diagnostics section upstream of the XUV-FEL. Because of its influence on the layout this emittance measurement section is described above in Section 7.5.3. Emittance measurement may also be performed in the periodic part of the HACL outward arc, using a similar method to that envisaged for the XUV-FEL branch.

Energy spread and the longitudinal phase space may be measured by a variety of methods, for example by performing phase scans of an accelerating RF structure and reconstructing the phase space by using tomography from screen/scanner images in a dispersive section.

7.9.2.5 Bunch Length and Bunch Profile

Bunch lengths — and importantly, longitudinal bunch profiles — must be measured at a variety of locations in the accelerator facility. In particular, bunch profile measurements will be required for tuning and for users upstream of each of the facility source points – XUV-FEL, VUV-FEL and each of the spontaneous source points. Bunch lengths longer than ~1 ps may be measured using streak cameras, whilst shorter bunch lengths require one of a variety of specialised techniques. Deflecting cavity-based measurements may be possible and appropriate in the XUV-FEL branch, the High Average Current Loop will almost certainly require a non-destructive measurement such as that offered by electro-optic sampling. Since this is a critical element of the diagnostic measurements envisaged for 4GLS, a review of electro-optic techniques is given below in Section 7.9.8.

7.9.3 Pre-Linac Diagnostics

The low energy injector diagnostic and tuning requirements are dealt with in Chapter 5. A schematic of this section is given in Figure 7.51. After the first-stage XUV-FEL acceleration, measurements of the longitudinal phase space may be performed using the merge (BC1) to confirm the beam properties exiting the injector and to tune compression prior to entering the Main Linac.

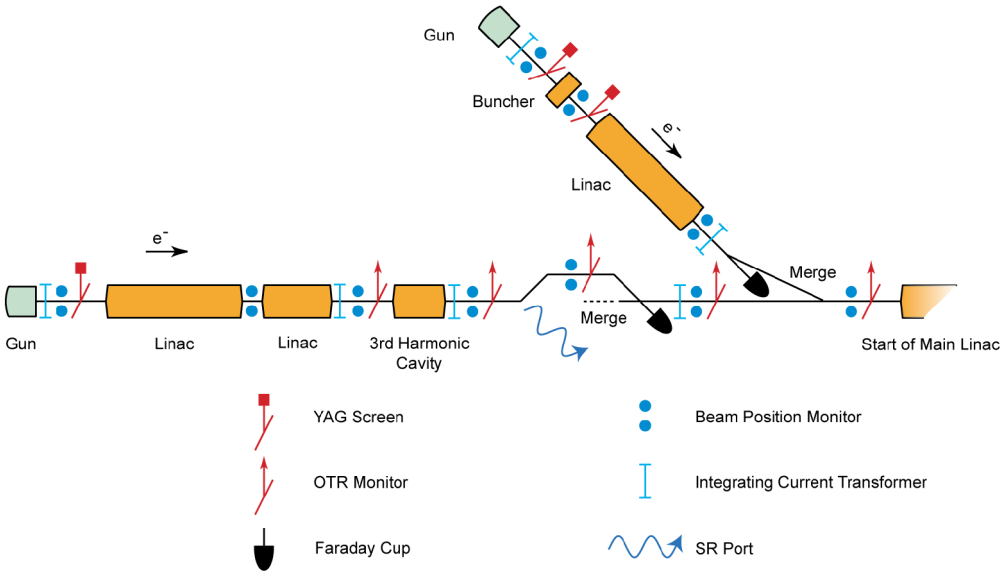

Figure 7.51 Schematic of XUV-FEL Branch and HACL Injector Diagnostics

7.9.4 Main Linac and Dump Extraction

A schematic of the Main Linac and dump region is shown in Figure 7.52. It is likely that emittance matching of the XUV-FEL and HACL beams will need to be performed separately. Matching of the return beam has previously been aided by using OTR screens with holes for the accelerating beam [72,73,74], but this will only be possible on 4GLS at low current due to the large beam power. Wire scanner measurements will complement the OTR diagnostics.

After extraction, the recovered HACL bunches must be expanded to a large transverse size (see Section 7.4.5), but the beam power at 100 mA current will still be too large in this region to use OTR or YAG imaging of the beam. At present it is envisaged that a YAG screen may be used to determine and tune the beam profile at lower current, but there is a requirement to study this issue during the technical phase of the project.

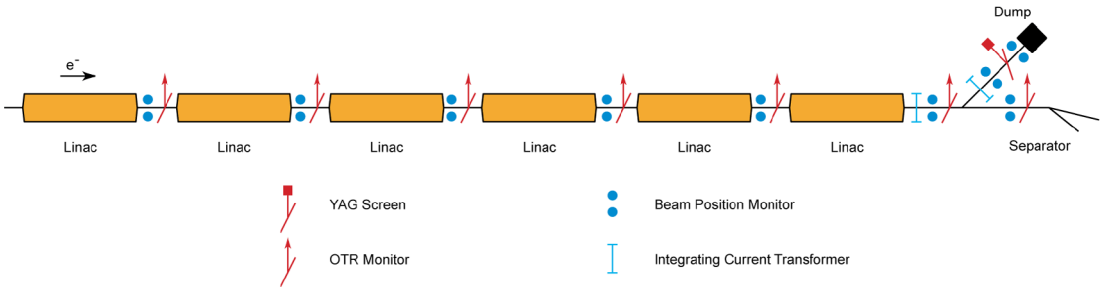

Figure 7.52 Schematic of Main Linac and HACL Dump Diagnostics

7.9.5 High Average Current Loop Diagnostics

A schematic of the HACL diagnostics is shown in Figure 7.53. It is envisaged that emittance measurements may be performed in the outward and return arcs using a combination of dispersion measurement and transverse profile measurements. At lower current, optical transition radiation (OTR) monitors or wire scanners may be used; it is possible that at full current it may not be possible to use wire scanners, in which case it may be possible to user laser-wire scanners. Details of this instrumentation will be developed during the technical phase of the project.

Beam loss is a complex area that has already been discussed in Section 7.8.1. In the HACL transport one of the principal difficulties is that most of the diagnostic instruments — OTR screens, BPMs, and longitudinal measurements — will only be sensitive to the core of the beam, and will be unable to detect the diffuse halo which can arise from instabilities, scattering and dark current throughout the accelerator system. Measurement and control of this halo, which must be done with a sensitivity down to 10^{-7} compared to the core beam, will be performed in a variety of ways. Firstly, a collimation system will be used to progressively scrape the beam halo in each of the Outward and Return HACL arcs. Secondly, long ionisation chambers will measure lost particles from the collimators and other locations in the transport to quantify the size of the halo at each location. It may also be possible to use wire scanners to probe the edge of the HACL bunches to make profile measurements of the beam.

The HACL outward arc is a FODO channel in which the longitudinal dispersion will be tuned to provide the desired compression at the first HACL user straight, depending upon the chosen Main Linac gradient and phase setup. Confirmation of this compression setup will be obtained using an electro-optic monitor upstream of the insertion device straights. There will be at least a second electro-optic monitor to confirm the small compression that occurs from straight to

straight, with perhaps more monitors to measure compression in the intervening straights (see below).

Energy spread measurements may be obtained from the undulator spectra and longitudinal phase space profiling may be performed by varying the accelerating RF phase at low current.

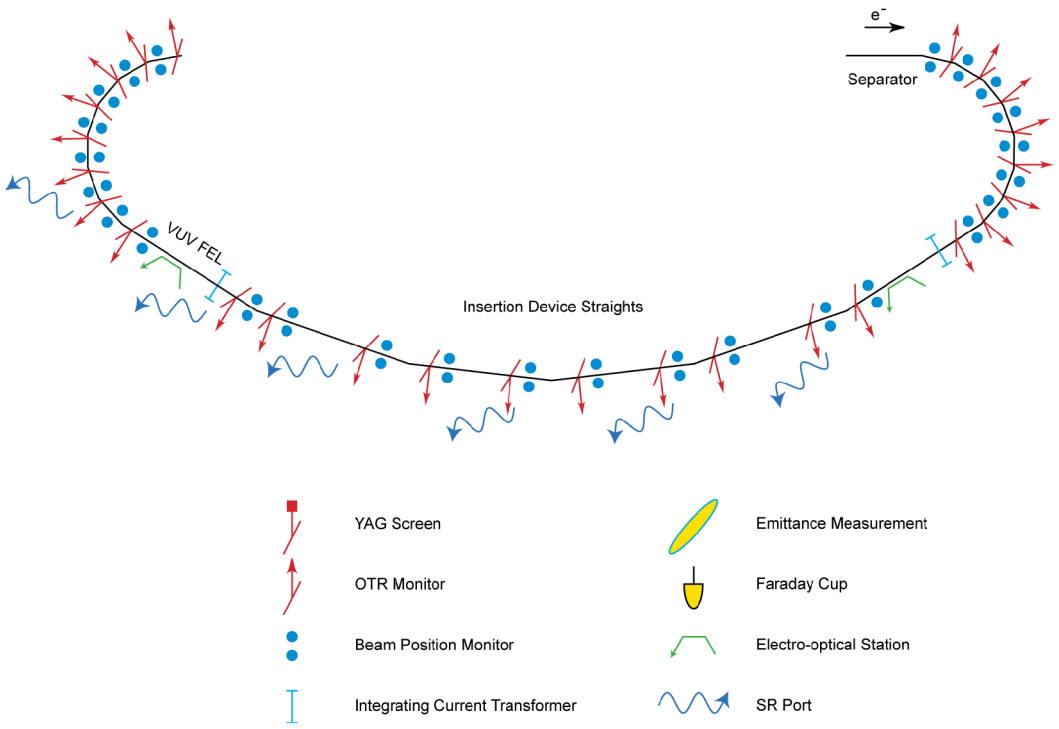

Figure 7.53 High Average Current Loop diagnostics. OTR monitor locations may also or instead include wire scanners.

7.9.6 XUV-FEL Branch Diagnostics

A dedicated emittance measurement section upstream of the XUV-FEL has already been described in Section 7.5.3; similar measurements are envisaged in the XUV-FEL branch arc. Synchrotron Radiation (SR) ports are available for transverse imaging. Electro-optic bunch length measurement will take place immediately upstream of the XUV-FEL – this technique is described in detail below, and will be used to tune the final acceleration and compression, in conjunction with measurements in the second compressor BC2. This will include measurement of the linearisation provided by the third-harmonic cavity and of non-linearities induced by the main accelerator RF and by the XUV-FEL branch arc.

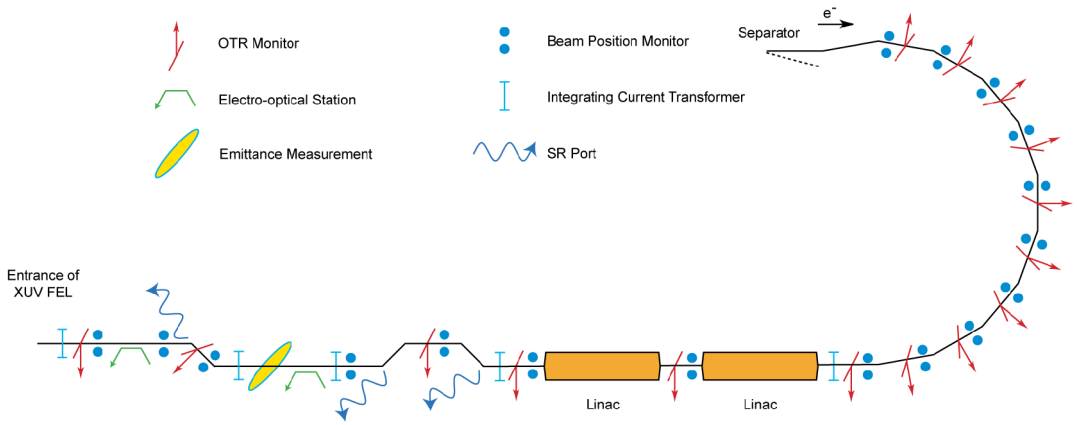

Figure 7.54 Schematic of XUV-FEL Branch Diagnostics

7.9.7 XUV-FEL and Spent Beam Undulator Diagnostics

A schematic of the diagnostics envisaged for the XUV-FEL itself and the downstream spent beam undulator is shown in Figure 7.55. Focusing and steering to accomplish and control lasing will be performed using beam-based alignment and using OTR screens and/or wire scanners to correctly match the beam. Electro-optic measurements upstream of the XUV-FEL and upstream of the spent beam undulator will both measure the longitudinal profile and provide timing information needed for synchronisation of the two sources.

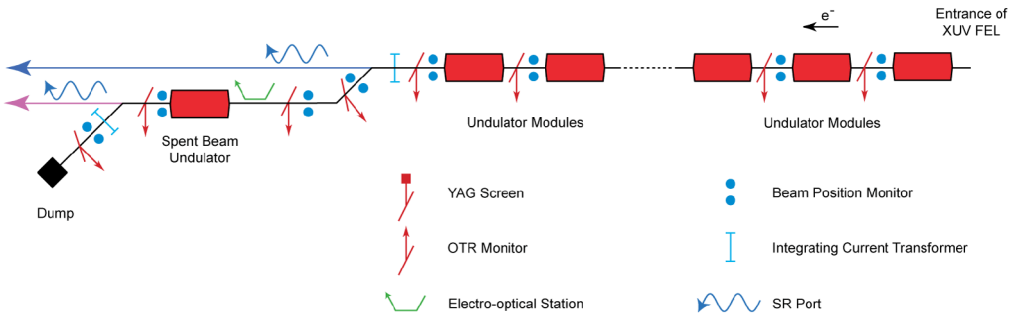

Figure 7.55 Schematic of XUV-FEL and Spent Beam Undulator Diagnostics. OTR monitor locations may also include wire scanners.

7.9.8 Longitudinal Diagnostics — Bunch Profile

7.9.8.1 Review of Available Techniques

Electron bunches in accelerators like 4GLS, which are typically 200 fs in length, are much shorter than those in previous generation machines (typically greater than 10 ps), and this results in a challenging requirement to measure the longitudinal (time) profile of bunches with a resolution approaching 40-50 fs. The potential of a number of diagnostics for attaining such time resolutions is discussed below.

7.9.8.2 Transverse-Deflecting RF Cavities

This technique uses a transverse-deflecting RF cavity operating at the RF zero-crossing to sweep the electron bunch transversely, transforming the bunch temporal profile into a transverse spatial profile. A time resolution approaching 10 fs is in principle achievable, although this will be strongly dependent on other bunch properties such as transverse profile. For the highest time resolution the location of the diagnostic is therefore coupled to beamline optics. At the energies required these cavities may be several metres long, providing a further constraint on location of the diagnostic. The diagnostic is also intrinsically a destructive measurement, and for the HACLL the cavity filling time of a few microseconds for a normal-conducting structure may present a difficulty in ensuring that only a limited number of bunches are influenced by the diagnostic. On the XUV-FEL arc the cavity filling time does not represent any constraint.

7.9.8.3 Electro-Optic Techniques

Electro-optic (EO) bunch profile measurements have been under systematic development for several years at various accelerator and FEL laboratories, such as the FELIX free-electron laser facility in the Netherlands, at TTF/VUV-FEL at DESY, and at SLAC and TJNAF. The electro-optic technique uses a non-linear crystal traversed by a chirped laser pulse to "transfer" the bunch profile information from the Coulomb field of the electrons to the laser pulse, via polarisation effects within the optical medium. Several variants of this technique exist, but all basically encode the bunch information on to a laser pulse, then optically process the pulse to extract the bunch profile. These techniques require only a short longitudinal space to make a bunch profile measurement, and appear capable of time resolutions approaching 10-20 fs in their ultimate development. Electro-optic techniques are well-suited to short (sub 1 ps) bunches at higher energy: for a specified time resolution there is a maximum distance of the monitoring crystal from the beam, R, which is proportional to the electron energy. The signal strength S is also proportional to the longitudinal charge density: $S \sim \left(Q/R\tau\right)^2$, where Q and τ are the bunch charge and duration respectively. Electro-optic diagnostics will therefore not usually be suitable for characterisation of low-energy beams (<< 50 MeV), or those with a low charge density (< 50 pC/ps).

Benchmarking of EO diagnostics with respect to other diagnostics, most notably the Lola transverse deflecting cavity, has recently been undertaken at TTF/VUV-FEL by a University of Dundee/FELIX/CCLRC/DESY collaboration [75]. Profile measurements with time resolution estimated at 100fs has been achieved to date. Further development should enable EO techniques

to reach 50 fs resolution. There are still significant obstacles to achieving higher time resolutions in the region of 10 fs, although research into achieving this goal is ongoing.

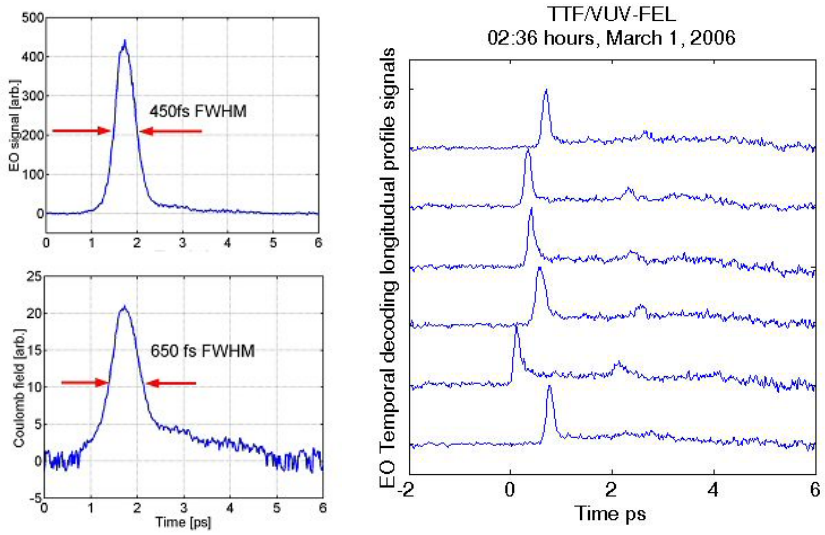

Figure 7.56 Left: an example of the electro-optic temporal decoding signal and the inferred bunch profile, obtained from measurements at the FELIX FEL facility [76]. Right: examples of electro-optic temporal decoding signals obtained for a sequence of bunches in the VUV-FEL at DESY (courtesy of G. Berden et al., FELIX/CCLRC/University of Dundee/DESY). The VUV-FEL measurements are preliminarily test measurements and were carried out while SASE was operating.

Three electro-optic laser diagnostics have been demonstrated in accelerator environments: spectral decoding (SD), temporal decoding (TD), and spatial encoding (SE). SD and TD have been developed and demonstrated by UK research teams, in conjunction with collaborators at FOM and DESY. The SE technique has been developed by University of Michigan and SLAC, and has been demonstrated at SPPS, with a further demonstration on TTF/VUV-FEL at DESY. Each technique has different characteristics as summarised below. Note the time resolution limits are only approximate, and are subject to particular implementation conditions. The potential time resolution of both TD and SD is given as a conservative estimate, with further advances likely in the medium term.

Table 7.20 Summary of electro-optic technique capabilities

Electro-optic technique	*Time resolution demonstrated (potential)*	*Repetition rate (laser limitations)*	*Laser system complexity*
Spectral decoding	~ 1ps (500 fs)	High (< 100 MHz)	moderate
Temporal decoding	~ 150 fs (50 fs)	Moderate (< 10 kHz)	moderate-high
Spatial encoding	~ 300 fs (50 fs)	High (< 100 MHz)	moderate

7.9.8.4 Monitors of Coherent Transition Radiation or Coherent Synchrotron Radiation

An established technique that has been applied at many accelerator facilities is the interferometric detection of coherent transition radiation (CTR) or CSR; for example the CTR generated by an oblique foil in the beam-line is analysed with a Michelson-type interferometer. The interferometer allows the reconstruction of the coherent radiation spectrum, which is dependent on the longitudinal profile of the bunch. Such diagnostics are relatively robust, and can provide a good indication of the *bunch length*. However, all implementations of this concept suffer from an absence of phase information on the spectrum. This leads to ambiguities and difficulties in accurately and reliably reconstructing a *bunch profile.* Where an accurate profile on sub-ps bunches is required, interferometric detection is not a suitable diagnostic. For more qualitative diagnostics, such as a relative bunch compression monitor, the overall power levels of CTR and CSR are likely to be sufficient (as seen in TTF measurements). In principle, the shorter the bunch length the easier this technique becomes.

Another common technique for bunch profile determination is based on spectral measurements of coherent millimetre-wave transition radiation or Smith-Purcell radiation, but such methods also suffer from the shortcoming of failing to account for the low-frequency spectral content of the signal, which inevitably introduces a bias into the final extracted profiles. Investigations have also been carried out into the use of variants such as diffraction and transition radiation as potential time and space diagnostics.

7.9.8.5 OTR-Based Streak Cameras

For long bunch lengths (>1 ps) streak cameras can be used to observe the OTR, with cameras capable of measuring a single bunch with a time resolution of ~ 1 ps. Such a measurement may be useful for injector diagnostics.

In general, the measurement of the phase and stability of the buckets in an accelerator with respect to the phase of the RF master oscillator is a major feature of streak cameras that operate with synchroscan and dual time base

7.9.8.6 Optical Replicas

A new concept for longitudinal bunch profile diagnostics, referred to as optical replicas, has recently been proposed by Saldin et al [77]. Briefly, the principle follows the sequence of (i) seeding an optically resonant undulator to impose small energy modulations, at the laser frequency, onto the electron bunch; (ii) the bunch is then passed through a dispersive section to produce a density modulation with the same period as the laser wavelength, (iii) the density modulated bunch enters a second resonant undulator, generating optical radiation with an envelope determined by the bunch longitudinal profile, and (iv) this ultrashort optical pulse is characterised with standard ultrafast laser diagnostics such as frequency-resolved optical gating (FROG).

While promising extremely good time resolution, at present the concept of optical replicas remains untested. Together with the overall complexity of the system, and the invasive nature of the diagnostic, it is not presently considered a feasible diagnostic for 4GLS. However, progress in this area will be monitored.

7.9.8.7 Recommendations

At the current time, transverse deflecting cavity diagnostics (TDC) arguably have the best time resolution capability of all longitudinal bunch profile techniques. It is also readily extendable to the provision of longitudinal slice measurements (see section 7.5.3). However, a TDC diagnostic has considerable space and electron beam optics requirements for optimal operation, and as such must be considered as an integral part of the machine design. The implications and feasibility of satisfying these requirements should be further considered during a technical design phase before a final recommendation on including a TDC diagnostic is made. Such a diagnostic is probably only justifiable on the XUV-FEL branch of 4GLS.

With the more modest requirements, it is currently recommended that electro-optic diagnostics be provided for temporal profile measurement on the XUV-FEL line and more widely on the energy recovery circuit of 4GLS. The possible inclusion of TDC diagnostics may be considered as a complement or expansion on the EO diagnostics capability.

Spectral decoding EO diagnostics should be incorporated at sites where the bunch profile is in the region of 500 fs – 2 ps, and where a profile would enable optimisation. Where the profile of sub-500 fs FWHM bunches is desired, a full temporal decoding system should be installed. Both spectral and temporal decoding bunch profile monitors should also integrate a signal from the RF timing distribution systems, enabling then to serve the dual purpose of high performance bunch timing detection. As the EO diagnostics are readily translatable into a real-time and operator-useable bunch profile, they should be incorporated into the control room information system.

It is recommended that for the XUV branch the laser to be used for EO diagnostics is derived directly from the laser producing the seed radiation, enabling the dual role of monitoring the HHG seed and electron bunch synchronisation. For the recirculation arm of 4GLS a separate dedicated diagnostics laser system is preferable because of the additional flexibility this affords.

7.10 Further Work

The studies presented in this chapter have sought to address the principal issues of concern in the design of the 4GLS electron transport system, and to identify particular physics and engineering work packages which must be carried out during the following technical phase of the project. This work will assess the feasibility of the various accelerator components envisaged in the facility. The studies in the present CDR also give an indication of what bunch properties are to be expected, and what the possible operating modes for the facility may be, so that user beamlines may be specified.

Detailed work remains to be done in a number of areas, particularly in producing an integrated design which includes simulation of the bunch properties from their generation at the three injectors, and their subsequent transport to the photon sources to generate either spontaneous or FEL radiation. Important work packages are described below.

7.10.1 Electron Optics and Start-to-End Simulation

Preliminary studies have been performed so far using simplified but indicative bunch distributions from the three injectors, and these have served to guide the output properties and to specify the injector requirements. Injector designs which give realistic bunch distributions have not yet been carried out, and this will have some effect upon the final bunch properties. The effects of magnetic and alignment errors, and the impact of various sources of jitter, must be performed to specify both the required quality of magnetic elements and their positioning, and to determine the expected variation in bunch shape, length and energy at the facility source points. Similar work has been carried out for the LCLS [78] and BESSY-FEL [79] projects, which will inform the 4GLS work to be carried out. In particular, attention must be paid to how fluctuations in the bunch properties from the HACL injector will produce varying CSR emission, which may have a significant effect upon the mean energy loss and bunch shapes provided at the HACL source points.

At lower energy, the effects of space charge must be determined. Although expected to be small in the XUV-FEL and IR-FEL injector regions [80], the emittance blow-up should be estimated. In the lower-energy region between the HACL injector and the Main Linac, an approximate emittance-compensated design has been achieved, but three-dimensional space charge simulations will be needed to arrive at an integrated design for the HACL injector including the low energy merger.

Non-linearities must be examined in greater detail, particularly to examine the sextupole scheme for phase space linearisation of the HACL bunches upstream of the source points, and their use to control the longitudinal phase space after deceleration. Energy recovery will also depend on the optical system used to control the final R_{56} prior to deceleration, and the requirements on path length control must be assessed.

A preliminary design has been proposed for the bunch separation scheme and for vertically separating the HACL from the XUV-FEL branch. The optical effects brought about by this scheme, particularly from the solenoids used to rotate the XUV-FEL bunch prior to transport through 180°, must be assessed including non-linearities.

7.10.2 Diagnostics and Tuning

An outline has been given of how diagnostic instrumentation is envisaged for the 4GLS facility. A number of issues are to be resolved. Firstly, an orbit correction scheme must be determined to allow adequate position feedback and to assist in the machine protection system; this is complicated by the presence of two types of electron bunches in the Main Linac with different charge and repetition rate, and will require study to determine how to commission, align and maintain beam steering in this important region. Similarly, a tune-up strategy is needed to determine the types and dynamic range of position measurement instruments which are required to achieve full-current operation of the XUV-FEL branch and HACL.

High-current operation will require profile measurement using instruments that will withstand the large beam power which is present in the HACL. At present, it is believed that wire scanners will provide the necessary resolution and can operate in this regime; a wire scanner design will be developed in future work, or alternative instrumentation will be designed. One possibility is to use laser-wire scanners, of which the 4GLS project has some experience through collaborative work [81,82].

7.10.3 Feedback, Collimation and Machine Protection

An extensive feedback system will be required to monitor and control beam loss, and to protect the accelerator in case of mis-steering or component failure. A collimation scheme will be developed to remove beam halo both in the HACL and in the XUV-FEL branch, and an instrumentation scheme developed to allow measurement and tuning of the beam halo, particularly in the high power parts of the accelerator complex. A fast machine protection system is required in case of machine errors.

7.10.4 Apertures and Wakefields

Wakefield effects have a strong influence on both the XUV-FEL and HACL bunches, especially in the longitudinal plane, and it is intended to carry out studies to calculate both the structure wakefields of the proposed seven-cell cavities, and to perform detailed calculations of the vacuum components in the beam transport that may disrupt the longitudinal phase space and the bunch compression. Estimates based on the nine-cell TESLA structure have already been performed which indicate that the seven-cell structures will be acceptable, and resistive wall estimates have been made to determine the smallest undulator and FEL magnet apertures that may be tolerated. Other sections of the machine must be examined so that their effect is at least as small as these primary components, in particular:

- The long sections of accelerator transport between the Main Linac and the source points;
- The collimators which are required in the high energy regions of the accelerator;
- The aperture openings which are required for diagnostic instrumentation;
- The BPMs and striplines used for position and charge measurement

7.10.5 RF Structures and Beam Break-Up

Simulations performed so far have used the nine-cell cavity structure, for example in predicting the impact of longitudinal wakefields. A seven-cell cavity is presently being designed, and this will provide more realistic HOM and wakefield data that can be used in start-to-end simulations and for beam break-up studies. Beam break-up estimates have been performed that indicate it should be possible to achieve a threshold current greater than 100 mA, but a transport scheme to do this must be designed using seven-cell cavity data and a realistic HACL transport optics.

7.10.6 Beam Power and Beam Dumps

Whilst the 1 kW beam power carried by the XUV-FEL bunches is modest, the 1 MW incident at the HACL beam dump is challenging because of the rather low 10 MeV energy which makes it difficult to distribute the heat load. Engineering development of the 1 MW beam dump design will be required during the technical project phase. Cornell University are developing a prototype for a similar dump as part of the Cornell ERL project, and much can be learned from their design work [25].

The IR-FEL dump design has yet to be determined. Depending upon the duty cycle of the IR-FEL accelerator a power handling requirement up to ~156 kW may be needed (156 kW results from assuming a beam energy of 60 MeV and a bunch charge of 200 pC at 13 MHz repetition rate). Although lower than the HACL dump, the shielding and accelerator environment around the IR-FEL may need to be different to accommodate user beamlines and accelerator components. A study will be carried out to assess the best solution for the overall dump transport – in particular to determine whether independent dumps are needed for the A and B branches – and to assess whether a 13 MHz repetition rate is appropriate.

REFERENCES

[1] C.A.J. van der Geer et al., 'Performance of the Felix Accelerator', Proceedings of EPAC'92 (3rd European Particle Accelerator Conference), Berlin, Germany (1992). Available at http://www.jacow.org

REFERENCES, Continued

[2] S. Benson et al., *Nucl. Inst. Meth.* **A429**, 27-32 (1999), http://dx.doi.org/10.1016/S0168-9002(99)00061-3

[3] C. Gerth et al., 'Start-to-End Simulations of the Energy Recovery Linac Prototype FEL', Proceedings of FEL 2004 (26th International Free Electron Laser Conference), Trieste, Italy (2004). Available at http://www.jacow.org

[4] D. Douglas, 'Design considerations for recirculating and energy recovery linacs', JLAB-TN-00-027 (2000).

[5] C. Tennant et al, 'Suppression of multipass, multibunch breakup in two pass recirculating accelerators' Proceedings of FEL 2004 p590.

[6] T. Limberg, P. Piot and F. Stulle, 'Design and Performance Simulation of the TTF-FEL II Bunch Compression System', Proceedings of EPAC 2002 (8th European Particle Accelerator Conference), Paris, France (2002). Available at http://www.jacow.org

[7] 'SASE FEL at the TESLA Facility, Phase 2', TESLA-FEL 2002-01. Available at http://www-hasylab.desy.de/facility/fel/

[8] V. Ayvazyan et al., *Eur. Phys. J. D* **37(2)**, 297-303 (2006). Available at http://www.springerlink.com/openurl.asp?genre=article&id=doi:10.1140/epjd/e2005-00308-1

[9] 'Linac Coherent Light Source, Conceptual Design Report', SLAC-R-593 (UC-414), (2002). Available at http://www-ssrl.slac.stanford.edu/lcls/cdr/

[10] 'The BESSY Soft X-ray Free Electron Laser, Technical Design Report', (2004). Available at http://www.bessy.de/FEL

[11] P. Piot, D. Douglas and G. Krafft, Phys. Rev. S.T. Accel. Beams 6 (2003), p0030702.

[12] H. Owen, '1D Bunch Compression in the FEL Branch', 4GLS Internal Report fgls-desn-rpt-0002 (2005).

[13] A Novokhatski, M. Timm and T. Weiland, 'Single Bunch Energy Spread in the TESLA Cryomodule', TESLA Collaboration Report TESLA 99-16.

[14] R. Brinkmann et al., 'Terahertz Wakefields and Their Effect on the Superconducting Cavities in TESLA', Proceedings of EPAC 2000 (7th European Particle Accelerator Conference), Vienna, Austria (2000). Available at http://www.jacow.org.

REFERENCES, Continued

[15] S. Miginsky, 'An optimiser for high-current beamlines', proceedings of the 3rd Asian Particle Accelerator Conference, Gyeongju, Korea (2004). Available at http://www.jacow.org

[16] H. Owen and J. Clarke, 'Consideration of Beam Separation in 4GLS', 4GLS Internal Report fgls-upcdr-rpt-0003 (2005).

[17] H. Owen, 'CW Loop Arc and ID Arc Preliminary Designs', 4GLS Internal Report fgls-desn-rpt-0006 (2005).

[18] S. Miginsky, unpublished code.

[19] S. Appleton, private communication.

[20] The MLC code is available at https://projects.astec.ac.uk/Plone/Codes/optics/madinputmlc/ . It is documented in H.L.Owen, 'MLC – Mathematica Lattice Code, A Framework for Accelerator Calculations', Daresbury Laboratory Internal Report erlp-desn-rpt-0005.

[21] G. Guignard E. T. d'Amico, 'First-order design of a new type of isochronous arc', CERN SL/95-120 (AP), CLIC Note 292, 1995.

[22] G. Guignard E. T. d'Amico, 'Special lattice computation for the CERN Compact Linear Collider', *Phys. Rev. S. T. Accel. Beams,* **4**:021002 (2001).

[23] P. Piot, D. Douglas and G. Krafft, *Phys. Rev. S.T. Accel. Beams* **6**, 030702 (2003).

[24] R. Hajima et al., *Nucl. Inst. Meth.* **A445**, 384-388 (2000).

[25] Colin H. Smith, Yun He & Charles K. Sinclair, 'Design for a 1.3 MW, 13 MeV Beam Dump for an Energy Recovery Linac', LNS Report ERL 05-4, available at http://www.lns.cornell.edu/public/ERL/.

[26] D.R.Walz et al., 'Beam Dumps, Energy Slits and Collimators at SLAC – Their Final Versions and First Performance Data', SLAC-PUB-0279 (1967).

[27] W.A.Reupke and D.R.Walz, 'Operating Experience with High Power Beam Absorbers in the SLAC Beam Switchyard', SLAC-PUB-878 (1971).

[28] TESLA Design Report, available at http://tesla.desy.de/new_pages/TDR_CD/start.html

[29] See for instance design work reported in N.Tesch et al., 'Design Studies for an 18 MW Beam Dump at the future e+/e- Linear Collider TESLA', presentation at ICRS 10 / RPS 2004 (Madeira) 13th May 2004

REFERENCES, Continued

[30] C. Gerth, M. Röhrs and H. Schlarb (2005) 'Layout of the Diagnostic Section for the European XFEL'. Proceedings of PAC 2005 (21st Particle Accelerator Conference), Knoxville, Tennessee, USA (2005). Available at http://www.jacow.org.

[31] C. Gerth (2005), private communication.

[32] F. Löhl (2005) 'Measurements of the Transverse Emittance at the VUV-FEL'. Diploma Thesis, Hamburg, DESY-THESIS 2005-014 and TESLA-FEL 2005-03.

[33] K. Honkavaara and F. Löhl (2005) Private communication.

[34] T. Bizen, T. Tanaka, Y. Asano, D.E. Kim, J.S. Bak, H.S. Lee and H. Kitamura (2001) 'Demagnetization of undulator magnets irradiated by high energy electrons'. Nucl. Inst. Meth. A **467**, 185.

[35] H. Schlarb (2004) 'Design and Performance of the Tesla Test Facility (TTF) Collimation System'. *AIP Conf. Proc.* **693**, 209, and Proceedings of EPAC 2002 (8th European Particle Accelerator Conference), Paris, France (2002). Available at http://www.jacow.org

[36] T. Kamps, 'Collimation System for the BESSY FEL', proceedings of FEL 2004 (International Free Electron Laser Conference), Trieste, Italy (2004). Available at http://www.elettra.trieste.it/fel2004/

[37] C. Hernandez-Garcia et al, 'Longitudinal Space Charge Effects in the JLAB IR FEL SRF Linac', proceedings of FEL 2004 (International Free Electron Laser Conference), Trieste, Italy (2004). Available at http://www.elettra.trieste.it/fel2004/

[38] T. Shaftan and Z. Huang, *Phys. Rev. S.T. Accel. Beams* **7**, 080702 (2004)

[39] M Borland, DUVFEL Accelerator and FEL Physics Workshop, 2004

[40] This function is defined in the 'CRC Concise Encyclopaedia of Mathematics' (2nd Edition), ed. E. Weisstein, Chapman and Hall/CRC (2002), ISBN 1584883472. Also available at http://mathworld.wolfram.com/ModifiedBesselFunctionoftheSecondKind.html

[41] G. Stupakov et al., *Phys. Rev. S.T. Accel. Beams* **5**, 0504402 (2002)

[42] M. Borland, *Phys. Rev S.T. Accel. Beams* **4**, 070701(2001)

[43] E.L.Saldin et al., *Nucl. Inst. Meth.* **A398**, 373 (1997)

[44] ICFA Beam Dynamics Mini Workshop, 'Coherent Synchrotron Radiation and its impact on the dynamics of high brightness electron beams', DESY-Zeuthen (2002). Available at http://www.desy.de/csr/csr_workshop_2002/csr_workshop_2002_index.html

REFERENCES, Continued

[45] C. Gerth, M. Bowler, B. Muratori, H. Owen, N. Thompson, B. Faatz and B. McNeil, 'Start to end simulations of the ERL Prototype at Daresbury Laboratory', Proceedings of PAC 2005 (21st Particle Accelerator Conference), Knoxville, Tennessee, USA (2005). Available at http://www.jacow.org

[46] E. Pozdeyev, unpublished work.

[47] A. Hutton, private communication.

[48] G. Hoffstaetter and M. Liepe, 'Ion Clearing in an ERL', to be published in the proceedings of the 32nd Advanced ICFA Beam Dynamics Workshop on Energy Recovery Linacs, Thomas Jefferson National Accelerator Facility, Newport News, USA (2005), to appear in *Nucl. Inst. Meth*. **A**. http://conferences.jlab.org/ERL/2005/index.html.

[49] A. Chao, 'The Physics of Collective Beam Instabilities in High Energy Accelerators', John Wiley & Sons (1993)

[50] K. Bane, 'The Short Range Resistive Wall Wakefields' SLAC/AP-87 (1991)

[51] K. Bane and M. Sands, 'The Short Range Resistive Wall Wakefield', SLAC-PUB-95-7074 (1995)

[52] N. Ashcroft and N. Mermin, 'Solid State Physics', Thomson Learning (1976), ISBN 0030839939.

[53] G. Reuter amd E. Sondheimer "The Theory of the Anomalous Skin Effect" *Proc. Roy. Soc. Lond.* **A195**, 336 (1949).

[54] G. Stupakov et al., *Phys. Rev. S.T. Accel. Beams* **2**, 060701 (1999).

[55] G. Stupakov, 'BNS Damping of Beam Breakup Instability', SLAC-AP-108 (August 1997).

[56], T. Wangler, 'RF Linear Accelerators', John Wiley & Sons Inc (1998), ISBN 0471168149.

[57] H. Padamsee, J. Knobloch and T. Hays, 'RF Superconductivity for Accelerators', John Wiley & Sons Inc (1998), ISBN 0471154326.

[58] I. Bazarov, 'bi' code, available at http://www.lepp.cornell.edu/~ib38/

[59] ERLBBU code, available from E. Pozdeyev (private communication, pozdeyev@jlab.org).

[60] E. Pozdeyev et al., Nucl. Instrum. Methods A 557 (2006), p176-188.

REFERENCES, Continued

[61] S. Gruner et al., 'Study for a proposed Phase I Energy Recovery Linac (ERL) Synchrotron Light Source at Cornell University', CHESS Technical Memo 01-003 and JLAB-ACT-01-04 (2001).

[62] 'Annual Report 2001 of the Institute of Nuclear and Hadron Physics', Forschungszentrum Rossendorf, Report FZR-341 (April 2002), available at http://www.fz-rossendorf.de/publications/004862/contents.html

[63] A. Fedotov, 'Resonances and Beam Loss in High Intensity Rings', Proceedings of PAC'03 (Particle Accelerator Conference), Portland, Oregon, USA (2003), p. 383. Available at http://www.jacow.org

[64] A. Fedotov, 'Beam halo formation in high-intensity beams', to be published in the proceedings of the 32nd Advanced ICFA Beam Dynamics Workshop on Energy Recovery Linacs, Thomas Jefferson National Accelerator Facility, Newport News, USA (2005), to appear in *Nucl. Inst. Meth*. **A**. http://conferences.jlab.org/ERL/2005/index.html.

[65] For example, see proceedings of the 29th ICFA Advanced Beam Dynamics Workshop on Beam-Halo Dynamics, Diagnostics, and Collimation (Montauk, New York), 19-23 May 2003 available at: http://proceedings.aip.org/proceedings/confproceed/693.jsp]

[66] See for example, M. Shirakata et al., 'Estimations on the Beam Halo Collection at the High Intensity Accelerator', proceedings of EPAC 2000 (7th European Particle Accelerator Conference), Vienna, Austria (2000). Available at http://www.jacow.org/

[67] D. Nölle et al., 'The Diagnostics System of TTF II', Proceedings of EPAC 2002 (8th European Particle Accelerator Conference), Paris, France (2002). Available at http://www.jacow.org

[68] A. Kalinin, ATF FONT December 05 Run, presented at ATF Weekly Meeting 5th December 2005. Available at http://hepwww.ph.qmul.ac.uk/~gcrist/FONT/mtg-dec2005.htm.

[69] D. Nölle et al., 'The Diagnostic System of TTF II', Proceedings of EPAC 2002 (8th European Particle Accelerator Conference), Paris, France (2002). Available at http://www.jacow.org

[70[K.Honkavaara et al., 'Transverse Electron Beam Diagnostics at the VUV-FEL at DESY', Proceedings of the 27th Free Electron Laser Conference (FEL 2005), http://www-ssrl.slac.stanford.edu/lcls/fel2005/index.php

REFERENCES, Continued

[71] K. Honkavaara, 'Optical Ttransition Radiation in High Energy Electron Beam Diagnostics' Hip-1999-04, Helsinki Institute of Physics, P.O. Box 9, FIN-00014, University of Helsinki, 1999. ISBN 951-45-7975-5

[72] G. Krafft et al., 'Electron Beam Diagnostics for Jefferson Lab's High Power Free Electron Laser', proceedings of EPAC 98 (6th European Particle Accelerator Conference), Stockholm, Sweden (1998). Available at http://www.jacow.org/

[73] D. Douglas, 'A 75% Solution for the FEL Upgrade', TJNAF Report JLAB-TN-99-040 (1999).

[74] G. Krafft and J.-C. Denard, Proceedings of the 2002 Beam Instrumentation Workshop, AIP Conference Proceedings 648 (2002), p118.

[75] S. P. Jamison, private communication.

[76] G. Berden et al. Phys. Rev. Lett. 93 (2004), 114802

[77] E. L. Saldin, E. A. Schneidmiller and M. V. Yurkov, Nucl. Instrum. Methods A539(3) (2005), pp499-526. Also 'A Simple Method for the Determination of the Structure of Ultrashort Relativistic Electron Bunches', DESY Report 04-126.

[78] see for example S. Reiche et al., 'Start-to-end Simulation for the LCLS Xray-FEL', Proceedings of PAC 2001 (19th Particle Accelerator Conference), Chicago, Illinois, USA (2001). Available at http://www.jacow.org.

[79] B. Kuske, M. Abo-Bakr, K. Goldammer and A. Meseck, 'Start-to-End Simulations for the BESSY Low and Medium Energy FEL Line Including Errors', Proceedings of the 27th Free Electron Laser Conference (FEL 2005), http://www-ssrl.slac.stanford.edu/lcls/fel2005/index.php.

[80] B. Muratori et al., 'Space Charge Effects for the ERL Prototype Injector Line at Daresbury Laboratory', Proceedings of PAC 2005 (21st Particle Accelerator Conference), Knoxville, Tennessee, USA (2005). Available at http://www.jacow.org.

[81] see for example J.Carter et al., 'Beam Profile Measurements and Simulations of the PETRA Laser-Wire', Proceedings of PAC 2005 (21st Particle Accelerator Conference), Knoxville, Tennessee, USA (2005). Available at http://www.jacow.org.

[82] S. Malton, 'PETRA Laserwire Analysis', presentation at ILC European Regional Meeting and ILC-BDIR Workshop, Royal Holloway College, London, United Kingdom (20-23 June 2005). Available at http://www.pp.rhul.ac.uk/workshop/.

8. Free-Electron Lasers

Free-electron laser (FEL) sources which operate in the XUV, VUV and IR regions of the spectrum are fundamental components of the 4GLS design. These sources will deliver ultra-short pulses of temporally coherent photons with peak brightness at least 10^8 greater than that available from state-of-the-art 3rd generation light sources such as Diamond [1]. All of the FEL sources have been designed to produce near-transform-limited variably-polarised variable-length photon pulses with excellent pulse-to-pulse reproducibility.

This chapter first presents the FEL physics necessary for the later justification and clarification of the 4GLS design choices (section 8.1.2 onwards). Three distinct FEL gain regimes, which correspond to the three FELs of 4GLS are discussed. The high-gain regime for XUV-FEL operation is discussed in section 8.1.3, the intermediate-gain regime of the VUV-FEL is discussed in section 8.1.5, and IR-FEL operation in the low-gain regime is considered in section 8.1.6.

The XUV-FEL specification is given in detail in section 8.2. This FEL will operate over the photon energy range 8-100 eV and will be seeded at its fundamental resonant wavelength by an externally injected high-harmonic (HH) source. The technical specification and modelling presented in section 8.2 are based on the original proposed photon energy range of 10 - 100 eV. Consultation through the last year with user groups has identified a revised requirement to operate the XUV-FEL from 8 - 100 eV and this has been adopted as the baseline specification. It is strongly emphasised that the small revision to the photon energy range is easily achievable with only minor adjustments to the design given here, as demonstrated in section 8.2.9. The peak output power of the XUV-FEL will vary from 2 GW at 100 eV up to over 8 GW at 8 eV with typical FWHM pulse length < 50 fs. Section 8.2.2 presents the undulator specification to achieve variably polarised FEL operation over the photon energy range. Optimisation of the beam focussing and undulator lattice design shows that a FODO lattice with short undulator modules of length ~2 m gives the optimum design for FEL coupling while maintaining sufficient space for beam diagnostics. Section 8.2.3 shows that a step-tapered vacuum vessel allows optimum seed focussing across the photon energy range and also helps to mitigate electron beam quality degradation due to wakefields. Electron beam quality requirements are estimated in section 8.2.4. Recent high-harmonic generation results are surveyed and used to inform the specification of the HH seed source in section 8.2.5. The proposed seeding design allows continuous tuning across the photon energy range 8 - 100 eV. Seed lasers are shown to have more than sufficient power to overcome the intrinsic noise. Numerical simulations using the three-dimensional code Genesis 1.3 [30] in both steady-state (section 8.2.6) and time-dependent mode (section 8.2.7) have validated the design against the predictions of the standard theory. The simulations present an extensive investigation of the FEL output, optimisation of the HH seed injection (section 8.2.7.4) and the effects of timing jitter between the electron bunch and seeding pulse (section 8.2.8).

The design specification of the VUV-FEL is given in section 8.3. The VUV-FEL design is based on the regenerative amplifier FEL (RAFEL) concept which operates in the intermediate-gain regime. A hole-outcoupled low Q cavity that uses robust low reflectivity optics provides sufficient feedback to allow FEL saturation after only a few cavity round-trips. The RAFEL allows an undulator length of ~ 11 m which is approximately one-third the length required for a Self Amplified Spontaneous Emission (SASE) FEL. In its standard operating mode the VUV-FEL will generate temporally coherent photon beams over the range 3 - 10 eV with peak power ~ 500 MW and with FWHM pulse lengths of ~ 170 fs. Cavity length adjustment allows superradiant operation with enhanced peak powers of ~ 3 GW and FWHM pulse lengths of ~ 25 fs. The specification of the undulator parameters and undulator lattice are given in section 8.3.2, followed by a discussion of the electron beam quality requirements in section 8.3.3. Preliminary specification and modelling of the feedback cavity is discussed in section 8.3.4. Steady-state Genesis 1.3 simulations in three dimensions are presented in section 8.3.5.1. Time dependent simulations starting up from noise have been carried out with a one-dimensional code in section 8.3.5.2. A parallel implementation of Genesis 1.3 has also been used and is reported upon in section 8.3.5.3. These simulations predict the effects of cavity length detuning and demonstrate the short-pulse, high peak power superradiant pulse evolution for a near synchronous cavity. The simulations demonstrate that the RAFEL output pulses are temporally coherent and close to transform limited.

The specification and conceptual design of the IR-FEL is presented in section 8.4. This FEL operates in the low-gain regime and will produce temporally coherent photon pulses from 2.5 - 200 μm. The electron beam will be switched between two separate undulator branches, each with its own optical cavity, to allow coverage of the wide spectral range of the design specification. Branch-A will operate with wavelengths from 2.5 - 25 μm and Branch-B will overlap slightly, operating from 20 - 200 μm. The parameters of the undulators, electron beam and optical cavities are presented in section 8.4.2 to section 8.4.7. Design formulae are used in section 8.4.8 to optimise the IR-FEL performance and to predict the photon pulse output parameters. Extensive one-dimensional simulations are reported in section 8.4.9 which characterise the photon output for a range of electron bunch lengths and output wavelengths. In standard mode of operation the IR-FEL maximum peak output power is ~9 MW with FWHM pulse length ~ 2 ps. The results of simulations investigating cavity detuning are reported in section 8.4.9.1. As with the VUV-FEL, operation of the IR-FEL with a near-synchronous cavity generates superradiant pulse evolution with maximum peak output powers increased above the standard mode of operation up to ~ 20 MW and with FWHM pulse lengths reduced to ~ 300 fs.

8.1 Introduction

The conceptual designs of the Free-Electron Laser sources that give the 4GLS facility its' name are presented. The fundamental difference between 4th generation FEL sources and 3rd generation synchrotron sources, such as Diamond [1], is the temporal coherence of the FEL emission. This coherence increases the peak brightness of the FEL over 3rd generation sources by at least seven orders of magnitude as shown in Chapter 9.

4GLS is intended to be a state-of-the-art facility that must operate over extended periods, generating stable, synchronous and reproducible radiation pulses over a wide spectral range to end-user stations. In this conceptual design, therefore, the aim has been to create a robust design that does not overly push the specification of its individual components. This mildly cautious approach should minimise the risk in proceeding to the future design phase and enable further, more advanced, designs to be incorporated as technological progress permits.

8.1.1 Overview of 4GLS FEL Sources

Three different types of FEL source are included in the conceptual design phase of 4GLS to cover the photon energy (wavelength) ranges 8 - 100 eV (155 - 12.4 nm), 3 - 10 eV (413 - 124 nm) and 0.0062 - 0.5 eV (200 - 2.5 μm). These FEL sources are respectively: a high-gain FEL amplifier of an externally-injected seed source (XUV-FEL); an intermediate-gain FEL that utilises a low-Q cavity in a regenerative amplifier design (VUV-FEL); a lower-gain oscillator FEL (IR-FEL) that utilises two undulators to cover the broad spectral range. Design specification parameters for all these sources are given in Table 8.1:

Table 8.1 Summary of parameter and performance estimates for the FEL sources of 4GLS

	XUV-FEL	*VUV-FEL*	*IR-FEL*
	FEL DESCRIPTION		
FEL design	High Gain Amplifier	Regenerative Amplifier	Oscillator
Seeding type	External seeding	Self-seeding	Self-seeding
Seeding mechanism	HHG source	Low-Q cavity	High-Q cavity
	FEL PHOTON OUTPUT		
Tuning Range	8 - 100 eV	3 - 10 eV	2.5 - 200 μm
Repetition rate	1 kHz	n × 4⅓ MHz	13 MHz
Polarisation	Variable elliptical	Variable elliptical	Variable elliptical
Max Peak Power	8 GW	500 MW (3 GW*)	9 MW (>20 MW*)
Pulse length FWHM	< 50 fs	170 fs (25 fs*)	2 ps (300 fs*)
Typical $\Delta\nu\Delta t$	≈ 0.6	≈ 1.0	≈ 0.9
Max pulse energy	400 μJ	70 μJ	50 μJ
	ELECTRON BEAM PARAMETERS AT FEL		
Energy	750 - 950 MeV	600 MeV	25 - 60 MeV
Bunch Charge	1 nC	77 pC	200 pC
RMS bunch length	266 fs	100 fs	1 - 10 ps
Peak Current	1.5 kA	300 A	8 - 80 A
Normalised emittance	2 mm mrad	2 mm mrad	10 mm mrad
RMS energy spread	0.1 %	0.1 %	0.1 %
	UNDULATOR PARAMETERS		
Undulator Type	PPM & APPLE-II	APPLE-II	APPLE-II
No of Modules	8 & 5	5	1 & 1
Module length	2 m	2.2 m	2.65 m & 5.07 m
Period	45 mm & 51 mm	60 mm	53 mm & 145 mm
Focussing	FODO	FODO	Natural
Minimum magnetic gap	10 mm	10 mm	23.5 mm & 74 mm

* indicates possible output in superradiant mode

The conceptual design incorporates three distinct electron beams for driving the three types of FEL and a range of spontaneous sources. The XUV-FEL branch has energy 750 - 950 MeV and is designed to give the high peak currents (1.5 kA, 1 nC pulses at 1 kHz) necessary to drive the single pass high gain XUV-FEL. The High-Average Current Loop (HACL) has energy 600 MeV and supplies 77 pC electron pulses. The HACL operates in energy recovery mode at up to 1.3 GHz, driving both spontaneous undulator sources and the VUV-FEL. The latter operates with repetition-rates at integer multiples of 4.33 MHz. The third branch is a 25 - 60 MeV beam which drives an IR-FEL with repetition rate 13 MHz. These repetition rates allow synchronism between sources.

8.1.2 FEL Physics

Before giving further details of the three individual FEL sources of the conceptual 4GLS design a brief overview of the FEL physics is presented and the main physical parameters that affect the FEL performance are introduced.

Coherent emission by the electron beam in a FEL relies upon the self-consistent interaction between the electrons and radiation as the electron beam undulates through the static magnetic undulator field. The undulator and resonant electromagnetic fields form a ponderomotive potential which co-propagates at the mean electron velocity along the axis of the undulator. This potential bunches the relativistic electron beam to form a periodic density modulation at the resonant radiation wavelength. Emission from this density modulated electron beam is therefore coherent and may be many orders of magnitude greater than the emission from a similar, but unbunched, beam such as occurs in conventional synchrotron sources.

The FEL interaction between a pulse of electrons and a linearly-polarised radiation field in a planar undulator FEL is considered. In deriving the equations that describe the FEL interaction, approximations are made that initially allow the neglect of explicit three-dimensional effects such as electron beam emittance and radiation diffraction. These effects may be re-introduced into the reduced one-dimensional model by using further approximations (e.g. the beam emittance may be modelled using an effective energy spread). When three-dimensional effects are included in FEL models they generally tend to degrade the quality of the FEL interaction by reducing saturation powers and decreasing the radiation gain per unit length. This may be seen from the FEL analysis of Ming Xie [2] which is used later to estimate key design parameters at the first design optimisation stage. The one-dimensional FEL model is therefore the 'best-case' model for a given set of parameters. Any limiting factors derived from the analysis of the one-dimensional model must generally be satisfied in the three-dimensional model.

For an undulator of peak magnetic field strength B_u and period $\lambda_u = 2\pi/k_u$ the fundamental resonant radiation field has the same wavelength as that for spontaneous undulator radiation:

$$\lambda = \frac{\lambda_u}{2\gamma_r^2}\left(1+\overline{a}_u^2\right) \tag{8-1}$$

where $\overline{a}_u = eB_u^{RMS}/mck_u$ is the RMS undulator parameter and $\gamma_r mc^2$ is the mean resonant electron beam energy. Unless otherwise stated, the peak undulator magnetic field is assumed in this chapter to be that for a pure permanent magnet planar undulator, as given in Chapter 10. Odd harmonics of the radiation field are also resonant, but for the purposes of this introduction are not considered as the interaction at the fundamental is dominant.

The equations used to describe the FEL interaction have been well established in the literature and may be written in various scaled forms. The scaling used here is the 'universal scaling' of [3]. By universal scaling it is meant that a set of scaled equations governing the FEL interaction is derived which have no free parameters. For a given set of initial and boundary conditions

there is therefore only one solution to these equations and all information regarding real physical quantities are determined by the scaling. The field evolution is described by a scaled Maxwell wave equation and the electron trajectories, which determine the source current for the radiation field, are governed by a similarly scaled Lorentz force equation. For our purposes, the relativistic beams used mean that space-charge forces may be neglected. This is the Compton limit of electron/radiation scattering. In terms of the universally scaled variables, and with their extension to include pulse effects [4,5], the coupled Maxwell/Lorentz equations may be written:

$$\begin{aligned} \frac{d\theta_j}{d\bar{z}} &= p_j \\ \frac{dp_j}{d\bar{z}} &= -\left(A\left(\bar{z},\bar{z}_1\right)\exp\left(i\theta\right)+\text{c.c.}\right) \\ \left(\frac{\partial}{\partial\bar{z}}+\frac{\partial}{\partial\bar{z}_1}\right)A\left(\bar{z},\bar{z}_1\right) &= \chi\left(\bar{z}_1\right)b\left(\bar{z},\bar{z}_1\right) \end{aligned} \tag{8-2}$$

Here $\theta_j=\left(k+k_u\right)z-\omega t_j$ is the phase of the j^{th} electron with respect to the ponderomotive potential that causes electron bunching, $p_j=\left(\gamma_j-\gamma_r\right)\big/\rho\gamma_r$ are the scaled electron energies, $\chi\left(\bar{z}_1\right)=I\left(\bar{z}=0,\bar{z}_1\right)\big/I_{pk}$ is the electron beam current scaled with respect to its peak value at the entrance to the FEL interaction region, $b(\bar{z},\bar{z}_1)=1\big/N\sum_{j=1}^{N}\exp\left(-i\theta_j\left(\bar{z}\right)\right)$ is the bunching parameter evaluated from the N electrons contained within one ponderomotive potential (of interval of $4\pi\rho$) centred at $\bar{z}_1$, and $A\left(\bar{z},\bar{z}_1\right)$ is the scaled complex radiation field envelope with magnitude defined by:

$$\left|A\right|^2=\frac{1}{\rho}\frac{P_{\text{rad}}}{P_{\text{beam}}} \tag{8-3}$$

where P_{rad} and P_{beam} are the radiation and electron beam powers respectively (hence $\rho\left|A\right|^2$ gives the efficiency of the FEL interaction). The scaled independent variables are [4]:

$$\bar{z}=\frac{z}{l_g} \quad \text{and} \quad \bar{z}_1=\frac{z-c\bar{\beta}_z t}{l_g\left(1-\bar{\beta}_z\right)}$$

where $l_g=\lambda_u\big/4\pi\rho$ will be identified as a nominal gain length of the FEL interaction, the initial z-component of the mean electron velocity within the interaction region is $c\bar{\beta}_z=\left\langle v_{z0}\right\rangle$ and ρ is the fundamental FEL, or Pierce, parameter [3] defined as:

$$\rho=\frac{1}{\gamma_r}\left(\frac{\bar{a}_u\omega_p f_B}{4ck_u}\right)^{\frac{2}{3}} \tag{8-4}$$

The plasma frequency, $\omega_p=\sqrt{e^2n_{pk}\big/\varepsilon_0 m}$, is for the peak electron number density of the electron pulse, n_{pk}, and the factor $f_B=J_0\left(\xi\right)-J_1\left(\xi\right)$, where $\xi=\bar{a}_u^2\big/2\left(1+\bar{a}_u^2\right)$ is the difference of Bessel function factor familiar to planar undulator FEL theory [17]. The parameter

ρ determines the strength of the FEL interaction in the one-dimensional limit with stronger coupling between electrons and radiation occurring for larger values of ρ. Typical values of ρ for functioning FELs are in the range $10^{-4} \lesssim \rho \lesssim 10^{-1}$.

In the steady state limit an infinitely long electron pulse of uniform current is assumed so that $\chi(\bar{z}_1) = 1$ and the scaled time derivative of the field $\partial A / \partial \bar{z}_1 = 0$. The set of equations (8-2) then simplifies to a set of coupled ordinary differential equations.

The scaling and equations above can be used to describe the principles of operation of the FEL and the main operating regimes. These regimes may be defined by the scaled interaction length $\bar{z}$ [3]:

- High gain regime: $\bar{z} >> 1$ - Here the FEL interaction is a collective, exponential instability and may saturate in a single pass through the undulator. This method of FEL lasing is required where no suitable cavity mirrors exist and is the principal route to lasing in the XUV and beyond. These high gain amplifier FELs may start up from an intrinsic noise signal (in the SASE case) or an externally injected signal. The latter is the chosen design option for the 4GLS XUV-FEL.

- Intermediate gain regime: $1 \lesssim \bar{z} \lesssim 10$ - Where the FEL experiences exponential instability but does not achieve saturation in a single pass through the undulator. A small amount of feedback via a low-Q cavity allows the FEL to saturate in a few cavity round trips [6]. This principle is known as a Regenerative Amplifier FEL [7,8] and is the chosen design option for the 4GLS FEL operating in the VUV region of the spectrum.

- Low-gain regime: $\bar{z} \lesssim 1$ - In this regime there is no exponential FEL instability and radiation growth is due to an interference-type Madey gain [17] requiring a relatively high-Q cavity to achieve saturated FEL output. These oscillator FELs are able to cover a wide range of the spectrum where good cavity mirrors exist, generally between the IR and the UV. This type of FEL is the design choice for the IR-FEL of 4GLS.

8.1.3 SASE and Amplifier FELs in the High Gain Regime ($\bar{z} >> 1$)

The above equations and definitions constitute the one-dimensional universally scaled Compton limit FEL equations. For a 'cold' electron beam p_{j0}=δ, a constant, where subscript 0 indicates the initial conditions of parameters on entering the undulator at $\bar{z} = 0$. Linear stability analysis of these equations [3] shows that for electrons uniformly distributed in θ the initial bunching $b_0 = 0$, and for $|A_0| = 0$ the system is stable, i.e. neither field nor electrons depart from their initial conditions. Any small deviation from these conditions however, in either the field or the uniformity of the electron distribution, and the system will be exponentially unstable for $\delta < \delta_{th} \approx 1.89$ - both field amplitude A and the electron bunching parameter b exhibit exponential growth for $z > l_g$. This is the high gain FEL amplifier operation.

8.1.3.1 Performance Estimates from Scaled Solutions

For a cold, resonant beam with no initial electron bunching $\delta = 0$ and $b_0 = 0$, then for a small initial radiation power of $P_{rad}(0)$, the radiation power grows exponentially as

$$P_{rad}(\bar{z}) = \frac{P_{rad}(0)}{9} \exp\left(\sqrt{3}\frac{z}{l_g}\right) \tag{8-5}$$

The parameter $L_g = l_g/\sqrt{3}$ therefore defines the e-fold gain length of the FEL instability. Following the exponential growth of the linear regime the system saturates at some value of $\bar{z} = \bar{z}_{sat}$ for a value of $|A| \approx 1$. Hence, from the definition of $|A|^2$ in equation (8-3), it is seen that the radiation power at saturation is $P_{sat} \approx \rho P_{beam}$.

An estimate for the undulator length required to achieve saturation may be obtained from the results of [2] and is given by:

$$L_{sat} = L_g \ln\left(9\frac{P_{sat}}{P_{rad}(0)}\right) \tag{8-6}$$

For radiation wavelengths where there are no external sources $P_{rad}(0) = 0$, and the only source is the inherent noise in the distribution of the electrons so that $b_0 \neq 0$. This *shot noise* is the source of spontaneous radiation. For any practical beam such noise always exists and so the system is inherently unstable. When an FEL amplifier starts from the electron shot-noise it operates in the SASE regime [3].

The equivalent spontaneous radiation power arising from shot noise may be calculated [9] and written in the form:

$$P_{rad}(0) = \frac{6\sqrt{\pi}}{N_\lambda \sqrt{\ln(N_\lambda/\rho)}} \rho^2 P_{beam} \tag{8-7}$$

where N_λ are the number of electrons in an optical period.

An energy spread in the electron beam may be modelled by a distribution of the scaled energy parameter $p_j = (\gamma_j - \gamma_r)/\rho\gamma_r$, where γ_r is the resonant electron energy for the radiation field. Linear analysis shows that for there to be exponential gain the RMS energy spread of the electron beam $\sigma_\gamma \lesssim \rho$. The effects of electron beam emittance may be modelled in a similar way by introducing an effective spread in the resonant energies γ_r of the electrons [10].

The natural linewidth of the FEL radiation emission is given by [3]:

$$\left.\frac{\Delta\lambda}{\lambda}\right|_{HWHM} \approx 2\rho. \tag{8-8}$$

8.1.3.2 Electron Beam Transport and Emittance Effects

From the above analysis it is seen that the FEL parameter ρ is required to estimate the growth rate, saturation length, equivalent input power and saturation power. However, ρ has so far only been defined via the electron beam density n_{pk}. Given the beam current it is therefore necessary to determine the transverse structure of the beam to calculate n_{pk} before estimates of more useful parameters can be obtained.

The radius of an electron beam envelope matched to a linear transverse focussing channel is determined by the normalised emittance of the beam ε_n, and the strength of the focussing channel via the relation:

$$r_b = \sqrt{\frac{\varepsilon_n \beta}{\gamma}} \tag{8-9}$$

where β is the β-function for the focussing channel. For a transverse gaussian distribution of charge this radius is the RMS value. A beam matched to a constant strength focussing channel maintains a constant radius as it propagates. If the beam is not matched and/or the focussing channel is not of constant strength, then the electron beam envelope oscillates as it propagates through the channel.

For natural undulator focussing (i.e. in the absence of any strong external focusing system, such as a FODO quadrupole lattice described below), the β -function is given by [11]

$$\beta = \frac{f\gamma}{\overline{a}_u k_u} \tag{8-10}$$

where the focussing parameter $f = 1$ for a helical undulator in both the x and y directions of the transverse plane. For a planar undulator with flat pole faces $f = 1$ in the plane of the undulator field, and for a planar undulator with curved or canted pole faces $f = \sqrt{2}$ typically in both the x and y directions of the transverse plane.

When strong external focusing is applied, such as that provided by a FODO structure, then the average β-function may be decreased further and the matched beam radius (8-9) decreases accordingly. For a FODO lattice the periodic spacing between quadrupoles means that a constant strength focusing channel cannot be achieved and the β -function oscillates between the values

$$\beta = \frac{2\gamma m_e c}{e L_Q B_Q} \pm \frac{\lambda_{FODO}}{2} \tag{8-11}$$

where L_Q [m] and B_Q [T] are the quadrupole lengths and strengths respectively, and λ_{FODO} is the FODO lattice period [12]. The mean value of the β-function is then given by the first term in (8-11).

Numerical studies indicate [11] that the FEL gain length, L_g, is optimised for a matched beam and this matching is assumed henceforth.

Use of the expression for the electron beam radius for the case of a gaussian transverse charge distribution now allows the ρ parameter to be expressed in more useful units as:

$$\rho = \left(\frac{e}{32\pi\varepsilon_0 mc^3} \frac{I_{pk}\overline{a}_u^2 f_B^2}{\gamma_r^2 k_u^2 \varepsilon_n \beta} \right)^{\frac{1}{3}} \tag{8-12}$$

where I_{pk} is the peak electron beam current.

It may initially appear beneficial to maximise ρ by increasing the strength of the focusing channel, thereby decreasing the β-function. In doing so it is seen that the one-dimensional gain length $L_g \propto \rho^{-1}$ decreases. However, the transverse dimensional effects of radiation diffraction and betatron motion of the electron beam have not been properly accounted for in the one-dimensional model and may introduce deleterious effects on the gain. If the electron beam is focussed too strongly then the matched beam radius r_b may be so small that radiation diffracts too quickly out of the electron beam and no significant radiation gain can take place. Also, if the betatron motion of the beam occurs on a scale less than the gain length then the growth of the beam bunching at the radiation wavelength is washed out by the electron betatron motion [11]. If however, diffraction and betatron motion occur on a length scale that is greater than the gain length, then the three-dimensional effects will not catastrophically affect the gain process, and the one-dimensional model will remain a valid approximation. Clearly a balance must be struck between increasing the one-dimensional interaction strength parameter ρ, by increased beam focusing, and reducing the effects of diffraction and betatron motion by reducing the focusing. This is an optimisation problem that has to date been carried out using three-dimensional analysis and numerical codes.

In summary, the effects of diffraction and betatron motion may be neglected when:

- $L_g \lesssim l_{ZR}$ - the gain length must be less than the Rayleigh range, $l_{ZR} = 4\pi r_b^2 / \lambda$;
- $L_g < \beta$ - the gain length must be less than the β-function.

The first relation for diffraction effects is similar to that derived from three-dimensional theory [13] where diffraction effects may be neglected for $B > 1$ where $B = (2l_{ZR}/l_g)^{2/3}$ is the diffraction parameter.

The ability to steer the electron beam through the undulator/focussing system is also of critical importance. In order to have a sustained FEL interaction in the undulator the radiation and electron beam must maintain a close transverse overlap. Whereas the radiation propagates in a straight line along the central axis of the undulator, the same is not true of the electron beam. Errors in both the alignment and field strengths of the magnetic focussing lattice and the

undulator mean that the electron beam will wander in and out of the co-propagating radiation field. If the RMS wander of the electron beam, δ_r, approaches the radiation beam transverse radius then the gain will be significantly reduced as the radiation and electrons will effectively decouple. Given that electron beam radii for SASE FELs designed to operate in the XUV are of the order of a few tens of microns and the radiation beam can be expected to be of similar size, state-of-the-art technology is required to maintain the transverse beam positioning to this order over tens of metres of propagation. To date the only way to effectively model these effects on the FEL interaction are via three-dimensional numerical codes which introduce the focusing/undulator errors as a random variation about some mean value.

From the above it is seen that the emittance affects the matched beam radius (8-9) and the interaction coupling via the one-dimensional FEL parameter ρ (8-12). Another effect of the emittance is to introduce an energy spread in the resonant energies of the beam electrons of RMS width [10]:

$$\sigma_\varepsilon = \frac{\varepsilon_n \overline{a}_u^2 k_u^2 \beta}{2\gamma_r \left(1+\overline{a}_u^2\right)} \tag{8-13}$$

8.1.3.3 Summary of Criteria for Optimum FEL Performance

The one-dimensional theory describes the best-case limit for FEL operation. The following summarises the limits required for the one-dimensional equations to be a valid approximation for a high gain FEL interaction that achieves saturation:

- $L_u \gg L_g$ - The undulator is significantly longer than the interaction gain length
- $L_g \lesssim l_{ZR}$ - The gain length is less than the Rayleigh range
- $L_g < \beta$ - The gain length is less than the betatron function
- $\delta_r \ll r_b$ - Electron beam wander off-axis is much less than the beam radius
- $r_b \approx$ constant - The electron beam radius is approximately a constant
- $\sigma_\gamma \lesssim \rho$ - Homogeneous relative energy spread is less than the FEL coupling parameter
- $\sigma_\varepsilon \lesssim \rho$ - Resonant relative energy spread due to emittance is less than the FEL coupling parameter

8.1.4 Design Estimates

While the one-dimensional formalism discussed above provides useful insight into the general principles of the operation of FELs, it is not best suited to providing more accurate estimates of important design quantities such as the gain and saturation lengths for high gain amplifier FELs.

Neither does it allow optimal cavity design or describe transverse modes in low gain oscillator-based FELs. Design formulae have been developed specifically for high gain FEL amplifiers that operate at higher photon energies [2] and also for FEL oscillators [16]. These formulae provide good estimates of the important design parameters and are utilised in the subsequent work to explore the available parameter space and to optimise, where possible, design parameter specification. The estimates provided by these formulae are then used as a basis for more detailed numerical simulation.

8.1.5 Regenerative Amplifier FEL in the Intermediate Gain Regime ($1 \lesssim \bar{z} \lesssim 10$)

For FELs with scaled undulator lengths $\bar{z} > 1$, the interaction between radiation and electrons is similar to the high gain interaction described in section 8.1.3. However, the undulator is of insufficient length to achieve saturation in SASE mode, i.e. starting from noise, and where no seed lasers are available to shorten the length required to achieve saturation. In a Regenerative Amplifier FEL a small fraction of the radiation emitted by an electron pulse at the end of the undulator is fed back to the beginning of the undulator to act as a seed field to a subsequent electron pulse [6,7,8]. The radiation feedback may readily be achieved by placing the undulator into a low-Q cavity. This self-seeding process rapidly builds up and allows the RAFEL to achieve saturation after only a few electron pulses have propagated through the undulator. Furthermore, the temporal coherence of the radiation may also improve greatly over that of SASE and the stability of FEL output with respect to mirror degradation is good [14]. The undulator length is also reduced significantly compared to a SASE FEL and the small number of passes required to reach saturation may also relax the mechanical alignment tolerances [8]. The duration of the pulse output may also be varied by detuning the cavity round-trip time from the electron pulse repetition-rate. Such detuning may also allow higher peak radiation powers via superradiant emission processes [15].

Assuming a mirror reflectivity of *R* and a fractional outcoupling through the mirror hole of α the fraction of the radiation power fed back via the cavity to the beginning of the undulator will be $F = (1-\alpha)R^2$. The total cavity losses are therefore $1-F$. For a sufficiently long FEL interaction the intra-cavity saturation power actually *increases* for larger total cavity losses. This can be seen from the results of one-dimensional steady-state simulations for a scaled undulator length $\bar{z} = 4$ shown in Figure 8.1. The modulus of the intracavity saturated scaled radiation field $|A_{cav}|$ (i.e. after many cavity round trips) are plotted against the total cavity losses. The radiation feedback was modelled by reducing the power of the output radiation pulse by the feedback factor *F* and using this power for the input radiation seed. It is seen that the intracavity intensity increases as the total cavity losses increase from 60 % and peaks for a loss of $\approx 97\%$.

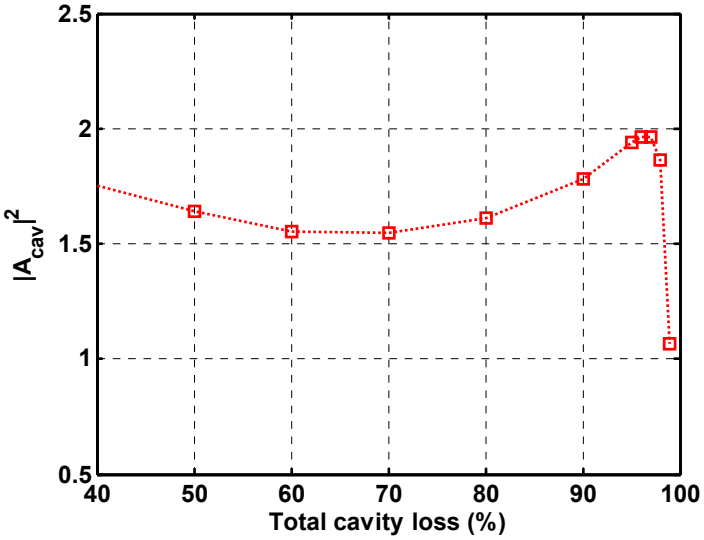

Figure 8.1 The intracavity scaled saturation power as a function of total cavity losses for RAFEL operation with scaled undulator length $\bar{z} = 4$

Figure 8.2 plots the maximum scaled output power (i.e. the maximum obtained in a scan over the outcoupling fraction α) as a function of scaled undulator length $\bar{z}$, for a range of mirror reflectivities. It is seen that for larger values of $\bar{z} \gtrsim 4$, the output power is relatively insensitive to the mirror reflectivity R, the power using 60 % reflectivity mirrors being only 5 % lower than that using 95 % reflectivity mirrors. For lower values of $\bar{z} \lesssim 3$ the FEL interaction leaves the high-gain exponential regime and enters the low-gain regime (see section 1.1.6) where higher Q cavities are required.

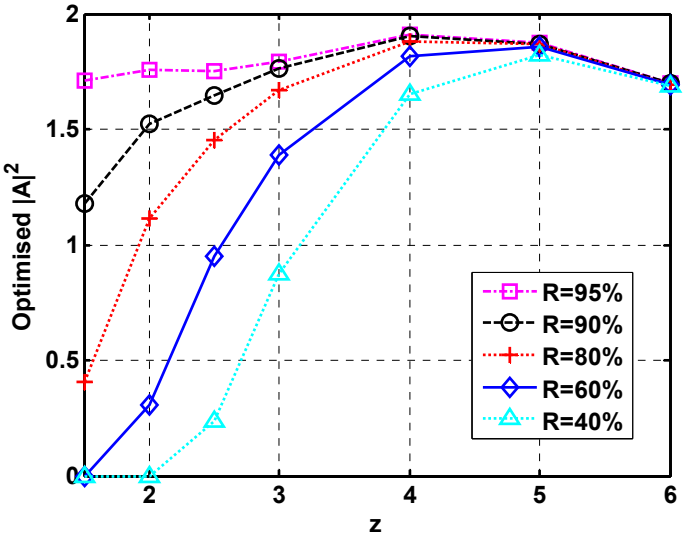

Figure 8.2 Scaled maximum output power as a function of scaled undulator length $\bar{z}$. *The output power is maximised by scanning over the outcoupling fraction* α.

In Figure 8.3 a scaled undulator length $\bar{z} = 4$ is assumed and the saturated scaled output power P_{out} is plotted as a function of the fractional hole outcoupling α for several mirror reflectivities. For mirror reflectivity of 60 % the optimised outcoupling fraction $\alpha \approx 92\%$. However, a small increase in α above this value is seen to provide insufficient feedback to allow lasing. A lower outcoupling of for example 75 %, would be preferred as although output power would be slightly lower, minor fluctuations would be less critical and allow greater stability. For outcoupling fractions in the approximate range $0.4 \lesssim \alpha \lesssim 0.85$ it is seen that the output power increases as mirror reflectivity is reduced, adding to the RAFEL stability: relatively large mirror degradation is seen to actually enhance the RAFEL performance.

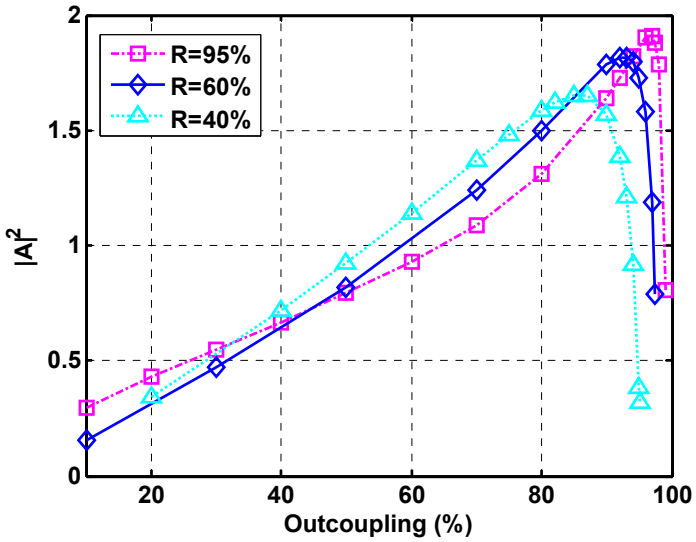

Figure 8.3 Scaled output power as a function of percentage outcoupling, α, for a scaled undulator length $\bar{z} = 4$, and for a range of mirror reflectivities

The above discussion relates to the steady-state only and does not include any pulse effects which yield further beneficial properties of the RAFEL. When an FEL operates in a cavity, and with electron pulses, the superradiant regime of electron pulse/radiation evolution may occur [15]. This regime is characterised by a simultaneous shortening of the radiation pulse length and an increase in peak power. Because the superradiant regime only occurs close to cavity resonance (when the round-trip time of light in the cavity is equal to an integer multiple of the duration between electron pulses), the radiation pulse properties may be controlled by altering the cavity length. This is called 'cavity detuning'.

8.1.6 High-Q cavity FEL in the Low-Gain Regime ($\bar{z} \lesssim 1$)

In this regime the exponential instability does not exist and a high-Q cavity is required to enable the FEL power to saturate. The single pass gain in such a system is low. This means the number of passes required to reach saturation (where a pass is the co-propagation of an electron bunch

with an optical pulse) is typically in the hundreds, over which time the radiation pulse is stored within the cavity and amplified pass by pass. As the intensity in the cavity increases so does the cavity power loss (due to absorption, diffraction and outcoupling) which is in direct proportion to the cavity intensity. Saturation is reached when the cavity power loss is equal to the power extracted from the electron bunch. Because the outcoupling fraction is low, typically about a fifth of the small signal gain, the intracavity intensity is very high compared to the output intensity.

The design of a high-Q cavity FEL is a multi-dimensional optimisation problem which involves many iterations to determine a satisfactory solution. The general approach taken can be summarised as follows:

- **Determination of fundamental parameters to maximise FEL coupling.** This involves assessment of suitable undulator types and parameters to cover the required tuning range with a sufficiently high undulator parameter $\overline{a}_u$ in parallel with determination of required electron beam parameters.

- **Assessment of beam quality and transverse overlap to minimise gain degradation.** This involves study of beam emittance and energy spread effects as well as the effect of the transverse overlap between the electron beam and optical mode.

- **Optical cavity design.** The aim is to give the required transverse overlap while minimising cavity loss and providing adequate stability.

These steps are iterated until a satisfactory design that meets all the output requirements is determined. This design is then validated and further characterised using simulations. In the following sections the methods used for each stage are outlined.

8.1.6.1 Determination of Fundamental FEL Parameters

The strength of coupling between the electron beam and optical field is most conveniently parameterised by the small signal gain coefficient g_0 [16] which is related to the gain length l_g of section 1.1.2 by:

$$g_0 = \frac{1}{\pi}\left(\frac{L_u}{l_g}\right)^3 \tag{8-14}$$

where L_u is the undulator length. An explicit expression for g_0, applicable for a planar undulator, is given by:

$$g_0 = \frac{16\pi\lambda L_u N_u^2 \xi f_B^2 J_e}{I_A \gamma}. \tag{8-15}$$

Here $J_e = I_{pk} \big/ 2\pi r_b^2$ is the electron beam current density and $I_A = 17$ kA is the Alfven current. The Bessel function factor f_B is omitted for helical undulators.

The threshold condition for FEL lasing is that the single pass gain must exceed the cavity loss. The philosophy is to optimise the strength of fundamental FEL coupling by choosing parameters to maximise the small signal gain parameter. This implies that:

- the undulator must have a certain minimum length ($g_0 \propto L_u N_u^2$);
- the electron beam must be suitably focussed to provide sufficient current density ($g_0 \propto J_e$);
- the on-axis field strength of the undulator must be sufficiently strong to give adequate coupling between electrons and the co-propagating optical field ($g_0 \propto \xi$) .

Once these fundamental parameters are determined the beam quality and transverse optical mode profile are considered.

8.1.6.2 Electron Beam Quality and Transverse Overlap

It is well known from the Madey Theorem [17] that the small signal gain is proportional to the negative derivative of the spontaneous emission spectrum. It thus follows that any effect causing an inhomgeneous broadening of the natural linewidth causes a reduction in the FEL gain. From this simple argument the beam quality criteria can be derived. Typically the normalised emittance should satisfy [17]:

$$\varepsilon_n < \frac{\gamma \lambda_r}{2\pi} \tag{8-16}$$

to avoid gain degradation due to inhomogeneous broadening of the natural linewidth. The relative energy spread in the beam should satisfy [17]:

$$\sigma_\gamma^{FWHM} < \frac{1}{4N_u} \tag{8-17}$$

The maximum single pass gain $G_{\max}$ is determined for the 4GLS IR-FEL designs by applying corrections to the small signal gain parameter which quantify gain reduction effects caused by beam emittance, energy spread and the transverse overlap between the beam and optical mode. The result for the maximum gain is then given by:

$$G_{\max} = 0.85\left(g_0 \kappa F_f\right) + 0.19\left(g_0 \kappa F_f\right)^2 + 4.12 \times 10^{-3}\left(g_0 \kappa F_f\right)^3 \tag{8-18}$$

The coefficient $\kappa = F_{inh} F_c$, where F_{inh} is an inhomogeneous broadening factor accounting for the gain reduction due to beam energy spread and emittance and F_c is a longitudinal mode coupling

factor accounting for the gain reduction due to the relative slippage between electron and radiation pulses.

The inhomogeneous broadening factor F_{inh} is given by:

$$F_{inh} = \frac{1}{1+1.7\mu_e^2} \cdot \frac{1}{1+\mu_y^2} \tag{8-19}$$

where $\mu_e = 4N_u(\sigma_\gamma / \gamma)$ is proportional to the relative RMS beam energy spread and for a planar undulator μ_y depends on the normalised emittance $\varepsilon_{n,y}$ along the vertical axis:

$$\mu_y = \frac{N_u \varepsilon_{n,y}}{\lambda_u} \frac{2\overline{a}_u}{1+\overline{a}_u^2} \tag{8-20}$$

A filling factor F_f [18], is used to account for the transverse overlap between electron beam and optical mode:

$$F_f = \frac{1}{1+\overline{w}^2/4r_b^2} \tag{8-21}$$

where $\overline{w}$ is the mean optical mode size, defined by the radius at which the intensity drops to $1/e^2$ of its on-axis value, averaged along the length of the undulator, and r_b is the RMS electron beam radius. It is interesting to note that from the definitions of g_0 and the filling factor F_f the product $g_0 F_f$, which is to first order proportional to the maximum gain $G_{\max}$, can be expressed as

$$g_0 F_f \propto \frac{1}{r_b^2} \frac{1}{\left(1+\overline{w}_2/4r_b^2\right)} = \frac{1}{r_b^2 + \overline{w}_2/4}. \tag{8-22}$$

This means that if the electron beam radius is much smaller than the optical mode size, as for example in a long wavelength FEL, then the gain is independent of the electron beam radius.

The method of gain calculation presented here has been checked for a wide range of parameter values against the values derived numerically from one-dimensional simulation codes and three-dimensional simulation codes such as Genesis 1.3 [30]. The calculated and numerical values are in very good agreement.

8.1.6.3 Optical Cavity Design

The choice of parameters for the high-Q optical cavity is crucial to FEL performance. It is necessary to optimise the strength of coupling between electron bunch and FEL pulse and also to allow a stable optical mode to be amplified over many passes without the cavity being oversensitive to mirror misalignment or distortion. Unfortunately, as will be seen, it is not possible to fully optimise performance and stability simultaneously: a level of compromise is required.

The optical resonator [19] consists of two spherical mirrors, radii of curvature (ROC) r_1 and r_2, separated by a distance L_{cav}. The optical mode within the cavity is not a plane wave, but has a curved front except at the waist where the wave-front is planar. At the mirrors the radius of curvature of the wave-front matches the mirror surface. The fundamental TEM_{00} mode has a Gaussian transverse intensity profile.

The cavity length L_{cav}, must ensure that the optical pulses in the cavity overlap with the electron pulses at the undulator entrance and is given by

$$L_{cav} = \frac{nc}{2f} \tag{8-23}$$

where n is an integer and f is the electron pulse repetition frequency. For a symmetrical cavity $r_1 = r_2 = r$ and the mode size at the waist is given by:

$$w_0^2 = \frac{\lambda}{2\pi}\sqrt{L_{cav}(2r - L_{cav})} \tag{8-24}$$

The mode size at a distance z from the waist is given by:

$$w^2(z) = w_0^2\left(1 + \left(\frac{\lambda z}{\pi w_0^2}\right)^2\right) \tag{8-25}$$

and the Rayleigh length, is given by:

$$l_{ZR} = \frac{\pi w_0^2}{\lambda} \tag{8-26}$$

This, substituting from equation (8-24), gives:

$$l_{ZR} = \frac{1}{2}\sqrt{L_{cav}(2r - L_{cav})} \tag{8-27}$$

So, for a given wavelength and cavity length, the ROC defines both the Rayleigh length and the mode profile along the whole resonator. However, only certain combinations of cavity length and ROC are stable. The wavefront propagation can be treated mathematically using element by element transfer matrices. For stability (i.e. the existence of a stable periodic solution) the condition:

$$\left|Trace(M)\right| < 2 \tag{8-28}$$

must be satisfied, where M is the round trip transfer matrix. This leads to the resonator stability condition for a symmetric cavity:

$$0 < g^2 < 1 \tag{8-29}$$

where $g = 1 - L_{cav}/r$.

The FEL gain scales with the filling factor F_f which depends on the ratio of the electron beam transverse area to the optical mode transverse area. The FEL interaction does not occur at a single point but along the whole length of the undulator so the filling factor is averaged along the undulator length. If the Rayleigh length is too short then, although the waist size is small, the diffraction of the optical beam is very strong and the filling factor is small. If the Rayleigh length is too long then although diffraction is minimised the average optical beam size is large, again giving a small filling factor. The averaged filling factor is maximised if the Rayleigh length is approximately one quarter of the undulator length [20]:

$$l_{ZR}^{(opt)} \approx L_u / 4 \tag{8-30}$$

This yields an optimum resonator configuration for maximum gain. However, the cavity length for an FEL is typically long, being defined by the electron bunch frequency and by the space required for dipoles and quadrupoles within the cavity. This means that the small Rayleigh length for optimum gain must be achieved simultaneously with a long cavity length. From (8-27) it is seen that this condition can only be satisfied if $2r \approx L_{cav}$ giving $g = 1 - L_{cav}/r \approx -1$ so that $g^2 \approx 1$ and the cavity is close to the boundary of stability. Thus the design of an FEL optical resonator involves a compromise between performance and stability. Typically [21] FEL cavities are designed so that the stability parameter $g^2 \leq 0.95$ giving a near-optimal filling factor while not pushing the cavity too close to an unstable configuration.

The angular alignment tolerances for the cavity mirrors depend on how close the cavity is to instability. For a symmetric cavity it can be shown [22] that the angular alignment tolerance should satisfy:

$$\theta_m \ll \sqrt{2\lambda/\pi L_{cav}}\,(1-g)^{1/4}\,(1+g)^{3/4} \tag{8-31}$$

Alignment tolerances are therefore more stringent for shorter wavelengths, longer cavities or cavities approaching the edge of the region of stability.

The cavity loss is estimated from the mirror reflectivity, by calculating the diffraction loss at the mirrors and the truncation loss suffered by a transverse gaussian mode as it passes through two ideal rectangular apertures, representing the vacuum vessel, positioned at either end of the undulator. In the cavity the optical fields at opposing mirrors can be represented by a pair of coupled integral equations [19]. Except for certain cases, no analytical solution is generally available, so the calculation of diffraction loss is found by numerical methods. Reference [19] presents graphs of numerical solutions that enable diffraction loss in symmetric cavities to be estimated for TEM_{00} and TEM_{01} modes and for discrete values of the stability parameter g, as a function of the Fresnel number $N_F = a^2/\lambda_r L_{cav}$, where a is the mirror aperture radius. A

MATLAB program has been written [23] that solves the integral equations numerically. This has been used and the results found to agree well with the graphical solutions in [19].

The TEM_{00} power transmission through a wide rectangular aperture of height a is given by [24]:

$$P_{trans} = erf\left(\frac{a}{w\sqrt{2}}\right) \tag{8-32}$$

The power transmission factor denoting mirror diffraction loss is notated D_m. The power transmission factors describing losses into and out of the undulator aperture are notated T_{in} and T_{out}. The total round trip power transmission is then given by:

$$P_T = (R \cdot T_{out} \cdot T_{in} \cdot D_m)^2 \tag{8-33}$$

where R is the mirror reflectivity and the total round trip passive loss, i.e. excluding outcoupling, is calculated as:

$$\Lambda = 1 - P_T \tag{8-34}$$

8.1.6.4 Output Power

When pulse effects may be neglected, the optimal efficiency for conversion of electron beam power into output radiation power is well known to be given by:

$$\eta_{\text{opt}} = \frac{1}{4N_u}. \tag{8-35}$$

In the case where i) the cavity losses are very low, ii) the output coupling is adjusted to its appropriate optimum value and iii) the outcoupling efficiency is high, this efficiency has been achieved experimentally. To account for the loss of output power due to cavity losses, and neglecting the efficiency of the outcoupling method, a generic efficiency is used in this report:

$$\eta = \frac{1}{4N_u}\frac{\alpha}{\alpha + \Lambda} \tag{8-36}$$

where α is the optimised outcoupling fraction and Λ is the passive cavity losses due to mirror reflectivity and all diffraction losses. An expression for the optimised outcoupling fraction, i.e. the outcoupling fraction that maximises output power, is given by Giannessi [25]. The calculations in this report use instead a third degree polynomial fit to extensive one-dimensional steady-state oscillator simulations for systems with single pass gain up to 500 %. This fit agrees very well with the Giannessi expression at small gain.

8.2 XUV-FEL Conceptual Design

8.2.1 General Specification

The XUV-FEL design will generate short, tuneable, high-brightness pulses of 8 - 100 eV photons from an undulator system directly seeded by an external laser source. This tuning range has recently been revised from the original specification of 10 - 100 eV in response to the latest information from potential user groups, as discussed earlier. For this reason the specification presented covers the tuning range 10 - 100 eV. However, as will be demonstrated in section 8.2.9, the extension to the lower photon energy can be easily achieved with only minor parameter changes. The radiation output will have good temporal and transverse coherence and also have variable polarisation. These specifications are expected to satisfy a wide range of current user requirements and also open up many new areas of science for exploration. It is also possible to utilise the exhaust electrons of the XUV-FEL in a spontaneous spent-beam undulator source, before the electron beam is dumped. The radiation from this source is then guaranteed to be synchronous with the XUV-FEL output for pump-probe type experiments.

A schematic of the design for the 4GLS XUV-FEL is shown in Figure 8.4. Only those components that have direct relevance to the XUV-FEL are shown. Further description of the electron beam transport system for the XUV-FEL is given in Chapter 8.

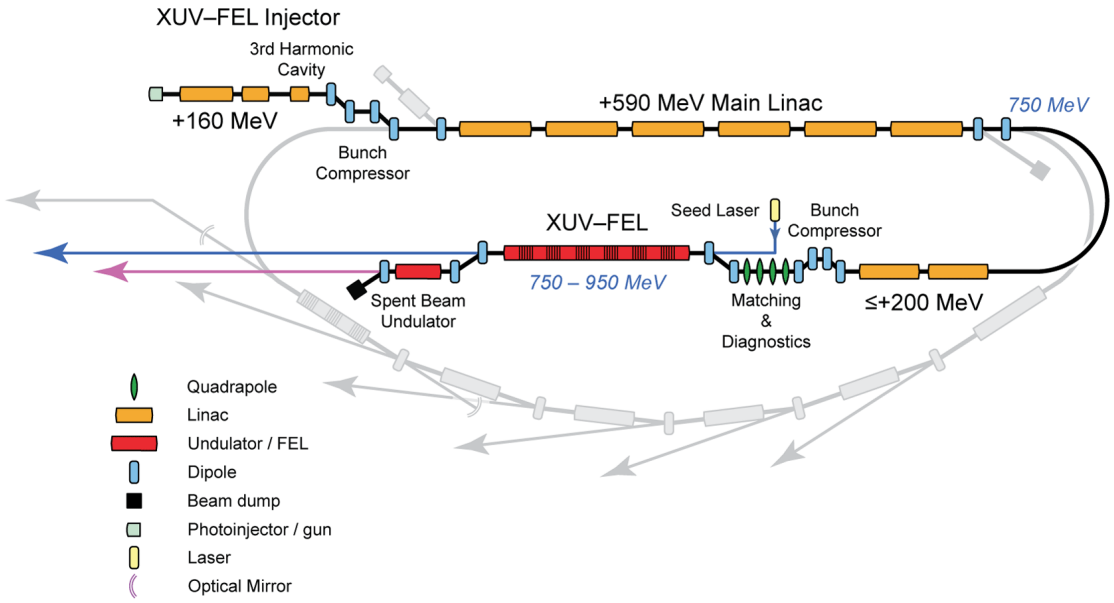

Figure 8.4 Schematic layout of the XUV FEL conceptual design

Photon energy tuning in the XUV-FEL will be achieved by a combination of both undulator gap tuning and electron energy tuning between 750 and 950 MeV. The FEL undulator will consist of a lattice of individual undulator modules allowing electron beam focussing elements and

diagnostics to be placed in between. The final undulator modules of the FEL will be of APPLE-II design that will enable the generation of variable elliptically polarised radiation.

Because suitable cavity mirrors for higher photon energies are unavailable, a single-pass high gain FEL amplifier is the only viable design option. Existing laser systems can provide seed energies of 10 - 100 nJ with pulse widths of 30 fs FWHM over this photon range (see section 8.2.5). These seed pulse widths will not be greatly increased in duration as a result of the FEL amplification and are significantly shorter than the pulse width resulting from a SASE interaction which is typically that of the electron pulse width. For the purposes of this design report the seed pulse energies are reduced by a factor of approximately ten at the entrance to the XUV-FEL undulator to account for transport losses. Even with this conservative factor, the seed will be of significantly higher power than the spontaneous power due to electron shot-noise present at start-up. Less conservative estimates for the seed powers will be made in future design phases as further information regarding improvements in the seed sources becomes available themselves and the seed transport into the undulator becomes better defined. Thus, the problems of the noisy radiation pulse output with poor temporal coherence and shot-to-shot power stability associated with the SASE mode of operation are circumvented. The higher seed powers also ensure that the amplifier will be shorter than that required for SASE operation. The quality of XUV-FEL output can be expected to be similar to that of the input seed pulse which has a high degree of both spatial and temporal coherence. The amplified pulse widths will also be only slightly longer than the seed pulse of typically $\gtrsim$ 30 fs FWHM.

Other seeding systems have been considered but are not pursued further here. For example, a self-seeding scheme at the VUV-FEL at DESY, Hamburg is currently under construction [26], but this system requires a complex system of XUV optics and magnet chicanes. There is also significant pulse-to-pulse variation in the power using this method. Given the current availability of suitable seed lasers and the continuing improvement in their characteristics for use as seeds, the self-seeding option is not preferred. Another seeding scheme that was investigated is high gain harmonic generation (HGHG) [27]. This method can extend the benefits of a seeded FEL interaction indirectly to higher harmonics of the seed laser. Again, such a scheme is not thought necessary for the 4GLS XUV-FEL as sources are available for direct seeding over the full spectral range.

The use of an external laser seed source requires synchronism between the seed and the electron pulses at the entrance to the undulator. The timing synchronisation required to deliver a high level of FEL pulse-to-pulse power stability can be met, as discussed in Chapter 12.

8.2.2 Undulator Lattice

The design for the XUV-FEL undulator (Figure 8.5) consists of a lattice of planar and variable polarisation undulator modules. Each type of module will have a fixed period and a variable magnetic gap that allows tuning of $\overline{a}_u$ via the undulator magnetic field. A schematic giving further detail of the undulator lattice is presented in Figure 8.6.

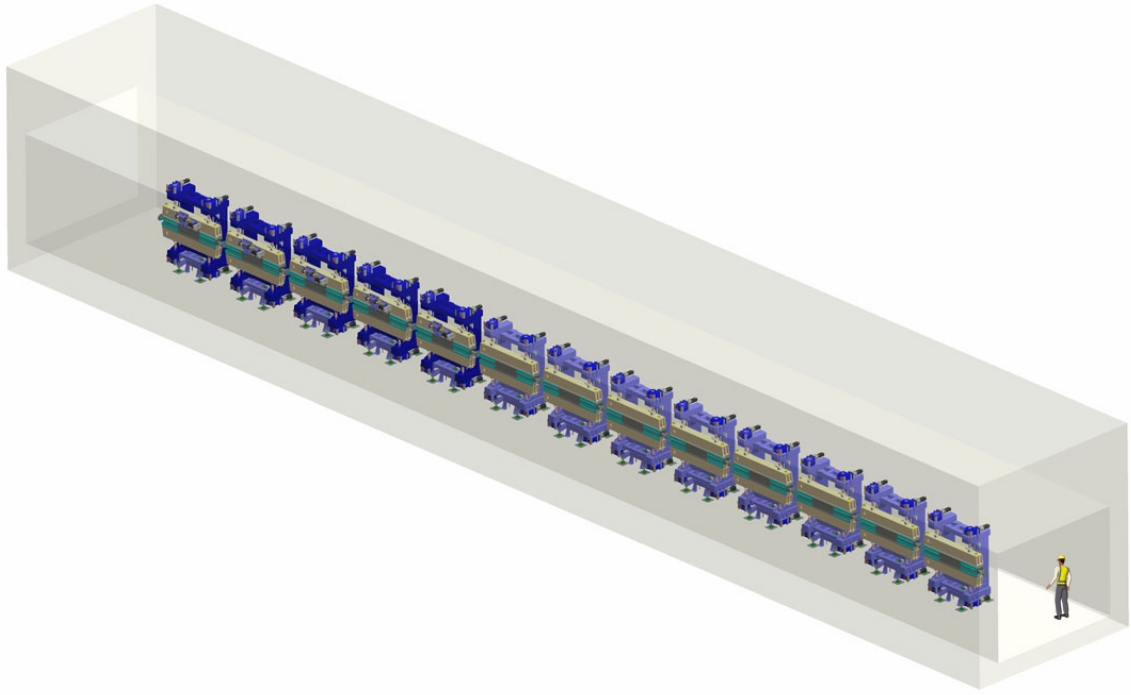

Figure 8.5 An engineering design drawing of the XUV-FEL undulator tunnel. The electron beam direction is right to left. The first eight undulator modules are planar and the last five are APPLE-II.

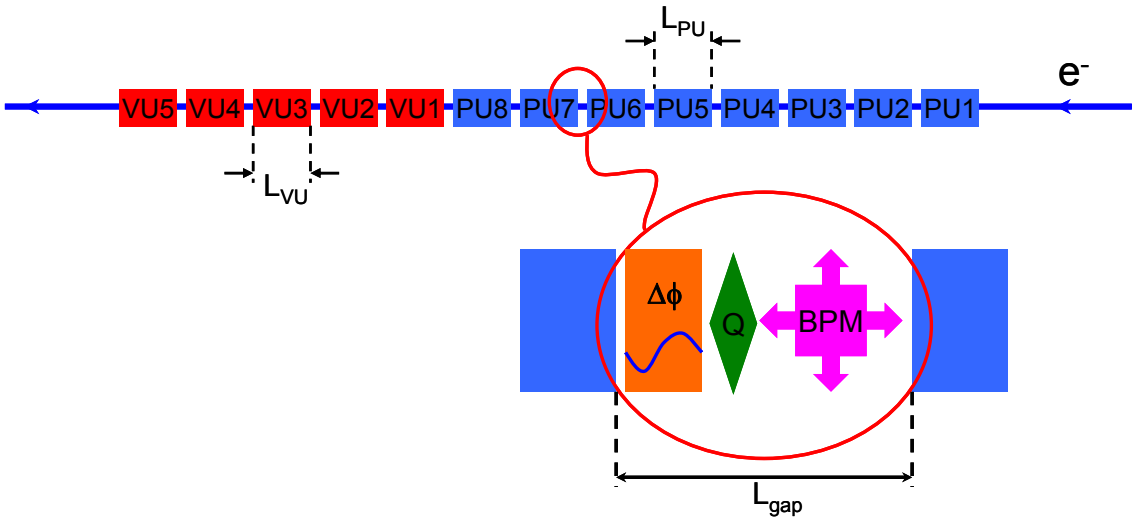

Figure 8.6 Schematic of the modular undulator system of the XUV-FEL. Undulator modules PU1..8 (blue) are planar undulators; VU1..5 (red) are variable polarisation undulators. The gap between undulator sections may contain a beam position monitor, quadrupole and radiation/electron phase matching unit.

Photon energy tuning is achieved by varying the electron beam energy and/or the undulator magnetic gap. The variable polarisation undulator sections, VU1..VU5, ensure that variable polarisation may be generated across the full design spectrum.

The resonance relation (8-1) shows that to tune an undulator to a shorter wavelength either the electron beam energy γ_r must be increased and/or the undulator parameter $\overline{a}_u$ decreased. Both changes reduce the FEL coupling mechanism (the Pierce parameter ρ of (8-12) is reduced) and result in longer gain and saturation lengths. In practice, operation of the XUV-FEL amplifier at the higher photon energies will require a longer undulator length to achieve saturation. The effective undulator length may be varied by opening the magnetic gaps of individual undulator modules to their maximum. Those modules that have maximum magnetic gap generate only small on-axis magnetic fields and are effectively switched off for the purpose of the FEL interaction.

For example, in Figure 8.7 for 80 eV photon operation, undulator modules PU1 and PU2 are open and the electron beam will have FEL interaction first with the planar undulator modules PU3..PU8 and then with the variable polarised undulator modules VU1..VU5. For 10 eV operation, all planar undulator modules PU1..PU8 are open and the electron beam will have FEL interaction first with the variable polarised undulator modules VU1..VU5.

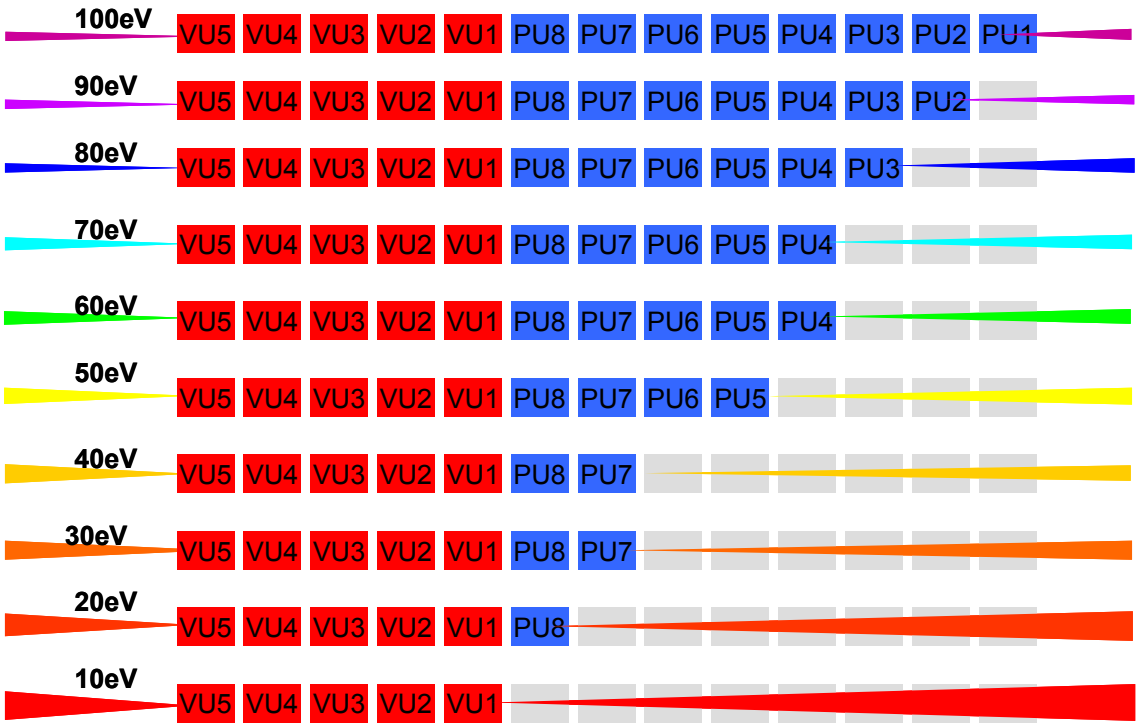

Figure 8.7 Schematic of the modular undulator system of the XUV-FEL demonstrating the different modes of operation across the photon energy range 10-100 eV. Undulator modules marked in grey have large magnetic gaps $\left(\lim \overline{a}_u \to 0\right)$ *and do not affect FEL operation. Electron beam transport is right to left. The minimum required undulator gap (and vacuum vessel internal aperture) decrease in gradual steps from 28 mm (25 mm) for PU1 down to 10 mm (7 mm) for PU8 and the variable polarisation modules VU1-VU5.*

8.2.2.1 Undulator Type and Periods

Three main undulator types are identified for this design proposal, details of which are given in Chapter 10. For the planar undulators a relatively simple pure permanent magnet (PPM) was chosen and an APPLE-II design was chosen for the variable polarisation undulators.

A minimum undulator magnetic gap of $g = 10\,\text{mm}$ is assumed for the design of both planar and variable undulators. Note that the gap between the vacuum vessel walls will be $\approx (g - 3)\,\text{mm}$, the 3 mm reduction from the magnetic gap being the estimated thickness of the vacuum vessel walls and the clearance between magnets and vacuum vessel. For magnetic gaps greater than this minimum the undulator parameters decrease. For the PPM undulator, when $g/\lambda_u \gtrsim 0.65$ the undulator parameter $\overline{a}_u < 1$, which results in only a weak FEL coupling between electrons and radiation field.

Resonant photon energy contours are plotted as a function of the period and magnetic pole-gap for a PPM planar undulator in Figure 8.8 and Figure 8.9 for electron beam energies of $E_0 = 750\,\text{MeV}$ and 950 MeV respectively, corresponding to the lower and upper electron beam

energies of the XUV-FEL. The same plots are repeated in Figure 8.10 and Figure 8.11 for a variable polarisation APPLE-II type undulator in helical mode.

The minimum undulator parameter due to undulator gap tuning is taken to be $\overline{a}_u^{\min} \approx 1$ to ensure sufficient FEL coupling. With this constraint then $g/\lambda_u \lesssim 0.65$ and for a beam energy of $950\,\text{MeV}$ the maximum planar undulator period that can achieve 100 eV FEL resonance is seen from Figure 8.9 to be $\lambda_u \approx 45\text{mm}$. Figure 8.8 shows that at the lower beam energy of $750\,\text{MeV}$ and for $\lambda_u \approx 45\,\text{mm}$, the resonant photon energy is $\approx 10\,\text{eV}$ for the minimum magnetic gap of $g \approx 10\text{mm}$. The period of $\lambda_u \approx 45\,\text{mm}$ is then the optimum for the beam energy, magnetic gap and photon tuning range.

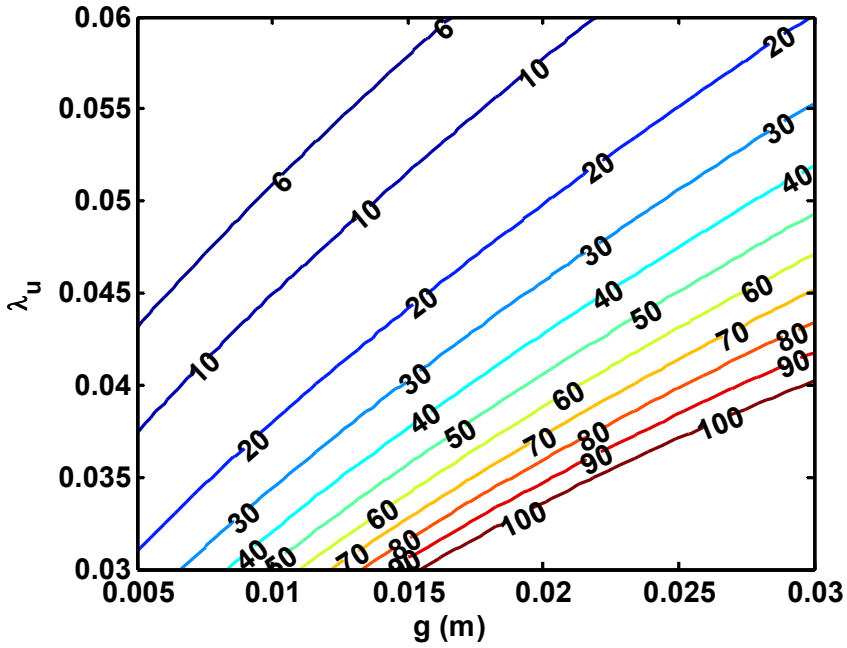

Figure 8.8 Resonant photon energy contours as a function of undulator magnetic pole gap and period for a planar permanent magnet pole undulator with beam energy of 750 MeV

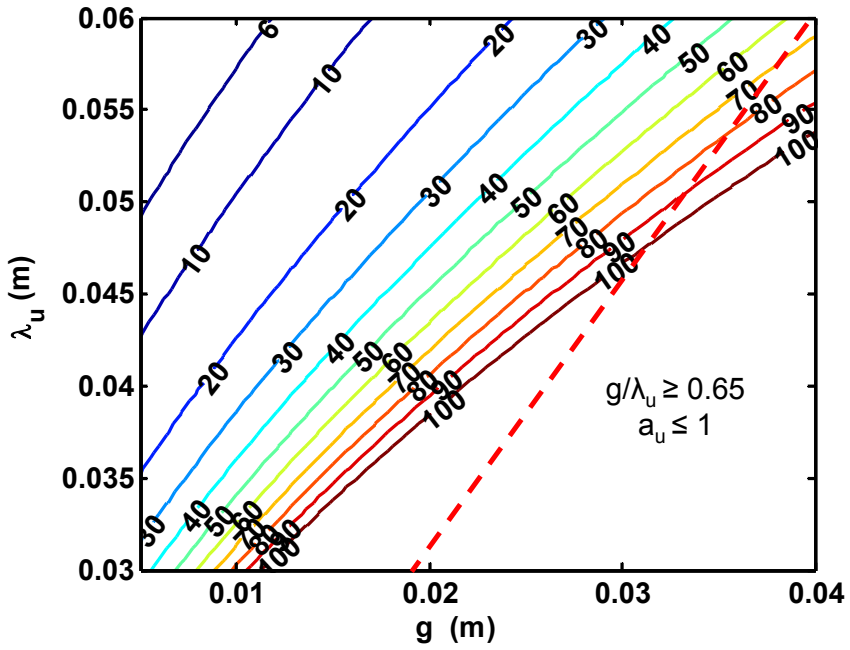

Figure 8.9 Resonant photon energy contours as a function of undulator magnetic pole gap and period for a planar permanent magnet undulator with beam energy of 950 MeV. The area beneath the dashed red line is the region in which $\overline{a}_u \leq 1$.

The period of the APPLE-II variable polarisation undulator is set at 51 mm, so that at minimum gap, g = 10 mm, and beam energy 750 MeV, the undulator is resonant at 10 eV in helical mode. This ensures electron beam energy and output wavelength correspondence between the PPM and APPLE-II modules.

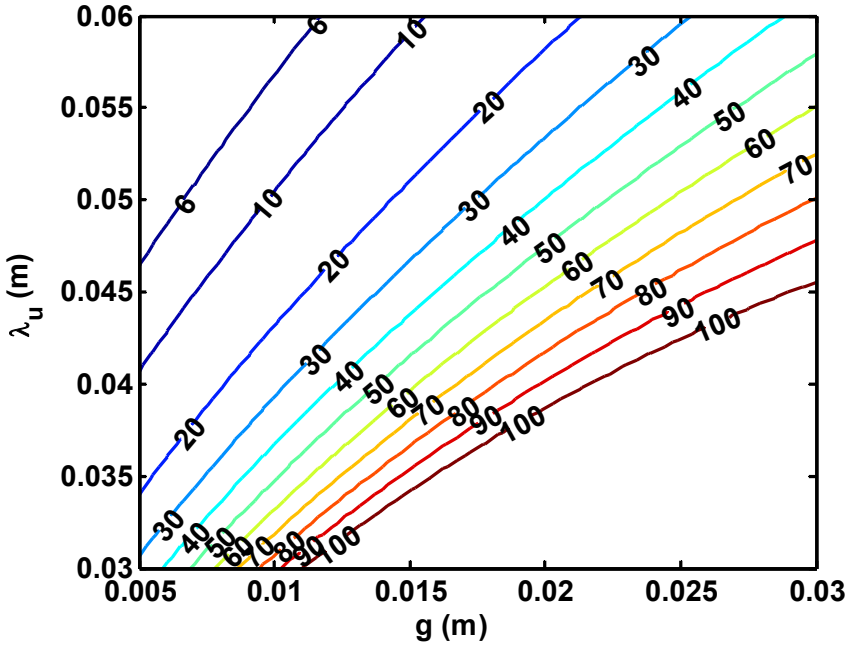

Figure 8.10 Resonant photon energy contours as a function of undulator magnetic pole gap and period for an APPLE-II undulator in helical mode with beam energy of 750 MeV

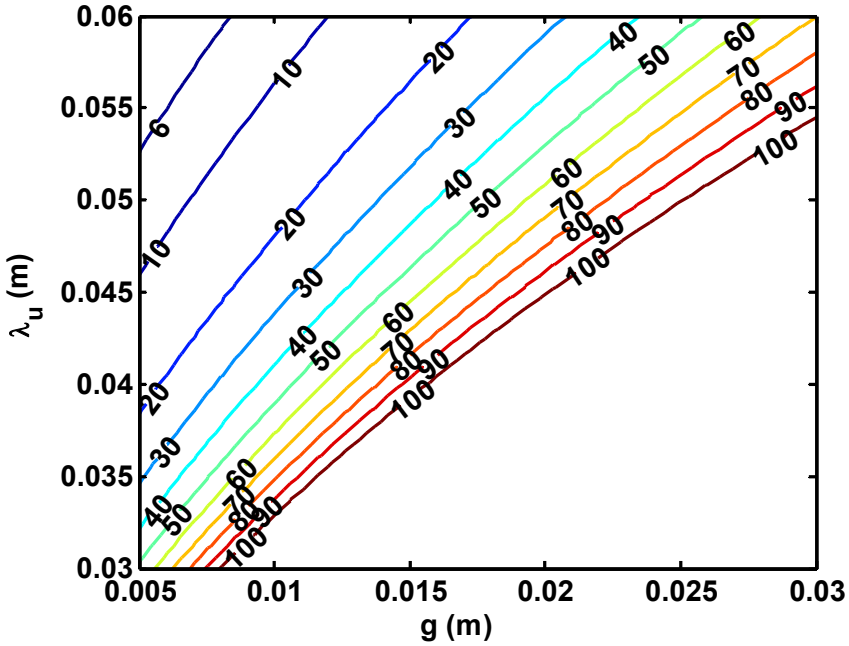

Figure 8.11 Resonant photon energy contours as a function of undulator magnetic pole gap and period for an APPLE-II undulator in helical mode with beam energy of 950 MeV

8.2.2.2 Undulator Beam Energy and Magnetic Gap Tuning

Having chosen the undulator periods, it is useful to summarise the resonant photon energies at which the XUV-FEL will operate as a function of both the parameters that will be used to tune the FEL in practice: the beam energy and the undulator gap. This information is shown in Figure 8.12 for planar mode operation and Figure 8.13 for helical mode operation. It should be noted that the red annotation only highlights the tuning range, not necessarily the optimum tuning curve.

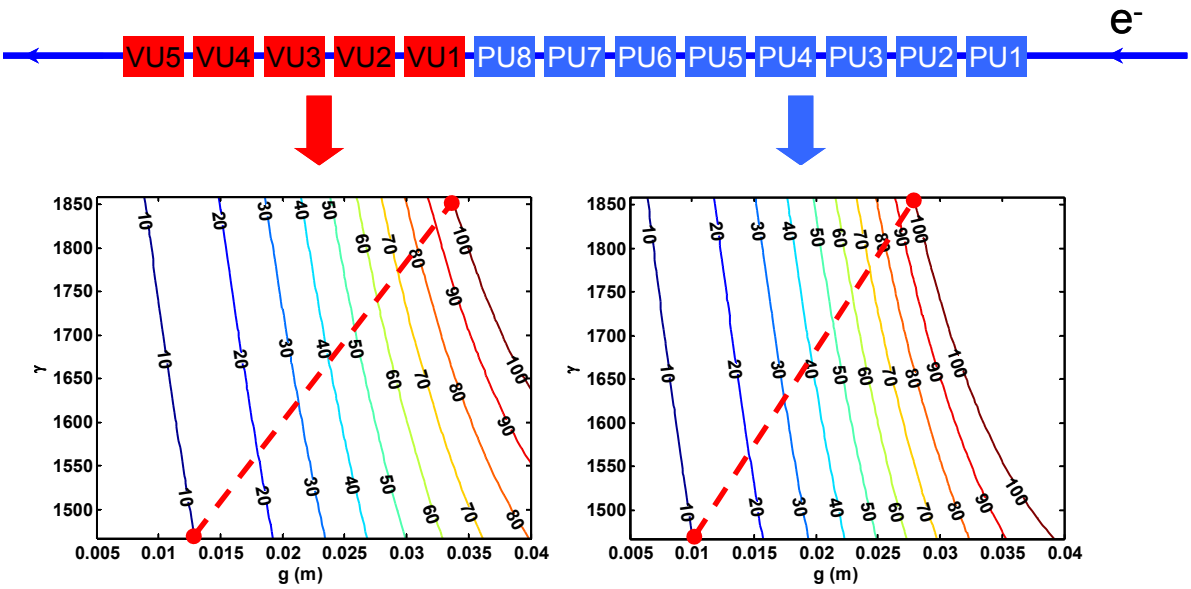

Figure 8.12 Tuning contours of the resonant photon energy (10 - 100 eV) as a function of the electron beam relativistic parameter (E_0 = 750 - 950 MeV) and the undulator magnetic gap g. The variable polarisation undulators VU1..5 are set to planar mode so that output radiation is linearly polarised. The red annotation shows the range only, not necessarily the optimum tuning curve.

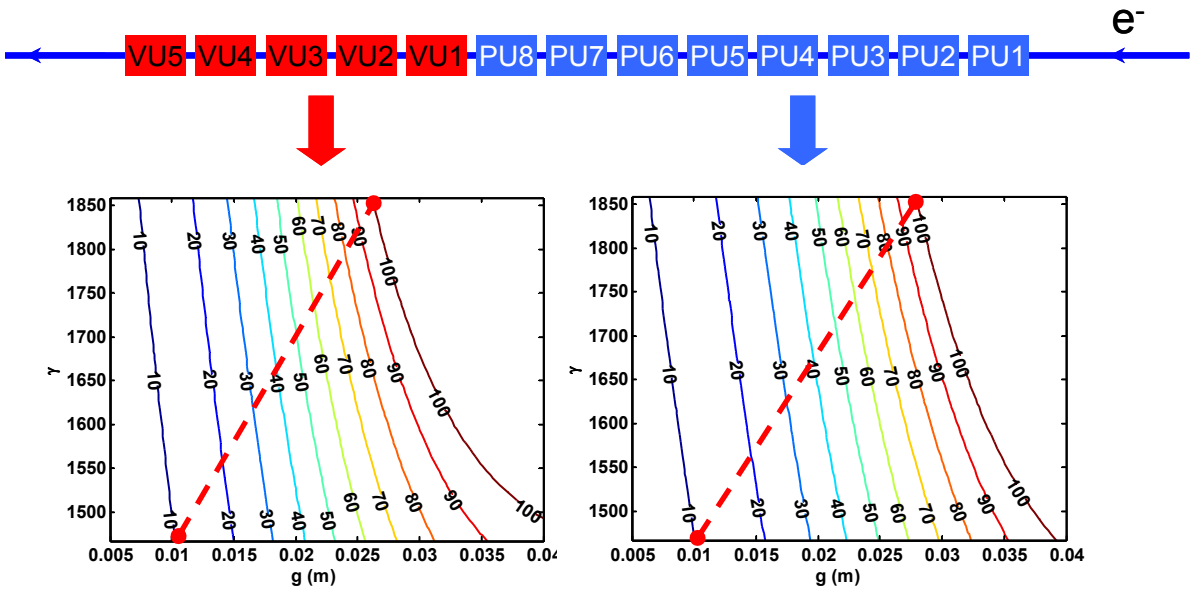

Figure 8.13 Tuning contours of the resonant photon energy (10 - 100 eV) as a function of the electron beam relativistic parameter (E_0 = 750 - 950 MeV) and the undulator magnetic gap g. The variable polarisation undulators VU1..5 are set to helical mode so that output radiation is circularly polarised

8.2.2.3 Focussing Lattice

A FODO focussing lattice has been chosen for the design. Other systems based upon quadrupole doublet and triplet focussing have been investigated [28] and rejected. These latter designs allow longer, and therefore fewer, undulator modules of up to 5 m in length to be used. However, the doublet and triplet quadrupole field strengths must be significantly greater by a factor of 3-4 than those required for a FODO lattice which is distributed between more modules. These larger field strengths mean that stricter alignment tolerances are required for the doublet and triplet positioning [29]. Furthermore, the smaller number of undulator section gaps mean that monitoring of the electron beam transverse position, critical to the FEL interaction, is limited. For these reasons, the simpler FODO focussing lattice is the chosen design option.

The Xie design formulae have been used to estimate the optimum average β-function of the FODO focussing lattice. The Xie results assume a constant, distributed focussing with no variation of the β -function due to the discrete quadrupole lattice as described by (8-11). The formulae also assume a fixed undulator type, so that the planar/variable polarisation of the XUV-FEL cannot be modelled exactly. For the purposes of this design, however, the assumption of planar PPM undulators for all sections still gives very useful design estimates. For 100 eV photon energy FEL operation, using the parameters above, the Xie formulae are used to plot in Figure 8.14, the contours of the gain length, L_g, and in Figure 8.15 the contours of the saturation power P_{sat}, as a function of the electron beam β -function and normalised emittance ε_n. In Figure 8.14 the dashed red line shows the beta function that minimises the gain length as a function of beam emittance. In Figure 8.15 the dashed red line shows the beta

function that maximises the saturation power, again as a function of beam emittance. For the design value of $\varepsilon_n = 2$ mm mrad , these figures show that the optimal value of $\beta \approx 2-3$ m .

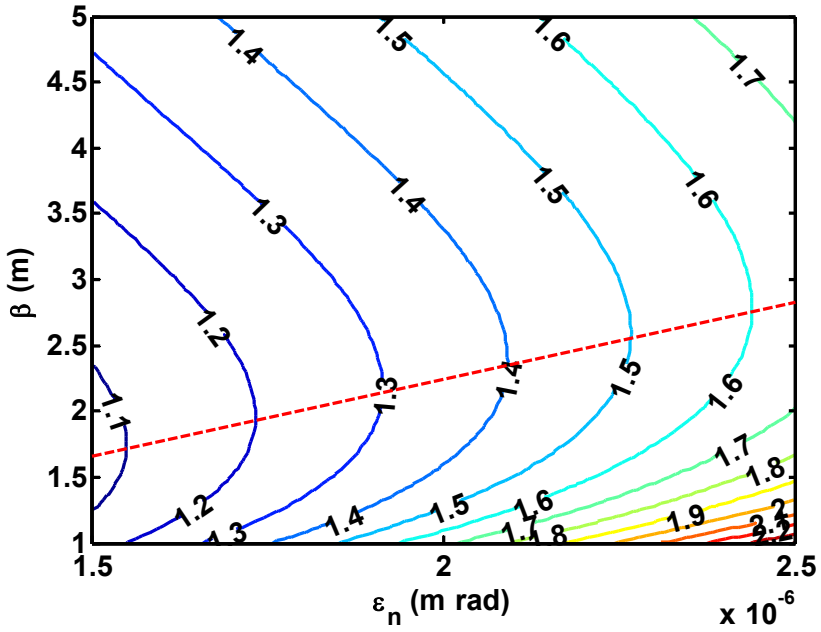

Figure 8.14 Gain length (m) contours: β -function vs emittance for 100 eV operation. The dashed red line indicates the beta function that minimises the gain length, as a function of emittance.

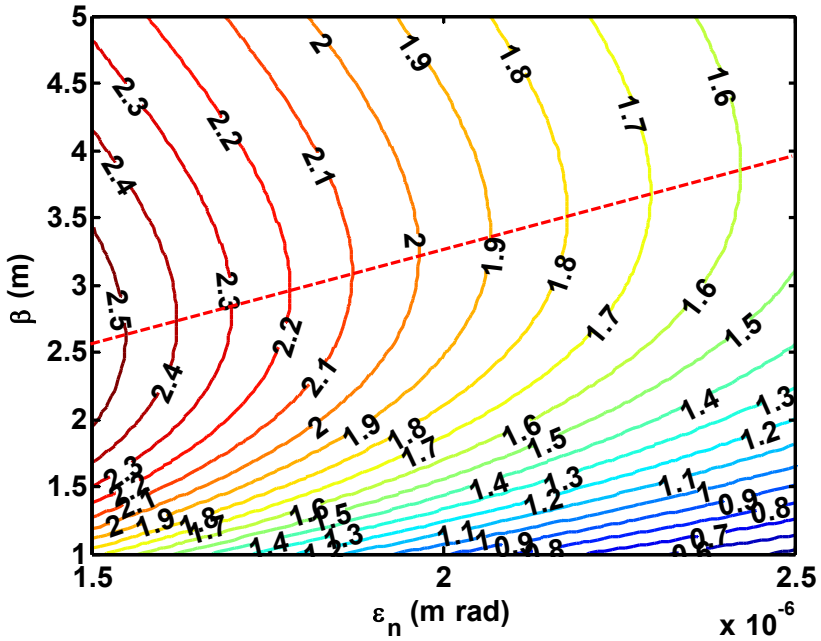

Figure 8.15 Saturation power (GW) contours: β-function Vs emittance for 100 eV operation. The dashed red line indicates the beta function that maximises the saturation power, as a function of beam emittance.

In order to investigate the effect of β-function variation due to the discrete focussing quadrupoles of the FODO lattice, the three-dimensional code Genesis 1.3 [30] was used to determine both the saturation length $L_{sat}\left(\propto L_g\right)$ and power P_{sat} as a function of average β-function. This was carried out for a planar undulator system and the results shown respectively in Figure 8.16 and Figure 8.17. It is seen that the β-function that minimised gain length is ~3.5 m, whereas the β-function that maximises the output power is ~ 5.5 m.

The results from both methods have been assessed, and the nominal value of the β-function is chosen to be that which gives the maximum output power: β = 5.5m. This is motivated by the fact that the planar modules PU1-PU8 produce a seed pulse (and pre-bunched beam) which will be amplified to saturation in the APPLE-II modules VU1-VU5, so maximising the power of the seed into the VU modules reduces the required length of the more technologically challenging APPLE-II modules. For the parameters used here a β-function of 5.5 m is satisfied by quadrupoles of magnetic length 0.09 m and of strength B_Q=13 T/m. The electron beam radius may be calculated from equation (8-9) as r_b = 77 μm for electron beam energy 950 MeV.

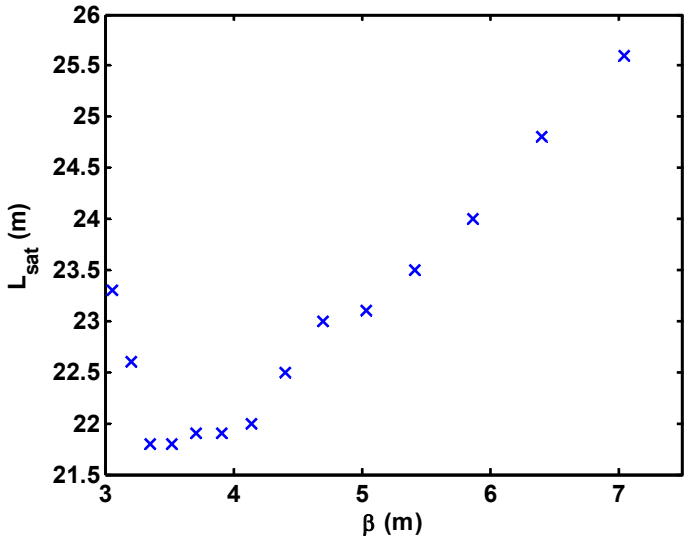

Figure 8.16 Saturation length as a function of the β-function in a FODO lattice for 100 eV operation. These results are from Genesis 1.3 simulations.

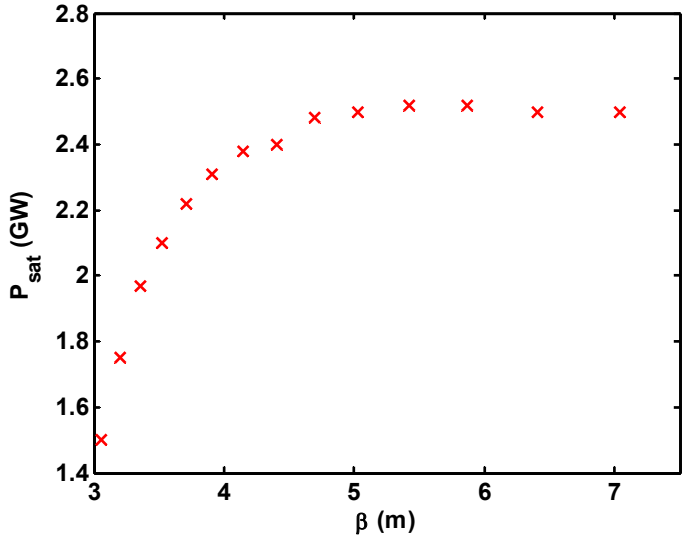

Figure 8.17 Saturation power as a function of the β-function in a FODO lattice for 100eV operation. These results are from Genesis 1.3 simulations.

The optimisation presented here has been done for 100 eV operation. The Genesis 1.3 simulations presented later in this report for longer wavelength output of the XUV-FEL adhered to the same philosophy for β-function optimisation, and it was found that a β-function of 5.5 m was near optimum across the wavelength range. This is the value used in the simulations. For operation of the XUV-FEL it would be convenient if the electron beam matching could be independent of wavelength. This would greatly simplify wavelength tuning of the FEL. It is recognised, however, that the photon beam divergence increases with wavelength and at the long wavelength end of the tuning range it may be necessary to operate with a larger β-function to reduce the divergence to a level that satisfies user requirements. This is not expected to be a problem for FEL operation because at the longer wavelengths the strength of the FEL coupling is much increased over that at shorter wavelengths and the available high harmonic generation (HHG) seed powers are higher.

8.2.2.4 Undulator Module Length and Inter-Module Gaps

The modular construction of the combined undulator and FODO focussing lattice requires the length of each undulator module, L_{PU} for planar and L_{VU} for variable undulators, and the spacing between modules L_{gap}, to be chosen. The FEL performance has a functional dependence on these parameters so optimisation is needed.

The energy dispersion induced into the electron beam by the FEL interaction, and the natural homogeneous energy spread, is transformed into a spatial dispersion in the gap between undulator sections which may disrupt the FEL bunching process.

It is seen from Figure 8.6 that the undulator module length and gap define the FODO focussing lattice period, $\lambda_{FODO} = 2\left(L_{PU} + L_{gap}\right)$. From equation (8-11), λ_{FODO} determines the variation in

the β-function of the electron beam and, via equation (8-9), the electron beam radius. Thus if L_{PU} or L_{gap} are too large, the electron beam radius will vary greatly as the beam propagates through the lattice, adversely affecting the FEL coupling.

Alignment of the electron beam through the undulators is of critical importance to maintain the electron-radiation coupling and an uninterrupted FEL interaction. This requires both beam alignment between undulator modules and careful construction of the undulators to ensure that the beam wander due to magnetic field errors and pole alignment are minimised. Ideally, beam wander off the optical axis should be no greater than ~ 20 % of the electron/radiation beam radius. This aspect is considered further in section Chapter 10.

The FEL design formulae of Xie offer no assistance in describing these processes and so Genesis three-dimensional simulations were carried out to simulate the FEL operating at 100 eV. Only the planar undulator modules were used, inclusion of the variable polarisation undulator modules being an unnecessary complication at this stage of the design.

Figure 8.18 plots the results of Genesis steady-state simulations for the saturation power, P_{sat}, as a function of the gap between undulator modules, L_{gap}, for three different module lengths, $L_{PU} = 2,\ 3,$ and 4 m. Care was taken to ensure the phasing between modules was matched correctly for all gap lengths. It is seen that the saturation power is nearly independent of the undulator module length and decreases almost linearly with the undulator gap. A gap of $L_{gap} = 0.6\,\mathrm{m}$ is chosen for the design specification. This is the estimated minimum length into which the quadrupoles, BPMs and phase matching units can fit.

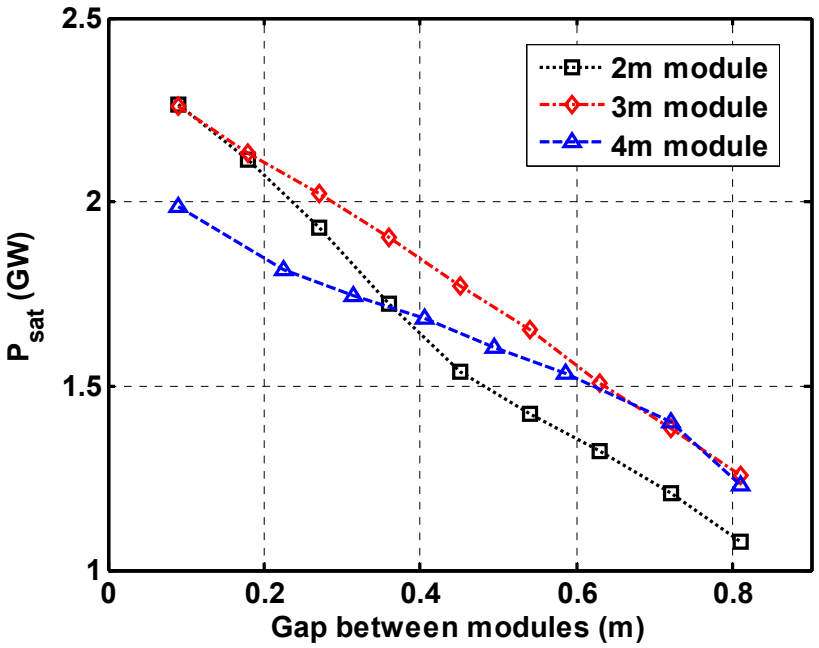

Figure 8.18 Genesis simulation of the saturation power P_{sat} for XUV-FEL planar undulator operation at 100 eV as a function of the gap between undulator modules L_{gap}. The results are plotted for three module lengths: L_{PU} =2, 3 and 4 m.

Results of Genesis 1.3 simulations of the saturation length L_{sat} of a seeded amplifier interaction, starting from a seed power of 30 kW at 100 eV, are shown in Figure 8.19. It should be noted that the saturation length is the length of undulator only: the gaps between modules are not included in the length. For each length of undulator module the saturation length is seen to increase with the module gap. However, there is a notable difference between each undulator module length, with the 4 m module having a saturation length that is $\approx 15\%$ longer than that of the 2 m module. This is attributed to the greater variation in the β-function for the longer module as discussed above. For this reason, and the greater opportunities for beam monitoring and control afforded by the greater number of undulator gaps, the module length for the design specification is chosen to be $L_{PU} = L_{VU} \approx 2\,\mathrm{m}$.

Hence, for the baseline design for 10 - 100 eV operation, each planar PPM undulator will have 45 periods of 45 mm giving a module length L_{PU} = 2.025 m and each variable undulator APPLE-II undulator will have 40 periods of 51 mm giving a length L_{PU} = 2.04 m.

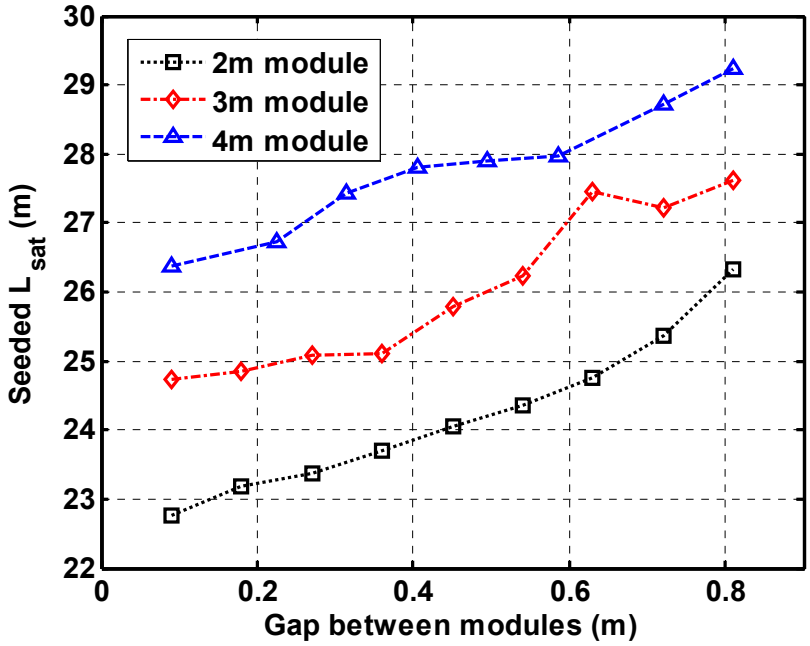

Figure 8.19 Genesis 1.3 simulations of the saturation length L_{sat} for XUV-FEL planar undulator operation at 100 eV as a function of the gap between undulator modules, L_{gap}. The results are plotted for three module lengths: L_{PU} = 2, 3 and 4 m. It should be noted that the saturation length given is the length of undulator only: the gaps between modules are not included in the length.

8.2.3 Step-Tapered Vacuum Vessel

It can be seen from Figure 8.7 that module PU1 is only required for 100 eV operation. For 100 eV resonance the magnet gap will be maximum (~28 mm). This module will never be required to operate at a smaller gap and therefore the vacuum vessel aperture can be large at this point. Similar considerations show that module PU2 will operate at a minimum gap slightly smaller than that required for PU1, and that module PU3 will operate at a minimum gap slightly smaller than that required for PU2, and so on. It is therefore proposed to use a step-tapered vacuum vessel that gradually decreases in aperture from module to module. The two advantages of this approach are that firstly resistive wall and surface roughness wakefields are much reduced compared to a constant minimum aperture, and secondly the tapered internal aperture allows for optimal focussing of the HHG seed pulse across the whole wavelength range. This is demonstrated in section 8.2.7.4 for the 10 eV case, where the seed must be introduced at the entrance to PU1 but focussed to a suitable spot size towards the beginning of module VU1.

8.2.4 Electron Beam Quality

The Xie design formulae are now used to investigate the effects of electron beam quality, particularly the normalised emittance ε_n and the RMS fractional energy spread σ_γ, for the nominal parameters required for 100 eV and 10 eV operation. These two beam quality parameters are critical for lasing. The design values assumed are a normalised emittance of

$\varepsilon_n = 2$ mm mrad and energy spread of $\sigma_\gamma = 10^{-3}$. These values may be considered to give a good quality beam in that they satisfy well the one-dimensional criteria of section 1.1.3.2. The values are not, however, overly optimistic in pushing at the boundaries of what is currently possible.

The gain length L_g and saturation power P_{sat} are plotted as contours as a function of the electron beam emittance and energy spread for 100 eV operation in Figure 8.20.

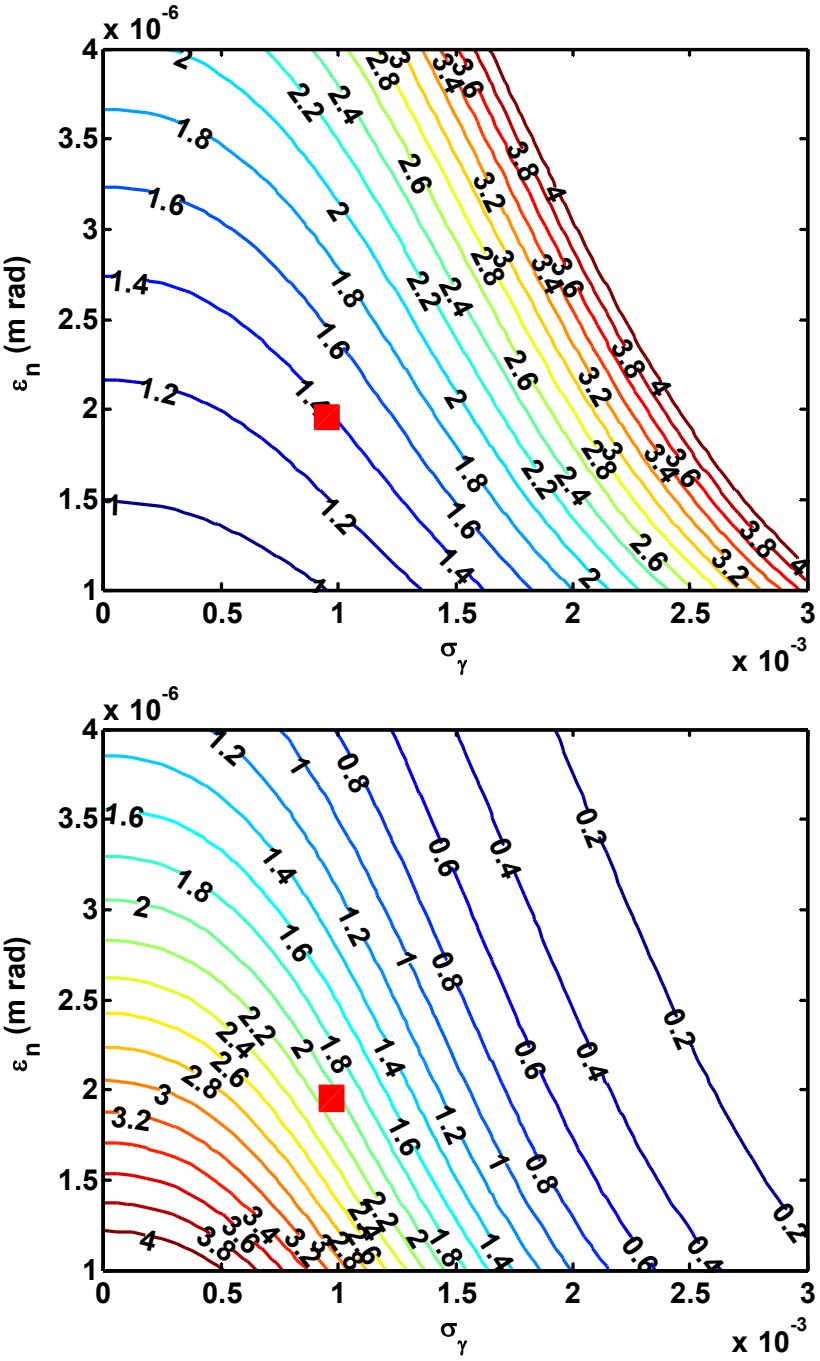

Figure 8.20 Gain length $L_g\,(m)$ [top] and saturation power $P_{sat}\,(GW)$ [bottom] contours for 100 eV photons as a function of normalised emittance and the RMS fractional energy spread. The red square indicates the design operating point.

The maximum saturation length of the XUV-FEL will be for 100 eV operation and therefore it is this length that determines the total overall length of the undulator lattice. The total number of gain lengths required for the FEL to saturate does not vary significantly [2] and so the saturation length is proportional to the gain length. It can be seen from the L_g contours that, even for relatively modest increases in emittance and energy spread from the design values, significant increases in the gain length, and therefore the saturation length, result. Therefore, the determination of electron beam quality is of critical importance to the overall design of 4GLS. Better specification of emittance and energy spread, conservatively estimated here, will be an important objective of start-to-end simulations at the next design phase. Work has already progressed in this vein in the design work carried out for ERLP [31].

For 10 eV operation, the dependence of the gain length and saturation power upon the electron beam quality is less restrictive as can be seen from Figure 8.21.

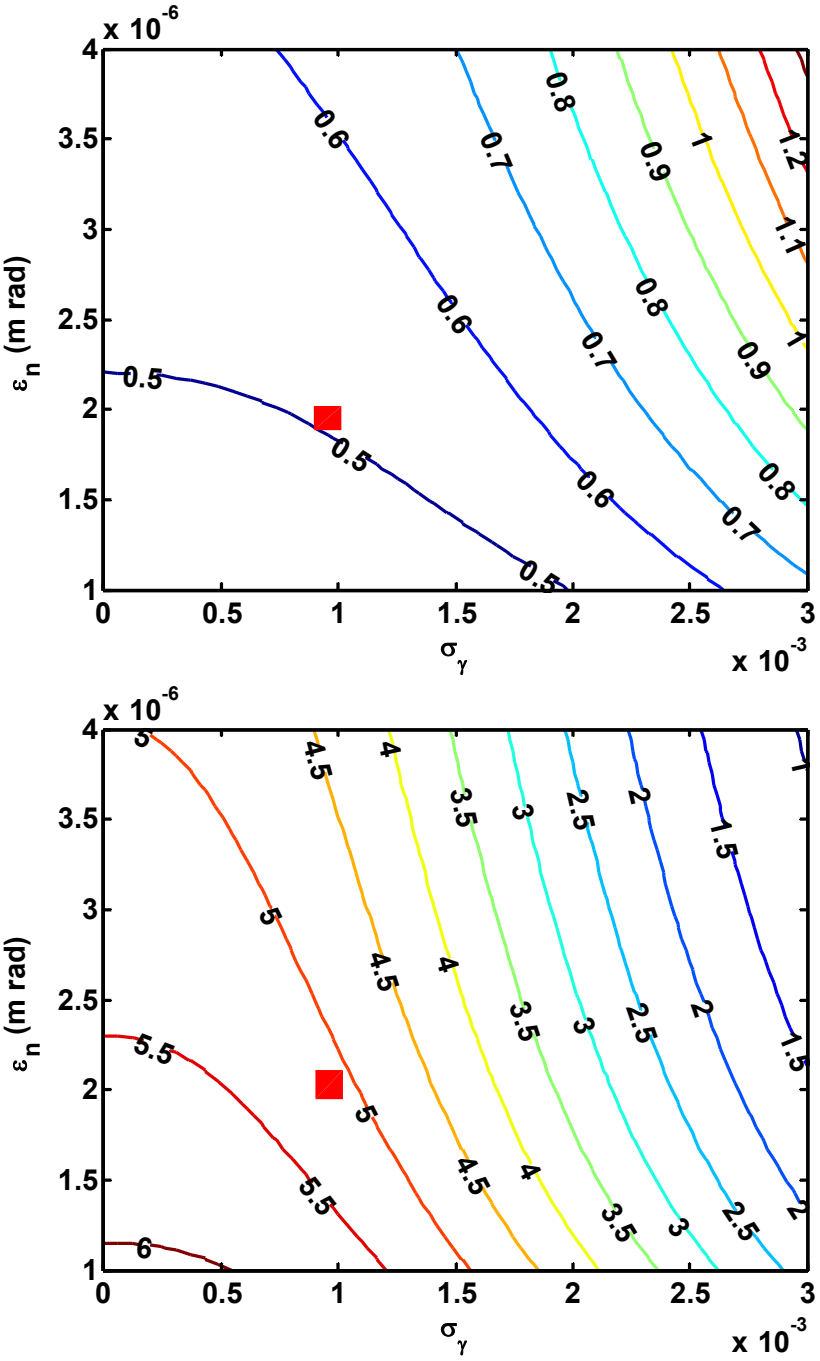

Figure 8.21 Gain length, $L_g\,(m)$ [top] and saturation power $P_{sat}\,(GW)$ [bottom] contours for 10 eV photons as a function of normalised emittance and the RMS fractional energy spread. The red square indicates the design operating point.

8.2.5 Seeding Specification

As discussed in section 8.2.1, sufficient energy for direct seeding is available from high harmonic sources across the photon energy range of the XUV-FEL. Unlike HGHG, when using HHG for direct seeding no multiple stages are required and a much less stringent synchronisation requirement is imposed. Direct seeding with an HHG source is the more suitable approach for the 4GLS XUV-FEL, and so will be the sole topic of the following discussions.

In considering the HHG seed, several issues need to be addressed. Firstly, harmonic generation has a low efficiency, so the most important question is the availability of sufficient seed power at a repetition rate of 1 kHz. Secondly, a tuneable output is desired, with minimal downtime and impact on system parameters (e.g. synchronisation) during tuning. Finally, the spectral and temporal properties of harmonics must be considered.

8.2.5.1 Seed Laser Powers

Previous simulations have shown that 60 kW of seed power is sufficient to seed the FEL [32]. This is three orders of magnitude above the spontaneous power generated from intrinsic density fluctuations in the electron density (shot-noise). Later simulations presented in this report, show that 30 kW seed power is adequate. For 30 fs pulses this represents an energy of 1 nJ. Figure 8.22 shows a synopsis of data from several experiments [33,34,35], representing the harmonic energies achieved to date, in several target gases, as a function of energy, using titanium sapphire based (~800 nm) ultrafast systems. These energies exceed 4GLS requirements by over three orders of magnitude at the low energy photon end of the XUV-FEL operating range, and by over an order of magnitude at the high energy end.

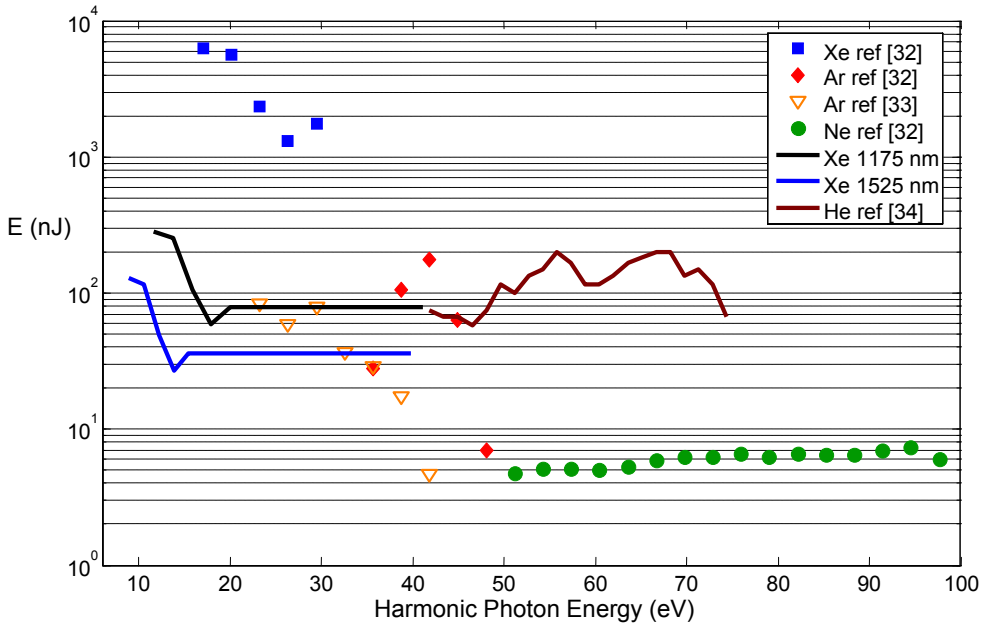

Figure 8.22 Recent experimental results scaled by energy and wavelength. The unconnected points were taken with an 800 nm fundamental, with pulse widths of 30-50 fs, and are scaled here to a pulse energy of 14 mJ. The solid Xe curves show the projected range of harmonic yields for the NOPA (2 mJ pulse energy), tuning between 1175 and 1525 nm. The solid He curve shows the results of a two-color experiment using 800 and 400 nm fundamentals, scaled to a 14 mJ pump energy. The minimum energy for seeding the XUV-FEL with a 30 fs pulse is 1 nJ.

With the exception of the neon data, all of the data in Figure 8.22 were taken at drive laser energies that are compatible with kHz operation. The neon data were taken using a 50 mJ laser pulse energy at low repetition rate, but scaling appropriately to a laser energy of 14 mJ, which is available in existing kHz systems [36] the required energies for seeding are still exceeded by a factor of six. It should be noted that ultra-fast lasers are a very rapidly developing field. There is no fundamental limitation preventing extending ultra-fast systems to higher powers, and there is considerable scientific motivation to do so. A number of recent developments, including the use of optical parametric chirped pulse amplification [37], high power Yb:YAG lasers [38], and enhancement cavities [39,40,41], offer new opportunities for larger systems. Several 100 W, kHz system designs have been proposed [42], and will likely be demonstrated soon.

High harmonic generation is also a very active research area, and a number of efforts are focused on extending the wavelength range and yield of harmonics. While the fundamental dynamics has been understood for about a decade, innovative approaches continue to make big strides in developing these sources. Very recent experimental work [35] using two-colour driving fields demonstrated an enhancement of over two orders of magnitude in harmonic yield in helium, producing 150 nJ in the 38th harmonic (59 eV), using only 2.8 mJ in the drive laser, an efficiency of 5×10^{-5}. Figure 8.22 shows the scaled results of that experiment, assuming that the yield is linear in the pump power and a 14 mJ pump is used. Since helium has the lowest

harmonic efficiency of the rare gas targets used, it is reasonable to expect that when these techniques are extended to other gases and longer pump wavelengths available seed energies over the XUV-FEL operating range will increase substantially.

8.2.5.2 Seed Laser Tuning

In HHG a harmonic series of frequencies is produced simultaneously up to an intensity and target dependent cut-off. When a single driving wavelength is used, parity restricts emission to the odd order harmonics, while both odd and even orders appear when a fundamental and its second harmonic are used to drive the process. In either case, a large number of frequencies other than the desired seed frequency are present and, for a fixed fundamental frequency, the desired frequency is likely to lie in a gap between harmonic orders.

The simplest way to tune between the harmonic orders is by controlling the amplitude and phase of the fundamental. This can be as simple as a chirp [43,44,45] but more general adaptive pulse shaping [46,47,48,49] allows greater tuning range and control over the harmonic pulse width. This permits tuning with minimal impact on synchronisation, and short adjustment times once the system has been calibrated. However, general adaptive pulse shaping does not function at low harmonic orders, as the tuning range is of the order of $q\Delta\nu_f$, where q is the harmonic order and $\Delta\nu_f$ is the bandwidth of the fundamental. Reitze et al [47] demonstrated complete tunability (i.e. a tuning range exceeding the separation of adjacent harmonics) down to 40 eV in Argon using 28 fs, 800 nm pulses, a tuning range of $\approx 2.2q\Delta\nu_f$. How far below 40 eV complete tunability can be extended is not known, but it seems clear that it will be lost somewhere before the lower end of the XUV-FEL tuning range (10 eV) is reached. For this reason a tuneable fundamental is proposed for the low-energy end of the XUV-FEL energy range.

The principal disadvantage of a tuneable fundamental is the loss in overall efficiency due to the frequency conversion and the lower harmonic efficiency [50] at longer wavelengths. Conversion to wavelengths shorter than 800 nm, where the harmonic efficiency is higher, is possible, but then the harmonic orders used to reach the very low end of the tuning range are smaller, and complete tunability cannot be obtained. For an infrared source tuneable from 1175 nm to 1525 nm, complete tunability would be obtained. Conversion efficiency for commercial optical parametric amplifier (OPA) systems in this range, pumped by a Ti:sapphire system, are typically 10 %, while laboratory systems have reported efficiencies of 20 % [51]. The harmonic efficiency drops as $1/\lambda^3$ [50,52,53], so it is 15-30 % of the harmonic efficiency at 800 nm. Fortunately, at these lower energies (see Figure 8.22), the efficiencies are high enough that, even with the losses, an adequate seed power is produced. For higher photon energies, the Ti:sapphire fundamental is used, and tuning is done by adaptive control.

The previously mentioned developments in laser technology will probably make this two-track system unnecessary in the near future, as new kHz ultrafast sources in the 1 - 2 micron wavelength range exceed 10 W average power. Because the high energy cut-off of harmonic production increases with λ^2 at longer wavelength, gases with higher harmonic efficiency can be used out to higher photon energies, offsetting some of the drop in efficiency. Figure 8.23,

from [52], shows the cut-off position for the rare gases as a function of the fundamental wavelength. While an 800 nm fundamental requires using Neon in order to reach 100 eV photon energies, at longer wavelengths, Argon and Xenon may be used. A longer fundamental wavelength also increases the wavelength range over which adaptive tuning may be used, as the harmonic order q for a given wavelength increases and the harmonic spacing decreases. For example, assuming an adaptive tuning range of $2q\Delta\nu_f$, a source with a fixed wavelength of 1.8 μm and 20 fs pulse width could cover the entire 10 - 100 eV XUV-FEL energy range using only adaptive tuning.

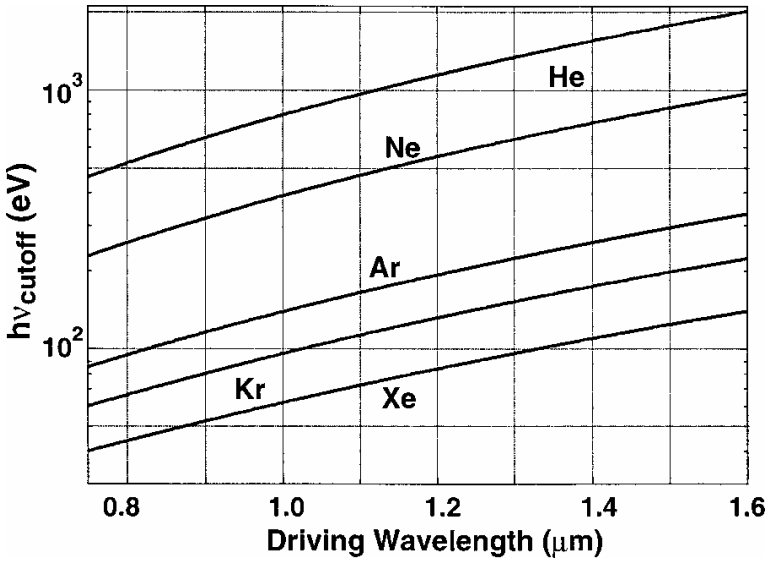

Figure 8.23 (from [52]) maximum harmonic energy (single atom cut-off) obtainable from the rare gases as a function of wavelength

Because of the rapid advances both in the laser technology and in HHG techniques, we expect that the optimal design for the seeding system will likely change before construction. In the interest of demonstrating the feasibility of the project, we outline a seeding system that could be constructed with currently available technology.

Figure 8.24 shows a block diagram of the system. An ultra-fast titanium sapphire oscillator will run at 81.25 MHz, the 16th sub-harmonic of the accelerator RF frequency, with which it will be synchronized (see Chapter 12). Amplifier chains preserving sub-20 fs pulse width with outputs of 14 mJ have been constructed [54] and improvements in commercial pump lasers expected in the coming year will raise the maximum possible output ~ 50 %, so that a 30 fs, 14 mJ system is conservative.

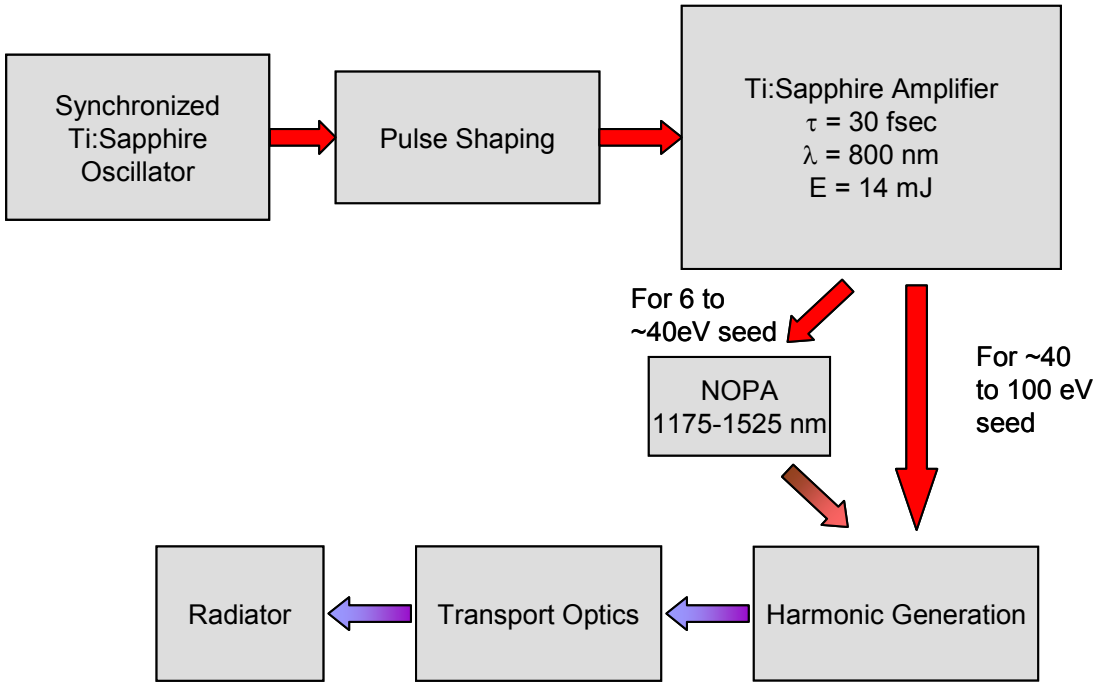

Figure 8.24 Functional block diagram of the high harmonic seed generation for the XUV-FEL

After amplification, one of two paths are selected, depending on the photon energy range needed for the seed. For low energies (10 to approximately 40 eV), a noncollinear optical parametric amplifier (NOPA) will be used to produce a tuneable fundamental for the HH generation. Note that the full tuning range of 1175 - 1525 nm is only required for an optional 6 - 10 eV, of this range. Utilising the low order harmonics, the rest of the low-energy range (10 - 40 eV) can be covered with the peak of the OPA signal spectrum, from 1200 - 1425 nm. At higher energies (40 - 100 eV), the 800 nm light is used for HHG, and the seed wavelength is varied using adaptive tuning. Pulse shaping for the adaptive tuning can be done either before the amplifier, as shown here, or afterwards. The best choice depends on the details of the final laser system design, and will be decided in the technical design phase.

The harmonic generation can be done in a variable-length cell, using loose focusing [33], although guided wave methods [55,56,57] will also be studied in a future design phase. The loose focusing geometry is the simplest to implement over the entire energy range of the XUV-FEL, and Kazamias et al. [58] have shown that loose focusing and guided wave geometries are equivalent in the long focusing limit. There may be some benefit in guided wave geometry in the low photon energy range, where the NOPA is used and there is less energy in the fundamental, but this will require more detailed studies to determine. Quasi-phase matching [59,60] (periodically varying waveguides) may also be beneficial, but will require multiple configurations to cover the XUV-FEL energy range.

8.2.5.3 Seed Laser Temporal Structure

The presence of the multiple odd order harmonics within the seed pulse is not considered to be a problem, as even if all frequencies are injected into the XUV-FEL, the FEL resonance is narrow enough (0.6 %) that only the one harmonic order interacts resonantly with the electron beam. However, another consideration is the temporal structure that the superposition of harmonics may create: the harmonics are coherent, with well-defined phase relationships, and so may interfere to create temporal structure on a time scale shorter than the optical cycle of the fundamental [61,62]. If all harmonics were in phase, the temporal structure would be that of atto-second pulses emitted every one-half of an optical cycle. This has been studied in some detail, as producing atto-second pulses is one of the driving interests of HH research. The phases of the harmonics in fact have a more complex relationship, so that a superposition of all of the harmonics broadens the structure considerably [61,63,64]. Temporal structures of a few hundred atto-seconds have been observed [65,66] but this requires selecting a sub-group of harmonics involved and/or compensating their intrinsic phase variation [67].

The interaction with the electron bunch effectively samples the temporal profile of the single harmonic that lies within the FEL resonance, which is a smooth envelope extending over several optical cycles of the fundamental [68,69]. However, even if this were not the case, the slippage of the electron bunch relative to the optical pulse will wash out the modulation. Since the optical pulse advances in the electron bunch by one wavelength of the FEL-resonant radiation for each period of the radiator, it takes a number of periods equal to one-half of the harmonic order to average over a half-cycle of the fundamental pulse. This is longest at the highest photon energy of the XUV-FEL, 100 eV, where it is still only one gain length. This worst-case scenario has been simulated using the three-dimensional Genesis 1.3 code (section 1.2.8.1), and it was found that the modulation is effectively eliminated by the end of the amplifier.

8.2.5.4 Seed Laser Optics

The soft focus, the low divergence of the harmonics, and the long imaging distance to the radiator indicate that grazing incidence optics would be appropriate for the transport. Critical angles are quite large in the XUV-FEL energy range for typical optical materials, so large effective apertures and high reflectivities can be attained over the entire operating range. Figure 8.25 shows reflectivity curves calculated for several potential materials at 2 degree grazing incidence angles. The optical waist of the seed in the radiator is relatively large so the demands on the optical surfaces are not exacting by synchrotron standards. The divergence of the harmonic radiation is lower than that of the fundamental, and the objective of the imaging system can be located far enough from the HHG focus that the fundamental intensity can be kept below the damage threshold. Silicon carbide has already been shown to have a high damage threshold (> 0.8 TW/cm^2) in similar applications [70] and is extremely versatile to form.

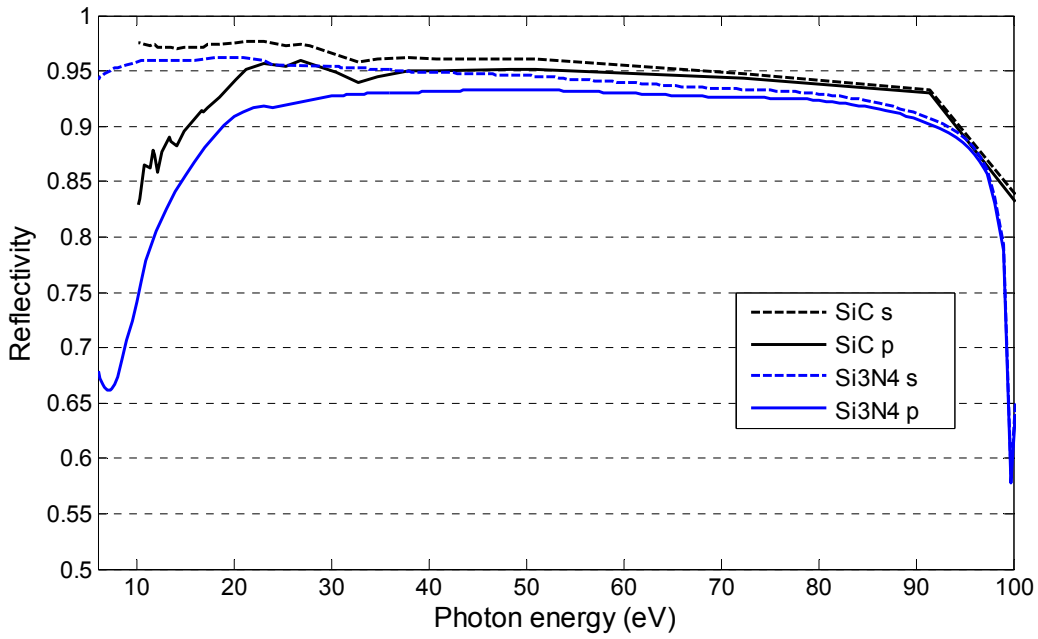

Figure 8.25 *Grazing incidence (2°) reflectivities for potential materials for the transport optics*

8.2.6 Three-Dimensional Steady-State Numerical Simulations

The steady-state analysis and optimisations discussed in the preceding sections may be summarised by plotting both the saturation powers and lengths across the operating spectrum of the XUV-FEL. It has been assumed that the XUV-FEL is operating in an amplifier mode with a seed power equal to 10 % of the peak power available from the seed pulses as described in section 8.2.5.1. The reduction in seed power by a factor of approximately ten conservatively estimates the power available following transmission and focussing losses from the seed laser into the undulator. The seed is assumed focussed to the centre of the first in-use undulator module with Rayleigh length equal to half the module length. This is the configuration shown schematically in Figure 8.7. The seed pulses are 30 fs FWHM and of energy 3 nJ for 6 to 40 eV photons and 1 nJ for 40 to 100 eV giving corresponding approximate peak powers of 100 kW and 30 kW.

The saturation power over the operational spectral range as calculated by both Genesis 1.3 (in steady state mode) and the Xie estimates are shown in Figure 8.26. Both planar and helical mode results are shown. Note that the Xie design formulae cannot take into account mixed planar/helical undulators, so the 'Xie Helical' estimates assume a helical-only undulator for the equivalent length of the planar-helical combination. The Xie estimates also do not include the effects of gaps between undulator modules. These differences account for the small discrepancy of the 'Xie Helical' estimates from the other simulations, in the slightly higher saturation power estimation. Notwithstanding this, the three-dimensional numerical and Xie estimates are in excellent agreement.

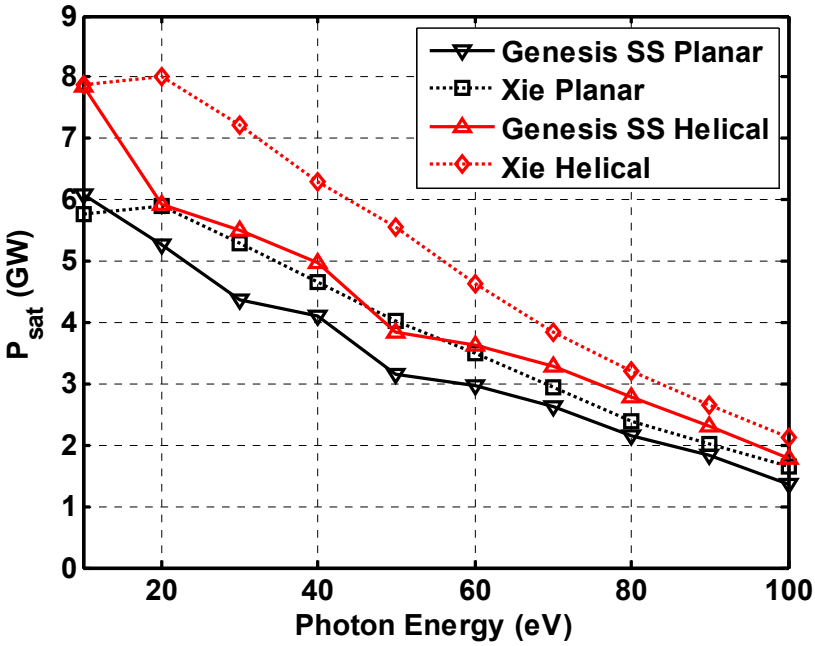

Figure 8.26: Summary of saturation power estimates for the XUV-FEL across its spectral operating range. Genesis 1.3 steady-state (SS) simulations and the Xie formulae are in excellent agreement.

In Figure 8.27, the length of undulator required for saturation, corresponding to that of Figure 8.30, is plotted as a function of photon energy. Note that the gaps between undulator modules are not included in this length and must be added on to obtain the total length of the combined undulator-focussing lattice.

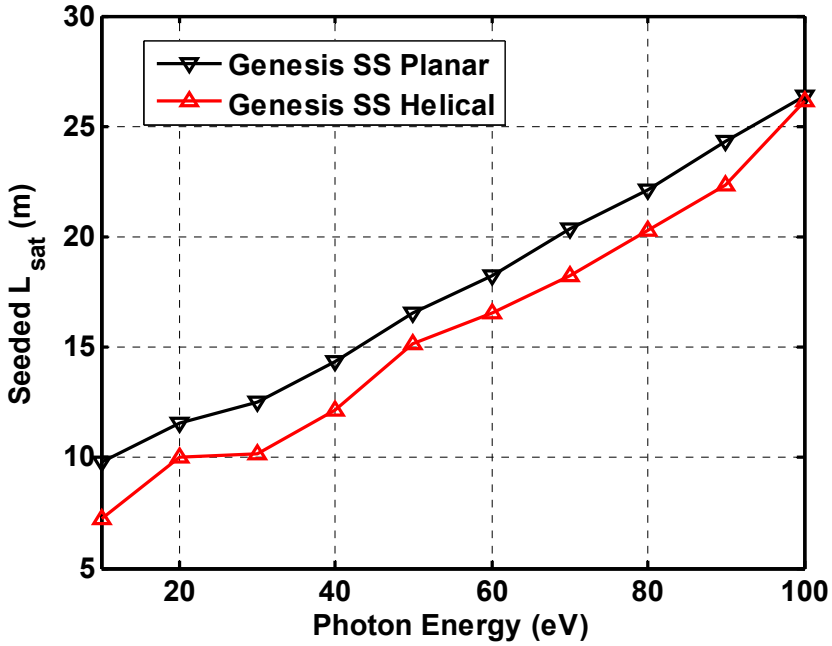

Figure 8.27 Summary of steady-state Genesis 1.3 simulation estimates for the XUV-FEL undulator saturation length across the spectral operating range

8.2.7 Pulsed Amplifier Operation

The preceding analysis and numerical simulations were all carried out in the steady-state limit in which all pulse effects are neglected. These effects are now included into the design model and examples of the HH pulse amplification are shown at the extremes of the XUV-FEL operational range for photon energies of 100 eV and 10 eV.

8.2.7.1 HH Seed Pulse Structure Amplification

The method of seed generation and specification across the XUV-FEL spectral range is described in detail in section 8.2.5. The HH seed has interesting spectral and temporal properties, being composed of a large number of narrow phase-coherent odd harmonics of a fundamental drive laser. This forms a comb structure in frequency-space. However only one of the harmonics, say the n^{th} harmonic, may interact resonantly with the electrons as the FEL gain bandwidth (8-8) is much less than the spacing between harmonics, giving the relation $\rho \ll 1/n$. Thus, it should be possible to inject all of the seed radiation, including all non-resonant harmonics, into the XUV-FEL without the need for band-pass pre-filtering of the seed, as all non-resonant harmonics will simply become negligible relative to the resonant harmonic as the FEL interaction proceeds through the undulator. For the purposes of investigating the effects of injecting all of these harmonics into the XUV-FEL, a Genesis 1.3 simulation was performed with a seed pulse with a power spectral density of the form plotted in Figure 8.28. The peak of the spectral distribution is at the resonant photon energy 100 eV (~ 12.4 nm).

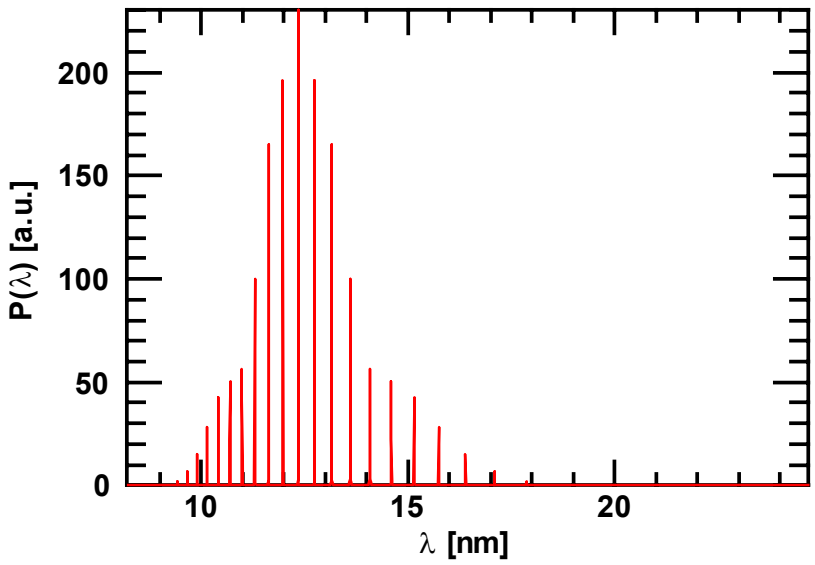

Figure 8.28 Simulated unfiltered HHG pulse power, showing harmonic structure, as a function of radiation wavelength at the beginning of the interaction, z = 0

Such a phase correlated comb in frequency space has a similar comb-like attosecond structure in the temporal domain, detail of which is shown in Figure 8.29. As discussed in section 8.2.5.3 this fine structure is washed out, due to the relative slippage of the radiation through the electrons, as the FEL interaction progresses through the undulator. This is seen from the same detailed region of the radiation pulse at FEL saturation in Figure 8.30: the atto second structure has left no artefacts, having effectively disappeared with only relatively small variations in power across the region. A similar conclusion may be drawn from the spectral power density of the pulse which, in Figure 8.31, shows a single high power emission at the resonant wavelength 12.4 nm. The average power across the simulation window is plotted as a function of distance through the undulator lattice in Figure 8.32. Again, no anomalies are apparent that may be attributed to the injection of the full harmonic seed field.

It is concluded that, at least for these three-dimensional simulations, the injection of the full harmonic content of the HH seed appears to have no adverse effects in the FEL evolution, or in the saturated emission. The same conclusion may be drawn for lower photon energy XUV-FEL operation as relative electron/radiation slippage effects are greater and the ‘wash-out’ process of the short temporal pulse structure may be expected to be enhanced.

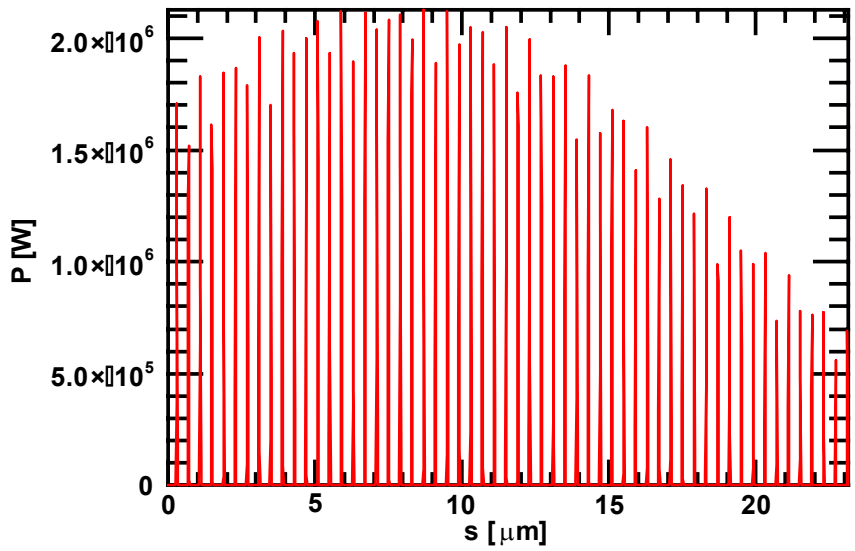

Figure 8.29 Simulated unfiltered HHG pulse power, showing atto-second structure, as a function of local pulse length s, at the beginning of the interaction, z = 0. Only the region about the peak of the electron pulse current is shown.

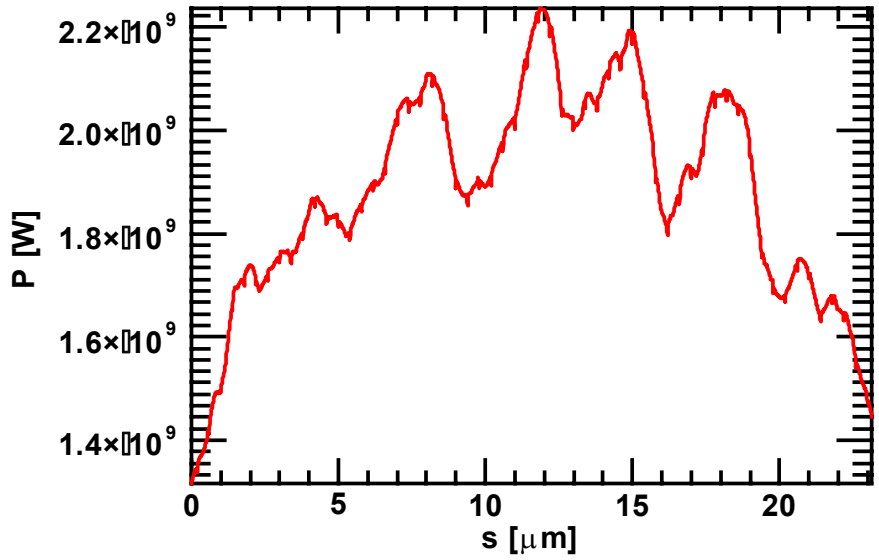

Figure 8.30 Pulse power as a function of local pulse length s, at saturation, z = 23. Only the region about the peak of the electron pulse current is shown.

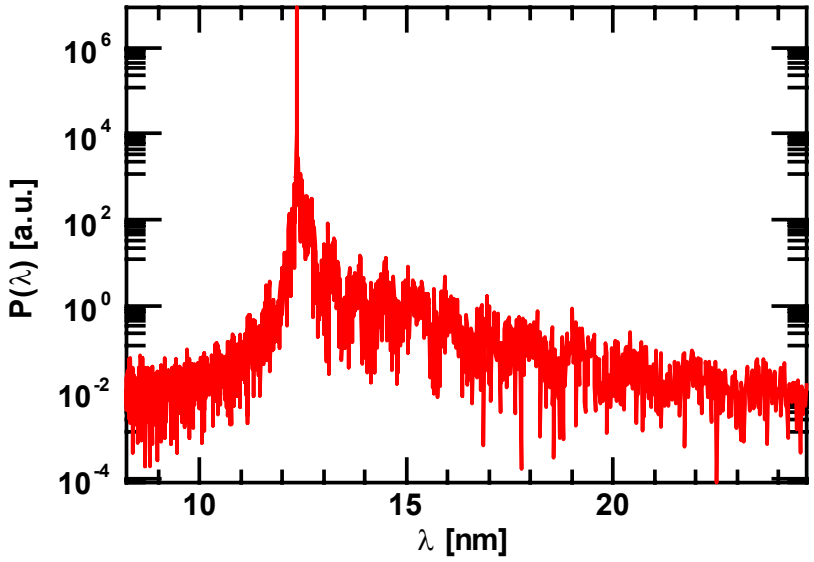

Figure 8.31 Pulse power as a function of radiation wavelength at saturation z = 23. Only the region about the peak of the electron pulse current is shown.

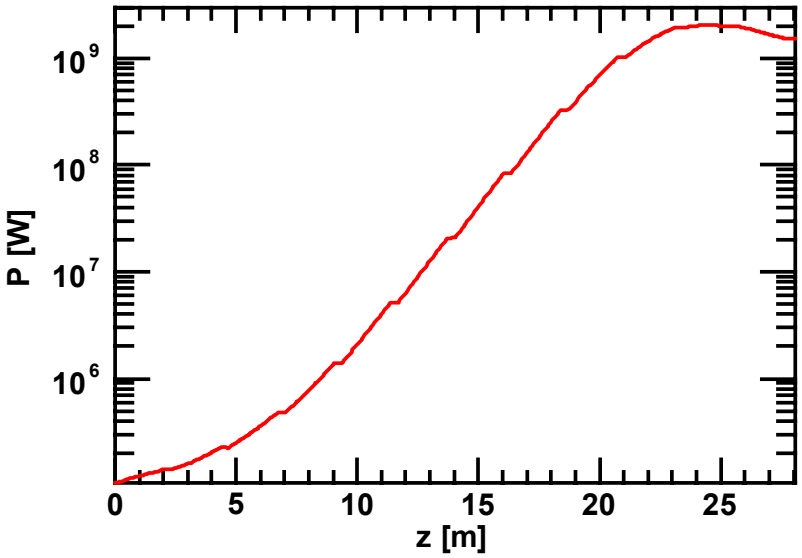

Figure 8.32 Radiation power, averaged over the region about the peak of the electron pulse current, as a function of distance z, through the FEL

8.2.7.2 100 eV Pulse Amplifier Lasing

A complete simulation of the design for the XUV-FEL operating at 100 eV is now demonstrated, using the full set of parameters chosen in the preceding sections. The system modelled is that shown in Figure 8.7 which, for 100 eV operation, uses the full set of planar and variable undulator modules with the FODO lattice incorporated between modules. The variable APPLE-II undulator modules VU1..5 are set to helical mode so that circularly polarised radiation is generated.

The radiation power is plotted in a spatial window that travels along the undulator axis at the speed of light. Figure 8.33 plots the power distribution of the seed pulse of peak power $P_{pk} = 30\,\text{kW}$ and duration 30 fs FWHM at the entrance to the first undulator section, PU1. The seed is assumed to have only the resonant harmonic component so that none of the atto-second structure discussed in the previous section is present. Also plotted to scale is the electron beam current, here assumed Gaussian, of peak current $I_{pk} = 1.5\,\text{kA}$ and duration 626 fs FWHM. At the exit of the planar undulator modules, it can be seen from Figure 8.34 that the peak radiation power has increased to $\approx 70\,\text{MW}$ with little change in the pulse structure or width. This pulse and the co-propagating electrons are then injected into the set of APPLE-II undulators, VU1 to VU5. By the end of this set of undulator modules, it is seen from Figure 8.35 that the FEL interaction has saturated, achieving a peak power of $P_{pk} \approx 2.5\,\text{GW}$ and with duration $\Delta t \approx 60\,\text{fs FWHM}$. The bandwidth of the spectrum is $\Delta\nu/\nu \approx 5.6\times10^{-4}$ which gives a very good time-bandwidth product of $\Delta\nu\,\Delta t \approx 0.8$. For comparison the time-bandwidth product for a transform limited Gaussian pulse is $\Delta\nu\,\Delta t \approx 0.44$. A log-plot of the same data clearly shows in Figure 8.36 the 'clean' central seeded region upon a noisier pedestal. This pedestal is the amplified SASE radiation which remains well below saturation because of the smaller initial spontaneous noise radiation (typically a few tens of watts), compared with the initial seed power of 30 kW. The shape of the saturated pulse power is not quite as gaussian as may be expected which suggests that the FEL interaction may have progressed just past saturation. Taking the output power at the end of the previous undulator module, VU4, and plotting it in a similar log-plot in Figure 8.37, a cleaner gaussian shape can be seen, with a slightly reduced peak power of $P_{pk} \approx 1.5\,\text{GW}$. The shape is confirmed from the pulse duration of $\Delta t \approx 43$ fs FWHM and spectral bandwidth of $\Delta\nu/\nu \approx 6\times10^{-4}$ giving a better time-bandwidth product of $\Delta\nu\,\Delta t \approx 0.63$.

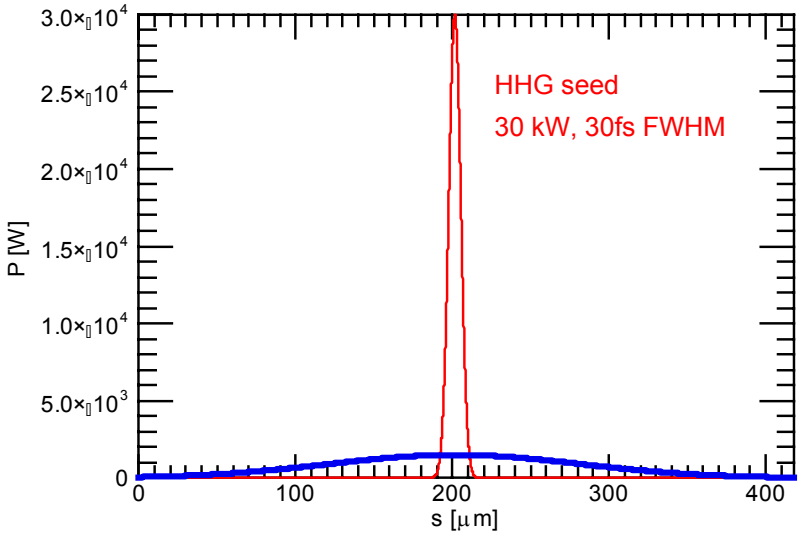

Figure 8.33 Input radiation seed power (red) to PU1 as a function of local distance, s. The electron beam current profile (blue) is also shown against the same numerical scale.

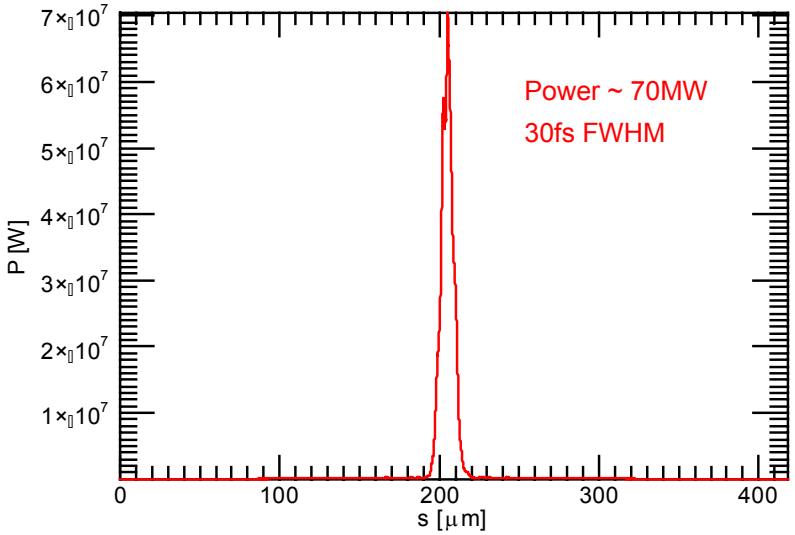

Figure 8.34 The radiation power at the exit of PU8 as a function of local distance, s

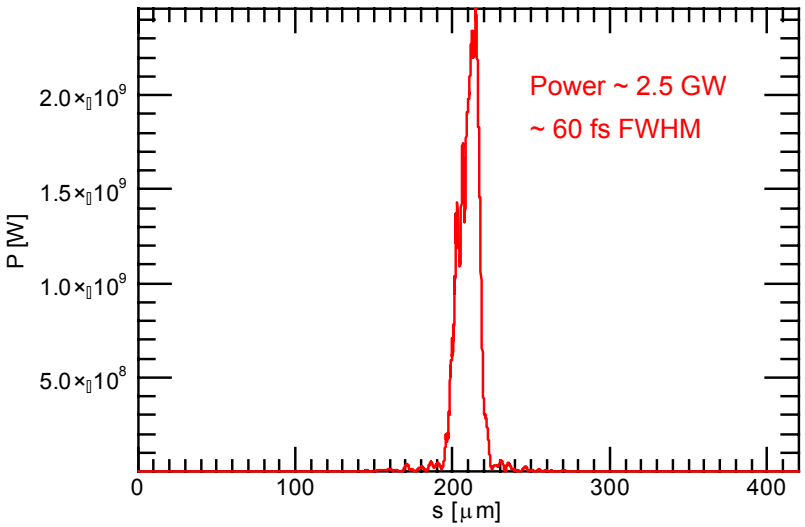

Figure 8.35 The radiation power at the exit of VU5 as a function of local distance, s

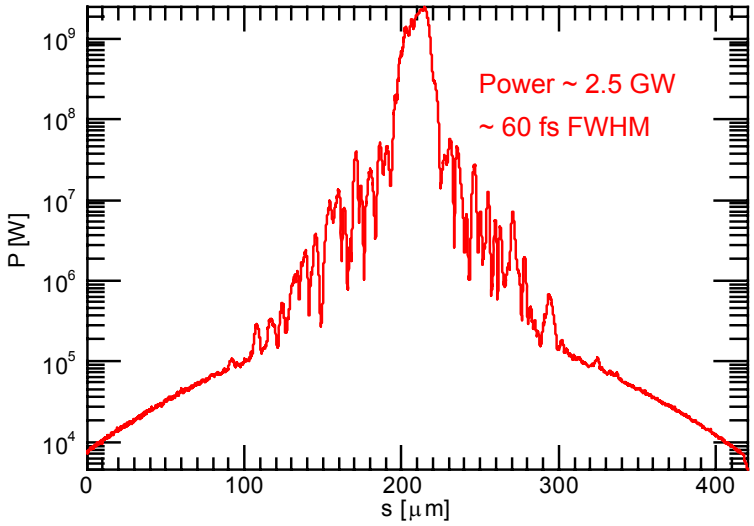

Figure 8.36 A log-plot of the radiation power at the exit of VU5 as a function of local distance, s

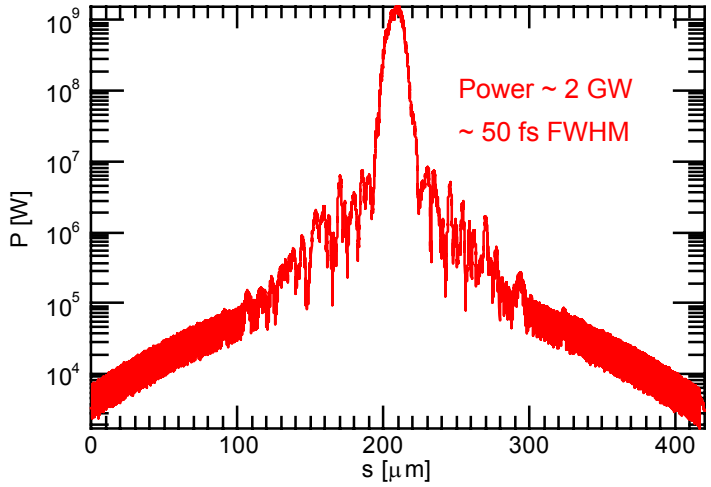

Figure 8.37 A Log-plot of the radiation power at the exit of VU4 as a function of local distance, s

8.2.7.3 10 eV Pulse Amplifier Lasing

Similar modelling to that performed at 100 eV was also carried out for the case of 10 eV operation of the XUV-FEL. Now however, only the APPLE-II type undulator modules VU1 to VU5 are required to achieve saturation as shown schematically in Figure 8.7.

The input seed power is shown in Figure 8.38 with a peak power P_{pk} = 100 kW and duration 30 fs FWHM. Note that the electron pulse current will be the same as that for the 100 eV case of Figure 8.33.

Radiation power output at the end of undulator module VU5 is shown in Figure 8.39 and Figure 8.40 using linear and log scales respectively. Pulse quality is very good with a peak power of $\approx 6\,\mathrm{GW}$ and pulse time-bandwidth product very close to that of a transform-limited gaussian ($\Delta\nu\,\Delta t \approx 0.44$).

If the radiation is instead extracted at the end of undulator VU4, the radiation power output is shown in Figure 8.41. A slightly better contrast between the peak power of $P_{pk} \approx 1\,\mathrm{GW}$ and the SASE pedestal power is seen from that of Figure 8.40, indicating that the power had saturated by the end of VU5. The time-bandwidth product is approximately the same at $\Delta\nu\,\Delta t \approx 0.48$.

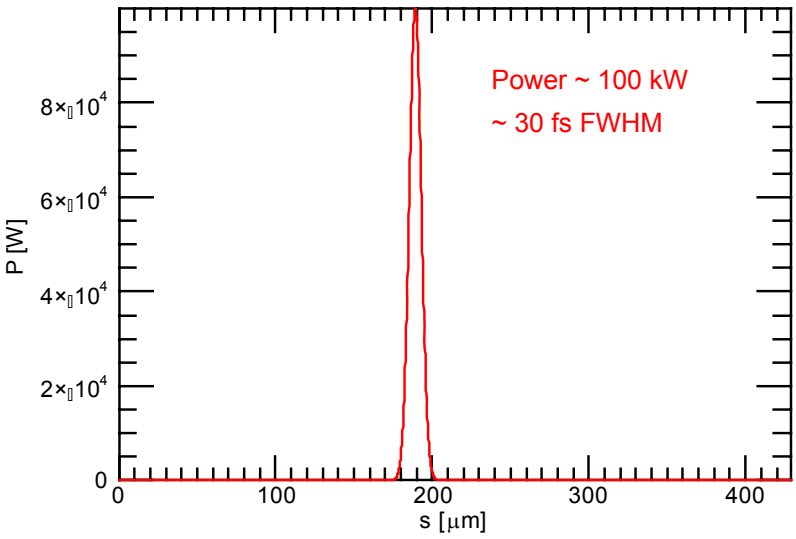

Figure 8.38 Input radiation seed power for 10 eV operation as injected into VU1 as a function of local distance, s. The electron beam current profile is the same as that of Figure 8.33.

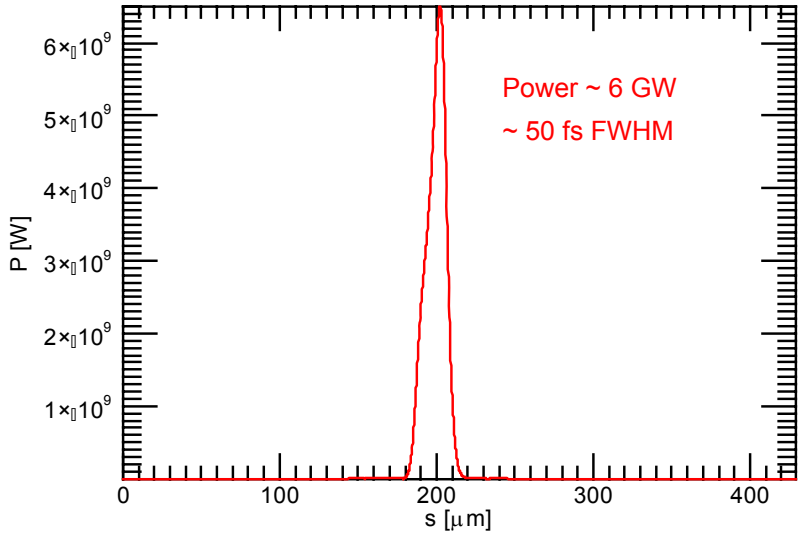

Figure 8.39 Radiation power for 10 eV operation at the end of undulator module VU5, as a function of local distance, s

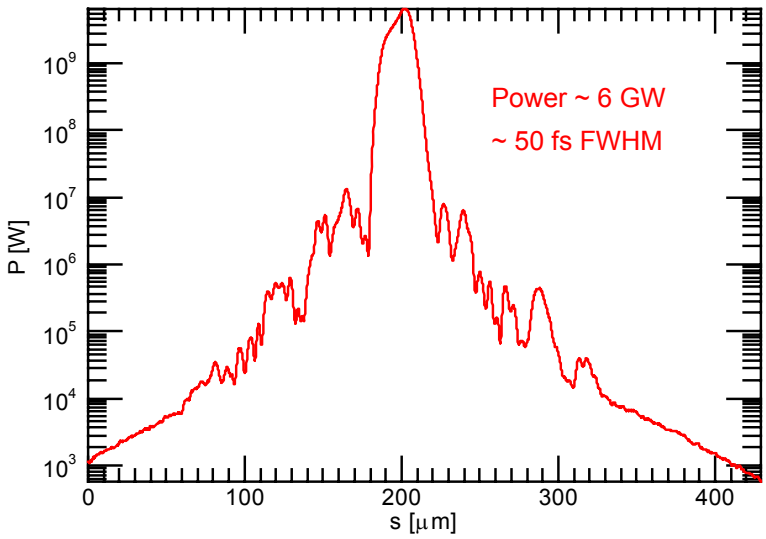

Figure 8.40 Log-plot of the radiation power for 10 eV operation at the end of undulator module VU5, as a function of local distance, s

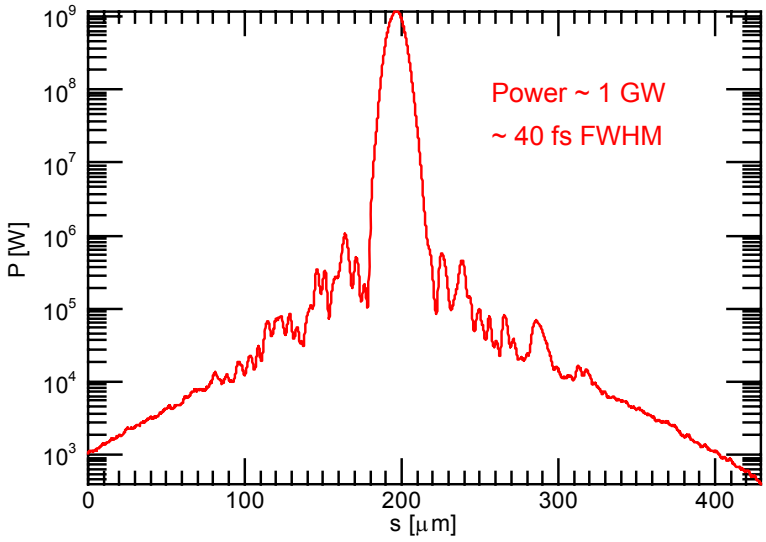

Figure 8.41 Log-plot of the radiation power for 10 eV operation at the end of undulator module VU4, as a function of local distance, s

8.2.7.4 Optimisation of 10 eV Seed Focussing

Time dependent Genesis 1.3 simulations have also been used out to assess the sensitivity of the XUV-FEL output power to the seeding geometry. The assumption is that 10 eV will be the most difficult energy at which to achieve the optimum geometry, because of the long distance between the seed injection point (before PU1) and the first in-use undulator (VU1). This distance is ~ 21 m.

The seed power used is 100 kW, focussed to a waist at the beginning of VU1. Table 8.2, Figure 8.42 and Figure 8.43 show the effect of varying the size of the waist at the focal point. It is found that the optimum seed waist is ~ 200 μm, giving a peak output power of 7.5 GW. The corresponding Rayleigh length is 1.01 m. Xie formulae estimate the gain length at 10 eV to be ~ 0.5 m. Expressed in terms of the gain length the optimum Rayleigh length for a seed focussed at the undulator entrance is found to be $Z_{r,opt} \approx 2L_g$ **.** For this optimum focussing the seed beam radius at the injection point (beginning of VU1) is 4.1 mm. If it is assumed that a full aperture at the injection point of six times the beam radius is needed to minimise diffraction effects, then a vacuum vessel aperture of ~ 25 mm (magnetic gap minus 3mm) at the injection point is sufficient. This can be achieved with the adoption of a step-tapered vacuum vessel, as discussed in section 8.2.2.

The results also show that the output power at the end of VU5 reduces as the seed waist size increases (and consequently the seed radius at the injection point decreases) because saturation is not reached in the fixed undulator length. It is seen from the simulations that the radiation profile is strongly gain guided such that by the start of the third module, VU3, the radiation size has become independent of the input seed size. It appears the seed is strongly focussed by the FEL interaction. It may therefore be beneficial to design for a larger seed waist size than the optimum value of 200 μm. There will be a small reduction in output power, which could be easily countered by focussing the seed to an earlier module (PU8 for example) because the power at saturation is independent of seed power, but due to the increased waist size the dependence of output power on seed source pointing stability will be reduced, leading to improved pulse to pulse stability.

This will be investigated further in future design work but the current conclusion shows that the optimum seed focussing geometry can be obtained with the use of a step-tapered vacuum vessel.

Table 8.2 Summary of investigations of the optimum seeding geometry for 10 eV operation

Seed waist w_0 ***(μm)***	***Rayleigh length (m)***	***Seed radius at injection point*** w_{inj} ***(mm)***	***Clear aperture*** ($\approx 6w_{inj}$) ***(mm)***	***Power at end of VU5 (GW)***
50	0.063	16.5	99.4	5.43
100	0.253	8.3	49.7	6.98
200	1.01	4.1	24.8	7.48
300	2.28	2.8	16.6	7.00
400	4.05	2.1	12.6	6.42
500	6.33	1.7	10.4	5.77
700	12.4	1.4	8.2	4.79
1000	25.5	1.3	7.7	3.52

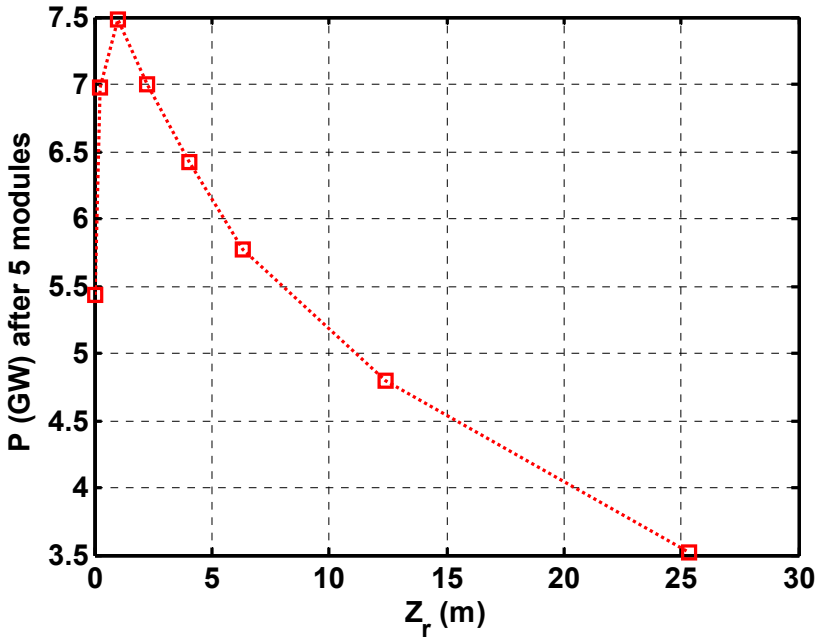

Figure 8.42 Peak radiation power for 10 eV operation at the end of VU5 plotted as a function of seed Rayleigh length

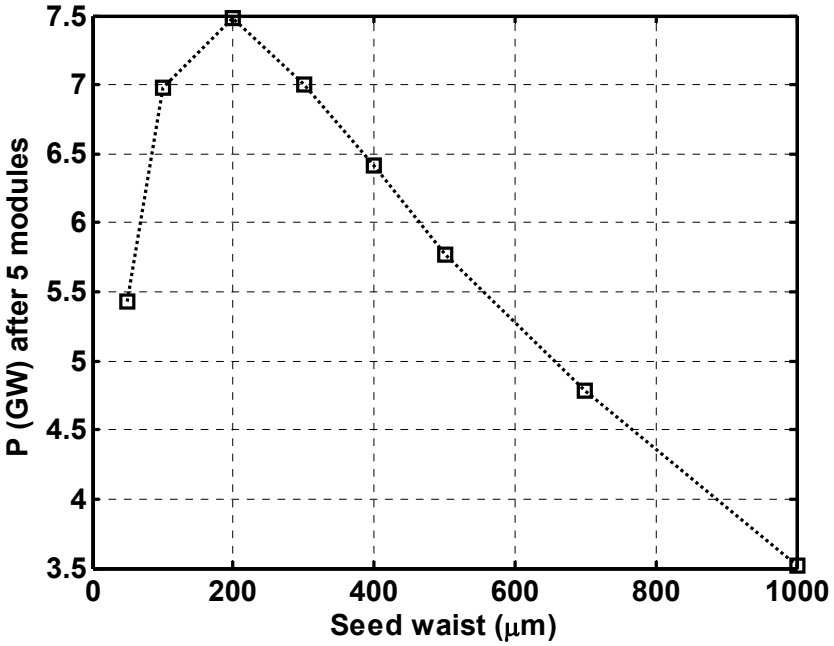

Figure 8.43 10 eV power after VU5 for different seed waists (w_0)

8.2.8 The Effect of Timing Offset Between Seed Pulse and Electron Pulse

The above results assume a coincidence of the HH seed laser peak power and the electron pulse peak current at the beginning of the undulator. However, as discussed in Chapter 12, there is an inherent noise associated with the arrival time of each pulse which results in a relative timing offset of magnitude Δt. For the Gaussian current of RMS width $\sigma_e = 266$ fs assumed here, the current that the seed pulse interacts with is then given by:

$$I(\Delta t) = I_{pk} \exp\left(-\frac{(\Delta t)^2}{2\sigma_e^2}\right) \tag{8-37}$$

The relation between timing offset Δt and current I_{pk} has been used with the Xie formulae [2] to estimate the effects of timing offset upon the gain length L_g and saturation power P_{sat}. It should be noted that this has been done for the parameters of the planar wiggler modules PU1-PU8, making the assumption that the interaction will proceed to saturation in a wiggler of these parameters. Contours of L_g and P_{sat} are plotted as functions of Δt and the resonant photon energy E_{ph} in Figure 8.44 and Figure 8.45 respectively. A fixed electron beam energy of 950 MeV was assumed and tuning over the photon energy range was achieved by varying the undulator gap over the range $0.01 < g(\mathrm{m}) < 0.028$.

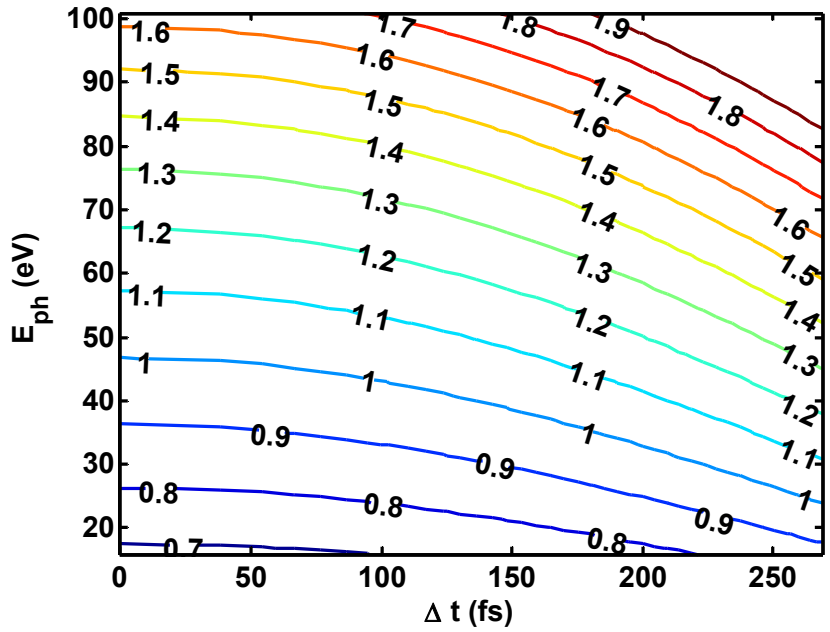

Figure 8.44 Xie formulae predictions of the effect of an offset of Δt from electron/seed pulse coincidence upon the gain length, L_g (m) of the planar modules PU1-PU8, for 950 MeV operation

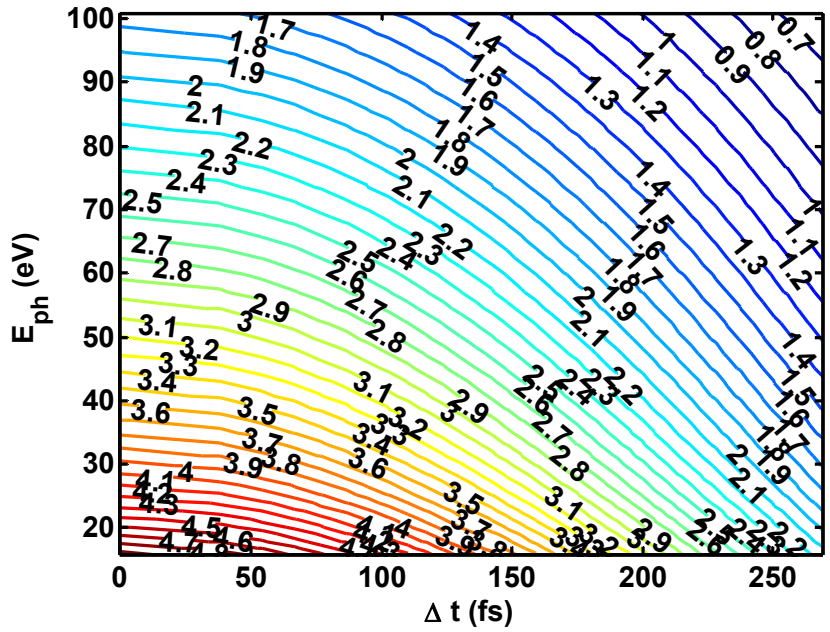

Figure 8.45 Xie formulae predictions of the effect of an offset of Δt from electron/seed pulse coincidence upon the saturation power, $P_{sat}\,(GW)$ for 950 MeV operation. The parameters of the planar modules PU1-PU8 were used for this investigation

From these estimates, for 100 eV operation a 50 fs offset increases the gain length (and hence saturation length L_{sat} from equation (8-6)) by ~ 1.3 %, and decreases the saturation power by ~ 4 %. A 100 fs offset increases the gain length by ~ 5 %, and decreases the saturation power by ~ 13 %.

Genesis 1.3 simulations have also been used to investigate the effect of timing offset on the 100 eV saturation power, again assuming the parameters of the planar modules PU1-PU8 only. The results are shown in Figure 8.46 where to ease comparison the simulation results and the Xie formula results are normalised with respect to their values at $\Delta t = 0$. It is seen that the simulations and the Xie formulae results are in very good agreement.

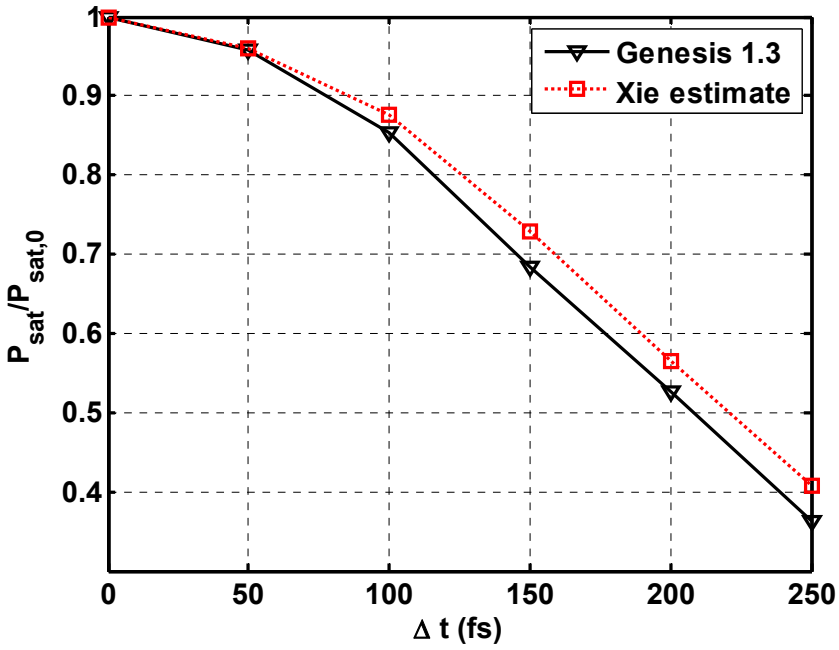

Figure 8.46 Results of simulations of the effect of an offset Δt from electron/seed pulse coincidence upon the saturation power, $P_{sat}(GW)$ for 100 eV output. The parameters of the planar modules PU1-PU8 were used for this investigation. Also shown for comparison are the Xie formula estimates from Figure 8.45. To ease comparison the Genesis 1.3 results and the Xie formula results are normalised with respect to their values at $\Delta t = 0$.

It may be possible to compensate for the effects of temporal offset upon the XUV-FEL output by allowing the FEL interaction to slightly over-saturate. It was seen in the simulations of Figure 8.36 and Figure 8.37 that an increase in length of one full undulator module (corresponding to ~ 8 % of the total undulator length) only slightly changed the properties of the output power and temporal width of the photon pulse.

These effects will need to be studied further in future design work which will also incorporate more realistic non-gaussian electron pulses from the start-to-end simulations, but the conclusion drawn now is that a timing offset of < 50 fs would have a negligible effect on the FEL output

power, and that a timing offset of 80 fs would cause a reduction of ~ 10 % in output power. The RMS timing 'jitter' (the statistical distribution of timing offsets) should therefore be kept to less than 50 fs: this would ensure that the FEL pulse-to-pulse power variation is less than 10 % for 90 % of the pulses.

8.2.9 Extension to 6 eV

An option to extend the lower photon energy range to 6 eV has been investigated. The design option considered requires reduction of the minimum undulator gap to 8 mm (5 mm vacuum gap) and an increase in the period of the VU modules to 53 mm. The tuning curves are shown in Figure 8.47 for planar mode and Figure 8.48 for helical mode. Investigations of the effects of increased wakefields on the electron beam are encouraging and the saturation powers predicted by the Xie design formulae and Genesis simulations only slightly reduced at higher photon energies from the baseline 10 - 100 eV design. The saturation power is slightly increased at 6 eV compared to 10 eV, and the saturation length slightly reduced. The seed design put forward in section 8.2.5 already covers the range 6-100 eV. Further work will be undertaken in the next design phase, but is clear that there are no technical obstacles to extending the photon energy range down to 6 eV and that this can be achieved with only small changes to some parameters.

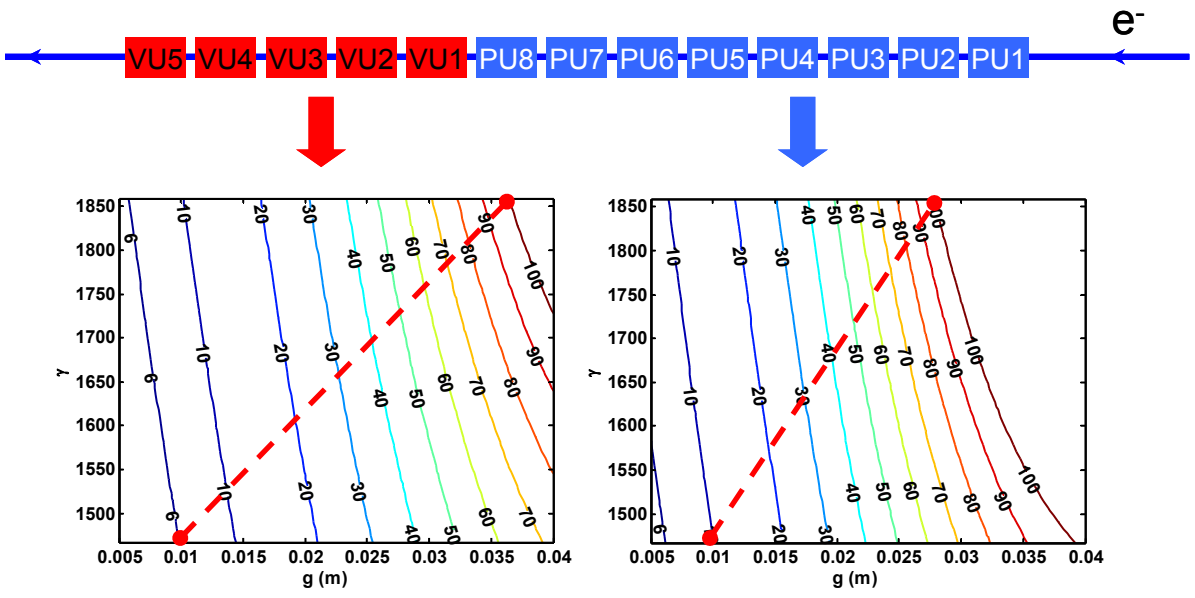

Figure 8.47 Tuning contours of the resonant photon energy (6 - 100 eV) as a function of the electron beam relativistic parameter (E_0 = 750 - 950 MeV) and the undulator magnetic gap g. The variable polarisation undulators VU1..5 are set to planar mode so that output radiation is linearly polarised.

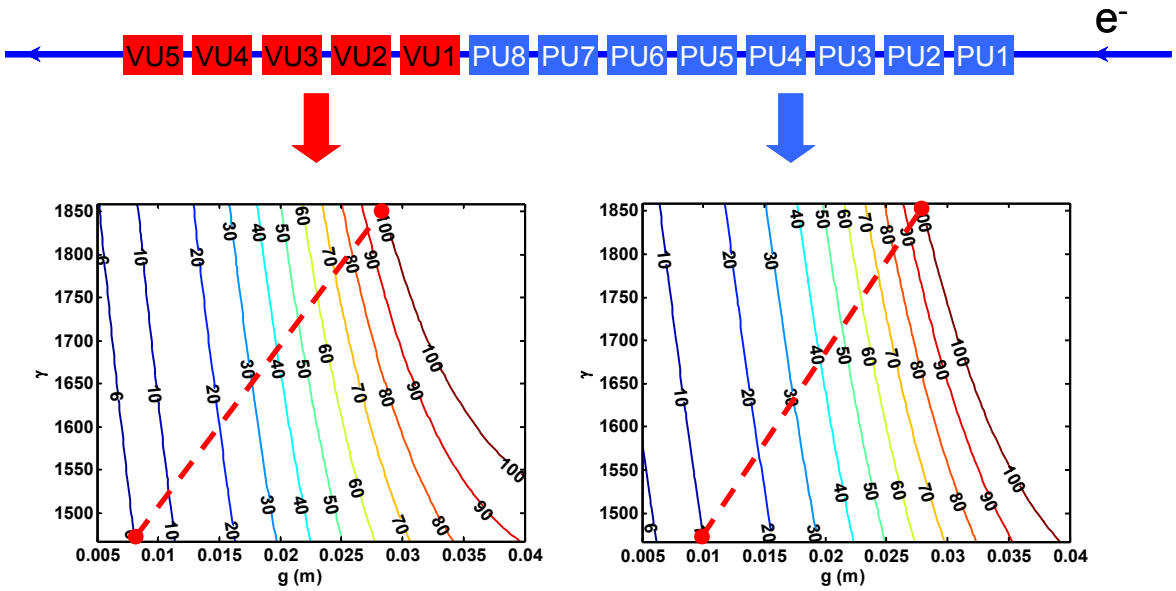

Figure 8.48 Tuning contours of the resonant photon energy (6 - 100 eV) as a function of the electron beam relativistic parameter (E_0 = 750 - 950 MeV) and the undulator magnetic gap, g. The variable polarisation undulators VU1 to VU5 are set to helical mode so that output radiation is circularly polarised.

8.2.10 Summary

A robust conceptual design for the XUV-FEL has been developed, the main parameters of which are summarised in Table 8.3. Established FEL theory and state-of-the-art simulation codes predict this free-electron laser will generate photons of giga-watt power levels in pulses of duration 40-60 fs FWHM. The design specification presented here is optimised for 10 - 100 eV operation but it is demonstrated that extension to the revised photon energy range of 8 - 100 eV requires only small parameter changes. The FEL pulses will have very good temporal and spatial coherence with time-bandwidth products close to the Fourier transform limit for a gaussian pulse. Unlike the SASE mode of operation, which effectively self-starts from intrinsic noise, the FEL interaction here is truly acting as a simple, bandwidth limited amplifier. So long as the radiation input seed pulses have sufficient spectral purity, the output radiation is very nearly a simple amplified version of the input. Recent advances in HHG sources ensure that the seed requirements for the XUV-FEL already exist.

Research in the next design phase will require full start-to-end simulations from the electron gun through to the end of the undulator. This will allow the modelling of the FEL interaction with a more realistic electron pulse than that used here which assumes a gaussian variation of most variables. Investigation of tolerances, for example in quadrupole position and undulator field errors, will also be required, as will a more detailed study of the effects of relative electron-seed pulse jitter.

Table 8.3 Summary of XUV-FEL parameters

DESCRIPTION	
FEL design	High Gain Amplifier
Seeding type	External seeding
Seeding mechanism	HHG source
PHOTON OUTPUT	
Tuning Range	8 - 100 eV
Peak Power	~8 - 2 GW
Repetition rate	1 kHz
Polarisation	Variable elliptical
Min Pulse length FWHM	< 50 fs
Typical $\Delta\nu\Delta t$	~0.6
Max pulse energy	400 μJ
ELECTRON BEAM PARAMETERS	
Energy	750 - 950 MeV
Bunch Charge	1 nC
RMS bunch length	266 fs
Normalised emittance	2 mm mrad
RMS energy spread	0.1 %
UNDULATOR PARAMETERS	
Undulator Type	PPM & APPLE-II
No of Modules	8 & 5
Module length	2 m
Period	45 mm & 51 mm
Focussing	FODO
Minimum gap	10 mm

8.3 VUV-FEL Conceptual Design

8.3.1 General Specification

The VUV-FEL is required to deliver intense sub-picosecond pulses of tuneable coherent radiation in the photon energy range 3 – 10 eV (413 – 124 nm). Figure 8.49 shows a schematic of the 600 MeV High Average Current Loop (HACL) operating in energy recovery mode (~77 pC bunches at up to 1.3 GHz) which will feed spontaneous sources and the VUV-FEL. The electron bunch repetition rate for VUV-FEL operation has a minimum value of 4.33 MHz to match the optical cavity frequency. It will also be possible to operate the VUV-FEL at integer multiples of 4.33 MHz subject to the limitations of average power load on the optics. The maximum repetition rate will be determined in future optics design work. A description of the HACL that provides the electron pulses is given in Chapter 8. The HACL generates electron pulses of duration ~ 250 fs FWHM and peak current ~ 300 A. The VUV-FEL is therefore an integral component of the HACL which limits the possible undulator length. This spatial limitation, in addition to the lower electron bunch charge than that available to the XUV-FEL, means that there are insufficient gain lengths to allow saturation of the FEL starting from noise, i.e. in SASE mode. An externally supplied seed laser, as used in the XUV-FEL, will reduce the number of gain lengths required to achieve saturation and may allow the VUV-FEL to saturate. However, the repetition-rates of the electron pulses in the HACL, from MHz frequencies to a maximum of 1.3 GHz, are much greater than those available from potential seed lasers, typically ~ 1 kHz.

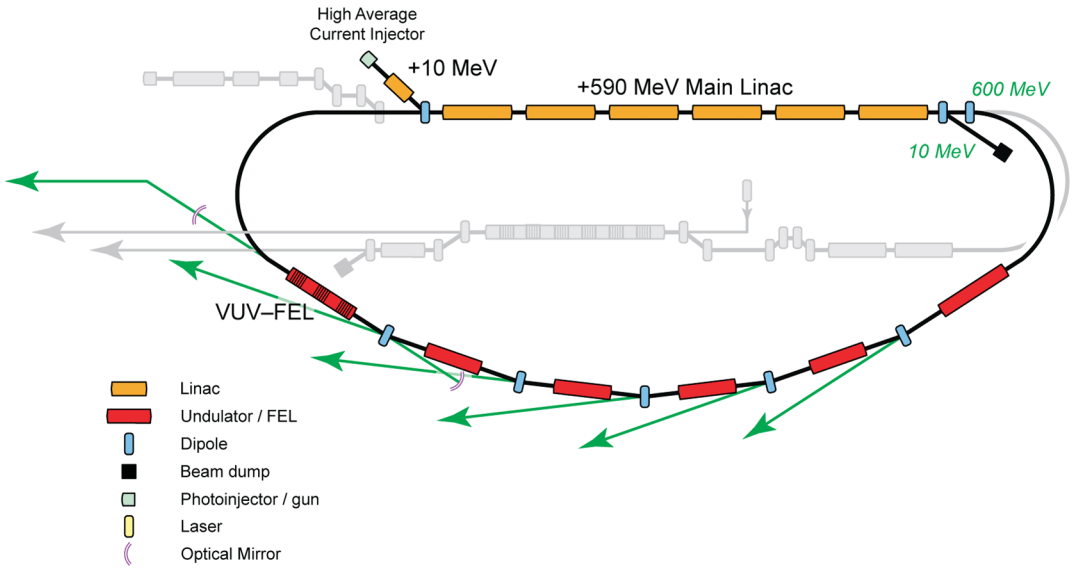

Figure 8.49 Schematic showing the main components relevant to the VUV-FEL

The design therefore uses a self-seeding scheme, the RAFEL, as described in section 8.1.5. The RAFEL uses a low-Q cavity constructed with relatively low reflectivity mirrors and mirror-hole out-coupling. It is anticipated that over the 413 – 124 nm wavelength range required, a broadband reflectivity of 60 % can be obtained using aluminium mirrors with a fluoride coating [71]. Due to the high gain, saturation can be achieved in a few passes of the radiation through the cavity (typically < 20).

8.3.2 Undulator Lattice and Module Specification

A similar undulator lattice design as the XUV-FEL has been chosen and is shown in Figure 8.50. As with the XUV-FEL, relatively short undulator sections are employed with a strong FODO focussing lattice and beam diagnostics distributed between the undulator sections. By keeping the undulator section length relatively short, a more tightly focussed electron beam with smaller variation in the electron beam β-function than that possible from longer sections is ensured. The better electron-radiation coupling that results yields shorter gain lengths.

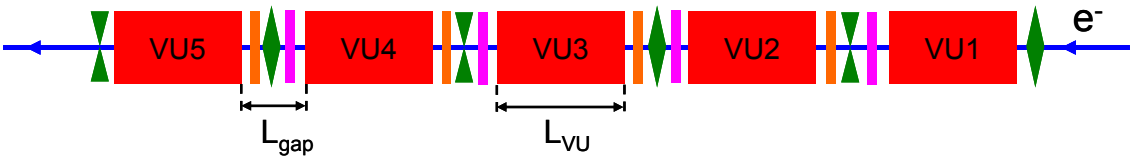

Figure 8.50 Schematic of the sectional undulator system of the VUV-FEL. Undulator sections VU1..5 (red) are variable polarisation undulators. The gaps between undulator sections contain a beam position monitor, focussing quadrupole and radiation/electron phase matching unit.

In order to achieve output with variable polarisation across the photon energy range 3-10 eV, APPLE-II type undulators are employed for all undulator sections. Resonant photon energy tuning contours for the fixed electron beam energy of 600 MeV of the HACL in an APPLE-II undulator are shown in Figure 8.51 for planar and helical mode operation.

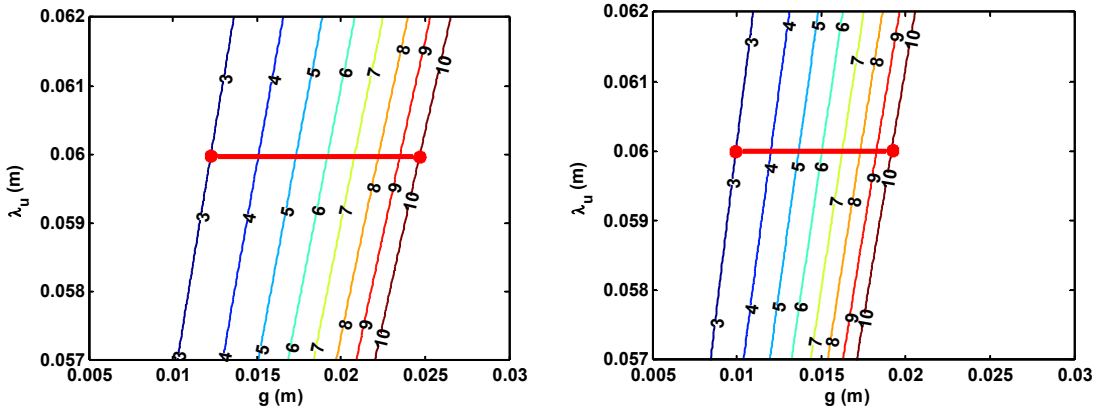

Figure 8.51 Resonant photon energy (eV) contours as a function of undulator magnetic pole gap and period for an APPLE-II variable polarisation undulator in planar mode (left) and helical mode (right). The electron beam energy is 600 MeV.

Because of the fixed electron beam energy, tuning of the VUV-FEL can only be achieved by variation of the undulator magnetic gap. To ensure a design minimum gap of $g = 10$ mm it is seen that a minimum undulator period of $\lambda_u = 60\text{mm}$ is required for 3 - 10 eV operation. With this undulator period, and for the $N = 37$ periods per module required to achieve sufficient gain over the five modules VU1 to VU5 as discussed below, the design length of the VUV-FEL undulator section is $L_{VU} = 2.2\,\text{m}$. As with the XUV-FEL, the gap between undulator sections is chosen to be $L_{gap} = 0.6\,\text{m}$ to allow space for the BPMs, focussing quadrupoles and phase matching units. The total length of the FEL interaction region, including undulator sections and section gaps is therefore, $L_U = 13.5\,\text{m}$. The quadrupoles of the FODO lattice have magnetic length 0.12 m and field gradients of 9 T/m.

In section (1.1.5), as part of the discussion of the RAFEL concept, it was shown that for a sufficiently long FEL interaction, $\bar{z} \cong 4$, the intracavity power can actually be increased by increasing the cavity losses. Steady state Genesis 1.3 simulations have been used to model the undulator and focussing lattice to numerically determine the gain length L_g, the FEL parameter ρ and hence the scaled undulator length $\bar{z}$. This was carried out for 3 eV and 10 eV operation, in both planar and helical modes. Due to the effect of the inter-module gap the calculated gain length is larger than the Xie estimate of section 8.3.3, so that a module length of 2.2 m is required to provide a good enough coupling for RAFEL operation over all wavelengths and polarisation modes. The numerical estimates for the 2.2 m modules are summarised in Table 8.4.

Table 8.4 Results of Genesis 1.3 steady state simulations used to estimate numerically the scaled undulator length $\bar{z}$

	Planar			***Helical***		
	L_g	ρ	$\bar{z}$	L_g	ρ	$\bar{z}$
10 eV	1.81 m	1.52×10^{-3}	3.52	1.24 m	2.22×10^{-3}	5.16 (5 mods)
						4.13 (4 mods)
3 eV	1.38 m	2.00×10^{-3}	4.64 (5 mods)	0.87 m	3.17×10^{-3}	7.38 (5 mods)
			3.71 (4 mods)			5.90 (4 mods)
						4.43 (3 mods)

8.3.3 Electron Beam Quality

Layout considerations dictate an undulator length no greater than approximately 10 m, plus some allowance for gaps between undulator modules. From the definitions of the gain length L_g and $\bar{z}$ given in section 8.1.2, the relation:

$$L_g = \frac{L_u}{\sqrt{3\bar{z}}} \tag{8-38}$$

yields the result that for the conditions $\bar{z} \geq 4$ and $L_u = 10$ then the gain length $L_g \leq 1.44$.

The Xie design formulae have been used to determine the peak current that meets this gain length requirement for 10 eV operation. Given the undulator parameters of section 8.3.2, the relative RMS energy spread of $\sigma_\gamma = 0.1\%$ and normalised emittance of $\varepsilon_n = 2$ mm mrad, it is seen from Figure 8.52 that the electron beam peak current must satisfy $I_{pk} \gtrsim 300\,\mathrm{A}$.

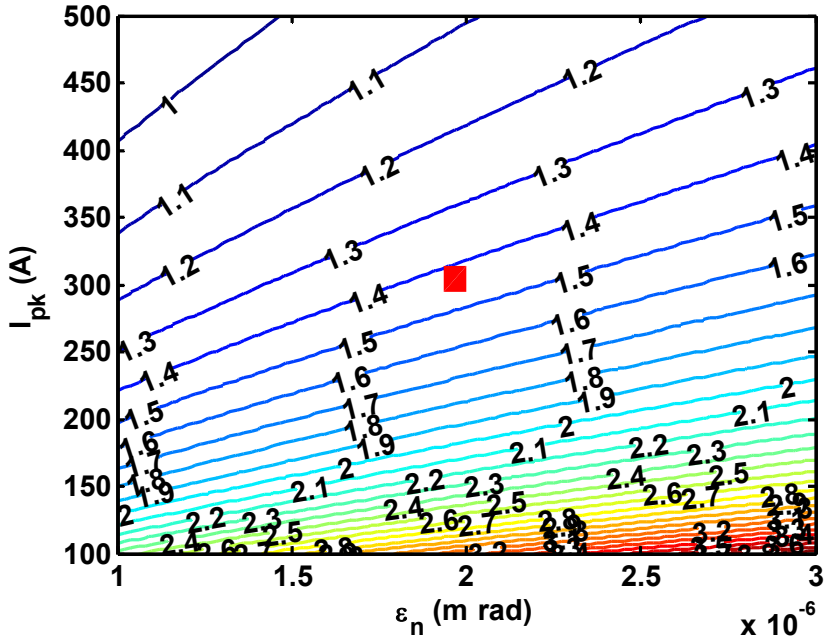

Figure 8.52 Contours of gain length L_g (m) as a function of electron beam peak current and normalised emittance, assuming an energy spread $\sigma_\gamma = 0.1\%$. The red square denotes the design working point.

8.3.4 Feedback Cavity

The aim of the cavity in a RAFEL is to provide just sufficient feedback of the radiation emitted by an electron pulse through the FEL to enable the FEL interaction of following electron pulses to saturate via the high-gain FEL mechanism. Because in the RAFEL the undulator is several gain lengths long, the gain is high and a low-Q cavity provides sufficient feedback allowing most of the FEL radiation generated to be out-coupled. While the combination of high gain and a low-Q cavity make the concept of cavity mode analysis as discussed below rather tenuous, it provides a useful starting point in the design of cavity geometry and will be used to inform a more complete three-dimensional model using a modified version of the Genesis 1.3 FEL code incorporating a full simulation of the cavity optical elements.

A schematic for the first iteration of the VUV-FEL cavity design is shown in Figure 8.53. The optical mode profile shown is the TEM_{00} mode for 10 eV output. Radiation is coupled out of the cavity by means of a hole-outcoupled mirror. The radii of curvature of the outcoupling mirror, r_2, the feedback mirror, r_1 and the lengths $L_{1,2}$ are chosen to achieve a radiation beam focussed towards the beginning of the FEL interaction region as shown. For each cavity round trip, this geometry results in a good coupling between the returned seed field and the new electron pulse entering the interaction region. For this design study: r_1 = 12.85 m, r_2 = 22.75 m, L_1 = 10 m and $L2$ = 11.1 m. The minimum repetition-rate of the electron pulses at the entrance to the undulator is the inverse of the cavity round trip time, $f_{cav} = c/2L_{cav} = 4.33\,\text{MHz}$. The cavity stability parameter is $g_1 g_2 = 0.88 < 1$.

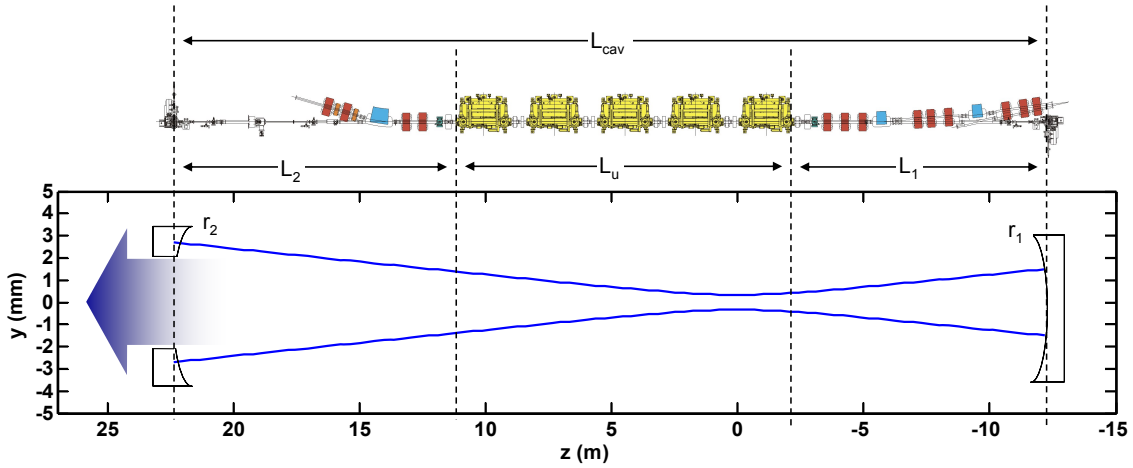

Figure 8.53 Schematic of the first iteration of the VUV-FEL low-Q cavity. Shown aligned on the same longitudinal scale is an engineering representation of the VUV-FEL. The radius of curvature, r_2, of the hole-outcoupling mirror is greater than that of the upstream mirror, r_1. This cavity design has a minimum beam waist nearer the entrance to the undulator assisting the self-seeding process.

While high reflectivity mirrors for photon energies $\lesssim 6\,\mathrm{eV}$ are in principle relatively simple to make, this becomes increasingly difficult with current transmissive mirror technology for photon energies exceeding 6 eV. However, by adopting a hole-outcoupled output mirror design, relatively robust mirrors may be constructed. Figure 8.54 plots a typical spectrum of a good VUV aluminium mirror with MgF_2 protection [72].

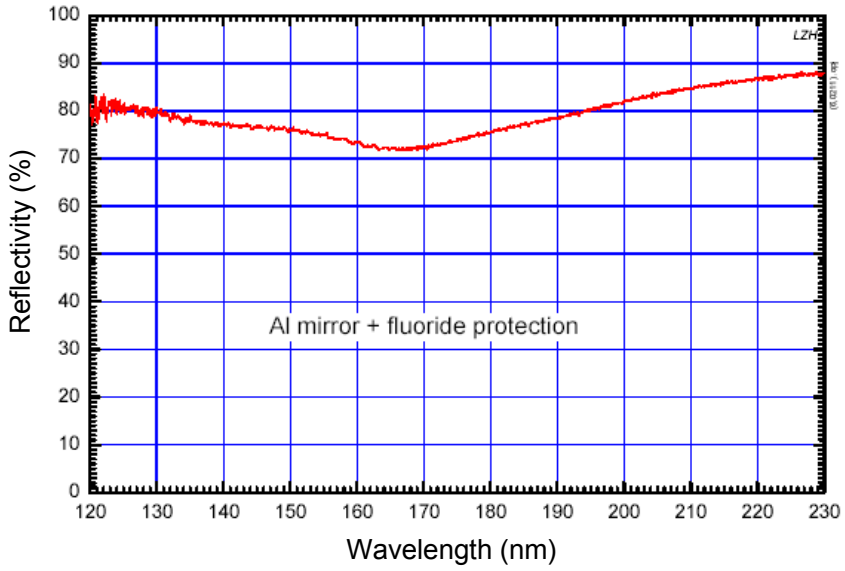

Figure 8.54 Typical spectrum of a good VUV Al mirror with MgF_2 protection

The next design phase of the 4GLS project will require further research to develop suitable mirror technology in the 6 - 10 eV photon energy range. For the purposes of this design it is assumed that mirrors of 60 % reflectivity will be available and used in the construction of the VUV-FEL cavity. It should be noted that this figure is not critical and, as was shown in section 8.1.5, lower mirror reflectivities of even 40 % will still allow effective VUV-FEL operation at the expense of increased power absorption and thermal load.

8.3.5 Simulation of the VUV-FEL

Simulations have been carried out in three-dimensions using Genesis 1.3 in the steady state approximation, which assumes an infinitely long electron beam, and also including full temporal pulse effects. At this stage of the design process, full modelling of the cavity has not been possible as Genesis does not include the option of including optical elements in the model. However, a Dutch group at the University of Twente are currently extending the code to include them. Collaboration of the 4GLS design team with this group has ensured that hole-outcoupling mirrors etc. will be included in a future release of Genesis expected mid-2006. In order to model the RAFEL in three dimensions here, we use sequential runs of the Genesis code with the radiation output fed back after being reduced by the feedback factor F (see section 1.1.5) and used as a seed field for the subsequent pass through the cavity. The first pass starts from shot noise.

In the simulations that follow, the parameters used were not identical to the design parameters given above because the work was done before the final design parameters were chosen. The simulation parameters yield results that differ only in fine detail and the conclusions drawn and FEL output parameters presented remain valid for the purposes of this design report.

8.3.5.1 Steady-State Simulation in Three Dimensions

Genesis 1.3 has been used in steady-state mode to model the RAFEL and confirms the main results and conclusions of the one-dimensional model of section 8.1.5, where it was seen that the RAFEL principle worked well for scaled undulator lengths of $\bar{z} \approx 4$. A discussed above this can be achieved, in combination with appropriate electron beam parameters, with an undulator length (excluding inter-module gaps) of 11 m. Typical undulator lengths required for SASE saturation using the same electron beam parameters are approximately a factor three greater at $\approx 30\,\mathrm{m}$. An undulator of such length would present significant challenges in the design layout of the facility.

A cavity with fixed outcoupling of α = 75 % is assumed and the RAFEL is simulated for a range of mirror reflectivities $R = 40\%, 80\%$ and 95% . In Figure 8.55 the evolution of the output power is plotted as a function of the number of passes through the cavity for 10 eV photon operation. The output power at saturation is seen to be $\approx 400\,\mathrm{MW}$ after six passes for mirror reflectivities of $R = 80\%$ and 95% . This increases to $\approx 430\,\mathrm{MW}$ for a decrease of the mirror reflectivity to $R = 40\%$. This perhaps counter-intuitive result is explained by the evolution of the intracavity radiation power through the undulator at saturation and is shown in Figure 8.56

for 95 % and 40 % mirror reflectivities. For 95 % mirror reflectivity, the high gain FEL interaction is seen to over-saturate (full saturation occurring at around 7 m). However, for 40 % mirror reflectivity, the intracavity power at the start of the pass at z = 0 is optimised so that full saturation occurs exactly at the end of the undulator at z = 9.3 m. This will take only a few extra passes to achieve, which is negligible on the time scale of the 4.33 MHz repetition-rate of the pulses.

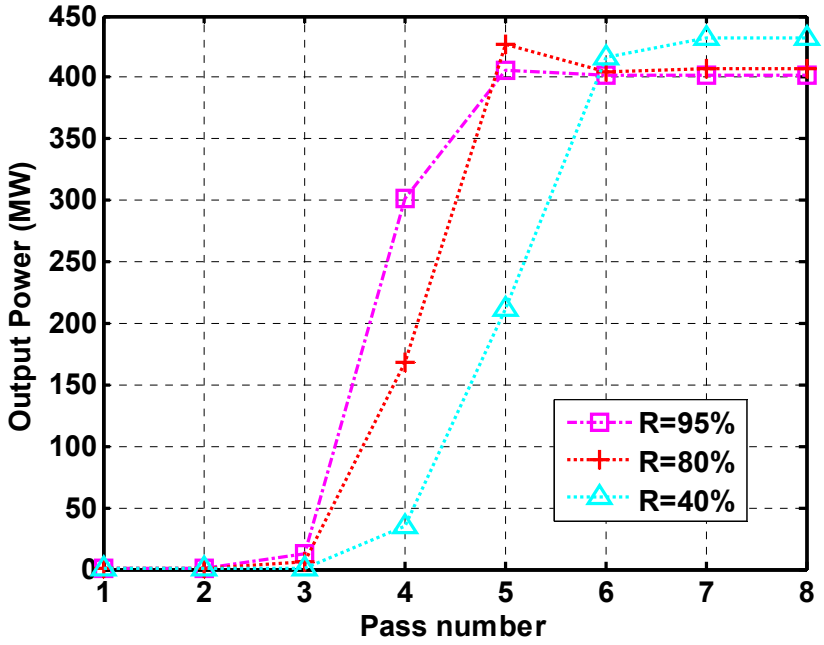

Figure 8.55 Three-dimensional steady-state simulation of the VUV-FEL operating at 10 eV photon energy. The output power is plotted as a function of optical pass number through the cavity for an outcoupling factor of α = 75% and for three different mirror reflectivities.

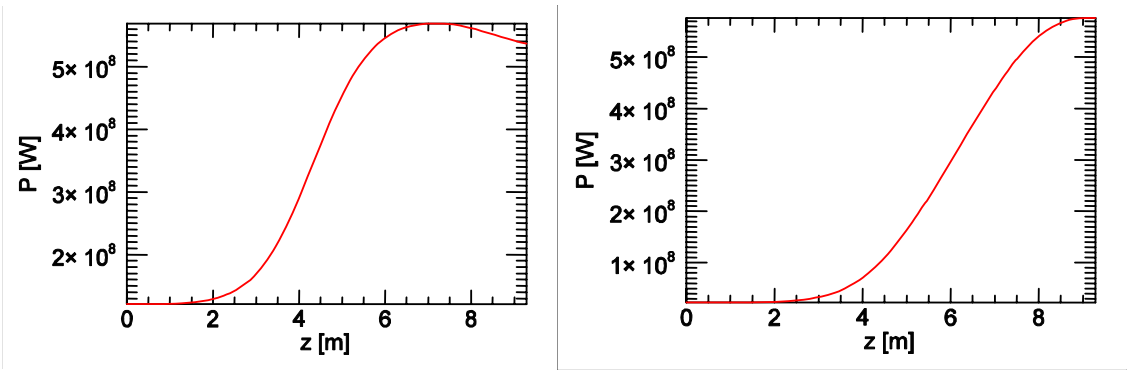

Figure 8.56 Power evolution of the radiation through the undulator at cavity saturation for the case of 95 % mirror reflectivity (left) and 40 % reflectivity (right). For 95 % reflectivity the FEL power oversaturates, whereas for 40 % reflectivity the power saturates exactly at the end of the undulator, leading to optimum outcoupled power.

8.3.5.2 Pulse Simulation in One Dimension

The additional contribution of the effects of finite pulse length on the operation of the VUV-FEL results in greater opportunities and flexibility in the expected performance. The two principal benefits that may be expected over that of SASE-type radiation pulses are an improved temporal coherence, and greater control over the radiation pulse power profile through the use of cavity detuning.

The latter effect can be seen clearly in one-dimensional simulations of the VUV-FEL at 10 eV, with parameters as above and with mirror reflectivity of $R = 60\%$. Figure 8.57 plots the peak power and pulse width (FWHM) as a function of the cavity detuning δ_c. Positive values of δ_c shorten the length from cavity-resonance. Shortening of the cavity may be used to compensate for the so-called radiation 'lethargy' where the group velocity of the radiation in the cavity appears to be less than the speed of light. This happens because the electron pulse emission occurs towards the end of the undulator (when the electrons are strongly bunched and emitting coherently) and so the radiation emission appears retarded.

From Figure 8.57 it can be seen that close to cavity resonance, $0 \lesssim \delta_c \lesssim 6\,\mu\text{m}$, the radiation pulse width is around 30 fs FWHM, an order of magnitude less than the electron pulse width of 250 fs FWHM. Also, pulse peak powers are significantly greater than the $\approx 400 - 430$ MW predicted by the steady-state simulations of Figure 8.55. A plot of the shape of the pulse output power, at cavity resonance $\delta_c \approx 0$ is shown in Figure 8.58. This pulse shape is typical of superradiant radiation with a narrow, high peak power spike followed by secondary pulses or ringing. Both the pulse narrowing and high peak powers typify emission of the superradiant FEL regime which also occurs in low-gain FEL oscillator systems – see section 8.4.9.

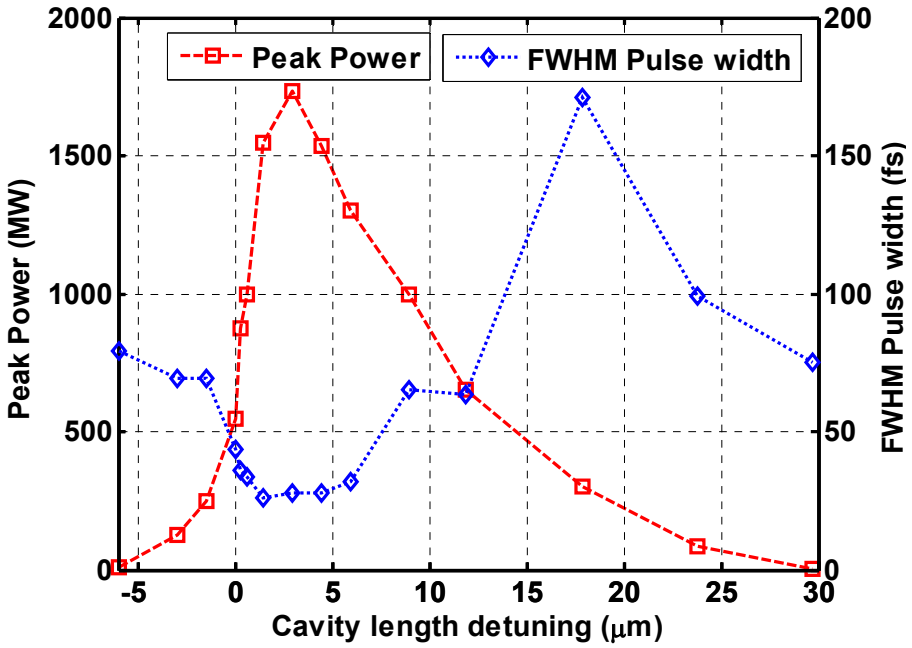

Figure 8.57 Peak power (red) and FWHM pulse width (blue) as a function of VUV-FEL cavity detuning. The parameters are for 10 eV photon output.

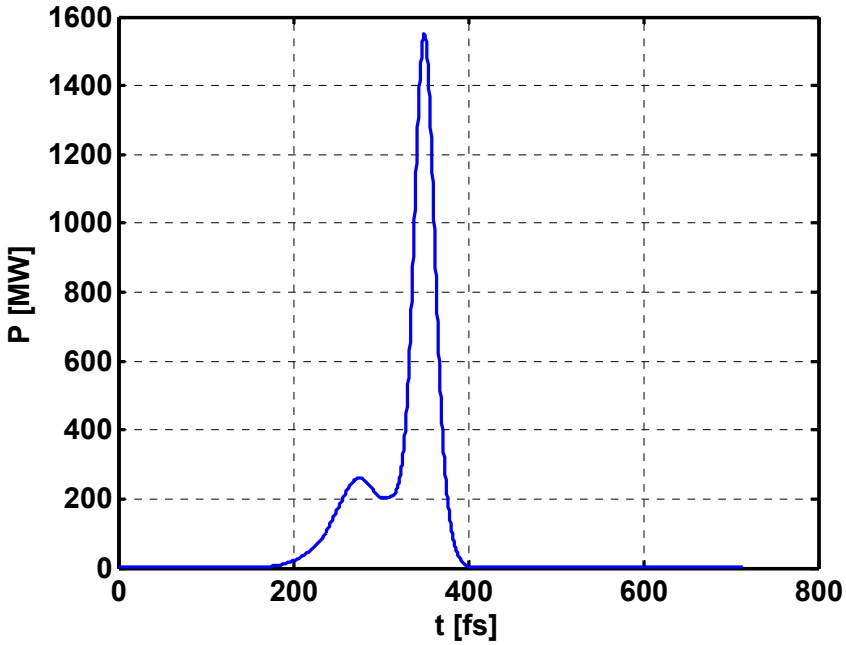

Figure 8.58 One-dimensional simulation result showing the 10 eV radiation power at saturation as a function of time for near- zero cavity detuning. The pulse shape demonstrates a spiking behaviour typical to FEL superradiance.

Larger values of the cavity detuning compensate for the effects of radiation lethargy and the output can be expected to be more like that of the steady state. This should occur when the cavity detuning δ_c is approximately equal to the relative slippage that occurs between the electron pulse and a radiation wavefront. For the parameters here this is $\delta_c \approx 20\,\mu\text{m}$. Indeed, it can be seen from Figure 8.57 that for $\delta_c \approx 20\,\mu\text{m}$, peak pulse power is approximately that expected of the steady-state model. A plot of the radiation pulse shape at saturation, similar to that of Figure 8.58 but for $\delta_c = 18\,\mu\text{m}$, is shown in Figure 8.59 and shows a wider pulse profile with no superradiant artefacts.

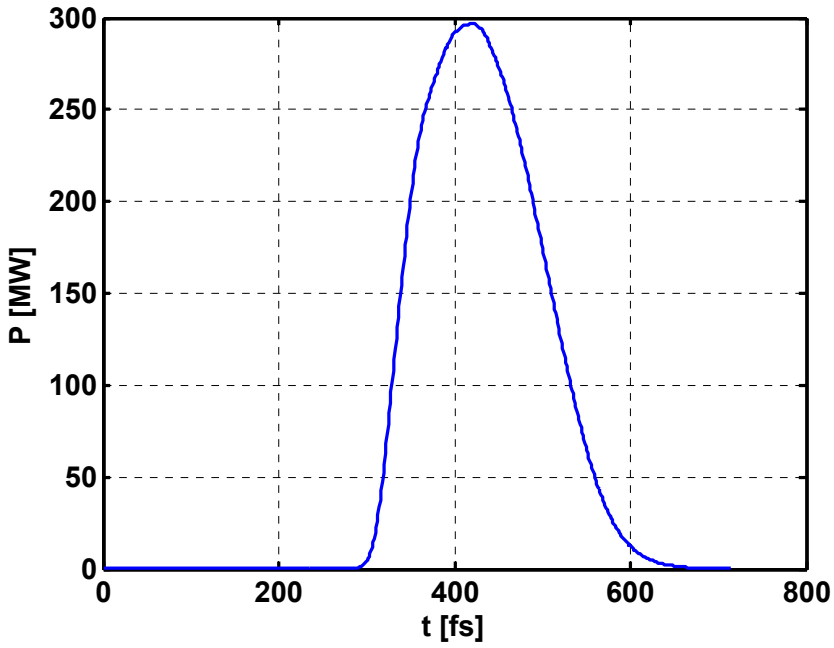

Figure 8.59 One-dimensional simulation result showing the 10 eV radiation power at saturation as a function of time for cavity detuning $\delta_c \approx 18\,\mu\text{m}$. The pulse shape demonstrates none of the superradiant behaviour of Figure 8.58

One-dimensional simulations have also been carried out for 3 eV photon output and are shown in Figure 8.60. In this case the parameters for helical mode operation were used. The increased coupling for this parameter set enables a scaled undulator of $\bar{z} = 4.43$ to be obtained even with only three undulator modules in use. The outcoupling fraction was again assumed to be 75 %. In practice, and assuming hole outcoupling, this would require a different mirror to that used at 10 eV due to the larger divergence of the longer wavelength radiation.

The cavity length detuning curve is shown in Figure 8.60 and exhibits the same characteristics as for the 10 eV case. In the steady state region the peak power is ~500 MW with a FWHM pulse width of 220 fs, whereas at near synchronous cavity length the peak power increases to over 3 GW and the FWHM pulse width reduces to around 40 fs.

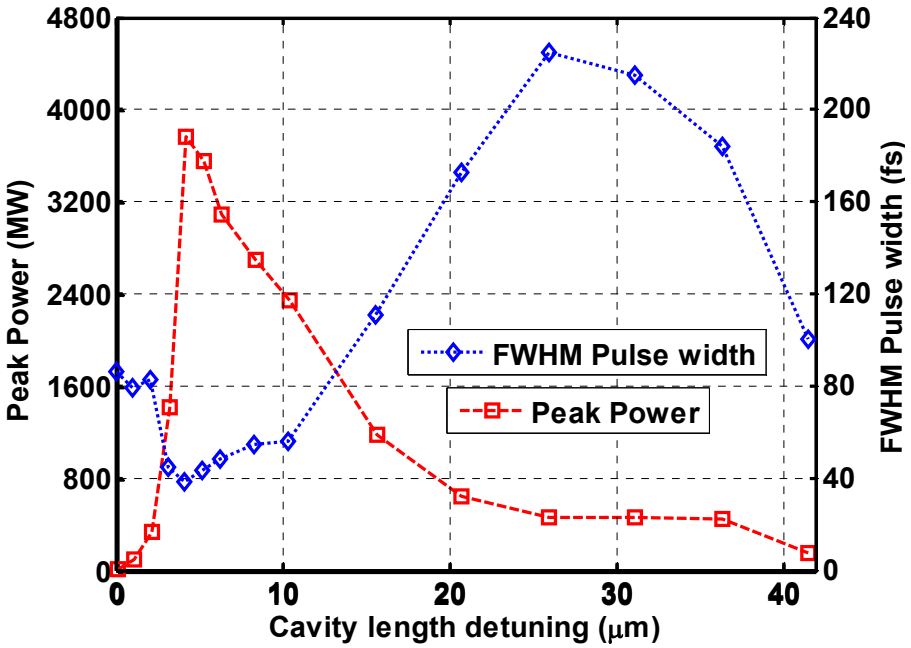

Figure 8.60 Peak power (red) and FWHM pulse width (blue) as a function of VUV-FEL cavity detuning. The parameters are for 3 eV photon output.

8.3.5.3 Pulse Simulation in Three Dimensions

Three-dimensional time-dependent simulations have also been carried out using Genesis 1.3, extending the predictions of the one-dimensional simulations to investigate the use of cavity feedback to improve longitudinal coherence over SASE output, and to investigate the possibility of controlling pulse widths and peak powers using superradiant effects and cavity-detuning. The parallel MPI implementation of Genesis 1.3 was used on 256 processors of a 1024-processor IBM computer [73]. This reduced code run-time by up to a factor of about one hundred over that of an equivalent single processor computer. As above, mirror reflectivity of $R = 60\%$ with hole outcoupling of $\alpha = 75\%$ were assumed, giving a feedback fraction of $F = 9\%$. The feedback was modelled simplistically by scaling the power of the output radiation pulse by the feedback factor and using this modified pulse as the input for the next pass. This simple approach will be improved in future modelling which will use the extended version of Genesis 1.3 currently being developed that includes full three-dimensional modelling of optical elements.

Figure 8.61 shows the evolution of the intracavity pulse power for a cavity length detuning of $\delta_c \approx 12\,\mu\text{m}$. After the first pass, the pulse power has a noisy profile characteristic of SASE. However, after only three passes a relatively well formed pulse has developed showing fewer signs of noise. Saturation occurs after eight passes where the intracavity peak power is 290 MW, equivalent to an output power of $\alpha \times 290 = 218\,\text{MW}$. The pulse length is ~ 50 μm FWHM, or ~ 160 fs. The corresponding spectrum at saturation is shown in Figure 8.62. As with the power, the spectrum is seen to be noisy after the first pass. On subsequent passes however

the spectrum narrows about a single wavelength. At saturation the spectrum has FWHM bandwidth 0.26 % giving a time-bandwidth product of ≈ 1.0. This is just over a factor two greater than a Fourier transform limited gaussian pulse and indicative of excellent longitudinal coherence.

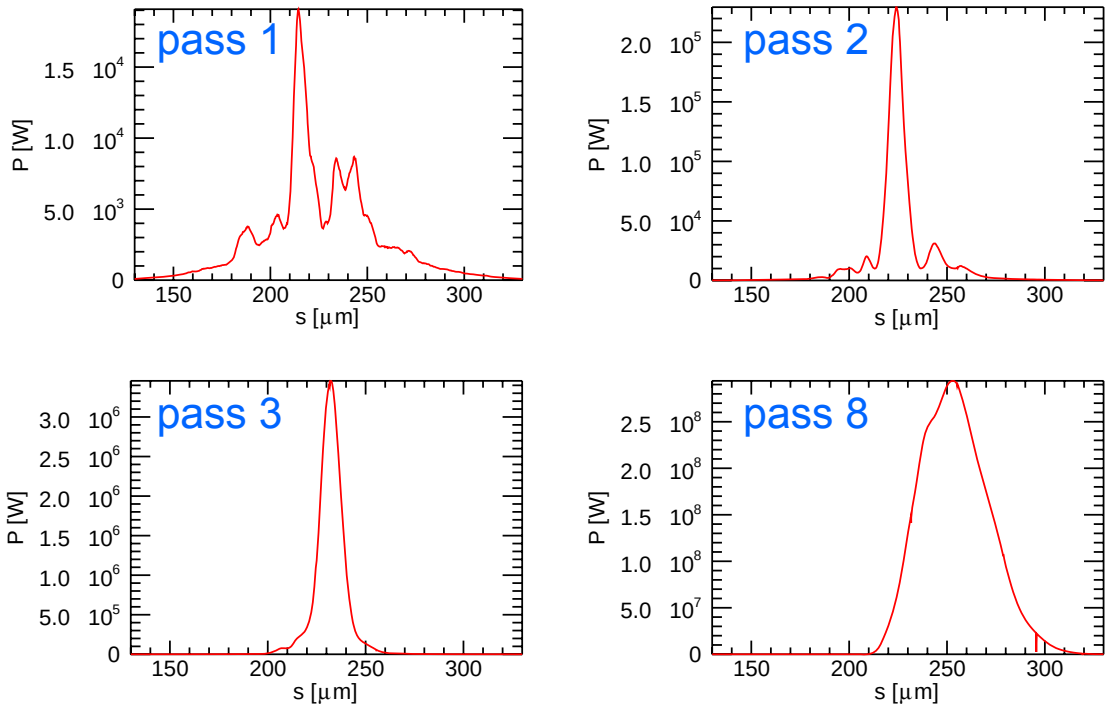

Figure 8.61 Genesis 1.3 simulation of the radiation pulse power after one, two, three and eight passes through the VUV-FEL for a detuned cavity of $\delta_c \approx 12\,\mu\text{m}$

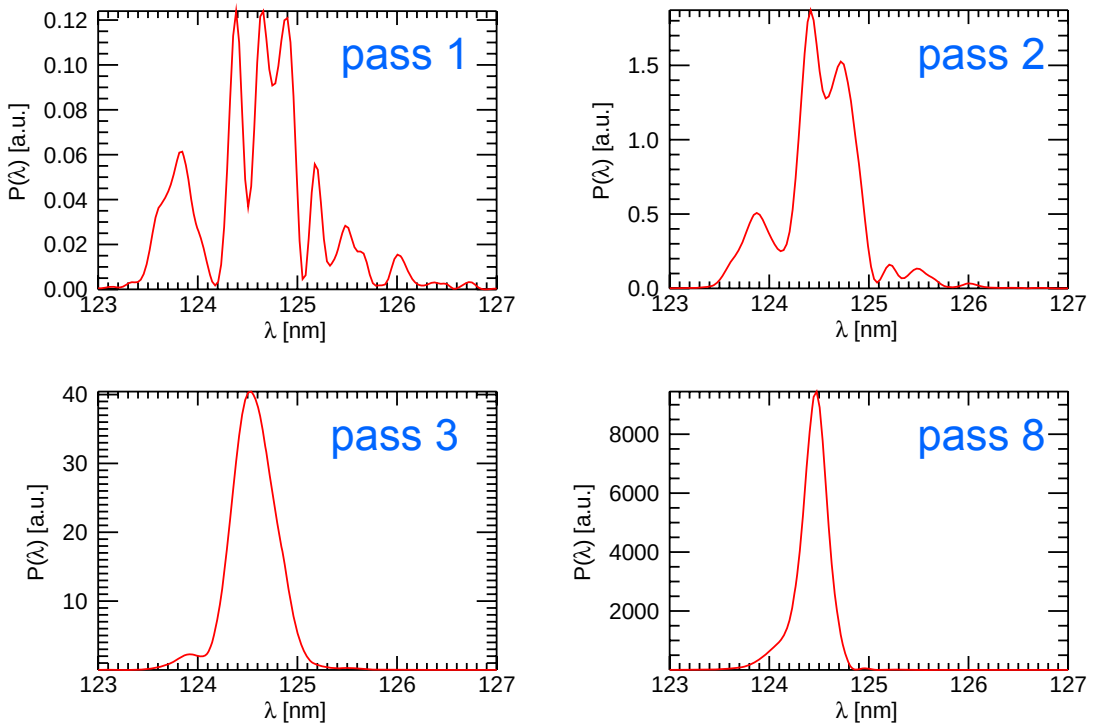

Figure 8.62 Genesis 1.3 simulation of the radiation pulse power spectral density corresponding to Figure 61 after one, two, three and eight passes through the detuned VUV-FEL cavity

When the above system has its cavity length made synchronous, i.e. $\delta_c \approx 0$, the pulse power at saturation is observed in simulations to appear more unstable. However, as seen in the left plot of Figure 8.63, the peak intracavity powers are greater, at 870 MW, and narrower, exhibiting the onset of the spiking behaviour associated with superradiance. The spectrum on the right of Figure 8.63 shows sidebands, although the FWHM bandwidth is slightly narrower at 0.2 % than for the previous cavity-detuned case. A richer behaviour is expected as the number of cavity passes grows and this will be the subject of investigation in future design studies.

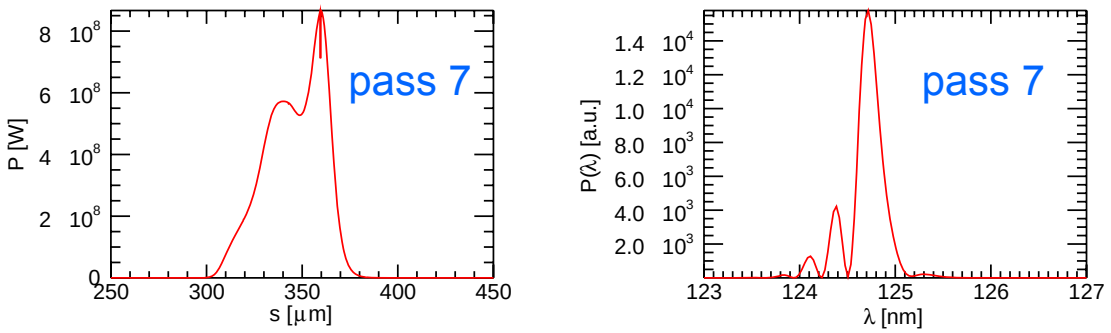

Figure 8.63 Genesis three-dimensional simulation of the radiation pulse power (left) and power spectral density (right) after pass seven through the VUV-FEL for a synchronous cavity of $\delta_c \approx 0$

Further simulations are required to characterise cavity detuning behaviour. However, the results here give indications that for a synchronous cavity the output power may be increased at the expense of pulse-to-pulse stability. By detuning the cavity length the pulse quality and stability can be improved at the expense of output power. In any event the self-seeding provided by the low-Q cavity is sufficient to dramatically enhance the spectral and temporal characteristics of the output compared to SASE.

8.3.6 Summary

The RAFEL is a promising design for fulfilling the 4GLS VUV-FEL requirements. The parameters of the device are summarised in Table 8.5. One-dimensional simulations have been used to determine suitable design parameters and a regime has been identified where the performance of the device is relatively insensitive to (and can even be enhanced by) degradation of mirror reflectivity.

Research into suitable mirror options, however, will be a future research requirement, both for assessment of the transverse radiation modes within the cavity and also to determine maximum allowed average power load on the optics which will hence determine the maximum repetition rate. Furthermore, the best method of cavity outcoupling is not yet clear. The simulations carried out so far have been independent of the outcoupling method. The possible options are mirror hole and annular outcoupling in either a Fabry-Perot or a ring cavity as well as unstable resonator configurations. The emphasis so far has been on determining a robust design for 10 eV operation because at this end of the wavelength range the optics challenges are more demanding and the FEL coupling is lower. Full three-dimensional modelling of optical elements is planned and is being incorporated into the time-dependent Genesis 1.3 model with the aim of developing a fully three-dimensional, start-to-end simulation of the VUV-FEL from its SASE-like start-up phase from shot-noise, through to saturation.

Table 8.5 Summary of VUV-FEL machine parameters and expected output parameters for standard user operation

DESCRIPTION	
FEL design	Regenerative Amplifier
Seeding type	Self-seeding
Seeding mechanism	Low-Q cavity
PHOTON OUTPUT	
Tuning Range	3 - 10 eV
Peak Power	500 - 300 MW (3 GW*)
Repetition rate	$n \times 4⅓$ MHz (n is integer)
Polarisation	Variable elliptical
Pulse length FWHM	170 fs (25 fs*)
Typical $\Delta\nu\Delta t$	~1.0
Max pulse energy	70 μJ
Maximum Average output power	$n \times 300$ W
ELECTRON BEAM PARAMETERS	
Energy	600 MeV
Bunch Charge	77 pC
RMS bunch length	100 fs
Peak current	300 A
Average current	n × 333 μA
Normalised emittance	2 mm mrad
RMS energy spread	0.1 %
UNDULATOR PARAMETERS	
Undulator Type	APPLE-II
No of Modules	5
Module length	2.2 m
Period	60 mm
Focussing	FODO
Minimum gap	10 mm

* indicates possible output in superradiant mode

8.4 IR-FEL Conceptual Design

8.4.1 General Specification

The IR-FEL is required to deliver intense pulses of tuneable coherent radiation with FWHM pulse lengths varying from less than 1 ps to 10 ps over the wavelength range 2.5 - 200 μm. The long wavelength limit is set to overlap with the onset of coherent bending magnet emission. The required photon pulse energy is up to at least 30 μJ to meet user needs.

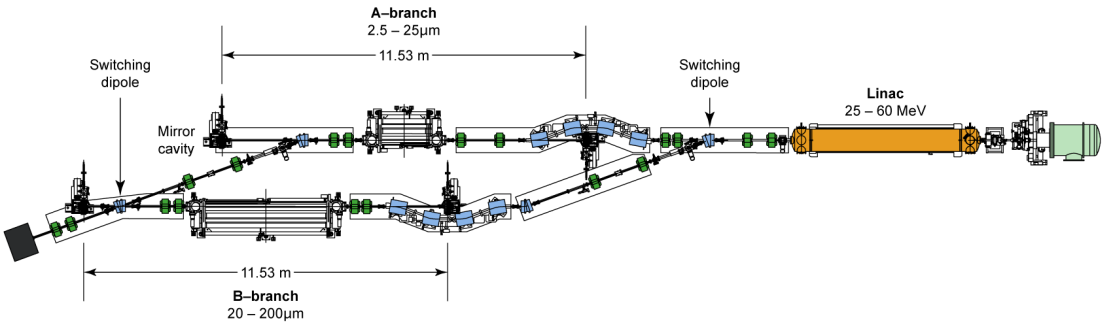

Figure 8.64 Conceptual layout of the IR-FEL showing the two undulator branches

The design of the IR-FEL is shown in Figure 8.64. The FEL design incorporates two undulators, each with their own optical cavity but driven by the same electron beam. The two branches of the system are notated IR-FEL A-branch and IR-FEL B-branch. Each branch is designed to be resonant over different subsets of the wavelength range with A-branch operating in the mid infrared from 2.5 μm to 25 μm, and B-branch operating from 20 μm into the THz regime at 200 μm (~ 1.5 THz). In order to cover these wavelength ranges the electron beam energy will be varied between from 25 MeV to 60 MeV, in combination with undulator gap tuning. The electron bunches supplied by the injector will be at a repetition rate of 13 MHz and will either be continuous or in macropulses. The macropulse duty factor is flexible and will depend on experimental needs. Fast magnetic switching, which will operate at up to 100 Hz, will allow the electron beam to be switched between undulator branches. The pattern of this switching will be determined on an operational basis dependent on user needs. Each branch of the IR-FEL will then lase within the supplied macropulse. It is expected that occasionally only one of the branches will be on-line. In this case the relevant branch will give continuous lasing. Both branch cavities must therefore be designed to cope with the associated high average power load and adequate cooling must be supplied.

In order to supply further flexibility to the pulse structures seen at the user stations, pulse chopping techniques will be employed outside each cavity. State-of-the-art electro-optic techniques for achieving this are currently being researched and developed. It is also proposed to offer the facility to pick out single pulses over a wide wavelength range. If suitable electro-optic techniques are not found over some of the wavelength range mechanical chopping would

offer an alternative solution, but it is be expected that the macropulse seen at the user-station will have a finite rise time.

8.4.2 Undulator Parameters and Tuning Curves

The wavelength tuning of each branch of the IR-FEL for both helical and planar geometries are shown in Figure 8.65 and Figure 8.66 as a function of beam energy and undulator gap. It is seen that the electron beam energy varies from $\gamma = 117$ (60 MeV) at the shortest wavelength for each device to $\gamma = 49$ (25 MeV) at the longest wavelength for the undulator parameters summarised in Table 8.6. The undulator periods are determined by the tuning requirements in the helical mode when the on-axis field is weaker than in the planar mode and it is necessary to use a longer period and a smaller gap to achieve resonance at a given wavelength. When switching from helical to planar configuration therefore, the wavelength contours in the tuning curves shown shift towards a larger gap. It is recognised that the undulator period for the B-Branch undulator is very long for an APPLE-II device and that the forces between arrays will pose an engineering challenge. For this reason it might be necessary to use an electromagnetic undulator. This issue will be investigated further in future design work.

Table 8.6 Summary of IR-FEL undulator parameters for A-Branch and B-Branch

IR-FEL	***A-Branch***	***B-Branch***
Type	APPLE-II	APPLE-II (or EM)
Period	53 mm	145 mm
Number of periods	50	35
Minimum Gap	23.5 mm	74 mm
Tuning range	2.5 - 25 µm	20 - 200 µm
Undulator parameter $\overline{a}_u$	0.58 - 1.12	1.65 - 2.39

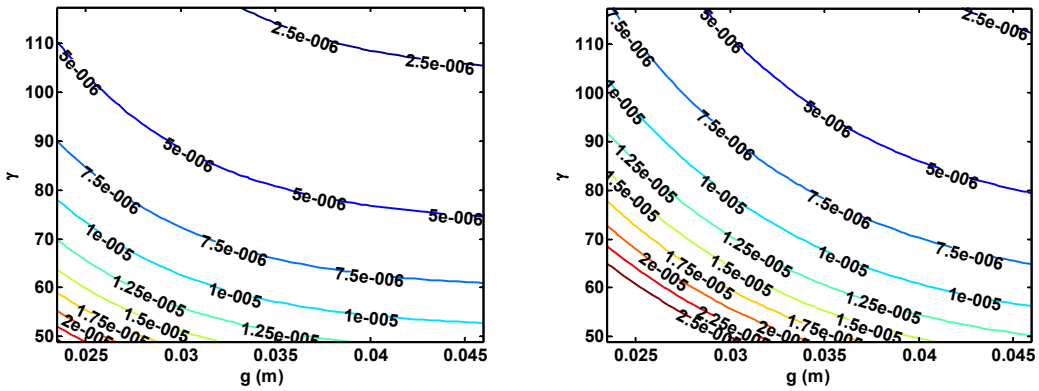

Figure 8.65 Energy and gap tuning of IR-FEL A-Branch from 2.5 µm to 25.0 µm in helical mode (left) and planar mode (right) . The contours show the resonant wavelength in m.

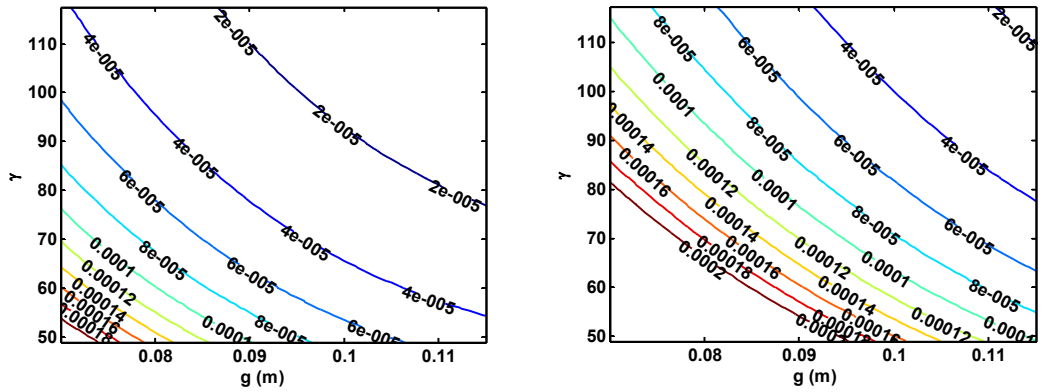

Figure 8.66 Energy and gap tuning of IR-FEL B-Branch from 20 μm to 200 μm in helical mode (left) and planar mode (right) . The contours show the resonant wavelength in m.

8.4.3 Electron Beam Quality

8.4.3.1 Emittance Requirements

The beam quality requirements are similar to those for the ERLP FEL [74], which is designed to operate at a minimum wavelength of 4 μm. It is found that for a 60 MeV beam and radiation output at 2.5 μm, the estimate (8-16) requires the normalised emittance to be less than 45 mm mrad. However, the effect of the emittance on the FEL performance is also due to its effect on the electron beam size. From equation (8-22) it is seen that the FEL gain will continue to increase as the emittance, and hence the electron beam radius, is reduced, until the electron beam size becomes significantly smaller than the optical mode size, at which point the gain becomes independent of the emittance. Figure 8.67 plots the single pass gain (normalised with respect to the gain assuming zero emittance: the one-dimensional limit) of the IR-FEL A-Branch branch at 2.5 μm, 12.5 μm and 25.0 μm, assuming 10 ps electron bunches with the undulator set to planar mode. It is seen that for ε_n = 10 mm mrad the gain at 12.5 μm and 25 μm is reduced only marginally over its value at the one-dimensional limit, whereas at 2.5 μm the gain drops to 68 % of its one-dimensional limit value. A normalised emittance of 10 mm mrad is specified as a threshold condition and defines the nominal value. This can be achieved relatively easily and any improvement will be beneficial for short wavelength operation of the IR-FEL A-Branch. The IR-FEL B-Branch operates at longer wavelengths where the detrimental effect of beam emittance is not so pronounced. The layout of the IR-FEL is designed to provide a straight through beam path for the A-Branch with the beam diverted via a dog leg into the B-Branch: this is because any emittance growth in the dog-leg is less important to B-Branch performance.

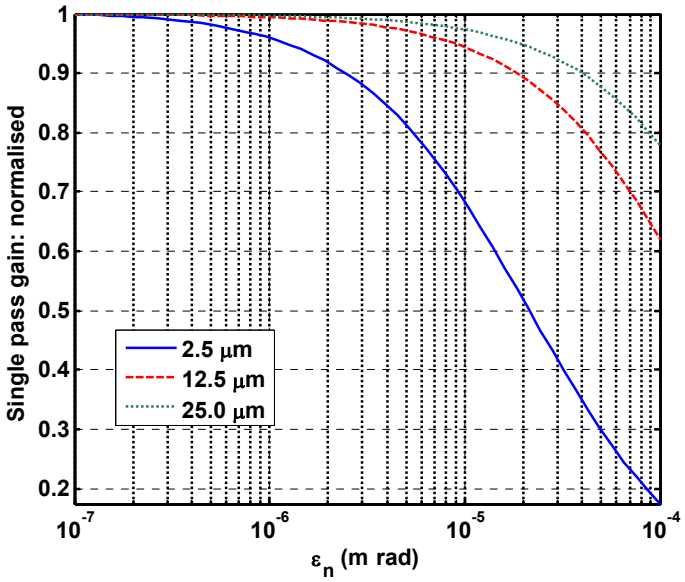

Figure 8.67 Single pass gain (normalised with respect to the gain at the one-dimensional limit) of the IR-FEL A-Branch at 2.5 μm, 12.5 μm and 25.0 μm, assuming 10 ps electron bunches with the undulator in planar mode

8.4.3.2 Energy Spread Requirements

The estimate (8-17) gives the requirement that for IR-FEL the relative RMS energy spreads should be less than ~ 0.2 % and ~ 0.3 % for branches A and B respectively. Figure 8.68 shows the calculated single pass gain of the IR-FEL A-Branch with 10 ps electron bunches, in planar mode, normalised with respect to the gain in the cold-beam limit and plotted as a function of relative RMS energy spread. The gain reduction is independent of the FEL wavelength, as seen from (8-19). An energy spread of 0.2 % degrades the gain to ~ 0.8 of the gain in the cold-beam limit, whereas an energy spread of 0.1 % degrades the gain to ~ 0.9 of that at the cold-beam limit. This latter energy spread is readily achievable and thus specified as the nominal value.

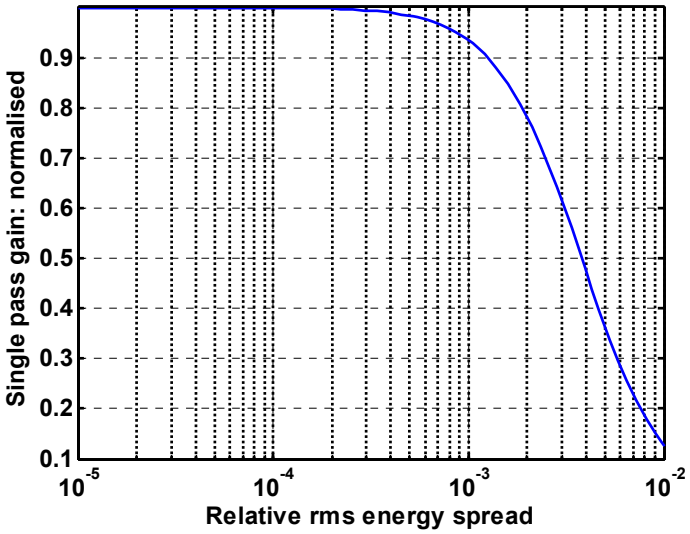

Figure 8.68 The single pass gain of IR-FEL A-Branch with 10ps electron bunches, in planar mode, normalised with respect to the gain in the cold-beam limit, plotted as a function of relative RMS energy spread

8.4.4 Bunch Charge and Bunch Length

Due to the requirement that the IR-FEL produces pulses with lengths of up to 10 ps, the bunch charge needs to be higher than that of ERLP or the 4GLS HACL . A bunch charge of 200 pC is proposed. It has been found, from extensive one-dimensional simulations over the full wavelength ranges of both branches of the IR-FEL, that in order to produce 10 ps FWHM pulses over the full tuning range, the RMS electron bunch duration σ_t needs to be as long as 10 ps and consequently the charge in the bunch needs to be high enough to give a sufficiently high peak current in these long bunches. The simulations have also shown that to produce sub-picosecond radiation pulses at the shorter wavelengths, an electron bunch length of 2 ps is sufficiently short, if cavity detuning is used to stimulate superradiant output at near synchronous cavity lengths. Assuming a 200 pC bunch charge in a gaussian charge distribution, an RMS bunch length of 2 ps gives a peak current of 40 A, which reduces to 8 A for a 10 ps bunch length. If it is decided after further user consultation that such long radiation pulses are not required the bunch charge can be reduced accordingly. Further reduction of the bunch length to < 1 ps would allow even shorter radiation pulses and the extension of enhanced superradiant output to shorter wavelengths. For sub-picosecond radiation pulses coinciding with the more stable shoulder of the cavity detuning curve, electron bunch lengths of ~ 1 ps are required.

8.4.5 Repetition Rate

The electron bunch repetition rate should be compatible with other 4GLS sources and appropriate to give a convenient optical cavity length. The proposed repetition rate is 13 MHz. This is three times the minimum repetition rate of the VUV-FEL and gives a minimum cavity length of 11.53 m in which configuration there will be a single optical pulse circulating in the

FEL cavity. Within the macropulse, the average beam current will be 2.6 mA with an average beam power (at 60 MeV) of 156 kW. The true average beam power will depend on the length and frequency of the electron beam macropulses.

8.4.6 Summary of beam parameters

The proposed beam parameters at the IR-FEL undulator entrances are summarised in Table 8.7.

Table 8.7 Summary of IR-FEL electron beam parameters

Normalised emittance ε_n	10 mm-mrad
Relative energy spread σ_E / E	0.1 %
Bunch charge Q	200 pC
Repetition rate f	13 MHz
Beam power (at 60MeV) *within macropulse*	156 kW
Electron bunch length σ_t	1 ps - 10 ps

8.4.7 Optical Resonator Design

The IR-FEL A-Branch resonator geometry is close to concentric. The Rayleigh length is near the optimum value, but has been slightly increased to aid cavity stability so that the stability parameter $g^2 = 0.90$. The undulator vacuum vessel gap, undulator length and cavity geometry have all been assessed to ensure that cavity loss due to diffraction on the undulator gap is nearly minimised at long wavelengths while at the same time the cavity geometry is near the optimum balance between performance (coupling between radiation and electron beam) and stability. The angular alignment tolerance calculated from (8-31) must satisfy $\theta_m \ll 50\,\mu\text{rad}$.

The IR-FEL B-Branch cavity is further from concentric with a Rayleigh length of 2.05 m and stability parameter $g^2 = 0.60$. In this case, the angular alignment tolerance must satisfy $\theta_m \ll 390\,\mu\text{rad}$.

This geometry has been chosen to minimise diffraction loss on the undulator vacuum vessel and provide a smaller mode size on the mirror than a near-concentric design would provide.

For the A-Branch mirror the diameter has been chosen to be three times the 25 μm mode diameter on the mirror. This ratio between mirror size and mode size reduces the intensity of diffraction ripples to a negligible amount. For the B-Branch the mirror diameter is provisionally restricted to 2.6 times the 200 μm mode size on the mirror to produce a more manageable optic. In the next design phase optics simulations will be performed to assess any degradation in transverse mode quality due to this aperture.

The design parameters are given in Table 8.8. Figure 8.69 shows the electron beam and TEM_{00} optical mode profiles within the undulator vacuum vessels of both IR-FEL branches. In each case the profiles are shown for the longest design wavelength.

Table 8.8 Summary of optical cavity parameters for IR-FEL A -Branch and B-Branch

IR-FEL	***A-Branch***	***B-Branch***
Cavity length	11.53 m	11.53 m
ROC Mirror 1	5.92 m	6.5 m
ROC Mirror 2	5.92 m	6.5 m
Rayleigh Length	0.94 m	2.05 m
Stability parameter g_2	0.90	0.60
Mirror angular alignment tolerance θ_m	« 50 µrad	« 390 µrad
Mode size (radius) at mirror w_m	5.4 - 16.9 mm	10.7 - 34.1 mm
Mirror diameter	100 mm	180 mm

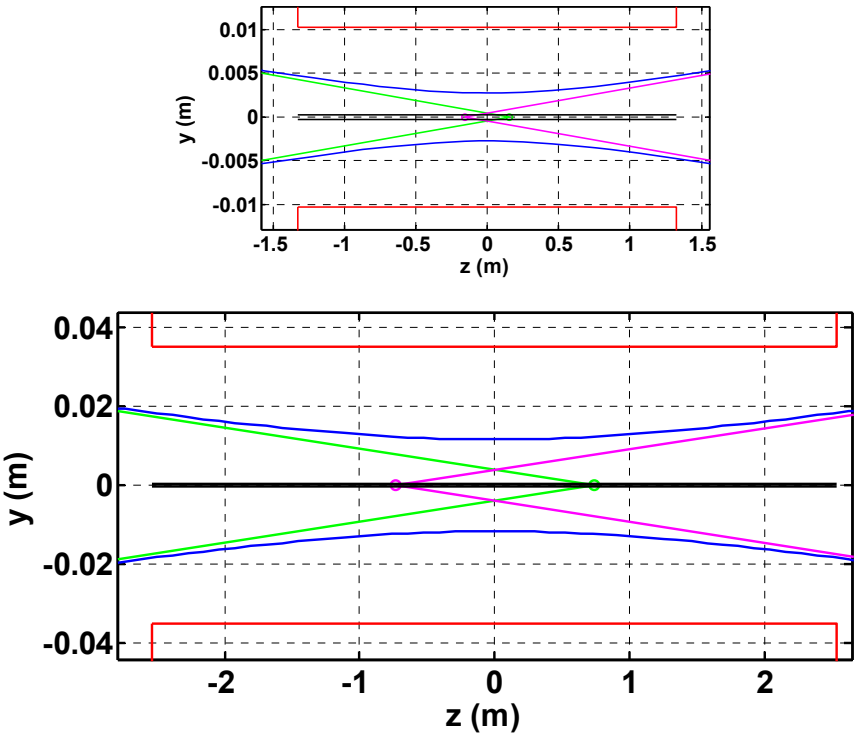

Figure 8.69 Schematic of cavity geometry for IR-FEL A-Branch at 25 µm (top) and IR-FEL B-Branch at 200 µm (bottom) through the undulator vessel. The red lines represent the undulator vacuum vessel, the black lines the electron beam which in this plane only can be matched to have a constant radius, and the blue curve the radius (w) of the TEM_{00} optical mode. The green and purple circles show the position of the centre of curvature of the mirrors.

8.4.7.1 Outcoupling and Materials

In the previous sections a generic outcoupling method has been assumed. The design assumes that IR-FEL A-Branch will utilise transmissive outcoupling to avoid mode distortion and to retain a constant outcoupling fraction with varying wavelength. In view of the wide output wavelength range, the use of coated optics is not feasible. Other facilities have used hole coupled mirrors [75, 76, 77], and whilst this method has significant disadvantages (variable output coupling with wavelength and mode quality) it remains the simplest and most proven approach and is being investigated for B-Branch. An alternative being explored is the use of a matrix of small holes, previously used to sample high power beams [78]. Theoretical developments in this area continue [79, 80].

Current diamond windows are of questionable suitability in the short wavelength region covered by A-Branch, in terms of absorption bands and retention of diffraction limited beam quality. However current rapid improvements in diamond windows may yield adequate quality material in time for 4GLS. Cadmium telluride [81, 82] or KRS5 are alternatives for the A-Branch, as we exclude on engineering grounds weak, hygroscopic materials with easy cleavage such as KBr and CsI. Well developed and readily available, zinc selenide gives good performance to

~ 16 μm [81, 82], but increasing absorption beyond this wavelength will limit average output powers.

8.4.8 Calculations of IR-FEL output

The semi-analytical model already presented in section 8.1.6 is used to predict the maximum single pass gain and peak power of both branches of the IR-FEL. The assumption is made that at every wavelength the optimum output coupling is used. In reality this will not be the case because in A-Branch, with the use of transmissive outcoupling, the outcoupling fraction will remain constant with wavelength and in B-Branch, with the use of hole coupling, the outcoupling fraction will vary with wavelength as the mode size on the mirror varies. However, for the purposes of the design at this stage it is assumed that near optimum outcoupling can be achieved across the wavelength range by changing mirrors accordingly. Further work on the mirror specifications will be presented in future design work.

Another simplifying assumption applied in the calculations is that in both planes the electron beam β-function is set according to (8-10) to take advantage of natural wiggler focussing and provide a constant radius electron beam through the undulator. In reality this will not be the case because the undulator natural focussing is dependent on the polarisation mode of the undulator, and in planar mode, for example, only exists in one plane: in this case, assuming zero dispersion, the electron beam Twiss parameters would be set to give $(\alpha, \beta) = (0, \beta_{\text{matched}})$ in the focussing plane and a waist in the centre of the undulator in the non-focussing plane. A full treatment of beam matching is given in [83].

It is stressed that the model used is not valid for the regime where the electron bunch length becomes much shorter than the slippage length. In later sections we present simulation results which allow us to:

- investigate the regimes where the bunch length is shorter than the slippage length;
- validate the semi-analytic predictions of this section;
- make predictions of other FEL output characteristics such as pulse length, and the dependence of pulse length and peak power on the cavity length detuning.

The calculated maximum single pass gain G_{max} and peak output power for A-Branch, for 2 ps electron bunches and 10 ps electron bunches, are shown in Figure 8.70 and Figure 8.71. The calculated maximum single pass gain and output power for B-Branch, for 10 ps electron bunches, is shown in Figure 8.72.

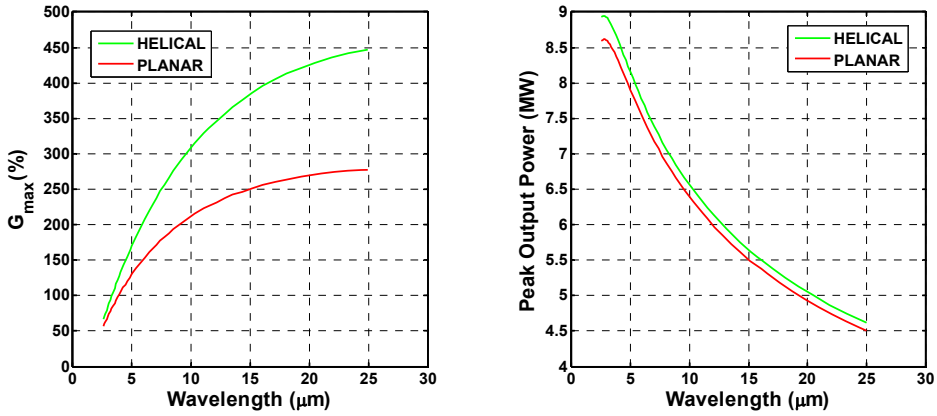

Figure 8.70 Calculated maximum single pass gain and peak output power for IR-FEL A-Branch, assuming 2 ps RMS electron bunches and an outcoupling fraction optimised for every wavelength to give the maximum output power. Calculations for helical and planar mode are shown in green and red respectively.

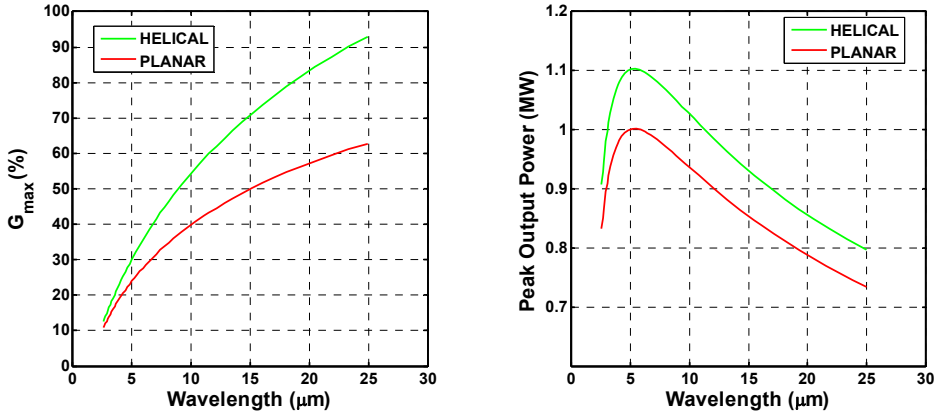

Figure 8.71 Calculated single pass gain and peak power for IR-FEL A-Branch, assuming 10 ps RMS electron bunches and an outcoupling fraction optimised for every wavelength to give the maximum output power. Calculations for helical and planar mode are shown in green and red respectively.

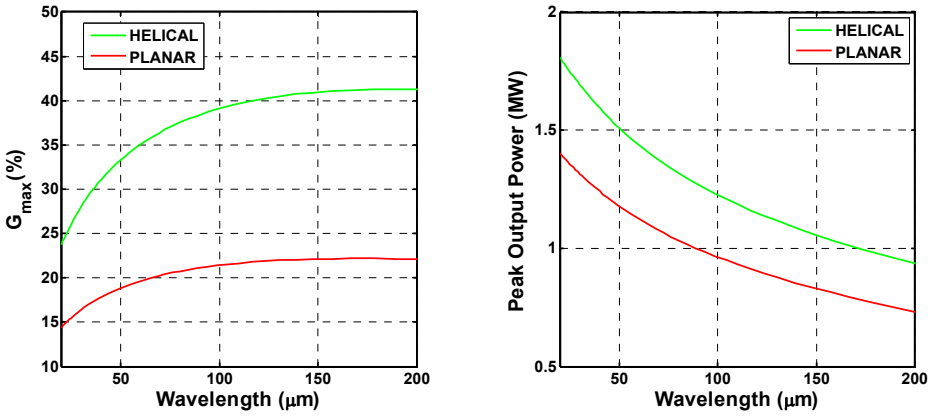

Figure 8.72 Calculated maximum single pass gain and peak power for IR-FEL B-Branch, assuming 10ps RMS electron bunches and an outcoupling fraction optimised for every wavelength to give the maximum output power . Calculations for helical and planar mode are shown in green and red respectively.

8.4.9 One-Dimensional Simulations

A one-dimensional pulse propagation simulation code has been used to model IR-FEL A-Branch and B-Branch in planar mode. The code numerically solves the FEL equations (8-2). After each pass the intracavity field intensity is modified according to the outcoupling fraction and estimated cavity loss. The relative longitudinal positions of the electron bunch and developing optical pulse can be adjusted at each pass to model the effect of cavity length detuning. In this way the cavity detuning curve can be determined. The effects of energy spread, beam emittance and transverse filling factor on the FEL interaction are accounted for by using an effective Pierce parameter:

$$\rho_{eff} = (F_{inh} F_f)^{1/3} \rho \tag{8-39}$$

when applying the universal scaling of [3] , where F_{inh} is the gain attenuation factor accounting for beam energy spread and emittance and F_f is the filling factor.

8.4.9.1 Simulation Results

Simulations have been carried out for 2 ps and 10 ps Gaussian electron bunches, for IR-FEL A-Branch at 2.5 μm, 12.5 μm and 25 μm and for B-Branch at 25 μm, 100 μm and 200 μm. For each of these twelve cases the peak power, FWHM pulse width at saturation, and hence pulse energy, have been determined as a function of cavity length detuning. In each case the plots of peak power and pulse width against cavity detuning exhibited the characteristic profiles seen experimentally at many facilities. The peak powers corresponding to the maximum stable pulse width correspond very well with the predictions of the calculated values. Closer to synchronous cavity length the peak powers are typically a factor of two to three higher and pulse widths are significantly reduced, indicative of superradiant pulse evolution. The shortest pulse lengths

observed correspond to approximately eight optical cycles, consistent with published experimental observations of superradiance in oscillator FELs [15].

As an example, the cavity length detuning curve for A-Branch, with 2 ps electron bunches and resonant at 2.5 μm, is shown in Figure 8.73. It is seen that the FWHM pulse width varies between 300 fs and 3.8 ps. The maximum peak power of 23 MW is seen at the synchronous cavity length where the FWHM pulse width is 300 fs. The peak power corresponding to maximum pulse energy (at a detuning of 9 μm) is 9.3 MW which is in good agreement with the semi-analytic theory which predicts 8.6 MW as shown in Figure 8.70. The saturation pulse profile for the cavity detuned by 9 μm is shown in Figure 8.74.

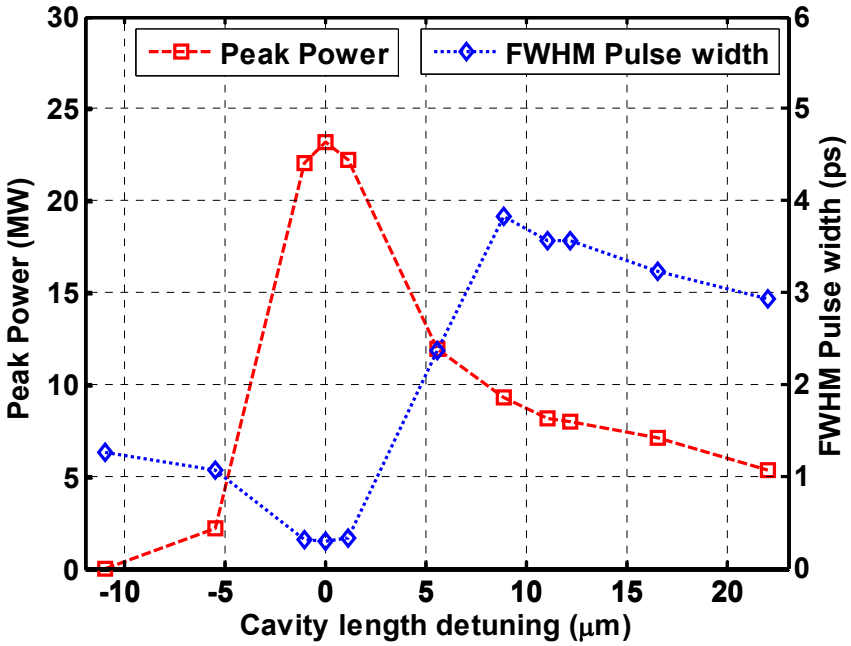

Figure 8.73 Peak power and FWHM pulse width as a function of cavity length detuning, for IR-FEL A-Branch at 2.5 μm with 2 ps electron bunches

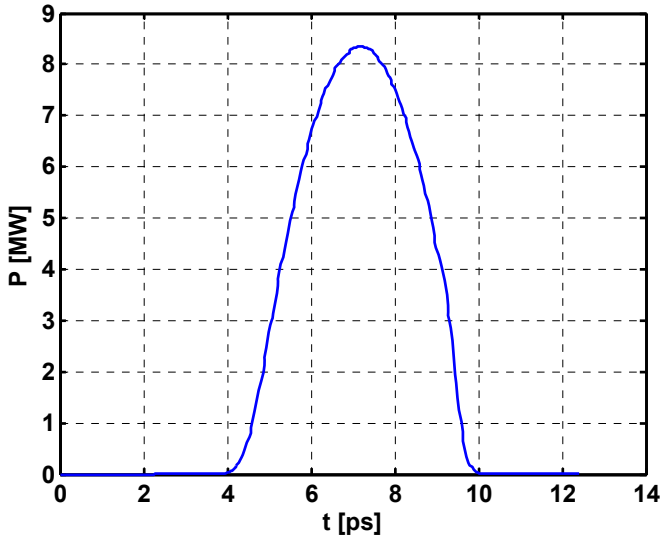

Figure 8.74 IR-FEL A-Branch 2.5 μm pulse profile corresponding to a cavity length detuning of 9 μm

As a further example, the detuning curve for A-Branch, with 10 ps electron bunches and resonant at 25 μm, is shown in Figure 8.75. It is seen that the FWHM pulse width varies between 2 ps and 18 ps. The peak power corresponding to maximum pulse widths is 0.75 MW which is in good agreement with the calculations which predict 0.75 MW as shown in Figure 8.71. The saturation pulse profiles for the synchronous cavity length detuned by 227 μm are shown in Figure 8.76. Summaries of the results of the one-dimensional simulations are given in Table 8.9 and Table 8.10. It should be noted that in these tables a range of values indicates the upper and lower values found over the range of electron bunch lengths and cavity detunings used in the simulations. Similarly, maximum values in different rows may not correspond to the same set of input parameters, so that for example the maximum pulse energy may be obtained at a different electron bunch length than the maximum peak power.

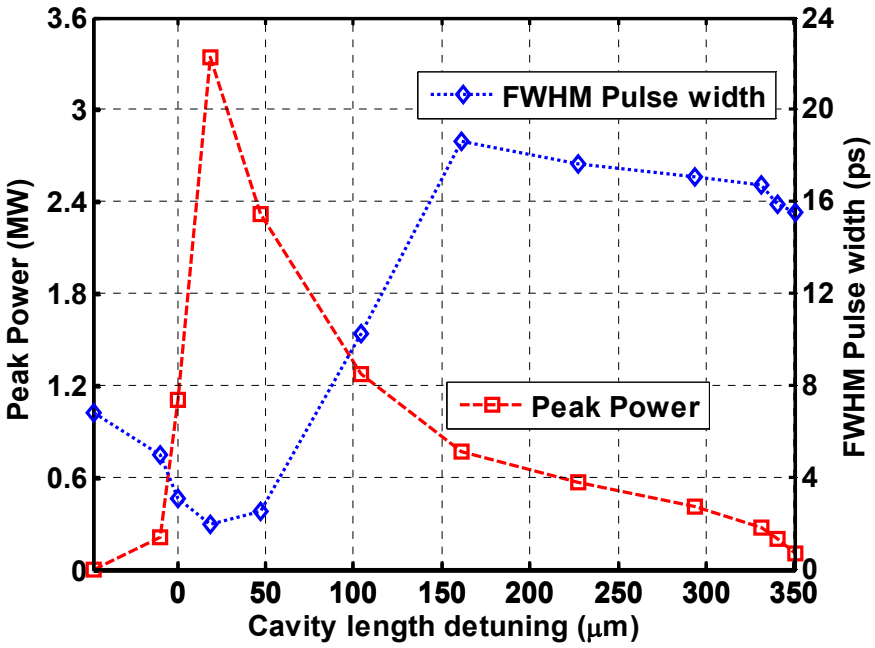

Figure 8.75 Peak power and FWHM pulse width as a function of cavity length detuning, for IR-FEL A-Branch at 25 μm with 10 ps electron bunches

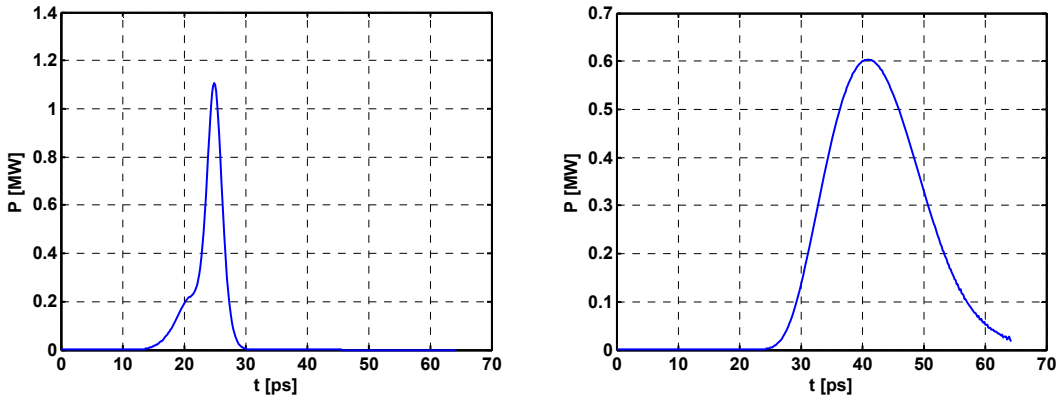

Figure 8.76 IR-FEL A-Branch 25 μm pulse profile corresponding to a synchronous cavity length (left) and detuned by 227 μm (right)

Table 8.9 Summary of IR-FEL A-Branch simulation results, for electron bunch lengths 2 ps - 10 ps. Where a range of values are given these represent the maximum and minimum values seen over the cavity length detuning range.

Output Wavelength	***2.5 µm***	***12.5 µm***	***25.0 µm***
FWHM pulse width (ps)	0.3 - 9.8	0.75-20.6	1.4-18.6
Maximum pulse energy (µJ)	29	48	27
Typical steady-state peak power (MW)	9.3	6.0	4.5
Maximum superradiant peak power (MW)	23	33	20
Maximum average power (W)	319	624	351
FWHM linewidth (%) (assuming $\Delta\upsilon\Delta t \approx 0.9$)	0.06-2.1	0.15-4.2	0.33-4.4

Table 8.10 Summary of IR-FEL B-Branch simulation results, for electron bunch lengths 2 ps - 10 ps. Where a range of values are given these represent the maximum and minimum values seen over the cavity length detuning range.

Output Wavelength	***25 µm***	***100 µm***	***200 µm***
FWHM Pulse width (ps)	1.2 - 15.5	2.8 - 20.1	5.4 - 29
Maximum pulse energy (µJ)	104	47.7	25.5
Typical steady-state peak power (MW)	12	8	1.0
Maximum superradiant peak power (MW)	55	16.3	4.5
Maximum average Power (W)	1352	620	331
FWHM linewidth (%) (assuming $\Delta\upsilon\Delta t \approx 0.9$)	0.40 - 5.2	1.24 - 8.9	1.7 - 9.2

8.4.10 Summary

The IR-FEL has been designed to produce high intensity, spatially and temporally coherent radiation with variable pulse lengths, flexible output pulse patterns and variable polarisation over the wavelength range 2.5 - 200 µm. The main parameters are summarised in Table 8.11. The design employs two undulators and hence offers the potential to satisfy user experiments at two different wavelengths simultaneously. The provision of short electron bunches offers the potential to operate the FEL in superradiant mode to produce shorter FEL pulses with higher peak intensities than available in 'normal' operation: simulations predict that FWHM pulse lengths of only a few optical cycles can be produced in this way. Analytical calculations and numerical simulations have been used to determine all major characteristics of the photon output. Further user consultation during the next design phase, as well as commissioning and operating the ERLP IR-FEL, will lead to further design optimisation and a complete specification of operating modes and pulse patterns. Analysis of the 4GLS Science Case makes it clear that the user need for the IR-FEL is very strong, particularly when used in combination with the other 4GLS photon sources.

Table 8.11 Summary of IR-FEL machine parameters and expected output parameters for standard user operation

DESCRIPTION	
FEL design	Oscillator
Seeding type	Self-seeding
Seeding mechanism	High-Q cavity
PHOTON OUTPUT	
Tuning Range	2.5 - 200 μm
Peak Power	9 MW (>20 MW) - 1 MW (>4 MW*)
Pulse length FWHM	2 ps (300 fs*) - 10 ps (6 ps*)
Repetition rate	13 MHz
Polarisation	Variable elliptical
Typical $\Delta\nu\Delta t$	≈ 0.9
Max pulse energy	≈ 50 μJ
ELECTRON BEAM PARAMETERS	
Energy	25 - 60 MeV
Bunch Charge	200 pC
RMS bunch length	1 - 10 ps
Normalised emittance	10 mm mrad
RMS energy spread	0.1 %
UNDULATOR PARAMETERS	
Undulator Type	APPLE-II
No of Modules	1 /1
Module length	2.65 m / 5.07 m
Period	53 mm / 145 mm
Focussing	Natural
Minimum gap	23.5 mm / 74 mm
OPTICAL CAVITY PARAMETERS	
Length	11.53 m
Rayleigh length	0.94 m / 2.05 m
Stability parameter g^2	0.90 / 0.60
Mirror diameter	100 mm / 180 mm

* indicates possible output in superradiant mode

REFERENCES

[1] V. P. Suller, Proc Euro Particle Accelerator Conference, Paris (2002) p757.

[2] Ming Xie, Proc. of 1995 Part. Accel. Conf., (1996) p183.

[3] R. Bonifacio et al., Opt. Commun. 50 (1984) p373.

[4] R. Bonifacio and B. W. J. McNeil, Nucl. Instrum. Methods A 272 (1988) p280.

[5] R. Bonifacio, B. W. J. McNeil and P. Pierini, Phys. Rev. A 40 (1989) p4467.

[6] B. W. J. McNeil, IEEE J. Quantum Electron., 26 (1990) p1124.

[7] B. Faatz et al., Nucl. Instrum. Methods A 429 (1999) p424.

[8] D. C. Nguyen et al., Proceedings of the XX International Linac Conference (2000) p731.

[9] Kwang-Je Kim, Phys. Rev. Lett., 57 (1986) p1871.

[10] R. Bonifacio, L. De Salvo Souza and B.W.J. McNeil, Opt. Commun., 93 (1992) p179.

[11] E. T. Scharlemann, Proc. INFN Int. School. on EM Radiation & Particle Beam Acceleration, North-Holland, 1989.

[12] J. Pflüger, Proc. 1999 Particle Accelerator Conference, New York (1999) p157.

[13] E.L. Saldin et al., 'The Physics of Free-electron Lasers', Springer.

[14] N. R. Thompson, B.W.J. McNeil and M.W. Poole, Proc. 27th Int. FEL Conf., Stanford (2005).

[15] D. A. Jaroszynski et al., Phys. Rev. Lett. 78, (1997) p1699.

[16] A. Torre et al., 'Insertion Devices for Synchrotron Radiation and Free Electron Lasers', World Scientific, 2000.

[17] W.B. Colson et al., 'Laser Handbook Vol 6', North Holland, 1990.

[18] D. Nutarelli et al., "Dynamic filling factor in the Super-ACO free electron laser", Nucl. Instrum. Methods A 393 (1997) p64.

[19] Kogelnik and Li, "Laser Beams and Resonators", SPIE MS68, 1993.

[20] P. Luchini and H. Motz, 'Undulators and Free-Electron Lasers', Oxford University Press, 1990.

REFERENCES, Continued

[21] K. Saeki, Nucl. Instrum. Methods A 375, (1996) p10.

[22] Charles A. Brau, 'Free–Electron Lasers', Academic Press Inc, 1990.

[23] R. Spero, "Update on diffraction loss and minimum mirror size", http://huey.jpl.nasa.gov/~respero/mirror-loss.pdf.

[24] R. Siegman, 'Lasers', University Science Books, 1986.

[25] L. Giannessi et al., 'Saturation and cavity-loss optimization in free-electron lasers', Phys Rev E, 48(2) (1993) p1401.

[26] E.L. Saldin et al., Nucl. Instrum. Methods A 475 (2001) p357

[27] L. H. Yu, Phys. Rev. A 44 (1991) p5178.

[28] B.W.J. McNeil et al., Proc. 27th Int. FEL Conf., Stanford (2005).

[29] B. Faatz and J. Pflüger, Nucl. Instrum. Methods, A 475 (2001) p603.

[30] S Reiche, Nucl. Instrum. Methods, A 429 (1999) p243.

[31] C. Gerth et al., Proceedings of 2005 Particle Accelerator Conference Knoxville, USA (2005) p1643.

[32] B.W.J McNeil et al., 'Design Considerations for the 4GLS XUV-FEL', Proc. 27th Int. FEL Conf., Stanford (2005).

[33] E. J. Takahashi et al., 'Generation of strong optical field in soft X-ray region by using high-order harmonics', IEEE Journal of Selected Topics in Quantum Electronics 10(6) (2004) p1315-1328.

[34] J. F. Hergott et al., 'Extreme-ultraviolet high-order harmonic pulses in the microjoule range', Phys. Rev. A 66(2) (2002) p021801-4.

[35] I.J. Kim et al., 'Highly Efficient High-Harmonic Generation in an Orthogonally Polarized Two-Color Laser Field', Phys. Rev. Lett. 94(24) (2005) p243901-4.

[36] Y. Nabekawa et al., 'Generation of 0.66 TW pulses at 1kHz by a Ti:sapphire laser', Opt. Lett. 23 (1998) p1384-1386.

[37] A. Dubietis et al., 'Powerful femtosecond pulse generation by chirped and stretched pulse parametric amplification in BBO crystal', Opt. Commun. 88(4-6) (1992) p437-440.

REFERENCES, Continued

[38] D. J. Ripin et al., '300-W cryogenically cooled Yb:YAG laser', IEEE J. Quantum Electron. 41(10) (2005) p1274-1277.

[39] R. Jones and J. Ye, 'Femtosecond pulse amplification by coherent addition in a passive optical cavity', Opt. Lett. 27 (2002) p1848-1850.

[40] R. Jones and J. Ye, 'High-repetition-rate coherent femtosecond pulse amplification with an external passive optical cavity', Opt. Lett. 29 (2004) p2812.

[41] F.Ö.Ilday and F.X. Kärtner, 'Cavity-Enhanced Optical Parametric Chirped-Pulse Amplification', Joint Conference on Ultrafast Optics V and Applications of High Field and Short Wavelength Sources XI, 2005, Nara, Japan, Springer, to be published.

[42] F. X. Kaertner et al., 'Experiments in Laser Seed Generation', MIT Workshop on the Physics of Seeded FELs, June 2004, Boston, MA.

[43] J. Zhou, 'Enhanced high-harmonic generation using 25 fs laser pulses', Phys. Rev. Lett. 76(5) (1996) p752-755.

[44] H. T. Kim et al., 'Continuously tuneable high-order harmonics from atoms in an intense femtosecond laser field', Phys. Rev. A 67(5) (2003) p051801-4.

[45] D. G. Lee et al., 'Coherent Control of High-Order Harmonics with Chirped Femtosecond Laser Pulses', Phys. Rev. Lett. 87(24) (2001) p243902-4.

[46] R. Bartels et al., 'Shaped-pulse optimization of coherent emission of high-harmonic soft X-rays', Nature 406(6792) (2000) p164-166.

[47] D. H. Reitze et al., 'Enhancement of high-order harmonic generation at tuned wavelengths through adaptive control', Opt. Lett. 29(1) (2004) p86-88.

[48] T. Pfeifer et al., 'Spatial control of high-harmonic generation in hollow fibers', Opt. Lett. 30(12) (2005) p1497-1499.

[49] T. Pfeifer et al., 'Controlling the spectral shape of coherent soft X-rays', Applied Physics B: Lasers and Optics 80(3) (2005) p277-280.

[50] M. Lewenstein et al., 'Theory of high-harmonic generation by low-frequency laser fields', Phys. Rev. A 49(3) (1994) p2117-2132.

[51] V. Yakovlev et al., 'Broadly tuneable 30-fs pulses produced by optical parametric amplification', Opt. Lett. 19(23) (1994) p2000-2002.

REFERENCES, Continued

[52] B. Shan and Z. Chang, 'Dramatic extension of the high-order harmonic cutoff by using a long-wavelength driving field', Phys. Rev. A 65(1) (2002) p011804-4.

[53] A Gordon and F.X. Kärtner, 'Scaling of keV HHG photon yield with drive wavelength', Optics Express 13(8) (2005) p2941-2947.

[54] Y. Nabekawa et al., 'Generation of 0.66-TW pulses at 1kHz by a Ti:sapphire laser', Opt. Lett. 23 (1998) p1384-1386.

[55] C. G. Durfee III et al., 'Phase Matching of High-Order Harmonics in Hollow Waveguides', Phys. Rev. Lett. 83(11) (1999) p2187-2190.

[56] A. Rundquist et al., 'Phase-Matched Generation of Coherent Soft X-rays', Science 280(5368) (1998) p1412-1415.

[57] H. T. Kim et al., 'Optimization of high-order harmonic brightness in the space and time domains', Phys. Rev. A 69 (3) (2004) p031805-4.

[58] S. Kazamias et al., 'Global Optimization of High Harmonic Generation', Phys. Rev. Lett. 90(19) (2003) p193901-4.

[59] A. Paul et al., 'Quasi-phase-matched generation of coherent extreme-ultraviolet light', Nature 421(6918) (2003) p51-54.

[60] E. A. Gibson et al., 'Coherent Soft X-ray Generation in the Water Window with Quasi-Phase Matching', Science 302(5642) (2003) p95-98.

[61] P Antoine et al., 'Attosecond Pulse Trains Using High-Order Harmonics', Phys. Rev. Lett. 77(7) (1996) p1234-1237.

[62] K. J. Schafer and K.C. Kulander, 'High Harmonic Generation from Ultrafast Pump Lasers', Phys. Rev. Lett. 78(4) (1997) p638-641.

[63] Y. Mairesse et al., 'Attosecond Synchronization of High-Harmonic Soft X-rays', Science 302(5650) (2003) p1540-1543.

[64] C. D. Lin et al., 'Attosecond atomic and molecular dynamics', in 340th Heraeus Seminar, High Field Attosecond Physics, 2005, Obergurgl, Austria.

[65] P. M. Paul et al., 'Observation of a Train of Attosecond Pulses from High Harmonic Generation', Science 292(5522) (2001) p1689-1692.

[66] M Hentschel et al., 'Attosecond metrology', Nature 414(6863) (2001) p509-513.

REFERENCES, Continued

[67] K. T. Kim et al., 'Single sub-50-attosecond pulse generation from chirp-compensated harmonic radiation using material dispersion', Phys. Rev. A 69(5) (2004) p051805-4.

[68] I. P Christov et al., 'High-Harmonic Generation of Attosecond Pulses in the "Single-Cycle" Regime', Phys. Rev. Lett. 78(7) (1997) p1251-1254.

[69] H. T. Kim et al., 'Continuously tuneable high-order harmonics from atoms in an intense femtosecond laser field', Phys. Rev. A 67(5) (2003) p051801-4.

[70] E. J. Takahashi et al., 'High-throughput high-damage-threshold broadband beam splitter for high order harmonics in the extreme-ultraviolet region', Opt. Lett. 29 (2004) p507-509.

[71] F. Bridou et al., Proceedings of SPIE 5250, p628.

[72] Stefan Gunster, private communication.

[73] http://www.hpcx.ac.uk

[74] N. Thompson, 'ERL Prototype Free-Electron Laser', Internal Report erlp-ofel-rpt-0001, 2003.

[75] M. Shinn et al., Proc. 2004 FEL conf., p222-225.

[76] R. J. Bakker et al., 'Broadband tunability of a far-infrared free electron laser', J. Appl. Phys. 74(3) (1993) p1501

[77] B. Faatz, 'Hole coupling in Free Electron Lasers', IEEE J. Quantum Electron. 29 (1993) p2229-2237.

[78] Harvey James E. and Scott Marion L., 'Hole grating beam sampler - versatile high energy laser (HEL) diagnostic tool', Optical Engineering 20(6) (1981) p881-886.

[79] X. Shu, 'Improved optical cavity quality of a waveguide free-electron laser with hole coupling by using a grating', Optical Engineering 39(6) (2000) p1543.

[80] H. N. Rutt, private communication.

[81] E. D. Palik, 'Handbook of Optical Constants of Solids, 1st Edition', Academic Press (1997).

[82] P. Klocek, 'Handbook of Infrared Optical Materials (Optical Engineering)', CRC (1991).

[83] N. Thompson, 'Electron Beam Matching', Internal Report erlp-ofel-rpt-0007, 2004.

9. Conventional Synchrotron Radiation and Laser Sources

4GLS will be an outstanding light source in every respect. It will produce sub-picosecond photon pulses over a very wide and continuous photon energy range, it will produce peak brightness and peak flux levels eight orders of magnitude greater than is presently available from 3rd generation sources, it will produce energies per pulse enhanced by ten orders of magnitude compared with today's synchrotron radiation sources and it will facilitate the combination of sources with femtosecond synchronisation to enable many exciting pump-probe experiments to be performed which are presently impossible.

In this chapter, all of the various 4GLS sources are discussed and their properties described. They are then compared against well known facilities such as DIAMOND, Max III and X-FEL. The impact of the undulators on the electron beam is then addressed and shown to be largely negligible.

9.1 Introduction

4GLS will contain a wide variety of photon sources. The free-electron lasers stand out as state of the art photon sources but additionally there will be undulator based sources which will have high average flux capability and high peak flux capability, wigglers, extremely intense sources of THz radiation generated by coherent effects and conventional dipole radiation. In addition to this a variety of conventional lasers will form part of the facility and advantage can be made of their intense photon output and ability to be synchronised with the electron generated sources. This chapter will explore all of the potential sources available in 4GLS except for the FELs which are covered in detail in Chapter 8.

9.2 Photon Output

The 4GLS Science Case [1] presents a wide range of possible experiments and an analysis of the photon parameters required has directed the selection of sources presented in this chapter. Table 9.1 gives a list of beamline requirements for use of spontaneous radiation output derived from the Science Case along with a proposed 4GLS source type. This demonstrates the ability of 4GLS to meet the science needs and is not a proposed definition of the final suite of sources. The photon output of representative sources is described in order to inform the user community.

Table 9.1 Analysis of photon sources required by the Science Case and suitable 4GLS solutions

Beamline requirement deduced from Science Case	***Science/technique area***	***Possible 4GLS source type***
THz (synchronised to IR-FEL)	THz pump probe, excitation dynamics, imaging	Bending magnet, short electron bunch location for CSR
IR 2-20 μm (synchronised to IR-FEL and VUV-FEL)	IR pump-probe, surface adsorbate IVR, dynamics at interfaces, RAIRS, IR spectroscopy	Bending magnet source
Visible-UV-VUV 1.5-50 eV, selectable polarisation	CD, UV RR, low energy photoemission, high resolution bandmapping, RAS, ROA	Undulator, period in range 90 to 50 mm; longer electron bunch location
UV-VUV 2-20 eV	CD, low energy photoemission	Bending magnet source, longer electron bunch location
VUV short pulse 3-20 eV selectable polarisation (synchronised to VUV-FEL)	Pump-probe, multiply charge molecular ions, free radical spectroscopy, negative ions and neutrals	Undulator, period ~ 60 mm; short electron bunch location
VUV/XUV 5-350 eV selectable polarisation (synchronised to VUV-FEL)	Photoemission, spin-polarised PES, two photon PES of excited states, dynamics of electron-hole pairs	Undulator, period ~ 30 mm; longer electron bunch location
XUV short pulse 10-200 eV selectable polarisation (synchronised to VUV-FEL and XUV-FEL)	Pump-probe, multiply charged molecular ions, photoionisation detection of neutrals	Undulator, period ~ 30 mm; short electron bunch location If in XUV-FEL branch can take advantage of higher electron energy for higher energy photon output
XUV-SXR 100-1000eV selectable polarisation	PEEM, XMCD, XAS, some photoemission	Undulator, period < 30 mm; longer electron bunch location If in XUV-FEL branch can take advantage of higher electron energy for higher energy photon output

From the table, it can be seen that the performance of 4GLS electron-based sources can be illustrated by studying the output from two representative undulators, U30 and U60, and a typical bending magnet.

For many of the pump-probe experiments, a second source is required. 4GLS will meet this by providing the most appropriate combination, utilising beams from spontaneous and FEL sources with laser sources for seamless coverage of the THz to SXR photon energy range.

9.2.1 Output from Undulators

Two representative undulators have been selected for 4GLS and the parameters for these are given in Table 9.2. To calculate brightness, the electron beam dimensions are also required and those assumed for the centre of the undulators are given in

Table 9.3. These assume a horizontal and vertical emittance of 1.7 nm rad (corresponding to a normalised emittance of 2 mm mrad) and a betatron function value of 2 m in both planes.

Table 9.2 Parameters for two possible undulators

Parameter	*U30*	*U60*
Period	30 mm	60 mm
Magnet Gap	10 mm	10 mm
Number of Periods	330	80
Peak Magnetic Field	0.79 T	1.33 T
K value	2.2	7.4
Length	10 m	5 m

Table 9.3 Electron beam dimensions (RMS values) used for the source brightness calculations

Parameter	*Value*
σ_x	58 μm
σ_y	58 μm
σ_x'	29 μrad
σ_y'	29 μrad

Important parameters to calculate and compare when dealing with very short pulse sources are the peak flux and brightness. An illustration of the concept of peak flux is given in Figure 9.1. The photon flux of a single pulse is plotted, with the peak flux simply being defined as the maximum value on the curve. The integral of the flux curve is the total number of photons in the pulse. If the number of photons per pulse is constant then a shorter pulse length will generate a higher peak value in general. For a gaussian photon pulse with RMS length of σ_l, the peak value is simply given by

$$F_{peak} = \frac{N_{ph}}{\sqrt{2\pi}\sigma_l} \tag{9-1}$$

Where N_{ph} is the number of photons per pulse. The peak brightness is similarly defined.

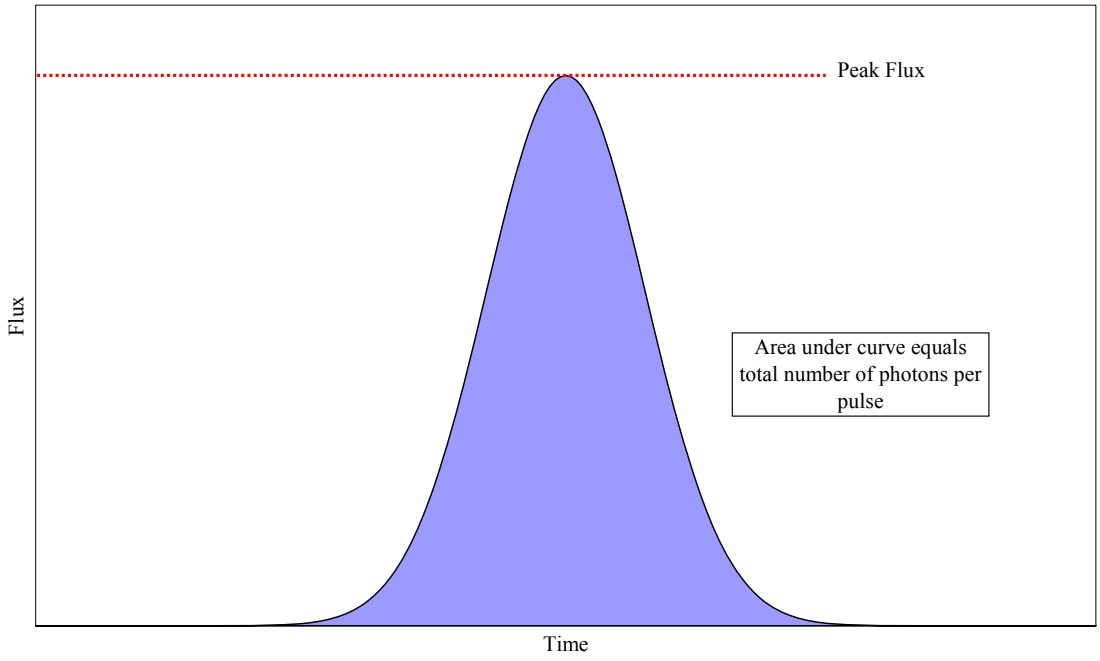

Figure 9.1 Illustration used to explain the concept of peak flux. A single photon pulse is plotted as a function of time, the peak flux is the maximum value observed. The integral of the flux equals the number of photons in the pulse.

The peak flux (in the central cone) and brightness levels achieved are very impressive when compared with other sources. This is illustrated in Figure 9.2 and Figure 9.3, where up to the ninth harmonic is plotted, which is readily achievable with modern undulators. The peak source levels are enhanced by the very short electron bunch lengths that are generated. They are typically a factor of ~ hundred to thousand times shorter than in 3rd generation light sources such as DIAMOND and Max III. Note that Max III has been selected as a representative modern low energy light source; other sources such as ELETTRA and ALS generate similar output tuning curves. The two DIAMOND undulators shown on the curves are presently under construction. The tuning range of the DIAMOND helical undulator, HU64, is shown for the linear horizontal polarisation mode.

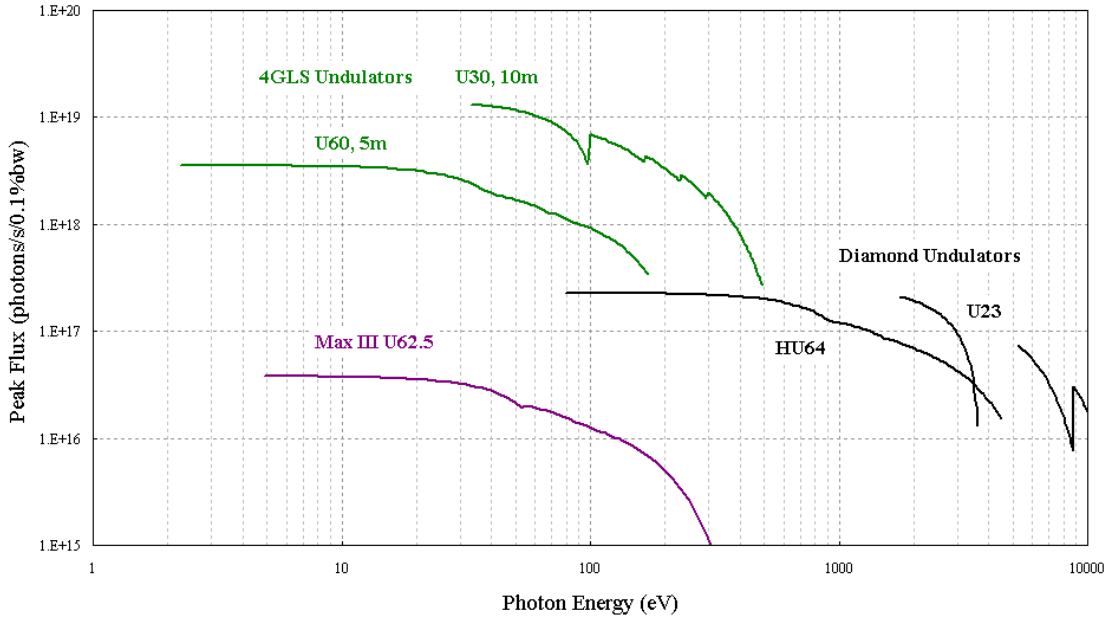

Figure 9.2 Peak flux for sample 4GLS undulators compared with DIAMOND and Max III devices. An RMS electron bunch length of 100 fs is assumed for 4GLS, 10.9 ps for DIAMOND [2]and 93 ps for Max III [3].

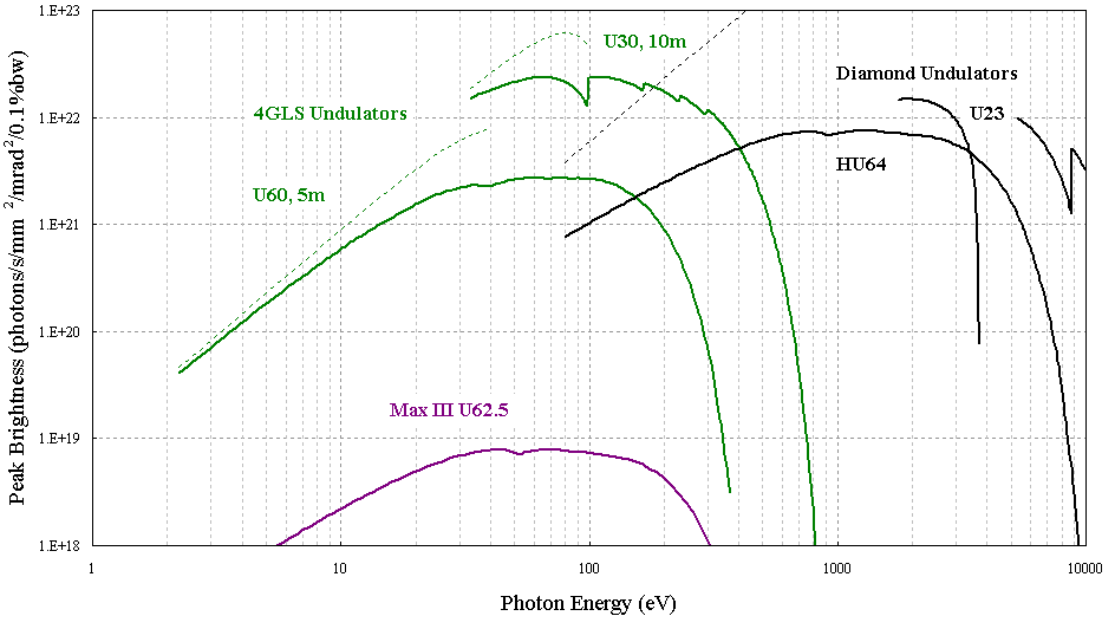

Figure 9.3 Peak brightness for sample 4GLS undulators compared with DIAMOND and Max III devices. The dotted lines indicate the maximum peak brightness possible, for 4GLS devices and also DIAMOND HU64, which is set by the inherent diffraction-limited size and divergence of the photon source.

The average flux and brightness for the two sample undulators is shown in Figure 9.4 and Figure 9.5. The brightness of every photon source has a maximum fundamental limit set by the diffraction-limited source size and divergence of the photon beam. Since longer wavelengths

naturally have larger photon source emittances [4], lower photon energies can never achieve the same brightness levels as higher photon energies. This brightness limit is illustrated for 4GLS by a dotted line on Figure 9.5.

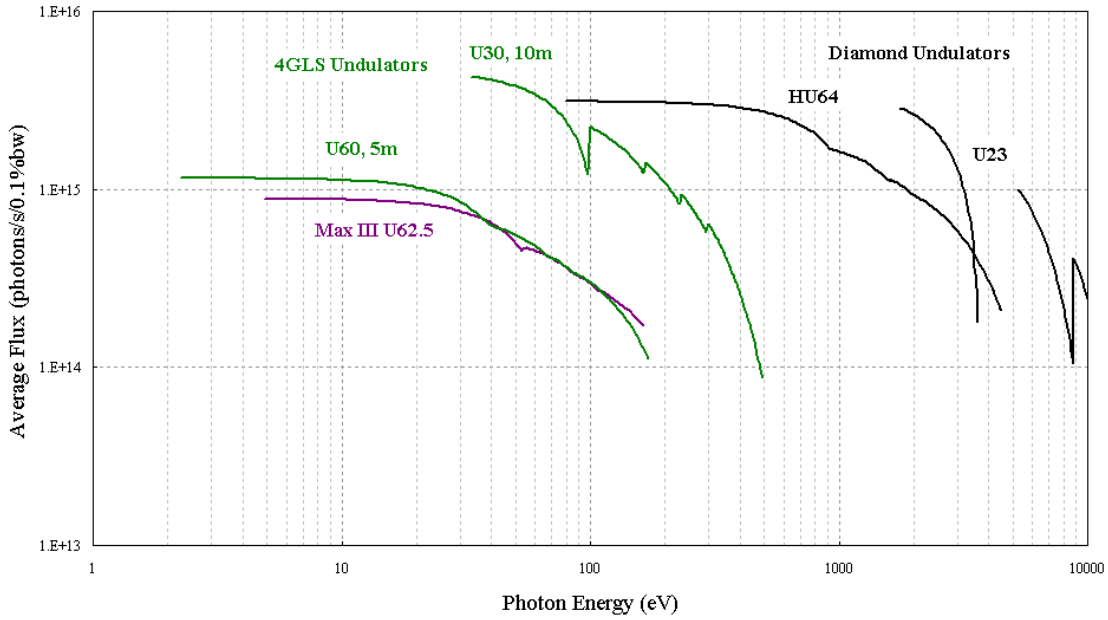

Figure 9.4 Average flux into the central cone for sample 4GLS undulators compared with DIAMOND and Max III devices

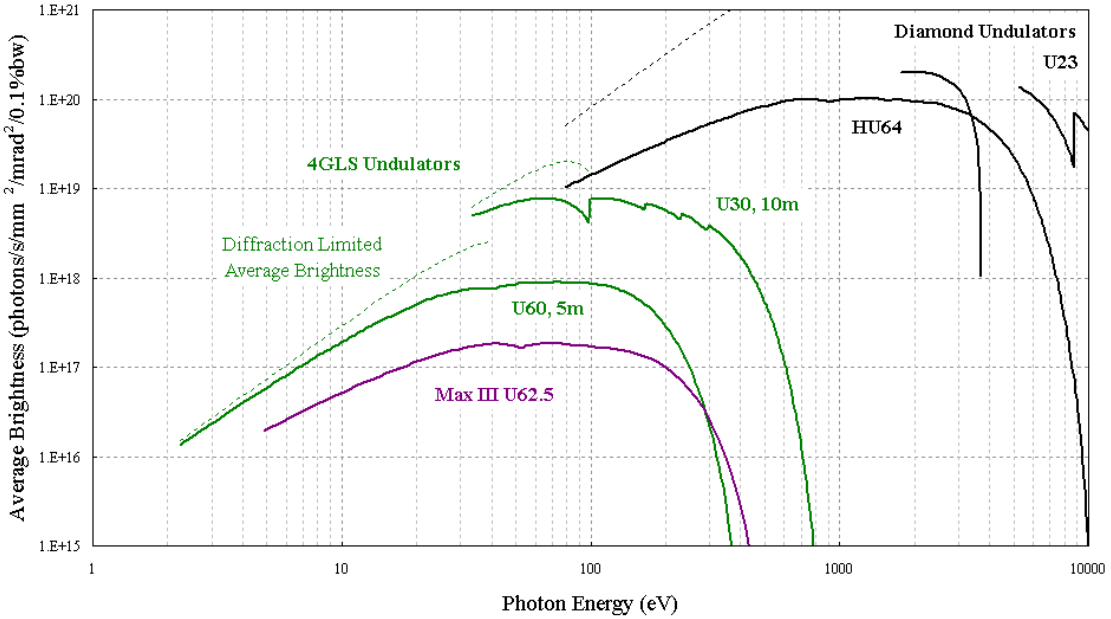

Figure 9.5 Average brightness for sample 4GLS undulators compared with DIAMOND and Max III devices. The dotted lines indicate the maximum brightness possible, for 4GLS devices and also DIAMOND HU64, which is set by the inherent diffraction-limited size and divergence of the photon source.

Since the power and power density levels generated by undulators scale very strongly with electron energy [4], 4GLS does not suffer from the extreme values encountered in many 3rd generation light sources. The power levels generated by the 4GLS example undulators are compared with those from DIAMOND [2] in Table 9.4.

Table 9.4 Comparison of power and power density for 4GLS and DIAMOND undulators

Parameter	*4GLS U30*	*4GLS U60*	*DIAMOND HU64*	*DIAMOND U23*
Power (W)	142	200	7500	1600
Power Density ($W/mrad^2$)	36	15	19200	15400

9.2.2 Output from Dipoles

The electrons in a bunch radiate coherently at wavelengths similar to and longer than the bunch length. Since 4GLS has very short bunch lengths this so-called coherent synchrotron radiation (CSR) is emitted over a broad wavelength range. Calculations for the radiation in the CSR regime are given in Figure 9.6 and Figure 9.7 for the High Average Current Loop. In this case the average values of flux and brightness are important and these are calculated assuming a 77 pC bunch, 100 mA average current, RMS bunch length of 100 fs (30 μm), magnet strength of 0.35 T (which is typical of the bends in the High Average Current Loop) and horizontal angular aperture of 50 mrad. The onset of the CSR is seen to occur at around 0.03 eV (40 μm) with the vacuum chamber long wavelength cut-off occurring at ~0.0001 eV (see section 9.4.3). At shorter wavelengths conventional synchrotron radiation is also emitted and available for user experiments.

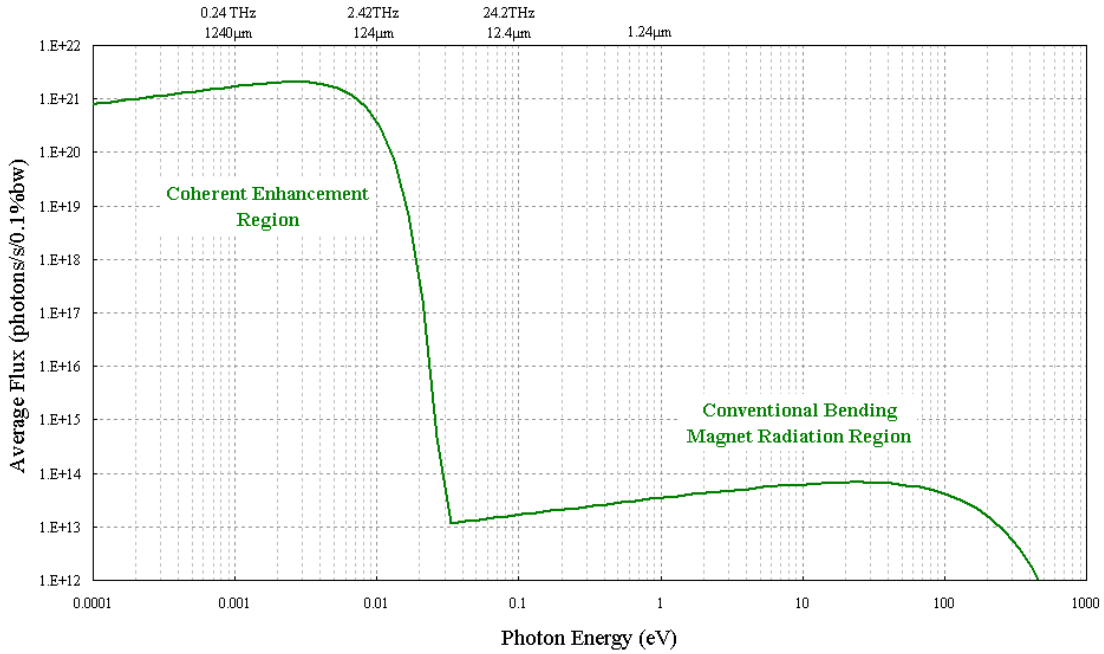

Figure 9.6 Average flux from a 0.35 T bending magnet into a 50 mrad aperture with 100 mA beam current and RMS bunch length of 100 fs

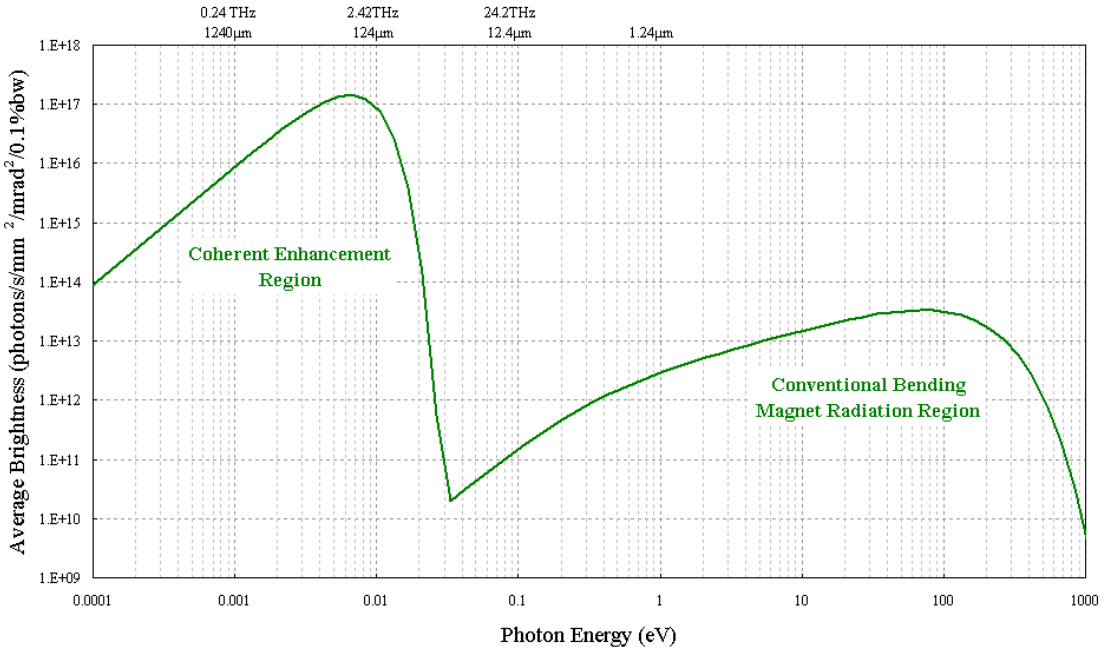

Figure 9.7 Average brightness from a 0.35 T bending magnet with 100 mA beam current and RMS bunch length of 100 fs

For the XUV-FEL branch, which has a 1 kHz repetition rate and a charge per bunch of 1000 pC, the pulse flux and energy are the important quantities and these are given in Figure 9.8 and Figure 9.9.

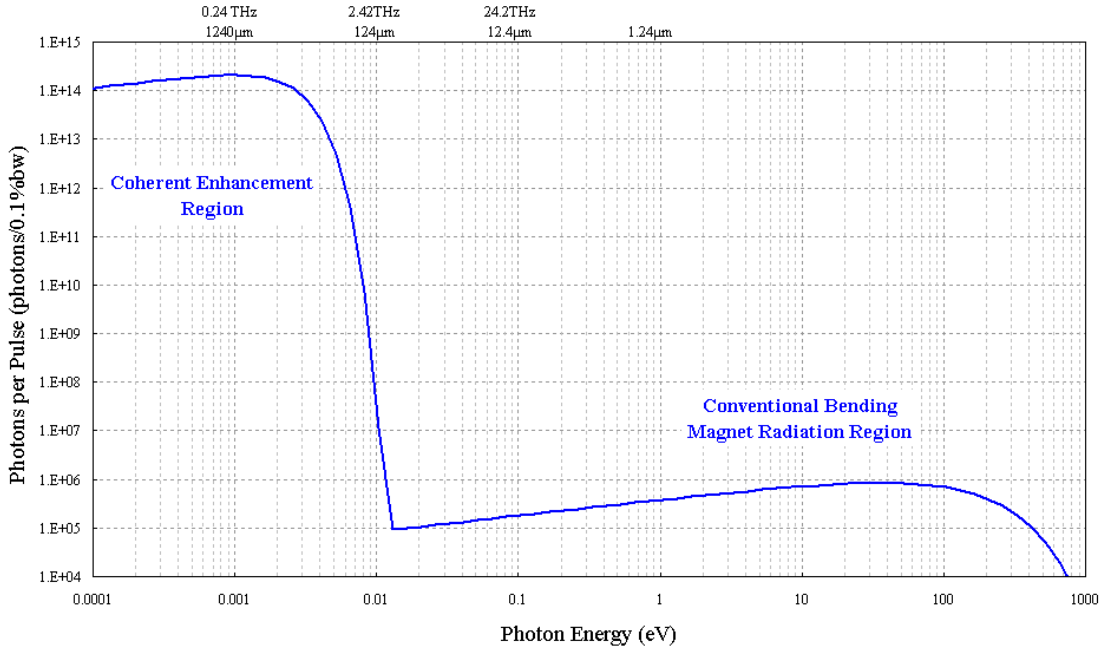

Figure 9.8 Flux per pulse from a 0.35 T bending magnet into a 50 mrad aperture with 1 nC bunch charge and RMS bunch length of 266 fs in the XUV-FEL branch at 750MeV

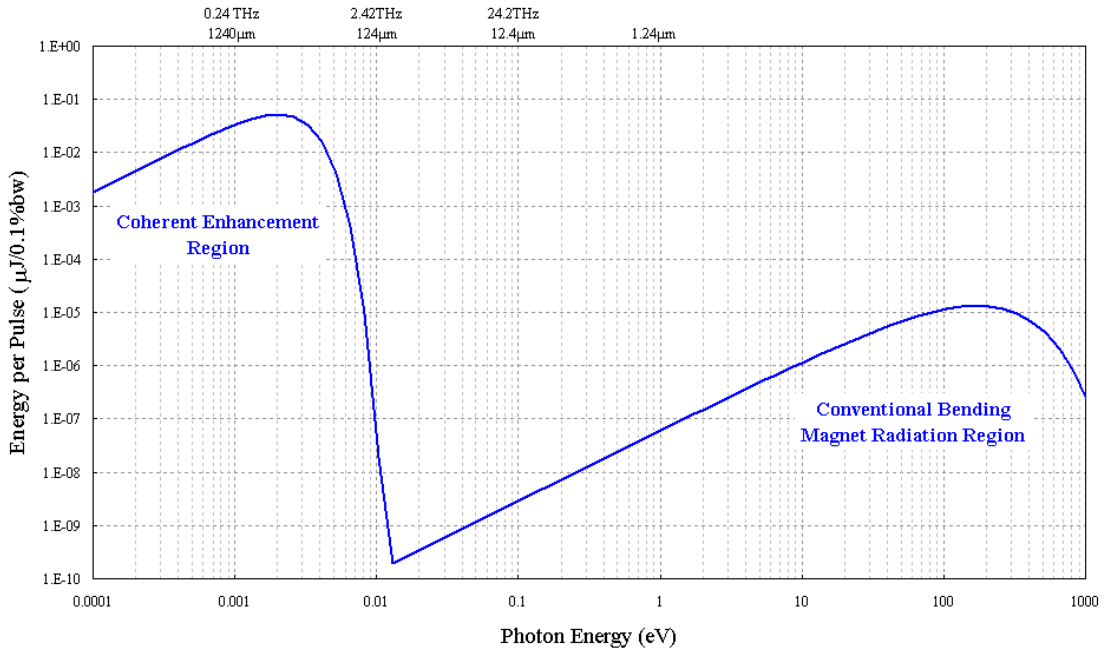

Figure 9.9 Energy per pulse from a 0.35 T bending magnet into a 50 mrad aperture with 1 nC bunch charge and RMS bunch length of 266 fs in the XUV-FEL branch at 750MeV

9.2.3 Output from Wigglers

4GLS is optimised to generate electromagnetic radiation at the soft X-ray and lower energy part of the electromagnetic spectrum, but there is also an opportunity to exploit the low emittance and short bunch electron beam as a source of hard X-rays (energy > 1 keV). Synchrotron radiation storage ring sources, although pulsed, are optimised to produce high time-averaged photon brightness. The pulse length of the X-rays in a storage ring is determined by the electron bunch length which is typically of the order of 10 to 100 ps. To achieve sub-picosecond X-ray pulses in such sources requires special measures such as laser slicing [5]. Linac based sources, such as 4GLS, are however able to generate shorter electron bunch lengths of ~ 100 fs. The short wavelength of hard X-rays allows ~ 100 fs pulses to be used without significant transform broadening of the bandpass beyond the 10^{-4} level of typical synchrotron experiments.

As an example, a 3.5 T wiggler with a 60 mm period and length of 1.5 m will be used. The total power and power densities emitted by such a multipole wiggler will be 419 W for a 100 mA average beam current, and an on-axis power density of 12 W/mrad^2. By comparison, a similar device under construction for DIAMOND [6] will emit ~ 30,000 W of power with an on-axis power density of ~ 21,000 W/mrad^2.

9.2.4 Output from Conventional Lasers

Using solid state lasers and non-linear processes, it is relatively straightforward to generate high repetition rate/low pulse energy or low repetition rate/medium pulse energy light throughout the spectrum from the XUV to the far infrared. Because a large number of experiments at 4GLS will need tunable optical radiation for use in pump-probe experiments with 4GLS sources, the facility will provide systems for this purpose at the end stations of a number of beamlines. A possible optical parametric amplifier (OPA) based system is described later in section 9.6.1 and the output from such a system is shown in the summary plots in the following section.

9.2.5 Output Comparisons

This section summarises the photon output from the full suite of 4GLS light sources. Since 4GLS has a number of possible operating modes and repetition frequencies it is difficult to summarise the possible output in a few graphs, and so the underlying assumptions for each figure need to be considered.

For the peak flux output given in Figure 9.10, the 4GLS undulators, a 1.5 m long wiggler and a dipole are in the High Average Current Loop and assume a 100 mA beam current and repetition rate of 1.3 GHz. The dipole output assumes that 50 mrad of horizontal fan is collected and 1 mrad for the wiggler. The repetition rates of the XUV-FEL, the VUV-FEL and the IR-FEL are assumed to be 1 kHz, 4.33 MHz and 13 MHz respectively. The results clearly indicate the advantage of the short electron bunches in generating very high peak intensities when compared with 3rd generation light sources. The assumed electron bunch length for the undulators, wiggler and dipole of 100 fs RMS (235 fs FWHM) is about 100 times shorter than that of DIAMOND

and MAX III. The FELs produce a tremendous enhancement when compared with the spontaneous undulators, with the FELs having an intensity of about eight orders of magnitude higher. The XUV-FEL output will contain higher harmonics (third and fifth are shown) and these also offer a very impressive performance. Filling in the region between the IR and VUV-FEL, with similar peak values, is the conventional OPA laser system which is assumed to have a repetition rate of 1 kHz. The peak brightness output is given in Figure 9.11 and similar enhancements are seen as for the peak flux. The output for some other FELs are also shown for comparison. The EUFELE FEL is currently the most advanced UV storage ring FEL in operation and this has about a thousand times lower peak brightness than the 4GLS VUV-FEL. Also shown are the design values for the DESY VUV-FEL and the DESY X-FEL.

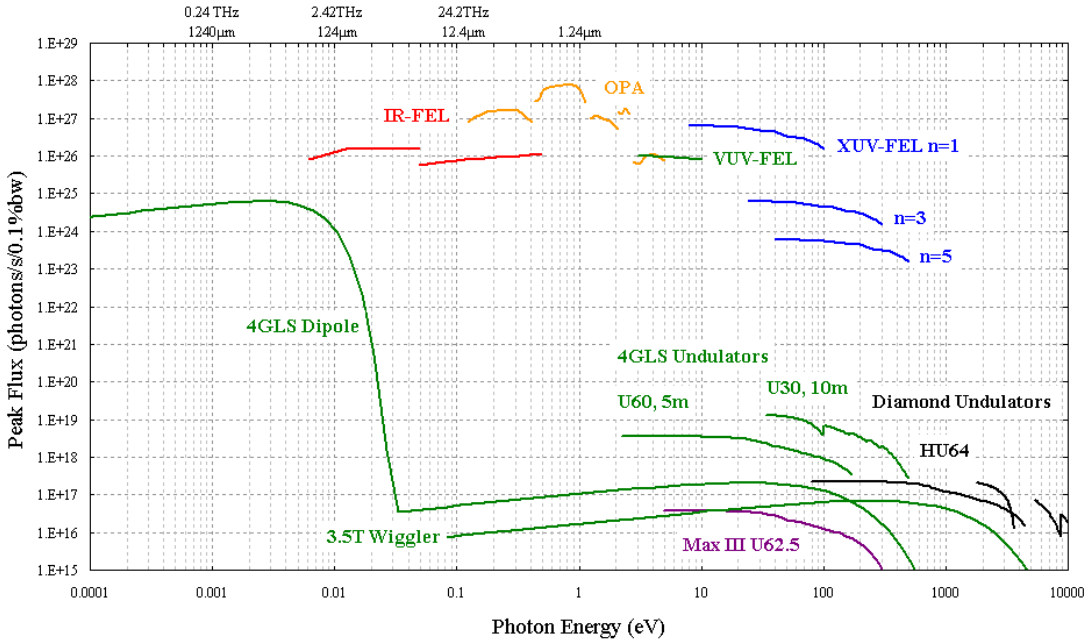

Figure 9.10 Peak flux for 4GLS FELs, undulators, wiggler, OPA and dipoles compared with DIAMOND and Max III undulators

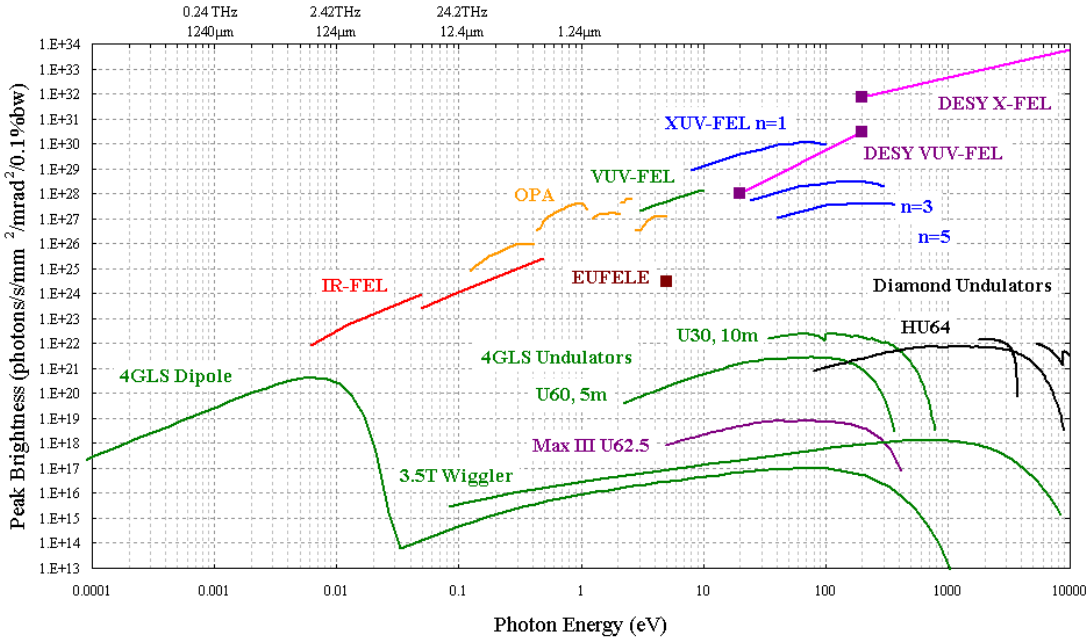

Figure 9.11 Peak brightness for 4GLS FELs, undulators, wiggler, OPA and dipoles compared with DIAMOND and Max III undulators, the EUFELE UV FEL at ELETTRA [7] and the DESY single pass FELs [8]

The energy per pulse is illustrated in Figure 9.12 and the flux per pulse in Figure 9.13. Similar assumptions are made as for the previous output curves. All of the FELs and the example OPA in general produce a similar pulse energy in the region of 10 to 100 μJ, again many orders of magnitude higher than the other possible sources. These high pulse energies are, of course, reflected in the number of photons per pulse.

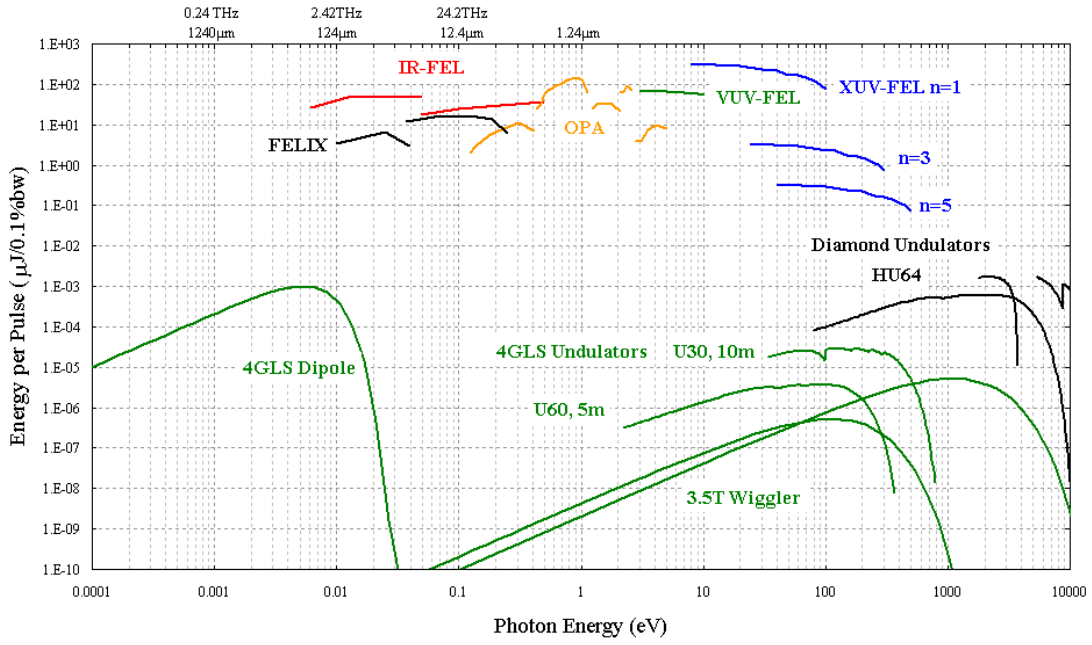

Figure 9.12 Energy per pulse for 4GLS FELs, undulators, wiggler, OPA and dipoles compared with DIAMOND undulators and the FELIX FEL [9]

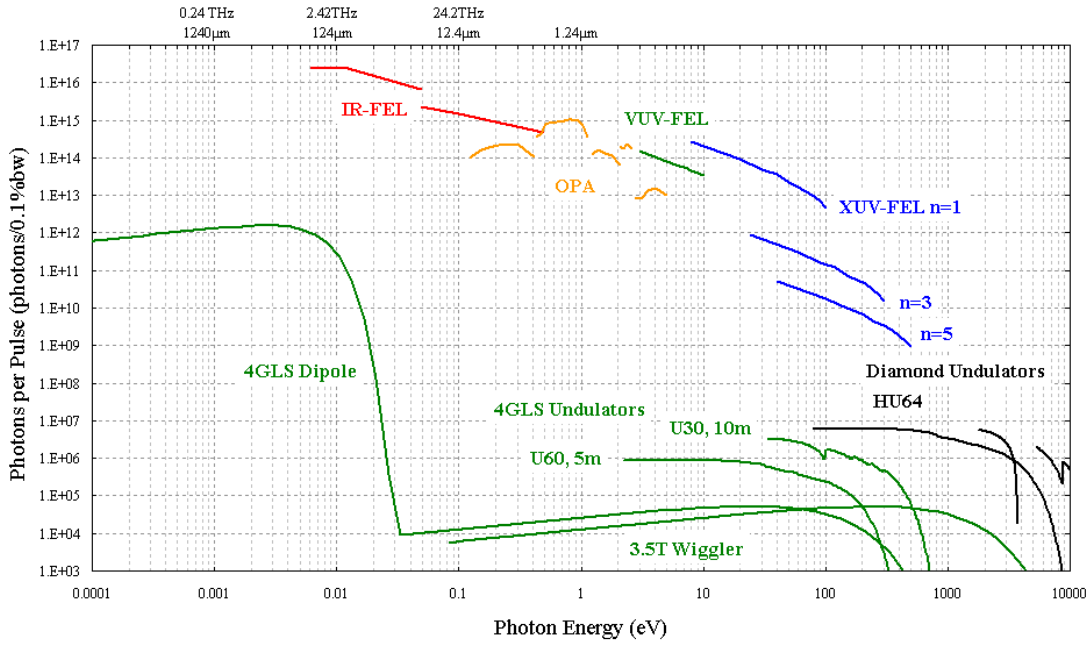

Figure 9.13 Photons per pulse for 4GLS FELs, undulators, wiggler, OPA and dipoles compared with DIAMOND undulators

For the average flux output given in Figure 9.14 the same beam currents and repetition rates as earlier are again assumed. The relatively high repetition rate of the VUV and IR-FELs ensures

that they outperform the other sources by about five and eight orders of magnitude respectively. For the average brightness output in Figure 9.15 similar comments apply.

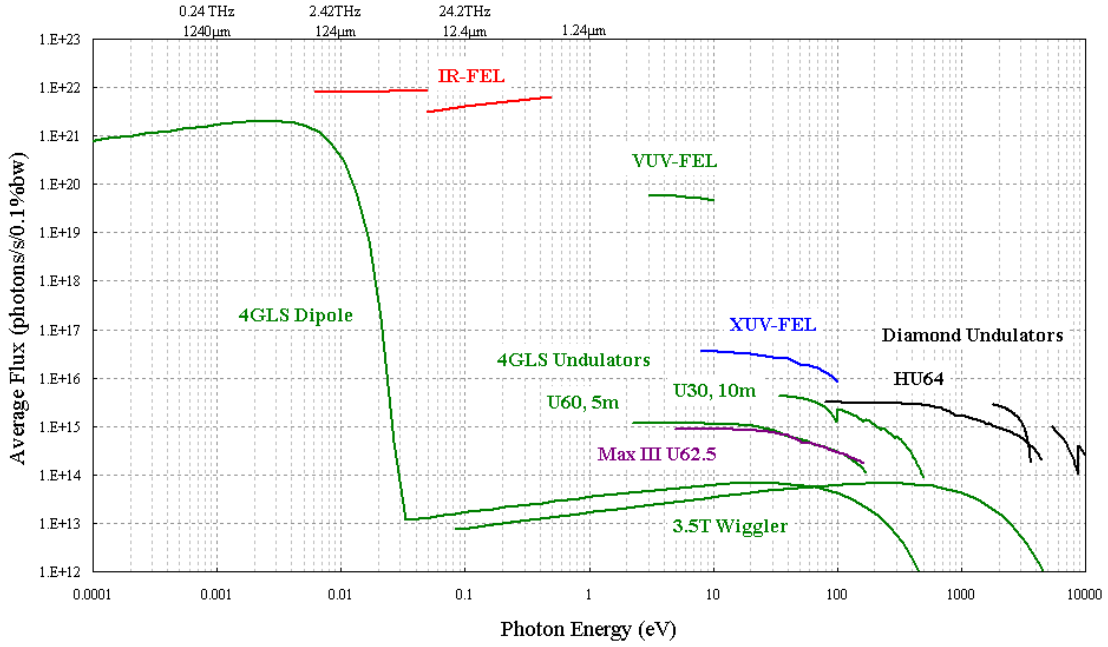

Figure 9.14 Average flux for 4GLS FELs, undulators, wiggler and dipoles compared with DIAMOND and Max III undulators

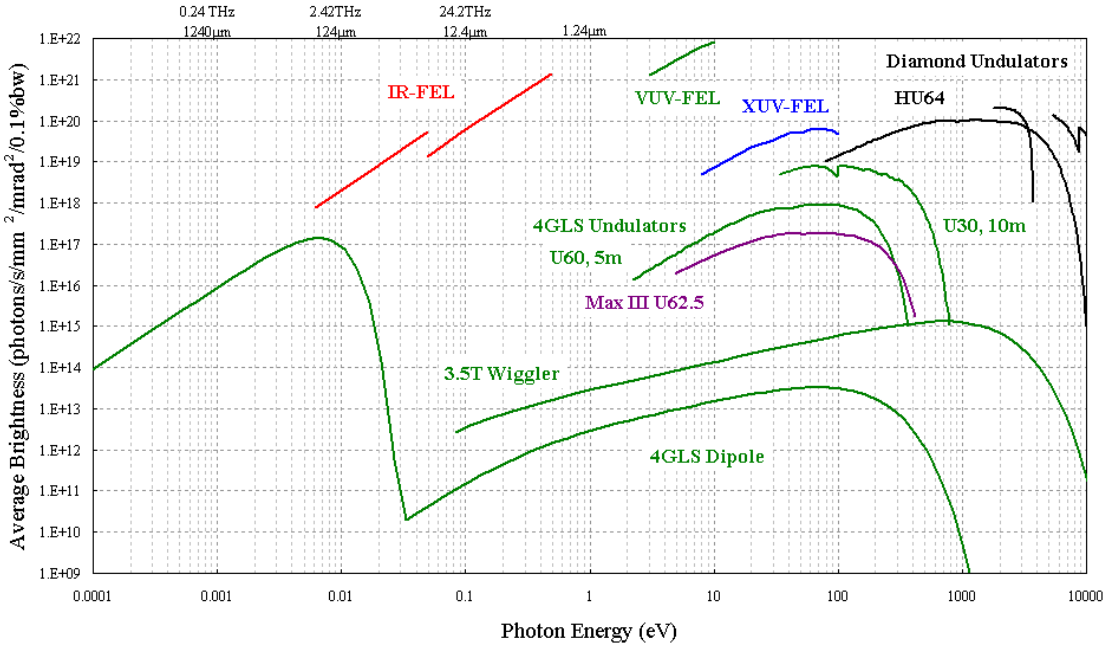

Figure 9.15 Average brightness for 4GLS FELs, undulators, wiggler and dipoles compared with DIAMOND and Max III undulators

Table 9.5 summarises the photon output from all of the sources mentioned above.

Table 9.5 Summary of the photon output from the various sources of 4GLS

	XUV-FEL	*VUV-FEL*	*IR-FEL*	*U30*	*U60*	*Dipole CSR (HACL)*	*Wiggler*	*OPA Laser*
Harmonic	1	1	1	1 to 9	1 to 9	—	—	—
Photon Energy Range (eV)	8 to 100	3 to 10	0.006 to 0.5	33 to 600	2 to 300	0.0001 to 0.03	1 to 5000	0.1 to 6
Wavelength Range (μm)	0.15 to 0.012	0.4 to 0.12	2.5 to 200	0.04 to 0.002	0.6 to 0.004	10000 to 40	1 to 0.0002	11 to 0.2
Repetition Rate	1 kHz	n x 4.33 MHz	13 MHz	1.3 GHz	1.3 GHz	1.3 GHz	1.3 GHz	1 kHz
FWHM Photon Pulse Length (fs)	50	170	2000 to 10000	300 to 2000	300 to 2000	235	500 to 2000	130
Peak Flux (/s/0.1%)	~5 x10^{26}	~1 x10^{26}	~1 x10^{26}	~1 x10^{19}	~3 x10^{18}	~6 x10^{24}	~6 x10^{16}	~1 x10^{27}
Peak Brightness (/s/mm^2/mrad^2/0.1%)	~1 x10^{30}	~1 x10^{28}	~1 x10^{22} to ~2 x10^{25}	~2 x10^{22}	~2 x10^{21}	~1 x10^{20}	~5 x10^{17}	~1 x10^{27}
Energy per Pulse (μJ/0.1%)	~200	~60	~40	~3 x10^{-5}	~3 x10^{-6}	~1 x10^{-4}	~1 x10^{-6}	~30
Photons per Pulse (/0.1%)	~5 x10^{13}	~1 x10^{14}	~6 x10^{14} to ~2 x10^{16}	~2 x10^{6}	~1 x10^{6}	~1 x10^{12}	~4 x10^{4}	~1 x10^{14}
Average Flux (/s/0.1%)	~3 x10^{16}	~6 x10^{19}	~7 x10^{21}	~3 x10^{15}	~1 x10^{15}	~1 x10^{21}	~5 x10^{13}	~1 x10^{17}
Average Brightness (/s/mm^2/mrad^2/0.1%)	~5 x10^{19}	~5 x10^{21}	~8 x10^{17} to ~1 x10^{21}	~7 x10^{18}	~7 x10^{17}	~1 x10^{16}	~7 x10^{14}	~1 x10^{17}

9.3 Undulators

9.3.1 Undulator Locations

There are six insertion device straights in the high average current loop and one of these is allocated to the VUV-FEL. There are three different undulator straight lengths; 2 of ~ 8 m, 2 of ~ 10 m, and 2 of ~ 14 m. Thus the total space available for undulators is ~ 64 m which compares very favourably with typical low energy 3rd generation light sources (see Table 9.6). In principle a number of devices can be inserted into the same straight with a small corrector magnet between them so as to angularly separate the photon beamlines. This technique is increasingly being used on 3rd generation light sources to increase the effective number of straights but has not been considered in detail at this stage for 4GLS. In addition to this there is an undulator straight after the XUV-FEL for the high bunch charge beam.

Table 9.6 Comparison of approximate space available for undulators in 4GLS and several low energy 3rd generation light sources

Light Source	*Total Undulator Straight Space (m)*
ELETTRA	52.8
BESSY II	60
ALS	50
4GLS	64

9.3.2 Undulator Design Options

A number of undulator magnet technology options exist and these are described below. In addition the polarization characteristics required will affect the design of the undulator. Another design option which exists is due to the 'round beam' properties of the electron beam. Conventional light sources, based upon storage rings, require an elliptical vacuum chamber since much greater aperture is always required in the horizontal plane for lifetime and injection processes. 4GLS does not rely on such processes with the consequence that the aperture requirements in both planes are broadly similar. The undulators could take advantage of this aperture by having the arrays mounted in the horizontal plane rather than the vertical one. This may be more straightforward from an engineering point of view, provided there is space available. An initial engineering assessment has been made and is presented in Figure 9.16. In principle the round aperture could be completely surrounded by the magnet to produce very intense fields but this makes magnet testing problematic, and also the production of the vacuum within the long vessel may not be possible without any side access for pumps. However, compromise solutions exist which partially surround the vacuum chamber [10] and these will be studied further.

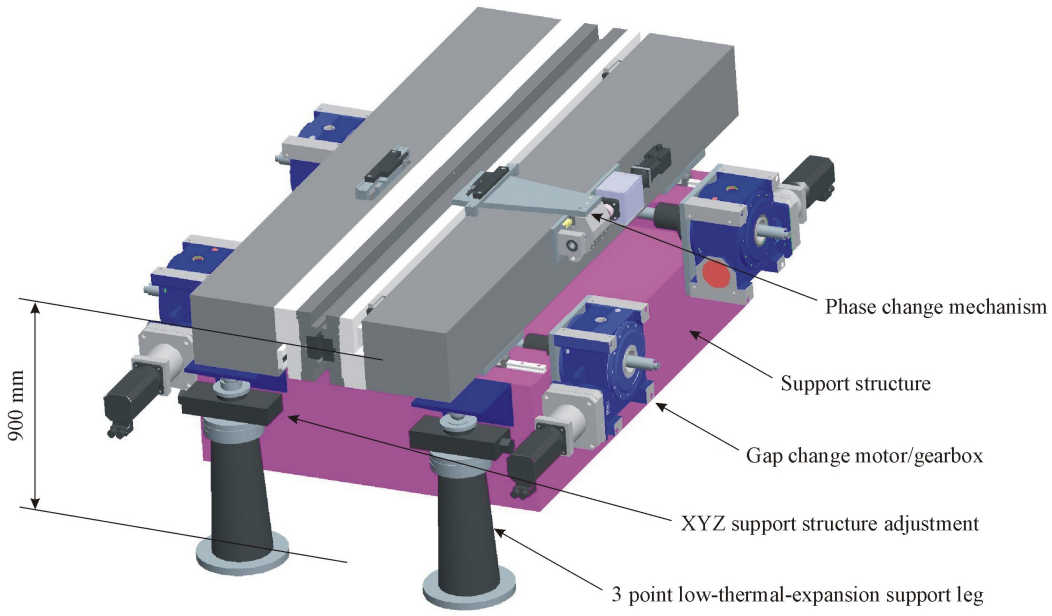

Figure 9.16 Engineering scheme for an APPLE-II undulator mounted horizontally rather than vertically

.

The magnet gap plays a crucial role in determining the peak fields that can be achieved. In general, the undulator design benefits from small magnet gaps. However, there are counter arguments for having large vacuum chambers, and hence large gaps, that relate firstly to the physical space available to the electron beam and secondly to the influence of the vacuum chamber on the electron beam due to wakefield effects (see section 7.7.6). A compromise must be reached and for 4GLS the undulator magnet gap in the High Average Current Loop has been limited to a minimum of 10 mm.

9.3.2.1 Permanent Magnet Based Designs

The vast majority of undulators in use today are based upon permanent magnet technology. The simplest form of these is the planar pure permanent magnet design which is widely used. The peak magnetic field produced on-axis by such a magnet, B_0, is given by [4]

$$B_0 = 1.72 B_r e^{-\pi g/\lambda_u} \tag{9-2}$$

where B_r is the remanent field of the magnet blocks, g is the gap between the magnet arrays and λ_u is the period of the undulator. Typical values for remanent field are between 1.1 and 1.2 T.

The magnetic field in a permanent magnet undulator can be enhanced by the inclusion of iron poles. These hybrid magnets are intrinsically non-linear so no simple analytical formula exists, but empirical studies have shown [11] that for a remanent field of 1.2 T the peak field level is given by

$$B_0 = 3.694 \exp\left(-5.068 \frac{g}{\lambda_u} + 1.52 \left(\frac{g}{\lambda_u} \right)^2 \right) \qquad (9\text{-}3)$$

A comparison of the two types of undulator in terms of the peak field achievable is given in Figure 9.17. Typically undulators are operated with g/λ_u values in the range 0.2 to 0.8.

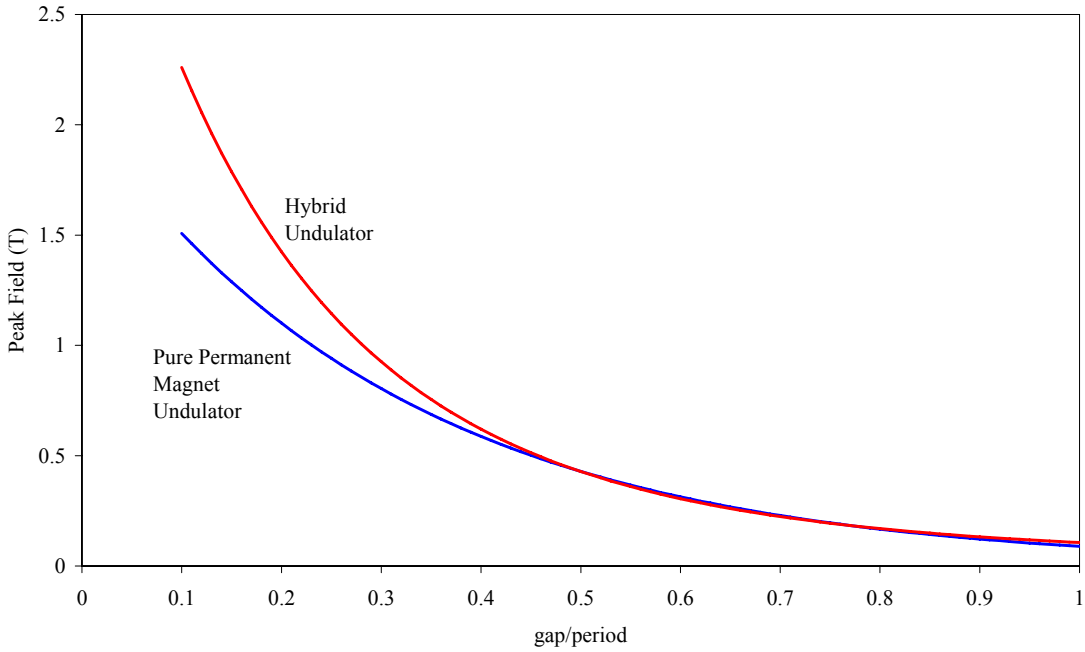

Figure 9.17 Comparison of the field levels achievable for pure permanent magnet and hybrid undulators

9.3.2.2 In-Vacuo Magnets

Many undulators are now put inside the vacuum system of accelerators so that the magnet gap can be made smaller. There is no requirement, in this case, for a vacuum chamber between the magnet arrays and so the magnet gap can be reduced typically by about 3 mm. However, producing variable polarisation undulators that operate inside a vacuum system is very challenging from an engineering point of view and probably not the best approach. At this stage it is not clear whether 4GLS will make extensive use of in-vacuo systems since variable polarisation is likely to be requested for many of the beamlines. However, for beamlines only requiring planar polarisation it is likely that in-vacuo technology would be strongly considered.

9.3.2.3 Superconducting Magnets

There is considerable interest now in the use of superconducting undulators. As yet they are still under development and so they do not have a proven record of operating successfully on 3rd generation light sources. Schemes have been produced for variable polarisation devices but these are less well developed than the simple planar field devices. The field enhancement

offered by a superconducting undulator is very attractive and strong consideration will be given to the extensive use of this technology in the future.

9.3.2.4 Cold Permanent Magnets

Reducing the temperature of a permanent magnet increases the remanent field. Experiments with available materials have been carried out in Japan [12] which show that the on axis field level for an undulator can be enhanced by about 30 % if the temperature is reduced to about 150 K. However, cooling magnet arrays to such low temperatures will almost certainly involve putting the systems inside an insulating vacuum which then means that these devices will suffer from the same limitations as the standard in-vacuo undulators with regard to variable polarisation production.

9.3.2.5 Variable Polarisation Devices

It is anticipated from the 4GLS Science Case [1] that there will be a strong demand for selectable polarisation of the light. This is achieved with undulators that are capable of generating horizontal and vertical fields that can be controlled independently. The most common device of this type is the permanent magnet based design, APPLE-II [13] and this is what has been assumed for the variably polarising undulators. Undulators of this type are in operation at several 3rd generation light sources, and one has recently been designed and constructed at Daresbury Laboratory and successfully commissioned in the SRS (see Figure 9.18 and Figure 9.19) [14, 15] and one is now being constructed for DIAMOND [6]. This magnet can produce elliptical polarisation and in particular linear horizontal, linear vertical, left circular and right circular radiation. With a further adaptation linear radiation of arbitrary inclination can also be generated. No analytical expression exists for the magnetic field on-axis when in the helical mode but an empirical equation has been developed based upon 3D magnet models [11], assuming a remanent field of 1.2 T, and it is given by

$$B_x = B_y = 1.614 \exp\left(-4.67 \frac{g}{\lambda_u} + 0.62 \left(\frac{g}{\lambda_u} \right)^2 \right) \tag{9-4}$$

Further enhancement of the field level is possible if the round beam aperture is exploited. A design has been developed [10] which produces a higher helical field by about a factor of 1.4. Such an increase is attractive and so serious consideration will be given to the use of such a design. The effect of the revised design on the mechanical forces, field quality at small gaps, shimming ability and so on will need to be carefully assessed in the next stage of the project.

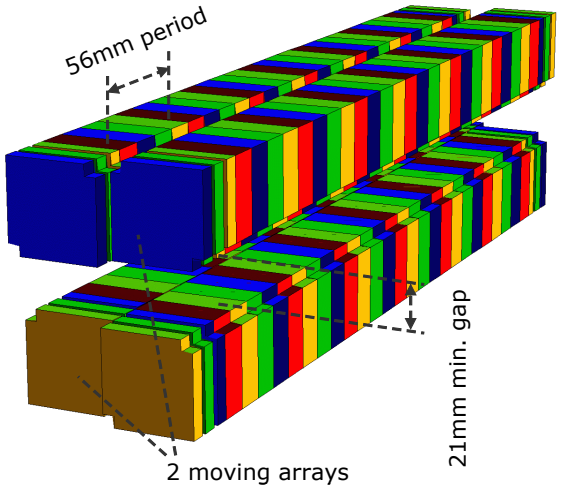

Figure 9.18 RADIA [16] model of HU56 APPLE-II undulator recently installed and commissioned in the SRS

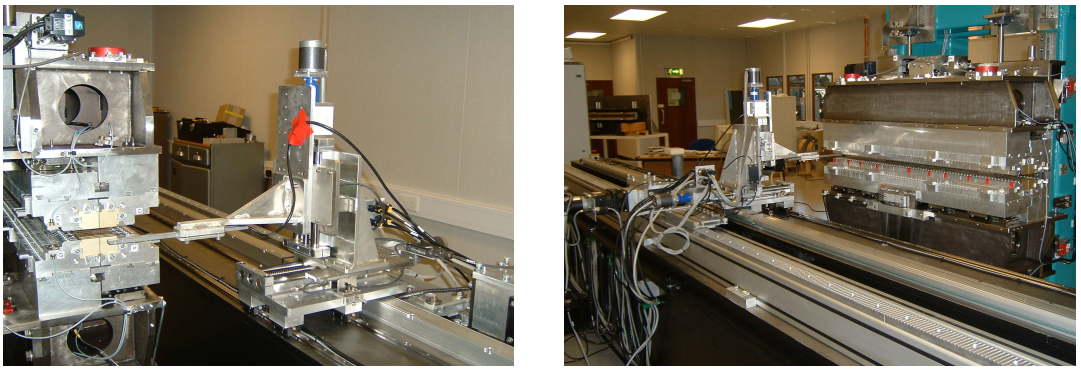

Figure 9.19 Photographs of the HU56 APPLE-II undulator being tested at Daresbury Laboratory

9.3.3 Effect of Undulators on the Electron Beam

4GLS is a single pass machine, unlike a storage ring, and so the effects due to undulators in 3rd generation light sources are not replicated. There is no emittance equilibrium for example and also an electron that loses energy due to the emission of synchrotron radiation will not have this energy replaced. This section looks at the effect of the undulators on the electron beam.

9.3.3.1 Energy Loss

An electron emitting synchrotron radiation in an undulator will lose energy. The equation for the energy lost by a relativistic electron, ΔE (in eV), travelling through a magnetic system of length L is given by [4]

$$\Delta E = 1265.5 E^2 \int_0^L B(s)^2 \, ds \tag{9-5}$$

where the energy of the electron, E, is in GeV. The largest energy loss is for a helical undulator since B(s) is effectively constant along its length. A 10 m long helical undulator with a 1 T transverse field will cause each electron to radiate ~ 4.6 keV on average, which is less than one part in 10^5 of the electron's energy. For an electron passing through a system of five undulators the total loss by the electron is ~ 23 keV, which is still less than 0.004 % of the electron's energy. The effect on the electron beam energy spread is negligible as shown later in section 9.3.3.4.

The electron will also radiate energy as it passes through the arc dipoles. Ignoring coherent effects an electron passing through a system of 1 T dipoles making up a 360° path will radiate ~ 5.7 keV on average. However, as mentioned earlier, the coherent effects are significant in 4GLS because the electron bunch lengths are so short. A calculation of the CSR energy radiated is complicated because the electron bunch length is not constant around the high average current loop. The code ELEGANT [17] has been used to calculate the energy radiated around the high average current loop, up to the entrance to the return arc. The results, which depend strongly upon the exact settings used in the model, suggest a loss of ~1 MeV due to CSR emission. Although this loss is relatively large it will remain constant so long as the bunch parameters do not vary. Further modelling will be carried out as part of the start to end simulations (see section 7.7.4) with realistic longitudinal bunch profiles to calculate these losses more accurately.

If we assume a worst case of an electron energy change of 0.005 %, due to a number of undulators being varied, then the change in undulator harmonic wavelength for a subsequent typical 48 mm period device, generating ~ 100 nm radiation, would be about 0.01 nm (or 0.01 %). This should be contrasted with the typical harmonic bandwidth of ~ 1 %. This effect may become important at higher undulator harmonics which naturally have narrower bandwidths.

9.3.3.2 Path Length Effects

Since an undulator affects the trajectory of the electron beam, and hence the path length, the adjustment of an undulator in one straight will affect the electron bunch arrival time at subsequent undulators and so could affect the timing synchronisation with another source. The maximum time delay that an undulator can introduce is the difference between the time it takes an electron to travel the length of the undulator when it is at maximum field (maximum path length) to when it is at zero field (minimum path length).

An example undulator with a K factor of 5 and a length of 10 m will introduce a time delay in the electron beam undulator exit time of 150 fs for a 600 MeV electron beam. A helical undulator with the same K parameter produces double the time delay. Two photon experiments which rely upon the same electron bunch to generate the photon pulses will be largely unaffected by these time delays since the relative timing between the two sources will remain constant. However, if these timing changes are cause for concern a simple three-pole chicane magnet arrangement could be used to counteract the effect of undulator gap changes so that the total path length of the electron beam is always kept constant. Simple modelling suggests that a

magnet with a peak field of 0.5 T and length of 1 m can easily introduce time delays of 400 fs which is more than adequate for the undulators considered here.

The time delay between two photons emitted by the same electron, one emitted at the entrance of the device and one at the exit, is Nλ, where N is the number of undulator periods and λ is the wavelength of the light emitted. The same example undulator as above with a K factor of 5 and a length of 10 m will introduce a maximum photon pulse lengthening of 163 fs with a 600 MeV electron beam. A helical undulator with the same K parameter in both planes produces double the pulse lengthening. In fact these are rather pessimistic estimates and modelling with an FEL code suggests that the actual FWHM only increases by about half these values. However, this does suggest that long wavelength experiments requiring the shortest possible pulses should be based upon relatively short undulators. For example, a planar undulator which is 5 m long and with a K of 3 will only contribute 33 fs of pulse lengthening. Note that the electron bunch length is unaffected by these path length effects.

9.3.3.3 Emittance

Emission of radiation in an undulator implies a loss of energy by the electron and so if dispersion is present within the undulator this could lead to an emittance growth. Although the dispersion (η) and its derivative (η') will be set to zero at the entrance to an undulator the device itself will generate its own dispersion and so this must be considered to see if the effect is significant. The dispersion generated by an undulator with a sinusoidal magnetic field is given by [4]

$$\eta(s) = \frac{\lambda_u^2}{4\pi^2\rho_0}\sin\left(\frac{2\pi s}{\lambda_u}\right) \tag{9-6}$$

$$\eta'(s) = \frac{\lambda_u}{2\pi\rho_0}\cos\left(\frac{2\pi s}{\lambda_u}\right) \tag{9-7}$$

The rate of change of emittance due to this dispersion can be estimated to be [18]

$$\frac{d\varepsilon_x}{ds} \approx 1.45\times10^{-19}\gamma^2 B_0^3 H(s) \tag{9-8}$$

where H(s) is defined as

$$H(s) = \frac{1}{\beta}\left(\eta^2 + \left(\beta\eta' + \frac{1}{2}\beta'\eta\right)^2\right) \tag{9-9}$$

If we make the reasonable assumption that the betatron function, β, remains approximately constant through the undulator (and so β' = 0) and substitute an average value for η'^2 then by integrating over the length of the undulator we can show that the emittance growth is

$$\Delta\varepsilon = 1.04\times10^{-15}\lambda_u^2 B^5 \hat{\beta} L \tag{9-10}$$

Furthermore, if we assume that the betatron function at the undulator centre is equal to half the undulator length then the average value of β through the device $\hat{\beta}$, is 2L/3. In these circumstances the emittance growth due to a 10 m undulator of 50 mm period and peak field of 1 T is 1.7 x 10^{-7} nm rad, which is 10^7 times smaller than the natural emittance and so is certainly a negligible effect.

A second effect on the emittance, due to the change in transverse momentum of the electron, has also been considered [19], but this effect is generally smaller than the effect above by a factor of ~ 0.2 K^2, so is also negligible.

9.3.3.4 Energy Spread

Since the electrons passing through an undulator will emit photons over a relatively wide energy range in a discrete process it might be anticipated that the energy spread in the electron beam could increase significantly as a result. An analytical approach to the energy spread induced by this quantum process suggests that the energy spread of the electron beam due to a helical undulator (the worst case) is given by [20]

$$\sigma_\gamma = 5.02\times10^{-13}\gamma K\left(\frac{F(K)L}{\lambda_u^3}\right)^{1/2} \tag{9-11}$$

where F(K) is a function of K which has been solved numerically to an accuracy of better than 1 % over the full range of possible K values:

$$F(K) = 1.42K + \frac{1}{1+1.50K+0.95K^2} \tag{9-12}$$

As an example, a helical undulator with a period of 50 mm, K value of 5 and length of 10 m would induce an additional energy spread of 0.0002 %, which is negligible in comparison with the nominal electron energy spread of 0.1 %.

An alternative numerical approach has been developed [21], which has also been applied to the 4GLS case. This method directly calculates the probability of a particular photon energy being emitted and assesses the consequences of this on the electron beam. For the undulator parameters above the additional energy spread is found to be 0.0001 %, less than the analytical result by about a factor of two.

9.3.3.5 Electron Bunch Length Growth

An additional consequence of the self dispersion generated by the undulators is the effect this will have on the electron bunch length. The change in the electron bunch length, $\Delta\sigma_l$, due to the undulator is given by

$$\Delta\sigma_l = \frac{R_{56}\sigma_E}{c} \tag{9-13}$$

where R_{56} is the change induced by the undulator in the linear (5,6) element for the system that couples the longitudinal coordinates (described in more detail in Chapter 7), and σ_E is the relative projected energy spread of the electron beam. For a planar sinusoidal magnetic field R_{56} can be written as [4]

$$R_{56} = \frac{L\lambda_u^2}{8\pi^2\rho_0^2} \tag{9-14}$$

An example undulator with a period of 50 mm, field of 1 T and length of 10 m, has R_{56} of 0.08 mm and will contribute an additional 0.3 fs to the electron bunch length, which is negligible.

9.3.4 Undulator Tolerances

Tolerances for the undulators need to be carefully considered so that they are able to meet the design goals of the project. Issues to be considered include the effect of a non-ideal magnetic field, misalignments, steering errors etc. In most instances the most demanding undulator system is that required for the XUV-FEL since the electron beam/photon beam transverse overlap needs to be maintained over ~ 30 m. A number of error sources will be considered in this section with regard to the XUV-FEL undulator. In general the tolerances of the other undulator systems will be more relaxed than this.

9.3.4.1 Trajectory Straightness

The ability to steer the electron beam through the undulator system is of critical importance. In order to have a sustained FEL interaction in the undulator the radiation and electron beam must maintain a close transverse overlap. Whereas the radiation propagates in a straight line along the central axis of the undulator, the same is not true of the electron beam. Errors in both the alignment and field strengths of the undulator mean that the electron beam will wander in and out of the co-propagating radiation field. If the RMS wander of the electron beam approaches the radiation transverse mode radius then the gain will be significantly reduced as the radiation and electrons will effectively decouple. Given that the electron beam size for the XUV-FEL is ~ 70 μm and that the radiation mode can be expected to be of similar size, state of the art technology is required to maintain the transverse beam positioning to this order over tens of metres of propagation. To date the only way to effectively model these effects on the FEL interaction are via 3-D numerical codes which introduce the undulator errors as a random variation about some mean value [22, 23, 24]. A conservative estimate suggests that the RMS electron beam trajectory should not wander by more than 20 % of the electron beam size [25]. This suggests a trajectory straightness of ~ 15 μm for the XUV-FEL undulator. Such a value is demanding but achievable with sophisticated magnet shimming techniques already used routinely at Daresbury Laboratory.

9.3.4.2 Gap Control

The undulator system is comprised of many modules and it is vital that they are all set to resonate at the same wavelength. Since the FEL process has a natural linewidth it is enough to ensure that the K values of all the modules are set so that the undulator resonance is within this linewidth: this then sets the minimum gap step size that is needed. The HWHM FEL linewidth is given by (see section 8.1.3):

$$\frac{\Delta\lambda}{\lambda} \approx 2\rho \tag{9-15}$$

where ρ is the Pierce parameter. The variation of wavelength with K can be derived from the undulator resonance equation to give (for large K):

$$\frac{\Delta\lambda}{\lambda} \approx \frac{2\Delta K}{K} \tag{9-16}$$

and so it is enough to ensure that

$$\frac{\Delta K}{K} = \frac{\Delta B}{B} < 2\rho \tag{9-17}$$

where B is the peak on axis magnetic field. However, to ensure that the resonance condition falls well within this linewidth an additional safety factor of four is introduced such that an equality that will define the gap control can be given as

$$\frac{\Delta B}{B} = \frac{\rho}{2} = \pm\frac{\rho}{4} \tag{9-18}$$

Assuming a planar pure permanent magnet it can be shown using the field equation given in section 9.3.2.1 that the field variation with gap change, Δg, is given by

$$\frac{\Delta B}{B} = \exp\left(\frac{\pi\Delta g}{\lambda_u}\right) - 1 \tag{9-19}$$

Hence a gap change of 1 μm will induce a field variation of 7 x 10^{-5} for the 45 mm period linear polarising undulator selected for the XUV-FEL (see Table 8.3). The smallest value of ρ for the XUV-FEL is 3 x 10^{-3} and so the gap control must be better than ± 10 μm.

Similar analysis of the APPLE-II field variation with gap when in helical mode, using the empirical equation of section 9.3.2.5 shows that

$$\frac{\Delta B}{B} \approx \exp\left(4.67\frac{\Delta g}{\lambda_u}\right) - 1 \tag{9-20}$$

Hence a gap change of 1 μm will induce a field variation of 9×10^{-5} for the 51 mm period helical undulator selected for the XUV-FEL (see Table 8.3). This implies the gap control for the APPLE-II modules must be better than ± 8 μm. The gap control resolutions derived are greater than those specified already by the insertion devices installed in the SRS [26] (± 5 μm) and so they would seem to not be unduly concerning.

9.3.4.3 Temperature Control

An additional source of error comes from the variation of the magnetic field strength with temperature. A typical temperature coefficient for NdFeB magnet material is -0.1 %/°C. Any temperature variation will have to be compensated by having better gap resolution control. Table 9.7 summarises how the allowable temperature variation of the undulator modules can be traded off against gap setting resolution.

Table 9.7 Variation of gap control resolution required as a function of temperature stability of the APPLE-II XUV-FEL undulator modules in helical mode for a Pierce parameter of 3×10^{-3}

Temperature Control (°C)	*Gap Control Resolution (μm)*
± 0.1	± 7.1
± 0.2	± 6.0
± 0.3	± 4.9
± 0.4	± 3.8
± 0.5	± 2.7

The combination of temperature and gap control required appears to be practical. If difficulties were to arise in attaining these values then consideration could be given to the use of a weaker magnet material, such as SmCo, since this has a three times smaller temperature coefficient.

9.4 Dipoles

9.4.1 Generation of Coherent SR

In all accelerator dipoles the electrons in a bunch radiate coherently at wavelengths of the order of, and longer than the bunch length. However, the electron bunch lengths of 3rd generation light sources are typically in the range 10 to 30 ps which means this radiation only occurs at multi-mm wavelengths. By contrast the 4GLS bunch length will be as short as 100 fs and so wavelengths of ~30 μm and greater will benefit from this effect. A consequence of the coherence is that the bunch of N electrons radiates with intensity proportional to N^2 rather than just N as it does for an incoherent source. Since N is in general a very large number this enhancement factor is enormous and this ensures that 4GLS will be one of the world's most powerful THz sources.

Observations of this coherent radiation have been made at Jefferson Laboratory [27] and dedicated beamlines are being built to exploit this radiation there and on the ERLP at Daresbury Laboratory [28, 29].

9.4.2 Possible Location of Dipole Sources

The most useful sources of THz radiation will be at the bending magnets where the electron bunches are shortest since this is where the shortest wavelengths of CSR will be generated. On the XUV-FEL branch, this will be either the last bending magnet before the entrance to the FEL, or on the bending magnet immediately after the FEL. On the high average current loop, where the bunch will be sequentially compressed round the loop, the most likely source for a THz beamline will be at the bending magnets just before or after the VUV-FEL.

9.4.3 Properties of Coherent SR

CSR is emitted over a wide wavelength range with the long wavelength limit being set by the vacuum chamber dimensions. More precisely, the observed long wavelength limit is [30]:

$$\lambda = 2b\left(b/\rho\right)^{1/2} \tag{9-21}$$

where b is the pipe diameter and ρ is the bending radius. This limit will typically be of the order of 10 mm wavelength (0.0001 eV) though it could be larger if special vacuum chamber designs are implemented.

For short pulses, the minimum bandwidth is given by the uncertainty principle and although the results in Figure 9.6 and Figure 9.7 are given in terms of a 0.1 % bandwidth to aid comparisons, this is not realistic in practice. For example, a radiation pulse with an RMS length of 100 fs would lead to an energy resolution ~ 0.0008 eV FWHM.

Some experiments utilise the radiation electric field directly. The peak field will depend on the pulse width and bandwidth. As an example of the field strengths that could be achieved, the field produced by a 10 % bandpass of radiation of energy 0.0025 eV (~500 μm) from the XUV-FEL electron bunch is calculated.

The shortest pulse that would achieve a (2 sigma) 10 % bandpass of 0.00025 eV would have an RMS length of 2.6 ps. From Figure 9.8 the flux per pulse at 0.0025 eV into a 50 mrad fan and a 10 % bandpass is 1.1 x 10^{16} photons. Note that 70 % of this flux will occur in a time of 5.2 ps, compared to the optical period of 1.7 ps for 0.0025 eV radiation. Focussing this radiation into a spot of radius 1 mm yields a power density of about 2 x 10^{11} W/m^2. The electric field is then calculated from

$$E = \sqrt{\frac{2I}{c\varepsilon_0}} = \sqrt{240\pi I}\ \text{V/m} \tag{9-22}$$

where I is the power density, giving a field of about 12 MV/m, very similar to the value of 5.5 MV/m/cm^{-1} for the THz line at Jefferson Laboratory (1cm^{-1} = 0.000124 eV) [31].

Instead of using bending magnet radiation, THz radiation can also be produced by firing the electron bunch through a metal foil, to generate transition radiation. As an example, THz transition radiation is produced at the DUV-FEL [32], where they have measured a pulse energy of 80 μJ with electron bunches of charge 0.7 nC and length 300 fs. Scaling this to the 1 nC bunch for the XUV-FEL would suggest that pulse energies of 160 μJ could be obtained compared to an estimated 90 μJ for bending magnet radiation. A major difference in the properties of bending magnet and transition radiation is the polarisation – transition radiation is radially polarised which gives zero intensity on axis, whereas bending magnet radiation is linearly polarised on axis, and elliptically polarised above and below the horizontal axis. Transition radiation could be generated after the XUV-FEL in the dump line. Further studies of coherent transition radiation will be made in the next phase of the project.

9.5 Wigglers

There are a number of methods that could be used to generate fs hard X-ray pulses from the 4GLS electron beam. Many of these methods rely on the interaction of the electron beam with a fixed target. When the electron beam collides with a target, in techniques such as coherent bremsstrahlung, channelling radiation, parametric radiation, transition radiation, the electron beam quality is disrupted and so these techniques have not been pursued further for 4GLS. Other methods seem more applicable and a wiggler source is suggested as the best option. A possible alternative technique that is considered a potential upgrade to 4GLS is Compton scattering of the electron beam with a laser beam and this is discussed in further detail in Chapter 12.

Multipole wigglers can be built using permanent magnet or superconducting technology. Three high field (2 T and 2.4 T) permanent magnet wigglers are presently in use on the SRS [26]. These devices have relatively long periods (200 and 220 mm) for the magnet gap of 20 mm. Shorter periods are possible using superconducting technology at the expense of the complication of operating a cold bore cryostat within an accelerator environment.

The effect of a wiggler on the electron beam is similar to an undulator. The increased field level of the wiggler tends to increase the magnitude of any effect but this is often balanced by the reduced length of the magnet and so in general the impact of a wiggler on the electron beam is broadly similar to that of the undulator examples.

For applications that require hard X-rays with very short pulse lengths (< 500 fs) care must be taken that the slippage effects discussed earlier in section 9.3.3.2 do not over lengthen the photon pulses. If this is found to be an issue then the wiggler parameters can be altered (by reducing the length of the magnet for instance) to reduce the effect or the alternative Compton method mentioned earlier could be implemented.

9.6 Conventional Lasers

One of the most important functions of the 4GLS facility is to provide the means for doing time-resolved studies of phenomena with resolution of tens of femtoseconds. This requires providing users with the means to conduct pump-probe experiments with sources that provide the best time resolution available. In some cases the pump or the probe source should be a conventional laser that is integrated into the facility.

Access to the XUV-FEL seed laser could be useful for users requiring pump or probe light that is synchronised to the XUV-FEL itself. It should be possible to make use of the high power (IR) fundamental but transport of the high harmonics is unlikely to be practical whilst the XUV-FEL is operational.

9.6.1 Additional Lasers

A large number of experiments at the 4GLS will need tuneable optical radiation for use in pump-probe experiments with 4GLS sources and the facility will provide systems for this purpose at the end stations of a number of beamlines. A possible system, shown in Figure 9.20, is used here to illustrate how broad spectral coverage can be obtained. The synchronized seed for the system could be derived directly by optical means from the master clock, or a separate oscillator could be locked to the clock at the femtosecond level [33]. The repetition rate of the seed is a sub-harmonic of the machine frequency in the 100 MHz range, and pulses are picked from this train at kilohertz rates for amplification. Currently available commercial chirped pulse amplification (CPA) systems produce energies in the 1-7 millijoule range at 1 kHz, in the near IR spectral region (~ 800 nm). From the millijoule pulses, other wavelengths are obtained through various nonlinear optical processes [34, 35]. Figure 9.20 shows a block diagram of the several processes used to reach the various regions of the spectrum. The amplifier pumps an optical parametric generator/amplifier system (OPG/OPA). Optical parametric generation produces signal and idler pulses that can be tuned throughout the wavelength range of 1150 – 2600 nm. The difference frequency between signal and idler can extend from 2400 to 11000 nm (although with only limited pulse energy at the longer wavelengths). Frequency-doubling (SHG) the OPA output or summing it with the residual pump radiation covers the visible and near-IR portion of the spectrum (475-1150 nm), while further doubling and sum-frequency mixing are used to extend the spectrum all the way to the boundary of the vacuum ultraviolet at 189 nm. Figure 9.12, shows a representative energy yield curve from a system driven by an amplified pulse of ~ 0.5 mJ, at a wavelength of 790 nm.

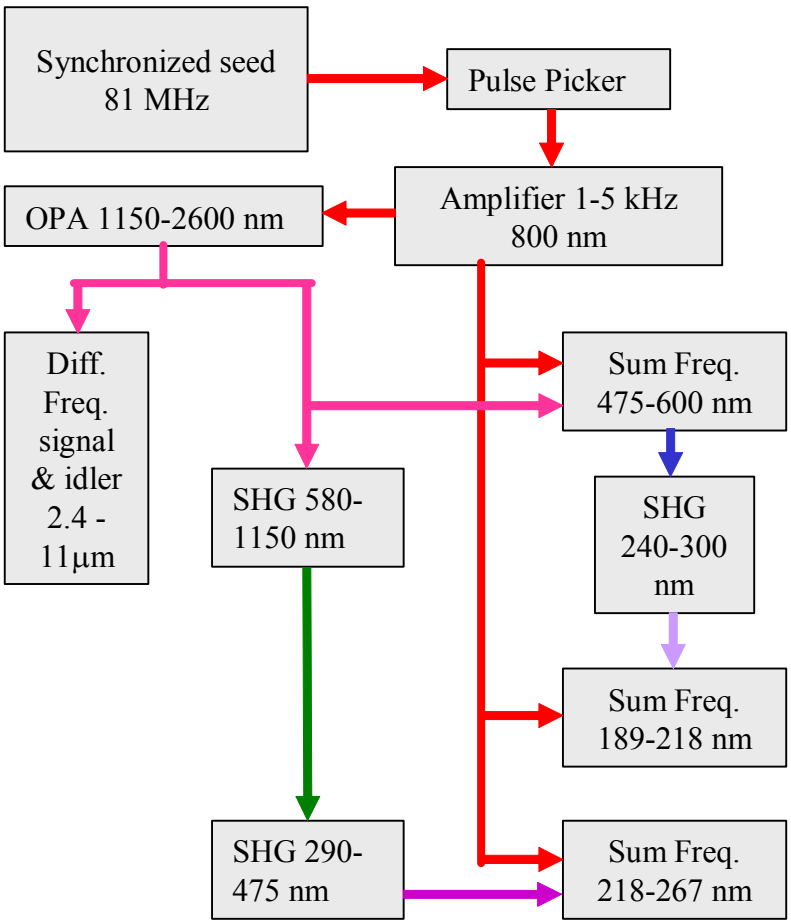

Figure 9.20 A Titanium sapphire based frequency synthesis system for providing broadly tunable ultrafast pulses for pump-probe experiments in conjunction with 4GLS sources. A near-IR amplifier pumps an optical parametric amplifier, and a number of frequency-mixing stages are used to cover the spectrum from 189 nm to 11 µm. Arrows are colour coded for the spectrum of the radiation they represent. The operation in a box operates on the spectra entering the box to produce the spectrum written in the box. OPA, optical parametric amplifier, SHG, second harmonic generation.

The frequency-synthesis system is very robust and relies on long-established technology. Commercial versions have been available for several years. While this is a mature and reliable technology, even the well developed commercial systems generally require trained specialist oversight to ensure reliable and optimal operation. With dedicated supervision of these laser systems, high efficiency, robust and trouble free operation would be expected. A fully automated system for tuning and synchronisation could be implemented, allowing for significant user control of experimental conditions. Such systems would be convenient "workhorses", fulfilling a wide range of user needs.

REFERENCES

[1] The Science Case for 4GLS, December 2001, http://www.4gls.ac.uk/Documents/EPSRC-Dec2001/Science_Case.pdf.

[2] DIAMOND Report of the Design Specification, June 2002.

[3] A. Andersson et al, 'The 100 MHz rf system for MAX II and MAX III', EPAC 2002, p2118.

[4] J. A. Clarke, 'The Science and Technology of Undulators and Wigglers', Oxford University Press, 2004.

[5] R.W. Schoenlein et al, 'Generation of Femtosecond Pulses of Synchrotron Radiation', Science 287, 2237 (2000).

[6] J. A. Clarke et al, 'Status of the DIAMOND insertion devices', PAC 2003, p1029.

[7] M. Marsi et al, 'Operation and performance of free electron laser oscillator down to 190 nm', Appl. Phys. Lett. 80, 2852 (2002).

[8] Interim Report of the Scientific and Technical Issues (XFEL-STI) Working Group on a European XFEL Facility in Hamburg, January 2005.

[9] http://www.rijnh.nl/n4/n3/n2/f1234.htm

[10] The BESSY Soft X-ray Free Electron Laser Technical Design Report, March 2004.

[11] P. Elleaume et al, 'Design Considerations for a 1 Angstrom SASE Undulator', TESLA-FEL-2000-16.

[12] H. Kitamura et al, 'Design Criteria and Technology Challenges for the Undulator of the Future', EPAC 2004, Lucerne.

[13] S. Sasaki, 'Analyses for a Planar Variably-Polarizing Undulator', NIM A 347, 1994.

[14] F. E. Hannon et al, 'Construction of an APPLE-II type undulator at Daresbury Laboratory for the SRS', EPAC 2004, p440.

[15] B. J. A. Shepherd, 'Commissioning of an APPLE-II undulator at Daresbury Laboratory for the SRS', PAC 2005, p4051.

[16] O. Chubar, P. Elleaume, J. Chavanne, 'A 3D Magnetostatics Computer Code for Insertion devices', J. Synchrotron Rad. (1998). 5, p481.

REFERENCES, Continued

[17] M. Borland, 'Simple method for particle tracking with coherent synchrotron radiation', Phys. Rev. ST-AB, 4 (2001) 070701.

[18] R. Glantz, 'A feasibility study of high intensity positron sources for the S-band and TESLA linear colliders', DESY-97-201, 1997.

[19] J. Rossbach, 'Positron recycling in high energy linear colliders', NIM A 309 (1991) p25.

[20] E. L. Saldin et al, 'Calculation of energy diffusion in an electron beam, due to quantum fluctuations of undulator radiation', NIM A 381 (1996) p545.

[21] J. C. Sheppard, 'Energy loss and energy spread growth in a planar undulator', Linear Collider Collaboration Tech Notes, LCC-0086, July 2002.

[22] B. Kuske et al, 'Tolerance studies for the BESSY FEL undulators', NIM A 528 (2004) p258.

[23] K. J. Kim et al, 'Performance characteristics, optimisation and error tolerances of a 4nm FEL based on the SLAC linac', PAC 1993, p1533.

[24] H. D. Nuhn et al, 'Alignment and magnet error tolerances for the LCLS x-ray FEL', PAC 1995, p231.

[25] B. Faatz and J. Pfluger, 'Field accuracy requirements for the undulator systems of the x-ray FEL's at TESLA', TESLA-FEL Report 2000-14.

[26] J. A. Clarke et al, 'Design of a 2 T multipole wiggler insertion device for the SRS', J. Synchrotron Rad., 5, p434, 1998.

[27] G. L. Carr et al, ‘Very high power THz radiation at Jefferson Lab’, Phys Med Biol 47 (2002) 3761.

[28] G. Neil et al, 'Conceptual Design Report for the THz Beamline at the Jefferson Laboratory Free Electron Laser', THz User Workshop Jefferson Laboratory, September 2004.

[29] M. Bowler, 'Extraction of the THz radiation in ERLP', Internal Report erlp-emout-bldes-rpt-03, 2005.

[30] J.B. Murphy and S. Krinsky, 'Millimeter wave coherent synchrotron radiation in the SXLS phase I electron storage ring', NIM A 346, (1994) p571.

[31] G. Williams, private communication.

REFERENCES, Continued

[32] H. Loos et al, 'Intense coherent THz pulses from the DUV-FEL linac - characteristics and potential applications', DUV-FEL workshop 2004.

[33] A. Winter et al, 'High precision optical synchronisation systems for x-ray free electron lasers', FEL 2005, Palo Alto.

[34] V. Yakovlev, B. Kohler, and K. Wilson, 'Broadly tunable 30-fs pulses produced by optical parametric amplification', Optics Letters, 19(23), (1994) pp2000-2002.

[35] K. Wilson and V. Yakovlev, 'Ultrafast rainbow: tunable ultrashort pulses from a solid-state kilohertz system', J. Opt. Soc. Am. B (1997) 14(444-448).

10. Photon Transport Systems

The purpose of this chapter is to explore the issues that will be important in designing the photon transport systems that will carry the light produced by 4GLS to the experimental systems of the users. The general issues of photon beam power, polarisation and coherence will be discussed first, and detailed consideration will be given to pulse timing and synchronisation as this is fundamental to the experimental program. The transport of light from each of the major types of source is then considered in more detail and with the aid of generic beamline case studies. Specific design solutions will not be presented as it is not appropriate at this stage to prejudge those experiments that might be funded.

10.1 Introduction

The function of the photon transport system is to provide an image of the source at the experiment. In general, the optical system will be required to provide spectral shaping and physical (de)magnification, whilst preserving properties of the source such as the temporal structure and polarisation, and delivering as many photons as possible.

Being the essential link between source and experiment, the optical transport system must be designed with both these in mind. The needs of the experiment determine the required flux and polarisation, and the spectral, temporal and physical properties of the photon beam. The optical transport system is then designed to give the best possible delivery from the chosen source.

The precise experimental specifications are an essential prerequisite to the detailed design of any of the optical transport systems, particularly when two or more photon beams from different sources on the facility are to be combined at the same experiment. At this stage of the project, the experimental specifications have not been firmly established. This chapter will therefore review the general principles and illustrate them with some generic case studies. There is an emphasis on the XUV and shorter wavelengths as this is the part of the spectrum where the greatest challenges are expected. However, all transport systems will be designed with the aim of meeting the requirements of the experiments as thoroughly as possible.

10.2 Effects of Beam Power

This section reviews the effects of the power of the photon beam on the performance of the photon transport system. It does not consider the impact on FEL cavity optics. There are two main ways in which the power of the photon beam may affect the performance of the photon transport systems. Firstly, power absorbed by a particular optical element will lead to a temperature gradient within the element that will cause a distortion of the surface of the element. Secondly, high instantaneous energy at a surface can lead to ablation of the surface.

The effects of thermal distortion are familiar from conventional synchrotron sources. The distortion of the optical surface degrades the imaging properties of the element leading to loss of

spectral or spatial resolution by deviating rays from their ideal Gaussian image point. In a conventional synchrotron source, the change in path length over the aperture of the beam caused by this deviation is not sufficient to affect the temporal properties of the beam. However, with ultra-short pulses from some of the sources on 4GLS, wavefront distortion and its effects on the temporal profile should also be considered.

Control of the thermal distortion is achieved by controlling the temperature gradient within the optical element. It is not the total absorbed power that is critical, but rather how the heat is distributed within the element that can lead to high temperature gradients and so high slope changes over the surface of the element. A poor cooling scheme can actually exacerbate the thermal distortion.

The experience gained in recent years on third generation storage ring based sources has shown how to control temperature gradients effectively. Insertion devices give high total output powers (multipole wigglers) or high power densities (undulators). Total powers of kilowatts are not uncommon. Finite element analysis modelling is able to predict the induced distortion and adjust cooling schemes to minimise it. Carefully engineered side-cooling bars are often sufficient and do not induce strain within the substrate. In extreme cases internal cooling of silicon or Glidcop substrates can be employed. Manufacturing techniques are now able to achieve high quality surfaces on internally cooled substrates.

A major advantage of 4GLS is that, in general, average photon beam power will not be as high as on many 3rd generation storage ring based sources. The total power in watts radiated by a planar undulator or wiggler is:

$$P_T = 632.8E^2B_0^2LI \tag{10-1}$$

where E is the electron energy in GeV, B_0 is the peak on-axis magnetic field in tesla, L is the length of the undulator in metres and I is the beam current in ampères.

The power is thus proportional to the square of the electron beam energy, which is only 600 MeV for the 4GLS high average current arc. Furthermore, the on-axis power density scales as the fourth power of the electron beam energy. We therefore expect significantly less total power and power density from spontaneous sources on 4GLS than on most 3rd generation storage ring sources. Table 9-4 in §9.2.1 compared power and power density for 4GLS and Diamond undulators. This table gives the total power for a 4GLS undulator to be ~ 150 W and the power density to be ~ 30 W/mrad^2.

The FEL sources will emit coherently and will thus produce many more photons per electron than spontaneous sources. For the XUV-FEL, the peak output power is very high (~ 6 GW), but the pulse length is very short (~ 22 fs) and the repetition rate is only 1 kHz. Therefore, the average continuous power is very low (< 1 W). The power density at 100 eV is ~ 60 W/mrad^2 due to the highly collimated nature of the light from the diffraction limited source, but this should not present a challenge as the average continuous power is still only ~ 80 mW.

The situation is rather different for the VUV-FEL. Although this emits at longer wavelengths and at lower peak power (~ 500 MW), the repetition rate is much higher (4.33 MHz minimum). The consequence of this is that the average continuous power is moderately high (~ 300 W). The power density will also be high (~ 3 kW/mrad^2) at 10 eV (assuming a diffraction limited source size of 90 μm RMS). These powers are still modest compared with that encountered on some 3rd generation light sources, but the acceptable level of deformation for preserving the beam quality on a FEL source is much lower and so thermal deformations must be controlled more tightly.

For the IR-FEL, the photon energy is very low but the repetition rate is high at 13 MHz and this gives an average continuous power of up to 1.4 kW (at 25 μm wavelength from IR-FEL undulator-B) but with a very low power density due to the high divergence. There is therefore no risk of ablation, but a lot of beam power to handle. However, this sort of beam power is not untypical of that successfully handled by other IR-FEL facilities. The longer wavelengths are more tolerant of deformations in the surfaces of the mirrors and since high reflectivities are readily achievable, absorbed power should be low and there should be no major problem with transporting the high power IR beams.

It is therefore expected that, with the possible exception of the VUV-FEL, the effects of the total average beam power on 4GLS will be well within the compass of techniques already developed for 3rd generation storage ring sources to control. For the VUV-FEL, consideration will need to be given to the effect on the coherent wavefront of any residual thermal distortions.

The continuous power output from any device on 4GLS will not be sufficient to ablate material from the surface of any sensibly cooled optical element by heating of the surface material through liquid and thence to vapour phases. This would require continuously high incident powers, which will not be present on 4GLS except at beam foci, which will of course not be coincident with optics.

However, sub-picosecond pulses can cause ablation as the high incident field strength is able to break the atomic bonds of the surface atoms and cause direct ejection of atoms from the surface. Ablation of mirror surfaces by this mechanism is only likely to occur with the ultra-short, high energy and highly collimated pulses from the XUV-FEL, especially at the high photon energy end of its operating range. The VUV-FEL also has ultra-short and high-energy pulses, but the divergence is much higher and so the energy density is only likely to be high enough to cause ablation at beam foci. This is illustrated by Table 10.1, which gives the estimated beam fluence for the VUV and XUV-FELs at 10 m from the source.

Table 10.1 Estimated beam fluences of the VUV and XUV-FELs at the nominal minimum and maximum operating photon energies

Photon Energy (eV)	VUV-FEL Fluence (mJ/cm^2)	XUV-FEL Fluence (mJ/cm^2)
3	0.09	
10	0.73	2.64
100		66.38

Measurements of the threshold beam fluence for ablation of some common mirror surfaces have been measured on the DESY VUV-FEL [1]. These measurements were performed at normal incidence and at a single wavelength of 98 nm (12.7 eV). Table 10.2 gives the measured thresholds for those materials studied that are suitable for mirror coatings. To understand whether the optical surfaces on 4GLS are at risk from ablation, it is necessary to infer from this data the threshold beam fluences at other wavelengths and when the surfaces are not at normal incidence.

Table 10.2 Threshold fluence for ablation at 98 nm at normal incidence

Material	Threshold fluence (mJ/cm^2)
Carbon	60
Silicon	30
Gold	40

The ablation threshold is determined by the energy absorbed per atom. Consequently, operation at grazing angles of incidence, as required for high reflectivity at VUV and shorter wavelengths, will naturally tend to dilute the beam over the surface by a factor equal to $1/\cos\theta$, where θ is the angle of incidence. However, as the angle of incidence increases (more grazing), the penetration of the refracted wave into the surface, as measured along the surface normal, decreases. The absorbed energy is thus deposited into fewer atoms and this acts to offset the spatial dilution on the surface i.e. the absorption volume remains essentially constant. This occurs until the grazing angle is below the critical angle, at which point total external reflection occurs and the penetration into the surface becomes essentially constant. The absorption volume then increases in proportion to $1/\cos\theta$.

The threshold beam fluence for ablation thus depends on three factors. The reflectivity of the material determines the amount of energy absorbed, whilst the cosine of the incidence angle and the penetration depth determine the volume over which that energy is absorbed and hence the energy absorbed per atom. Thus, the factor F_a we must calculate to scale the measured threshold is:

$$F_a = \frac{(1-R)\cos\theta}{d_e} \tag{10-2}$$

where R is the reflectivity and d_e is the penetration depth normal to the surface. The penetration depth depends on the angle of refraction θ', which, for an absorbing media, is complex, meaning the refracted wave is inhomogeneous. If $\tilde{n}$ is the complex refractive index, then the component of the wave vector of the refracted wave that is normal to the surface is given by:

$$k'_\perp = \frac{2\pi}{\lambda}\tilde{n}\cos\theta' \tag{10-3}$$

which by Snell's law can be written as:

$$k'_\perp = \frac{2\pi}{\lambda}\sqrt{\tilde{n}^2 - \sin^2\theta} \tag{10-4}$$

The 1/e attenuation length of the amplitude of the electric vector in the direction normal to the surface is given by the imaginary part of Equation (10-4). Consequently, the 1/e penetration depth of the intensity is given by:

$$d_e = \frac{\lambda}{4\pi\left|\mathrm{Im}\left(\sqrt{\tilde{n}^2 - \sin^2\theta}\right)\right|} \tag{10-5}$$

The absolute value of the imaginary part of Equation (10-4) is taken because its sign depends on how the complex refractive index is defined; in the x-ray region it is more usual to use the definition $\tilde{n} = n - \mathrm{i}\,k$, and then (with n, k real and positive) the imaginary part will be negative.

The threshold beam fluences given in Table 10.2 can thus be scaled to another wavelength and incidence angle by multiplying them by the ratio of F_a at the wavelength and incidence angle of interest to F_a at 98 nm and normal incidence. Figure 10.1 shows the increase in threshold fluence for various materials at 5° grazing angle of incidence and shows that the threshold is significantly increased by operating at grazing angles. The reflectivity used is the average of the s- and p- reflectivities. Note that the calculation gives the increase in the beam fluence i.e. measured at a plane normal to the direction of the beam, since the factor F_a includes the effect of the angle of incidence at the mirror surface.

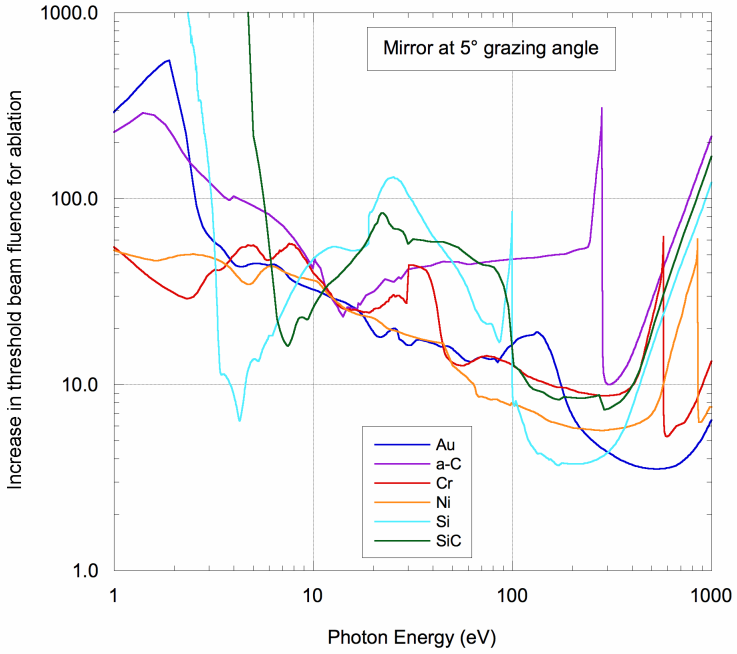

Figure 10.1 Increase in the threshold beam fluence for ablation, relative to the threshold measured at 12.7 eV and normal incidence, for possible mirror coatings (gold, amorphous carbon, chromium, nickel, silicon and silicon carbide) at 5° grazing angle of incidence

Reducing the risk of ablation from an optical element will in general involve using materials with a higher threshold and/or operating below the critical angle at increasingly grazing angles of incidence. However, it is not always possible to make a free choice of incidence angle. For example, in the SX700 type of monochromator [9], the incidence angles at both the plane premirror and plane diffraction grating are determined by the operating wavelength and the grazing angles increase rapidly at lower energies.

The most significant risk that will be posed by the XUV-FEL is at 100 eV, where the light is most collimated. A particular concern will be the diffraction grating used in any monochromator. The periodic structure of any grating means that some parts of the surface will be at much larger grazing angles than the mean surface plane. This is not only true for a blazed grating, where the blaze facets are tilted towards the incident beam, but also for a lamellar grating. In reality, lamellar gratings have a trapezoidal profile and the sides of the grooves are typically at only 10° inclination to the surface plane. Hence there is always a significant fraction of the surface that is at relatively high grazing angle to the incident beam.

The current state of knowledge of the fluence limits for safe operation is not sufficient to say if the diffraction gratings will have to be operated with appreciably less incident energy than a mirror at equivalent angle. Furthermore, recent work [2] reported noticeable damage to the surface at fluences well below the previously reported threshold for ablation. For example, the onset of changes to the refractive index of silicon occurred at a fluence of only 5 mJ/cm^2. This is one area where more research is needed before final design choices are made.

In addition to ablation damage to optical elements, the impact on apertures within the beamline must also be considered. Beam defining apertures and slits are usually at normal incidence to the beam and so absorption and flux density is high. However, apertures away from beam foci will see only low flux density and will be safe. The greatest risk will occur if the FEL output is focussed onto the entrance slit of a monochromator. Therefore, the beamline concepts presented in this document employ entrance slitless monochromator designs. Exit slits are a necessity in any monochromator, but the light is spectrally dispersed at the slit and so the energy density will be reduced to safe levels.

10.3 Polarisation

Much of the research on 4GLS will require photon beams of adjustable and well-defined polarisation. The IR-, VUV- and XUV-FELs and many of the spontaneous insertion device sources will use helical undulators that can produce photon beams with polarisation adjustable between horizontal linear, through left or right circular to vertical linear. The degree of polarisation from these sources is expected to be very high.

However, in the VUV and XUV energy range, mirrors will have to be at grazing angles of incidence to achieve high reflectivity, and there is then a difference between s- and p-reflectivities and so a net polarising effect. There is also a phase shift between the s- and p-components in the light. As the photon energy increases, the required angles become more grazing. Above about 200 eV, the difference between s- and p- reflectivities of typical mirror coatings becomes small and the phase shift approaches zero and so can generally be neglected. An optical system that employs an equal number of horizontal and vertical deflections may help to reduce the overall polarising effect, but, if the reflections are inherently polarising, this will be at the expense of transmission efficiency.

A design criterion for 4GLS beamlines in the 5 to 100 eV range will be to ensure that any polarising effect is minimised by suitable choice of optical coatings. By measuring the polarisation state of the output radiation, the residual effect can then be compensated for by tuning the photon source polarisation at the undulator such that the final beamline output is the desired polarisation state [3].

The s- and p-reflectivities and relative phase shift are easy to calculate using the generalised Fresnel equations provided the complex refractive index of the material is known. In the XUV region and above, the refractive index can be calculated from the atomic scattering factors, and compounds approximated to a summation of their atomic constituents. Atomic scattering factors are tabulated for energies above 30 eV, and above this energy the atomic model works well, provided the density of the material is known. The density may be an issue for thin optical coatings in which it may deviate significantly from the bulk value. But below this energy, the optical behaviour of materials is more complex and the refractive index must be measured directly at the wavelength of interest.

A considerable body of measured refractive indices does exist [4], but there is always the concern that the exact form of the material that may be used as a mirror coating has not been measured and in the VUV this will make a significant difference to the reflectivity.

A particular example of this is carbon. Due to its high ablation threshold and good measured reflectivity, amorphous carbon films have been suggested as a suitable coating for use on FEL's [5, 6]. But, thus far, reflectivity measurements for actual coatings have only been performed with s-polarised light.

There is only limited refractive index data for amorphous carbon films [7]. The applicability of this data to any actual mirror coating will depend on how strongly the method of forming the film affects the optical properties. In addition, there is also data for graphitic carbon [4]. Calculations of the reflectivity at 85° incidence angle of amorphous and graphitic carbon in the range 1 to 1000 eV are shown in Figure 10.2 and Figure 10.3 respectively. In both cases, the p-reflectivity drops significantly at 13 eV, and the mirror will be strongly polarising at this energy.

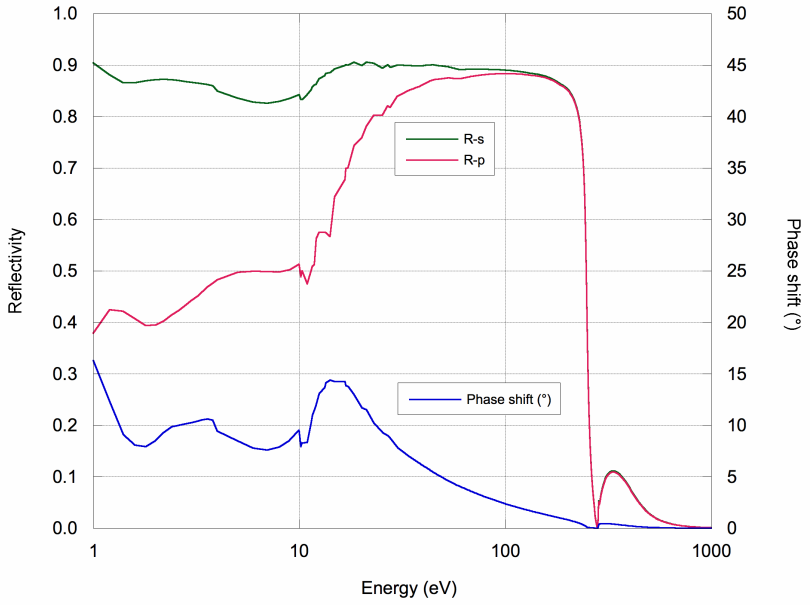

Figure 10.2 Calculated reflectivity of amorphous carbon at 85° incidence angle and the phase shift between s- and p- components. There will be an increasingly strong polarising effect below c. 20 eV.

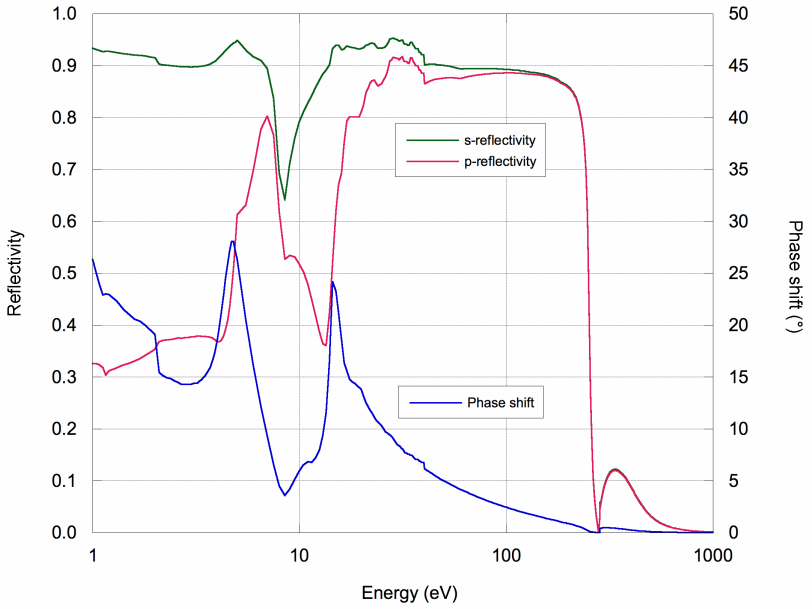

Figure 10.3 Calculated reflectivity of graphitic carbon at 85° incidence angle and the phase shift between s- and p- components. There will be a strong polarising effect at c. 13 eV.

If carbon films are to be used as optical coatings for operation below c. 20 eV, it is therefore essential that the s- and p-reflectivities are measured for the actual form of carbon to be used. Should the actual reflectivities show the same effect as the calculated ones, then the cumulative effect of using carbon coatings throughout the optical system of a beamline operating in this energy range will be very detrimental to the polarisation characteristics of the beam delivered to the experiments.

The coatings used in the optical system of the VUV- and XUV-FELs will therefore have to balance the polarising effects against the likely damage from ablation. Coatings like carbon may have to be restricted to use on only those optical elements most at risk from damage.

10.4 Coherence

The FEL beams are expected to be essentially fully transversely coherent. At longer wavelengths, even the spontaneous undulator sources will show a high degree of transverse coherence. For example, the coherent fraction will be ~ 0.9 at 5 eV and ~ 0.2 at 100 eV for a typical undulator with the electron beam properties given in Table 9.3 of §9.2.1.

Whilst coherent light beams can open up many scientific opportunities, the challenges associated with transporting them are already known from 3rd generation storage rings. The blurring of images due to diffraction from imperfect windows is widely known. For THz (terahertz) and IR (infra-red) radiation, diamond windows can be thick and so polished to a high degree of optical perfection. In the VUV to SXR (soft x-ray), all the beamlines will necessarily be windowless, but the use of traditional I-zero monitoring foils or grids will not be possible without degrading the beam quality. An alternative way of monitoring the incident flux is to

measure gas ionisation signals from a differentially pumped absorption cell (see §10.8.1.1), or the drain current from the coating of the last mirror in the beamline.

The quality of the optical surfaces must also be higher when handling coherent beams. Small defects on a surface will diffract the beam and lead to speckle patterns in the outgoing beam, which may even cause damage to downstream optics. The optical surfaces must also be kept scrupulously free of dust particles that can cause a similar effect.

At VUV and XUV wavelengths, diffraction effects from the edges of optical elements are unlikely to be a serious problem. The generally large physical apertures necessitated by grazing angle operation means that such diffraction effects will be concentrated at the very edges of the beams. However, 4GLS optical systems will be designed wherever possible with the optics sufficiently large to span at least 4σ of the expected beam footprint to minimise such disturbances.

For IR and THz radiation, diffraction from the optics must be considered more carefully. Since these wavelengths are inherently more transportable than VUV and XUV beams, it is the IR and THz beams that will be more heavily manipulated to bring them into coincidence with the shorter wavelength beams. Transport paths are likely to be long and multiple intermediate foci will be required. The build up of diffractive ripple from each element in the chain into the body of the beam will need to be avoided.

10.5 Photon Beam Timing

The unique capability of 4GLS to deliver multiple short-pulse photon beams at the experiment with a defined time delay between them is the enabler behind much of the scientific research. Delivering this will therefore be the main design driver behind many of the beamlines.

The XUV-FEL will produce the shortest pulses, determined by the pulse length of the HHG seed laser and slippage within the FEL. Pulses with RMS length in the range 20 to 30 fs are expected. Spontaneous sources will produce longer pulses, limited by the electron bunch length. This will vary along the high current arc and will be a minimum in the VUV-FEL straight. In general, spontaneous sources will produce pulses with RMS lengths in the range of 100 to 1000 fs.

10.5.1 Pulse Length Preservation

To deliver a pulse from source to experiment whilst preserving the pulse length at the level of 10 fs will require a transport system that has a closely matched optical path length over the aperture of the system. In general, geometrical aberrations and the effect of manufacturing and thermally induced slope errors will have to be tightly controlled.

However, the biggest factor affecting the pulse length will be the spectral bandwidth. For simplicity in this overview, we are assuming the FEL pulses will be Gaussian and transform

limited and hence the RMS pulse length and RMS bandwidth will be related by the transform limit:

$$\Delta E_{rms} \Delta \tau_{rms} = \frac{h}{4\pi} \tag{10-6}$$

If the pulses are not fully longitudinally coherent or not Gaussian, then the time-bandwidth product will be greater than h/4π. This will be the case in practice since the pulses inevitably deviate from the Gaussian ideal even when fully longitudinally coherent. Typically, the output of the VUV- and XUV-FELs is expected to be about twice transform limited i.e. the pulse bandwidth is about twice that calculated from (10-6) and the actual pulse length.

In units of eV and fs, (10-6) can be conveniently approximated to:

$$\Delta E_{rms} \Delta \tau_{rms} \approx \frac{1}{3} \tag{10-7}$$

A 10 fs pulse thus has a limiting bandwidth of 33 meV. Any attempt to reduce this bandwidth will lengthen the pulse. The bandpass of any monochromator used to condition the FEL beam, for example by removing the spontaneous and SASE (self-amplified spontaneous emission) background generated by the FEL undulator, must be no smaller than 33 meV if the pulse length is to be preserved.

In the VUV and XUV part of the spectrum, diffraction gratings are employed as the dispersing elements in monochromators. When a beam passes across a diffraction grating, each illuminated groove gives a path length difference equal to the wavelength of the diffracted light times the order of diffraction. Thus, if the illuminated length of the grating is L and the line density is N, the total optical path length difference along the grating is:

$$\Delta l = LNm\lambda \tag{10-8}$$

The time stretch to the pulse caused by the grating is thus:

$$\Delta \tau = \frac{LNm\lambda}{c} \tag{10-9}$$

Since a grating in uniform illumination has a diffraction limited resolving power given by:

$$R_G = LNm \tag{10-10}$$

the pulse stretch caused by the grating and the resolving power of the grating are clearly linked. Thus, the grating resolving power defines the minimum amount by which the pulse will be stretched due to the optical path length difference along the grating. Even though the total monochromator resolving power will inevitably be worse than the grating resolving power, the pulse will still be stretched by the amount determined by the grating resolving power. For

example, opening up the exit slit to reduce the monochromator resolving power will not reduce the pulse length below the limit set by the grating illumination.

The bandwidth of the pulse after the grating will be the convolution of the input pulse bandwidth and the grating bandpass. The output pulse length will thus be the convolution of the input pulse length and the pulse stretch produced by the grating. If a monochromator with a single grating is to preserve the input pulse length, it is clear that the grating bandpass must be larger than the natural bandwidth of the pulse.

The output from the FELs will be, to a good approximation, Gaussian both transversely and (to a lesser extent) longitudinally. The illuminated footprint on the grating will thus be Gaussian and so the expression for the grating resolving power given in (10-10) will no longer be correct. In fact, in uniform illumination, the diffracted orders have a $\mathrm{sinc}^2(x)$ lineshape, and equation (10-10) is the Rayleigh resolving power i.e. the separation of the maxima and first minima of the $\mathrm{sinc}^2(x)$ profile.

In Gaussian illumination the diffracted orders will have a lineshape that is Gaussian. Strictly speaking, this is the lineshape when the grating is infinitely long. For an infinite grating with Gaussian illumination of RMS extent along the grating σ_L, the grating resolving power, defined by the FWHM (full width at half maximum) of the diffracted orders, is given by:

$$R_G = \frac{\lambda}{\Delta\lambda_{FWHM}} = \frac{2\pi}{\sqrt{2\ln 2}}\sigma_L Nm \approx 5.34\sigma_L Nm \qquad (10\text{-}11)$$

When the grating length is finite, the Gaussian illumination is truncated and so the diffracted orders have a lineshape that is the square of the convolution of a Gaussian and a sinc(x) function. Initially, we assume the grating is long enough to approximate to infinite. This will be the case if the grating is about $6\sigma_L$ long or greater. The RMS pulse stretch from the grating is:

$$\Delta\tau_{rms} = \frac{\sigma_L Nm\lambda}{c} \qquad (10\text{-}12)$$

We can combine (10-11) and (10-12) to give, converting wavelength to energy in eV and with the pulse stretch in femtoseconds:

$$R_G = 1.29E\,\Delta\tau_{rms} \qquad (10\text{-}13)$$

Thus, if the pulse stretch is to be limited to 10 fs at 10 eV, the grating resolving power must be no greater than 129. This is exceptionally low, and implies (from (10-11)) that the product of the line density N and RMS illuminated length σ_L must be less than 24. In other words, the RMS number of illuminated grooves must be less than 24!

This is clearly not achievable in practice. Therefore, at low energies, a single grating monochromator cannot be made to preserve pulse lengths in the range below ~ 100 fs. At higher

energies, or as the input pulse length gets longer, a single grating can be illuminated with sufficiently few grooves to give the desired resolving power. If the product of E and $\Delta\tau_{rms}$ is greater than ~ 1000 eV fs, then limiting the pulse stretch to an acceptable with a single grating is feasible. It must however be remembered that a single grating will always introduce some pulse stretching and thus will unavoidably introduce a spatial chirp to the output beam, i.e. it shears the output beam. The impact of this on the experiment must be considered.

When a single grating cannot be used, the only solution is to use a second grating that reverses the pulse stretch (spatial chirp) caused by the first grating. To do this, the optical path difference across the aperture of the beam must be equal and opposite for the two gratings. Figure 10.4 shows a so-called 4f configuration that achieves the required time compensation. This is an example of Fourier domain pulse shaping in which the time shaping occurs in the frequency domain.

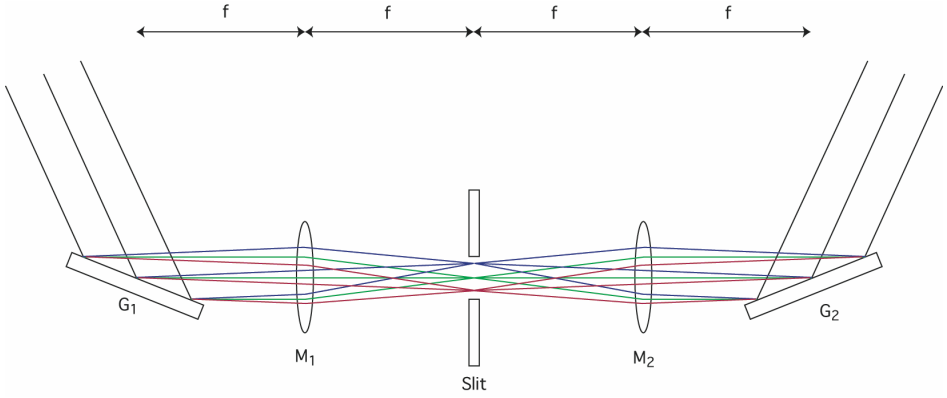

Figure 10.4 Schematic of 4f system for pulse length preservation

The two focussing mirrors (shown as lenses for simplicity in the figure) and the mirror-imaged grating pair are spaced at distances equal to the focal length f of the mirrors. The grating G_1 disperses the light and M_1 performs the Fourier transform, converting angle of dispersion into position at the slit plane between the two mirrors. M_2 performs the inverse Fourier transform but maintains the dispersed spectrum. The grating G_2 recombines the dispersed beam into a single collimated beam. G_2 must work in the opposite order of diffraction to G_1 in order for the path lengths to be correctly balanced. The slit is a simple spatial modulator; its purpose is to filter out the undesired spectral components but leave the required ones intact.

The slit should be set wide enough to pass the complete transform limited bandwidth of the input pulse. Since the spectral shape is assumed to be Gaussian, the term "complete" needs to be qualified. The slit of size *S* will transmit a bandwidth given by:

$$\Delta\lambda_{slit} = \frac{S}{f}\frac{1}{Nm}\cos\beta \qquad (10\text{-}14)$$

where β is the diffraction angle. The slit transmission is a "top-hat" function and so it will truncate the Gaussian spectral distribution at some level. The truncation needs to be at a level

that does not appreciably affect spectral shape of the transmitted pulse. It will be assumed that the slit will be set to transmit four times the RMS bandwidth of the pulse.

We must also consider what the source for the second part of the 4f system is, as this will be the source that is imaged to the experiment. The grating G_1 and mirror M_1 will produce a spectrally dispersed image of the FEL source at the slit plane. The spatial extent of the illumination at the slit plane is determined by the spectral bandwidth of the source, the dispersion of the grating and the magnification of the monochromator.

For a conventional monochromator on a continuum source, to which a conventional spontaneous synchrotron source is a good approximation, the illumination at the slit plane is continuous and homogeneous and so the slit is uniformly illuminated and the slit defines the source size (in the dispersive direction) for the following optics.

For the 4f system on a FEL source, the source bandwidth is limited by the time-bandwidth product, and the exit slit is set to give an (assumed) bandpass of four times the RMS source bandwidth. The spatial extent of the illumination at the slit plane is given by the convolution of the monochromatic image size and the size of the dispersed source spectrum, both of which are taken to be Gaussian.

At low energies, the source size limited bandpass is small compared with the spectral width of the source (which is why the 4f monochromator is being used, the source size limited bandpass being the same as the diffraction limiting bandpass of the grating for a Gaussian and diffraction limited source). Therefore, the illumination across the slit opening is Gaussian with essentially the same width as the dispersed source spectrum, and so the transmitted intensity distribution through the slit is Gaussian, truncated by the slit at 4σ.

At higher photon energies, the source size limited bandpass becomes closer to the transform limited bandwidth of the source. The illumination at the slit plane is therefore broader than the width of the dispersed source spectrum. The exit slit set to pass 4σ of the source spectrum now truncates the Gaussian illumination on the slit plane at a narrower point and the transmitted intensity becomes more uniform and the transmitted fraction of the pulse is reduced.

Ultimately, at high enough photon energy, when the source size limited bandpass is large compared with the source spectral bandwidth, the illumination over the slit opening will be effectively uniform. The exit slit, still set to 4σ of the source bandwidth, will now be small compared with the monochromatic image size. At this point, the 4f system is not needed to preserve the pulse length and the slit is only passing a small fraction of the intensity of the pulse.

To illustrate this, the optical layout described in §10.6.3.1, requires a 1.5 mm exit slit to pass 4σ of the source bandwidth of the XUV-FEL at 10 eV, meaning the source spectrum is dispersed at the slit plane with an RMS spread of 375 μm. However, the monochromatic image of the FEL

source at the slit has an RMS size of only 17 μm. Therefore, the illumination at the slit plane is entirely determined by the dispersion, and the transmission is ~ 95 % (i.e. 4σ of a Guassian).

However, at 100 eV, the RMS spread of the dispersed spectrum has reduced to 12 μm, and the slit size is set to 48 μm. The monochromatic image is still 17 μm RMS, so the RMS size of the illumination is now 21 μm, and the 48 μm slit cuts the spectrum at 2.3σ of the illumination. Thus, whilst the spectral range passed by the slit is still 4σ of the source spectrum, the intensity transmitted has decreased to ~ 75 %.

At 200 eV, the RMS spread of the dispersed spectrum will be just 4.2 μm, and the illumination size will be 17.5 μm and is dominated by the monochromatic image size. The exit slit size, set to 4σ of the dispersion, will be just 17 μm and so will cut the illumination at about 1σ. The transmission through the slit will be just 38 %, and the transmitted intensity will be nearly uniform.

Therefore, as long as the source bandwidth is larger than the source size (and hence diffraction) limiting bandwidth, the optical system after the slit sees a source (in the dispersive direction) that is a (truncated) Gaussian but with a spatial extent given by the dispersed pulse bandwidth. The size of the source will therefore depend on the dispersion of the grating and the pulse length. Since the truncation will become narrower at higher photon energies, it may be desirable to design the monochromator with sufficient dispersion to ensure the source size limited bandpass is always much smaller than the source bandwidth and hence so the truncation does not change the transmitted intensity distribution appreciably from Gaussian. This will also maximise the throughput. For a wide energy range of operation, this would require additional gratings.

The transform limited bandwidth of the pulse in eV (so h in eV s) is, from equation (10-6):

$$\Delta E_{rms} = \frac{h}{4\pi \Delta \tau_{rms}} \tag{10-15}$$

The bandpass of the slit in eV is, from equation (10-14):

$$\Delta E_{slit} = \frac{S}{f} \frac{1}{Nmhc} E^2 \cos\beta \tag{10-16}$$

If the slit is to be maintained at q times the pulse bandwidth, then the slit size in μm is given by:

$$S = 0.408\, Nm\, q\, f \frac{1}{\Delta \tau_{rms}} \frac{1}{E^2 \cos\beta} \tag{10-17}$$

Even with a fixed magnification monochromator, the size of the slit will need to vary to keep the slit at 4σ of the pulse bandwidth. The effective source for the second part of the 4f system

will also change in size with photon energy. This will inevitably cause a change in photon beam spot at the experiment.

Alternatively, (10-17) can be used to define the diffraction angle at each energy such that the slit size is fixed. The required incidence angle is then calculated from the grating equation. Such a mode of operation will require a monochromator that can operate with freely chosen included angle such as a collimated light SX700.

10.5.2 Beam Synchronisation

In addition to preserving the photon pulse lengths from the various sources, pump-probe experiments will require the synchronisation of pulses from two different sources via different beamlines whilst giving a variable time delay between the pulses.

The strategy to achieve this consists of three basic principles. Firstly, the facility will be designed from the outset with the lowest possible level of inherent timing jitter between the different sources. Secondly, delay lines will be used to introduce the appropriate level of temporal separation between the different sources. Finally, diagnostics will be used to measure the imposed delays for system calibration and the residual temporal jitter for error correction in the experimental data.

Achieving low inherent jitter will require close control of the total photon path length from source to experiment for each beamline and also the electron path length between the sources. In general, bringing two spatially separated sources together at a common experiment will not be possible with zero total path difference between the two transport paths.

Therefore, any delay line will have to correct for the natural path difference and then introduce sufficient additional path difference to allow the timing between the two pulses to be adjusted as needed by the experiment. Some flexibility will also be needed to provide a one-off correction for any difference between the design and actual path lengths of the systems as constructed.

Since the delay only adds path length, the beamline with the delay line will depend on the relative path lengths of the two beamlines. If the pump pulse naturally arrives ahead of the probe pulse, the pump beamline will have the delay line with maximum retardation giving coincidence and minimum retardation giving maximum separation. Conversely, if the pump-pulse path is longer, the probe beamline will require the delay line to allow it to be retarded.

It is clear that to achieve the desired synchronisation, the design of the experiments, beamlines and the sources will have to be considered as a whole. Since the exact photon beam requirements will depend on the experiment, and approved experiments will be the result of future peer review, at this stage we can consider only the general issues that must be addressed.

To illustrate these issues, the XUV-FEL and the spent beam undulator will be used as an example. The provision of the spent beam undulator after the XUV-FEL allows for the

production of photon pulses with the same timing structure and with closest synchronisation to the XUV-FEL pulses.

For the pulses from the FEL and spent beam undulator to arrive at the experiment at the same time, we require the photon transit time down the XUV-FEL beamline to be matched to the summation of the electron bunch transit time from the FEL to the spent beam undulator and the photon transit time down the undulator beamline to experiment.

The first point to consider is the longitudinal positional stability of the apparent beam waist of the radiation output of the FEL. The beam waist defines the effective source for the beamline, even though radiation is emitted up to the end of the FEL undulator. Consequently, a change in the position of the waist along the FEL undulator means the optical path length from source to experiment will change. Furthermore, there will be a small difference between the time it takes for the electrons and the FEL radiation to reach the end of the undulator. This time difference will consequently give a relative change in the timing of the pulses from the FEL and the spent beam undulator. The time delay will be largest at 10 eV operation, when the electron energy is lowest and the undulator deflection highest, and will be ~ 7 fs per metre of beam waist shift. Determining the position of the beam waist requires longitudinal propagation of the radiation field given by the GENESIS simulation of the FEL output [8]. This work will be undertaken in the TDR (Technical Design Report) phase, but here it is sufficient to say that the beam waist should occur after saturation and the FEL will be designed to ensure saturation occurs near the end of the undulator as this gives the best transverse radiation properties. Therefore the magnitude of this relative delay should always be small.

Secondly, we must consider the stability of the electron path from the FEL to the spent beam undulator. This path needs to be tightly controlled to prevent jitter between the two photon pulses. A fluctuation in the path of only 3 μm will give a jitter of 10 fs. Whilst the design will minimise this jitter, timing diagnostics will be used on the electron beam to measure the actual jitter.

Thirdly, the optical paths of the two beamlines must be such that the total transit times are matched to within the level of achievable adjustment from the optical delay system, whilst also allowing for the introduction of extra path length to give the required relative time delay between the two pulses. This must be achieved simultaneously with bringing the two photon beams into physical coincidence at the appropriate relative angle and with the required beam spot size in the experimental system.

At this stage of the design process, the type of monochromator being considered for operation above 10 eV is the variable included angle plane grating monochromator known as the SX700 [9]. When operating with collimated light, this monochromator is highly flexible and is a well proven design [10, 11]. It allows the operation of the monochromator to be adjusted, for instance, to give high or low resolving power, good harmonic rejection, or on-blaze operation. This type of monochromator is also ideally suited to operation without an entrance slit, which is

a requirement for the XUV-FEL beamline at least, and for operation in a pulse length preserving mode such as the 4f system described above.

However, a disadvantage of this type of monochromator is that the variation in included angle is accompanied by a change in the optical path length through the monochromator as the photon energy is changed. This change is typically a few millimetres, and so will impose a considerable time delay in the range of tens of picoseconds.

A further complication is that the variation in included angle is usually achieved by reflection of the input beam by a plane mirror with an off-axis rotation. The off-axis rotation allows the mirror to rotate and still reflect the beam to almost exactly the centre of the grating over a wide range of mirror angles. Otherwise, a rotation and translation is required, which usually introduces more errors. However, there is always some small movement along the grating as the energy and hence mirror angle is adjusted. This would also give a small variation in the optical path length through the monochromator.

Both these effects are, in principal, a predictable function of the photon energy, and so could be allowed for in the beamline control system. But, the magnitude of the movement of the beam along the grating is very sensitive to the dimensional accuracy of the mechanism and more importantly to the position and angle of the photon beam as it enters the monochromator. Therefore, micron level metrology of the finished mechanism and very high levels (micron position and micro-radian angle) of positional stability of the photon beams from the source will be required.

However, it should be noted that it is possible to operate an SX700 monochromator at fixed included angle (i.e. with the premirror fixed). In collimated light, this does not affect the focussing, but will change the magnification and beamline efficiency. This is thus not a general solution for the entire operating range of the monochromator; rather the angle is set to the design angle for the middle of the scan range and then left fixed. This mode of operation (so-called “fixed mirror”) removes all the mechanical path length changes.

This then leaves the issue of path length changes caused by movement of the beam into the monochromator. To some extent, any monochromator operating without an entrance slit will be vulnerable to this effect, but the SX700 will be more sensitive than optically simpler designs. Detailed design must establish if the practically achievable photon beam stability is sufficient to prevent this effect from giving too much timing jitter in the beam in the SX700 design.

10.5.3 Optical Delay Lines

Pump-probe experiments will require a controllable delay to be introduced between the pump and probe pulses. This delay should ideally be variable between zero and a maximum time determined by the dynamics of the system being studied. The delay will be created by adjusting the path length between the source of the probe (or pump) pulse and the experiment. This path length can either be added in the optical transport system (which will be considered here) or in

the electron beam transport system. Since the electrons are relativistic, the correlation between temporal delay and path length is the same in either case. Table 10.3 gives path difference required to achieve typical maximum delays.

Table 10.3. Transport system path difference required for different time delays

Required maximum delay	Transport path difference
100 ps	30 mm
1 ns	300 mm
10 ns	3 m

Producing an optical path difference is typically achieved by reflection from two or more mirrors, at least one of which will be required to translate as well as rotate. The characteristics we require from any such system are:

- high transmission;
- minimal polarising effect;
- minimum number of translations and rotations;
- fixed input and output directions and positions;
- no beam movement as the delay is varied;
- compact, ideally within one vessel;
- a high ratio of optical path difference to mirror travel.

The ratio of OPD (optical path difference) to travel depends on the angular deflection of the beam at each mirror. At the grazing angles necessary for high efficiency in the XUV, this ratio is very low at ~ 0.02. For 90° deflection it is ~ 1, and the maximum ratio is two for 180° deflection (i.e. normal incidence). Achieving a 10 ns delay will therefore be quite straightforward if 90° or greater deflections can be used. This is realistic for visible and longer wavelengths, and for the VUV (up to 10 eV) if aluminium coated mirrors can be used. Conversely, for XUV wavelengths, such a delay is impractical as the delay line will become tens to hundreds of metres in size. Here delays will have to be limited to ~ 1 ns.

10.5.3.1 Two-Mirror Delay Lines

Figure 10.5 shows a two-mirror system working at (a) grazing angles (b) near normal incidence.

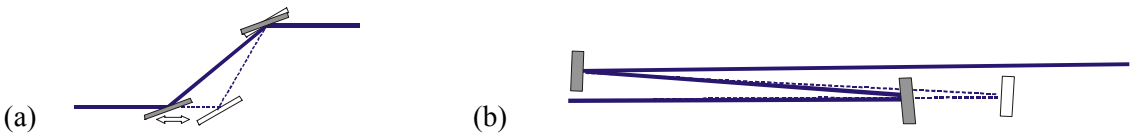

Figure 10.5 Grazing (a) and normal incidence (b) configurations for two mirror delay systems

The chief advantage of the two mirror system is that it has the minimum of reflections and hence losses and is also mechanically the most simple. This is important as mechanical errors in

the rotations and translations will result in movement of the output beam and uncertainty in the delay being introduced.

The main potential disadvantage is that the output beam has to be offset from the input beam. At normal incidence, this offset can be small and is determined by the size of the mirrors needed to capture the beam. At grazing angles, the offset must be large if a large path difference is to be achieved.

Because the offset must be fixed, it is necessary to translate the mirror parallel to the beam direction. This reduces the OPD/travel ratio and also limits the range of path difference this system can introduce. A large offset will increase the maximum path difference for a given maximum grazing angle, but will require more longitudinal separation at the minimum working grazing angle. Consequently, the minimum useable angle is determined not by physical acceptance of the mirror but by the overall size of the delay line.

In general, the two-mirror system needs to be physically very large and requires large translation if high grazing angles are to be avoided. For example, a delay line of 14 m overall length and 1 m offset will give a minimum deflection angle of 4.1°, and the range of delay with a maximum grazing angle on the mirrors of 10° will be 0.47 ns. The mirror will have to translate 11.2 m to achieve this range of delay. This sort of travel may be impractical.

However, the two-mirror system at normal incidence is very attractive for a number of reasons. At normal incidence, there is no polarising effect from the reflections. The travel required to produce a given delay is much reduced and so the mechanism will be much simplified. If the mirrors have sufficient reflectivity, then two systems can be used back to back (making a four-mirror system) and the beam offset will be cancelled. Furthermore, it will no longer be necessary to rotate any of the mirrors as the beam movement caused by the movement in the first half of the system will be cancelled by the opposite beam movement in the second half of the system.

10.5.3.2 Three-Mirror Systems

Introducing a third mirror into the delay line (Figure 10.6) allows for greater OPD within a given overall length and also allows the delay line to have no overall offset of the beam.

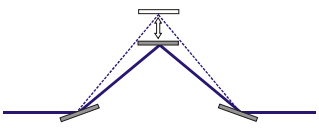

Figure 10.6 Configuration of three-mirror optical delay line

Adjustment of the path length can be achieved by either translating the second mirror normal to the beam direction and rotating the first and third mirrors in equal and opposite directions, (see Figure 10.6) or by rotating and translating the first and third mirrors along the beam direction

and leaving the third mirror fixed. The first method is generally to be preferred as it gives a greater OPD for a given translation.

Whilst this scheme only introduces one extra reflection, it has a key disadvantage in that the grazing angle on the second mirror is twice that on the first and third mirrors. This will have a significant effect on the upper operating energy of the system as the mirror will more rapidly reach the critical angle.

A flexibility of the three-mirror system is that the beam can be offset from its input position by a freely chosen (within reason) amount and this offset can be used to compensate for a beam shift elsewhere in the transport system. However, doing this requires the second mirror to rotate as well as translate when the delay line is adjusted.

10.5.3.3 Four-Mirror Systems

The four-mirror system (Figure 10.7) overcomes the main disadvantage of the three-mirror system by ensuring all the mirrors are at the same grazing angle whilst still maintaining the zero beam offset geometry. This solution is therefore to be preferred when higher energy operation is required.

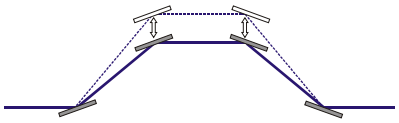

Figure 10.7 Four-mirror optical delay line

The four-mirror system is essentially two two-mirror systems back to back. The spacing between the second and third mirrors contributes nothing to the delay and so should be as small as the physical size of the mirrors allows. In the limit of zero separation, the four-mirror system gives twice the delay as the two-mirror for a given overall system length.

Adjustment of the delay can be achieved by antiparallel translation of the first and last mirrors and rotation of all four mirrors. However, this adjustment mode has the same disadvantage of the two-mirror adjustment in that it limits the minimum operating angle for a given length of system.

The preferable adjustment mode is the translation of the middle two mirrors normal to the beam direction and rotation of all four mirrors. This also gives a larger OPD/travel ratio. Furthermore, introduction of a positional offset between input and output beams is possible without further complication to the scanning mechanism; specifically, the angles at each mirror can be the same though the path length in each half of the system then becomes different.

With a 90° deflection, it is possible to achieve variable path length and maintain a fixed output beam position with just a translation of the middle mirrors. This gives a very simple mechanism

for adjustment, but is of course limited photon energies where reasonable reflectivity at 45° incidence can be achieved.

In fact, the four-mirror system will give a fixed output beam position if the mirrors are not rotated even when not operating at 45° incidence angle. However, this causes the beam to move along the second and third mirrors as the mirrors are translated, and so the achievable delay is limited by the length of these mirrors. Practically, this limits such a system to delays of only ~ 10 ps at angles of incidence sufficient to give good reflectivity in the XUV. But, such a system would be mechanically much simpler and hence likely to give better precision in the delay. For example, with grazing angles of 3°, the delay range is 14 ps with a starting offset of 1 m and translation of 0.02 m. The beam will move along the mirrors by 0.38 m.

10.5.3.4 Comparison of Delay Line Options

To assess the relative merits of the delay lines described above, the performance for each system is presented for operation from 10 to 100 eV where:

- the range of achievable delay is 1 ns;
- the maximum travel is 2 m;
- the minimum grazing angle is 1° (to limit the length of the mirrors);
- the maximum overall length of the delay line is 10 m;
- the maximum transverse size is 2.0 m.

The three- and four-mirror systems are assumed to have no overall beam offset and use a translation perpendicular to the beam direction.

The transmission of each system is calculated assuming a perfect gold coating at 10 and 100 eV. Because each system uses a different angle for a given energy and delay, the optimum coating for each system may be different. But gold gives a good reflectivity over a wide range of energies and angles and so is used for this comparison. The ratio of s- to p- reflectivity is similarly calculated for each case to assess the polarising effect of the systems. Table 10.4 summarises the results.

Table 10.4 Comparison of two-, three- and four-mirror optical delay lines operating in the XUV energy range

	Two-mirror	Three-mirror	Four-mirror
Delay Range (ns)	1.00	1.00	1.04
Travel Required (m)	2.00	1.07	1.049
Total Length (m)	4.34	10	10
Total Width (m)	2.0	1.25	1.21
Grazing angle at min delay	12.375°	1° & 2°	1°
Grazing angle at max delay	20.25°	7° & 14°	7.5°
Total Rs at min delay @ 10 eV	0.49	0.88	0.89
Total Rs at min delay @ 100 eV	0.32	0.88	0.89
Total Rs at max delay @ 10 eV	0.42	0.45	0.43
Total Rs at max delay @ 100 eV	0.14	0.38	0.39
Total Rs/Rp at min delay @ 10 eV	5.95	1.34	1.34
Total Rs/Rp at min delay @ 100 eV	1.18	1.03	1.04
Total Rs/Rp at max delay @ 10 eV	17.36	7.72	8.84
Total Rs/Rp at max delay @ 100 eV	1.49	1.19	1.18

In general, the two-mirror system performs the worst due to the need for high grazing angles to get the required delay within the permitted travel. The only advantage for the two-mirror system is the shorter overall length.

The performance of the three- and four-mirror systems is broadly similar. Both have a strong polarising effect at 10 eV with the maximum delay. This is because of the use of gold as the reflecting material. Gold has a good overall reflectivity from 10 to 100 eV, but the p-reflectivity is markedly less than the s-reflectivity below c. 40 eV. An alternative coating such as silicon would give much better performance at 10 eV (if the surface oxidation can be controlled), but could not be used above c. 60 eV. The mirrors would thus have to have two coatings (e.g. gold and silicon) and be translated in the beam. This will make the mechanisms more complicated.

The above examples show that it is possible to achieve optical delays of up to 1 ns in the range 10 to 100 eV without excessive transmission loss. The real world performance of such a system will depend upon the mechanical design. The large translations required and coupled rotations will place great demands on the mechanism if jitter of the beam position, angle and timing are not to be induced. The systems are also all large, and designing a suitable vacuum envelope will be demanding.

Longer delays can be achieved with larger systems and by using higher grazing angles. The practical limit for a grazing angle system will still be a few nanoseconds before the system becomes too large or the losses too high. Delays as long as 10 ns can only practically be achieved with non-grazing angles or even more complicated multi-mirror systems. A four-mirror system with 45° incidence angle will give 10 ns of delay with 1.5 m of travel. Multilayer

mirrors could be utilised to give good reflectivity at this angle, but will only work over a limited energy range and will have a very strong polarising effect. This may be acceptable for some experiments. Each substrate could be coated with many multilayers to give a wide energy coverage. At 45° there is no need to rotate the mirrors and so each multilayer will give the full delay range within its bandpass and the mechanism needed to translate to each multilayer will be easier to implement.

10.6 Beamlines for FEL Sources

In the following sections, the issues discussed above will be explored with the aid of specific beamline concepts. The concepts are not intended to relate to any particular experiment and nor are they intended to be definitive design solutions. Rather, the intention is to explore issues and establish broad performance indicators. There is an emphasis on the shorter wavelength sources, since these are likely to pose the most significant challenges.

10.6.1 Direct Light Beamline for XUV-FEL

A direct light beamline with the minimum of optical elements but high demagnification will give the highest possible flux density at the experiment. The practical minimum number of elements is two. Firstly, a plane mirror will deflect the light away from the FEL axis at an angle 4.6°, chosen to fit in with the other FEL beamlines described in later sections. This is also desirable as it moves the beamline from the axis of the high energy radiation from the accelerator. The mirror will optimally have silicon and gold coatings for operation at low and high energies respectively, or otherwise just gold.

Focussing will thus be accomplished by a single mirror, which will necessarily be ellipsoidal in form. The demagnification achievable is limited by the minimum desired working distance after the mirror and the maximum length of the mirror that can be manufactured to the required quality.

The tangential image size in particular will be limited by the tangential slope errors of the mirror. Shorter mirrors can be made more accurately, so a smaller image may be achieved with a better quality but shorter mirror even though this will require lower demagnification (the shorter mirror has lower acceptance and so must be closer to the source). Reducing the image distance reduces the magnitude of the image blurring caused by the slope errors. Shorter image distances also require shorter mirrors to give sufficient space for the experiment.

The distance of the mirror from the source, the angle of incidence and the radiation divergence will determine the length of the mirror required to capture the FEL radiation. The mirror length can be reduced by increasing the grazing angle, but with a penalty in lower reflectivity and increased polarising effect. Larger grazing angles also increase the relative image blur due to sagittal slope errors.

For this initial beamline concept, a mirror of 50 cm total length is assumed, which can be made with RMS slope errors better than 2.5 μrad (tangential) and 10 μrad (sagittal). The image distance is 75 cm, which will allow approximately 40 cm of space between the mirror vessel and the focus for the experimental system.

With a grazing angle of 5°, the mirror can be 53 m from the source point and the beam footprint at 10 eV will be c. 50 cm by 4 cm (at 6σ level, ensuring minimal diffraction effects). To achieve high reflectivity over the entire range 10 to 300 eV, a nickel coating will be used on the mirror. This will give c. 60 % reflectivity at 300 eV.

The geometrical demagnification of the mirror is thus 71:1. With an assumed source size of 70 μm RMS, the ideal image would be 2.3 μm in diameter at FWHM. Because the transverse size of the source is so small, a perfect ellipsoidal mirror will give no aberrations if the source also has essentially zero depth, but the image will degrade if the source depth is large. Wavefront propagation of the calculated radiation field from the FEL is the ideal method to determine the source properties, including the source size, and such calculations will be performed in the TDR phase. However, the FEL output is expected to be a good approximation to a TEM_{00} Gaussian mode and so there should be no apparent source depth in the far field. Nevertheless, Figure 10.8 shows the result of a SHADOW ray-trace of a perfect ellipsoid imaging a Gaussian source of 70 μm RMS size and 141 μrad RMS divergence (equivalent to the FEL at 10 eV) and with 1 m uniform depth, equivalent to half the length of an undulator module. The horizontal axis is the sagittal image and the vertical axis is the tangential image. The scale is in microns. This shows a source depth of 1 m has little effect on the final image quality.

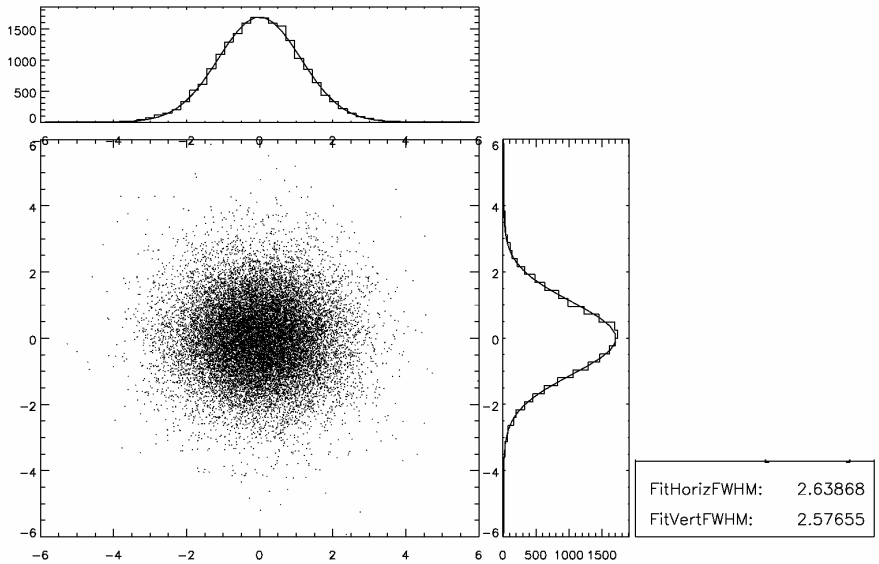

Figure 10.8 Ray-trace image of FEL at 10 eV with perfect ellipsoidal mirror

However, the slope errors of the mirror will degrade the image. Table 10.5 gives the expected final image size with slope errors included. Also given in the table are indicative key

performance parameters of the beamline. Whilst the image size is calculated on purely geometrical grounds, the mirror aperture is large enough so that diffraction from the truncated Gaussian beam is not significant and so the system is not expected to be diffraction limited even at 10 eV. However, some caution is needed over the geometrical treatment of the slope errors. With coherent illumination, the height errors in the mirror will result in a phase error in the reflected wavefront and this adds in amplitude at the image plane, rather than in intensity as in the geometrical case.

Table 10.5 Performance of focused direct light beamline on XUV-FEL

Parameter			***Unit***
Photon Energy	10	100	eV
Peak output power of FEL	6080	1370	MW
Pulse length (rms)	22	22	fs
Beamline efficiency	75	61	%
Energy / pulse at experiment	251	46	μJ
Photons / pulse at experiment	2.10^{14}	3.10^{12}	
Image size (FWHM)	9 x 4	9 x 4	μm^2
Photon density	4.10^{12}	7.10^{10}	1 / μm^2 / pulse
Pulse energy density	6.10^{5}	1.10^{5}	mJ / cm^2 / pulse
Peak power density	$1.\ 10^{16}$	2.10^{15}	W / cm^2

To increase the power density to ~ 10^{17} W/cm^2 will require a decrease in the FWHM image size to ~ 2 μm diameter at 10 eV and ~ 1 μm diameter at 100 eV. This can only be achieved by a combination of higher demagnification and lower mirror slope errors. The focal length of the mirror will need to be reduced as this lowers the diffraction limit by increasing the numerical aperture (NA) and also reduces the magnitude of the slope error blurring. The mirror will thus have to operate at a higher grazing angle (to reduce its length) and be integrated in to the experimental system. It is likely that the distance of the focus from the end of the mirror would be ~ 10 cm or less and the grazing angle would be as high as 20°. There will inevitably be a reduction in reflectivity and increase in polarising effect.

Even with reduced focal length, the mirror will have to be of much lower slope error. Tangential slope errors of ~ 1 μrad RMS or lower would be required and the sagittal slope errors would need to be similar if the mirror operates at 20° grazing angle. Ellipsoids (and other aspherics) are difficult to manufacture and achieving such a mirror will require close collaboration with a manufacturer capable of precise surface finishing techniques such as ion-beam milling and world leading metrology to determine where the milling needs to be performed.

An alternative focussing mirror scheme is the Kirkpatrick-Baez arrangement of crossed plane-ellipses. The advantage of this system is that each mirror is formed by the controlled bending of a flat substrate, which can be made with sub-microradian RMS slope errors. Micron and sub-micron spot sizes have been achieved (in the hard x-ray region) with such systems at various SR

sources [12, 13]. The disadvantage of the Kirkpatrick-Baez arrangement is that the demagnification is not the same in each plane and the demagnification of the first mirror is limited by the length of the second mirror. This is not a major problem on conventional SR sources as the source is asymmetric, but it does mean that for high demagnification the mirrors are too short to accept the full output of the source.

For the XUV-FEL, the acceptance of the mirrors needs to be very large ($> 4\sigma$) otherwise the required spot size will not be achieved due to diffraction. However, the lower photon energy means that higher grazing angles can be used and so the mirror can be short and still accept the full beam aperture. But the high divergence of the light at long wavelengths will ultimately limit the minimum mirror length and even with 20 cm long mirrors with 2 cm separation at 20° grazing angle and a 10 cm final working distance, the demagnification of the first mirror will be about two times lower than that of the second mirror. Thus the performance of the Kirkpatrick-Baez system is compromised. Also, the reflectivity of such a system at high grazing angle will be very much lower than the single mirror as there is always one p-reflection in the system. There is no overall polarising effect however.

Schwarzschild objectives have also been used for producing sub-micron spot sizes [14]. These objectives work at normal incidence and so need to have multilayer coatings to achieve reasonable reflectivity in this energy range. The spectral operating range of each objective is thus limited. They also have a low geometric acceptance due to the central obstruction and small size of the primary mirror. So, while they can achieve small spot sizes, they do not have high efficiency and their usefulness in this application is questionable.

In summary, achieving a micron sized spot from the XUV-FEL will require a high NA mirror system with exceptionally high manufacturing tolerances. Detailed study will be required to assess the relative merits of a single mirror against a Kirkpatrick-Baez or other system.

10.6.2 High Resolving Power Beamline for the XUV-FEL

This beamline concept illustrates the possible performance from a beamline optimised for high resolving power (RP) over the range of the 1st and 3rd harmonics of the XUV-FEL (10 to 300 eV). The beamline would also be able to operate at lower resolving power to give higher flux. As the design criterion is high resolving power, no attempt is made to preserve the short pulse length and such a beamline will not be appropriate for time resolved studies. It is therefore assumed that synchronisation with other sources is not required, though this will not preclude combining with the more easily transportable wavelengths (IR, THz) and independent laser sources.

The beamline concept is based around the SX700 variable included monochromator, operating in collimated light [10]. In this design, there are four key optical elements to the monochromator.

A collimating mirror (CM) receives light from the source and collimates it in the dispersive plane of the grating (usually vertical). It may also perform horizontal focussing at the exit slit. It is normal to have this mirror horizontally deflecting and sagitally collimating as this helps to reduce the effect of slope errors on the resolution. If the mirror also focuses in the horizontal, it will be toroidal in shape.

A plane grating (PG) receives the collimated light and disperses it. The included angle between incident and diffracted beams can be varied by a plane mirror (PM), which is (usually) just in front of the grating. This mirror utilises an off-axis rotation to ensure the beam always strikes the centre of the grating. Normally, both mirror and grating will deflect vertically.

After the grating a focussing mirror (FM) produces a monochromatic focus at the exit slit. This mirror is usually horizontally deflecting and sagittally focussing and is thus a sagittal cylinder in shape.

After the exit slit, the beam is refocused to the experiment by one or more mirrors depending on the beam spot requirements.

Since the grating operates in collimated light, the monochromatic magnification at a given energy can be readily varied by changing the angle of incidence at the plane mirror. This allows the resolving power to be adjusted. A key parameter in the operation of the SX700 type of monochromator is the c-parameter defined by:

$$c = \frac{\cos\beta}{\cos\alpha} \tag{10-18}$$

where α and β are the angles of incidence and diffraction at the grating. Increasing c will improve the ultimate resolution but decrease the efficiency of the monochromator through reduced diffraction efficiency and spectral bandpass (the premirror reflectivity will actually improve).

Since this type of monochromator operates without an entrance slit, the resolution is normally limited by the source size. However, as the source from the FEL is assumed to be diffraction limited and Gaussian, it can easily be shown that the source size limited resolving power is always equal to the diffraction limited resolving power of the grating given by equation (10-11) (if the grating is infinite in length). If the grating is finite, the grating resolving power will always be worse than the source size resolving power, which can therefore be ignored.

The practical limit to the resolving power is therefore the RMS illuminated length of the grating. This will depend on the divergence of the photon beam from the FEL and the distance of the collimating mirror from the source.

Since the output of the FEL is assumed to be diffraction limited, the relation between the RMS source size and RMS divergence in the far field is given by:

$$\sigma_r \sigma_{r'} = \frac{\lambda}{4\pi} \tag{10-19}$$

The source size will depend on the electron beam size, and this will vary slightly as a function of photon energy because the beam energy will be adjusted. The exact accelerator settings will be the subject of later detailed study, and so at this stage precise source sizes and divergences cannot be determined. Therefore, this initial study has assumed a constant RMS source size of 70 μm, which is in line with the current predictions. In the future, simulations of the FEL output with the code GENESIS [15] will be performed to find the far field divergence and allow the effective source size to be calculated.

A consequence of equation (10-19) is that the divergence over the energy range 10 to 300 eV varies considerably. Operation over such a wide range is therefore problematical. To achieve the required resolving power at high photon energy, the collimating mirror must be far from the source. However, at low photon energy, this will make the beam section too large at the monochromator and the required optics will be impractically large and introduce too many aberrations.

Therefore, a double collimating mirror system is proposed. A plane switching mirror SwM will deflect the light horizontally from the FEL onto one of two collimating mirrors which are so arranged to deflect the light horizontally along a common path and collimate vertically. The first CM will be at a higher grazing angle of incidence and closer to the source and will be used for the lower energy range (10 to 100 eV). The second CM (which will have to be moved aside when the first CM is in use) will deflect through a smaller angle and will be further from the source and so will be used for the higher energies (up to 300 eV). Figure 10.9 shows the general layout.

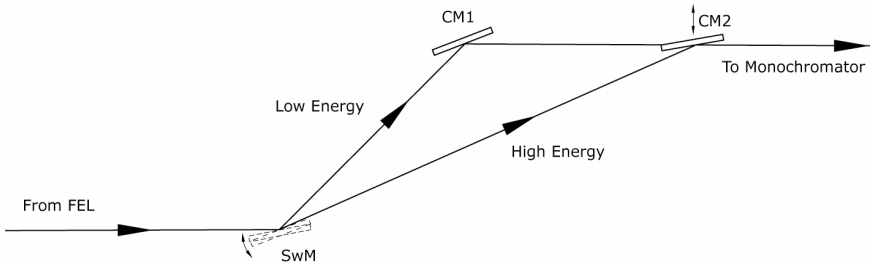

Figure 10.9 Double collimating mirror system for high resolving power FEL beamline

The exact choice of angles and distances must bear in mind the following factors:

- The plane mirror will be relatively near the source. It will also be at a relatively high grazing angle when deflecting to CM1. The peak energy density on it is a major concern. This will be worst at 100 eV, when the radiation divergence is lowest.

- The grazing angles of incidence have to be low enough to give a reasonable reflectivity, but not too low so as to make the mirrors too long.

- The optical paths to each CM must be long enough to give the required grating illumination and hence resolving power, but not so long so as to make the beam footprints too big and introduce aberrations.

Table 10.6 gives the parameters for the double collimating mirror system used for this initial study. With the switching mirror at only 17.4 m from the source, the peak of the beam fluence at the position of the switching mirror is high at 50 mJ/cm^2 at 100 eV. From Figure 10.1, the ablation threshold at this mirror will be about sixteen times the value in Table 10.2 for a gold coating and fifty times for an amorphous carbon coating. The ablation threshold of the switching mirror is thus 640 mJ/cm^2 for gold and 3000 mJ/cm^2 for amorphous carbon. This mirror can easily be made wide enough to have two (or more) coatings to suit different parts of the spectral range.

Table 10.6 Parameters for double collimating mirror system

	SwM	CM 1	CM2
Optical path from source (m)	17.392	23	36
Grazing angle (low energy) (°)	5	5	N/A
Grazing angle (high energy) (°)	1.5	N/A	1.5
Distance between CM1 and CM2 (m)		13.060	

Using this double collimating mirror system, four modes of beamline operation are considered, as described in Table 10.7.

Table 10.7 Operation modes of high RP XUV-FEL beamline

	Mode 1	*Mode 2*	*Mode 3*	*Mode 4*
Energy range (eV)	10 – 100	10 – 100	50 – 300	50 – 300
Description	High RP	High Flux	High RP	High Flux
Grating Line density (l/mm)	1200	600	1800	1800
Monochromator c	6	2	6	2
Collimating Mirror	CM1	CM1	CM2	CM2

Table 10.8 summarises the optical elements and Figure 10.10 shows the layout of the key optical components of the beamline

Table 10.8 Optical elements for High RP XUV-FEL beamline

Element	SwM	CM1	CM2	PM	PG	FM
Shape	Plane	Toroid	Toroid	Plane	Plane	Cylinder
Geometrical surface size (mm^2)	110 x 50	190 x 40	180 x 25	310 x 30	160 x 30	220 x 110
Optical surface size (mm^2)	100 x 40*	160 x 30	170 x 15	300 x 20	150 x 20	210 x 100
Source distance (tangential / sagittal) (m)	17.392	23	36	∞ / ∞	∞ / ∞	- / ∞
Image distance (tangential / sagittal) (m)	-	41.96 / ∞	28.9 / ∞	∞ / ∞	∞ / ∞	- / 20
Grazing angle of incidence (°)	1.5 or 5	5	1.5	variable	variable	2
Curved mirror radius (tangential / sagittal) (m)	-	R = 340.92 ρ = 4.009	R = 1224.8 ρ = 1.885	-	-	ρ = 1.396
Slope error RMS (tangential / sagittal) (µrad)	1	2 / 5	2 / 5	0.2	0.4	1.25 / 3
Line density (l/mm)	-	-	-	-	600 1200 1800	-
Blaze angle (°)	-	-	-	-	See Table 10.10	-

**allows for two coatings*

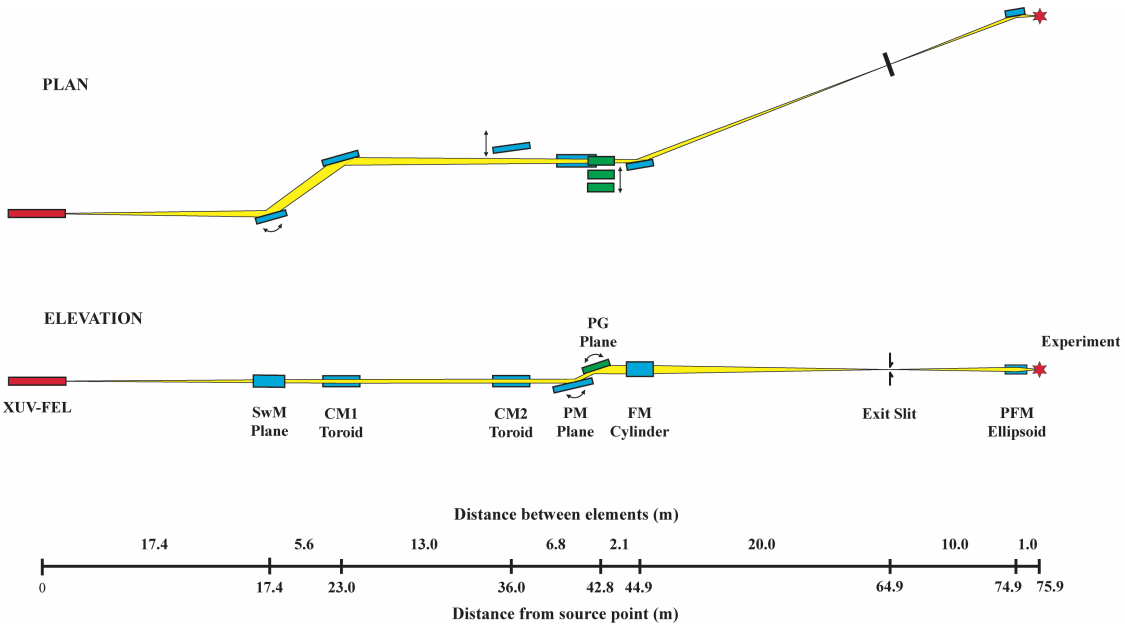

Figure 10.10 Layout of the key optical components of the high resolving power XUV-FEL beamline

10.6.2.1 Resolving Power

The resolving power has been calculated by using standard analytical tools. The infinite grating resolving power in equation (10-11) is adjusted for the finite actual length of the grating using the results of a numerical convolution to give the FWHM of the diffracted orders. The infinite grating resolving power is reduced by the factor shown in Figure 10.11, where the reduction factor is plotted against the grating length divided by the RMS illumination at the grating.

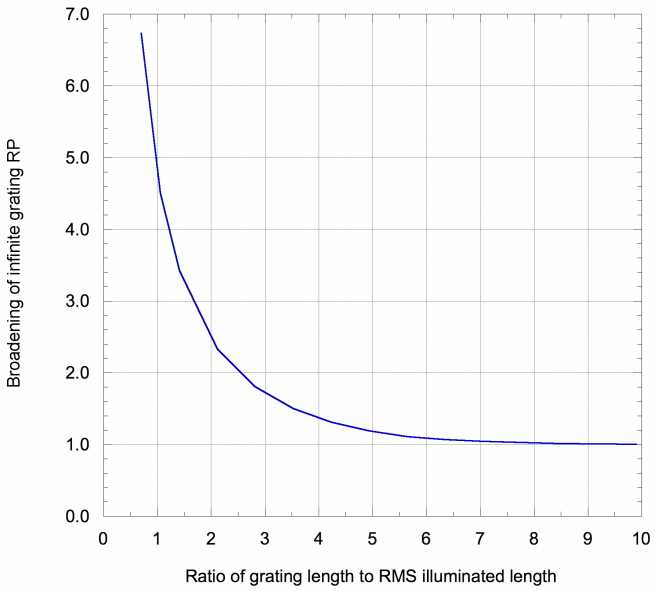

Figure 10.11 RP degradation due to the finite length of the diffraction grating. The infinite grating RP given by (10-11) is reduced by the factor shown.

The effect of slope errors on of each element is calculated assuming the errors are randomly distributed and so give a Gaussian broadening to the image formed by each element. The slope errors used are given in Table 10.8 and are demanding but achievable with the latest manufacturing and metrological techniques.

The effect of optical aberrations on the resolution is not included in the calculated resolution. With collimated light, the only aberrations are at the collimating mirror and the focussing mirror. Ray tracing shows the collimating mirror has negligible aberrations. The focussing mirror has a long focal length of 20 m to reduce the sagittal curvature and so reduce the effect of aberrations. This is necessary as the sagittal footprint on the mirror is the monochromator c-parameter given by Equation (10-18) times the beam height into the monochromator. With c = 6 for high RP in mode 1, the footprint at low energies increases rapidly due to the large beam divergence. Below about 20 eV, there will inevitably be some aberrations. The effect of these has not yet been calculated. Masking of the focussing mirror can be used to eliminate the aberrations at the expense of throughput, but will reduce the resolving power in any case as it is equivalent to reducing the illuminated length of the grating. For the other modes, there should be negligible aberrations and resolution will be limited by the illuminated grating length and slope errors.

The expected resolving power of the four modes is shown in Figure 10.12. The contribution of the exit slit is taken as the convolution of a Gaussian, representing the image at the slit, and a top-hat, representing the bandpass of the slit. For the high RP modes (modes 1 and 3) and slit size of 10 µm is used as the practical minimum size that could be employed in practice. This size of slit adds only slightly to the total resolution. For the high flux modes, the slit size is set to match the source size limit. For mode 2 the size was 70 µm and for mode 4 it was 45 µm.

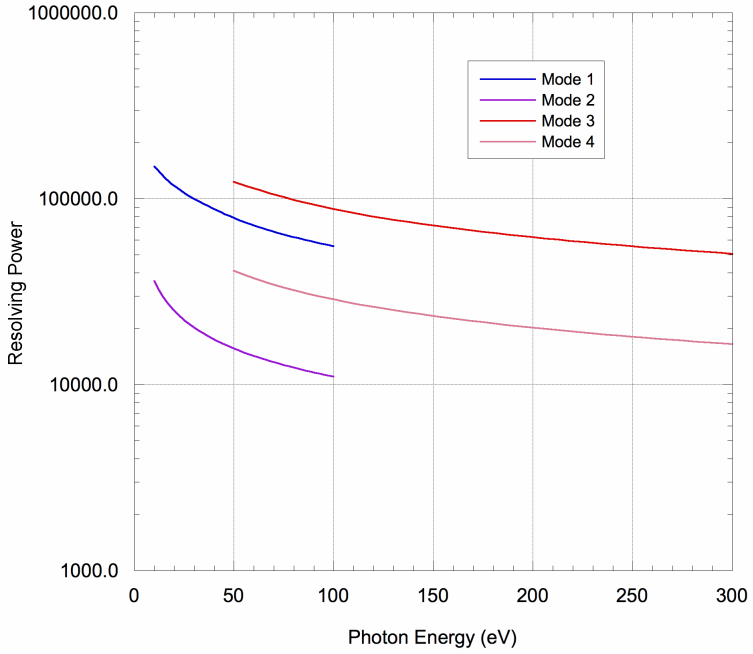

Figure 10.12 Predicted resolving power from high RP XUV-FEL beamline

10.6.2.2 Post Focussing Optics

Because the beamline is designed to achieve a high resolving power, the optical system is designed around achieving the necessary magnification in the dispersive direction and reducing the dispersive errors in the system. Specifically, sagittal focussing has been used in the dispersive direction whenever possible to reduce the effect of the slope errors on the resolution. Consequently, no special regard has been given to the non-dispersive imaging. The collimating mirror is used to focus the source at the exit slit in the non-dispersive direction, and the non-dispersive magnification is large compared with the dispersive magnification. Table 10.9 summarises the magnifications.

Table 10.9 Magnifications of high RP XUV-FEL beamline

Mode	Dispersive magnification	Non-dispersive magnification
1	0.145	1.82
2	0.435	1.82
3	0.093	0.80
4	0.278	0.80

Higher non-dispersive demagnification could simply be achieved by using a toroidal focussing mirror. But one reason for using the collimating mirror to focus in the non-dispersive direction at the exit slit is that this reduces the footprint on the focussing mirror significantly and so helps to control the aberrations. Allowing the light to diverge from source to focussing mirror will certainly not be acceptable. However, if the collimating mirror were to collimate in both planes, the non-dispersive magnification would be 0.87 (modes 1 and 2) and 0.56 (modes 3 and 4). However, this will increase the tangential radius of the CM1 to c. 528 m and CM2 to c. 2750 m. The latter is certainly beyond that which can be achieved by polishing and so CM2 would have to be based on an actively bent cylinder, with possible impact on the image quality. A third option will be for the collimating mirror to produce an intermediate horizontal focus which is re-imaged by the focussing mirror. The optimum solution will be determined in a detailed design study once the detailed experimental requirements for the beamline are known.

So, with the system as proposed, the image at the exit slit will be highly asymmetric, even though the source is symmetric. This is a consequence of the system having been designed to give high spectral resolving power. For the optics after the slit imaging to the experiment, the source in the dispersive direction will be the exit slit. Aberrations and slope errors only degrade the energy resolution. In the non-dispersive direction however, the image of the source at the slit will be enlarged by the slope errors of the optics. This will be a significant effect as the tangential slope errors of the collimating and focussing mirrors will be dominant. In modes 1 and 2, the FWHM non-dispersive image size is likely to be about 500 μm. In modes 3 and 4, the image will be about 300 μm FWHM. Since the nominal exit slit settings are 10 μm, 70 μm, 10 μm and 45 μm for the four modes respectively, the source for any post focussing optics is thus very asymmetric with the beamline operating as intended

To produce a symmetric beam spot at the experiment without enormously degrading the spectral resolving power will thus be impractical without spatially reducing the size of the non-dispersive image at the exit slit by aperturing, or with higher demagnification and better quality mirrors. Therefore, in the absence of a specific experimental driver to demand a symmetric spot, a simple post focussing system is modelled consisting of a single ellipsoidal mirror deflecting at an incidence angle of 88° with a high demagnification of 10:1. To preserve the properties of the source seen by the ellipsoid, the sagittal focus is set for the dispersive direction. With RMS slope errors of the ellipsoid of 10 μrad sagitally and 2.5 μrad tangentially, there is negligible slope error blurring of the final image.

10.6.2.3 Mirror Reflectivities and Grating Efficiencies

Because carbon is likely to have a strong polarising effect on the beam below 20 eV (§10.3), it will be assumed that carbon will not be used unless it is absolutely necessary to prevent damage of the optical surfaces.

For the fixed mirrors, the material that gives the best overall coverage from 10 to 300 eV is gold. There is still a relatively strong polarising effect at the lowest energies, but this can be minimised by using as grazing an angle of incidence as possible. At 5° grazing angle, the ratio of s- to p-reflectivity is 1.4, which is acceptable. Gold also has a good damage threshold.

The two optical elements that will have the biggest polarising effect are the premirror and the grating, as they operate at high grazing angles at low energies. The optimum material for limiting the polarising effect below 20 eV is silicon, but clearly this cannot be used at 100 eV due to the *L*-edges. Figure 10.13 shows the reflectivities and Figure 10.14 the ratio of s- to p-reflectivity of gold, amorphous carbon, nickel and silicon coatings for the premirror in mode 1. It should be noted that the calculation for silicon does not include the effect of any oxide on the surface. This will reduce the reflectivity and increase the polarising effect at low energy. The magnitude of the effect will depend on the thickness, stoichiometry and density of the oxide layer. Direct measurement of the reflectivity of polished silicon surfaces will probably be the best way to assess the true usefulness of reflection from uncoated silicon in this energy range.

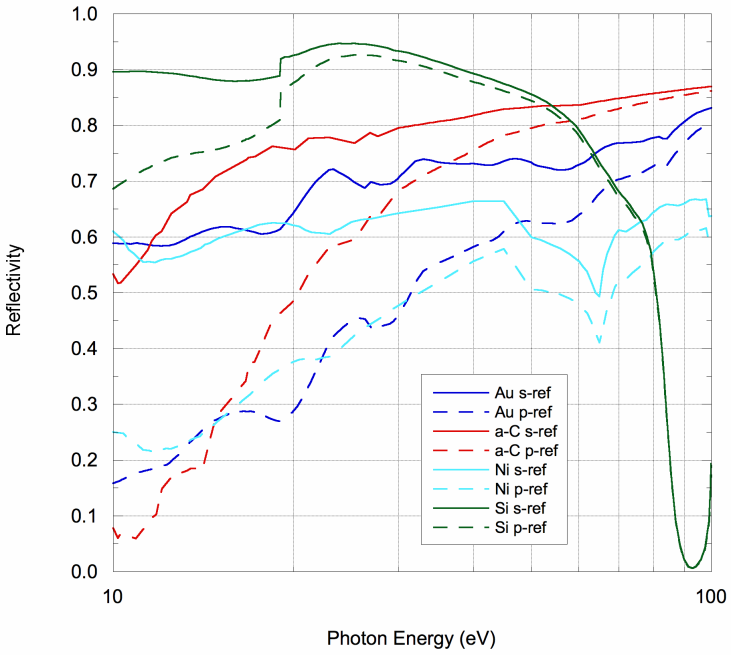

Figure 10.13 s- and p-reflectivities of various premirror coatings in mode 1 operation

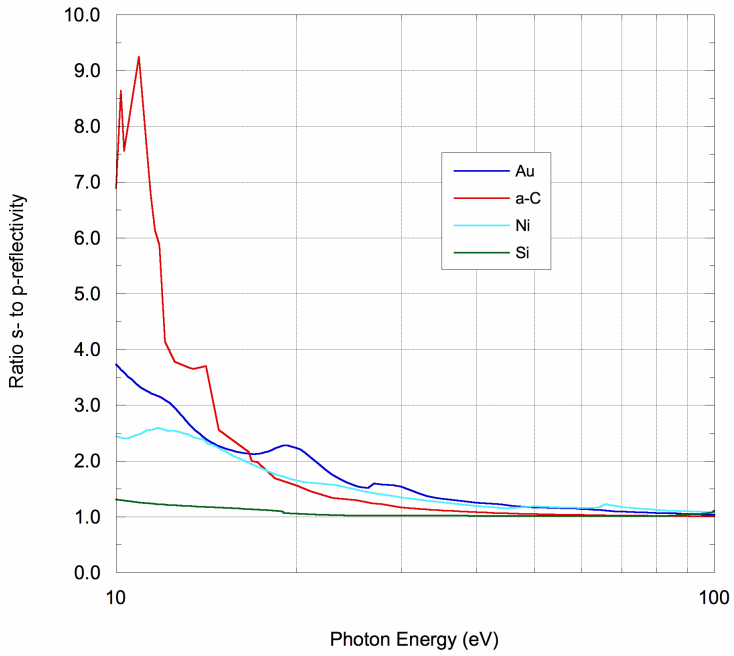

Figure 10.14 Ratio of s- to p-reflectivity of various premirror coatings for mode 1 operation. All except Si have a strong polarising effect below 20 eV.

Figure 10.15 and Figure 10.16 give the premirror reflectivities and ratio of s- to p- reflectivities for mode 3 operation for gold and nickel coatings (carbon and silicon will not be useable in this range, whilst chromium would be an alternative to nickel unless the beamline operation should need to be extended to cover the 5th harmonic of the FEL). Whilst neither coating will give a significant problem in terms of polarisation, the reflectivity of gold falls markedly above 150 eV and the nickel is much better above 200 eV.

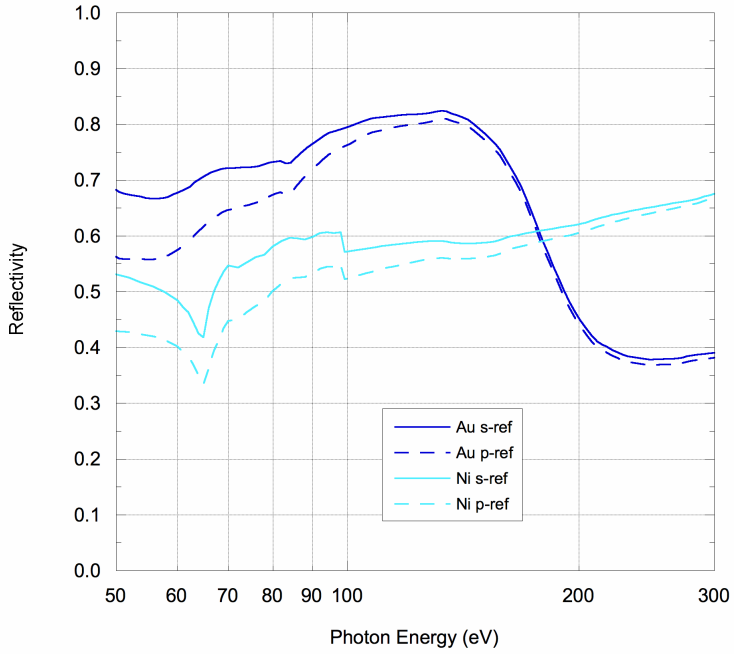

Figure 10.15 S- and p-reflectivities of gold and nickel premirror coatings in mode 3 operation

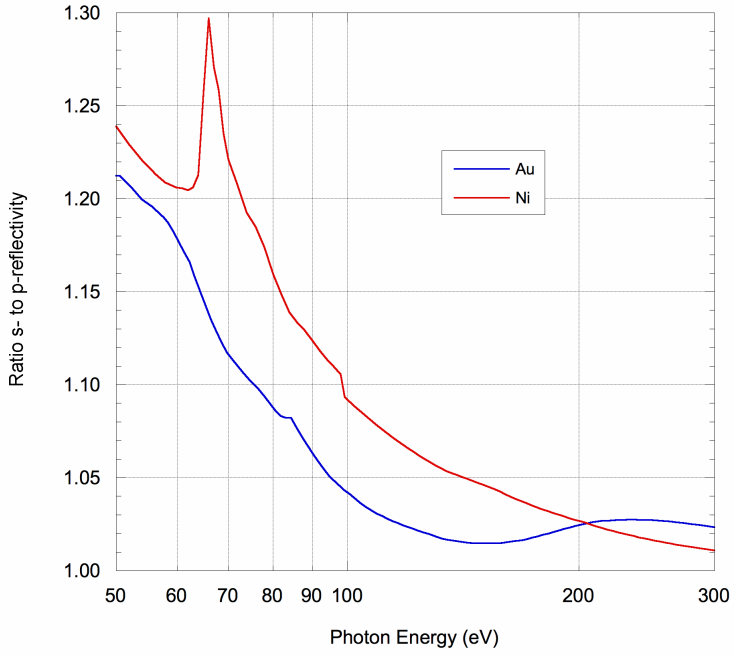

Figure 10.16 Ratio of s- to p-reflectivity of gold and nickel premirror coatings for mode 3 operation

Calculations of grating efficiencies using the code of Neviere [16] show that achieving high diffraction efficiency at 10 eV requires the use of a blazed grating. With a lamellar grating, it is not possible to make the grooves deep enough to work well at 10 eV. This is because lamellar gratings in fact have trapezoidal grooves with the groove walls inclined at typically only 10° to 30° to the groove floor. With a high line density, there is thus insufficient land space to make

the grooves very deep. Furthermore, even if the grooves could be made deep enough, this would severely compromise the efficiency at high energy.

As with the premirror, the best coating for the grating both in terms of absolute efficiency and especially in terms of low polarising effect at 10 eV is silicon. With a gold coating, the ratio of s- to p-efficiency is typically greater than three. With a silicon coating, the ratio is about 1.2.

There is thus a clear problem with trying to cover the energy range 10 eV to 100 eV with a single premirror and grating. The best practical solution is to have two coatings on each element and translate the most suitable coating into the beam for the energy range of operation. Thus, up to c. 50 eV, the silicon coatings would be employed and beyond this the gold coatings would be used.

Similarly, covering the range 100 to 300 eV presents a problem in terms of reflectivity. Gold is to be preferred below 150 eV, but above 200 eV has quite a low reflectivity at the angles used in modes 3 and 4. Above 200 eV, nickel is a better choice. Nickel can be used down to 50 eV, but has a fairly strong edge at ~ 65 eV (chromium has the advantage over nickel here as the edge is at ~ 45 eV). Therefore, it would seem that the ideal premirror should have silicon, gold and nickel coatings and the high energy gratings should have gold and nickel coatings.

It may seem that three coatings on the premirror will be problematical. But in practice, this will be no more difficult than two coatings. The beam width will be very small, and if the facility exists to use two coatings, then three can also be employed.

For the gratings, the optimum blaze angle naturally changes as the energy changes. However, calculations show that a single blaze angle is able to give good efficiency over the whole range of each mode. It is thus not necessary to have more than three gratings (600, 1200 and 1800 l/mm). Table 10.10 summarises the blaze angles and operating ranges for each grating.

Table 10.10 Grating blaze angles, coatings and operating ranges for each mode

	Grating number	Energy (eV)	Line density (l/mm)	Blaze angle (°)	Coating
Mode 1	1	10 to 50	1200	6	Si
		40 to 100			Au
Mode 2	2	10 to 60	600	3.5	Si
		40 to 100			Au
Mode 3	3	50 to 170	1800	3.5	Au
		150 to 300			Ni
Mode 4	3	50 to 170	1800	3.5	Au
		150 to 300			Ni

There are two disadvantages to using a blazed grating. The first is that the higher order contamination is usually worse than with a lamellar grating. The second is that the blaze angle

effectively increases the incidence angle to the beam and thus may increase the risk of ablation or other surface damage.

The overall beamline efficiency in modes 1 and 2 is shown in Figure 10.17. The beamline still shows quite a large polarising effect at lower energies. This is because of the two 5° grazing angle reflections from the gold coated switching and collimating mirrors which have an appreciably lower p- than s- efficiency. Also, since all the fixed mirrors are deflecting in the non-dispersive direction, this makes the non-dispersive efficiency larger that the dispersive efficiency at lower energies. The overall scheme may need to be refined to improve this situation.

The overall efficiency increases by roughly a factor of two in going from mode 1 (high RP) to mode 2 (high flux). Combining this with the increase in exit slit bandpass, this means mode 2 will give roughly twenty times the flux of mode 1.

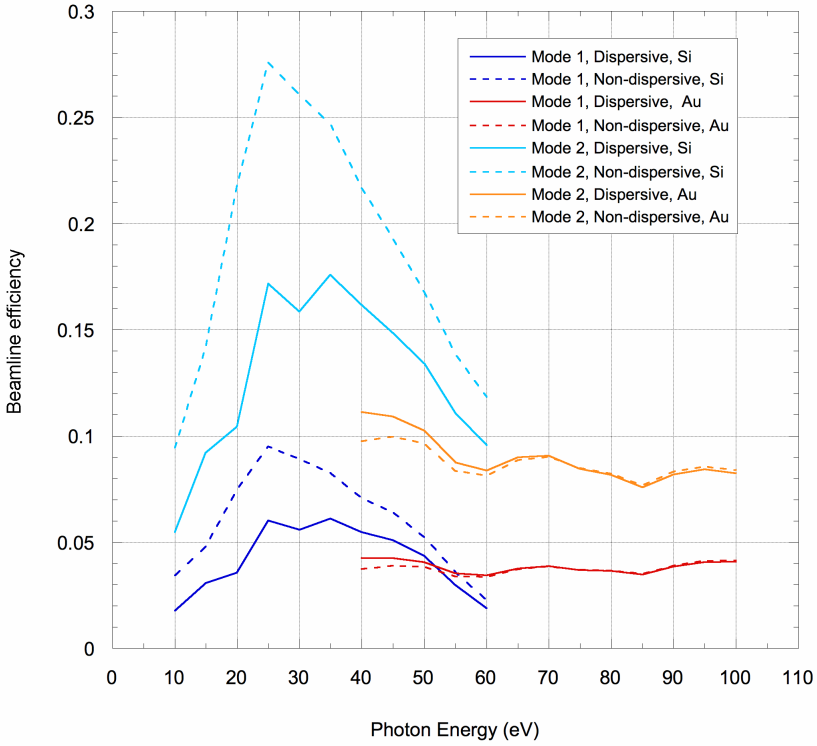

Figure 10.17 Calculated beamline efficiencies for modes 1 and 2 of the high RP XUV-FEL beamline. Silicon premirror and grating are used from 10 to 60 eV, gold coatings are used 40 to 100 eV. All other mirrors are gold coated.

Figure 10.18 shows the beamline efficiency in modes 3 and 4. The calculation is for gold and nickel coatings on the premirror and grating. Above 200 eV, the efficiency with gold coatings becomes very low, and is worse for mode 4, the so-called high flux mode. This indicates the poor efficiency is due to the premirror, which operates at higher grazing angles with lower monochromator c-value and so has lower reflectivity. Using nickel coatings, the beamline efficiency varies from 2 % to 1 % from 100 to 200 eV. This could be improved by reducing the

grating blaze angle so that it is closer to the optimum at these higher energies. Alternatively, the angle at the premirror can be reduced to improve its reflectivity by inclining the exit arm relative to the entrance arm. This doesn't change the included angle at the grating but does increase the required length of the premirror, which could impact on the achievable slope errors and hence resolution. In general, however, the efficiency is good considering the energy range and the fact that the beamline has six optical elements including high line density gratings, and is similar to that of other comparable beamlines [17,18].

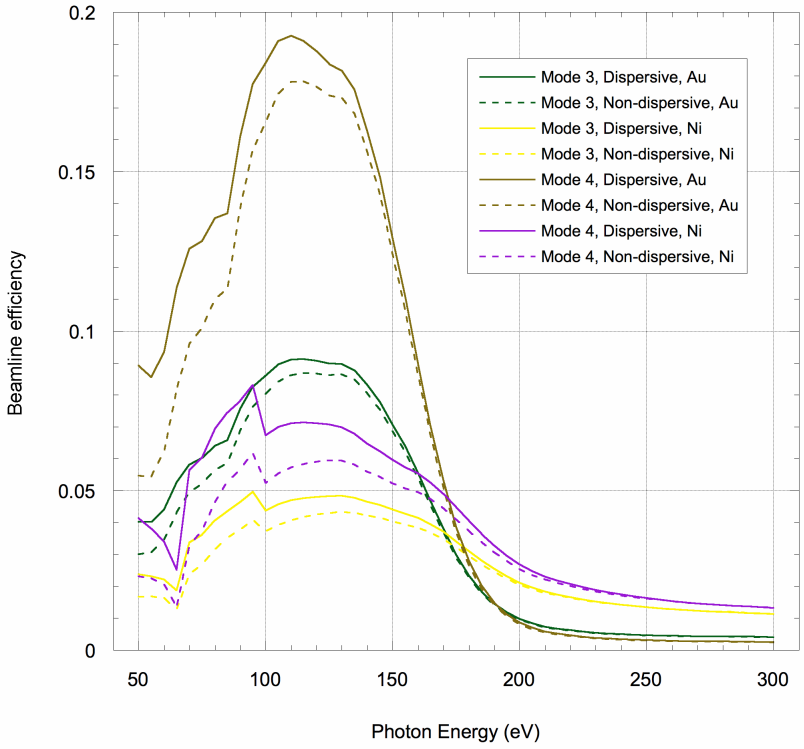

Figure 10.18 Calculated beamline efficiencies for modes 3 and 4 of the high RP XUV-FEL beamline. Calculations are for gold and nickel coatings on premirror and grating.

10.6.3 Combined XUV-FEL and Spent Beam Undulator Beamline with Pulse Length Preservation and Synchronisation

Combining two beams from separate sources with high timing precision is clearly a demanding task. This section presents a preliminary design concept that is not intended to be a realistic beamline solution. Rather, the issues raised in producing the concept are used to inform the design challenges that will be presented by the actual beamline design.

The idea behind the spent beam undulator is to provide a spontaneous source with the same repetition rate and minimal temporal jitter relative to the XUV-FEL for pump-probe experiments on the XUV-FEL. It is therefore necessary to provide two beamlines that can deliver the two photon beams to the same experimental system with the following general requirements:

- physical coincidence of the focused beams at the experiment;
- focused beam spots from each beam to be as similar in size as possible;
- the two beams should be as close as possible to being collinear;
- the inherent pulse lengths of each beam should be preserved;
- spectral filtering should be applied to remove the unwanted background from each source (but photon energy resolution should not be better than the transform limited bandwidth);
- the transport efficiency should be as high as possible.

To this end, the following design principles have been used:

- the chief rays from the two beamlines will be coincident at the final focus;
- the overall magnifications of each beamline should be similar. (But note, the sources will not be the same size and the final spot size may be limited by other factors e.g. slope errors on the mirrors);
- the two beams should converge at a small included angle;
- both beamlines will use monochromators. The FEL beamline will use a double monochromator system as described in §10.5.1. The undulator beamline will use a single grating monochromator in order to reduce transmission losses;
- the spectral bandpass of each beamline will not be less than the limit required to preserve the pulse length;
- the geometry of each beamline will not include excessive deflection angles.

Currently, there are many areas of uncertainty that prevent a more thorough and realistic approach to the beamline concept. The exact properties of the sources are not defined. In particular, the electron bunch size and length through the spent beam undulator has not been modelled. The relative position of FEL and spent beam undulator is also unknown. More importantly, the experimental requirements have not been established. So the required spectral and spatial properties are not known.

10.6.3.1 Pulse Length Preserving XUV-FEL Beamline

The pulse length preserving beamline will follow the general principles described in §10.5.1. The design will be based on the collimated light SX700 monochromator already described. In order to fit in with the conceptual high resolving power beamline (§10.6.1), this beamline will utilise the same switching mirror of the high RP beamline. The switching mirror will horizontally deflect to a collimating mirror at the same location as CM2 of the high RP beamline (a translation will move between the mirrors). The collimating mirror for the short pulse beamline will deflect horizontally through an angle of 7° to separate the two beamlines. The collimating mirror focuses in the horizontal at the slit between the gratings.

The first plane mirror and grating pair will be located at 8 m from the collimating mirror. This first SX700 monochromator will operate in outside order with a monochromator c = 0.7, and so

the grating will be placed before the mirror to reduce the effect of the mirror's slope errors on the image quality. A low line density grating of 50 l/mm will be used.

Positioned 2 m after the grating will be the first focussing mirror, focussing in the vertical to the exit slit at 6 m from the mirror. The mirror will be a sagittal cylinder but the short focal length will not cause aberrations because the outside order operation of the preceding grating will compress the vertical section of the beam from the collimating mirror and so reduce the sagittal footprint on the focussing mirror.

The beamline after the exit slit becomes a mirror image of that before the slit, except the collimating mirror is replaced with a post-focussing mirror focussing to the experiment. The second SX700 monochromator works in inside order with c = 1/0.7 to ensure the time stretch of the first is exactly reversed.

The post-focussing mirror (PFM) sees a horizontal source at the exit slit but a vertical source at infinity. The PFM is thus toroidal in shape and focuses at a distance of 6 m.

The spectral transmission of the beamline is set to four times the RMS bandwidth of the pulse by suitable adjustment of the exit slit. The spectral width of a 30 fs transform-limited Gaussian input pulse is 11 meV RMS (26 meV FWHM). The required exit slit size for this pulse varies between 1.5 mm at 10 eV and 47 μm at 100 eV. The spectral resolving power of the beamline, defined at the FWHM of the energy spread, is the photon energy E in units of eV divided by 0.026, i.e. 385 at 10 eV and 3846 at 100 eV. The resolving power cannot be made higher without lengthening the pulse.

10.6.3.2 Spent Beam Undulator Beamline

The key design choice for the spent beam undulator beamline is whether or not it will need a double grating monochromator to preserve the pulse length. Because the undulator is only a spontaneous source and the beam current through it will be only ~ 1 μA, the beamline should have as high efficiency as possible. Therefore, a single grating design is to be preferred if it is technically possible.

The exact pulse length that will be achievable from the undulator will be the subject of a later technical design study. The pulse length will be determined by the electron bunch length and will necessarily be longer than the FEL pulses (whose length is determined by the HHG seed pulse). Note that slippage between the electron bunches and photons emitted along the length of the undulator will lengthen the pulse unless the undulator is kept relatively short and operated at modest value of the deflection parameter (see §9.3.3.2). The experimental demands will set a minimum acceptable level to the pulse length.

In this study, a single grating monochromator will be used with a very short RMS pulse length of 80 fs to test the feasibility of such a design. The beamline will be allowed to increase this pulse length by 20 % to c. 100 fs RMS. The pulses are assumed to be Gaussian, so this means the grating stretch must be no more than 70 % of the input pulse length, i.e. 56 fs. This will be

very difficult to achieve (§10.5.1) with a single grating monochromator and will have important consequences that will be explored here.

Equation (10-12) gives the relation between the pulse stretch from the grating and the RMS illuminated length of the grating. For a grating with incidence angle α and at a distance r from a source of RMS divergence $\sigma_{r'}$, the RMS illuminated length is:

$$\sigma_L = \frac{r\sigma_{r'}}{\cos\alpha} \tag{10-20}$$

By combining (10-12) and (10-20), we can define the incidence angle required to maintain a fixed pulse stretch as:

$$\cos\alpha = \frac{Nm\lambda}{c}\,\frac{r\sigma_{r'}}{\Delta\tau_{rms}} \tag{10-21}$$

To maintain the correct incidence angle at each wavelength will require a monochromator that is able to operate with a free choice of included angle. Hence a collimated light SX700 monochromator is again considered.

To give a pulse stretch of only 56 fs the grating will need to have a very low line density to ensure sufficiently few illuminated grooves whilst ensuring the incidence grazing angle is not excessively large. Between 10 and 55 eV, a line density of 30 l/mm will be considered. This is feasible with mechanical ruling. Higher energies permit a higher line density without stretching the pulse, see (10-12). Between 50 and 200 eV a 300 l/mm grating could be used. It is also necessary to place the collimating mirror as close to the undulator as possible to minimise the beam height at the grating. A distance of 12 m has been assumed.

With the incidence angle determined by (10-21) and the radiation divergence from the undulator of length *L* given by the convolution of the natural radiation angle from diffraction (see equation (10-22), §10.7.1.1) and the electron beam divergence, the monochromator c-value and hence magnification must vary with photon energy. At 10 eV, the monochromator c-value becomes close to unity and so there is only a small separation between the diffracted and zero order light. This will increase the amount of scattered light passing down the beamline and the monochromator energy calibration will be more susceptible to small angular misalignments of the premirror and grating. The c-value increases with the photon energy and hence the operating range of a given grating is limited before the c-value becomes too large. Figure 10.19 shows the c-values of the two suggested gratings. (The assumed undulator length is 6 m).

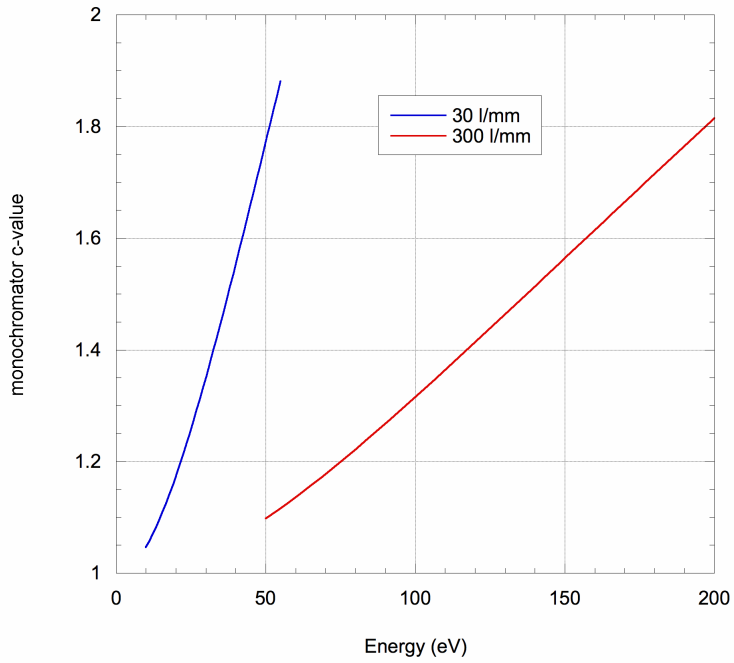

Figure 10.19 Monochromator c-values of spent beam undulator beamline in pulse length preserving mode

Whilst preservation of the temporal pulse length determines the number of illuminated grooves on the grating, the monochromator spectral resolving power is limited by the angular subtense of the source size at the grating. This is because the undulator source is not Gaussian and diffraction limited, and so this source size limited resolving power is necessarily worse than the grating resolving power determined by the number of illuminated grooves. Consequently, the spectral resolving power of the monochromator is low, especially at low energy, and certainly well below the limit set by the transform-limited bandwidth of the pulse.

Figure 10.20 gives the total RP (based of FWHM energy spreads) for each grating and the contributions from the source size and a 150 µm exit slit. The grating RP, defined by the number of grooves that can be illuminated whilst achieving the required pulse length, is also shown, and can be seen to be significantly above the source size RP. At 10 eV, the total RP falls to only c. 300, though this is not too dissimilar to the RP of the FEL beamline.

If the spectral resolving power falls below the natural bandwidth of the undulator harmonic, then the monochromator is just filtering the background radiation between the undulator harmonics and reducing the relative intensity of the higher harmonics (depending on the higher order efficiency of the grating). This is unlikely to occur in practice as the spectral width of the harmonics is determined by the number of periods in the undulators and this must be limited to prevent the output photon pulse being temporally stretched due to slippage between the photons and electrons.

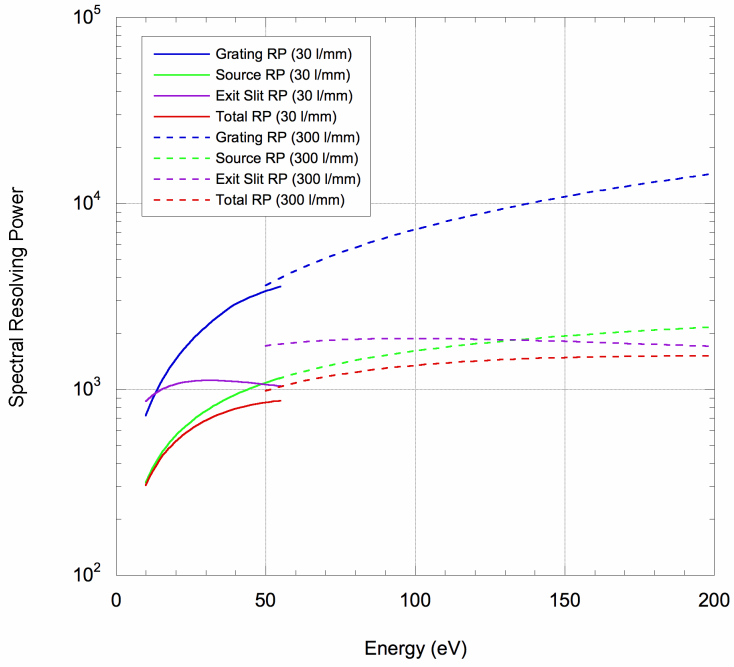

Figure 10.20 Predicted resolving power for pulse length preserving spent beam undulator beamline

If the exit slit bandpass becomes large compared with the spectral width of the undulator harmonic, then the slit will no longer define the source for the following post focussing mirror (see §10.6.3.3 below). Figure 10.20 shows that the slit RP for a 150 μm slit is ~ 1000 or above and so this would not be the case for this slit setting.

After the exit slit, and ellipsoidal or toroidal mirror can be employed to focus at the experiment with a horizontal deflection. Whilst a single mirror limits the image size that can be achieved, it is simpler to achieve coincidence with the FEL beamline.

10.6.3.3 Issues for Combining the Two Beams

Achieving coincidence of the two beams in the horizontal plane is not particularly challenging. Both optical designs use mainly horizontal deflections and there are enough degrees of freedom in both beamlines to allow the angles and lengths to be adjusted to give the required coincidence. Figure 10.21 shows the overall layout of the beamlines in schematic form.

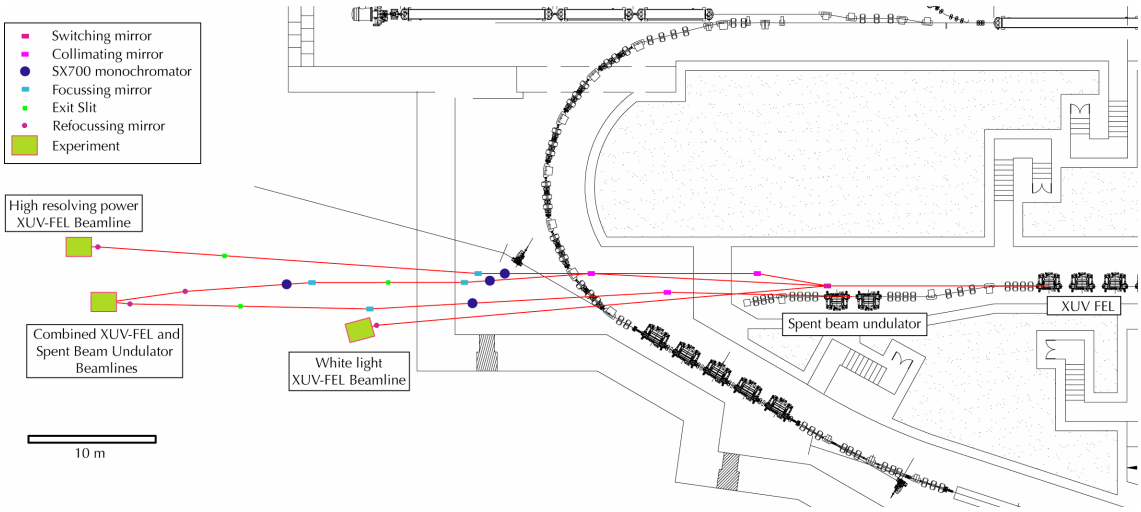

Figure 10.21 Layout of conceptual XUV-FEL beamlines. The combined pulse length preserving FEL and spent beam undulator beamlines are shown in relation to the high resolving power and white beam FEL beamlines. The XUV-FEL axis is above the plane of the high current loop, so the beamlines pass over the top of the return arc and VUV-FEL cavity.

In the vertical plane, the FEL beamline is height neutral (the final image and source are in the same horizontal plane) since the vertical offset from the first SX700 monochromator is reversed by the second. But the spent beam undulator beamline will have a ~ 20 mm height offset, depending on the mechanical design of the SX700 monochromator. This can be corrected by angling the beam after the monochromator by a very small amount. Alternatively, an asymmetric three- or four-mirror delay line giving an overall vertical offset could be used to correct the height difference (see §10.5.3). This would necessitate the delay line to use vertical deflections and translation.

Far more challenging is trying to match the image sizes of the two beamlines. In fact, this has not really been tried with the above concept. Rather, the target was to match the magnifications in both the vertical and horizontal. If the magnifications can be adjusted to be roughly the same, then they can also be adjusted to compensate for differences in the source sizes, once these are known. Table 10.11 gives the magnifications of the two beamlines as outlined in §10.6.3.1 and §10.6.3.2. The vertical magnification of the spent beam undulator beamline changes because the c-value is adjusted to keep the pulse length constant.

Table 10.11 Source to experiment magnifications of XUV-FEL and spent-beam undulator beamline concept

	XUV-FEL Beamline	*Spent-beam Undulator Beamline*
Vertical magnification	0.167	0.089 to 0.160
Horizontal magnification	0.167	0.167

Since the magnification required depends on the source for each beamline, some discussion of the nature of the source is relevant. For the FEL, the source will be Gaussian and diffraction limited to a good approximation. The source size will depend on the size of the radiating electron bunch, which will be a function of photon energy via the tuning scheme of the FEL. But the variation in electron beam size is not expected to result in the source size being a strong function of photon energy.

The undulator presents a more conventional source. The source size is taken to be the convolution of the electron beam size and the natural radiation size. The RMS of the Gaussian approximation to the natural radiation size from an undulator of length L is given by equation (10-22), §10.7.1.1. The source size is thus a function of photon energy as long as the electron beam size is not significantly larger than the natural radiation size.

Consequently the size of sources for each beamline have a different energy dependence and two beamlines working with fixed magnification cannot produce identically sized images at all energies. It may therefore be desirable to have a large electron beam size in the spent beam undulator to reduce the energy dependence on the source size.

The two beamlines also have quite different imaging characteristics. In the dispersive direction for the XUV-FEL beamline, the exit slit does not define the source for the second monochromator. But the size of the dispersed illumination at the slit plane is a function of photon energy unless the monochromator is operated specifically to keep this constant (§10.5.1). The image at the experiment is thus an image of the FEL source as seen through an intermediate and dispersed image at the slit plane, which will have a truncated Gaussian intensity distribution. In the non-dispersive direction, where there is no slit, the source for second monochromator is the geometrical image of the FEL source.

The situation is quite different for the spent beam undulator since its spectral output should be broader than the bandpass of the exit slit. Therefore, the exit slit is fully illuminated with dispersed light and so the slit defines the source for the post-focussing mirror in the dispersive direction. If the exit slit is a fixed size (and it need not be), then the size of the source for the PFM in the dispersive direction will be constant with energy, but with a uniform not Gaussian intensity distribution. The vertical image size at the experiment is thus determined by slit size and the magnification of the PFM.

However, the non-dispersive source for the PFM will still be the image of the real source at the exit slit. If the horizontal size of the electron beam in the undulator is small or of the order of the natural radiation size (which is generally *not* the case in a conventional storage ring based SR source), then the horizontal image size at the experiment will still be a function of wavelength.

Furthermore the source size and system magnification is not the only factor in determining the image size at the experiment. The slope errors of the optical elements will play a large part. As has been described in §10.6.2.2, the non-dispersive imaging is likely to be dominated by the

tangential slope errors of the horizontally deflecting mirrors. This will tend to reduce the energy dependence of the non-dispersive image size.

Therefore, one can say that matching the spot sizes of the two beamlines, let alone tailoring the spot sizes to the needs of the experiment, will be a non-trivial exercise. There are unlikely to be enough degrees of freedom in the design to achieve exactly the optimum spot size required by the experiment, and some compromise will be required.

Achieving the required timing synchronisation is the next matter to consider. The exact solution cannot be specified until more definite information is available on the electron transport path from FEL to the spent beam undulator. For the beamline concepts described above, the total transport path lengths for the two beams (including an estimated electron path) are likely to be similar.

If the spent beam undulator beam is to act as the probe beam, then it must timed to arrive after the FEL pulse. If the optical delay line is located in the spent beam undulator beamline, then, with the delay set to its minimum amount, the path lengths of the two systems should be the same to give coincidence.

If the total path of the spent beam undulator beam tends to be shorter than the FEL beam path, then the optical delay line will have to be set above the minimum value to get simultaneity with the FEL beam. Some of the range of adjustment of the delay line will then be lost. Since it is hard to get appreciable delays in this energy range, it would therefore be desirable to introduce an additional electron beam path length between the FEL and spent beam undulator that compensates for the minimum delay discrepancy.

In the case where the total path length of the spent beam undulator line is unavoidably longer than the FEL beam path length, then the delay line will have to be put in the FEL beamline. The delay line will need to add enough extra path length to bring the two beams into temporal coincidence, whilst also being able to reduce the path length sufficiently to give the required temporal separation of the two beams. The delay line thus works with maximum delay giving minimum separation and reduced delay giving larger separation.

In summary therefore, we can at present only understand the issues that will influence the design choices. The detailed technical design will have to be built up with close collaboration between accelerator and optical system designers with the objective of meeting a carefully specified experimental need.

10.6.4 Beam Splitting and Recombining

Another approach to providing combined beams for multi-beam experiments is the combination of a photon beam with itself, such as in interferometric systems.

Experiments exploiting this cover ultra-high resolution interferometry and autocorrelation based diagnostics. The incoming beam is split, one pulse is delayed with respect to the other and then both are recombined at the sample or detector.

At wavelengths longer than 170 nm, efficient beam splitters using amplitude division are readily available. For shorter wavelengths, several different methods have been proposed to address the technical challenge. Multilayers on Si_3N_4 membranes have been developed for use up to 100 eV [19], but these are narrow bandpass devices. Transmission grating structures have been proposed for use at 60-80 eV [20].

For coherent sources such as in 4GLS, wavefront division by reflecting different parts of the beam in slightly different directions or by intercepting only part of the wavefront offers a more widely applicable solution for VUV and SXR systems [21]. Typical schemes are shown in Figure 10.22 where different portions of the incoming wavefront are reflected at different angles and separated, overlapped or delayed.

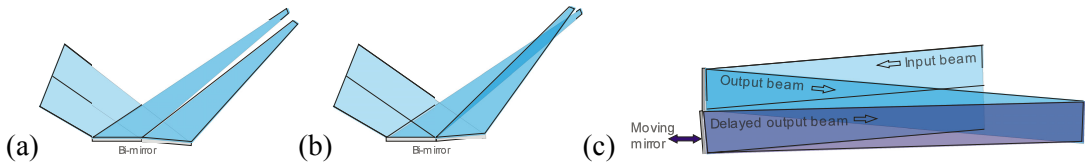

Figure 10.22 Scheme for wavefront division to (a) split beams, (b) to overlap and interfere, and (c) with delay for interferometry.

At normal incidence, a translation and a small rotation can merge to two parts of the beam with a variable delay. More grazing angles are required to use this technique at higher energies. A scanning interferometer for the range visible to 20 eV based on wavefront division by a pair of 90° roof mirrors has been built and successfully used on a storage ring undulator beamline [22].

In summary, beam splitting has been demonstrated to be feasible over the photon energy range of 4GLS. Amplitude division can be used from the THz to the near UV; multilayers can extend this for specific energies up to 90 eV; wavefront division can be used for shorter wavelength applications. The exact solution employed will be very dependent on the experiment so it is envisaged that such systems are located at the end of the beam transport system.

10.6.5 VUV-FEL Beamlines

Similarly to the XUV-FEL, the VUV-FEL source can be exploited by the scientific community as either a very brilliant source that allows very high resolving powers to be achieved with high flux at the experiment, a high intensity source without monochromator for the highest possible flux density at the experiment, or as a short pulse source for time dependent measurements.

The first use will clearly require a monochromator, whilst the second by definition does not. Whether the third use requires a pulse length preserving monochromator in the manner of the

XUV-FEL will depend on the experimental requirement for spectral purity outside the bandwidth imposed by the transform limit.

The VUV-FEL will produce a significantly higher contrast ratio than the XUV-FEL since there is effectively no part of the electron bunch that is not seeded. The full bunch will therefore radiate coherently, as demonstrated by the GENESIS simulation of the pulse profile at 10 eV shown in Figure 10.23, and the background of spontaneous and SASE light will be much reduced. Therefore, it is likely that the short pulse beamline will not require any sort of monochromator and the beamline will consist of just relay and focussing mirrors, similar to the direct light beamline, but with a final image optimised for combining with other photon beams.

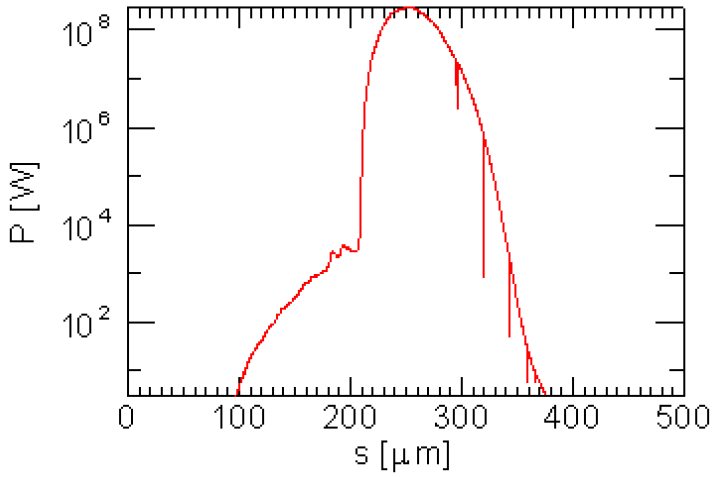

Figure 10.23 VUV-FEL pulse profile at 10 eV photon energy from GENESIS simulation; s is the longitudinal length of the pulse. Note the logarithmic scale for the pulse power covering eight orders of magnitude. The FWHM of the pulse is ~ 40 μm (130 fs).

The main difference between designing a direct light beamline on the VUV-FEL and one on the XUV-FEL is that the photon beam divergence will be larger and so the ultimate demagnification will be lower if aberrations are to be controlled and a good working distance maintained. For the same reason, the first mirror will need to be closer to the source, but this will not create a risk of ablation (see §10.2), though thermally induced slope errors from the high average power may degrade the image quality.

The polarising effect of the mirrors can also be much more significant in the VUV-FEL operating range. Whilst near-normal incidence can still give good reflectivity in this range and of course negligible polarising effect, the use of normal incidence mirrors is not always convenient in terms of laying out the beamlines. Also, the high output power of the FEL in a limited spectral range means that any normal incidence mirror will absorb a considerable amount of power unless the reflectivity is very high, and intensive cooling for such a mirror will be essential. Some grazing incidence reflections may therefore be desirable or inevitable, and these could have a strong polarising effect. Figure 10.24 shows the calculated reflectivity of

silicon as the angle of incidence changes from very grazing to near normal and shows that while the reflectivity is good even at normal incidence, there is a strong polarising effect at grazing angles. For comparison, the figure also shows the normal incidence reflectivity of MgF_2 coated aluminium. The coating is necessary to prevent oxidation of the aluminium surface, which would significantly reduce the reflectivity in this range. However, the stability of the MgF_2 coating under high incident fluxes is not well understood. Silicon will also suffer from surface oxidation and this will also affect the reflectivity. Accurate simulation of this is difficult without knowledge of the form of the oxide layer.

Ultimately, the detailed design of a direct light beamline (in terms of beam spot size, floor layout etc) will be determined by the specific experimental specification.

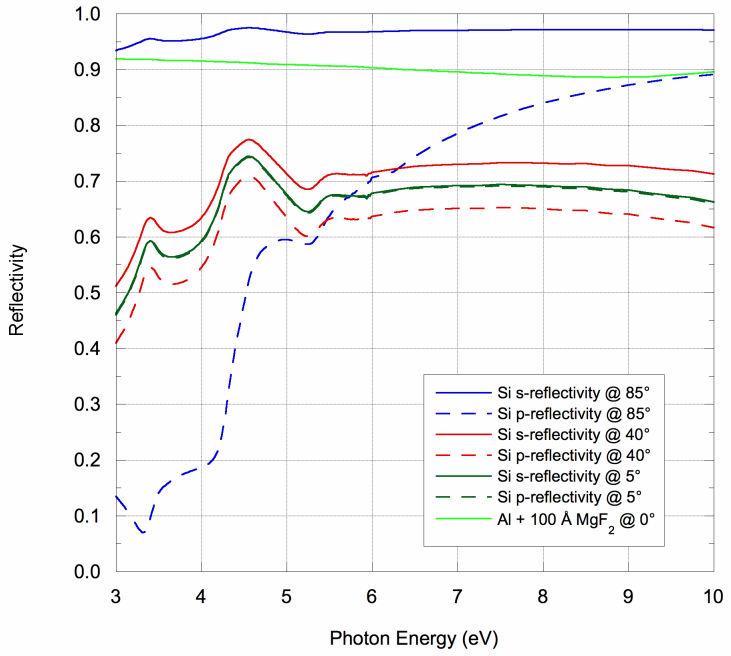

Figure 10.24 Calculated reflectivity of silicon at incidence angles of 85° (very grazing), 40°, and 5° (near normal). The calculation is for pure silicon; the presence of an oxide layer on the surface will reduce the normal incidence reflectivity at 10 eV significantly, but also reduce the polarising effect at more grazing angles. The calculated normal incidence reflectivity of MgF_2 coated aluminium is shown for comparison.

For high resolving power in the energy range 3 to 10 eV, most monochromators on SR sources are (near) normal incidence designs, usually variations on the Rowland circle principle. Normal incidence gratings are useable at these energies as the reflectivities are still reasonable. The historical reason for the use of normal incidence is the need to collect a large vertical fan of light with a finite grating length from a dipole source, which has a high divergence at these wavelengths. However, the use of normal incidence monochromator designs has continued even with undulator sources. This is in part because the divergence from an undulator will still be quite high at these wavelengths, unless the undulator is very long, as it is limited by diffraction. A consequence of using normal incidence is that the grating must have a very high

line density to get high resolving power (the cos α factor in equation (10-24) tends to unity). This tends to make the gratings inefficient.

A practical consequence of the use of a normal incidence monochromator is that an entrance slit is employed. This is because the monochromatic focus and hence exit slit will lie at or near the Rowland circle and will therefore be vertically above or side by side with the source. This is scarcely practical on a synchrotron (or FEL) and so a secondary source must be made by focussing the light at an entrance slit. The slit also performs the useful function of defining the source as seen by the grating and so allows the source size limiting resolution to be changed and decouples the energy calibration from movements in the real source.

It is not, however, essential that there is a physical slit; the focus acts as a source for the grating whether the slit is there or not. Without the slit, the quality of the focus will impact on the achievable resolution and so high demagnification to the virtual slit may not be advisable. The advantages of adjustable source size limiting resolution and energy calibration stability are also lost. Also, diffraction at the slit always ensures that enough grooves on the grating are illuminated (assuming the grating is long enough) to make the diffraction limited resolution match the resolution defined by the slit size. Without a slit, the grating line density and its distance from the focus will have to be chosen so that the natural divergence from the focus illuminates the required number of grooves.

For the VUV-FEL on 4GLS, the likely energy and power density at an entrance slit is a concern. With a pulse energy of ~ 55 μJ and continuous power of ~ 240 W at 10 eV, a beam focussed onto a slit even with high fractional transmission will give a significant risk of both ablation and thermal damage. For example, with a 3:1 demagnification in one plane only and the slit at 27 m from the source, the peak energy density at the slit will be ~ 10 mJ/cm^2 and the spatial-peak time-averaged power density will be ~ 40 kW/cm^2, which will put conventional slits under some strain. Certainly, any slit would have to be made in such a way as to spread the power or reflect as much of light that does not pass through the aperture as possible.

Detailed study will be needed to see if an entrance slit can be designed that can be safely used. If this is possible, a likely choice of monochromator will be the off-plane Eagle. This derivative of the Roland circle monochromator, in which the entrance and exit slits are adjacent but on opposite sides of the plane of the Roland circle, is a popular choice for high resolving power at many SR sources due to its low aberrations [23].

As explained above, it is technically possible to use this type of monochromator without a physical entrance slit. However, achieving the ultimate resolution with an off-plane Eagle requires the entrance slit to be rotated slightly with respect to the direction of the grooves. With no physical slit, this is not possible. Inclination of the Roland circle plane would achieve the same result, but would be difficult to fine tune in practice. It may therefore be better to use an in-plane design if the entrance slit is to be omitted. In any case, without a physical entrance slit, the ultimate resolution will depend on the achievable demagnification of the source at the

entrance plane of the monochromator and the overall size of the monochromator. To compensate for any limit to the demagnification, the monochromator will have to be made very large if very high resolving power is to be achieved.

An overriding concern for a normal incidence monochromator is the power absorbed at the grating. As already noted (§10.2) the VUV-FEL has a very high continuous power output of ~ 300 W. The FEL also has a narrow spectral output and so earlier mirrors at more grazing angles to give high reflectivity will do little to reduce the power incident on the grating, which will absorb a large amount due to the inefficiency of the inevitable high line density and normal incidence mounting. This grating will certainly need to be internally cooled to cope with the power and the effect of thermally induced slope errors on the resolution will have to be carefully modelled.

An alternative approach is to use a near-normal incidence plane mirror reflecting back onto a near-normal incidence grating. The mirror, which is more easily cooled as it will not need to rotate, will reduce the power at the grating somewhat, but probably not enough to remove the need for internal cooling. However, the main advantage of this approach is that the diffracted beam is now travelling in the same direction as the incident beam. This may be advantageous in terms of floor layout.

This approach has been used in a modification to the collimated light SX700 monochromator already discussed allowing it to work down to 5 eV [24, 25]. The gratings can be rotated to a very large grazing angle and an additional fixed premirror is used to illuminate them at near normal incidence. Resolution is limited by the number of illuminated grooves on the grating, which is determined by the radiation divergence and the distance of the collimating mirror from the source, and so high line densities (2400 l/mm and 3000 l/mm respectively) are necessary to achieve the design resolving power of 10,000.

Using an SX700 type monochromator in the usual grazing incidence mode can reduce the power absorbed by the grating as the efficiency will be higher because the reflectivity is greater and because a lower line density can be used for the same source size limited resolving power. However, the smallest grazing angle that can be used in practice is limited by the large beam divergence, the minimum distance of the grating from the source of about 25 m due to the presence of the cavity mirror, and the practical limit to the grating length of about 200 mm. In addition, the sagittal footprint on the focusing mirror will become very large with such divergent radiation and so the resolving power will be limited by aberrations.

In general, grazing angle monochromators are difficult to engineer for use at such low photon energies with high resolving powers due to the beam divergence leading to large beam footprints and hence high aberrations. The performance that can be achieved in such a design will be investigated in the TDR phase when additional detailed information is available on the properties of the FEL source.

10.6.6 IR-FEL Beamlines

10.6.6.1 Source Properties

The IR-FEL will utilise two undulators to produce output over a wide spectral range reaching into the THz part of the spectrum. The source is expected to have the following properties:

Table 10.12 IR-FEL undulator output properties

Wavelength range	Undulator A	2.5 to 25 μm (500 to 50 meV)
	Undulator B	25 to 200 μm (50 to 6 meV)
Pulse duration	Undulator A	~ 1.6 ps at 2.5 μm, ~ 600 fs at 25 μm
	Undulator B	~ 1 ps at 25 μm, ~ 600 fs at 200 μm
Energy per pulse	Undulator A	~ 40 μJ at 2.5 μm, ~ 30 μJ at 25 μm
	Undulator B	~ 110 μJ at 25 μm, ~ 6 μJ at 200 μm
Repetition rate		13 MHz
Photon energy spread		~ Transform limited

The source size will depend on the type of outcoupling from the FEL, whether pinhole, semi-transparent mirror or scraper mirror, and in a diffraction limited source this will also determine the radiation divergence.

10.6.6.2 Radiation Transport

In this wavelength range, high reflectivity is obtained using metal mirrors and the radiation can be transported over long distances with several reflections to experiments without appreciable reflection loss. Such beamlines have already been built on, for example, the IR DEMO FEL at Jefferson Laboratory, and at the IR-FEL FELIX at the FOM Institute. At FELIX, radiation is piped along a 30 m path from the laser to the farthest end-station, with only a factor of two loss in intensity [26]. We have designed a beamline for 4 μm radiation from an IR-FEL on the Energy Recovery Linac Prototype (ERLP) at Daresbury Laboratory, and this is currently under construction.

The radiation can be transferred to the end stations either by collimating the radiation or by using a series of intermediate foci. The former is preferred, as the focussing of the radiation at the end station onto a spectrometer entrance slit or directly onto a sample is independent of the distance of the end station from the source. However, at longer wavelengths, the Rayleigh range will be too short to allow collimation over appreciable distances. Which transportation scheme

is actually used will be dependent on the divergence of the radiation, and any restrictions on where mirrors can be placed.

On the ERLP, the out-coupling from the FEL is by a pinhole which effectively then becomes the source for the radiation transport system. The divergence due to diffraction at the pinhole leads to a spot of diameter 14 mm at the collimating mirror 4 m downstream. For a diffraction limited source, this will lead to a divergence in the "collimated" beam of the order of 140 µrad RMS, which is not a problem over the 10 m from the mirror to the diagnostic optical bench. Standard size optics (50 mm) can be used; on ERLP these will be made of copper.

On 4GLS, the radiation from the IR-FEL may need to be transported about 100m to different experimental stations. This will require detailed modelling to determine the focussing or collimation required in the beamlines. Such modelling has been carried out for the ERLP beamline, using the wavefront propagation code Synchrotron Radiation Workshop (SRW) [27]. Figure 10.25 shows the computed vertical profile at the collimating mirror and 10 m further downstream, illustrating the good degree of collimation obtained.

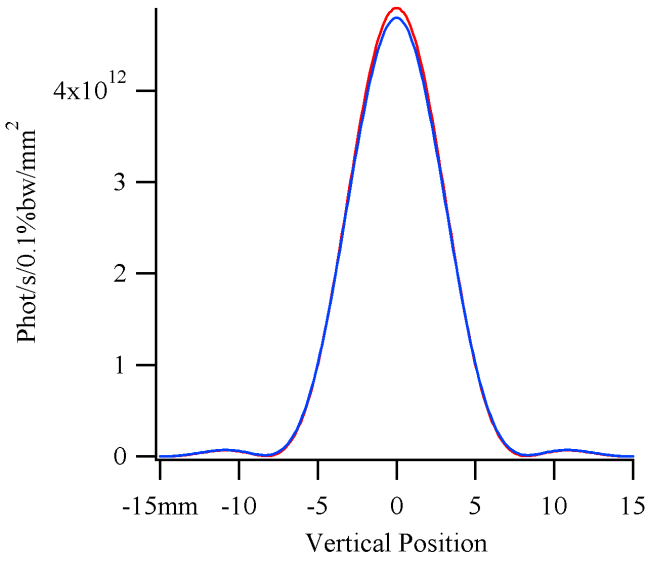

Figure 10.25 Vertical cut through the centre of the beam at λ = 4.2 µm from the IR-FEL on ERLP. Blue - at the collimating mirror, red – 10 m down stream from the collimating mirror.

The beampipe needs to be at rough vacuum, in particular to avoid water absorption, which is strong at wavelengths below 20 µm. A potassium bromide (KBr) window will separate the beamline from the machine vacuum.

10.7 Beamlines for Spontaneous Sources

10.7.1 Undulator Beamlines

10.7.1.1 Source Modelling

The photon source size and divergence are taken to be the convolution of the electron beam size and divergence and the natural (diffraction limited) radiation size and divergence from the undulator. The exact electron beam size and divergence along the high average current arc will be the subject of later technical design, but §9.2.1 gives likely parameters as $\sigma_{x,y}$ = 58 μm and $\sigma_{x',y'}$ = 29 μrad. The natural radiation size and divergence for an undulator of length L at a radiation wavelength λ are given by:

$$\sigma_r = \frac{\sqrt{2\lambda L}}{2\pi}$$
$$\sigma_{r'} = \sqrt{\frac{\lambda}{2L}} \qquad (10\text{-}22)$$

These formulae, derived by Walker [28], are the Gaussian approximations to the radiation size and divergence for "zero detuning" (i.e. at the harmonic energy). It should be noted that whilst the divergence is reasonably Gaussian, the physical source is not particularly well fitted by a Gaussian. In addition, the radiation source size predicted here is larger than that given by other approximations [29, 30]. However, modelling undulators with a simple ideal imaging system in the code SRW has shown that the formulae are in good practical agreement with the propagated and focussed undulator output, and are therefore used here.

It should be noted however, that undulators are often operated detuned from the harmonic at a tuning that gives peak integrated flux into an aperture. The spatial and angular properties of an undulator source when operated detuned are highly complicated and not amenable to simple analytical modelling.

As described above, for zero detuning, the RMS photon source size and divergence are given by:

$$\Sigma_{x,y} = \sqrt{\sigma_r^2 + \sigma_{x,y}^2}$$
$$\Sigma_{x',y'} = \sqrt{\sigma_{r'}^2 + \sigma_{x',y'}^2} \qquad (10\text{-}23)$$

Figure 10.26 shows the predicted total FWHM source size and divergence as function of photon energy from 30 to 500 eV for an undulator that is 8 m long. For comparison, each plot shows the contributions from the electron beam emittance and the undulator.

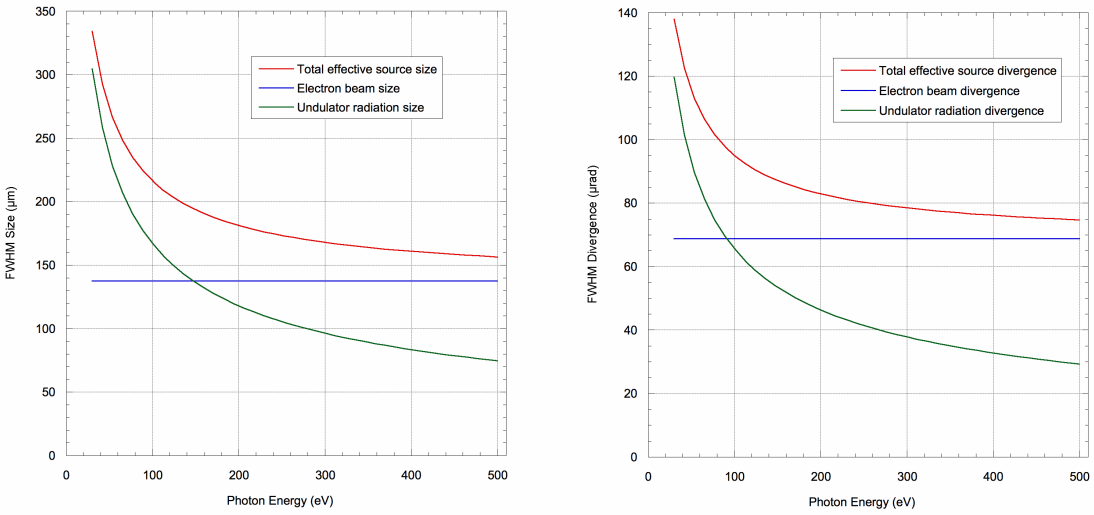

Figure 10.26 FWHM source size and divergence in both planes from an 8 m long undulator as a function of photon energy

10.7.1.2 Monochromator Resolution

An important consequence of (10-22) is that the product of the source size and divergence is not given by (10-19), even when the electron beam adds negligibly to the overall size and divergence. This is a consequence of the undulator source not being Gaussian. When the effect of the beam emittance is added, the undulator source deviates further from the diffraction limited ideal represented by (10-19).

Therefore, for a monochromator operating without entrance slit, the source size limiting resolving power will always be worse than the diffraction limiting resolving power determined by the number of illuminated grooves, at least when the grating is not significantly overfilled. The source size resolution for a source of FWHM size S at a distance r from the grating at angle of incidence α is given by:

$$\Delta E_{source} = \frac{S}{r}\frac{1}{Nmhc}E^2\cos\alpha \qquad (10\text{-}24)$$

As the angle of incidence at the grating is increased to improve the source size resolution, a finite grating will become increasingly overfilled. At some point, the diffraction limiting resolution will become equal to, and ultimately worse than, the source size resolution. The point at which this occurs will depend on the contribution of the electron beam emittance to the overall source size, and will therefore be a function of photon energy. At higher energies, the beam emittance will dominate the source size and the grating will have to become more overfilled before the monochromator resolution is limited by diffraction from the grating.

Whilst overfilling the grating is a possible way of improving the resolution, it necessarily involves a loss of throughput. The initial monochromator design should therefore strive to

achieve the required resolution without resorting to overfilling, whilst allowing this as an option to achieve better resolution if required.

Suppose we define a vertically dispersing grating of length L_G to be fully illuminated when it is filled at the qσ level. Then:

$$L_G = \frac{q\Sigma_{y'} r}{\cos\alpha} \tag{10-25}$$

And hence the source size limited resolving power is:

$$\Delta E_{source} = \frac{q}{Nmhc} \frac{S\,\Sigma_{y'}\,E^2}{L_G} \tag{10-26}$$

At a given energy, the source size and divergence are fixed and so the length of the grating and the line density (i.e. number of illuminated grooves) still determine the resolution of the monochromator, even though the resolution does not approach the diffraction limit. For the resolving power, the distance from the source and the angle of incidence are important only in that they determine the operating point of the monochromator required to just fill the grating. This means that a given grating (line density and length) can achieve the same ultimate resolving power whatever the distance to the source. The actual distance is chosen in view of the diffraction efficiency, optical aberrations, the effect of slope errors and general layout restrictions.

10.7.1.3 Collimated Light SX700 Monochromator for High Resolving Power in the XUV

To illustrate these points, a collimated light SX700 monochromator similar to that proposed for the XUV-FEL is considered. The grating length will be taken as 180 mm, and this will be considered fully filled at 3σ illumination. The less than complete transverse coherence of the undulator source should mean that diffraction effects caused by aperturing at this level are not problematical. This also allows for increasing the incidence angle to improve the resolution without reducing the flux excessively. The operating range will be 30 to 500 eV. This is slightly larger than the operating range of a 10 m long U30 undulator (see §9.2.1), but the beamline is conceptual and not intended to match to a particular source or scientific need.

Table 10.13 shows the monochromator c-values required to fill the grating at 500 eV with various distances of the collimating mirror from the source and grating line densities. At a given line density, the tabulated combination of the c-value and collimating mirror distance result in the same source size resolution. But, as the line density is increased for a given collimating mirror distance, the source size resolution improves as shown in Figure 10.27.

Table 10.13 Monochromator c-value required to fill grating at 500 eV for various line densities and collimating mirror distances

Collimating mirror distance (m)	Grating line density		
	1200 l/mm	1800 l/mm	2400 l/mm
20	7.50	9.10	10.50
40	3.83	4.65	5.31
60	2.66	3.20	3.62

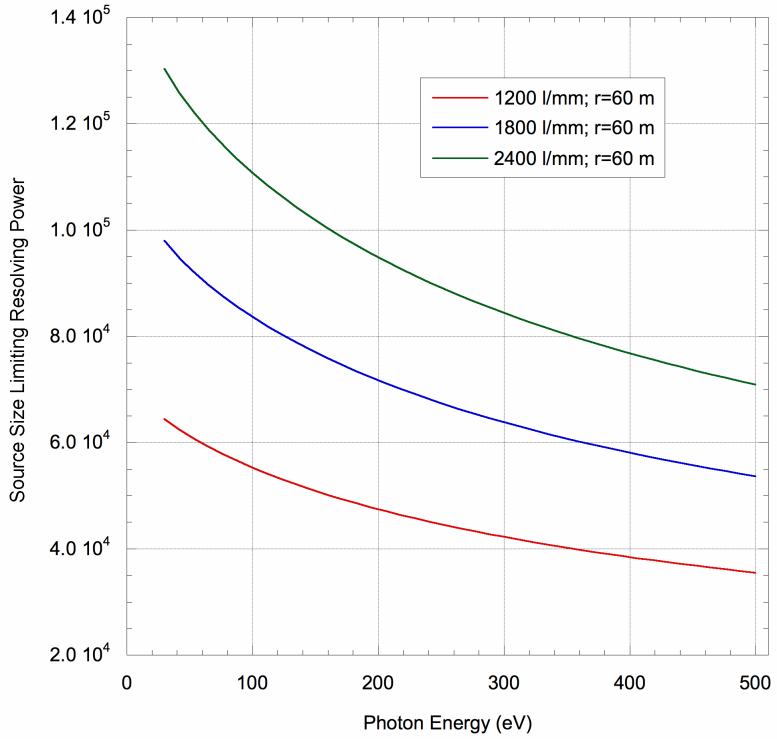

Figure 10.27 Source size resolving power for 'just filled' gratings of 1200, 1800 and 2400 l/mm. Collimating mirror is 60 m from the source. Required c-values are given in Table 10.13.

Although the source size resolving power is same at each combination of collimating mirror distance and c-value for a given line density, this does not mean the beamline resolving power will be the same. The higher c-values tend to reduce the effect of the slope errors on the resolution. Figure 10.28 shows the estimated resolving power with contributions from slope errors added to the source size resolving power. A contribution from the exit slit has not been added, though a 10 µm slit would degrade the resolution only slightly, and the calculation assumes zero aberrations. The RMS slope errors assumed were the same as given for the equivalent mirrors in Table 10.8.

Figure 10.28 is useful in that it shows what limiting parameters are required to achieve a certain resolving power at a given energy. For example, to achieve a resolving power of 40000 at 400 eV (nitrogen *K*-edge), a 1200 l/mm grating will not be sufficient. An 1800 l/mm grating could

be used, but the c-value would have to be at least 4.65. With a 2400 l/mm grating, there is more flexibility in operating point, though slope errors make the resolving power at 60 m collimating mirror distance similar to the 1800 l/mm grating with 20 m collimating mirror distance.

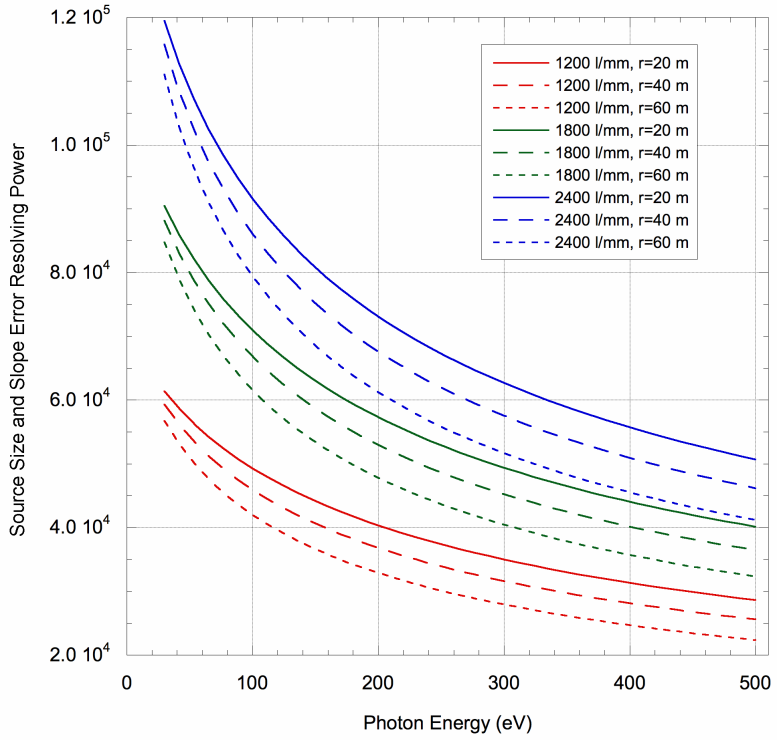

Figure 10.28 Resolving power with the effect of slope errors added to the source size resolving power. There is no contribution from the exit slit and from aberrations. A 10 μm exit slit will not affect the resolving power significantly. Focussing mirror aberrations will affect the resolving power at lower energies unless the mirror is masked.

Another contribution to the resolution is aberrations from the focusing mirror. This is sagittally focusing at the exit slit and aberrations increase rapidly as the sagittal footprint, determined by the beam height after the grating, increases. The beam height after the grating is the monochromator c-value times the height after the collimating mirror. But the height after the collimating mirror increases linearly with distance of the mirror from the source. The overall effect is that footprint *increases* with the higher line density cases. Table 10.14 shows the 4σ sagittal footprint in cm at 30 eV. The footprint rapidly falls with energy since the source divergence decreases, so the extra aberrations with the higher line density gratings will only be a significant factor at lower energies.

Table 10.14 4σ sagittal footprints at 30 eV in cm on the focussing mirror for the grating, collimating mirror distances and c-values given in Table 10.13

Collimating mirror distance (m)	Mirror footprint (cm) for grating line density		
	1200 l/mm	1800 l/mm	2400 l/mm
20	3.24	3.93	4.54
40	3.31	4.02	4.59
60	3.45	4.15	4.69

Once the possible options to achieve the required resolving power are known, the choice between them will come down to a balance of beamline efficiency and floor layout, which influences the non-dispersive imaging of the beamline.

Beamline efficiency falls with higher c-value. Also, grating efficiency drops significantly as the line density increases. The maximum efficiency at 500 eV of a gold-coated 1200 l/mm lamellar grating in first-inside order of diffraction is 12 %. This falls to 8 % for a 1800 l/mm grating and 5 % for a 2400 l/mm grating [31]. High line density gratings will generally need to be blazed to get reasonable efficiency, but this will impact on the higher order content in the beamline output. Higher c-values also make the higher order content worse. Complete calculation of the efficiency is therefore necessary to decide which option will have the best throughput and higher order suppression. This will form part of the TDR phase.

As with the high resolving XUV-FEL beamline described in §10.6.1, the non-dispersive imaging properties here are compromised by the need to use sagittal collimation and focussing to the exit slit. This reduces the effect of mirror slope errors on the resolution, but conversely increases the effect on the non-dispersive image. In addition, the closer the collimating mirror is to the source, the larger the horizontal magnification, assuming the focussing mirror to exit slit distance is kept large in order to control aberrations. This will exacerbate the asymmetry between horizontal and vertical image sizes at the exit slit. The use of intermediate foci in the non-dispersive plane may alleviate these problems, but there will inevitably be some residual asymmetry. Therefore, the ability to achieve a given beam spot size at the experiment will be different between the options, and the choice between them will depend on the needs of the proposed experiment. This will be considered in the TDR phase

10.7.2 THz Beamlines

Two different beamline locations are planned which will exploit the very intense coherent radiation at sub-millimetre wavelengths (see §9.4.2), one on the high average current loop for high average flux and one of the XUV FEL branch for high peak fluxes and high field studies. Beamlines for THz radiation have already been designed at Jefferson Laboratory [32] and on the ERLP at Daresbury [33].

10.7.2.1 Source Characteristics

The onset of the coherent radiation depends on the length of the electron bunch. Sample graphs of the flux output for both sources have been given in §9.2.2 for a bunch of RMS length of 100 fs for the high average current loop and for 266 fs for the XUV-FEL branch.

The maximum flux and power per pulse for the coherent radiation are given in Table 10.15.

Table 10.15 Properties of CSR for sources in the XUV-FEL branch and the high average current loop

	High average current loop	XUV-FEL branch
Maximum Average flux	2.10^{21} phot/s/ 0.1 % BW at 3 meV	
Maximum Average brightness	~ 10^{17} phot/s/0.1 % BW/mrad^2/mm^2 at 7 meV	
Maximum Flux per pulse		2.10^{14} phot/ 0.1 % BW at 1 meV
Energy per pulse		90 μJ mainly from 0.4 to 4 meV
Repetition rate		1 kHz

10.7.2.2 Radiation Transport.

The challenge of transporting THz radiation arises from the large natural divergence of the radiation, as shown in Figure 10.29, and diffraction from the extraction aperture and from the edges of any optics that are overfilled. In order to maximise the flux, a large aperture of 50 mrad by 50 mrad will be accepted by the beamline. All the preceding points mean that the radiation cannot be easily collimated and instead will be transported using intermediate foci. This is the solution adopted at Jefferson Laboratory and on ERLP at Daresbury Laboratory.

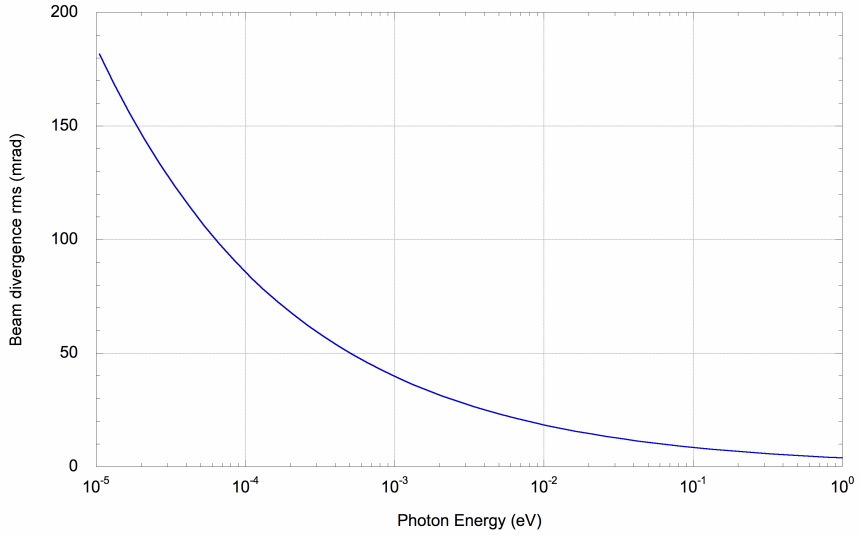

Figure 10.29 The RMS radiation divergence of the THz beam

As an example, the layout of the THz beamline on ERLP is given in Figure 10.30. The total path length from the source to the diagnostic room is about 17 m. The radiation is focussed twice, using a toroidal mirror M1 just after the 37 mm diameter extraction aperture in the dipole vessel and by M3 at the entrance to the labyrinth in the shielding. The reflectivity of aluminium at 0.584 THz (2.4 meV) has been measured to be > 99 % [34], and so reflectivity losses for the system will be small.

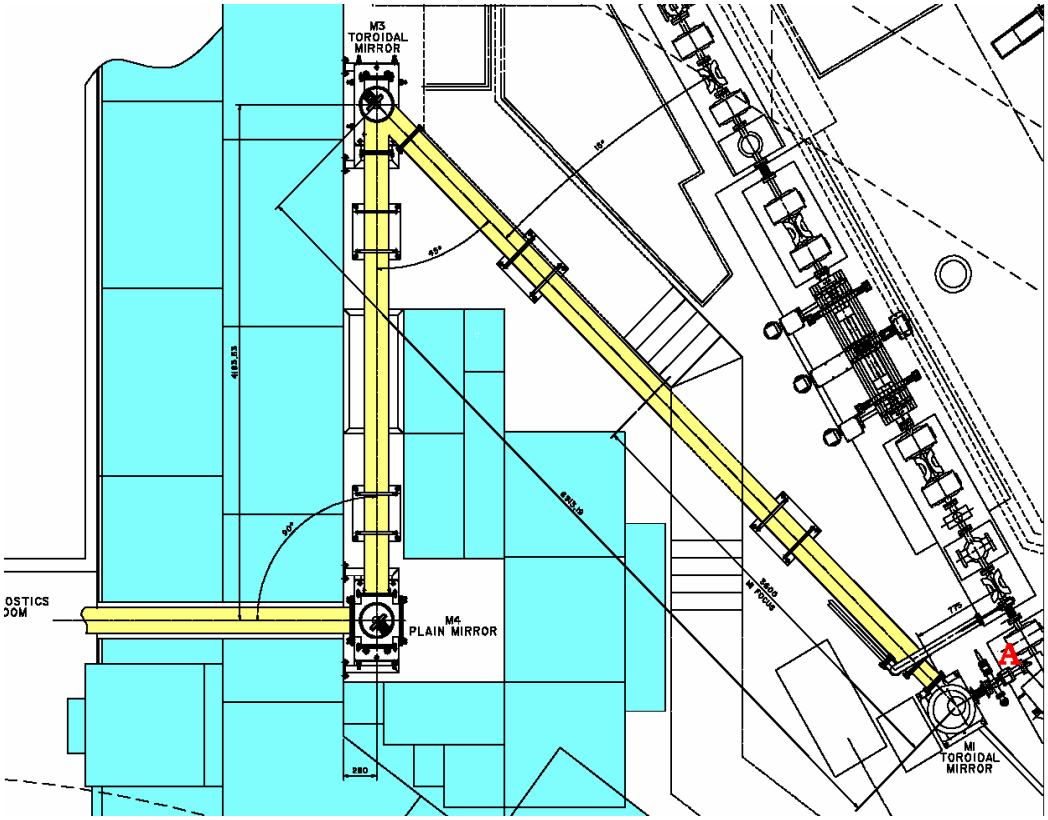

Figure 10.30 Section of the engineering layout for ERLP, showing the THz beamline (yellow) from the extraction aperture in the dipole vessel at A through the shielding coloured blue into the diagnostic room (bottom left of picture).

Diffraction by the extraction aperture is important, as can be seen from the computed beam profiles of the radiation at M1 obtained using the SRW code (Figure 10.31). As the wavelength increases, the angular spread of the radiation due to diffraction becomes comparable to the angular acceptance from the source, and there is then no single effective source point to image. This leads to different beam sizes for different energies as illustrated in Figure 10.32, which shows the beam cross-section in the diagnostic room for two different wavelengths.

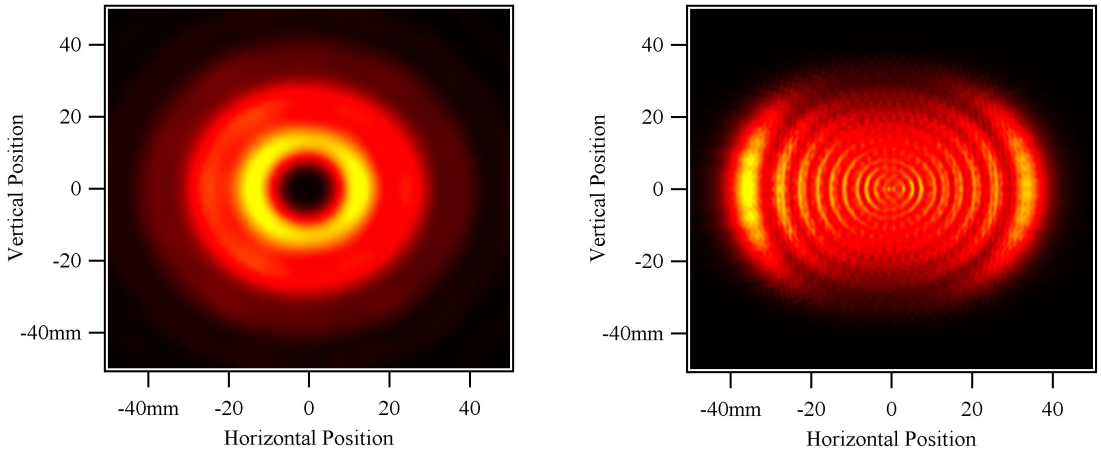

Figure 10.31 Calculated intensity of the THz beam on ERLP at the position of the first toroidal mirror M1, at a photon energy of 2 meV (LHS) and 20 meV (RHS)

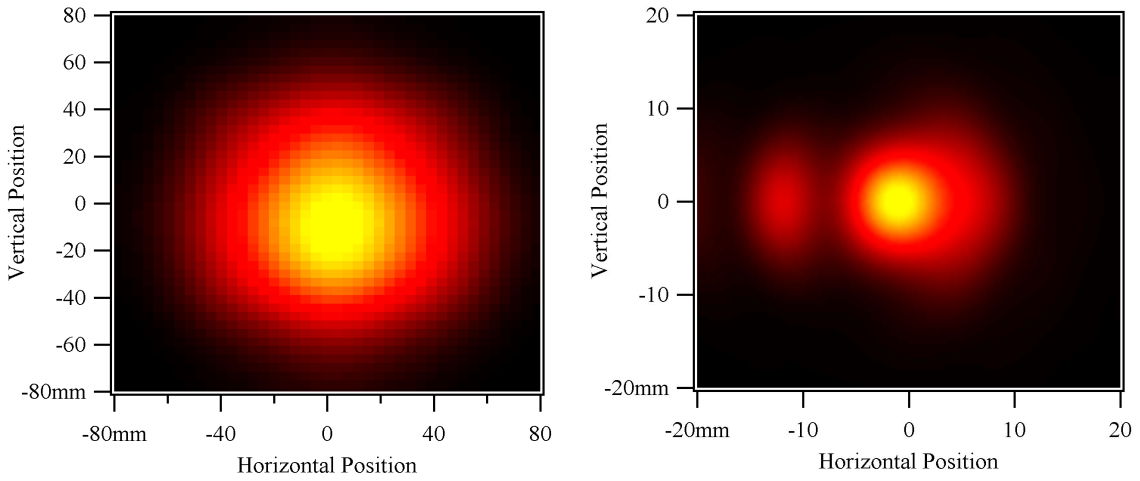

Figure 10.32 Calculated intensity of the THz beam on ERLP in the diagnostic room at a photon energy of 2 meV (LHS) and 20 meV (RHS). Note that the scale is a factor four larger for the 20 meV case.

On 4GLS, the transport length could be as high as 100 m if the THz is to be combined with, for example, experiments on XUV undulator beamlines. This will require more intermediate foci, and hence more mirrors. Optimisation of the number of intermediate foci and the size and shape of mirrors will be achieved by modelling with wavefront propagation codes to ensure the effects of diffraction are included.

The losses in a long relay system for the longest wavelengths will be mainly due to the aperturing at each mirror rather than reflectivity losses. From the modelling for ERLP described above, the total beam widths are of the order of 100 mm for the longer wavelengths. Whilst the THz source is not Gaussian, an estimate of the losses can be made by assuming Gaussian propagation with an equivalent Gaussian beam with waist w_0 of ~ 34 mm, (17 mm RMS of the

intensity profile). At 0.1 THz (3 mm wavelength), the Rayleigh range is only ~ 1.2 m, and the far-field divergence is ~ 4 mrad RMS. The RMS beam size at 5 m from the beam waist will be ~ 72 mm. A mirror of size 200 x 300 mm^2 at 45° incidence angle will thus accept ~ 2.8σ of the beam intensity, equivalent to about 17 % loss at each mirror. A relay of nine mirrors required to transport 100 m would have a total loss of 81 % even with perfect reflectivity.

However, this is very much a worst case situation. As the wavelength decreases, the divergence falls rapidly and so the loss at each mirror decreases. For this relay system, the Rayleigh range would be equal to the distance between a focus and following mirror at a wavelength of ~ 0.7 mm (~ 0.4 THz), and for this and shorter wavelengths the light is essentially collimated between mirrors and the aperture losses will be negligible. If high transportation efficiency is essential for wavelengths as long as 3 mm, larger mirrors are quite feasible but would result in considerable over-specification at shorter wavelengths.

Another challenge with transportation of THz radiation is that diffraction from the edges of optics and any restricting apertures in the beam path lead to a high level of scattered light, especially at longer wavelengths where the diffraction is stronger. This can be prevented by using beam pipes that are transparent to the THz, or by lining pipes with a metal foam absorber, as is done at the THz diagnostic lines at BESSY [35].

As water has many absorption lines in the THz spectral range, the beam pipes will either be at rough vacuum or purged with dry nitrogen, and separated from the machine vacuum by a suitable window. Ideally, a diamond window would be used as this transmits both in the THz and visible regions of the spectrum and therefore makes alignment easier. A cheaper alternative would be a silicon window, but this does not have such a wide range of transmission, being opaque between about 7 and 40 μm.

10.7.3 IR Bending Magnet Beamlines

Infra-red radiation will be available from the bending magnets with an expected flux of about 10^{13} phot/sec/100 mA/0.1 % BW (see Chapter 9) on the high average current loop. Major problems designing an appropriate beamline are not expected as the divergence will be less than for THz and there are many IR beamlines on storage rings.

10.8 Overview of Photon Beam Diagnostics

Successful experiments using 4GLS will require a range of diagnostics covering the spectral range from terahertz to soft x-ray. As the intensity, ultra-short pulse lengths and the ability to combine sources are key features of 4GLS, this places a high importance on measuring very high intensities and temporal properties on the femtosecond scale. A full suite of more conventional diagnostics is also required to ensure reliable operation.

The function of the photon diagnostic instrumentation is three-fold:

- to commission and optimise the photon sources (including some electron beam parameters);
- to characterise and help control the photon beam properties for the experiment programme;
- to help develop these 4th generation sources.

Some will be used primarily for characterisation at intervals and can therefore be invasive; others, more challenging, are necessary to provide online, pulse-by-pulse information and must be non-invasive and not interfere significantly with the photon beam performance.

The parameters to be measured include:

Table 10.16 Photon beam parameters to be measured by the diagnostic systems

Parameter	*Requirement*
Intensity	Online, both average and per pulse (and to distinguish the pedestal and 'dark' counts)
Spectrum, bandwidth and harmonic content	Online, both average and per pulse
Beam size and position	Online, both average and per pulse
Pulse length, shape	Online for selected pulses
Pulse arrival time and jitter	Online, per pulse and in relation to selected other sources
Coherence	Average measurement
Polarisation	Average measurement

10.8.1 Key FEL Diagnostics

Of the parameters to be measured, some of the instrumentation is well established via 3rd generation storage ring and laboratory laser developments. The following sections highlight the principle challenges and solutions relating to 4GLS; well-established diagnostics are not covered in this conceptual design document.

10.8.1.1 Intensity/Position

The XUV-FEL power is capable of ablating most surfaces. In combination with the need to preserve the coherence, this renders conventional methods of measuring intensity unsuitable.

A system based on photoionisation of rare gases has been developed for the VUV-FEL at DESY [36]. This has the advantage of being > 99 % transparent with a wide dynamic range allowing measurement of both the spontaneous and FEL output. With the use of split electrodes and a temporal resolution of a few nanoseconds, the gas ionisation detector can measure beam position of individual XUV-FEL pulses.

Control of the FEL intensity can be delivered by absorption in a gas cell as proposed at both the DESY VUV-FEL and LCLS [37]. While preserving the beam properties, this can deliver many orders of magnitude attenuation. The layout needs to allow lengths of 10-20 m for such systems.

10.8.1.2 Spectral Distribution of Photon Pulses

The spectral distribution within the bandwidth of the FEL output is a critical diagnostic. A system is under development to measure the spectral distribution of single pulses by use of a special grating spectrometer (a collaboration with DESY, SAS and Daresbury Laboratory) [38]. The technique consists in replacing an upstream mirror with a varied line spacing (VLS) grating, reflecting most of the radiation in zero order while a small fraction (< 1 %) is dispersed onto a CCD array. This spectrometer accepts a bandwidth of 10%, readily covering the natural FEL linewidth, and allowing a resolving power of 10^4 at the CCD. By scanning the detector arm, the wavelength range of the FEL can be covered (Figure 10.33).

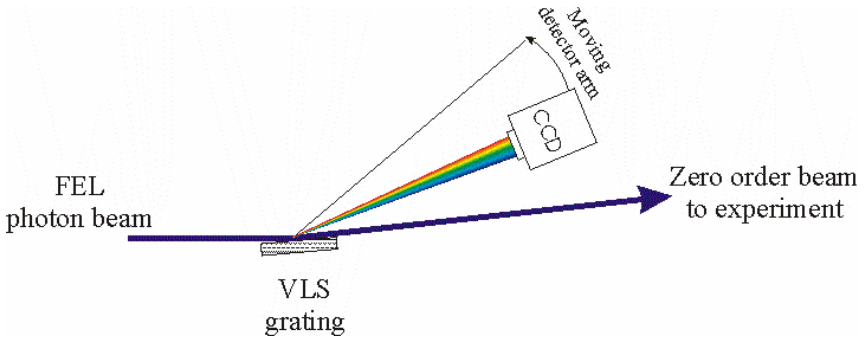

Figure 10.33 Schematic of a single shot spectrometer for measuring the spectral output from a FEL. Most of the light is reflected to the experiments; a small fraction is imaged by a VLS grating onto a CCD on a moveable detector arm.

The spectrometer relies on designing a diffraction grating surface with high zero order efficiency and a first order efficiency of ~ 1 %; calculations for this system performed by the 4GLS team are presented in Figure 10.34. The intensity of the FEL output provides sufficient photon flux for pulse by pulse data.

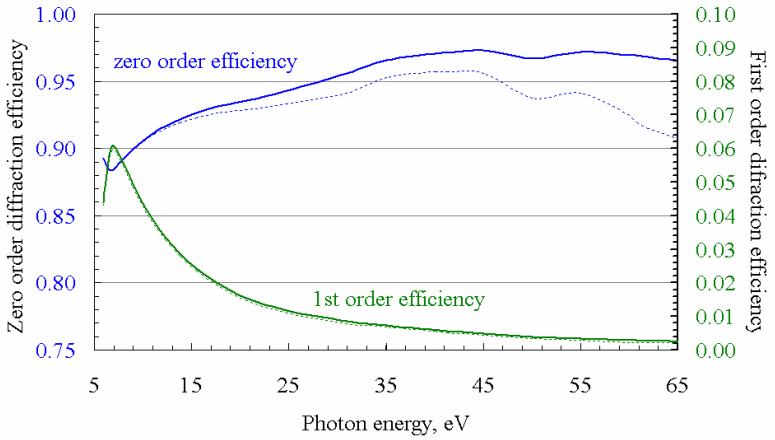

Figure 10.34 Zero and first order efficiencies for a 1200 l/mm, 1° blazed grating. Solid lines are for s-efficiencies, dashed for p-efficiencies.

A single shot spectrograph based on this concept will be designed for the XUV-FEL and VUV-FEL beamlines on 4GLS following commissioning tests on the VUV-FEL at DESY.

10.8.1.3 Pulse Length

4GLS photon sources will generate light pulses with durations from tens of femtoseconds to tens of picoseconds. The primary challenge for this facility is to extend the characterisation techniques familiar to IR and visible lasers up to the XUV-FEL regime.

For the far infra-red to near ultra-violet regions, pulse length characterisation techniques developed for laser systems are readily available [39, 40] and will not be discussed in this CDR. Such systems will be used for the lower photon energy 4GLS sources, the THz, IR-FEL and low energy bending magnet beamlines.

For the VUV region covered by the VUV-FEL, autocorrelation techniques using second harmonic generation (SHG) as the non-linear detector will be used up to the limit of availability of these SHG materials at 5 eV [41]. Above this, two-photon photo-ionisation of gases can be used as the non-linear detector. The range of this technique depends on the ionisation potential of the gas. For first ionisation potentials, this ranges from 12–24 eV for helium [42], to 4.5–9 eV for toluene [43]. Using an atomic beam is also an option: alkaline metals would extend this range down to 2–5 eV. Autocorrelation with two photon photoelectron (2PPE) detection will also cover the lower photon energy region of the XUV-FEL.

Autocorrelation involves splitting the photon pulse, adding a variable delay of the order of the time window of interest, and recombining the two pulses to detect the autocorrelation function (see Figure 10.35). Wavefront division techniques to split the incoming beam have been discussed in §10.6.4, and while non-trivial, several systems have been developed for the XUV region.

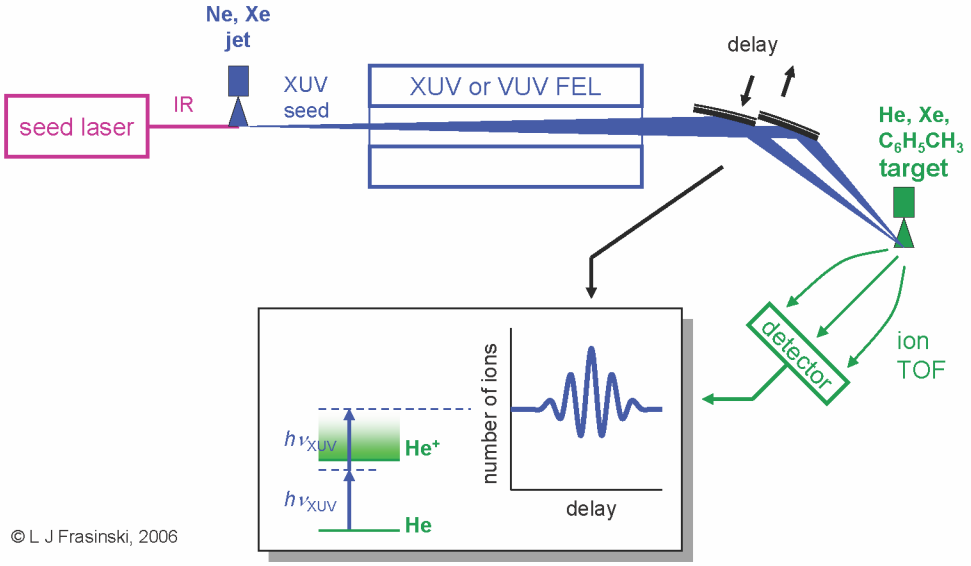

Figure 10.35 The principle of an XUV second-order autocorrelator. A split mirror with one half movable by a piezo translation stage acts as a beam splitter. Two-photon ionisation is monitored as a function of the piezo position. Although the total beam energy remains the same, the intensity distribution of in the focal spot varies sufficiently to induce nonlinearities in the ion signal, albeit with a reduced fringe contrast [44].

Using two photon single ionisation autocorrelators above 24 eV is likely to be impractical. Such an autocorrelator would have to discriminate against single-photon ionisation events, which give a strong background of unusable, first-order signal. The best theoretical candidate here is two-photon double ionisation of helium, which can cover the range 40-54 eV [45]. This scheme can be extended to heavier elements (Li, Be, B, etc.) and their higher ionisation stages. However, there would be some gaps not covered in the XUV-FEL photon energy range. An attempt to employ photoionisation of core electrons will encounter similar problems.

Above 24 eV, cross-correlation with an IR laser and detection by measurement of photoelectron side bands has been demonstrated successfully in the femtosecond to attosecond regime [46]. The experimental arrangement for cross-correlation is shown in Figure 10.37 using the IR component from the HHG seed laser system for optimum synchronisation with the XUV-FEL photon beam. This IR reference beam split from the seed laser has to be available at the diagnostics station to produce sidebands on the photoelectron energy spectrum. As the sidebands are spaced by the IR photon energy, a crude photoelectron energy resolution (~ 1 eV) is sufficient to separate the cross-correlation signal from the single-XUV-photon background. A magnetic bottle type spectrometer is preferable to ensure high collection efficiency. The IR intensity should be in the range 10^{10}–10^{12} W/cm^2 [47].

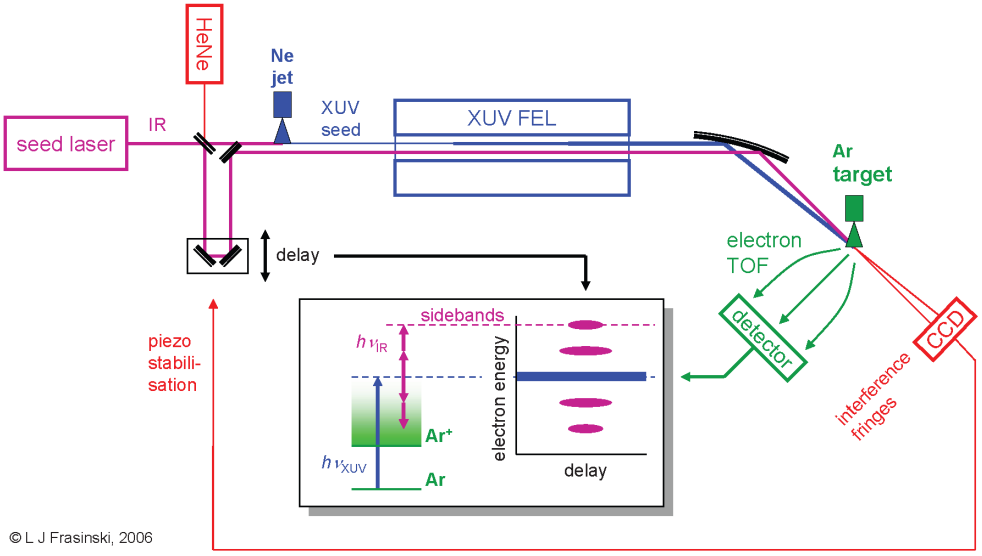

Figure 10.36. The principle of an XUV-IR cross-correlator based on sideband generation on photoelectron spectrum. To ensure good mechanical stability the IR and XUV beam should be guided in close proximity with rigid connections between their optical components. The optional HeNe laser can provide a substantial improvement by an active compensation of vibrations. The optical setup is simplified; more optical components are needed to overlap the IR and XUV pulses and to image the interference fringes on the CCD. An interferometric accuracy should be possible. For practical reasons the variable delay stage can be moved to the target side of the FEL.

Spectral techniques, such as FROG or SPIDER, have been recently extended to the XUV region of the spectrum to measure the temporal variation of the E-field in attosecond pulses [47]. One must be cautious, however, to propose them for characterisation of the XUV-FEL as the longer temporal range Δt of its pulses requires a finer energy resolution ΔE in the spectrometer. According to the uncertainty relation $\Delta t\, \Delta E \sim \hbar = 660$ fs meV, an electron spectrometer with a challengingly high resolution of 1 meV probes a temporal range of only about 660 fs, which may be insufficient to monitor FEL pulses.

Current XUV auto- and cross-correlators are multi-shot instruments as they require scanning the pulse delay. However, it is not difficult to envisage single-shot techniques, which require tilting the pulse wavefronts and employing spatial imaging of the photoelectrons. There is a fast technological development in this area, driven by the need to characterise attosecond pulses and FEL sources. The diagnostics outlined in this section should be regarded as a demonstration of feasibility rather than the choice of finalised techniques.

The proposed pulse length diagnostics techniques for the VUV and XUV sources on 4GLS are summarised in Figure 10.37.

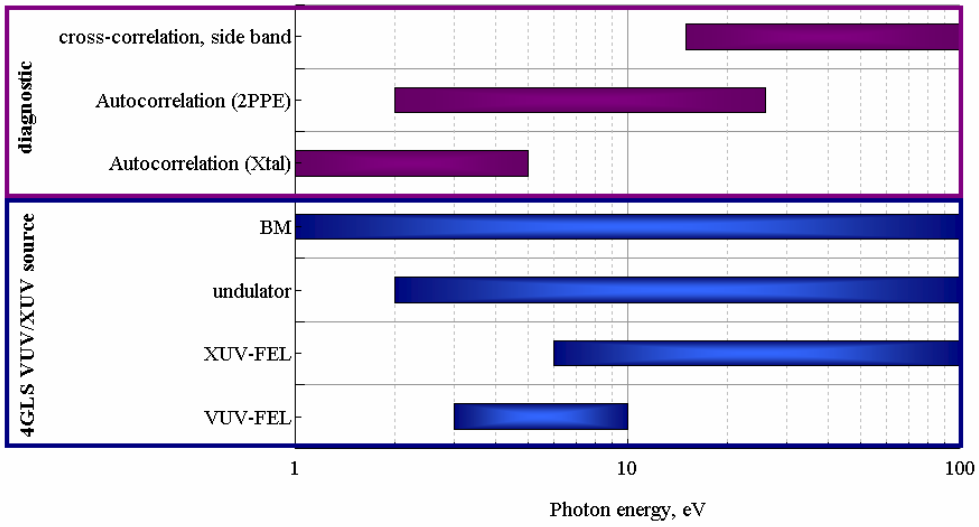

Figure 10.37 Pulse length diagnostics for VUV and XUV photon sources on 4GLS

For the bending magnet sources (including THz), electron beam diagnostics will provide useful information on the photon pulse length as these are directly related. For the XUV-FEL, the electron bunch length (626 fs FWHM) is much longer than the output photon pulse length (50 fs FWHM) due to the choice of HHG seed, and electron bunch length measurements will not provide useful information on the photon output pulse length. The VUV and IR-FEL pulse lengths are related to the electron bunch length in some modes and so electron beam diagnostics will be partially useful.

10.8.1.4 Arrival Time

Accurate measurement of the time delay between pump and probe beams is required for many time-resolved experiments. Additionally, set up of the electron and photon beam paths such that genuine t=0 data can be obtained will require an initial total path calibration and correction determined by pulse separation measurement. The accuracy of the latter is less than that required for experiments and only needs to bring the t=0 path length to within the adjustment of the experiment delay line range. Conventional streak cameras with temporal resolution of 0.2-1 ps will be adequate for much of the calibration range.

Observation of side bands in photoelectron spectra allow the extension of cross-correlation techniques to measurement of pump-probe delay and jitter down to the attosecond regime as described in the preceding section. Such a system, giving the fine detail of arrival time in the sub-200 fs region, will be considered as part of the end-station equipment for specific techniques.

For analysis of jitter in arrival time, measurement of the electron bunch timing will provide additional data and the beamlines will make use of the data from the electro-optical diagnostics system described in §7.9.8.

10.8.2 Summary of Diagnostic Instruments

4GLS will require a complete suite of more familiar diagnostics not covered above. These include Young's slits system for coherence measurement, polarisation analysers, conventional beam position monitors and imaging devices. The list of proposed instruments is shown in Table 10.17. Also included in the table are diagnostics prioritised for detailed design work in the TDR phase.

Table 10.17 List of proposed diagnostic instruments

Parameter	*Rrequirement*	*Further work TDR phase*
Intensity	Online gas ionisation detector Radiation hard calibrated photodiodes Bolometers Imaging thermopiles	
Spectrum, bandwidth and harmonic content	Online VLS spectrometer Beamline monochromator system FT interferometers	Design of VLS spectrometer for 4GLS
Beam size and position	Online gas ionisation detector Online photon beam position monitors (P-BPMs) Scanning wire systems	Design of scanning wire system
Pulse length, shape	Autocorrelator (conventional interferometers and special XUV two photon systems with ion and electron detection) Cross-correlator and PES side band detection Online CSR spectral monitors	Design of XUV/VUV autocorrelator and layout in beamline Design and layout of cross-correlator system
Pulse arrival time and jitter	Online electro-optical detection system Cross-correlators Streak camera	Selection of cross-correlation system
Coherence	Young's slit + CCD detector	
Polarisation	Multilayer and mirror polarimeters	

10.8.3 Photon Diagnostics Layout

A layout showing the position of specific photon beam diagnostics is not possible at this conceptual design stage for several reasons. Firstly, the layout of the beamlines, especially for the FEL lines, will require extensive consultation on the requirements of the experiment programme in order to derive a specification for the detailed design stage. Secondly, in comparison to a 3rd generation storage ring system, 4GLS beamlines must incorporate more complex control and diagnostics elements such as optical delays, beam splitters, beam combining optics and optical correlators. Thirdly, significant components of the diagnostics will be very dependant on the experiment to be performed and in some cases, reliant on the experiment itself for part of the measurement (for example, two photon detection for autocorrelation).

The following sections therefore only give schemas of the sequence of diagnostics for selected photon transport systems to develop the layout of the facility as a whole.

10.8.3.1 XUV-FEL

Figure 10.38 shows proposed position for instrumentation on the XUV-FEL beamline. As the intensity of the FEL output requires the first optical elements to be 20-30 m downstream to avoid ablation, this space is ideal for a gas ionisation intensity and position monitor and attenuator. Electron beam arrival time and bunch length will be derived from electro-optic measurements on the exiting electron beam, backed up by streak camera or imaging diagnostics on the bending magnet output.

A VLS single shot spectrograph will be designed for one of the first two mirror locations, giving pulse-to-pulse spectral readout. Optical delay lines and autocorrelators are best placed after any monochromating elements. 2PPE detection and cross-correlation with combined beams will be incorporated at the endstation. Depending on the design of any monochromator, the zero order beam can also be used for online diagnostics.

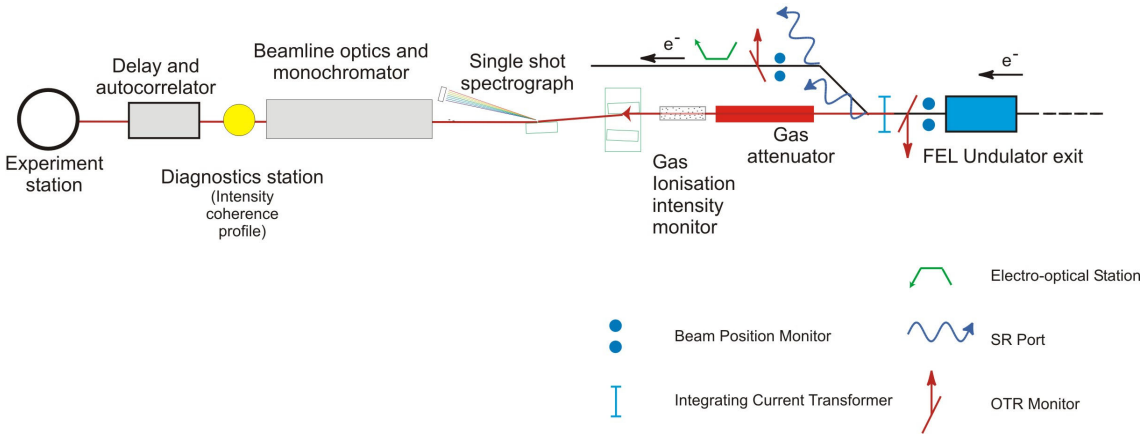

Figure 10.38 Diagnostics on a schematic XUV-FEL beamline (note the scheme does not show other XUV-FEL lines or photon transport from other sources)

10.8.3.2 VUV-FEL

The VUV-FEL diagnostics scheme is shown in Figure 10.39. Gas ionisation intensity monitoring is not possible for some of the VUV-FEL first harmonic output as this is below the ionisation potential of most gases. However, it can be used at the high end of the range and will become more important should this range be successfully extended. Timing and bunch length measurements of the electron bunch are more relevant for this FEL as they are strongly related to the photon output pulse length for the normal operating mode. Hence, there are diagnostics of the electron bunch upstream of the FEL.

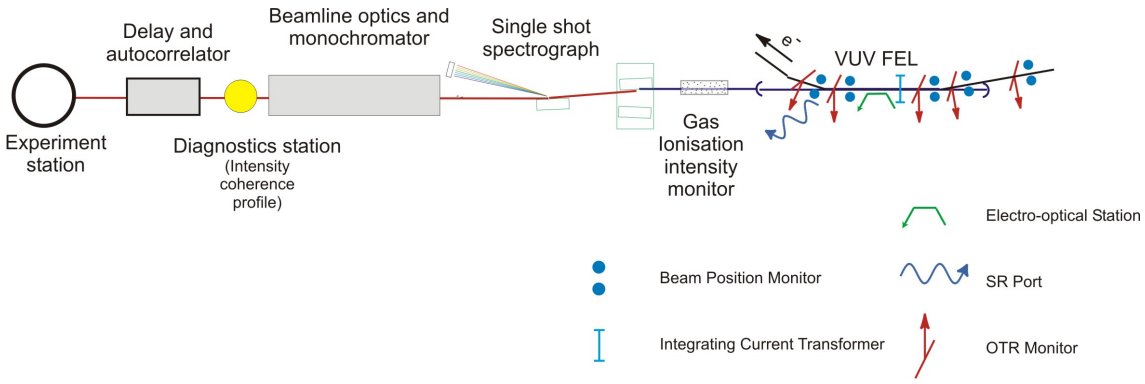

Figure 10.39 Diagnostics on a schematic VUV-FEL beamline (note the scheme does not show other VUV-FEL lines or photon transport from other sources)

10.8.3.3 IR-FEL/CSR THz/Lasers

Due to the relative ease of transporting long wavelength radiation and the availability of beamsplitters, long wavelength facilities generally transport the unmonochromated beam into a series of experiment areas. For IR, THz and conventional laser sources on 4GLS, a diagnostics station (Figure 10.40) will be set up in a dedicated area to operate in two modes; to intercept a small fraction of the beam for online measurement, or to condition the beam (polarisation, repetition rate, intensity) for downstream experiments.

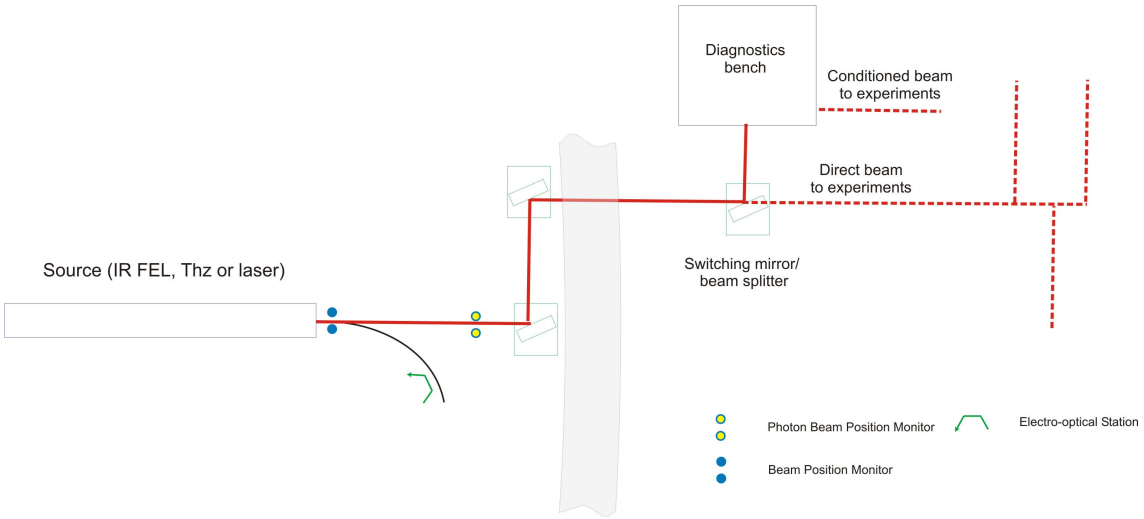

Figure 10.40 Proposed location of photon beam diagnostics bench in the distribution system scheme for the IR-FEL, THz or laser sources

This station will contain a range of diagnostic instruments:

- autocorrelation measurement for pulse length (using Martin Puplett interferometer, FROG);
- IR dispersive spectrometer (for multi-channel spectrum and wavelength measurement on a fraction of beam);
- power and image measurement (MCT, pyroelectric array, bolometer, micro-pulse power measurement);
- switching, attenuation, delay and chopping capability for control of output beam;
- polarisation conditioning;
- IR dump;
- beam splitters, filters.

Many of the above systems are readily available commercially in the mid-IR to visible range The THz region is not so well provided for and prototype systems are being developed. For example, a high aperture, step-scan Martin Puplett interferometer is being built by the Millimeter and THz Instrumentation Group of the Space Science and Technology Department of CCLRC for use on ERLP and which combined with the appropriate detector, will provide spectral and pulse length analysis of the THz sources at 4GLS.

On the IR-FEL and THz sources, the output radiation pulse length and arrival time is directly related to the electron bunch length, and the electro-optic diagnostics system will provide relevant information.

10.8.3.4 Spontaneous Undulators

Diagnostics on the insertion device beamlines in the high average current loop will be based on well-developed schemes for 3rd generation sources and so are only briefly discussed. Measurement of pulse length and arrival time can be provided using similar methods described for the FEL beamlines; these will only be necessary for instruments designed for time-resolved experiments.

The layout in Figure 10.41 shows a general approach. A pair of conventional photon beam position monitors (P-BPMs) are located before any optics. Typical distances from the source will be ~ 20 m. For a pointing accuracy of 0.9 μrad FWHM achieved with a P-BPM accuracy of 1 μm, then the separation between the monitors needs to be ~ 2 m.

Diagnostics stations containing intensity monitors such as Si diodes, imaging screens and conditioning baffles and filters will be located before and after the monochromators.

Part of the photon beam characterisation will make use of electron beam diagnostics as these are directly related. The distributed electro-optical system described in §7.9.8.3 will provide electron bunch length and hence photon pulse length data. Streak cameras on bending magnet SR (synchrotron radiation) ports will provide information of source size and pulse arrival time.

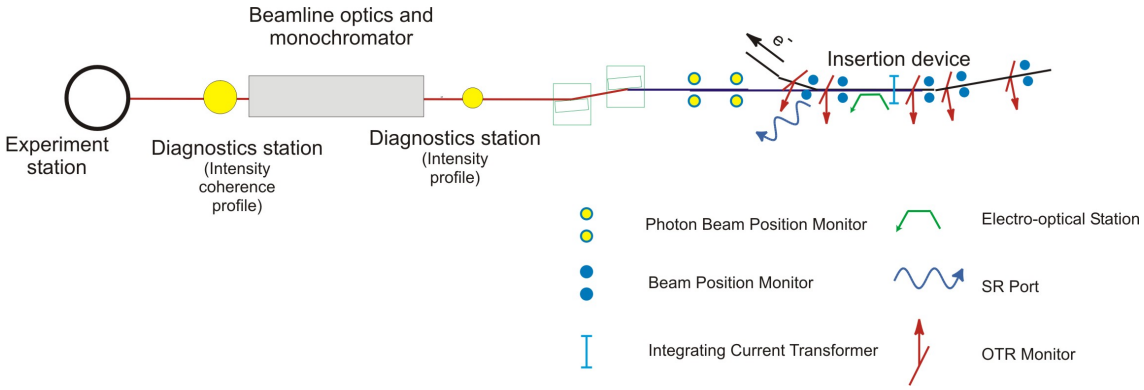

Figure 10.41 Proposed location of photon beam diagnostics on a insertion device beamline in the high average current loop

10.9 Conclusions and Future Work

This chapter has shown that achieving world leading photon beams to experiments on 4GLS is challenging but achievable. Anything that intends to be world leading cannot be a routine application of current techniques, and the areas of beamline design that go beyond the current techniques have been identified and solutions suggested.

The next stage in developing the photon transport systems for the TDR will be to define the photon properties needed by the experiments and to distil these requirements into sets of key performance parameters required on each of the source types on 4GLS. Detailed design work on the transport systems can then commence. There are some key design tools that are needed for the next phase, such as software codes to perform wavefront propagation through the systems. Existing codes such as SRW [27] and PHASE [48] will be used and extended as necessary to ensure the coherent nature of the photon beams on 4GLS is correctly modelled.

There are several areas where engineering studies need to be performed. The short pulse applications are relatively new in the field of SR optics. Achieving the required temporal jitter over long transport paths will require optical mounts with a high level of vibration isolation. More challenging will be the design of optical delay lines that will function in the XUV. These systems will be large and require very high precision coupled rotations and translations.

Some development in optics will be required. Optical constant and damage threshold measurements will be needed to establish the optimum mirror materials and coatings. Optical manufacturing techniques, which have improved rapidly in response to the demands of 3rd generation SR sources, will need to be even better for some critical applications, especially where aspheric surfaces are needed. Metrological techniques will need to improve in line with the accuracy of optical surfaces required.

Photon beam diagnostic techniques will need to be developed. Achieving photon pulse timing at the femtosecond level will be essential to the success of 4GLS. Here we will draw on and extend the large knowledge base developed in ultra-fast laser physics.

The key to the successful delivery of the photon transport systems on 4GLS will be the pooling of the wide range of techniques and expertise already developed in various applications of optical physics (such as synchrotron radiation, high power and ultra-fast lasers, optical manufacturing, surface form metrology) and to lead development in those areas where there is a shortfall to the requirements for 4GLS. International collaboration will form a key part of these development activities.

REFERENCES

[1] A. Andrejczuk et al., 'Investigations of damage thresholds of optical components at the VUV TESLA FEL Phase I', HASYLAB Annual Report (2001)

[2] J. Krzywinski et al., 'Interactions of intense ultrashort XUV pulses with different solids – results from the TESLA test facility FEL Phase 1' Proceedings of the 2004 FEL conference. p. 675-678

[3] L. Nahon, C. Alcaraz, 'SU5: a calibrated variable-polarisation synchrotron radiation beam line in the vacuum-ultraviolet range', Appl. Opt. 43(5), (2004), 1024-1037

[4] E. D. Palik (editor), 'Handbook of Optical Constants of Solids', Academic Press, 1985. 'Handbook of Optical Constants of Solids II', Academic Press, 1991

[5] 'BESSY FEL: The BESSY Soft X-ray Free Electron Laser'. Technical Design Report (2004)

[6] G. Materlik, T. Tschentscher (eds.) 'Tesla Technical design Report, Part V: The X-ray Free Electron Laser', DESY TESLA report 2001-23, (2001), http://tesla.desy.de/new_pages/TDR_CD/start.html

[7] D. Windt, from the data base contained within the program 'imd - Multilayer optical properties: modelling and curve-fitting'. http://www.bell-labs.com/project/imd/

[8] A. Meseck et al., 'Source Characterisation of the BESSY Soft X-Ray FEL', Proceedings of the 27th International Free Electron laser Conference, JACoW/eConf C0508213 (2005)

[9] H. Petersen, 'The plane grating and elliptical mirror: A new optical configuration fro monochromators', Opt. Comm. 40 (1982) 402-406

[10] R. Follath, F. Senf, 'New plane-grating monochromators for third generation synchrotron light sources', NIM A 390 (1997) 388-394

REFERENCES, Continued

[11] R. Follath, 'The versatility of collimated plane grating monochromators', NIM A 467-468 (2001) 418-425

[12] M. R. Howells et al., 'Theory and practice of elliptically bent x-ray mirors', Opt. Eng. 39(10) (2000) 2748-2762

[13] O. Hignette et al., 'Efficient sub-100 nm focusing of hard x-rays', Rev. Sci. Instrum. 76(6) (2005) 063709

[14] F. Barbo et al., 'Spectromicroscopy beamline at ELETTRA: Performance achieved at the end of commissioning', Rev. Sci. Instrum. 71(1) (2000) 5-10

[15] S. Reiche, code 'Genesis 1.3', http://corona.physics.ucla.edu/~reiche/

[16] M. Neviere, P. Vincent, R. Petit, Nouv. Rev. Opt. 5 (1974) 65

[17] S. A. Gorovikov et al., 'Optical design of the high energy resolution beamline at a dipole magnet of BESSY II', NIMA 411 (1998), 506-512

[18] R. Follath, F. Senf, W. Gudat, 'Plane grating monochromator at BESSY II using collimated light', J.Synchrotron Rad. 5 (1998), 769-771

[19] Ph. Zeitoun et al., 'Recent developments in X-UV optics and X-UV diagnostics', App. Phys. B, 78 (2004) 983-8

[20] M. R. Howells et al., 'Toward a soft X-ray Fourier transform spectrometer', NIM A 347 (1994) 182-91

[21] F. Polack, D. Joyeuz, J. Szatos, D. Phalippou, 'Applications of wavefront division interferometers in soft X-rays', Rev. Sci. Instr. 66 (1995) 2180

[22] D. Joyeux, N. de Oliveira, D. Phalippou, J. C. Rodier, M. Vervloet, F. Polack & L. Nahon "A spectrometer by Fourier transformation without separating wave, for VUV-XUV. Principles, implementation, and primary results" Journal de physique IV 127: (2005) 77-85

[23] M. Koike, 'Normal-incidence monochromators and spectrometers', from Vacuum Ultraviolet Spectroscopy II, eds. Samson & Ederer, Academic Press (1998). ISBN 0-12-475979-3

[24] R. Follath, J. S. Schmidt, 'A grazing incidence monochromator for the photon energy range 5 – 250 eV', SRI-03: AIP Conference Proceedings 705(1) (2004) 631-634

REFERENCES, Continued

[25] U. Flechsig, L. Patthey, C. Quitman, 'Extended SX700 type monochromator combining normal and grazing incidence optics for a new undulator beamline at SLS', NIM A 467-468 (2001) 479-481

[26] http://www.rijnh.nl/n4/n3/n2/f1234.htm

[27] O. Chubar, P. Elleaume, 'Accurate and Efficient Computation of Synchrotron Radiation in the Near Field Region', proc. of the EPAC98 Conference (1998) 1177-1179.

[28] R. P. Walker, 'Insertion devices: Undulators and wigglers', Elettra report ST/M-97/2 (1997)

[29] K-J. Kim, 'Brightness, coherence and propagation characteristics of synchrotron radiation', NIM A 246 (1986) 71-76

[30] R. Coisson, 'Effective phase space widths of undulator radiation', Opt. Eng. 27/3 (1988) 250-2

[31] V. Martynov, private communication

[32] G. Neil et al., 'Conceptual Design Report for the THz Beamline at the Jefferson Free Electron Laser', (2004)

[33] M. A. Bowler, 'Extraction Of THz Radiation In ERLP', internal report: erlp-emout-bldes-rpt-0003- THL extraction.doc, (2005)

[34] A. J. Gatesman, R. H. Giles and J. Walman, 'High Precision reflectometer for sub-millimeter wavelengths', J. Opt. Soc. Amer. B 12 (1995) 212

[35] K. Holldack, S. Khan, R. Mitzner, T. Quast and G. Wustefeld, 'Terahertz diagnostics for the femtosecond X-ray source at BESSY', EPAC 2004

[36] M. Richter et al, 'Measurement of gigawatt radiation pulses from a vacuum and extreme ulttraviolet free-electron laser', Appl. Phys. Lett., 83 (2003) 2970; K. Tiedtke, 'The SASE FEL at DESY: Photon Beam Diagnostics for the user facility', SRI-03: AIP Conference Proceedings 705(1) (2004) 588-592; and 'Intensity Monitor for FELs, http://www.ptb.de/en/publikationen/news042/artikel/04203.htm

[37] D. Ryutov, A. Toor, LCLC-TN-00-10

[38] R. Reininger, J. Feldhaus, E. Plonjes, R. Treusch, M. D. Roper, F. M. Quinn, M. A. Bowler 'Spectrometer based on a VLS Grating for Diagnostics of a Vacuum-Ultraviolet Free Electron Laser', SRI-03: AIP Conference Proceedings 705(1) (2004) 572-575

REFERENCES, Continued

[39] C. Iaconis and I. Walmsley, 'Self-referencing spectral interferometry for measuring ultrashort optical pulses', IEEE J. Quantum Electron. 35 (1999) 501

[40] R. Trebino et al., 'Measuring ultrashort laser pulses in the time-frequency domain using frequency-resolved optical gating', Rev. Sci. Instrum. 68 (1997) 3277

[41] V. Petrov, F. Noack, D. Z. Shen et al., 'Application of the nonlinear crystal SrB_4O_7 for ultrafast diagnostics converting to wavelengths as short as 125 nm', Optics Letters, 29 (4): (2004) 373-375

[42] Y. Kobayashi, T Ohno, T Sekikawa, et al. 'Pulse width measurement of high-order harmonics by autocorrelation', Appl. Phys. B: Lasers and Optics 70 (3) (2000) 389-394

[43] N. A. Papadogiannis, G. Nersisyan, E. Goulielmakis et al, 'Temporal characterization of short-pulse third-harmonic generation in an atomic gas by a transmission-grating Michelson interferometer', Optics Letters 27 (17) (2002) 1561-1563

[44] P. Tzallas, D Charalambidis, N. A. Papadogiannins et al., 'Direct observation of attosecond light bunching', Nature 426 (2003) 267–271

[45] T. Nakajima and L. A. A. Nikolopoulos 'Use of helium double ionization for autocorrelation of an XUV pulse', Phys. Rev. A 66 (2002) 041402(R)

[46] J. Mauritsson, P. Johnsson, R. López-Martens et al, 'Measurement and control of the frequency chirp rate of high-order harmonic pulses', Phys. Rev. A 70 (2004) 021801(R)

[47] P. Agostini and L. F. DiMauro 'The physics of attosecond light pulses', Rep. Prog. Phys. 67 (2004) 813–855

[48] J. Bahrdt, U. Flechsig, 'Wave front propagation in synchrotron radiation beamlines', Proc. of SPIE 3150 (1997) 158-170

11. Timing and Synchronisation

The 4GLS timing and synchronisation system has been designed to meet the wide-ranging needs of the experimental user community and also to enable integrated operation of the facility's many subsystems.

The timing system will be physically distributed across the 4GLS installation, with its performance enhanced by additional local subsystems where required. Pulses will be synchronised using a combination of passive and active techniques. Timing monitors will be developed and implemented on line to verify the system's operation and, if required, to provide additional data to the 4GLS users.

Users carrying out multi-beam experiments should generally expect the pulses from different sources to be delivered with a relative timing jitter of 100 - 200 fs RMS or less. It will be possible to reduce this to 10 - 20 fs RMS, although the choice of sources, the beam time structures and the machine's availability to other users may then be limited.

The technical components needed to generate the required time structures and to meet the general synchronisation levels are either already available or are in development. Achieving 10 - 20 fs synchronisation will involve extending the technology beyond what has currently been demonstrated. However this should be possible without resorting to fundamentally novel approaches.

This chapter covers two aspects of the 4GLS design: the time structures of the trains of photon pulses which the machine produces (timing) and also the delivery of those pulses with the required timing accuracy (synchronisation). In many ways these are quite separate issues, but there are some important points of contact between them. These include the fact that common hardware elements influence both aspects and also that the chosen time structures can limit the performance of some synchronisation systems.

11.1 Requirements

There are two sets of requirements for the 4GLS timing and synchronisation system. The first is determined by the facility's users, who need to manage the arrival of photon pulses at their experiments. The sources of these photons include the FELs, undulators and bending magnets on the 4GLS accelerators and also external conventional lasers. A key aspect of the timing management is the delivery of compatible repetition rates and adequate pulse synchronisation for multi-beam experiments. In addition the users may need electrical pre-triggers for their own equipment and information about the photon pulse arrival time(s) for analysis of their results. Issues which relate to these requirements are:

- the timing and time structure of the electron bunches as they travel around the accelerators;

- the timing of external lasers which deliver beams directly to users' experiments;
- the management of photon beam transport path lengths;
- the provision of pre-triggers;
- the provision of timing diagnostic information.

The second set of requirements covers what is needed for the successful operation of the machine itself. It includes:

- the generation and distribution of the low-level 1.3 GHz RF;
- the control of the time structure and arrival time of laser pulses at the photoguns;
- the need to accelerate both XUV FEL and HACL electron bunches in the main linac;
- the control of ions in the electron BTS, possibly by gapping the electron beam;
- the control of the time structure and arrival time of seed pulses at the XUV FEL undulator;
- the need to limit the power loading on certain optical components.

4GLS will operate across a range of different timing modes. The details of these will evolve as the 4GLS design continues and as the machine comes into operation, but some illustrative examples are outlined in chapter 4.

A high average current mode will consist of a continuous train of electron bunches at 1.3 GHz feeding the spontaneous sources in the High Average Current Loop (HACL). In addition the XUV-FEL branch will operate with a pulse rate of 1 kHz. It may be necessary to gap the HACL bunch train so that the XUV-FEL bunches can be accelerated, but if this is done the interval between the last of the HACL bunches and the XUV-FEL one will be kept very short, allowing synchronous delivery of photons from both sources to user experiments. The IR-FEL time structure will consist of a pulse train at 13 MHz (which can be modulated into macropulses with a duty cycle yet to be decided) and with the electron beam switched between two separate undulators. There may be additional beam chopping outside the FEL cavities. More details are given in section 8.1.4.

The minimum pulse rate from the VUV-FEL will be 4.333 MHz. It may be possible to operate at integer multiples of this, depending on the damage threshold of the cavity mirrors. The output photon beam may also be chopped, to reduce the pulse rate below 4.333 MHz, but this will not affect the operation of the FEL itself. Running the VUV-FEL will involve reducing the HACL electron bunch rate or, perhaps, finding a way to reduce the laser gain associated with most of the electron bunches.

11.1.1 Timing Management for User Experiments

The users' timing requirements will vary from experiment to experiment, both in time structure and in timing accuracy. For many users a time structure based on the maximum possible pulse repetition rates will be ideal, delivering the maximum average powers with the minimum temporal disruption.

The simplest time structure change which users will need will be a reduction in the pulse rates. This will be important, for example, when relatively slow relaxation processes are being studied, when an inherently slow experimental technique (e.g. time-of-flight) is used, or when a sample simply needs to be renewed between pulses.

More sophisticated time structuring may be required for multi-beam experiments, perhaps to control an experimental system's progress through a complex sequence of transitions or to enhance measurement sensitivity by taking interlaced readings with and without sample stimulation.

From a timing accuracy point of view experiments will fall into one of three broad classes. The least demanding experiments are those which are completely insensitive to timing accuracy. Either they have no time dependency or the time dependency is handled intrinsically (e.g. when any sample relaxation is much faster than the source's inter-pulse period).

The second group of experiments are those where the characteristic timescales are substantially longer than the duration of the 4GLS light pulses. The light pulses will then behave as delta functions in the time domain and the tightest requirement will be for a timing accuracy comparable with their duration. For the 4GLS sources as currently planned the timing in this case will need to be accurate to ~ 100 - 200 fs RMS.

The third and most demanding group of experiments will investigate processes which take place on the same timescale as the 4GLS pulse durations. In the case of the lasers (both the FELs and the conventional lasers) these can be as short as a few tens of femtoseconds. If timing jitter is not to affect these results significantly then it must be reduced to a level of ~ 10 - 20 fs RMS.

As well as the value of the jitter, the other important parameter which characterises the timing accuracy is the period over which it needs to be managed. With the high pulse rates and fluxes of the 4GLS HACL sources some experiments may involve data acquisitions lasting only a fraction of a second. At the other extreme integration times of many minutes, or even hours, may be needed for the study of dilute samples for example. Such long integrations place corresponding demands on the stability of timing sensors and control systems.

The user experiments which require the timing to be managed, either at the ~ 100 fs or the ~ 10 fs level, will generally only need accurate *relative* timing between pulses. Absolute timing stability will not usually be required.

Pulse timing for user experiments can be managed in two different ways. The first is "timing control", where the pulse timing fluctuations are low and the arrival times at the sample can be varied on user demand. The second is "time stamping", where the pulse timing cannot be completely controlled, but it can be accurately measured and the resulting experimental data can be stamped with the measured timing. Time stamping can be an effective solution when full timing control is too challenging. Relevant considerations are:

- That the technique works most efficiently when pulse timing is one of the experimental variables. Experiments which need the timing to stay fixed can use time stamping, but only to reject data taken when the timing falls out of range;

- It must be possible to measure and record the timing accurately enough and quickly enough. The measurements may not need to be single-shot, but they will need to be completed before the timing changes significantly;

- The timing jitter distribution should be of the right size and shape. So, for example, if time stamping is to be used to map out a decay process then the distribution should not be much wider than the decay time, nor should it be clustered around a few distinct values. If the jitter distribution is narrower than the decay time then an element of coarse control can be added to allow time stamping to be used across the full timescale of the process.

11.1.1.1 Single-beam experiments

The timing requirements for almost all single beam experiments are covered above. Time structuring will be limited to control of the pulse repetition rate and if any synchronisation is needed then it will be between the photon pulses and the electrical signals used to trigger data acquisition hardware. In some cases (e.g. for time-correlated single photon counting, or for integrating streak camera studies) the accuracy of the experiment may depend on the accuracy of these triggers. The fastest photon detectors have sub-picosecond time resolution, so a similar jitter will be required between the photons and the triggers if the capabilities of these detectors are to be fully utilised.

11.1.1.2 Multi-beam experiments

In terms of their time structuring the simplest of the multi-beam experiments are those where two different pulses e.g. with two different photon energies are used to irradiate a sample simultaneously. An example might be the characterisation of an excited state which cannot be accessed by a single photon because selection rules forbid it. In this type of experiment good time control is desirable, since data must otherwise be rejected.

A variant of the synchronous multi-beam experiment is when the pulses need to be delivered with some fixed, but not zero, delay. This approach can be used to guide an experimental system down a particular reaction pathway or to transfer population out of a relatively long-lived state following its selective excitation [1]. Again good time control is needed if this is to work efficiently.

A large fraction of time-resolved experiments use the pump-probe technique, where one photon pulse stimulates the sample and a subsequent one diagnoses it. The sample's response is mapped out as a function of the delay between these pump and probe pulses i.e. the delay is one of the experimental variables. The range over which the delay needs to vary is usually limited at the low end by the duration of the pump and/or probe pulses and at the high end by the sample's

characteristic response time(s). Pump-probe experiments can be carried out using either time stamping or timing control.

11.1.2 Timing Management for Machine Operation

11.1.2.1 Electron generation, acceleration and transport

There is a possible need for gaps in the bunch train to allow simultaneous acceleration of the HACL and XUV FEL bunches and also for ion clearing (see chapter 7). There are no other generation, acceleration or transport requirements for time structuring of the electron beam.

For the electron bunch timing accuracy, the first impact of any timing fluctuations will be on the 4GLS FELs. Successful operation of these requires good temporal overlap between the electron bunches and the FEL photons and also effective compression of the bunches to maximise the peak electron current and therefore the FEL gain. Bunch timing and compression are influenced by:

- the time at which the electrons are generated in the guns;
- the relative phases of RF fields in guns, bunchers and accelerator cavities;
- factors affecting the electron beam path such as magnet positions, magnet supply voltages, real-time machine tuning, insertion device settings etc.

Variations in these parameters arise largely independently but their effects on the electron bunch timing can be strongly coupled, with coupling coefficients which depend on the precise machine configuration. This makes estimation of the jitter in the electron bunch timing and duration difficult without a detailed machine design (an example of the analysis which can then be done is given in [2]). This information will not be available for 4GLS until the Technical Design Report (TDR) has been produced. So instead of specifying absolute stability levels for the electron generation time, the RF phases and the transport path length, the approach taken here will be to discuss these in the point design below (section 11.3.1) and then, during the TDR phase, to iterate the design to deliver the required overall stability.

The electrons will be generated in guns based on laser-irradiated photocathodes (for the XUV- and VUV-FELs) or on a thermionic cathode with pulsed electron extraction (for the IR-FEL). In the former case the timing of the drive lasers will determine the initial timing stability of the electrons. In the latter it will be controlled by RF electrical signals delivered to the gun. In both cases the electron bunch durations will be compressed substantially as the electrons travel through the machine and this process will, as a side-effect, tend to suppress the downstream effects of any timing jitter in the guns (see section 11.3.1.4). As a consequence the timing of electron production at the cathodes can be relatively relaxed. Jitter levels of a few hundred femtoseconds RMS should be adequate.

The SCRF cavities in the accelerator modules have a very high quality factor, Q, which reflects the ratio of the cavities' resonant frequency to the resonance's linewidth. The narrowness of the resonance demands a correspondingly high level of long-term RF frequency stability from the

drive source. This is essentially an absolute, not a relative requirement. The output of good quality commercially available microwave synthesisers, which have very good low frequency performance, are well suited to meeting this need.

In addition to the operation of the photon sources, the requirement for high-efficiency energy recovery also sets limits on the timing stability of the HACL electron bunches, in this case as they return to the main 4GLS accelerator. However since acceleration and deceleration take place near crest, a phase error on return of ~ 1°, corresponding to ~ 2 ps, is tolerable. This requirement will be relatively easy to meet.

11.1.2.2 FEL operation

Two different design schemes will be used for the 4GLS FELs. The VUV- and IR-FELs will be oscillators whose beam properties will be shaped by optical cavities, while the XUV-FEL will be a high gain single-pass amplifier fed by a low-energy photon seed pulse. This difference is reflected in the details of the FEL timing. The fundamental timing requirements, though, are common to all three FELs. They are:

- that the electron bunch and photon pulse time structures match;
- that there is good temporal overlap between the photon pulses and the electron bunches as they propagate through the FEL undulators.

The XUV-FEL will operate continuously at a pulse rate of 1 kHz. The XUV-FEL electron bunches will be generated in an independent photoinjector (see chapter 5) with the sole purpose of driving the FEL so there will be no time structure conflict between machine operating modes.

The requirement for temporal overlap between the electron bunches and the seed photon pulses in the XUV-FEL has been analysed in section 8.2.8. The data in figure 8.46 suggest that a timing offset between the electrons and the photons of ~ 80 fs corresponds to a reduction of ~ 10 % in the XUV-FEL pulse energy. Taking this energy to mark the boundary of acceptable FEL operation and assuming the timing offset to be normally distributed, it follows that a timing jitter of less than 50 fs RMS is required for more than 90 % of the XUV-FEL pulses to have an acceptable energy. This value of the electron-to-photon jitter will be set as the target for acceptable operation of the XUV-FEL.

Turning to the VUV and IR-FELs, the photon pulse time structure will be fundamentally constrained by the lengths of the optical cavities. Pulses will circulate within these, leaving through the output coupler at a rate equal to c/2NL Hz, where c is the speed of light, L is the cavity length and N is the number of pulses in the cavity at any given time. For a steady pulse train out of the FEL the electron bunches must amplify the photon pulses each time the latter travel in the same direction as the former. This sets an absolute minimum pulse rate corresponding to N=1. N will be greater than this if the electron bunch time structure allows i.e. if there is a steady electron bunch rate of c/2NL Hz. Of course the bunch rate must also be a sub-harmonic of the RF frequency.

In the case of the IR-FEL the chosen pulse rate of 13 MHz (the one hundredth sub-harmonic of the RF frequency) corresponds to a cavity length of 11.54 m. The FEL will operate with just one photon pulse in the cavity. The minimum pulse rate of the VUV-FEL, 4.333 MHz, is one third of that of the IR-FEL so its cavity will be three times longer, at 34.62 m.

Electron-to-photon synchronisation in the cavity FELs raises different issues than the XUV-FEL amplifier. The source of photons is now internal to the FEL, allowing their properties to change in response to local conditions. An important point is that photons are continuously lost through the cavity output couplers, which means that their effective lifetime is rather short (it is unlikely to exceed a few microseconds). The consequence for synchronisation is that the need to sustain the relative phase between the photons and the electron bunches is relaxed. Provided that good electron-to-photon overlap is maintained over the photon lifetime the FEL will operate effectively. Over longer periods the photon timing will simply follow any changes in the electron timing as the electrons move into synchronism with, and amplify, photons towards the head or tail of the circulating pulse.

Although cavity FEL operation is relatively insensitive to slow electron bunch timing changes, it is affected by changes in either the electron bunch or optical cavity frequencies. The sensitivity to frequency can be estimated from the data in figure 8.57. This shows that an RMS change in the cavity length on the order of 2 μm can significantly affect the FEL output. As the VUV-FEL cavity will be operated with a feedback fraction of only 9 % this sensitivity to cavity detuning can also be taken as an indication of the bunch-to-bunch timing jitter sensitivity. A change of 2 μm in a cavity length of 34.62 m corresponds to a rate of change of timing of 58 ns/s. Such a large timing variation is not typical of real accelerator systems, even where RMS timing jitters of picoseconds have been measured [3]. These jitters tend to reflect phase noise in the hertz to kilohertz region of the spectrum, corresponding to rates of change of timing between ~ 10 ps/s and ~ 10 ns/s respectively. Since these are well below the 58 ns/s level calculated above it is not surprising to find that cavity FEL operation has been reliably delivered with this level of electron timing jitter [4].

11.1.2.3 Conventional laser sources

Many of the multi-beam experiments proposed for 4GLS depend on at least one beam from a conventional laser. 4GLS will be designed so that lasers fit seamlessly into the overall installation. As far as possible users should be unaware of whether the photon beam they are using comes from a laser or from an accelerator-based source. This principle will apply as much to the timing properties as to everything else, which explains why the laser timing requirements are covered in the machine operations section of this report.

To make full use of 4GLS's capabilities a range of conventional laser beams will be required. Some will need to have properties similar to those from the accelerator-based sources, i.e. femtosecond pulse duration, comparable timing jitter and up to gigahertz repetition rate. The provision of these will be discussed in section 11.2.1.1 below. In addition to these general-purpose lasers there may be a need for more specific ones with beam characteristics

very different from the accelerator-based sources. Practical examples of what is available include single-pulse energies of more than a joule and spectral linewidths of less than a hertz. These types of lasers may well have a timing performance which is limited by the need to satisfy other requirements. They will generally be dedicated to particular experiments which have yet to be specified. For this reason, although the need to incorporate them is noted, they will not be discussed further in this chapter.

11.1.2.4 Laser-based machine elements

As well as the lasers discussed above (i.e. the photoinjector lasers, the laser producing the HHG seed for the XUV-FEL and the lasers which provide beams directly to users) there may be other lasers integrated with 4GLS. Their timing will also need to be managed to ensure effective machine operation.

Non-invasive sensing of the electron bunch timing will be implemented using the electro-optic (EO) effect [5, 6, 7]. This technique will also be used for measuring the bunches' longitudinal profile. An EO crystal placed close to the electron beam will alter the polarisation state of light passing through it in response to the electric field generated by each electron bunch. This will allow the electron bunch timing to be deduced by measuring the time-dependent polarisation of the light. The measurement is a relative one, so to convert this to an absolute timing the light source (typically a femtosecond laser) must be very well synchronised to the absolute master clock. The technique is capable of a few tens of femtoseconds resolution if the laser timing jitter can be kept below this. The rate at which measurements can be made will be limited either by the rate at which the polarisation data can be acquired or by the rate at which the laser can operate, whichever is the slower. Currently data acquisition limits the measurement rate to a few hertz, but development work is under way to increase this. The timing system will be designed to cope with laser pulse rates of at least 10 kHz.

Among the options for time structuring the 13 MHz output of the IR-FEL may be the use of a separate laser to modulate the transmission of a semiconductor window [8]. When the laser is fired it transiently turns the window into a mirror, which then reflects a single pulse from the 13 MHz train. The laser typically operates with nanosecond pulses delivering fluences at the window/mirror of ~ 1 mJ/cm^2. Clearly the laser will need to be synchronised to the IR-FEL pulses, but the jitter will only need to be less than the laser pulse duration i.e. sub-nanosecond for the system to work. This level of jitter has already been demonstrated with a high pulse rate laser [9]. The maximum pulse rate will be set either by the average power handling capability of the semiconductor or by the average power limit of the laser. Lasers delivering tens of watts at tens of kilohertz repetition rates are already commercially available [10].

One possibility for simultaneously managing the requirements of low pulse rate and high pulse rate users may be to use a similar technique to laser pulse slicing [11]. A laser pulse could be used to interact at low repetition rate with a single bunch in the HACL such that the energy spread of the electrons is significantly increased. Following a dispersive section advantage could be taken of this increased energy spread such that the direction of photon emission from

the disrupted bunch (at least from a fraction of the electrons) is different from the standard bunches. A beamline which can select only those photons generated by the disrupted bunch will operate at the lower repetition rate without affecting any other users. The timing requirements for the laser would be that its pulse length would be longer than the whole electron bunch (few ps), its repetition rate would be matched to the users' needs (a maximum value of 10 - 100 kHz should be sufficient) and its jitter would be low enough to ensure reliable overlap with the selected bunches (perhaps ~ 1 ps RMS).

11.1.3 Timing Requirement Summary

The conclusions of the above sections are summarised in Table 11.1

Table 11.1 Summary of timing requirements

Requirement	Time structure	Timing accuracy
Standard user experiments	High average current - 1.3 GHz Optimum FEL operation - N × 4.333 MHz IR-FEL - 13 MHz (can be modulated) Reduced pulse rates - ~ 1 kHz -100 kHz Conventional lasers - ~ 10 Hz -1.3 GHz Multi-beam (timing controlled) Pump-probe (variable timing) Pump-pump-probe etc	 100-200 fs RMS 100-200 fs RMS 100-200 fs RMS
High temporal resolution user experiments	As above	10-20 fs RMS
Photoinjector laser beams	1.3 GHz, 1 kHz (13 MHz optional)	Few hundred femtoseconds RMS
RF source	1.3 GHz	Stability to match SCRF
Seeded XUV-FEL	1 kHz	50 fs RMS
VUV-FEL	N × 4.333 MHz	<< 100 fs RMS over ~ 5 μs and < 58 ns/s
EO sensing laser	Up to 10 kHz	~ 20 fs RMS
IR pulse laser-chopping	Few nanosecond pulses at low rate (to be determined)	Sub-nanosecond

11.2 Practical Techniques

The timing and synchronisation requirements have been covered in section 11.1. In this section the techniques which can be used to meet those requirements will be discussed.

Time structuring will be covered in section 11.2.1. This will include the generation of both the basic pulse patterns and the delays between pulses from different sources.

The measurement of pulse timing is the subject of section 11.2.2. In addition to verifying the system's performance, accurate, precise measurement will also be vital for time stamping and as an input to timing control systems.

Synchronisation is synonymous with the stable arrival time of photon pulses and/or electron bunches with respect to one another or to an accelerating RF field or to an absolute clock. In some circumstances the intrinsic timing stability delivered by a well-designed machine operating in a stable environment – the so-called passive stability – will suffice. Otherwise an active stabilisation system, based on dynamic measurement and correction of the timing error, will be needed. These two approaches will be covered in sections 11.2.3 and 11.2.4.

11.2.1 Time structuring

11.2.1.1 Pulse repetition rate and patterning

For spontaneous sources the time structure of the photon pulse trains can be controlled most easily by structuring the output of the photoinjector drive lasers to vary the structure of the electron bunch trains in the accelerator. A scheme for doing this is described in section 11.3.1.3.

The time structure of the amplifier FEL beam can be controlled either by altering the time structure of its electron bunch train or its seed pulses. The former option would automatically match the time structures of all sources which share the electron bunches whilst the latter would leave the spent beam undulator unaffected.

As explained above, the time structure of the beam from a cavity FEL is dominated by the length of the cavity. Simple changes to the electron bunch time structure can only be used to increase the pulse rate to multiples of its lowest value. Alternative techniques must be used if other changes to the cavity FEL pulse patterns are required.

There are two practical constraints which restrict the ability to match the time structures of the beams from conventional (e.g. photoinjector) lasers to those from accelerator-based sources. Firstly laser systems usually contain an oscillator whose pulse rate is determined by the length of its optical cavity. It is possible to make femtosecond lasers with cavities short enough to deliver gigahertz pulse rates, corresponding to the highest pulse rates from the accelerator-based sources. However it is difficult to fit all of the required optical components into such a small space, so the laser performance may still be compromised. High pulse rates can be achieved with a long cavity if it is seeded with multiple pulses from an external source [12] but again it is

difficult to produce short pulses with low timing jitter. The simplest solution for operating the laser oscillator at a convenient pulse rate is to use a power-of-two sub-multiple of the accelerator frequency, then to add a passive optical pulse stacker to increase the pulse rate as required [13].

A second restriction on the conventional laser pulse rate may arise from the relatively low average powers (typically 10 - 100 W) available from practical systems. Operating at high pulse rates inevitably means reducing the pulse energy proportionately. The repetition rate may therefore be determined by the user pulse energy requirements of the experiment (e.g. the induction of ultrafast melting) or where a nonlinear frequency conversion scheme such as frequency doubling or optical parametric generation is used to deliver coherent photons across a range of wavelengths.

An illustrative laser system is described in section 9.6. This would deliver femtosecond pulses at kilohertz pulse rates with very broad wavelength tunability. Commercially available systems based on simple, bulk-media oscillators can also operate at 70 - 200 MHz although with more limited tuning ranges. With the addition of a cavity dumper pulse rates can be reduced to a few megahertz without substantial loss of average power. Fibre lasers can span the pulse rate gap between these two options and have recently been scaled to hundreds of watts of average power (see chapter 5 for more detail). Regenerative laser amplifiers can cover the range from a few hundred kilohertz down to ~ 10 Hz. All of these systems are inherently regularly pulsed.

If controlling the photon pulse rate or pattern by modifying the electron bunch trains is unattractive or ineffective (as with cavity FELs or conventional lasers) then an alternative will be to structure individual photon beams after they have left the source. The technique of stacking, used to increase the photon pulse rate, has already been mentioned. Reducing the rate may be achieved by beam chopping. The options for this depend on the energy of the photons to be chopped.

Beams of photons with energies between ~ 0.3 eV and ~ 5 eV can be chopped using either the acousto-optic effect or the electro-optic effect. In the first case a high frequency acoustic wave is generated in a transmissive crystal, forming a diffraction grating which deflects the photon beam. In the second the beam is passed through a crystal whose birefringence can be modulated by the application of an electric field. Changing the field alters the polarisation of the photons. If the modulator is placed between crossed polarisers an effective shutter is formed. Acousto-optic systems are generally slower to switch than electro-optic ones and have poorer efficiencies and contrast ratios between their on and off states. However they can handle very high average photon powers, operate at few-megahertz switching rates and, with the use of appropriate materials, can switch photons with low pulse energies [14, 15].

Electro-optic modulators can either be optical fibre coupled, for < 50 ps switching times at up to gigahertz rates, or formed in bulk crystals (Pockels cells) for handling high power beams. Their direct electrical drive makes the delivery of complex pulse patterns possible, particularly in the

case of fibre modulators which can be driven with just a few volts. Contrast ratios can be as high as 40 dB in fibre modulators and 30 dB in Pockels cells with beam power limits of a few hundred milliwatts and a few tens of watts respectively. In the high power regime the cell has to be up to 10 mm in transverse size but a switching time of several nanoseconds is still feasible. Rates up to 200 kHz have been reported [16] although high average power is required from the cell driver. For switching with energies below 0.3 eV, the practical challenges are substantial [17], and the alternative technique described in 11.1.2.4 of switching a semiconductor's infrared transmission with shorter wavelength light can be an effective way to shift the switching problem to a more convenient photon energy.

With photon energies higher than 5 eV or with very high average power photon beams chopping in crystals is no longer viable. The alternative is to use a mechanical system. This is significantly slower than electro-optic switching, with rotating blades limited to minimum switching times of a few hundred nanoseconds. However this can reduce the megahertz pulse rates typical of cavity FELs to ~ 100 kHz or below, which would be optimum for applications such as time-of-flight spectrometry. Such mechanical choppers are in regular use on synchrotron sources [18]. For handling high power visible/near infrared beams they can be crossed with Pockels cells to combine the power handling capability of the former with the switching speed of the latter.

Where the electron bunch rate is so high that a chopper cannot switch cleanly between pulses an option is to gap the bunch train around single bunches. The gap length is chosen so that the chopper has time to select the photon pulses corresponding to the isolated bunches.

11.2.1.2 Delays between pulses from different sources

Multi-beam experiments will usually need the timing between the beams to be managed. If time stamping is used then the management simply amounts to allowing the timing to fluctuate naturally, with additional coarse control if needed, and then measuring it (see section 11.2.2) and binning the experimental data accordingly.

In timing controlled experiments the simplest scenario is where the two photon sources are powered by the same electron bunches (thus minimising the relative timing jitter). If the required delay is conveniently sized then it can be produced by varying the physical length of one of the beam transport paths using an optical delay line. The design of these is discussed in detail in sections 10.5.2 and 10.5.3. In principle the delay line technique can be extended up to tens, or even hundreds of nanoseconds provided the photon pulse rates can be reduced to avoid overlapping with subsequent pulses.

If longer pump-probe delays are needed then the photon pulses will have to be derived from sources driven by different electron bunches. If the sources are on the same branch of the machine, and if the experiment is unaffected by a train of probe pulses, then long delays can be achieved by time-gating the detector to select the signal corresponding to a particular probe pulse. Otherwise sources which are on different branches, or whose timing is completely

independent (e.g. a conventional laser) will have to be used. Again pulse rates may need to be adjusted to avoid irradiating the sample between the pump and probe pulses.

If one of the photon sources has an independently controllable pulse rate then it is possible to scan the time delay without using a mechanical delay line. When the pulse rates differ by a small amount then the interval between pulses will slowly vary and the task will become one of acquiring and binning the data in the same way as with time stamping. The advantage of this approach is that the delay will be predictable, so a fast, very accurate timing measurement system will not be required. The technique has already been demonstrated with sub-picosecond timing jitter with laser sources [19] and with an accelerator [20] and sub-hundred-femtosecond performance seems possible.

11.2.2 Timing measurement

Tools to measure the timing of photon pulses will be needed to label experimental data for the 4GLS users (if time stamping is used), to confirm the machine's setup and performance and also to feed into active timing control systems where these are employed. It will also be necessary to measure electron bunch timing for performance management and to enable active timing control.

Timing can either be measured directly, in the time domain, or it can be deduced from measurements made in the frequency domain. Frequency domain techniques can be extremely sensitive and can also make use of relatively slow detectors, but they are inherently average in nature, giving a value for timing variations over a finite sampling period. This limits their usefulness (for example they cannot time stamp experimental data on a shot-by-shot basis). Their strengths and capabilities are discussed in reference [21] and they will be mentioned again in section 11.2.4.1 but for the remainder of this section only time domain techniques will be considered.

Of course timing measurements will always need to be made with respect to a reference. Sometimes the choice is obvious, so for pump-probe experiments the reference for the probe timing will clearly be the pump pulse. If there is not an obvious alternative then in the following discussion the reference will be taken to be the signal from the master clock.

11.2.2.1 Photon pulses

The optimum technique for measuring photon pulse timing depends on the timescale involved and the photon energy (see sections 10.8.1.3 and 10.8.1.4).

Initial timing setup will depend on a sequence of increasingly fast detectors. When photon energies are above ~ 1 eV the slowest of these can be semiconductor photodiodes, which can generate signals with sub-ns precision. They can have a timing window limited only by oscilloscope memory capacity, which can easily stretch to milliseconds. Faster than photodiodes are streak cameras. Standard models have a temporal resolution below 10 ps, with a nanosecond timing window. The state of the art in resolution is currently a few hundred femtoseconds. Once

this stage is reached it may be practical simply to scan the pulse timing and to use the onset of the experimental effect itself to find the pulse overlap point i.e. time zero. If the timing is well controlled then offsets can be established by measuring the changes in the physical length of a delay line. Alternatively a pulse correlator based on nonlinear optics may serve the same purpose. (It is worth bearing in mind, however, that many correlator designs are not single-shot and the ones that aren't will only give an average measure of timing.) Commercial units designed for visible and near infrared wavelengths have 10 fs resolution and similar values are becoming possible at shorter wavelengths as appropriate nonlinear processes are being identified [22, 23, 24, 25].

Timing of pulses with low photon energies e.g. from the IR-FEL or from a source based on a conventional laser is more difficult but the actual pulse lengths are longer anyway. Photon drag detectors can have few-nanosecond risetimes. Relative timing between two photon sources can be measured with picosecond accuracy provided one of them has a photon energy high enough to cause optically-induced opacity in some material (often a semiconductor) and the photon energy of the other is low enough that the material normally transmits it. If both pulses are spatially overlapped on a piece of the material then the point at which they arrive simultaneously can be found by scanning the timing of one of them and looking, with a slow detector, for the transition from transmission of the low energy one to absorption. Careful scanning can deliver sub-picosecond accuracy. Alternatively exotic streak cameras have been developed based on cathodes consisting of Rydberg atoms. These are described in [26] which also includes information about nonlinear techniques for extending infrared timing measurements into the femtosecond regime.

If the results of timing measurements are to be used for time stamping with a high repetition rate photon source then the rate at which the measurements can be taken may limit the rate at which an experiment can proceed. Likewise if measurements are used to correct timing the data acquisition rate may limit the extent to which jitter can be reduced. Single channel detectors, such as the photodiodes used for frequency domain timing analysis, provide data which can already be streamed to memory in real time at gigahertz rates. This is fast enough for it not to be limiting. One-dimensional array detectors, which might be used to measure the output of a single-shot correlator, can be read out at 1 kHz [27] with extensions to 10 kHz available in the near future. Readout at 10 kHz will deliver detailed timing information at rates fast enough to cover much of the phase noise spectrum of typical photon sources.

11.2.2.2 Electron bunches

The measurement of electron bunch timing using the electro-optic effect has already been described in section 11.1.2.4. Slower measurements of the bunches' electromagnetic field can be made using pickups in the wall of the accelerator vacuum envelope. A timing resolution of a few hundred femtoseconds is practical [28] provided a sufficiently fast signal acquisition system is available.

Electron bunch timing can also be inferred by measuring the timing of electromagnetic radiation that the bunch emits. The example of picosecond resolution measurements using a streak camera has already been given [3]. If nonlinear optics are substituted for the streak camera then the technique can be extended to give a resolution as low as 30 fs with a time window of ~ 10 ps [29].

11.2.3 Passive Timing Stabilisation

In general passively stable systems are easier to design, construct and operate than actively stabilised ones and they also provide the best foundation for active systems to work from. They will therefore be implemented first on 4GLS and the only limits to their implementation will be budgetary ones. Factors which limit passive stability are discussed below.

11.2.3.1 Mechanical vibration

Like all accelerator based light sources the physical subsystems of 4GLS will be affected by mechanical vibration. The consequent effects on timing and synchronisation can arise simply through path length changes which occur when vibration causes beam transport elements to move [30]. More subtle effects include microphonic vibrations in the accelerating cavities which can influence electron bunch timing through energy modulation.

The same general principles of vibration management apply across the whole range of physical scales (from movement of the whole building down to ringing of small optical components inside lasers) and also across the whole range of frequencies (from sub-Hz seismic effects to tens-of-kHz crystal oscillations). They are:

- minimisation, including elimination where possible, of any sources which might drive vibration. Examples include the siting of 4GLS in a locality with very low ground vibration (see chapter 14), the selection of the quietest plant machinery and the control of personnel access to critical areas of the facility;

- isolation of sensitive machine elements and sources of vibration from one another (either by isolating the element or the source). Measures such as the use of remote plant buildings with isolated floor slabs, the location of the whole 4GLS complex away from the road and railway and the decoupling of vacuum envelopes from sensitive photon beam transport components fall into this category;

- control of vibrational resonances. Resonant mechanical systems can have Q's of tens, with a corresponding increase in the amplitude of vibrational motion. It is common practice in 3rd-generation light sources to tune the frequencies of resonances away from any significant drive frequencies (e.g. in magnet girders) and this will be the philosophy adopted by 4GLS. If this is not practical any resonances will be suppressed, as far as possible, by damping. Among the areas where damping techniques have already been developed are in the design of magnet girders and in the use of honeycomb tables for

supporting optical components. The damping of laser enclosures to avoid acoustic resonances is also being investigated.

11.2.3.2 Temperature variation

Like vibration, temperature variation is a ubiquitous effect operating over a very wide range of length and time scales. It can affect timing by changing the physical length of beam and signal transport paths, through the expansion and contraction of structural elements, and also by altering the refractive index of transport media. The latter effect will be a less common problem for photon and electron beam transport, since on 4GLS this will generally take place in vacuum, but it may be a significant factor in the distribution of timing signals because it affects both coaxial cable and optical fibre. Temperature-related timing problems can be mitigated by controlling the temperature changes, by minimising the physical size of vulnerable systems and by using materials whose properties are relatively insensitive to temperature. These might include phase stabilised cable [31] and fibre [32].

The slowest temperature variations will be seasonal and diurnal. These will be controlled through the design of the 4GLS building and the operation of its HVAC and lighting systems. Care will be taken with the use of insulation to minimise the effects of external temperature changes. As well as controlling the indoor mean temperature, efforts will be made to minimise any local variations occurring when daylight gives way to artificial lighting, or when heating during the winter or the night-time is replaced by cooling in the summer or the day. As pointed out in chapter 14 the presence of a large quantity of concrete for radiation shielding will help to stabilise the temperature simply through its large thermal mass.

11.2.3.3 Electrical effects

Fluctuations in electrical supplies may affect timing across 4GLS via a wide range of system components. Examples include:

- The magnets in the electron beam transport system. Clearly if the current in these should change the resulting change in the field strength would alter the beam path length. A sensitivity analysis will be carried out to establish which magnets need the most stable supplies. It may also be possible to group some of the magnets together on a common supply and balance their opposing effects on the path;

- The power supplies for the RF system. Amplitude changes in the RF accelerating field will change the electrons' energy and thus the path they follow through the machine. The same considerations of power supply stability will apply in this case as they will to the magnet supplies.

11.2.3.4 RF cavity effects

The RF cavities in the bunching and accelerating modules are high-Q structures, so their resonances are narrow and strong. The energy stored in their internal fields corresponds to ~ Q times the energy transferred in each cycle by the RF driver. So the effects on the fields of any

short-term variations (phase or amplitude) in the drive signal are very strongly suppressed. The cavities act, in effect, as high-frequency rejection filters for noise. This can be very useful, since active techniques for noise control become difficult at high frequencies. In the case of the SCRF accelerating cavities the Q is sufficiently high that the phase noise spectrum rolls off in the kilohertz region. This is a rare example of a passively stable system (the high-Q cavity) sitting "on top of" an actively stabilised one (the RF supply).

11.2.3.5 Cross-talk between machine sub-sections

A particular feature of multi-user facilities such as 4GLS is the effect of one user's experiment on another's. Many experiments will be coupled through the use of a common electron beam, and timing can be affected if the beam's properties are changed. The most obvious example is the opening of an undulator gap to tune the photon energy. As the magnetic field strength falls the electron path length will shorten and the delay introduced by the undulator will drop proportionately. An example calculation (see section 9.3.3.2) suggests that changes of > 100 fs could result, altering the electron beam arrival time at all downstream devices. Fortunately a simple feedback magnet will be able to negate this effect.

Although cross-talk effects are not negligible they are deterministic and, therefore, reproducible so the relationship between the machine's parameter settings and the electron bunch timing can be established in advance. It can then be used either to inform downstream users of any timing changes or, if a timing actuator is available, fed forward to correct the downstream timing automatically (this solution has been proposed for the undulator described above). For this reason cross-talk effects should not pose a fundamental timing problem.

11.2.4 Active Timing Stabilisation

Active timing stabilisation involves measuring timing variation and then attempting, in real time, to correct it. It is a widely used technique in accelerator control systems. The elements of an active system are a timing sensor, an actuator to change the timing and a link which reads the output from the sensor and controls the actuator. Systems such as this have been developed to control many parameters in addition to timing. They are now widespread in everyday life and their design and implementation are the subject of many textbooks. A succinct and practical introduction is given in [33]. Timing stabilisers can operate in the frequency domain or the time domain. Both options will be discussed in more detail below.

The performance of active timing stabilisers depends on the performance of all three elements. The link electronics can be optimised to extract the maximum sensor signal without saturation and to deliver the fastest actuator response without exciting structural resonances. A combination of actuators is routinely used to cover a wide adjustment range. The useful bandwidths of all three elements can be tailored to deliver a stable system response. Standard stabilisation techniques can also cope with any sensitivity of detectors to environmental factors.

The system performance can be enhanced by:

- using phase-locked-loop (PLL) control techniques;
- locating sensors close to the places where stability is most important and, if practical, having actuators nearby to reduce latency (which can otherwise amount to hundreds of nanoseconds);
- arranging for as much passive stability as possible (active stabilisers often suppress noise by a fixed factor, not to a fixed level);
- designing the system as an integrated whole (simulation tools play a vital role in this respect);
- placing an actuator where it controls the pulse frequency, i.e. the time derivative of the phase, rather than the phase itself, thereby increasing its range of control at low frequencies;
- if working in the frequency domain, using high harmonics of the fundamental pulse rate to increase the sensitivity to phase noise.

An example of the effectiveness of a state-of-the-art timing stabiliser, combined with sophisticated passive stabilisation, is given in reference [34]. The stabiliser combines three separate actuators and two PLLs (one operating on the 140^{th} harmonic of the fundamental pulse rate) using carefully optimised filters. It synchronises one laser to another, via an electronic link, with a control bandwidth of 200 kHz and it delivers a timing jitter of 1.75 fs RMS over a noise spectral range from ~ 0.1 Hz to 2 MHz. A custom synchronisation system applied to commercial laser oscillators is described in [35]. A jitter of 20 fs was sustained under working laboratory conditions for several hours. Fully commercial laser synchronisers are available with guaranteed jitters of less than 400 fs, and in well-controlled environments these can deliver ~ 100 fs performance on a day-to-day basis.

11.2.4.1 Frequency domain

The reduction of timing jitter to ultra-low levels in high pulse rate systems is almost invariably carried out using frequency domain techniques. The reasons for this, which are largely technological, are a) that sophisticated spectrum analysers are available which can dramatically reduce measurement noise [21] and b) that the jitter spectrum is typically dominated by low frequency components (few kilohertz and below, arising from vibration, power supply fluctuations etc.). Frequency domain techniques allow these components to be measured using low-bandwidth sensors which cannot resolve the timing jitter directly.

A number of approaches can be used to derive the timing error signal. Traditionally this has been done electronically, using a low-noise analog RF mixer to combine the signal to be stabilised with a reference. The beat signal from the mixer contains information about both amplitude and phase noise. If the inputs to the mixer are filtered to transmit just high harmonics then the phase noise component will increase with harmonic number more quickly than the

amplitude one and it will eventually come to dominate. This approach generates the largest error signal, making it particularly useful as the input to a closed-loop controller. Alternatively signals at the fundamental frequency can be fed into the mixer in quadrature. If perfect quadrature can be maintained then the amplitude component will be eliminated completely and the mixer will accurately reflect the phase noise. The signal level will not be as high as with the harmonic approach, so a PLL controller based on it may not work so well, but the signal will contain no high-order terms so it will reflect the actual timing jitter more accurately. In summary the second approach should be better if the aim is to measure the phase noise whereas the first one should be more effective in a system designed to eliminate it.

Electronic phase noise measurement has reached a high level of sophistication, but more recent developments in optical measurement are promising to deliver improved long-term stability with, in the case of balanced schemes, insensitivity to amplitude noise [36].

Once the phase noise signal has been generated it can be used to estimate an RMS value for the timing jitter via the formula:

$$\Delta t_{RMS} = \frac{1}{n\omega_0 K_\phi}\sqrt{\int_{f_1}^{f_2}\left[V_\phi(f)\right]^2 df} \tag{11-1}$$

where n is the harmonic number, ω_0 the fundamental frequency, K_ϕ the phase detector constant (a calibration factor which needs to be measured), $V_\phi(f)$ the spectrally resolved signal from the detector as measured with a spectrum analyser and f_1 and f_2 the limiting frequencies between which the timing jitter is measured.

There is one important practical consideration for measuring phase noise in the frequency domain. The signal, $V_\phi(f)$, needs to contain only phase noise information. As discussed above, if the amplitude noise is sufficiently low then this can be achieved either by working with high harmonics or by mixing in quadrature. But if the pulse train is time structured i.e. if pulses are completely missing then the amplitude noise level for those pulses will be 100 %. The impact of this on the phase noise measurement is discussed in terms of sampling theory in [37]. In essence, $V_\phi(f)$ will become corrupted at frequencies above half the time structuring frequency by the appearance of shifted copies of the unstructured spectrum in a process known as aliasing. This will limit the frequency range over which timing variation can be measured and, therefore, corrected. The degree of corruption, i.e. the amplitude of the aliasing, will depend on the duty cycle of the time structuring. As more pulses are removed from the train the amplitude will increase. It might be imagined that the problem could be contained if the duty cycle could be kept small. However it must be remembered a) that the purpose of time structuring is often to change the pulse rate substantially by removing very many pulses and b) that in a low jitter system the phase noise signal will be extremely small and therefore very quickly obscured (picosecond jitter corresponds to values of $[V_\phi(f)/K_\phi]^2$ around -110 dBc/Hz [21]).

Despite these limitations frequency domain techniques can still be used when pulse rates are very low. If the pulses are short then they can generate a high frequency signal with a well-defined phase by excitation of an appropriate resonant structure. This signal can then be compared with a reference to extract the relative phase. If the major source of phase noise in the system is the phase variation of the exciting pulses then repeated phase measurements will reveal the jitter as the statistical width of the phase distribution. A fairly extreme example of this is reported in [38] where a tuned cavity filter was used to generate 2856 MHz radiation from a 10 Hz photodiode signal. The photodiode was monitoring the output of a high power laser system. The resulting phase distribution allowed an upper limit of ~ 1 ps to be set on the timing jitter of the laser.

11.2.4.2 Time domain

Despite the predominance of frequency domain techniques in practical timing stabilisers, measurements in the time domain can offer significant advantages at both ends of the phase noise spectrum. At the high end the frequency domain approach cannot be extended beyond half the pulse rate of the signal which is to be stabilised – the familiar Nyquist limit. As pointed out above, this limit becomes increasingly severe as the pulse rate falls, preventing the measurement and correction of a significant fraction of the phase noise which occurs in real systems. A time domain measurement with a high-resolution, fast-readout detector can, in principle, yield the timing error for every pulse (the basis of time stamping) and the only effect of a falling pulse rate is to allow the measurement system more time to return the result – an advantage rather than a disadvantage. Again in principle the result of a pulse-by-pulse measurement could also be used to correct the timing of each pulse. However this would require a system, including an actuator, capable of acting quickly enough to modify its optical length in the time between the measurement and the pulse arrival. Such systems ("noise eaters") have been developed for correcting amplitude noise in large, single-shot laser installations.

Very low frequency phase noise corresponds to slow timing drifts. Its detection in the frequency domain requires long sampling times during which the near-DC response of the spectrum analyser must remain stable. Standard RF analysers are not suited to making measurements in this regime so FFT analysers may need to be employed. Problems with DC blocking capacitors, used to prevent amplifier saturation, can also limit the low frequency response of frequency domain systems [21]. Such problems have prompted the investigation of low frequency time domain techniques [39]. While these have allowed phase noise spectra to be measured down to < 2 mHz [40] the minimum timing deviation which could be detected was still ~ 50 ps which would be much too large to be useful as the input to a timing control system.

In summary, while time domain techniques offer the potential for improved performance over the frequency domain approach, the practical problems have so far prevented this potential from being realised in most cases. However developments over the next few years, particularly in the readout speed of detectors and in the processing power of computers, are likely to have a significant impact.

11.2.5 Timing System Architectures

The most fundamental choice concerning the architecture for a timing and synchronisation system is between a global approach, where signals are generated centrally and then distributed across the whole facility (hereafter referred to as a "distributed"scheme) and a suite of "local" systems, where the signals are derived close to their point of use. The advantages of a distributed system are:

- that it is infrastructural, so it is widely available to users and requires minimum preparation;
- that it is global, so it can link any source with any other;
- that it does not depend on the operation of the local source, so it can be available for the setup of user experiments when the accelerator is shut down or is configured in a different mode;
- that it can make use of features which are not available locally. In particular it can use the continuous, high pulse rate nature of the front-end signals to stabilise its output over a very wide noise bandwidth, even though the timing of the local signals might be too strongly structured to allow this;
- that its access to the master clock allows it to provide users with accurate pre-triggers; and
- that its components and design can be standardised, allowing economies of scale in procurement, operation and maintenance.

Local systems, however, have their advantages too. These include:

- they are independent. They can therefore be modified without disturbing other users and single-point failures only affect one experiment;
- they are compact, with relatively few components spread over relatively small distances. This means primarily that they have fewer contributions to their jitter budgets than a distributed system does, so they can perform better. The most demanding applications will almost certainly require local timing systems;
- A secondary advantage of local systems' simplicity is that individually they can be inexpensive.

11.3 Timing and Synchronisation - Point Design

The timing and synchronisation requirements for 4GLS have been analysed and summarised in section 11.1. Possible approaches to meeting these have been discussed in terms of specific techniques and overall architectures (section 11.2). In this section a skeleton scheme based on these techniques and architectures will be considered. Its potential performance will be estimated and compared with the requirements. However it will simply be an example of what might be proposed for the final 4GLS facility. The final design will take advantage of future developments in this rapidly advancing technology.

The timing and synchronisation system will operate in an environment where the passive stability has been maximised. The performance figures for the active subsystems described below are based on current technology, as implemented in existing facilities where the conditions were not always optimal. The quoted performance figures should therefore be conservative.

4GLS is fundamentally a multi-source machine and many of its users will need access to a number of synchronised outputs. A distributed timing system will therefore be essential and its elements are described in detail in section 11.3.1 below. In addition there are areas where the exceptional performance of a local timing system will be required. These are noted in section 11.3.2. and one is discussed in more detail.

11.3.1 Distributed Timing System

The component parts of the 4GLS distributed timing system are shown in Figure 11.1:

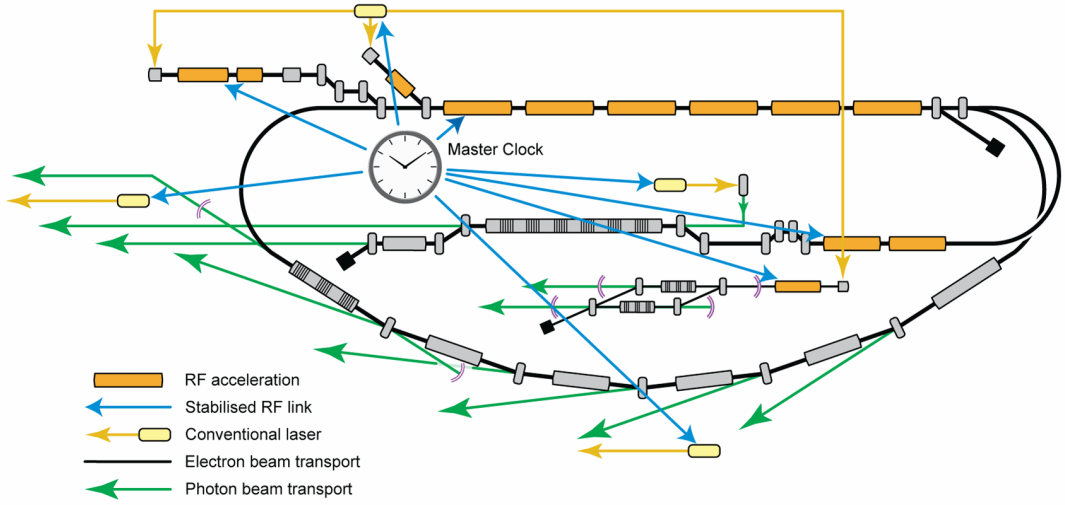

Figure 11.1 Components of the 4GLS distributed timing system

11.3.1.1 Master clock

The requirements of the master clock are that it should have the lowest phase noise across a very wide frequency spectrum and that it should generate a signal which can easily be distributed with high temporal fidelity. Practical considerations include the need for very high reliability.

A suitable optical master clock has recently been developed and demonstrated by Winter *et al* [41]. Figure 11.2 illustrates their technique. The high frequency phase noise characteristics of a fibre laser are superior to microwave sources, while the latter are better at low frequencies and may themselves be locked to atomic frequency standards to ensure long-term stability. By phase locking the repetition rate of the fibre laser to an ultra-stable microwave source (shown at upper left in the figure), the best performance is obtained. The laser is locked to the RF via feedback to a fibre stretcher, around which part of the fibre comprising the laser cavity is wound. A piezoelectric transducer varies the fibre length, and thus the laser cavity length, in response to a control voltage. The optical pulse train of the locked laser then functions as the master clock for the facility. An exception to this could be the most sensitive stages of the accelerator RF system, which may be fed directly from the microwave source. As explained above the SCRF cavities will filter out any high frequency noise that this produces. However they need the very best stability at low frequencies and this might be provided by a direct link to the 1.3 GHz synthesiser. In either case the resulting clock will meet the requirement in Table 11.1.

Erbium-doped fibre lasers, which have been intensively developed for the telecommunications industry, are attractive candidates for this application. Their operating wavelength (~ 1550 nm) matches the absorption minimum in fused silica fibre and, by frequency-doubling, the laser light can be converted to 775 nm. This is a convenient wavelength for direct seeding of the ubiquitous short-pulse Ti:sapphire laser system. The pulse repetition rate is set by the length of the fibre laser cavity, which needs to be at least a few metres to accommodate all of the optical components. A convenient pulse rate is 40.625 MHz which is the 32^{nd} subharmonic of the accelerator RF.

The choice of pulse length from the laser will be a compromise between a) providing enough high harmonics of the 1.3 GHz RF for use when needed (the use of these significantly improves the performance of frequency-domain synchronisation schemes [42]) b) delivering sufficiently short pulses for direct laser seeding and c) preventing dispersion and nonlinear effects in the fibre from corrupting the laser pulses in transit.

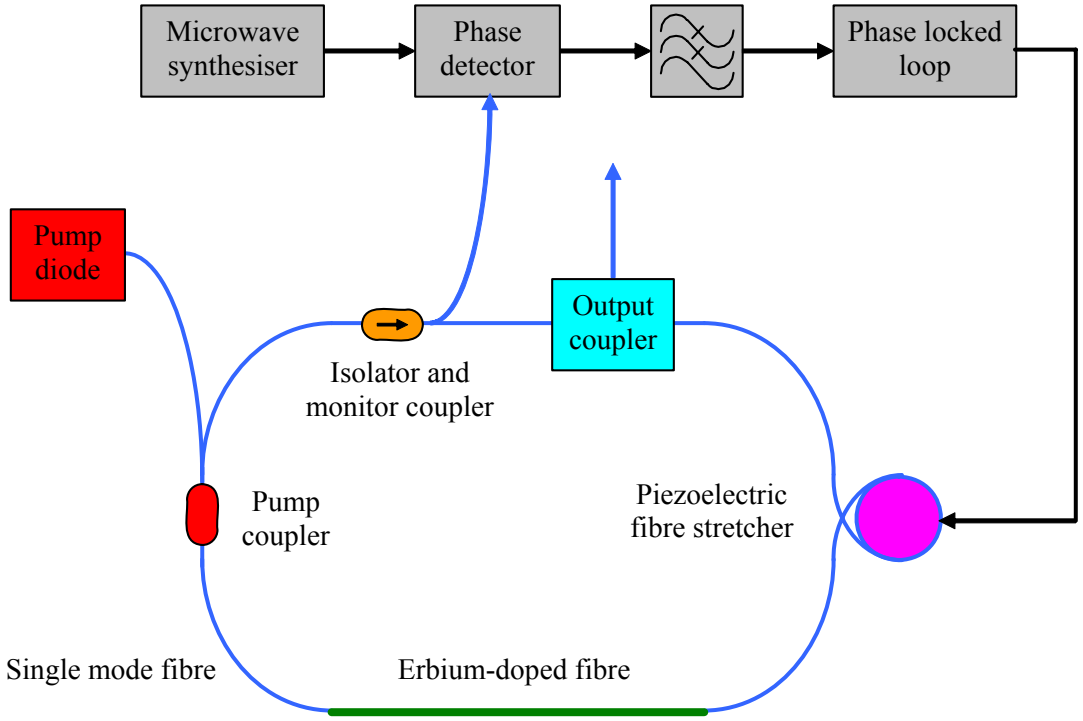

Figure 11.2. Schematic of the master clock based on a fibre laser locked to a microwave synthesiser

11.3.1.2 Low-level RF distribution

The 4GLS site will be sufficiently large that distributed RF signals will take ~ 100 ns to cross it. If they are to arrive with ~ 10 fs accuracy then the distribution path length must be stabilised to at least 1 part in 10^7. Options for distributing the low-level RF (LLRF) include free-space broadcasting, transmission of RF EM waves on copper conductors (coaxial or waveguide) and transmission of light pulses on optical fibres.

In principle free-space broadcasting could be attractively flexible. Receivers could be positioned wherever they were needed and once the propagation time from the source had been established an absolute timing signal could be derived. Practical problems arise, however, because in a free-space scheme the RF propagates from the central transmitter to the receivers through a large volume of space whose contents are difficult to control. The effective path length will change with the air density (and hence with the weather) and also with the positions of objects (including people) in the 4GLS building. In addition the receivers may be vulnerable to RF interference and in some parts of the site (e.g. where metal partitioning is used) the signal strength may be very low. Of course the effects of all of these factors can be measured and compensated for. It is possible that some existing technology, e.g. that developed for the GPS, might be adapted to do this. However at present free-space distribution schemes with the required stability do not seem either to have been demonstrated or to be under development. This option has therefore not been considered for the 4GLS conceptual design.

RF distribution using cable and waveguides has a long history, and sophisticated techniques have been developed, not least by the accelerator community, to deliver very low jitter performance. Stability of ~ 50 fs is possible over cable runs of several hundreds of metres [43]. A fundamental noise-correction limit is set by the frequency of the RF. It is practical to detect and correct phase errors down to a few tens of millidegrees of the oscillation period i.e. a few tens of femtoseconds at 1.3 GHz. 4GLS will be a relatively compact accelerator so 1.3 GHz distribution with ~ 10 fs stability may just be possible using temperature-stabilised and phase-stabilised coaxial cables. However it will be very challenging and, because cable-based technology is mature, significant technical improvements do not seem likely.

A third option is to distribute the timing signals as trains of short laser pulses on optical fibre. The advantages of this are a) direct compatibility with the clock described above and b) that both the intrinsic period (a few femtoseconds) and the typical pulse duration (~ 100 fs) of laser radiation are very much shorter than those of 1.3 GHz RF. The short period means that interferometry can be used to detect changes of much less than 1 fs in transit times down fibres.

Alternatively frequency domain techniques can be used to detect and correct changes in the transit time down long lengths of fibre. A state-of-the-art demonstration of this is reported in [41] and illustrated in Figure 11.3. At the bottom of the figure is the laser-based clock described above. The clock output coupler extracts the pulse train, which is divided into two parts. One part is directed to a high-bandwidth photodiode and the other transported on the “distribution” leg, here a 500 m length of fibre. In the demonstration experiment, this fibre was an existing link running through an accelerator environment. Part of the distribution leg was wound around a fibre stretcher to control the optical length of the leg. Part of the signal was reflected back from the end of the distribution leg through the fibre, its polarisation rotated by 90° with a Faraday rotator mirror to cancel any birefringent effects in the fibre. The return signal was coupled out and sent to the second high-bandwidth photodetector. Both the outgoing and returning pulse trains generate RF spectra in the photodetectors. A harmonic of the repetition rate was selected from each of the spectra with a filter, and these were mixed in quadrature to derive an error signal that, via the fibre stretcher, held the length of the fibre in the distribution leg constant. Using a non-optimal RF configuration and the existing non-dispersion-compensated fibre a jitter of 12 fs between the outgoing and returning trains was obtained. Straightforward improvements to the system hardware should yield jitter at the femtosecond level.

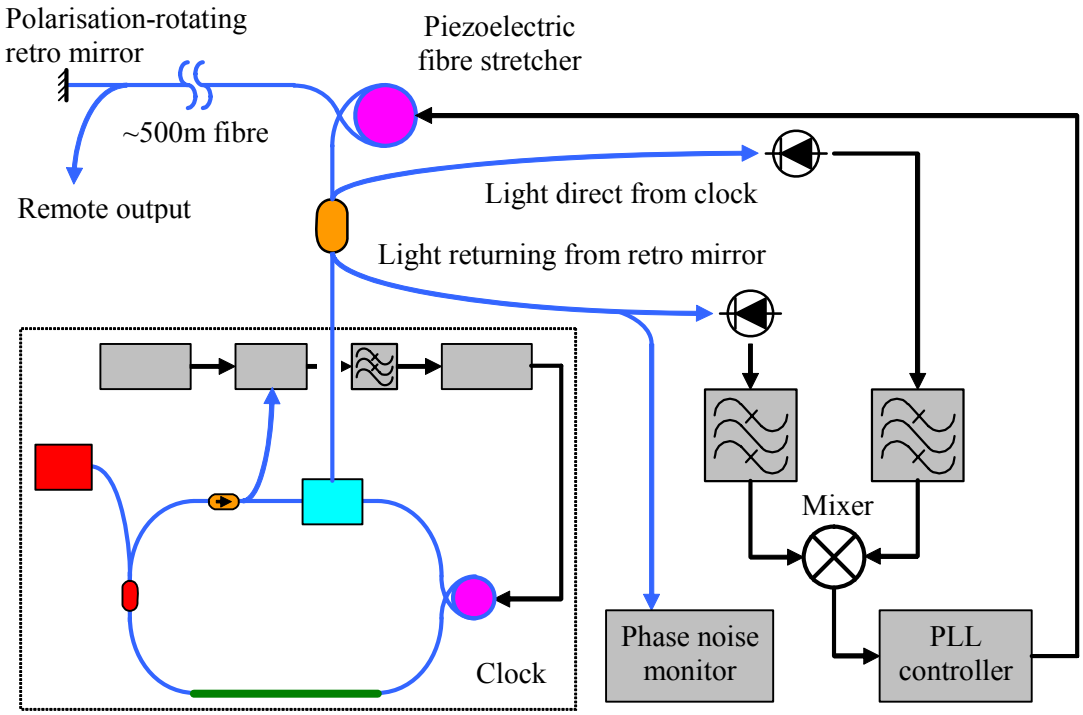

Figure 11.3. Scheme for stabilisation of the delay in a long "distribution" fibre

Other optical sources may be locked to the optical master clock with femtosecond accuracy, either by direct seeding using light optically derived from the pulse train, or by balanced cross-correlation [36]. Extracting necessary RF signals from the optical master clock is also required. In principle, a synchronised RF signal at all harmonics of the repetition rate is encoded in the pulse train, and may be extracted by converting the optical signal to an electric signal in a high-speed photodetector. Such a simple approach is limited by excess phase noise contributed to the electrical signal by optical power fluctuations, beam pointing instabilities, and photodetector nonlinearities [44]. However since this is an important problem in the development of both optical frequency standards and ultrafast accelerator-based sources, considerable effort is being focused on its solution, and progress has been substantial. The power fluctuations are the dominant contribution, and power stabilisation has been shown to reduce the phase noise dramatically [44,45].

It is possible to avoid such limitations through more sophisticated approaches. A recently developed approach removes the sensitivity to fluctuations by transferring the timing information into an intensity imbalance between two pulse replicas while still in the optical domain [46]. Figure 11.4, adapted from [46], illustrates the method. Optical pulses from the clock entering the Sagnac loop are divided and propagate through the loop in opposite directions. A phase modulator is driven at the desired harmonic of the repetition rate (here the 20^{th} harmonic) and positioned in the loop such that the counterpropagating pulses arrive at the modulator 180° out of phase relative to the modulation. An additional bias phase shift of 90° is introduced into the path of one of the pulse replicas in the interferometer using a thin film coating. Balanced detection is used for the output beams, and the difference signal is filtered

and fed back to the voltage controlled oscillator (VCO) that drives the phase modulator, varying the frequency until the detector outputs are balanced. The VCO output is then phase-locked with the optical pulse train.

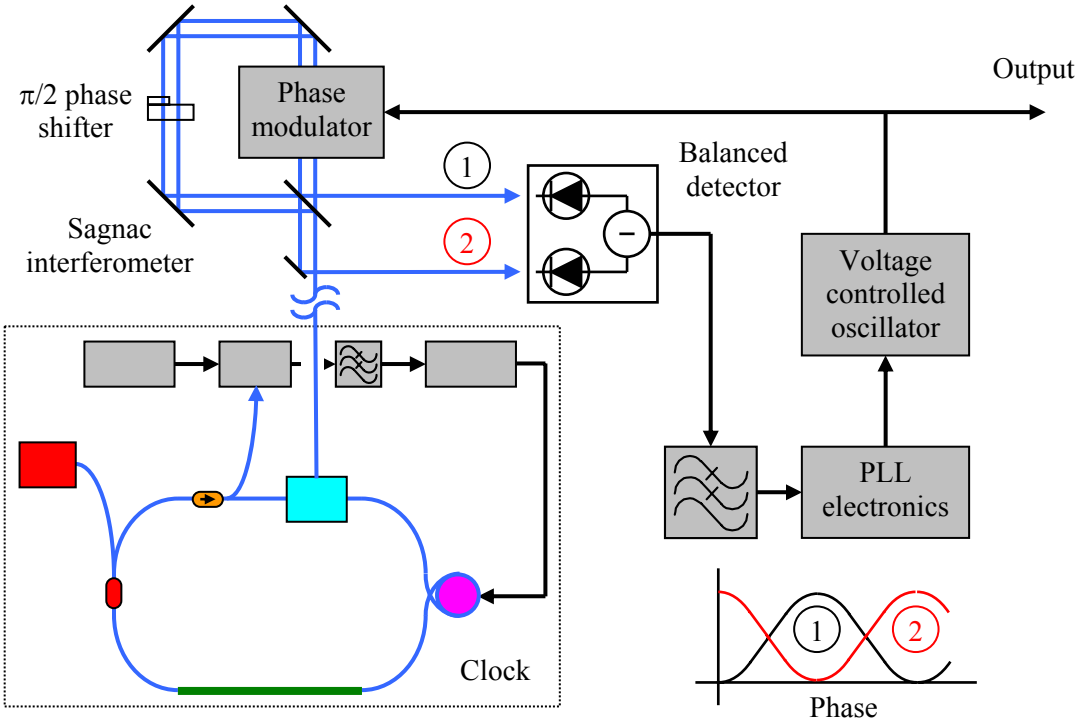

Figure 11.4 Setup for locking RF signal to optical pulses from master clock (inset graph shows the variation of optical intensity from the Sagnac interferometer as the RF-to-optical phase varies)

This method is very stable and robust against drifts. In a demonstration experiment, using a free-space Sagnac loop and modest quality VCO, timing jitter of 60 fs in a bandwidth from 100 Hz to 10 MHz was obtained [46]. Recent improvements, including a fibre implementation of the Sagnac loop to reduce acoustic noise, have resulted in jitter of ~ 9 fs, measured from 1 Hz to 1 MHz [47]. In principle, the technique is scalable to the sub-femtosecond level.

11.3.1.3 Photoinjectors and other conventional laser applications

Most aspects of the 4GLS photoinjector lasers have been discussed in Chapter 5. In this section the control of their timing will be covered. The issues are:

- how to generate pulses at rates up to 1.3 GHz with better than few-hundred-femtosecond timing jitter;
- how to effect changes to the time structure without disturbing the other properties of the pulses.

These will be addressed using components in the Laser Oscillator and Time Structuring modules which are shown in figure 5-2 and which are expanded in Figure 11.5 below. The 1.3 GHz trains will be generated by 32-fold stacking of the outputs from two 40.625 MHz

YDFL oscillators, labelled "primary" and "dummy", which are independently synchronised to the master clock. Each stacker will produce two output beams. The first will feed the HACL amplifier. The second will supply pulses into the XUV-FEL and (if used) IR-FEL amplifiers via electro-optic modulators to reduce the pulse rates. Several schemes exist for the synchronisation of fibre laser oscillators [48] and a timing jitter of 10 fs has already been demonstrated [49]. Satisfying condition a) above should therefore be straightforward.

Satisfying condition b) is potentially more challenging. The impact of laser gain dynamics and thermal effects on the output stability of transiently pulsed laser systems can be substantial. The need to manage these has required careful laser system design and the development of sophisticated real-time controls. Remarkable successes have been achieved [50]. However the 4GLS HACL injector will need to operate over a very wide range of pulse rates and would ideally have the flexibility to accommodate almost arbitrary time structuring. An alternative approach has therefore been adopted.

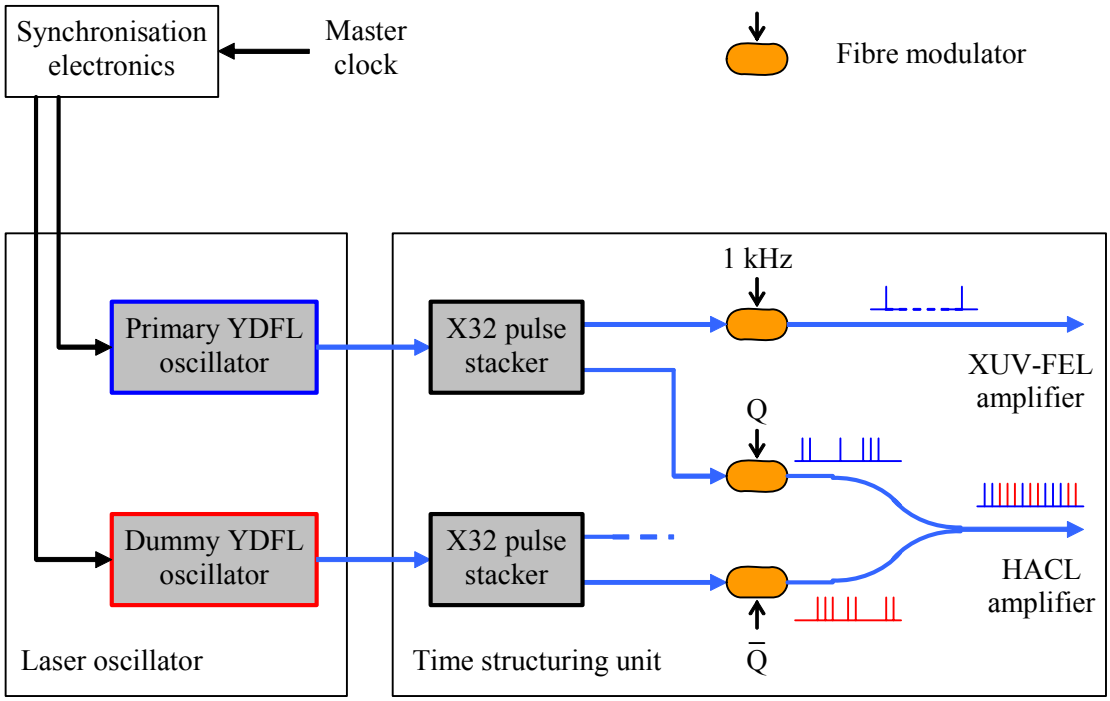

Figure 11.5 Details of the photoinjector laser oscillator and time structuring modules

The primary and dummy oscillators will operate at different wavelengths. The YDFL gain profile is broad enough to accommodate two spectrally separate beams without restricting their linewidths to the point where sub-picosecond pulses can no longer be sustained, although the details of the laser kinetics are complex [51] and the choice of wavelengths may need to be made with care. In fact only the primary beam will need to have good synchronisation and broad linewidth because the dummy will be used simply to maintain stability in the laser amplifier chain when the primary beam is time structured. The HACL time structuring will again be carried out using fibre modulators – one in the primary beam and one in the dummy.

These will operate with complementary timing so that the downstream amplifiers always see an uninterrupted train of pulses no matter what time structure is imposed on the primary beam. At the end of the amplifier chain a dispersive system, probably based on high-efficiency transmission gratings, will separate the primary and dummy beams. The primary will be fed to the frequency doubler and thence to the photocathode. The dummy pulses will be dumped. A time structured output will thus be generated without gross changes in amplifier beam loading.

One of the requirements for the time structured beam is that ghost pulses are minimised. These are low-intensity pulses present when none are expected. If present they are troublesome because they generate low-charge electron bunches which may travel far enough around the ERL to draw energy from the accelerators but not far enough for it to be recovered. They can arise in the scheme described above if the modulators have poor contrast ratio or if there is cross-talk between the dummy and primary beams. In fact fibre modulators can have very good contrast ratios and spectral separation can be a very low cross-talk technique (hence the success of Raman spectroscopy). In addition any low intensity pulses leaving the HACL amplifier will be very strongly suppressed in the frequency doubling stage. Recent unpublished work on the ERLP photoinjector laser has shown ghost pulse energies after frequency doubling of $< 10^{-6}$ of the main pulses, at which level their effects are negligible. Therefore, suppression of ghost pulses should not present any significant difficulty. When running at low repetition rates the integrated charge in the ghost pulses could become significant, in which case a simple mechanical chopping scheme will be introduced to block the beam completely for most of the time between primary pulses.

The success of dummy pulses in stabilising the laser system when the beam has to be time structured depends to some extent on their equivalence to the primary pulses. In fact they will certainly differ in their wavelengths and they may also have different durations and spectral widths. These differences may lead to some residual effects on the primary pulses' amplitude and/or timing as a result of the time structuring. Fortunately, if any such effects are found then it will be possible to mitigate them using a feature of the fibre modulators. This is that they are not simply switches. In fact their throughput can be continuously varied by changing their control voltage. Since any time structuring effects will be reproducible rather than noisy it will be possible to attenuate them by tuning the modulator transmission, thereby introducing an extra element of control into the system.

The time structure properties of conventional lasers, and techniques for modifying them, have been discussed in section 11.2.1.1. Synchronisation levels ranging from ~ 100 fs for carefully installed commercial equipment operating for many hours, down to ~ 2 fs for a state-of-the-art experimental system (stable at least for minutes) are reported in section 11.2.4. In judging the performance of lasers against the requirements in Table 11.1 a contribution from the LLRF distribution system must be included. However even when this is done it seems clear that all of the laser requirements can be met.

11.3.1.4 RF acceleration and electron beam transport

The RF acceleration and electron beam transport systems are described in detail in chapters 6 and 7. Only their timing properties will be discussed in this section. The electron beam transport system has no effect on the time structure of the bunch trains but in a very basic sense the RF linacs do. Their 1.3 GHz RF frequency (corresponding to a bunch spacing of 769 ps) sets the highest electron bunch rate, corresponding to the high average current operational mode. However lower bunch rates will also be perfectly practical. In general the linacs operate at their best with an electron bunch time structure which is simply periodic. So bunch rates which are integer submultiples of 1.3 GHz (e.g. electrons in every second bucket, at 650 MHz, or every 50^{th} bucket, at 26 MHz) will be preferred.

At low repetition rates, the energy recovery process starts to become inefficient and eventually fails as the RF cavities cannot store the energy from the returned electron bunch indefinitely. For the 4GLS cavities the energy decay time will be of the order of milliseconds and so at kilohertz bunch rates energy recycling will cease. However the current will now be of the order of one millionth of its design maximum, so the power cost will be insignificant and energy recovery is not required for the facility to operate.

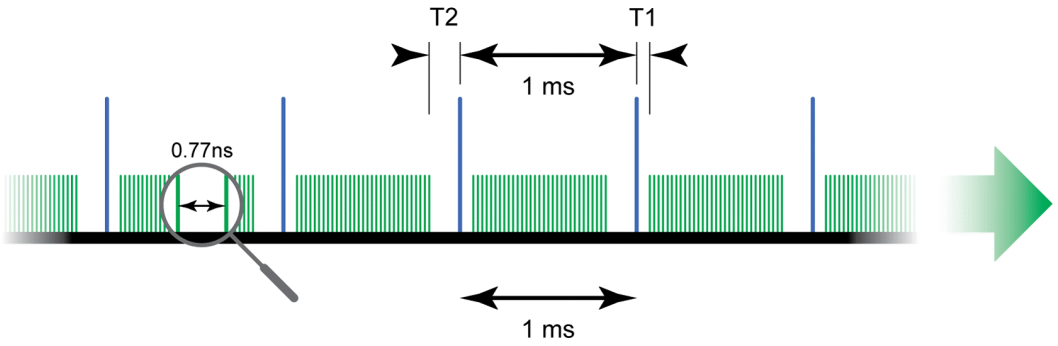

Figure 11.6 Time structure of the electron bunch train at the main linac, showing 1 nC XUV-FEL bunches (blue) and 77 pC HACL bunches (green)

A generalised snapshot of the bunch train at the main linac is shown in Figure 11.6 with time running from right to left. If gaps are required to accommodate the 1 nC bunches then T1 (the duration of the one before each 1 nC bunch) will be kept short to allow synchronous delivery of pulses from the XUV-FEL and the HACL sources to a target.

The timing of electron bunches as they travel round the 4GLS machines will be influenced by the combined properties of the RF modules and the magnetic beam transport system. This combination is deliberately designed to alter their timing, both in time-of-flight electron bunchers and also in magnetic bunch compression systems. In the absence of space-charge and wakefield perturbations the bunchers and compressors will not only compress the bunch but also the upstream jitter. In practice the perturbations will prevent perfect synchronism [52] but any initial timing differences between the electrons and the RF phases will still be substantially

reduced. From the point of view of electron timing stability this will tend to cancel the effects of any timing jitter between the photoinjector lasers and the cavity RF. This could be particularly useful in the main accelerator where it will tend to lock the timing of the HACL and the XUV-FEL branch electron bunches together. But in return it will stamp onto the electron timing any phase error between the cavity RF and the master clock, to which the rest of the 4GLS system will be locked. One option might be to consider deriving the 1.3 GHz signal for locking the master clock laser from an RF cavity in the main linac. At the expense of a slightly noisier clock the synchronisation of other sources to the train of electron bunches may be improved.

The overall 4GLS bunch compression scheme will be a complex combination of several RF modules and magnetic compressors. Electron bunches will generate photon pulses not only at the places where they are maximally compressed, but also at intermediate points where their timing may not be so strongly influenced by the cavity RF. In addition, the effects of RF amplitude variations, magnet power supply instabilities, physical movement of beam transport components and changes in the machine tuning may all alter the electron timing independently of the RF phase. Unfortunately the complexity of these effects and of the interactions between them means that quantitative prediction of the overall performance can only be delivered by sophisticated modelling. This will not be carried out until the 4GLS TDR, so at this stage it is not possible to say definitively how stable the electron timing will be.

What is known is that an RF phase stability of <0.02º has been achieved in a similar linac cavity [53], corresponding to a timing jitter of <40 fs at a frequency of 1.5 GHz. Performance down to 0.01º has been reported informally and this will be the target stability for the RF in the 4GLS injector sections which generate the bulk of the energy chirp needed for bunch compression. Additional electron bunch phase noise will arise in the main linac, but since this will be operating near crest it will make a smaller contribution to the electron bunch phase noise than the injector cavities. In the absence of any detailed modelling the electron timing jitter can be estimated by adding, in quadrature, 20 fs for each of the modules in the injectors and 30 fs for all of those in the rest of the machine.

11.3.1.5 Photon beam transport

Photon beams will need to be transported from the 4GLS sources to the users' experiments, from the photoinjector lasers to the photocathodes, from the XUV-FEL seed laser via the HHG chamber into the undulator and from any diagnostic and control lasers to their points of use. Transport path lengths of tens of metres including several turning mirrors are likely to be involved. In almost all cases the beams will be enclosed in sealed pipes. These will be evacuated if they are transporting high energy photons, which gases would absorb, or femtosecond pulses which would otherwise be stretched by dispersion, or if the beams are being image-relayed to preserve their near field uniformity, since this will involve a high-intensity focus. Otherwise they will contain static gas at a fixed density, subject to no bulk movement due to draughts or, given the small pipe diameters, convection. Disruption of the beam timing by the propagation medium will therefore not be an issue.

If timing problems do arise they will be caused by movement of the mirrors, leading to path length shifts. A change of just 3 μm corresponds to a timing change of 10 fs. Fortunately there exists substantial experience of designing optical systems to hold mirrors with much higher stability than this. Examples can be found in the fields of interferometric optical testing, precision metrology and gravitational wave detection (where the stability requirements are orders of magnitude more demanding). However perhaps the most relevant confirmation that the problem is tractable comes from the successful operation of FELs. It was noted in section 11.1.2.2 that the 35 m long VUV-FEL cavity will need to have a length stability of ~ ±2 μm i.e. an RMS variation of perhaps five parts in 10^8 for the FEL to operate reliably. The same technology used to achieve this can be transferred to the beam transport system to keep timing variations within limits. Possible additional measures are:

- the inclusion of beam transport paths inside the control loops used to maintain synchronisation. This simply involves moving the photon timing sensor to the end of the transport path. Changes in the path length will then be compensated by the synchronisation system;

- the use of optical interferometry to monitor path lengths, again feeding back to a timing actuator e.g. an adaptive mirror, elsewhere in the system. The simplest form of frequency stabilised HeNe lasers can have frequency drifts of less than one part in 108 over a few minutes and a few parts in 108 (i.e. a few micrometres over 100 m of optical path) over a day. Slightly more sophisticated transverse Zeeman stabilised lasers can deliver a stability of one part in 109. In the latter case the laser's frequency variation will generate less than one fringe shift to a monitor interferogram.

If the photon beam transport stability can be improved by a factor of five over the FEL cavity requirement i.e. to one part in 10^8 then this will correspond to a length stability of ~ 1 μm RMS or four optical fringes for a 100 m path. The temporal stability will then be ~ 3 fs RMS.

At least some of the photon beam transport paths may contain mechanical choppers for time structuring of the beams. The example that has been studied in most detail so far is the VUV-FEL beamline. The details of choppers for relatively low energy photons are rather different from those for typical synchrotron X-ray choppers. The longer photon wavelength means that VUV beams have shorter Rayleigh ranges i.e. they expand more quickly on either side of a focus. This limits the chopper blade thickness and forces the use of a rotating slotted disc geometry. To ensure clean chopping of single pulses from a train, the disc must rotate quickly enough to move the slot across the beam within twice the interpulse interval. Working back from the 4.333 MHz pulse rate and the material-limited maximum edge velocity, the required slot width can be shown to be ~ 50 μm. The coherence of the FEL beam should allow it to be focused relatively easily to this width. However with a peak power in the gigawatt regime the focus will need to be astigmatic (long axis parallel to the slot) to spread the power over a large enough area to avoid plasma generation. The beam footprint will be increased further by using as thick a blade as possible and bevelling the edge, where the beam lands, at a

shallow angle. This will maximise the fraction of the beam power which is reflected, rather than absorbed. This is important because with an average beam power of ~ 300 W there would otherwise be an issue with heat dissipation from the blade, which can only cool radiatively. At present the preliminary analysis suggests that a mechanical chopper for the VUV-FEL will be viable, allowing pulse rates below the lower limit set by the FEL cavity length.

11.3.2 Locally Derived Timing

It is expected that the distributed timing system described above will satisfy most of the requirements for operation and use of 4GLS. Two possible exceptions are the synchronisation of the XUV-FEL electron bunches and HHG seed source and the operation of the machine for ultra-low (10 - 20 fs) jitter experiments. In these cases locally derived timing systems may offer significant advantages.

Analysis of the 10 - 20 fs jitter scenario will require more detailed knowledge of the various machine subsystems than is currently available. It will therefore be deferred to the 4GLS TDR. The issues surrounding the XUV-FEL seeding, however, are reasonably clear and the option of local timing control can be usefully considered.

Successful seeding of the XUV-FEL will require a jitter of < 50 fs between the seed source and the electrons. If the distributed timing system was used to synchronise the two then the relevant processes would be:

- the generation of a master clock signal;
- the distribution of the RF clock signal to the HHG laser;
- the locking of the HHG laser to the distributed RF;
- the transport of the HHG photons into the XUV-FEL undulator;
- the generation of an RF field, locked to the master clock, in the accelerating structures;
- the delivery of the electrons, properly phased, to the accelerating structures;
- the transport of the accelerated electrons to the XUV-FEL undulator.

Process a) should not contribute to the timing jitter but the remainder, to some extent, will. The strength of this scheme is that the XUV-FEL photons, whose timing depends on the seed source timing, will be relatively well synchronised to the master clock which controls several of the other sources. Its weakness is that with a relatively large number of processes involved, all of them will need to work with low jitter if the overall performance is to be adequate.

The processes making up a locally derived system are:

- the generation of a timing signal from a local electron bunch monitor;
- the distribution of the timing signal to the HHG laser;
- the locking of the HHG laser to the timing signal.

Now the obvious strength is that the remaining processes are few and they include ones which are less prone to jitter, so the FEL output should be more stable. A more subtle strength is that the output pulses will now be synchronised more directly to the electron bunches, and thus to the output of the downstream devices including the spent beam undulator. However the timing link from the FEL output to the master clock is now more tenuous, so it will be more difficult to synchronise the FEL with the HACL devices. The local electron bunch rate is also just 1 kHz so the Nyquist limit prevents the HHG laser from tracking any noise on the electron bunch train above 500 Hz.

In the absence of quantitative information about the strengths and weaknesses it is not clear whether the locally derived timing scheme will be better than the distributed one. In practice the best solution may be to install both and switch between them as required.

11.3.3 Jitter Budgets

Table 11.2 lists the 4GLS subsystems which contribute to the timing difference between the photon beams from different sources. This picture is oversimplified because the contribution from each subsystem may vary with the source combination but, broadly speaking, the more contributions there are, the more difficult the overall jitter control is likely to be.

Table 11.2 Contributions to the timing jitter between beams from different photon sources

	Conventional laser	XUV-FEL spent beam undulator or dipole	XUV-FEL	VUV-FEL	IR-FEL
HACL undulator or dipole	1,2,3,4,6,10		1,2,3,4,6,9	4,6,8	1,2,3,4,6,7
IR-FEL	1,6,7,10		1,2,3,6,7,9	1,2,3,4,6,7,8	
VUV-FEL	1,2,3,4,6,8,10		1,2,3,4,6,8,9		
XUV-FEL	1,2,3,6,9,10	5,6,9			
XUV-FEL spent beam undulator or dipole	1,2,3,5,6,10				

1. Low level RF distribution system *2. Photoinjectors*
3. Accelerator modules and RF amplifiers *4. HACL electron beam transport system*
5. XUV branch electron beam transport system *6. Photon beam transport system*
7. IR-FEL (including injector and electron BTS) *8. VUV-FEL*
9. XUV-FEL (including HHG seed system) *10. Conventional laser*

11.3.3.1 Example of XUV-FEL combination with VUV-FEL

The most challenging of the source combinations is the XUV-FEL with the VUV-FEL. Not only are a large number of subsystems involved (including a conventional laser embedded in the XUV-FEL seeding system) but the short pulse duration of each of these sources means that a demand for very low jitter is more likely to arise. This combination has therefore been analysed in more detail to illustrate the possible timing jitter performance of 4GLS.

The analysis consists of estimating the jitter contributions from each of the subsystems and combining the results in quadrature, assuming that they are uncorrelated. In some slowly varying cases, e.g. when the timing responds to building-wide temperature changes, this assumption will not be valid. But quantitative allowance for effects like this will not be possible until the 4GLS design has been developed much further.

Two sets of jitter estimates have been made. The first is conservative, using figures based on performance demonstrated at the time of writing or, where no demonstration has been attempted, on what might reasonably be expected given current technology. The second set of figures are projected forwards to the date at which 4GLS will come on line. They use data

which are either the current state-of-the-art (but are expected to be readily available in a few years time) or which are plausible extrapolations from current performance levels.

Considering the individual subsystems in Table 11.2:

1, 2 **Conservative:** The LLRF distribution system will be used to synchronise the two photoinjector lasers and the XUV-FEL seed laser to the master clock. Because of the effects of bunch compression, timing variations in the photoinjector lasers should be suppressed by more than an order of magnitude. The main contribution to the quadrature sum will therefore come from the XUV-FEL seed laser. If this, in turn, can be optically synchronised directly from the LLRF distribution fibre then only the transport jitter along this fibre needs to be considered. A value as low as 12 fs has already been achieved for this (section 11.3.1.2). If the seed laser needs to be locked electronically, which using today's technology it probably will, then additional jitter from the optical-to-RF conversion must be added. 9 fs has been demonstrated, yielding a quadrature total of 15 fs. There may be a contribution to the jitter from electron beam transport elements in the photoinjectors. This will be treated with the other beam transport contributions below.

Projected: Using optimised dispersion-shifted fibre and carefully controlled RF signal levels a timing jitter from 1 Hz to 100 kHz of ~ 20 fs over a 4.5 km fibre length has been achieved [54]. The authors expect that in an accelerator-based facility using fibre lengths an order of magnitude shorter than this a timing transfer jitter of a few fs could be achieved. On this basis a distribution jitter of 5 fs would be practical for 4GLS.

3, 4 **Conservative:** Without a detailed design of the electron beam transport system it has not been practical to estimate the overall timing jitter of the electron bunches when they arrive at the FELs. However some estimates can be made for the RF bunching and accelerating cavities. This sets a lower limit to the electron jitter since the bunch compression scheme will act to compress the upstream jitter, so the electron timing jitter will simply be the same as the overall RF jitter. A minimum HACL electron bunch jitter might then be ~ 40 fs, made up of contributions from the buncher, injector linac and main linac. The XUV-FEL electron bunches will not contribute to the timing jitter of the XUV-FEL pulses since provided the overlap between the electrons and the seed photons is adequate the output pulse timing will depend only on the seed laser (see below).

Projected: Instead of using the system master clock as a reference it should be possible to lock the XUV-FEL seed laser to a harmonic of the 4.333 MHz electron bunch rate, measured close to the VUV-FEL undulator. This would eliminate the major contributions to the jitter budget from the RF acceleration and electron transport, replacing them with the effects of a slightly noisier clock signal and leaving the high-frequency timing jitter between the VUV-FEL electrons and photons. The

resulting jitter is even more difficult to estimate than in the conservative case, but the high resolution target could be met by reducing the clock and electron-photon total to ~ 15 fs. This will be the target figure for the TDR design.

6, 8 **Conservative:** Independent of the timing requirements it will be necessary to achieve a photon transport stability of five parts in 10^8 for reliable operation of the cavity VUV-FEL itself. This is not considered a problem since many FELs have operated reliably with similar specifications without resorting to special measures. Assuming the same stability level in the rest of the photon transport system the timing jitter can be estimated for each of five photon transport paths – two of length 15 m, from the photoinjector lasers to the photocathodes, one of the same length from the XUV-FEL seed laser to the undulator and two of length 50 m, from the FELs to the experiment. The 15 m paths would have length variations of 0.75 μm i.e. 2.5 fs. The 50 m paths would each contribute 2.5 μm, or 8 fs. If, as seems likely, the target stability of one part in 10^8 is reached, then these jitters would fall by factors of five. On the other hand the number of mirrors per unit length of each transport path is substantially higher than the number in the FEL cavity and for this reason the larger values have been used for the conservative analysis.

The timing of the VUV-FEL output pulses is influenced most strongly by the electron bunch timing, which has been accounted for above. The only other contribution to the timing jitter arises from variations in the length of the VUV-FEL cavity. A detailed analysis of the interaction between the cavity length and the electron bunches is complex but a simple upper-limit estimate can be made by assuming that the electrons exert no restoring influence on the photon timing over the timescale of one round trip in the cavity. This corresponds to an optical path length of ~70 m which, using the same stability criterion as in the previous paragraph, would contribute a jitter of 12 fs.

Projected: The photon transport stability figures given above were chosen on the basis of an optical system that just met the VUV-FEL cavity specification. It seems very likely that better performance than this will be achieved and that significantly better could be achieved if special measures such as interferometric stabilisation are used. If a factor of five can be delivered for the FEL cavity and even a factor of two achieved for the remaining optics then the contributions to the jitter budget would fall to ~ 3 fs and ~ 6 fs respectively.

9 **Conservative:** The timing jitter of the XUV-FEL pulses reflects the jitter of the seed pulses. For the FEL to work properly these must have a jitter of < 50 fs with respect to the electron bunches. This may well be achieved most reliably by using a local timing system to lock the laser pulses to the electron bunches (see section 11.3.2). However for the purposes of this analysis it will be assumed that the laser is locked to the master clock via the LLRF distribution system and that the jitter in the electron beam transport is not so large as to disrupt the XUV-FEL operation. In this case the FEL jitter will arise

predominantly in the laser oscillator at the start of the seed pulse generation train. If this was simply a commercial unit then a jitter of ~ 100 fs might be expected. However for this application better performance will be needed and a system similar to that described in [35] will probably have to be developed. The jitter level would then be reduced to ~ 20 fs.

Projected: The state-of-the-art in locking a laser system to a reference RF signal currently has a jitter of < 2 fs [34]. Transferring that technology to the more complex XUV-FEL seed laser could reduce the associated timing jitter to perhaps 3 fs.

The individual contributions to the jitter budget are summarised in Table11.3.

Table11.3 Analysis of individual jitter contributions for the worst case photon source combination of the XUV-FEL with the VUV-FEL (conservative estimates in plain, projected in italic).

	Individual jitter contributions
LLRF distribution	12 fs, 9 fs *5 fs*
Electron beam generation, acceleration and transport (via VUV-FEL output)	20 fs, 20 fs, 30 fs *15 fs*
Photon beam transport	2.5 fs, 2.5 fs, 2.5 fs, 8 fs, 8 fs *1.5 fs, 1.5 fs, 1.5 fs, 4 fs, 4 fs*
VUV-FEL cavity	12 fs *3 fs*
XUV-FEL	20 fs *3 fs*
RMS total	**51 fs** ***17 fs***

11.4 Conclusions

The requirements of the timing and synchronisation system have been assessed and it has been shown that in most circumstances an RMS jitter of 100-200 fs is acceptable. For very high temporal resolution experiments an RMS jitter of 10-20 fs is the target.

A point design for the 4GLS timing and synchronisation system has been presented to meet the wide-ranging needs of the experimental user community and also to enable integrated operation of the machine's many subsystems.

The timing system will be physically distributed across the 4GLS installation, with its performance enhanced by additional local subsystems where necessary. Photon pulses will be synchronised using a combination of passive and active techniques. Timing monitors will be developed and implemented on line to verify the system's operation and, if required, to provide additional data to the 4GLS users.

Analysis of jitter contributions from all the possible sub-systems has demonstrated that pulses from different sources will be routinely delivered to the experiment with a relative timing jitter of much better than the specified 100-200 fs RMS in general. Projecting the performances of timing systems forward and using a dedicated timing architecture it seems clear that the high resolution target of 10-20 fs jitter is achievable even for the most difficult photon source combinations.

REFERENCES

[1] I. Powis et al, 'Quantum chemical control', draft 4GLS flagship proposal

[2] B. Kuske et al, 'Impact of realistic bunch profiles and timing jitter on the output of the BESSY low energy FEL line', Proc 27th International Free Electron Laser Conference (2005) p35.

[3] S. Zhang et al, 'Temporal characterization of electron beam bunches with a fast streak camera at Jlab FEL facility', Proc 27th International Free Electron Laser Conference (2005) p640.

[4] G. R. Neil et al, 'The Jlab high power ERL light source', Nucl Instr Meth A 557 (2006) p9.

[5] S. P. Jamison et al, 'Electro-optic techniques for temporal profile characterisation of relativistic Coulomb fields and coherent synchrotron radiation', Nucl Instr Meth A 557 (2006) p305.

[6] I. Wilke et al, 'Real-time single-shot electron bunch length measurements', Nucl Instr Meth A 483 (2002) p282.

[7] A. L. Cavalieri et al, 'Clocking femtosecond X-Rays', Phys Rev Letts 94 (2005) p114801.

REFERENCES, Continued

[8] S. Marchetti et al, 'Controlled dumping of pulses of laser radiation ranging from MIR to the MM by means of optical semiconductor switching', Appl Phys B 72 (2001) p927.

[9] S. Pearce and C. L. M. Ireland, 'Performance of a CW pumped Nd:YVO_4 amplifier with kHz pulses', Opt Laser Technol 35 (2003) p375.

[10] K. J. Snell, D. Lee and J. G. Manni, 'High average power, high repetition rate Nd:YVO_4 MOPA laser system', paper CDP-1 at CLEO/QELS99 (1999).

[11] R. W. Schoenlein et al, 'Generation of femtosecond pulses of synchrotron radiation', Science 287 (2000) p2237.

[12] C. Hovater and M. Poelker, 'Injection modelocked Ti-sapphire laser with discretely variable pulse repetition rates to 1.56 GHz', Nucl Instr Meth A 418 (1998) p280.

[13] C. W. Siders et al, 'Efficient high-energy pulse-train generation using a 2^n-pulse Michelson interferometer', Appl Optics 37 (1998) p5302.

[14] S-H. Shim et al, 'Femtosecond pulse shaping directly in the mid-IR using acousto-optic modulation', Opt Letts 31 (2006) p838.

[15] T. Kanai et al, 'Free electron laser pulse control by acousto optic modulators', Proc 27th International Free Electron Laser Conference (2005) p332.

[16] D. Nickel et al, '200 kHz electro-optic switch for ultrafast laser systems', Rev Sci Instr 76 (2005) p033111.

[17] G. Coppola et al, 'Visualization of optical deflection and switching operations by a domain-engineered-based $LiNbO_3$ electro-optic device', Opt Express 11 (2003) p1212.

[18] M. Gembicky et al, 'A fast mechanical shutter for submicrosecond time-resolved synchrotron experiments', J Synchr Rad 12 (2005) p665.

[19] A. Bartels et al, 'Femtosecond time-resolved optical pump-probe spectroscopy at kilohertz-scan-rates over nanosecond-time-delays without mechanical delay line', Appl Phys Letts 88 (2006) p041117.

[20] X. Yan et al, PRL, 85 (2000) p3404.

[21] R. P. Scott, C. Langrock and B. H. Kolner, 'High-dynamic-range laser amplitude and phase noise measurement techniques', IEEE J Sel Topics in QE 7 (2001) p641.

[22] M. Drescher et al, 'X-ray pulses approaching the attosecond frontier', Science 291 (2001) p1923.

REFERENCES, Continued

[23] T. Sekikawa, T. Kanai and S. Watanabe, 'Frequency-resolved optical gating of femtosecond pulses in the extreme ultraviolet', Phys Rev Letts 91 (2003) p103902.

[24] T. Nakajima and L. A. A. Nikolopoulos, 'Use of helium double ionization for autocorrealation of an xuv pulse', Phys Rev A 66 (2002) p041402.

[25] J. Mauritsson et al, 'Measurement and control of the frequency chirp rate of high-order harmonic pulses', Phys Rev A 70 (2004) p021801.

[26] M. Drabbels, G. M. Lamkhuijzen and L. D. Noordham, 'Demonstration of a far infrared streak camera', IEEE JQE 34 (1998) p2138.

[27] M. Towrie et al, 'Development of a broadband picosecond infrared spectrometer and its incorporation into an existing ultrafast time-resolved resonance Raman, UV/visible and fluorescence spectroscopic apparatus', Appl Spectrosc 57 (2003) p367.

[28] H. Schlarb, 'Overview on the longitudinal diagnostics for ERLs', WG4 paper presented at ERL2005 (2005).

[29] V. Tenishev et al, 'On-line diagnostic tool for measurement of the time delay between two ultrashort light pulses', Meas Sci Technol 15 (2004) p1762.

[30] R. O. Hettel, 'Beam stability at light sources', Rev Sci Instr 73 (2002) p1396.

[31] D. McCormick et al, 'Thermal stabilization of low-level RF distribution systems at SLAC', Proc PAC 1993 (1993) p1975.

[32] T. Kobayashi et al, 'RF reference distribution system for the 400-MeV proton linac of the KEK/JAERI joint project', Proc LINAC2002 (2002) p187.

[33] A. Abramovici and J. Chapsky, 'Feedback control systems – A fast-track guide for scientists and engineers', publ Kluwer Academic Publishers (2000) ISBN 0-7923-7935-7.

[34] R. K. Shelton et al, 'Subfemtosecond timing jitter between two independent, actively synchronized, mode-locked lasers', Opt Letts 27 (2002) p312.

[35] D. J. Jones et al, 'Synchronization of two passively mode-locked, picosecond lasers within 20 fs for coherent anti-Stokes Raman scattering microscopy', Rev Sci Instr 73 (2002) p2843.

[36] T. R. Schibli et al, 'Attosecond active synchronisation of passively mode-locked lasers by balanced cross correlation', Opt Letts 28 (2003) p947.

REFERENCES, Continued

[37] Agilent Application Note AN 386, 'Pulsed carrier phase noise measurements using the Agilent 3048A phase noise measurement system', (2000).

[38] M. Bellaveglia et al, in presentation by A. Ghigo, 'JRA2 – PHIN Charge production with photo-injectors', presented at CARE 05 (2005).

[39] H. Tsuchida, 'Wideband phase-noise measurement of mode-locked laser pulses by a demodulation technique', Opt Letts 23 (1998) p286.

[40] H. Tsuchida, 'Time-interval analysis of laser-pulse-timing fluctuations', Opt Letts 24 (1999) p1434.

[41] A. Winter et al, 'High precision optical synchronization systems for x-ray free electron lasers', Proc 27th International Free Electron Laser Conference (2005) p676.

[42] M. J. W. Rodwell, D. M. Bloom and K. J. Weingarten, 'Subpicosecond laser timing stabilization' IEEE JQE 25 (1989) p817.

[43] G. R. Neil, private communication.

[44] E. N. Ivanov, S. A. Diddams and L. Hollberg, 'Analysis of noise mechanisms limiting the frequency stability of microwave signals generated with a femtosecond laser', IEEE J Sel Top QE 9 (2003) p1059.

[45] E. N. Ivanov, S. A. Diddams and L. Hollberg, 'Study of the excess noise associated with demodulation of ultra-short infrared pulses', IEEE Trans on Ultrasonics, Ferroelectrics and Frequency Control 52 (2005) p1068.

[46] J. Kim, F. X. Kärtner and M. H. Perrott, 'Femtosecond synchronisation of radio frequency signals with optical pulse trains', Opt Letts 29 (2004) p2076.

[47] J. Kim et al, 'A balanced optical-RF phase detector', preprint submitted to CLEO 06 (2006).

[48] F. X. Kärtner et al, 'Progress in large-scale femtosecond timing distribution and RF-synchronization', Proc PAC2005 (2005) p284.

[49] D. D. Hudson et al, 'Mode-locked fiber laser frequency-controlled with an intracavity electro-optic modulator', Opt Letts 30 (2005) p2948.

[50] I. Will, G. Koss and I. Templin, 'The upgraded photocathode laser of the Tesla test facility', Nucl Instr Meth A 541 (2005) p467.

REFERENCES, Continued

[51] L. Orsila and O. G. Okhotnikov, 'Three- and four-level transition dynamics in Yb-fiber laser', Opt Express 13 (2005) p3218.

[52] J. B. Rosenzweig and G. LeSage, 'Sychronization of sub-picosecond electron and laser pulses', UCLA internal publication (1998).

[53] M. Liepe and J. Knobloch, 'Superconducting RF for energy-recovery linacs', Nucl Instr Meth A 557 (2006) p354.

[54] K. W. Holman et al, 'Remote transfer of a high-stability and ultralow jitter timing signal', Opt Letts 30 (2005) p1225.

12. Potential Upgrades to the Core Facility

12.1 Introduction

4GLS has an extraordinarily flexible design, with a number of possible upgrade paths. It is therefore important that, even at this early stage, upgrades are borne in mind so that decisions now do not result in the exclusion of upgrade options at a later date. It is also possible that a decision taken now with little extra cost implication will permit very cost effective upgrades at a later date.

Potential upgrades fall into two broad classes; those that if implemented would have a large physical impact on the whole facility and those that represent an upgrade to a subsystem or an additional capability with little impact on the shape and scope of the rest of the facility.

12.2 Potential Upgrades of High Physical Impact

Undoubtedly the highest impact upgrade would be to enable much shorter wavelength synchrotron radiation production from GeV electrons by taking the electron beam twice through the main linac. Multiple acceleration of electron beams in this way is achieved at the CEBAF nuclear physics facility at Jefferson Laboratory. As the electron beam energy progressively increases then progressively stronger magnetic fields are required for steering and focusing. At CEBAF this requirement is met in a very space-effective manner by stacking the arcs vertically.

On 4GLS this approach could enable a set of X-ray beamlines at an upper level. However, such a development would have major implications for low-energy work on 4GLS and would change the scientific remit of the source. 4GLS is also a more complicated machine than CEBAF in terms of the requirements of the main linac and considerable accelerator physics work would be required to develop this proposal further.

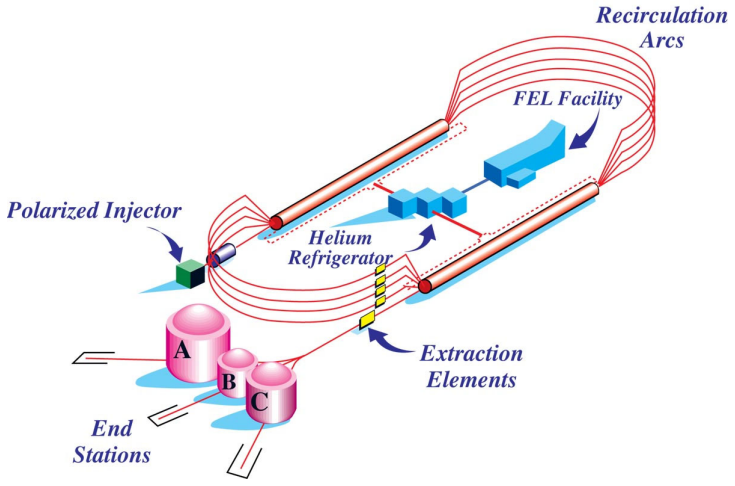

Figure 12.1 Schematic of the CEBAF multi-turn accelerator

Taking the electron beam several times through the main linac would have shielding implications and open up the possibility of a much shorter wavelength FEL in a straight-on configuration to the main linac.

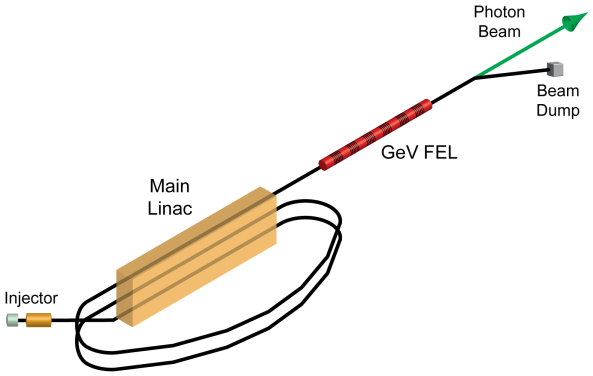

Figure 12.2 GeV energy FEL in the straight on position

This option would require development space in-line with the main linac and means that the orientation and position of the 4GLS building on the Daresbury Laboratory site should be chosen with this in mind. Use of reconfigurable shielding (*i.e.* shielding that is assembled from blocks rather than cast *in situ)* at the end of the main linac would in a very cost-effective manner to allow for this upgrade possibility at some stage in the future. Long-term if the UK were to decide to house such an in-line FEL facility then the 4GLS linac would be an ideal starting point.

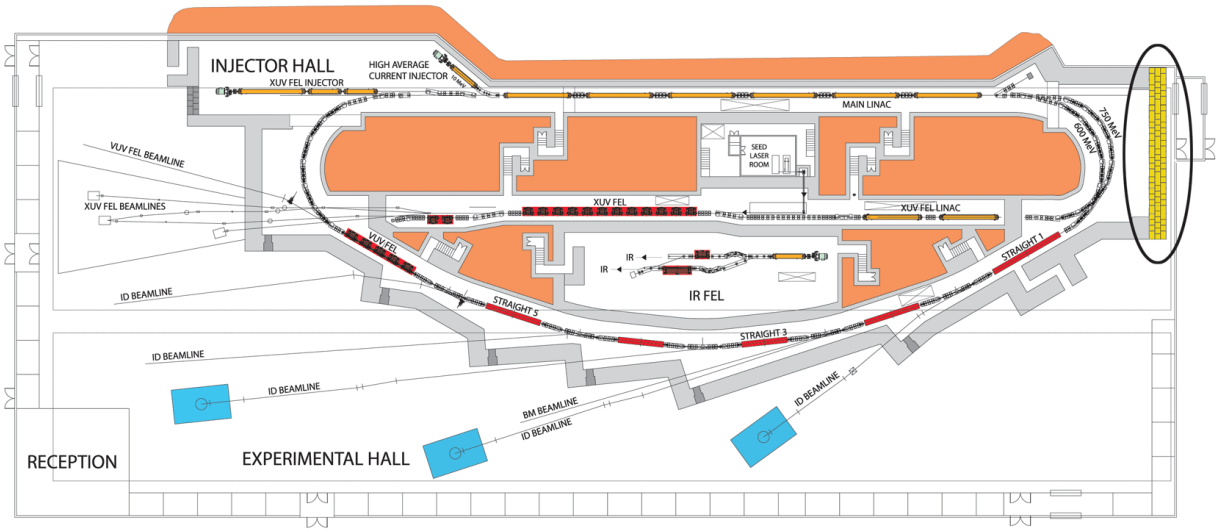

Figure 12.3 Area of demountable shielding at the end of the main linac

An approach to enhancing the upper photon energy of the XUV-FEL is to increase the energy of the radiating electrons by inserting additional accelerating modules after the main linac. This would extend the arc of the XUV-FEL branch beyond the current limit of the building (see Figure 12.4).

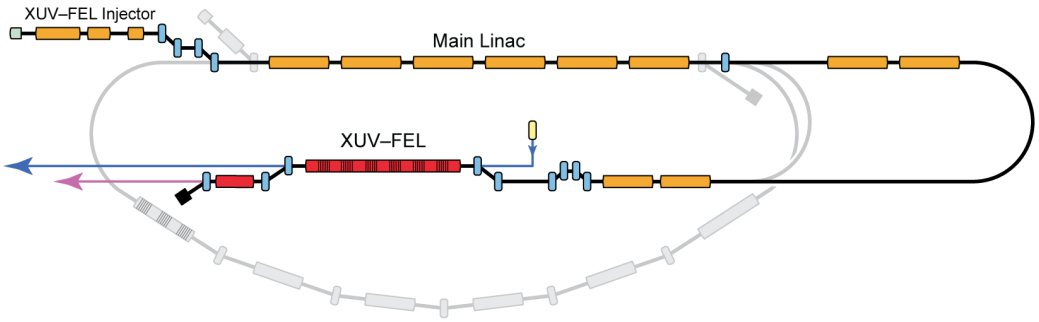

Figure 12.4 Increasing the electron energy at the XUV-FEL by increasing the number of accelerating modules

The core design of 4GLS allows for a maximum electron energy of 950 MeV in the XUV-FEL branch of the accelerator which in turn results in a maximum (fundamental) photon energy of 100 eV. The possibility of increasing this photon energy by additional modules could be easily realised by using reconfigurable shielding at the end of the main linac. An alternative to additional SC modules is operation of the same number of modules at a higher gradient. This has very significant risk and operating cost implications.

12.3 Potential Upgrades of Low Physical Impact

The easy inclusion of technology developments with concomitant improvements in the overall machine performance is a key strength of the 4GLS energy recovery linac light source approach. On a medium term time-frame this is likely to involve incorporation of photoinjector developments as this technology is the focus of much attention globally. Fortunately enhancements in photoinjector performance will improve the performance of the whole machine but are very unlikely to result in a significantly larger photoinjector footprint.

Easy incorporation of future enhancements to the FELs is an important consideration. Schemes are already under evaluation that would, for example, increase the peak power of the XUV-FEL. Whilst these have cost and complexity constraints, space is not felt to be a major constraint.

There is a strong and increasing science drive to produce sub-femtosecond pulses from FEL sources. This interest is fuelled by the fact that the dynamics of electron transfer in atoms and molecules are on the femtosecond and sub-femtosecond timescale. There are currently two main

schemes to produce attosecond FEL pulses led by Emma at SLAC [1] and Zholents at Lawrence Berkeley National Laboratory [2]. More work will be needed to ascertain the best route forward in a 4GLS context.

Utilisation of the electron beam of the IR-FEL branch to generate short X-ray pulses by Compton back-scattering is a potential upgrade route that has received some attention. The electron beam energies here can be varied between around 20 and 50 MeV which would result in X-rays in the energy range of 6 - 38 keV. Whether to proceed with such a development will be informed by Compton back-scattering activities which are currently at a very early stage of development on the ERL Prototype at Daresbury Laboratory.

Other developments that do not involve light sources *per se* but which would broaden still further the science output of 4GLS include utilisation of the energy recovered electron beam either in free radical dynamics studies using pulse radiolysis or in an EBIT source. Both of these activities would involve use of a low energy electron beam from 4GLS (probably extracted from an early part of the dump line) with suitable target materials.

12.4 Summary

Future-proofing of 4GLS has been embedded in the proposed conceptual design by the use of reconfigurable shielding at the end of the main linac and provision of development space in the siting of the building.

During the technical design phase, schemes for production of sub-femtosecond pulses will be studied further.

The Compton back-scattering activities on the Energy Recovery Linac Prototype will inform future strategies for short pulse X-rays.

REFERENCES

[1] Femtosecond and Subfemtosecond X-Ray Pulses from a Self-Amplified Spontaneous Emission–Based Free-Electron Laser, P. Emma, K. Bane, M. Cornacchia, Z. Huang, H. Schlarb, G. Stupakov and D.Walz, Phys. Rev. Lett., 92 (2004) 74801(4).

[2] A proposal for Intense Attosecond Radiation from an X-Ray Free-Electron Laser, A. A. Zholents and W. M. Fawley, Phys. Rev. Lett., 92 (2004) 224801(4).

13. Technical Systems

A range of conventional technical systems must be integrated together to ensure a smooth design, planning, construction, installation and commissioning process. Further detailed work will follow in the Technical Design Review (TDR) phase. Nevertheless enough knowledge has been established to be confident that the key technical challenges can be solved within the cost and timescales of the project.

Firstly, the system integration methodology is presented in the introduction. In the following sections, most attention has been given to the more challenging technical systems.

The 1.8 K cryogenic plant will be amongst the largest in the UK and will be a significant cost for the project. Additionally, part of the plant will require housing remotely from the main 4GLS facility, and thus affects the site requirements.

Ultra-fast, ultra-bright photon beams place high demands on stability and alignment and an initial approach is presented.

Lastly, the more conventional systems are discussed, highlighting any special requirements for 4GLS. The magnets require tight engineering tolerances and careful design at a similar level to other modern particle accelerators. The slow control requirements again do not differ significantly from those of 3rd generation storage rings, but the digital feedback and feedforward systems need special attention as does the interaction between the control system and the timing and synchronisation system. The vacuum system requirements differ from a 3rd generation storage ring in the need for extremely high vacuum in some photoinjector guns and in the need for particulate control in all areas of the accelerator vacuum system to ensure very low levels of particulates in the superconducting linac modules.

13.1 Introduction

The methodology for construction of 4GLS is based on assembling in subsystems to enable full testing prior to installation into the accelerator tunnel complex to limit the work required in confined spaces and enable many of the technical problems to be solved at an early stage. As with 3rd generation light sources and the Energy Recovery Linac Prototype (ERLP), girder modules will be employed to ensure the stable support of magnets, diagnostics and vacuum systems in an integrated approach (see Figure 13.1). Key elements such as the focussing magnets and electron beam position diagnostics will be accurately pre-aligned on the girders, while local services will also be temporarily attached to enable testing to ensure full functionally prior to installation. These mechanical, electrical and controls system tests will be conducted in an assembly area, which will include all the key facilities, including a magnet test room, ISO class 4 clean rooms and adequate space for assembly, survey and alignment.

Figure 13.1 ERLP support girder modules installed in the Accelerator Hall

To maintain extremely good levels of mechanical and thermal stability of key accelerator and beamline optical components, careful attention to detail will be required in the structural and thermal management of the facility. Further details on stability requirements are covered later in this chapter and those influencing the building design are described in Chapter 14. The concept is to employ a two building approach comprising the main 4GLS building and a remote plant room that houses noisy equipment that could disturb the operation of the facility.

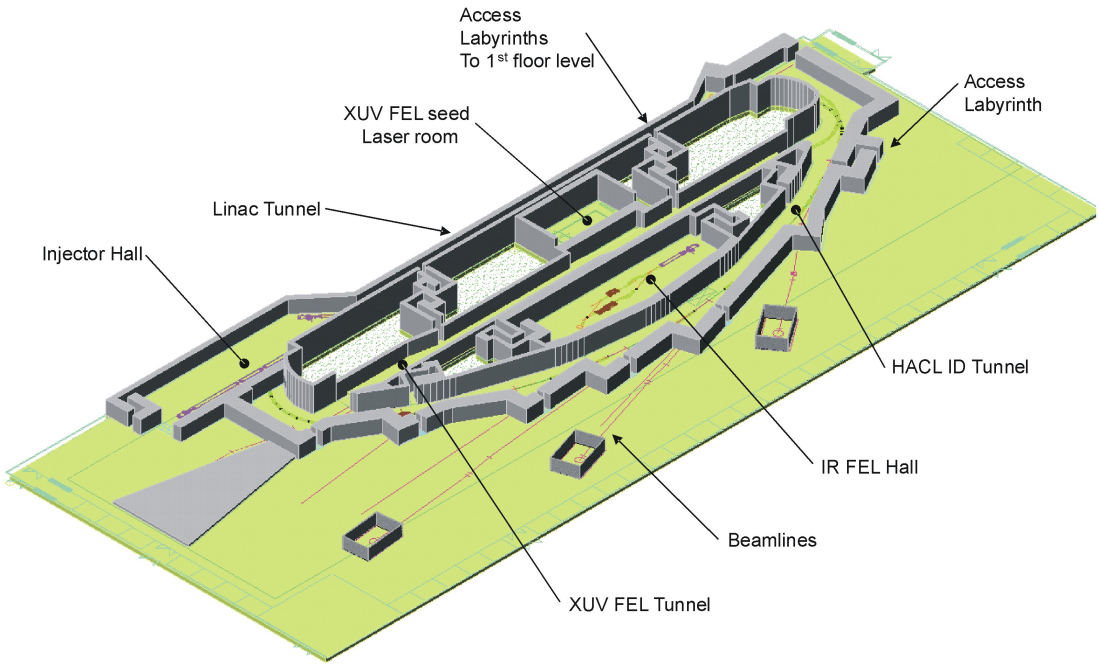

Figure 13.2 Accelerator tunnel complex

Figure 13.2 shows the concrete tunnel complex that will house the accelerator components. The walls and ceiling are shown at three metres thick but can be thinner where backfill can be

accommodated. At this stage, cast concrete is assumed to reduce costs, with removable walls at key locations to enable a staged commissioning schedule. Access holes in the ceiling will be required to build and remove the temporary walls, while a range of additional access holes will be required to lower or lift equipment from the tunnels. Two ten tonne cranes are considered adequate at present. The heaviest devices located in the tunnels will be the 12 m long superconducting accelerating modules, weighing eight tonnes. During construction the main equipment access will be through large doors constructed from removable shielding blocks. Access points through removable walls are planned at each beamline front end. To enable some operational flexibility, permanent walls are planned at the start and end of the XUV-FEL tunnel to allow access to the tunnel for planned maintenance when the high average current loop is operating.

It will be desirable to minimise the number of systems in the accelerator tunnels that could be adequately located in a more accessible location on technical gallery above the accelerator tunnel. These systems will include the magnet power supply racks, control racks, inductive output tubes, gun power supplies, 4 K coldbox and general services distribution. This will lower the thermal gain in the tunnels and ease problem solving during operation. Laser rooms for the photoinjectors and laboratories for terahertz (THz) and infrared (IR) output are located on the mezzanine level as shown in Figure 13.3. Overhead cranes allow lifting of equipment weighing less than ten tonnes from ground to mezzanine level, while an equipment access doorway at this level is approached via an elevated road ramp for the installation of heavy equipment such as the 4 K coldbox.

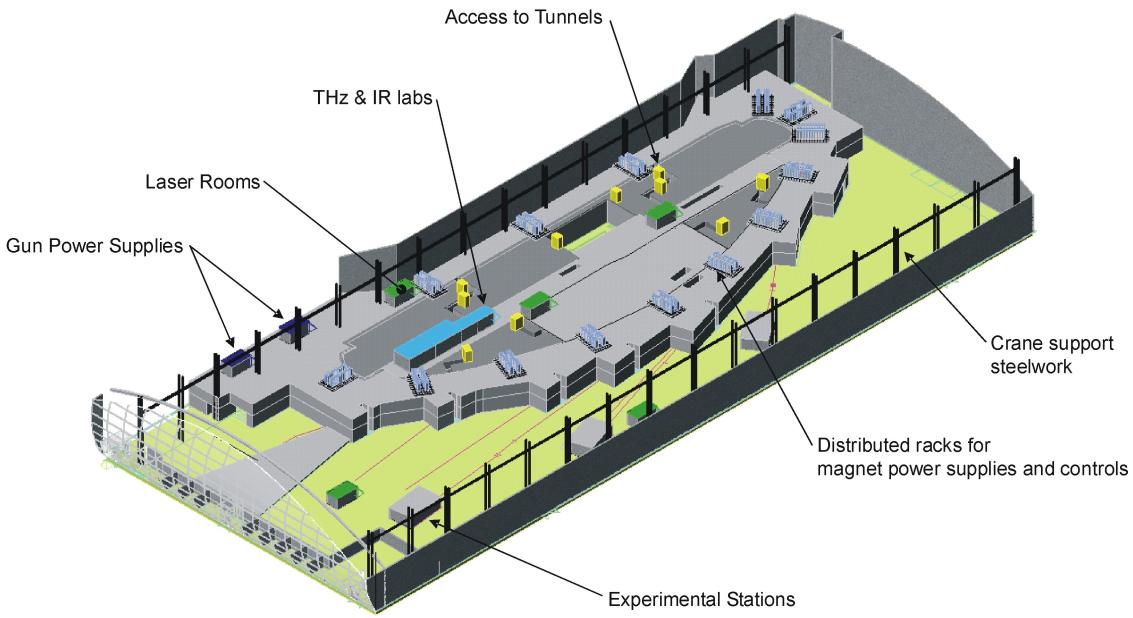

Figure 13.3 Technical gallery and mezzanine layout

13.2 Cryogenic Systems

The cryogenic system for 4GLS will be amongst the largest helium cryogenic plants in the United Kingdom to date. Although large in scale, cryogenic plants of the size and operating temperature proposed have been built and proven at other accelerators.

To fully specify the cryogenic systems for 4GLS, several key criteria are required, which at the time of writing this Conceptual Design Report (CDR), have not been finalised. Chapters 5 and 6, detailing the proposals for the injector and accelerator systems provide further information. For the purposes of this document the cryogenic requirement has been restricted to the 4GLS accelerating structures.

In order to progress the technical requirements of the cryogenic system, considered assumptions have been made for key parameters based on the experience of other accelerator laboratories (see Table 13.1). Any significant deviation from these assumptions will have an effect on the scope of the cryogenic system and the likely impact of any change is covered later in this document.

Table 13.1 Parameters of the cryogenic system

Parameter	*Value*
Operating Temperature	1.8 K
Number of Modules	14
Number of Linacs	7
Module Combined (Static + Dynamic) Heat Load	2.03 kW @ 1.8 K
Radiation Screen & RF Coupler Heat Loads (50-80K) (Static + Dynamic)	3.75 kW @ 80 K
HOM load (80K)	15.2 kW
Radiation Screen Heat Load (4 – 10K)	642 W @ 5 K
Distribution Losses	500 W @ 1.8 K
Operational Regime of RF System	Constant Wave (CW)
Operational Regime of the Cryogenic system	The 7 linacs will have different operating parameters and therefore independent control is required for each linac.
Redundancy / Factor of Safety	1.5
Flow Rate	183.7 g/s
Size of Refrigerator / Liquefier	5250 l/hr at 1.8K

Table 13.2 gives the current dynamic losses. The static and distribution losses are based on those achieved at other laboratories and are highly dependent upon the design of the cryomodules and the layout of the cryogenic system. These figures will be finalised in the TDR.

Table 13.2 Losses for the cryogenic system

Linac	Modules	Cavities per module	Total Cavities	*1.8 K losses, W* Static per module	Dynamic per cavity	Total	*80 K HOM losses, W*
LINAC 1 *10 MeV High Average Current Injector*	2	5	10	10.0	19.5	214.5	1694.0
LINAC 2 *95 MeV XUV-FEL Injector*	1	8	8	10.0	19.5	165.6	1355.2
LINAC 3 *95 MeV XUV-FEL Injector*	1	8	8	10.0	19.5	165.6	1355.2
LINAC 4 *XUV-FEL Injector 3rd Harmonic Cavity* (details to be further developed)	1	4	4	10	*	*	*
LINAC 5 *590 MeV Main Linac*	6	8	48	60.0	19.5	993.6	8131.2
LINAC 6 *200 MeV XUV-FEL*	2	8	16	20.0	19.5	331.2	2710.4
LINAC 7 *60 MeV IR-FEL*	1	8	8	10.0	19.5	165.6	1355.2
Total	**14**		**90**	**120**		**2036. 1**	**15246.0**
		Distribution Losses				500.0	W
		Total losses at 1.8K				**2536.1**	W
Total refrigeration requirement (with safety factor of 1.5)						**3499.8**	**W**
		Helium Consumption				5249.7	l/hr

** These losses are assumed to be relatively very low and will not affect the overall estimates. They are therefore neglected until the details of the 3rd harmonic cavity are further developed.*

13.2.1 Cryogenic System Overview

The initial assumptions made for this conceptual design report including a safety factor of 1.5 lead us to the proposed use of a 4 kW liquefier/refrigerator. It is probable that in order to prevent vibration caused by possible film boiling of nitrogen, helium gas at around 50 to 80 K from the refrigerator could be used to cool the radiation screen and the intercepts on the RF couplers to 80 K. This would require the size of the liquefier to be increased to around 4.5 kW. The cryogenics system is composed of several different components and is shown in Figure 13.4.

The compression system will consist of multiple compressor units, of medium and high pressures, along with oil removal and gas management systems. These will be housed in a remote plant room, ensuring no vibration from the rotating machinery is transmitted to the accelerator.

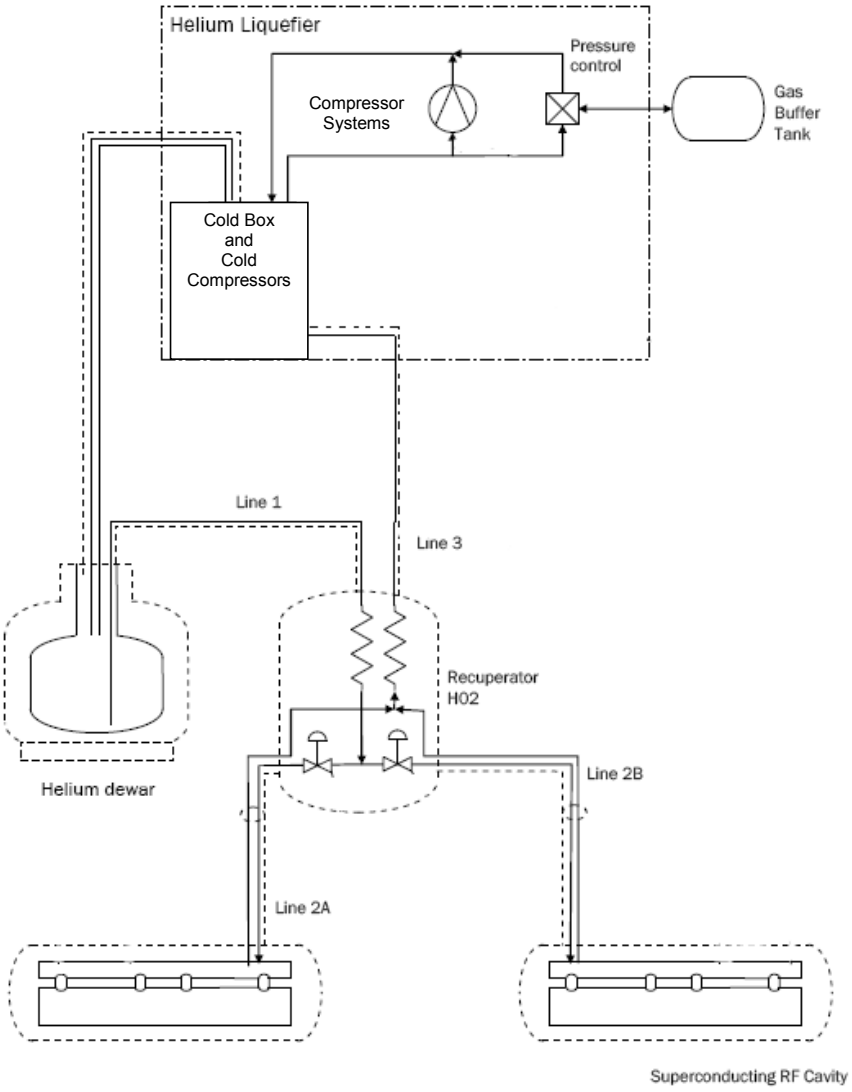

Figure 13.4 Schematic of 1.8 K cryogenic system

Assuming a heat load of 3.5kW the liquefaction capacity required will be in the region of 5250 litres per hour. Such a large scale helium liquefier will probably be of horizontal design. In order to minimise transmission heat losses it will probably be housed local to the accelerator.

Liquid storage capacity should be sufficient to allow continuous operation of the cryostats and provide resilience in case of failure. It is anticipated that the total system helium inventory will be in the order of one tonne.

To obtain temperatures at or below 1.8 K, the cryostats must be controlled at a pressure less than atmospheric. To achieve this sub-atmospheric condition, the evaporated gas must be pumped from the cryostats; this can be done by the use of cold compressors, ambient vacuum pumps or a combination of both. It is anticipated that in order to maximise operating efficiency, cold compression will be used for part of the process. There may be a requirement for one or more cold compression systems to be sited close to the cryostats. Additionally, there may be in

excess of seven 1.8 K cold boxes (or cold box units integral to cryostats) due to the different operating conditions and heat loads of each of the seven linacs. The 1.8 K cold boxes which form part of this system contain additional heat exchangers and valves. To aid in this temperature reduction, these cold boxes must be situated as close as possible to the cryostats.

In addition to the liquid helium requirement, there is also a need for large amounts of liquid nitrogen, in excess of 1300 l/h. A significant part of the cost of liquid nitrogen to the customer is the delivery from the production site to the laboratory: it may be more cost effective to have an air separation unit on site. At what point an air separation unit becomes the most cost effective option and how it could be operated will be considered in the TDR.

13.2.2 Cryogenic Systems Safety

All components of the cryogenic system including cryostats will be designed, manufactured and operated in compliance with all relevant statutory UK and EU legislation. Particular attention will be paid to the following regulations:

- Pressure Equipment Directive 97/23/EC;
- IEE Wiring Regulations 16th Edition BS7671: 2001 Amendment No2 2004;
- The Construction (Design and Management) (Amendment) Regulations 2000;
- Control of Substances Hazardous to Health 2002 (COSHH) (amended).

Once a detailed design has been agreed in principle, a 'hazard and operability' (HAZOP) study will be conducted on the entire cryogenic system. This will examine the safety of the system in order to minimise the possibility of accidents, which have the potential to damage equipment or injure personnel. The study will also characterise the operation of the system as a whole. Designers and process engineers from Daresbury Laboratory, the cryogenic system vendors and cryostat manufacturers will be required to participate in the HAZOP study.

In order to minimise the risk of venting cryogens into the buildings, the cryostat designs must include a specification of a safe working pressure, which ensures that a sufficient pressure drop is available for pressure relief devices to vent externally.

Due to the high volume of cryogens that will be in use, it will be necessary to install a multi channel oxygen depletion monitoring/alarm system. This system will include the functionality to set off audible/visual alarms, close process valves and start extract systems automatically.

13.2.3 Sensitivity to Cryogenic System Specification

This report has been based on information from Chapters 5 and 6 and also from experience at other accelerator laboratories. This section describes the impact of making fundamental changes to the assumptions made in the system overview.

13.2.3.1 Operating Temperature

All static and dynamic heat loads have been calculated based on a cryostat operating temperature of 1.8 K. Due to superconducting RF module design and also the significant increase in losses, it is highly unlikely that the operating temperature will increase. On similar systems, 1.8 K is considered to be the most efficient operating temperature.

13.2.3.2 Cryostat Design

The design of the cryostat for the superconducting RF cavities has a significant impact on the cost and complexity of the cryogenic system. The static load is relatively small in comparison to the dynamic load and makes very little difference to the capacity of the plant. However, the design of the cryostat impacts a number of areas which can affect the design of the system. The number of additional requirements at each operating temperature will affect the distribution of the cryogens and the complexity of the process control system (for example, cooling of couplers, radiation shields, etc.). The fluid dynamics of the liquid helium within the cryostat also needs careful consideration.

13.2.3.3 Number of Cryostats and Independent Control

The number of separate cryogenic modules and the level of independent control required can have a significant effect on the cost. An increase in the number of modules will increase the number of transfer lines and valve boxes required, this will increase the cost of the distribution system and also raise the static heat load. The degree to which these modules are independently controlled will have a significant cost implication. Currently, independent warm-up and cool-down of modules has not been studied in detail. This is likely to be required in the final design, as some independence will be desirable for fault conditions and possibly redundancy. Options in this area will need to be considered in conjunction with redundancy in the superconducting linac.

13.2.3.4 Size of Refrigerator/Liquefier

This system has been based on a single 4.5 K large liquefier and a number of smaller 1.8 K systems. This is proven technology and is in reliable operation at other accelerator laboratories. However, there are a number of other systems in use which could be considered. For example:

1) Two complete 1.8 K systems, one for the static load and the other for the greater dynamic load;
2) One large 4.5 K system, with a small local 1.8 K system per cryomodule;
3) Smaller multiple 4.5 K liquefiers.

Any of these options will alter the complexity of the process control and have a cost implication.

13.3 Stability

To maintain a photon beam position in the order of a few microns or better at the experimental stations on 4GLS, it is essential that measures are taken to control both mechanical and thermal stability. 4GLS must function as an integrated facility so the source, beamline optics and experimental systems must be treated as one unit, with careful attention to detail in all critical areas from the accurate alignment and positional stability of the quadrupoles and diagnostics in the accelerator to the stability of slits, mirrors, gratings and crystals in the photon beamlines.

The overall timing jitter from source to experiment needs to be in the order of 100 fs and in some cases tens of femtoseconds. Hence, the path length of the optical transport system must be stable to much less than 30 µm. Control of mechanical vibration and thermal drift is essential.

The floor for the accelerator complex and adjoining beamlines is required to be very stable. Long and short-term variations as well as higher frequency motion must also be dealt with. A stable site foundation is a crucial starting point, followed by careful design of the facility to ensure vibrationally noisy equipment is not located close to critical devices. A remote plant room at a safe distance from the main 4GLS building will house any such equipment. An air conditioning specification in the order of ± 0.2 ˚C for the accelerator tunnels, beamline optics and experimental stations will be necessary.

This section considers these points in further detail, while Chapter 14 discusses the building and air conditioning systems in more detail.

13.3.1 Ground Motion Measurements on the Daresbury Site

The techniques used to make the most recent vibration measurements are described in [1], while the measurement results are in [2]. Figure 13.5 shows the comparison of these results with those from other sites around the world.

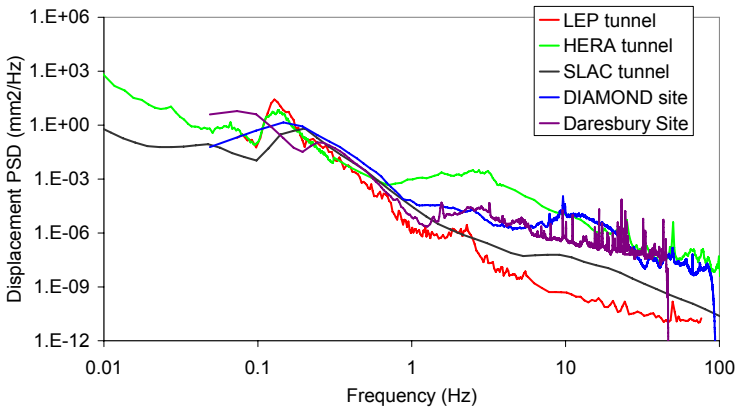

Figure 13.5 Comparison of ground motion measurements at Daresbury Laboratory with those from other sites around the world (comparison data courtesy of Andrei Seryi)

13.3.2 Accelerator and Experimental Hall Floor Slab

Once estimates of the volume of shielding required have been made, it will be straightforward to calculate the initial settlement expected due to the elastic deformation of the sandstone stratum during construction. This effect will be counteracted by the upwards motion of the sandstone due to any excavation work required, due to the removal of the loading.

It is proposed that the accelerator is built on a concrete floor in intimate contact with the un-weathered sandstone. Any areas of sandstone exposed that are not well-bonded should be excavated and filled with concrete prior to pouring the floor. It is considered that this approach, which to some extent trades the best possible deflection characteristics when a load is applied against slightly worse vibration transmission characteristics (both from within and outside the facility) is the optimum. It is not possible to stop the floor from transmitting vibration as any gaps introduced into the structure to provide breaks would always be bridged by the sandstone below. In addition, the combination of the low water table and permeable sandstone base means that there will be little seasonal expansion and contraction of the underlying stratum.

For the accelerator tunnels and experimental areas, a monolithic floor slab is desirable but technically not practical as, due to the size of the complex, the slab would crack during curing. The segmented slab arrangement will require keying techniques engineered and constructed to high standards to ensure that the floor acts as close as possible to that of a monolithic slab. In addition to lateral displacement already discussed, it is essential that angular stability is also considered. Angular stability of the light source to the optical gratings of beamlines will be required in the order of 1 μrad. Consequently the design and construction of the floor slab is crucial to meet the very high demands of 4GLS.

Some displacement due to settling of the foundation and concrete shrinkage will be inevitable. Following the initial period of settlement after the construction work the facility components will tend to move with a kind of diffusive motion which can be modelled using the ATL law. This random walk-like motion of the accelerator and beamline components must be corrected by periodic survey and realignment.

To minimise the frequency of manual survey and realignment programmes it is possible to include a remote method of realignment. This requires a source of positional information plus a motorised mechanism to move the most crucial magnets to a better aligned position.

13.3.3 Higher Frequency Motion

Even if the levels of ground motion are within acceptable limits, it is all too easy to design support structures that amplify the ground motion by a factor of ten by behaving in a resonant manner. This is most likely to be a problem in the 5 to 35 Hz range. Therefore it is necessary to undertake careful design and modelling of all critical structures, such as magnet support girder assemblies, insertion devices, optics and experimental equipment. Finite Element Analysis (FEA) will be used to predict resonant frequencies of all critical structures and the design

modified as appropriate. In the worst case, the amplitude of any oscillation can be reduced with the addition of damping mechanisms, but with good design this should not be necessary. Careful consideration will be given to determining the optimum floor-to-beam height in both the accelerator tunnel complex and the experimental hall: a lower beam height will improve mechanical stability and the effect on the absolute position of components due to thermal expansion. It will also be necessary to be careful not to introduce sources of vibration from compressors, reciprocating pumps, cooling water etc. Where possible such devices will be located in a remote plant room on a separate foundation at a safe distance away from the main 4GLS building.

Inevitably there will still be some sources of vibration in the main 4GLS building. The main accelerator and experimental floor slab will require isolation from the overhead crane supports and main building support steelwork to reduce vibration transmission from wind loading. Noisy equipment will require vibration attenuation material such as vibration isolation mats, springs, or other approaches that will require careful engineering. Decoupling of pipes that can transmit vibrations with soft bellows and spring hangers will also be required. Air flow in ducts and high velocity water cooling circuits will also require special attention to avoid resonant frequencies. Even the most sophisticated anti-vibration measures will only result in the attenuation of vibration amplitudes and not in their complete elimination.

At higher frequencies, beam-based feedback can be employed to overcome a certain amount of positional instability of the magnets, again over a frequency range that needs to be defined.

13.3.4 Considerations for Stable Beamline Optics

To prevent vibrations from the ground and air being transmitted to the optical components, optical systems must be decoupled as much as possible from the vacuum envelope, thereby reducing the effects of vacuum chamber deflections and thermal effects. Mounting of the optical mechanisms to a stable support structure constructed from materials with low thermal expansion and good vibration damping properties is good practice. Supporting structures will be rigidly coupled to the facility floor and designed to minimise resonances. Whilst air-tables and active vibration isolation techniques are widely available for isolating local systems, they are not appropriate for 4GLS where positional stability over the whole facility is required.

The temperature stability of water used for the cooling of optics will also need to be carefully considered as experience has shown that even with water regulated at a temperature stability of ± 0.5 °C, many re-adjustments of a beamline mirror are required to maintain photon beam intensity. This can be improved significantly by introducing a buffer reservoir in the cooling line before the water reaches the mirror, where the water is mixed to produce a cooling supply that is stable to ± 0.05 °C. Similar considerations are required for the cooling of the accelerator quadrupole magnets, where small changes in their position become amplified by the magnetic focussing applied to the electrons by the field producing a much larger change in position and angle of the electron beam.

13.4 Alignment

The alignment of an accelerator requires consideration of a number of stages:

- initial setting out of the walls and floor of the building;
- fiducialisation of components to references, e.g. magnets to their magnetic centres;
- pre-alignment of vessels and magnets on girders in an assembly area;
- positioning of components in the tunnel complex before the beam is switched on;
- adjustment of magnets from beam based alignment results after the machine is running;
- monitoring and correcting for long term drift.

There are two general types of equipment used for these stages: generic and integral. Generic survey equipment can be used for a number of different tasks, types of such equipment are; laser trackers, total stations, digital levels and dial test indicators (DTIs). Each of these equipment types has advantages and disadvantages. Other generic equipment types may be further developed by the time 4GLS requires surveying, including indoor global positioning system (GPS), portable precision measuring arms, and laser scanners. All of this equipment is fairly versatile and does not inherently affect the design of the machine. Further to generic equipment is integral equipment. These are systems integral to the design of the machine such as hydrostatic levelling, which cannot easily be removed from the facility, and is generally set up to monitor a few pre-selected points to establish a height datum.

13.4.1 Initial Setting out of Walls and Floor

A primary survey network will be used, consisting of a number of pillars firmly attached to the bedrock located outside the area occupied by the building. The survey monuments on the pillars generally allow for force-centring of theodolites and total stations to establish and maintain the network, while the building is being constructed. Force-centring the theodolites ensures that they are on a stable platform while survey work is undertaken. Required accuracy for dimensions taken from these posts is in the order of millimetres.

13.4.2 Fiducialisation and Pre-Alignment

It is important that fiducialisation of accelerator components is done as accurately as possible as any error takes up part of the overall ‘error budget’. Co-ordinate measuring machines (CMM, see Figure 13.6) will be used for smaller components as they are very accurate, require little set-up time, and are able to measure a complete component from one set-up. They are prohibitively expensive for large components, and so this will be done using other methods, for example, laser trackers.

Once the fiducials on the components have been measured, the components will be pre-aligned on a girder, generally performed in a temperature controlled, stable environment.

The exact method of alignment for the magnets will depend upon the number of fiducials chosen. Currently magnets and vessels are generally positioned using laser trackers, but it may be advantageous to do this using a simple indoor GPS network.

Figure 13.6 A CMM at Daresbury Laboratory measuring the repeatability of the EUFEL optical cavity mirror mechanism

13.4.3 Positioning of Components in the Tunnel Complex

There are a number of different philosophies for positioning girders within the tunnel complex, very generally, the two-dimensional plus one-dimensional (2D + 1D) and the three-dimensional (3D) approaches. Both of these methods require carefully laid out survey networks within the tunnel complex to avoid errors through lateral refraction, and are capable of delivering the required geometrical accuracy.

The 3D approach uses free-stationing of laser trackers to measure all the fiducials on the girders with respect to a reference network of points (Figure 13.7). The 2D + 1D approach generally uses total stations to measure the X and Y values of the fiducials and reference network points, and precision levels to measure the Z values. Within the 2D + 1D approach there are further options, free-stationing or force centring. Force-centring requires more expensive reference network points, however, once they have been established, instrument set-ups are faster.

Once the positions of the fiducials are known, the components are positioned by motorising the girders or through manual adjustment. Many different methods are used to adjust the position of girders including six-strut systems, hexapods, cams, three-jack systems, and wedge jack systems. These methods need to be analysed with respect to performance, cost, ease of adjustment, vibration characteristics, and stiffness before a final choice can be made.

While the girders are being moved it is necessary to track their position, and a selection of different feedback methods are available. Generic survey equipment such as DTIs, precision levels, and laser trackers can be used or systems such as encoders or hydrostatic levelling

systems can be made integral to the girder design. It is likely that a combination of different techniques will be required.

Figure 13.7 Magnets on the ERLP are positioned using the 3D free stationing approach and a laser tracker

The survey network in the tunnel complex will also require linking with the technical gallery and experimental hall survey networks to ensure good integrity of theses networks across the entire facility. Investigations will be made into the different approaches of relating the tunnel complex to these other areas.

13.4.4 Beam Based Alignment

This occurs after the beam is switched on and is used to assess any final minor adjustments of magnets/girders. Components are adjusted as described in the previous two sections, depending upon whether an individual magnet or a complete girder requires adjustment.

13.4.5 Long Term Drift

Monitoring of long term drift can be done in a variety of ways, using either generic or integral measuring devices. Generic devices can only be used during accelerator shutdown periods, while integral measuring devices can be used at any time and can monitor any trend in the drift, allowing for readjustment of components to be better planned.

13.4.6 Conclusions

The philosophy of alignment chosen will have an impact on the girder, and adjustment mechanism design. While choosing a philosophy during the Technical Design Report phase of the project, all stages of operation of the facility will be considered, not just the issues during installation.

13.5 Magnets

The majority of the lattice magnets within 4GLS are ‘conventional’ in the sense that they are of the same type as those for familiar particle accelerators such as SRS, Diamond and ERLP, and include DC dipoles, quadrupoles and sextupoles. Although all the 4GLS magnets will require tight engineering tolerances and careful design, most are not expected to be any more challenging than those used in other modern particle accelerators. In the sections below the magnet designs for the different sections of 4GLS, as currently envisaged, are discussed: these include a small number which have unusual or demanding features.

No pulsed magnets are presently needed within the 4GLS design.

13.5.1 High Average Current Outward and Return Arc Magnets

The two High Average Current loop (HACL) arcs are each built up from six identical modules, with a total bend of 120º in each arc. A diagram of one of the modules is shown in Figure 13.8.

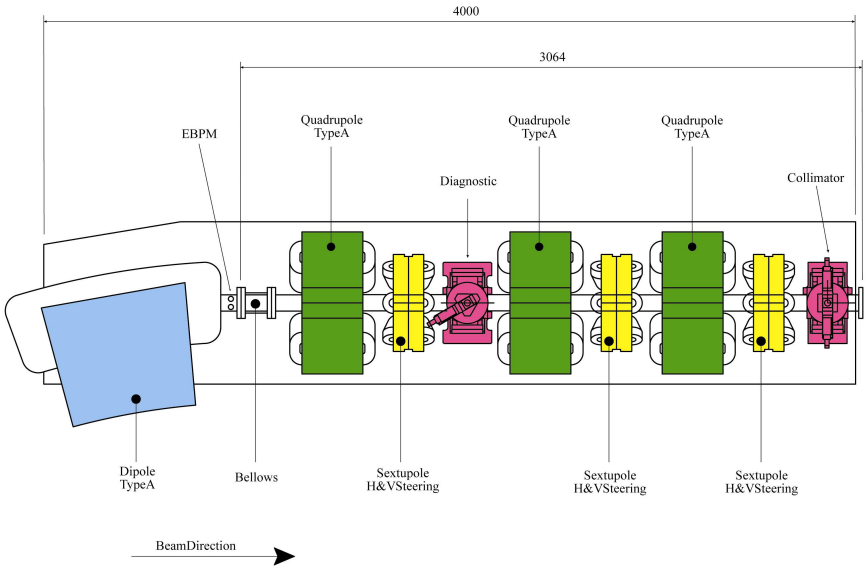

Figure 13.8 HACL arc module (dimensions are mm)

It can be seen that in addition to the single dipole in each module, three quadrupoles and three sextupoles are required. These are completely conventional magnets, with the dipole operating at a modest flux-density of 1 T at an electron energy of 600 MeV and the quadrupoles with a maximum gradient of 20 Tm^{-1}; with the anticipated small inscribed radius in the quadrupole (27 mm) this is an easily achievable gradient.

These magnets form a basis for the complete facility; it is economically attractive to use identical designs in other parts of the beam-transport system, wherever similar parameters allow. Whilst, therefore, the arc dipole (described as 'Dipole Type A' in the diagram) could be either an 'H' or a 'C' design, the use of the 'C' yoke provides easy access to vacuum vessel and allows radiation beam-lines to diverge tangentially outwards through the jaws of the dipole. It is

therefore recommended for this generic dipole magnet. The current feasibility design indicates the following set of parameters for the A type dipole:

magnetic length:	0.7 m;
bend angle:	20º;
flux density at beam:	1.0 T.

Likewise the arc quadrupole ('Quadrupole Type A' in the diagram) is of a standard construction, with a design which can be used elsewhere in the facility. Current estimated parameters are:

magnetic length:	0.3 m;
inscribed radius:	27 mm;
maximum gradient:	20 Tm^{-1}.

13.5.2 High Average Current ID Arc Magnets

Five arcs separate out the six straight sections which are available for insertion devices; a diagram of one of the five arc modules is given in Figure 13.9:

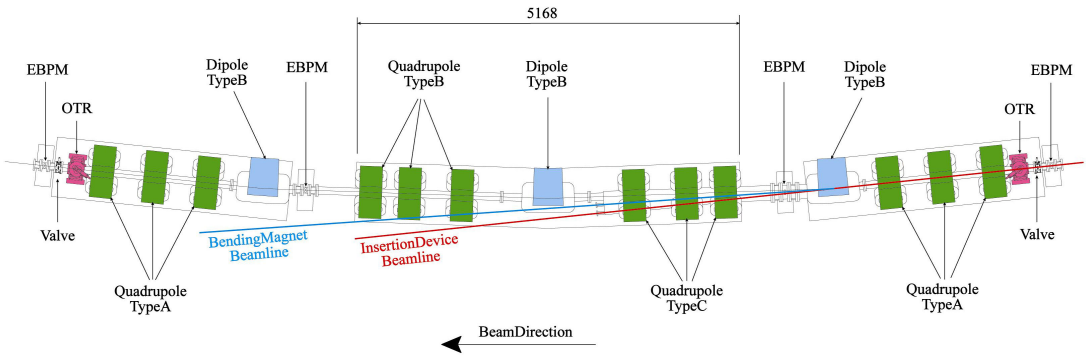

Figure 13.9 HACL Insertion Device Arc modules (dimensions in mm)

The bending magnets in the ID arcs have significantly different parameters to the outward and return arc dipoles; they are shorter and weaker and consequently a different design is required; they are therefore designated as 'Dipole type B'. Current parameters are:

magnetic length:	0.4 m;
bend angle:	4º;
flux density at beam:	0.33 T.

Again, for flexibility and access, a 'C type yoke' is proposed.

The quadrupole magnets in the ID arcs will probably require three different designs. As indicated in the diagram, the extreme up-stream and down-stream quads can be of the 'Quad type A' design, with the same gradient and excitation requirements. However, the two central triplets need to make provision for radiation emerging from up-stream insertion devices and

bending magnets, which would clash with the outward return yoke of a conventional quadrupole. This is a well understood and documented problem [3, 4].

In the case of the quadrupoles labelled 'Quad B' in Figure 13.9, the solution adopted at both the ESRF and Diamond is fully adequate. The magnetic return paths are restricted to the top and bottom yoke limbs and the side limbs are replaced by non-magnetic support structures. This then allows the geometry in the outer limb to be adjusted to allow the passage of photon beams at various radial positions, without affecting the magnetic behaviour of the quadrupole. Photographs of Diamond quadrupoles constructed to accommodate two extreme cases of photon beam positions with respect to the electron beam are shown in Figure 13.10. This solution is suitable for the 4GLS Quad B magnets, which otherwise will have identical parameters to the Quad As.

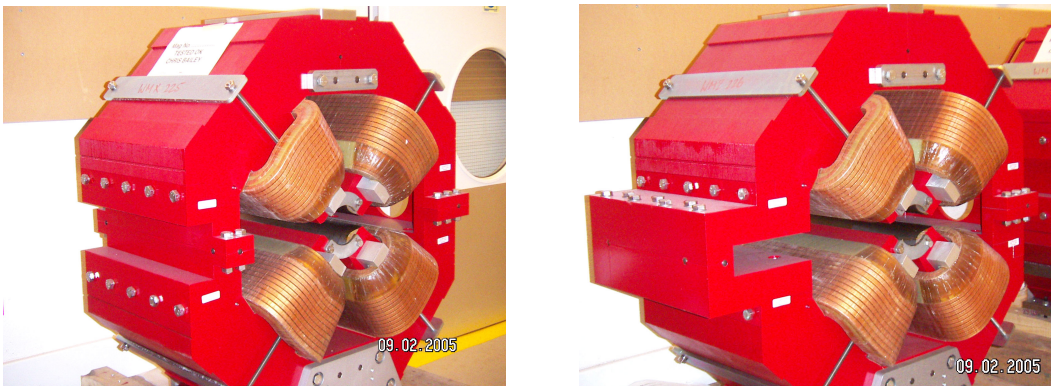

Figure 13.10 Photographs of two Diamond quadrupoles constructed to accommodate the extreme cases of photon beam positions

The quadrupoles indicated as 'Quad C' in Figure 13.9 are closer to the photon beam source points than the type B's and the emerging radiation will have only a small radial displacement outwards from the electron beam. This corresponds to the region occupied by the quadrupole's outer pole tips, where the vertical aperture is a minimum. This constriction at the pole tips is illustrated in Figure 13.11, which is also a 'close-up' of a Diamond production quadrupole.

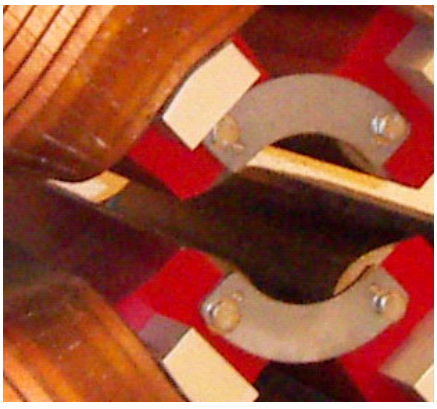

Figure 13.11 Close-up of the pole region of a Diamond quadrupole, showing vertical constriction region

Current estimates indicate that, with a 27 mm inscribed radius, the vertical gap between the pole tips in the quadrupole C position will be in the order of 12 mm, pole tip to pole tip. However, a terahertz beamline will need a larger vertical aperture in this region. There are two possible solutions - either to significantly increase the inscribed radius of the C type quadrupole or to insert a mirror for vertical reflection into the photon beamline prior to this quadrupole triplet. The latter solution is proposed for 4GLS and will be included in the beamline designs for the TDR.

13.5.3 XUV-FEL Branch Arc Magnets

This arc, which will handle 750 MeV beams, is required to provide a 180º bend with appropriate focusing. This will be achieved by eight identical modules plus an additional dipole. One of the modules is shown in Figure 13.12.

The dipole in these modules can have an identical geometry to those in the HACL arcs (i.e. the type A dipole) but, because of the higher energy beam, they need to operate at a slightly higher flux density, as indicated by the following parameters:

magnetic length:	0.7 m;
bend angle:	20º;
flux density at beam:	1.25 T.

The value of 1.25 T is easily achievable and the type A dipoles would be engineered to operate at this level. The small increase in capital cost associated with this enhanced performance is more than offset by the saving resulting from having common designs for the HACL and XUV-FEL arcs.

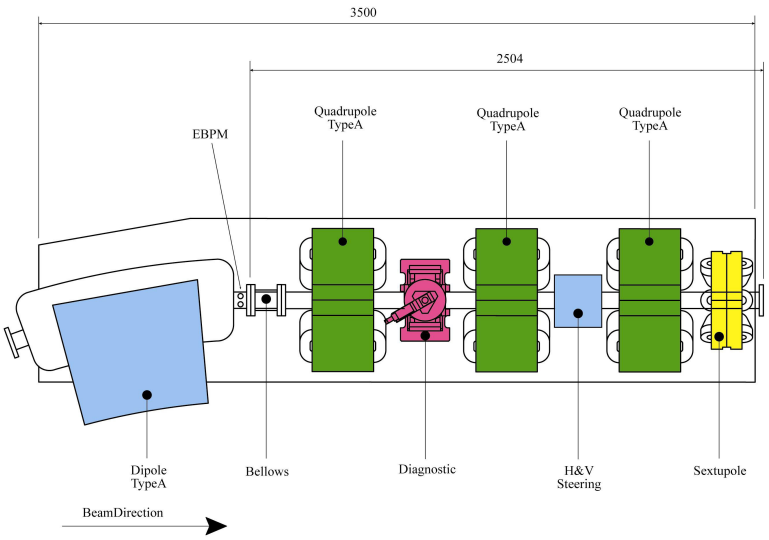

Figure 13.12 XUV-FEL branch arc module (dimensions in mm)

The quadrupoles in the XUV-FEL are currently expected to have identical specifications to those needed for the HACL arcs and so a common design can be used (the type A quadrupole).

13.5.4 Solenoids

Two identical solenoids are used in the XUV-FEL arc to provide transverse rotation to the beam at the entrance and exit of the 180° arc. Each solenoid has a magnetic length of 500 mm, a longitudinal field of 0.35 T and provides a rotation of ~ 2°. A simple model has been developed using the Radia code to confirm that the field level required is practical and also to perform particle tracking to measure the rotation applied. The design and manufacture of these solenoids appears to be quite straightforward and offers no particular concerns.

13.5.5 Spreader Magnet

A spreader magnet is used after the main linac to separate the beams of different energy for the two arcs. This magnet follows a standard dipole of ~ 0.5 T which separates the beams by 2°. One meter downstream of this dipole the beams will be transversely separated by ~ 35 mm and at this point a spreader is envisaged which bends the two beams in opposite directions to each other to enhance the separation to 10°. The specification for the spreader is a field strength of ± 0.35 T over a 400 mm magnet length. Clearly each beam needs to see a dipole field of opposite polarity in order to bend in different directions and this will be a challenge given the small separation between the two beams. An electromagnetic solution will be difficult since the space available for coils is very limited and it seems likely that a permanent magnet solution will be used.

An alternative design might be to use a large aperture defocussing quadrupole that is centred between the two beams so that each goes through off-axis. One beam will see a positive field and the other a negative field as appropriate. Simple modelling suggests that a typical quadrupole field would be sufficient to obtain the necessary beam divergences but accelerator physics studies are required since this would clearly be a change to the beam optics.

Although the magnet specification looks achievable, one concern will be the ability to change the field level seen by one beam without the other being affected. Adjustment of this magnet could be quite an awkward procedure due to the coupling of the two beams and so additional correctors may need to be included within the overall design to achieve independent beam tuning.

13.6 Vacuum Systems

The ultra-high vacuum (UHV) levels in an electron accelerator are such that it is not pressure that is important; rather it is the number density of gas molecules inside the vacuum envelope. Number density plays an important role in two general types of process, *viz*., scattering and ionisation, and impact rate on surfaces.

A full discussion of the various processes is beyond the scope of this report. We simply note that in 4GLS, processes to be minimised include -

- the build up of contaminant layers on optically-reflecting surfaces such as *in vacuo* FEL mirrors (although it should be noted that IR mirrors are less susceptible to hydrocarbon contamination – the most common type – than ultraviolet or visible light mirrors);
- cryodepostion of contaminant layers on the cold surfaces of superconducting cavities.

Ion impact on surfaces leads to damage of the structures. This is likely to degrade delicate multi-layer mirrors. GaAs cathodes in the photoinjector are known to be particularly sensitive to damage caused by the impact of hydrogen ions, which are the dominant gas species to be found in most accelerator vacuum systems.

The requisite outgassing rates and chemical cleanliness will be obtained by the application of well-characterised processing techniques. CCLRC Daresbury Laboratory has many years of experience of such processing, and possesses a unique body of expertise in this area which has been documented as a series of procedures and specifications [5].

In addition to chemical cleanliness, the photoinjectors and the superconducting cavities are sensitive to particulate contamination which leads to enhanced field emission of electrons. Therefore steps have to be taken to minimise particulate counts inside the vacuum envelope.

It is important that these different aspects of vacuum – pressure level, chemical cleanliness and particulates - are distinguished and treated separately.

13.6.1 Pressures and Cleanliness Required in Individual Areas

13.6.1.1 Photocathode Injector and Light Box

The requirements for high quantum efficiency cathodes in the photoinjector guns places stringent vacuum requirements on the gun chamber, since hydrogen ion back bombardment of the photocathode degrades its performance. To obtain reasonable cathode lifetimes, the partial pressure level of hydrogen in the gun chamber must be below 10^{-11} mbar.

Good UHV cleaning techniques will be needed for the gun chamber and internal components. For stainless steel components, the standard “full” DL chemical cleaning process followed by a vacuum bake at 300 C or more for a minimum of forty-eight hours will be applied. It may be necessary to use vacuum fired stainless steel as the main chamber material to reduce hydrogen

outgassing. If the vessel is electropolished to remove short wavelength roughness, then air baking should be done after polishing to deplete the surface layers of hydrogen. The bellows will be treated with particular care to ensure cleanliness and the ceramic should be air fired at as high a temperature as possible before flanges are welded on.

13.6.1.2 First Transfer Line

To minimise gas "beaming" back onto the photocathode, this part of the machine should be at a pressure in the low 10^{-10} mbar range. Insofar as is possible, these components will be treated as for the gun itself.

13.6.1.3 Superconducting Linear Accelerators

The linacs will be superconducting RF structures. It is likely that they will possess no applied vacuum pumping and no pressure measurement devices. When cold, they act as intrinsic pumps and the internal pressure will be very low. The main gas source will be gas flow from the warm bore sections on either side. These will need to be maintained at a sufficiently low pressure that beaming does not lead to build-up of cryosorbed layers of a thickness which affect the RF performance in reasonable operating times. This may require some measure of differential pumping at each end.

Initially, the linacs (warm) will be pumped through the beam entry and exit ports. The pressure required before cool down will be low enough to minimise cryodeposition of gas on the surface.

Waveguides and cryostat insulating vacuum will operate at pressures between about 10^{-4} mbar and 10^{-5} mbar respectively, with no stringent cleanliness requirements.

13.6.1.4 Transfer Lines, Return Path and Machine Branches

The pressure level along the electron paths is determined by ion effects on the beam and an average pressure of about 5×10^{-8} mbar is expected to be adequate. The requirement to minimise gas bremsstrahlung radiation for safety may demand a lower pressure. Preservation of the optical surfaces in the VUV-FEL cavity and close-in optics will also require lower pressures.

Pressure levels in beam tubes not traversed by the electron beam (optical paths, etc.) will be determined individually, once the appropriate limitations are understood. It may, for example, be necessary to have a slightly better pressure in the mirror chambers to prevent mirror degradation. Differential pumping may be required to minimise gas transfer between various parts of the machine.

13.6.2 Particulate Control

All items will have to be particulate "free" and installed under controlled conditions. Generation of particulates inside the vacuum system will have to be minimised.

It is not sufficient to ensure that the sensitive areas of the machine are particulate "free". Experience shows that particulates readily migrate so that if there is a source of particulates somewhere, undesirable particles will eventually turn up where they are not wanted. The standard to be aimed for inside the machine is that it should conform to Federal Standard Class 10 (equivalent to ISO Class 4). [6]

Suitable preparation, handling, cleaning and monitoring techniques and procedures have been developed at CCLRC Daresbury Laboratory during the construction of ERLP.

13.6.2.1 Design Considerations

All moving pieces of equipment such as beam screens, moveable impedance reduction tapers and valves should be designed to minimise the rubbing of surfaces together.

Viton sealed valves (especially those with vulcanised seals) are preferable to metal sealed ones. This must be counterbalanced by two factors: (a) the degradation of Viton due to radiation exposure and (b) the outgassing is too high for use in areas such as the gun, where, in any case, high temperature bakeout is required.

In the mechanical design of vessels, etc., attention should be paid to ensuring that there are no nooks, crannies or crevices which can act as temporary particulate traps. Many of the design approaches required are similar to good ultra high vacuum practice and are well understood.

To minimise the possibility of migration of particulates from ion pumps and gauges, they will be installed below the machine plane so that the pump or gauge body forms a well to maximise particulate trapping. Pump and gauge ports should be screened by a discharge shield if there is no other form of RF screening installed for impedance reasons. Roughing pumps will be selected from those types known to minimise particulate generation.

13.6.2.2 Pre-installation Cleaning and Assembly

The normal cleaning processes adopted at CCLRC Daresbury Laboratory for vacuum vessels and components, which involve rinsing with filtered high pressure clean water jets, help to remove particulates from vacuum components. To assist this process, vessels are suspended in a way which maximises the possibility of particles being flushed out. A final gas flushing stage with particle agitation has proven to be highly successful in removing particulates.

Following cleaning, individual vessels are sealed off in a dust "free" atmosphere and smaller items are bagged under dry, dust free nitrogen. Ideally, all assembly work should take place in a ISO Class 4 clean room, in order to ensure Class 10 conditions inside the completed machine. However this is impractical and would be extremely expensive. Girder sub-systems will be assembled in an off-line area which will be a clean room of Class 100 (ISO Class 5) standard or better. It has been demonstrated at CCLRC Daresbury Laboratory that local conditions equating to Class 10 (ISO Class 4) or better can be established and maintained during assembly work by means of local filtered air flows and plastic screening curtains inside the Class 100 area (Figure

13.13). Completed sub-systems will be filled with particulate-free dry nitrogen or air and sealed until required for installation.

Figure 13.13 ERLP gun being assembled in the ISO class 4 clean room at Daresbury Laboratory

In the machine hall local cleanliness approaching Class 100 or better will be achieved by erecting "tents" of clean plastic around work areas and using locally filtered, dry air flows, directed downwards where possible. The exterior of all items will be cleaned thoroughly before opening vessels, etc. For smaller jobs, it may be possible to set up systems analogous to Class 100 (ISO Class 5) glove boxes around the items to be manipulated, with workers outside the clean area wearing gloves and armlets. In either case, it is imperative that a thorough and careful clean-down of the area and items to be worked on is undertaken prior to the erection of the tent; with a final clean just before switching on the air flow. A particulate count should be made on the exhausting air to verify satisfactory conditions exist before any sealed item is opened.

13.7 Control System

13.7.1 Introduction

The 4GLS control system will be a facility-wide monitoring and control system integrating all parts of the 4GLS accelerator including experimental beamlines. The control system will extend from the interface of the equipment being controlled through to the operator. It will include all hardware and software between these bounds: computer systems, networking, hardware interfaces and programmable logic controllers.

The control system will not include data acquisition for the experimental stations and will only provide control of those elements and devices that are considered to be part of the beamline rather than the experiments themselves. The personnel safety system will be interfaced to, and monitored by, the 4GLS control system. Timing and synchronisation of the laser(s), RF and experiments is covered in Chapter 11 and is not considered to be part of the control system. A separate event synchronisation system will be implemented as part of the control system to ensure synchronisation of critical control operations and to provide a common high-resolution time-stamping capability.

13.7.2 Architecture

The control system will adopt the standard three-layer client/server architecture. This is a well tried and tested approach that lends itself to incremental development and ease of future expansion. It will use a proven software tool kit with well-defined interfaces at both the server and client to enable fast integration and development. It will enable the use of commonly available hardware and provide a collection of ready-to-use application software and device drivers.

The various elements of the control system will be connected to a conventional 100 Mb or faster Ethernet network. This should be a private class C network connected to the site network infrastructure via a router. Access will also be provided to the site office network. Wireless access will be provided in the accelerator halls to enable quick commissioning and maintenance to be carried out using laptops next to the relevant equipment.

Standard commercial PCs will be used as operator interface consoles. Both the Windows and Linux operating systems will be supported although it will not be possible to run all applications on either platform. A preferred option will be specified with the other system being available to support specialised application software.

Application software will be installed on a central file server rather than on the local hard disk to ensure consistent operation from any console on the control system network.

A number of development languages and tools will be supported. These are expected to include: C/C++, Java, Tcl/Tk and Visual Basic.

13.7.3 Application Software

The great majority of the application software requirements for commissioning and operating 4GLS can be met by a limited number of generic applications:

- **operator menu bar** - provides single-click access to all key operator facilities;
- **graphical display manager** – for designing and displaying graphical control panels used to produce a wide range of screens ranging from a high-level overview of the whole accelerator down to detailed engineering information for a single device;
- **plotting** – a general purpose stripchart or trend plotting application should be available that will display one or more parameters plotted against time;
- **alarm management** – a set of coordinating applications to detect, filter, categorise, display and log alarm and fault conditions from any part of the control system in a uniform manner;
- **archiving** – a series of tools is required to collect and archive the state and/or value of specified devices at a regular interval (typically < 1 Hz) and store in a database. A corresponding tool will be used to retrieve and display the information;
- **event capture** – in addition to slow archiving, there is a need for a high speed (typically > 1Hz) "transient capture" mode of archiving that can be triggered by certain pre-defined events such as a beam-loss or a quench of the cryogenic system;
- **logging** – all significant control events and operations should be recorded and archived by a central logging system. A suite of electronic logbooks should be available;
- **data analysis** – wherever possible, standard commercial packages should be used to perform data analysis and processing.

13.7.4 Equipment Interface

In order to ensure uniformity of design across 4GLS it will be necessary to specify a number of supported interface standards that should be used when interfacing plant into the control system. These standards should be used wherever possible although it may be possible to use alternatives for certain specialised equipment.

- **analogue** – the preferred option will be ± 10 V high impedance inputs and outputs controlled or monitored to 16 bit precision. Simple low-pass filtering may be provided by the control system if required; more complex filtering or signal processing should be performed within the equipment;

- **digital** – optically isolated digital input and output signals at either TTL or 24 V logic levels will be provided;

- **serial** – serial interfaces are often used to interface to devices with low data rate requirements such as power supplies and vacuum instrumentation. The 4GLS control system will support a number of physical standards including RS232, 422 and 485;

- **field bus** – field buses are widely used to connect intelligent controllers to the control system. CANbus, GPIB and Ethernet will all be supported in the 4GLS control system;

- **motion control** – a number of alternatives are available for control of motor systems including serial or Ethernet interfaces for intelligent systems or direct motor control from within the control system.

13.7.5 Equipment Protection

A specialised equipment protection system will be provided based on that originally developed for the SRS and further enhanced for use on ERLP. It will provide low-level interlock protection of critical devices as well as providing a consistent status control mechanism for the operation of non-intelligent devices such as vacuum valves, simple power supplies etc.

13.7.6 Machine Protection

The Beam Loss Monitoring and Machine Protection Systems for 4GLS are vital areas required both for efficient commissioning and for hardware protection during operation.

13.7.6.1 Requirements

The requirement is to produce a system which will, in the event of a mis-steered beam, prevent vacuum contamination and damage to vital machine components. The system must be able to detect a mis-aligned beam and return the machine to a safe operating level before damage to vacuum or machine hardware can occur. The system should take into account the different operational modes of the machine, including train length and beam path.

At this time it would be reasonable to assume that the systems being developed for ERLP will be used for 4GLS: these are heavily based on those currently used on ELBE at Rossendorf.

13.7.6.2 Long Ionisation Chamber (LIC)

The LIC system uses a series of air filled coaxial cables which will detect the ionising radiation emitted when electrons hit an obstacle. A chamber will be mounted along each section of the machine at a uniform distance from the design orbit to give good accuracy and resolution.

13.7.6.3 Beam Loss Monitors (BLM)

The BLM system uses the beam position monitors (BPM) to calculate the beam current level at various points around the machine. A comparison between two points will show a reduction in current when a mis-steer occurs.

13.7.7 Event Synchronisation

One of the major difficulties with a network distributed control system is the synchronisation and accurate time-stamping of events spread across several physically and geographically separated systems. An example of this is the simultaneous measurement of beam position around the entire beam transport system. This operation will typically require the involvement of a number of front end computer systems. Synchronisation hardware developed by APS and further enhanced by SLS and Diamond is available to coordinate software operations and to produce timing output signals with an accuracy of less than 1 ns.

13.7.8 Digital Feedback

Digital feedback systems will be required in a number of places on 4GLS. The primary requirements are:

1. Stabilisation of the RF field within the accelerating structures. There are a wide range of processes that can affect stability of the amplitude and phase of the RF field within the superconducting accelerating structures of the linac. These microphonics must be reduced to acceptable levels by the application of feedback and feedforward systems. This can be achieved using either conventional analogue techniques or by utilising a fast digital signal processing-based digital system such as recently developed for use on the Cornell energy recovery linac project. Although state-of-the-art techniques are required designs already exist that can be used as the basis of a system for 4GLS.

2. Global stabilisation of electron beam position within the accelerator. The performance is expected to be similar to that normally required for a 3rd generation light source for which a number of proven designs exist.

3. Local stabilisation of the photon beams from the various available sources. Again, the performance is expected to be equivalent to 3rd generation sources using conventional techniques and designs.

13.7.9 Signal distribution

Key diagnostic signals will be made available for monitoring in the control room by test equipment such as oscilloscopes, spectrum analysers etc. The system will use a combination of digital multiplexing and analogue multiplexing to transfer the signals over from the plant to a diagnostic patch panel in the control room. There will also be the option of monitoring remote

test equipment through the control network, or integrating data from remote measurement devices directly into the control system.

13.7.10 Control Room

The Control Room will be controlled from a dedicated room. The operator interface will be through workstations on the control system network. There will be a limited requirement for hardwired interfaces to technical system such as personnel safety lockout keys and wide band connection to monitor RF signals.

An annex to the control room will house the central computer systems that make up the control system. In this area all network cables connecting the central computers to the control stations will be terminated. Also located in the annex will be central systems for generating timing and event information and managing global machine protection. The Control Room should also have adequate heating, ventilation and air conditioning (HVAC) facilities.

13.7.11 Conclusions

On the whole, the slow controls requirements for 4GLS do not differ significantly from those required by a conventional 3rd generation light source and so should not present any major difficulties in design and implementation. There are however, a small number of areas that need to be better understood before a full design can be completed. These areas are:

- digital feedback and feedforward systems for stabilisation of the RF field in the accelerating structures;
- digital feedback systems for global stabilisation of the electron beam position within the accelerator;
- digital feedback systems for local stabilisation of the photon beam position;
- the interaction between the control system and the timing and synchronisation system.

In addition to these areas, work also needs to be done to evaluate a number of different control system software toolkits to decide on the correct choice for 4GLS.

13.8 Electrical Engineering

This section is focused on three main areas; general electrical distribution, power converters and motion control. A number of assumptions have been made to assess performance in particular comparisons with 3rd generation light sources.

13.8.1 Mains Electricity

Power for the facility will be provided via the existing Daresbury Laboratory main 11 kV substation from which a number of 11 kV feeds will be run to the 4GLS building and associated plant rooms.

13.8.1.1 Transformers

11 kV/400 V transformers will be required in or close to the 4GLS building to feed the main distribution 400 V switchboards. Loads are likely to be segregated into areas such as power converters, beamline and general building and then fed via 400 V switchboards supplied through separate 11 kV ring-mains or radial feeders. The various types of transformer available will be assessed taking into account capital and running costs including environmental impact and location restrictions.

13.8.1.2 Back up Power

Limited back-up power (uninterruptible power supplies and possibly generator) will be provided for important control equipment and building services plant (see section 14.4.1.1).

13.8.1.3 Harmonic Suppression

The site will comply with the Electricity Association Engineering Recommendations G5/4.

The techniques to be considered will require analysis of current harmonic levels on the site and likely future additions due to new facilities. Suitable harmonic suppression equipment can then be specified. This is likely to include some or all of the following:

- vectored 11 kV/400 V transformers;
- active filters;
- passive filters.

13.8.1.4 Power Factor Correction and Flicker

An assessment of the anticipated power factor for the facility will be undertaken and appropriate correction measures will be provided in accordance with value engineering considerations and Daresbury Laboratory's present charging structure for electricity.

As a precautionary measure space, and, if appropriate, switches will be provided so that further power factor correction equipment can be added if future tariff charges justify it's installation.

An assessment of the anticipated flicker caused to the supply network by the facility will be carried out in line with Electricity Networks Association Engineering Recommendation P29.

13.8.1.5 Earthing and Bonding

Earthing of the 11 kV and 400 V mains systems will be carried out in line with the standards required by BS7671, BS7430, BS IEC 61000-5-2 and The Electricity Supply Regulations of 1988.

The following items will be bonded to the earthing network:

- building structure;
- mechanical services entering/leaving the facility;
- lightning protection system;
- all trays/trunking/ distribution boards/ cable armouring.

Extensive interconnected bonding will minimise circulating noise currents and reduce overall levels of interference. This is considered essential for a world class research facility where precise control, stability and measurement of very small signals is fundamental to its operation.

13.8.2 Power Converters

13.8.2.1 Introduction

The main magnet power converters for 4GLS are all DC supplies. The power converters should be rated for maximum operational energy plus a 10% safety factor on both current and voltage, plus an additional 5% on the voltage to allow for cable voltage drop.

It is anticipated the electron beam transport system will be divided into sections each with its own dedicated instrumentation area. The power converters for the dipole, quadrupole and sextupole magnets will all be unipolar, as opposed to the correction power supplies, which are bipolar. These instrumentation areas will house racks for magnet power supplies, vacuum pump supplies and control & instrumentation equipment. The dipole converters may need a dedicated room due to their predicted higher power ratings.

The voltage drop in cables from the instrumentation area to each magnet have, non-negligible effects. The access arrangements (labyrinths) into the accelerator tunnel and the cable's cross-sectional area, determine both the voltage drop and the power loss in each cable. These calculations should be considered when assessing the loading on the heat management systems of the accelerator tunnel and the output voltage ratings of the power supplies.

The current for each magnet family will be optimised to ensure a balance between simplification and feasibility of the magnet design against minimising the losses in the cable and power converter efficiencies. A simplistic view is the number of turns and the current density for each magnet are fixed and only the conductor length increased. The power rating for each magnet type will then be controlled by the voltage level only. This allows common power converter

units to be specified, minimising the required spares and simplifying replaceability. It is envisaged that the power ratings for the individual units will be < 3 kW for the quadrupole magnets and < 1 kW for the sextupole magnets.

The need for such a large number of low (< 3 kW) power converters, means the reliability and replaceability of the units is a major consideration. The size and weight of each unit will depend on the technology chosen, and also affects operating efficiency, input supply harmonic levels and power factor correction. All these topics will need to be addressed, along with their commercial availability and cost.

All power converters will be measured against the performance parameters in Table 13.3:

Table 13.3 Performance specification for power converters

	Dipole and Quadrupole	*Sextupole*
Long-term Stability (8 hrs to 6 mths)	50 ppm	200 ppm
Short-term Stability (100 sec to 8 hrs)	10 ppm	100 ppm
Resolution (minimum)	18 bit	16 bit
Ripple (perturbation error)	< 10 ppm	< 100 ppm
Reproducibility	10 ppm	100 ppm

13.8.3 Motion Control

4GLS will require a variety of motion control techniques such as stepper motors (closed and open loop), ac and dc servo systems, piezo actuators and possibly hexapods. The controller must be capable of managing this variety of motor technologies. Ideally a common controller will be specified throughout which will minimise spares required and will allow a common interface and common software. Many of the axes are controlled discretely, but multiple axis interpolation will also be required.

The topology will depend much on the final machine and beam line design but the options are likely to be:

- Rack installed control electronics remote from the controlled device or actuator (i.e. installed within instrumentation rooms). This configuration provides accessibility when the machine is operational but is time consuming to install. In addition this configuration requires long cable runs between electronics and the device, which can be a source of electromagnetic noise;

- Distributed control electronics mounted on or close to the device being controlled. This option will make the electronics inaccessible during machine operation but is easier to install and has short cable runs, minimising the electromagnetic noise issues;

- A hybrid of the above two options.

REFERENCES

[1] Basics of Site Vibration Measurement as Applied to Accelerator Design, *AP-BU-rpt-001*, D J Holder, CLRC Daresbury Laboratory, 11th January 2000.

[2] Site Vibration Measurements at DL and RAL, December 1999, AP-BU-rpt-002/AP-BLD-REP-0002, 16th February 2000

[3] 'Foundation Phase Report', Ch II, section 4, 'Magnet Systems', European Synchrotron Radiation Facility, Feb 1987.

[4] 'DIAMOND Synchrotron Source - Report of the Design Specification', Volume 2, p E2-29, CCLRC, June 2002.

[5] ASTeC Vacuum Quality Control Documentation, available from CCLRC Daresbury Laboratory

[6] BS EN ISO 14644-1:1999

14. Building and Engineering Services

This chapter describes the concept for the facility building to house 4GLS and the required engineering services. The main facility building is laid out primarily over a ground floor. The footprint and photon beam transport is optimised by locating some experimental areas and technical support systems on a mezzanine level above the electron accelerator tunnels, taking advantage of the high stability of the thick concrete shielding. A remote plant room will house the cryogenic, electrical and cooling plant.

The suitability of the site geology is discussed; this relates to the proposed design of the experimental floor slab in Chapter 13.

Floor layouts, three dimensional views and architectural concepts are shown to illustrate how the final facility will house the experiments, accelerators, technical systems and preparation areas essential to a research environment.

Significant power and water cooling will be required: these are covered in the final sections.

14.1 Building Structure and Layout

The proposed building structure has been driven by the science and engineering requirements of the 4GLS project. It will be in the order of 200 metres long, 100 metres wide and 25 metres high. The footprint of the building is determined by the requirement to house the accelerator and adequate shielding with sufficient space in the experimental area to accommodate the wide range of experiments envisaged (see Figure 14.1).

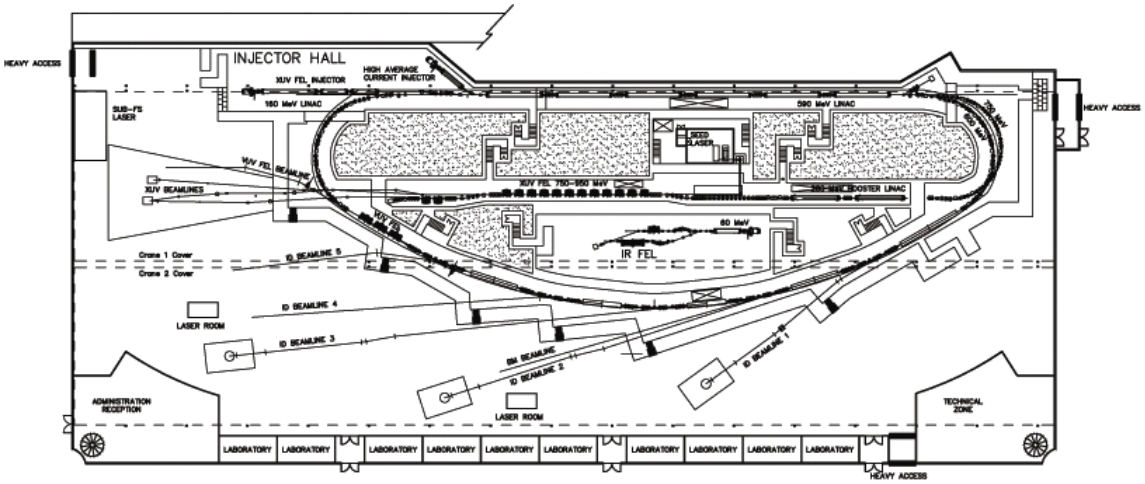

Figure 14.1 4GLS concept building design plan view at ground floor level

The overall building height has been determined by the working headroom required for the experimental processes, including some located above the tunnel complex, and the provision of

electrically operated overhead travelling cranes to lift and move items of equipment and shielding blocks (see Figure 14.2).

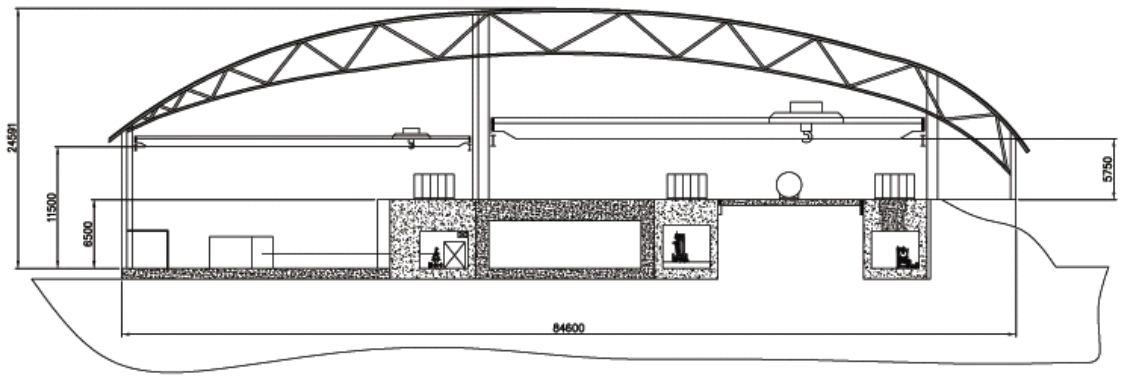

Figure 14.2 4GLS concept building design plan view cross section (dimensions in mm)

The current proposal is a single storey structure with the accelerator tunnel complex contained within it and to one side at ground floor level. The layout requires the superstructure to have large-span, column-free areas so that the experimental area can be laid out without the interference of major structural elements. Column-free areas are also important to ease the transportation and installation of the experimental equipment within the building.

14.1.1 Construction Style

The building will be constructed with a steel frame, which is similar to other technical buildings present at Daresbury Laboratory and is also in line with the construction approach at similar facilities around the world. A steel-framed building structure will support the building envelope over the large areas required and will present a high-technology appearance. Within the limits imposed by the requirement to maintain stable temperature levels, areas of glazing will provide natural lighting and solar gain as far as reasonably practicable.

As well as improved appearance, a steel-framed structure also provides more flexibility to accommodate modifications than a reinforced concrete-framed building. This flexibility is important because of the long timescales of scientific developments of this scale and caters for unexpected building changes. Alterations to a steel-framed building can be implemented more rapidly and generally with less disturbance to the areas of the building which are to remain unchanged.

The selected form of construction for the tunnel complex is reinforced concrete. This will provide the necessary shielding characteristics and strength where it is also required to be load bearing. A further advantage of reinforced concrete is its large thermal mass, which will help maintain temperature stability within the tunnel complex. The disadvantage of entirely cast in-

situ reinforced concrete shielding is a lack of flexibility for future developments. Therefore it is envisaged that certain key areas of shielding will be constructed from movable concrete blocks.

14.1.2 Mezzanine Floor and Crane Coverage

As well as experimental areas at ground floor level, it proposed to have further experimental areas located above the tunnel complex in a technical gallery at a mezzanine level (see Figure 14.3). This will determine the overall building height; the height of the tunnel complex plus the working headroom required at mezzanine level and including clearance for the operation of the overhead travelling cranes.

Crane coverage will be required for lifting large or heavy experimental equipment items, as well as shielding blocks, both during the construction of the experimental area and throughout its life. Electrically operated overhead travelling cranes will be installed, with a safe working load capacity of approximately fifteen tonnes. Secondary lifting devices will also be provided to be used for lifting lesser loads.

Some areas of the building may be only single storey - where the building height is not driven by the need to accommodate a mezzanine area above the tunnel complex and an overhead travelling crane.

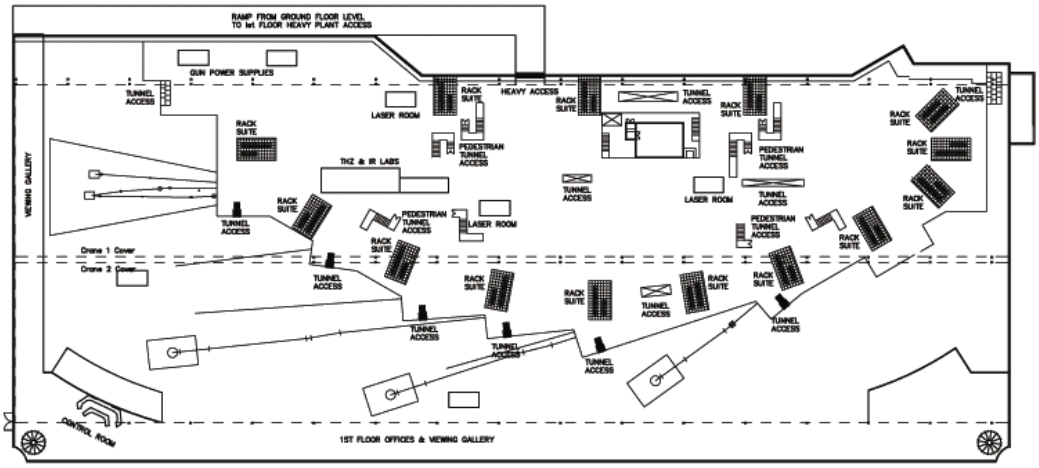

Figure 14.3 4GLS concept building design plan view at the mezzanine level

14.1.3 Ground Floor Layout

Analysis of the crane requirements as well as the need to propose an economic solution leads to a division of the building widthways into two main construction bays. Another result of dividing the building like this is that there are now two spans available in which to locate the overhead travelling cranes, one in each bay. A single span building would require an inordinately large

span for the overhead crane whereas two lesser spans would bring economy in initial costs and also during operation.

Such a division of the internal space would probably be along the line of the tunnel complex walling towards the edge of the mezzanine level so as to have the minimum influence on the layout at this level. This would achieve two approximately equal bay dimensions, and is the most desirable configuration for economy of building cost, which would include two equal span cranes. A proposed arrangement is shown in Figure 14.4.

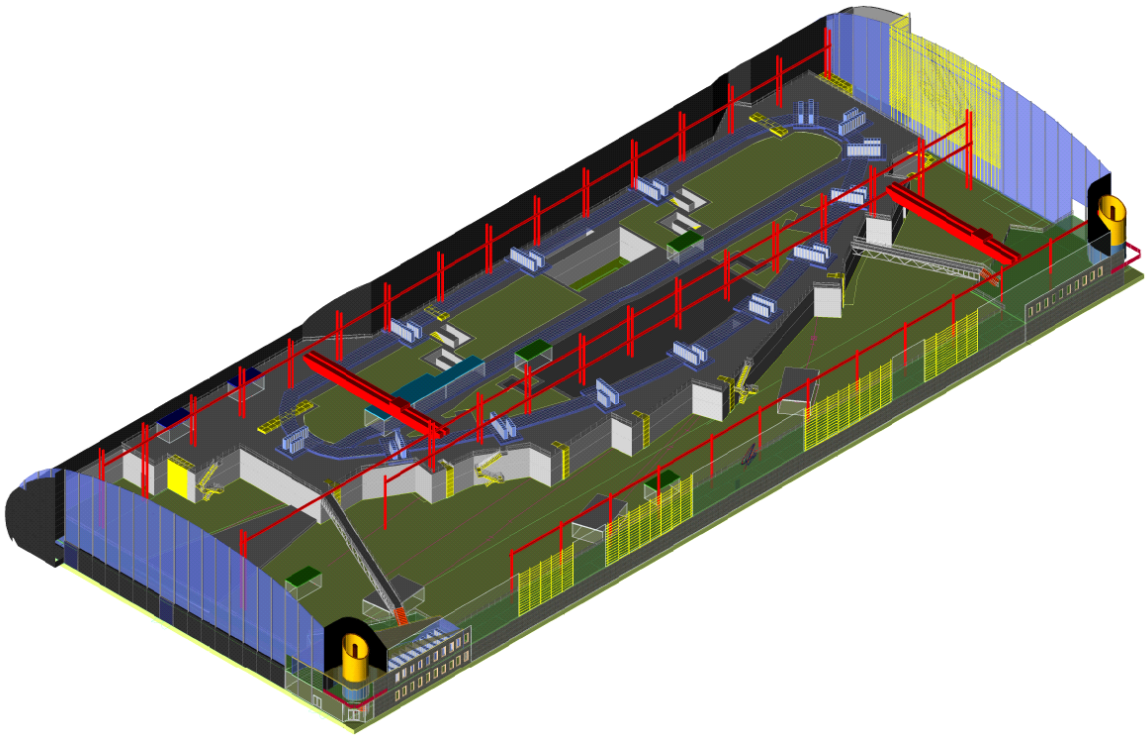

Figure 14.4 4GLS concept building design view of internal layout

14.1.4 Environmental Management

Strict requirements will be laid down for the tunnel and experimental area environments during the future development of the 4GLS design. This will require careful design of the temperature control and ventilation systems: consideration will also be given to providing enhanced general building insulation. Better temperature control in the experimental hall will help to achieve the required temperature stability within the tunnel (assumed to be the more stringent requirement). This will be considered during the 4GLS project development process in conjunction with the building services engineer and may have a key bearing on the selected type of building cladding system.

14.1.5 Ancillary Buildings

A remote plant room building will be required to house building services equipment such as cooling or heating plant that is required to support the operation of 4GLS. This will be in a separate building to minimise transmission of vibration to the machine. An existing building on the Daresbury Laboratory site might be suitable.

14.1.6 Planning Permission

Outline planning application will be made during the technical design review to Halton Borough Council and a detailed planning application will follow the detailed design phase.

14.1.7 Land Ownership

The majority of the proposed site is owned by CCLRC; investigation will be required into the site boundary and compensatory exchange of land.

14.2 Site Geology

14.2.1 General Description

Underlying the Daresbury site is a layer of Bunter sandstone approximately 300 m thick, running close to the surface and inclined downwards in the south-westerly direction at 6 to 8º. There is generally a top layer of brown sandy clay topsoil 0.3 - 0.75 m thick as well as gravel and red brown, slightly silty fine sand, occasionally very weakly cemented (weathered Bunter sandstone) which is 0.5 - 2.5 m thick, all on top of the Bunter Sandstone. Figure 14.5 shows the concrete foundations for the Nuclear Structure Facility (NSF) being cast directly on to the Bunter sandstone on the Daresbury site.

Figure 14.5 The concrete foundations for the Nuclear Structure Facility being cast directly on to the Bunter sandstone on the Daresbury site

The Bunter sandstone is permeable, and the height of the water table has apparently been dropping; from 16 m above ordnance datum in 1962 (this corresponds to more than 12 m below the surface) to 11 m above in 1969 and 4.5 m above in 1972.

Results from sandstone cores obtained from boreholes and also from static loading experiments have produced a wide range of values for Young's modulus and Poisson's ratio. Eventually an averaged value for Poisson's ratio of 0.25 was accepted.

A study [1] based on accurate survey data showed that the NINA synchrotron actually sank 2 mm during construction, conferring on the sandstone a Young's modulus of 1.0 GPa. This value agreed with another study being carried out at the time by the Building Research Station [2] who were assessing the long term creep properties of the sandstone.

14.2.2 Experimental Measurements

Most of the information on the Daresbury site comes from three periods: initial investigations around the time of National Institute Northern Accelerator (NINA) construction (1962/3), during consideration of the NINA booster (1969) and in preparation for the Diamond project (1999). Many of the early results are described in detail in the Diamond "Red Book" [3] and only a few salient points are recorded here. A report was produced in June 1964 that combined the findings of a geological survey of several sites in the North West to assess the suitability of their load bearing rock strata as a foundation for the NINA electron synchrotron. Extensive laboratory tests to define the structural properties of the Daresbury site rock strata, borehole in-situ 'Menard' pressure meter tests and plate loading tests in a surface pit [4] were all undertaken.

In 1969, a booster ring extension to NINA was proposed which required tunnelling into the hillside. Because of concerns over the nature of the sandstone, as well as its variable properties, a further borehole survey was commissioned to determine more accurately the properties of the sandstone [5]. As part of this work, some blast tests were also performed [6, 7].

Once NINA had been constructed, further tests were completed to measure the actual settlements experienced and also work was undertaken to measure the long term creep properties of the sandstone [8, 9]. Ground vibration measurements were made in 1999 as part of the Diamond site evaluation exercise [10].

14.2.3 Summary

There is no evidence for any structural problems related to ground conditions or geology with any existing developments at the Daresbury Laboratory site. No major geological or geotechnical hazards are present at the site that would affect the feasibility of the proposed development:

- there is no evidence for any slope instability on the hillside on which the existing and proposed facilities lie;
- no geological faults are known to cross the site;
- no coal, salt or other mine-workings have been carried out beneath the site and therefore the existing and proposed facilities are free from mining subsidence hazard.

The weathered sandstone is of adequate capacity for the building structure foundation and to support the concrete tunnel complex. The ground stiffness and loading defines the building settlement and values for Young's modulus and Poisson's ratio are well established for this site from numerous surveys and historical evidence from previous construction projects of similar scale. Once estimates of the volume of shielding required have been made, it will be straightforward to calculate the initial settlement expected due to the elastic deformation of the sandstone stratum during construction. This effect will be counteracted by the upwards motion of the sandstone due to any excavation work required, due to the removal of the loading.

14.3 Architectural Concept Design and Images

Based upon the requirements outlined in the previous sections, the following architectural scheme has been devised to show how the finished 4GLS building will look. Two views are shown in Figure 14.6 and Figure 14.7; these give an impression of the building, though the final detail will depend on a full technical performance assessment.

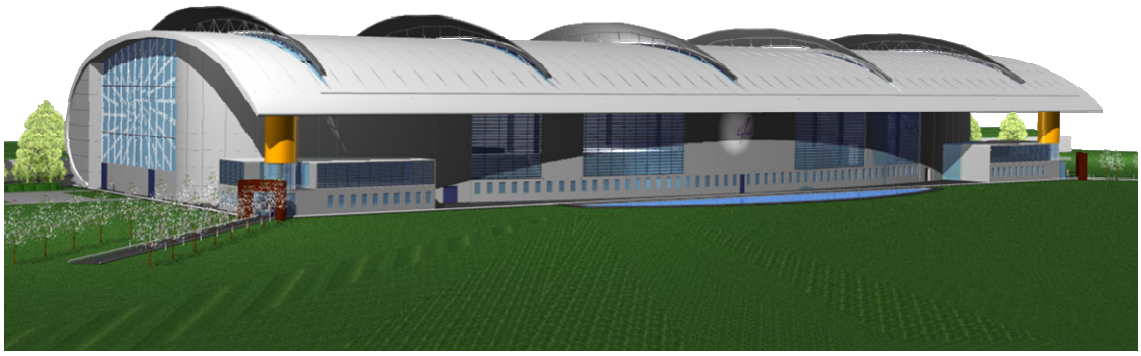

Figure 14.6 4GLS concept building design north facing view

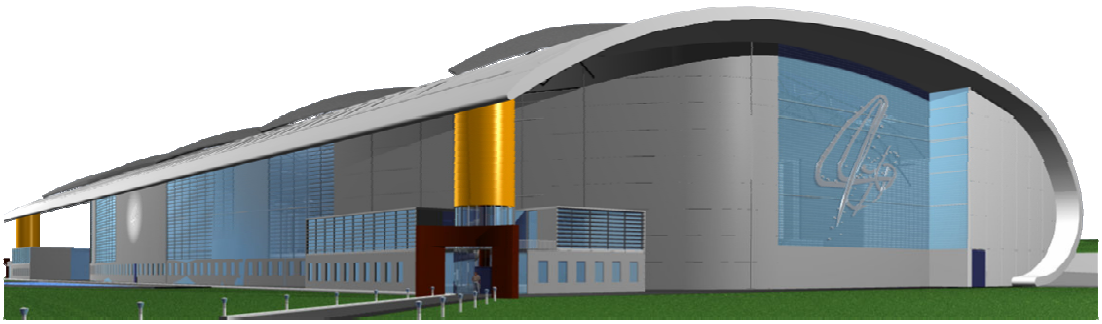

Figure 14.7 4GLS concept building design west facing view

Figure 14.8 shows a cross section through the building, allowing a view of the crane cover and construction. The precise height will be determined by the final layout for the ground and mezzanine levels. Figure 14.9 shows an end view of the facility.

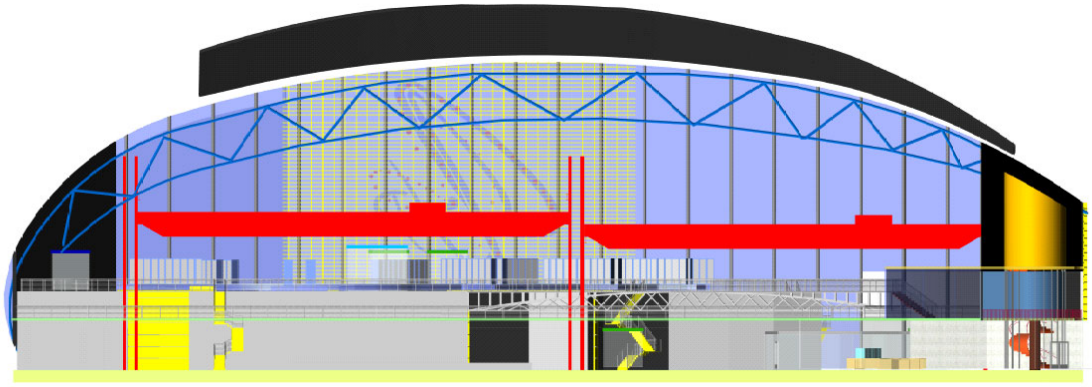

Figure 14.8 Cross-section of conceptual design for 4GLS building

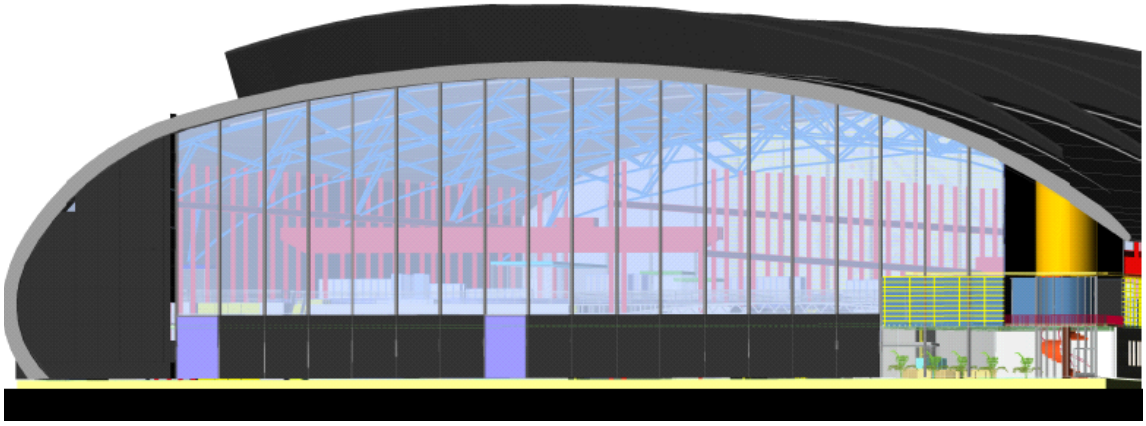

Figure 14.9 4GLS concept building design view of end elevations

14.4 Engineering Services

14.4.1 Electrical Power

It is anticipated that 4GLS would have a power demand in the region of 15.4 MW. The breakdown of this is shown in Table 14.1:

Table 14.1 Estimated electrical power requirements

Machine		***Total load kW***
Electron gun(s)		135
RF - injectors	(200 mA – 2 MW RF power @ 40 % efficiency)	5000
RF – linacs	(cryomodules will require 80 x 25 kW IOT)	2000
Power converters (magnets)		850
Electron gun control		6
Vacuum		160
Diagnostics		20
Network/control		54
Front-end		20
Insertion devices		20
RF control		60
FELs		24
Laser room		12
Cryogenic system		5024
Beamlines (20 beamlines at 20 kW each)		400
Total machine kW		**13,785**
Ancillary plant		
Lighting		20
Climate Control	Accelerator tunnel area	300
(heating not required)	Experimental and auxiliary area	400
Chiller System	Canal raw water pumps	100
	Magnet chiller	300
	Magnet water pumps	50
	IOT water pumps - canal	75
	Cryogenics cooling water pumps - canal	100
Compressed Air		200
Offices/laboratories		50
Total ancillary load kW		**1,595**
Total 4GLS electrical load kW		**15,380**

If alternative sources of electrical energy to the site's electrical connection to the national grid are to be included, the electrical distribution scheme will need to be altered accordingly. In the case of large-scale power generation, such as combined heat and power (CHP) plant, or large scale wind turbines, the resultant power will be delivered to the system via an auxiliary input on the main 11 kV switch panel. For smaller scale distributed systems the power will be supplied to the system at the low voltage switch panels.

14.4.1.1 Backup power systems

Backup power systems will be provided to cater for power outages for the critical or essential loads. In the case of critical loads, a ten minute static uninterruptible power supply (UPS) will be included to cater for the most common power supply transients and dips. Due to the limited fault currents available from these systems, dual-setting air circuit breakers will be included in the scheme to maintain discrimination while backup systems are in operation.

Generally, backup power provision shall be considered for at least the following:

- facility control computer systems;
- vacuum equipment;
- critical cryogenic systems;
- extract systems for COSHH;
- mechanical services systems associated with the control of temperature within the tunnel areas.

All backup equipment will be located in the remote plant room. Noise generating plant will be acoustically treated to limit the sound pressure level to 75 dBA at one metre. All such plant will be installed on anti-vibration mounts to eliminate vibration transfer to the main facility.

While UPS systems protect against transients and short term power dips, diesel generators would be required for protection against longer term blackouts. Such a blackout is very unlikely; none has occurred in the last ten years of running the SRS. For this reason coupled with the prohibitive cost of large scale generators, these are not included in the current proposal.

14.4.2 Cooling Systems

14.4.2.1 Primary Cooling Source

Several options exist for the source of primary cooling for 4GLS:

- geothermal;
- gas cycle cooling;
- vapour compression cooling;
- thermionic cooling;
- canal water.

CCLRC Daresbury Laboratory currently has a licence with Peel Holdings to use the adjacent Bridgewater Canal as a cooling water source. The current maximum load agreement is 3 MW of cooling, with summer and winter design differential temperatures of 5 ºC and 10 ºC respectively. The canal is currently the primary cooling source for the existing accelerator facilities on the Daresbury site. The initial cooling concept for 4GLS is for the use of canal water in conjunction with water chillers, water-cooled condensers and air blast water coolers.

14.4.2.2 Estimated Cooling Water Loads

Table 14.2 shows the present estimate of the water cooling requirements for 4GLS:

Table 14.2 Estimated significant cooling water loads

System	*Estimated cooling load (MW)*	*Water Quality*
Radiofrequency	1	De-ionised
Cryogenics	1	Canal
Magnets	1	De-ionised
Beam dumps	1	Canal
Beamlines	0.5	De-ionised
Air conditioning (climate control)	2.5	Chilled

14.4.2.3 Cooling Water Distribution Systems

Existing Synchrotron Radiation Source (SRS) primary water cooling pumps and circuits can be up-graded, renewed and modified to incorporate the new cooling circuits to 4GLS. Primary chilled water circuits will supply the air conditioning systems as required to supplement the adiabatic air handling systems. Cooling water will also serve heat exchangers in secondary cooling circuits for de-ionised water. These secondary circuits will have water treatment, filtration, mixing valves and pump sets to achieve required pressure, temperature, volume flow and water quality. Conductivity of de-mineralised water will not exceed 0.1 μS/cm with 10 μm filtration. Circuits will have de-oxygenation to reduce copper corrosion.

Where possible, energy recovery options will be considered in order to make use of the waste heat, for example from the beam dumps.

14.4.3 Environment Control Systems

14.4.3.1 Heating

Packaged heat-pump systems will be installed in the reception and perimeter accommodation areas to satisfy both heating and cooling loads. Heating in the experimental hall will be by direct gas-fired air handling induction systems. The heating load is not known at this stage. The system will be designed allowing for an external temperature of - 4 ºC and with 100 % saturation. Subject to suitable cooling and heating load profiles, CHP could be used to generate electricity and thermal energy for heating applications.

14.4.3.2 Air Conditioning and Ventilation

This will be provided in the following areas:

- accelerator tunnel;
- experimental hall;
- beam line enclosures;
- control rooms;
- reception and general accommodation areas.

14.4.4 Vacuum Exhaust and COSHH Systems

These will be twin systems to remove exhaust air from vacuum pumps and COSHH enclosures.

14.4.5 Gas Distribution Systems

The following gas distribution systems will be required to some parts of the building:

- compressed air;
- nitrogen;
- helium;
- liquid nitrogen (possibly).

14.4.6 Water Supplies

Water supplies will be provided for a ring main of fire hydrants around the outer wall of the experimental hall and for other uses as required. Cold water mains will also provide make-up water to boilers and domestic local hot water heaters in toilets.

14.4.7 Drainage Systems

Trade waste drainage will be required as needed.

14.4.8 Other Building Services Required

- artificial lighting;
- fire detection and alarm;
- telecommunications and data;
- security systems;
- safety alarm systems;
- building management system;
- lightning protection;
- public address system;
- information display systems;
- lifts

REFERENCES

[1] In-situ deformation of Bunter sandstone' by Messrs Moore and Jones of Building Research Establishment and Daresbury respectively.

[2] 'A long term plate test on Bunter sandstone' Oct 1973 by JFA Moore of the Building Research Establishment.

[3] DIAMOND Synchrotron Light Source Report of a Feasibility Study, May 1997.

[4] Report number 4042/1 "Preliminary site investigation at Daresbury, Cheshire for a proposed Nuclear Physics Laboratory" Dec 1962 by 'Soil Mechanics Ltd.', 65 Old Church St., London SW3.

[5] Report number 4274 "Site investigation at Daresbury, Cheshire for a proposed synchrotron" Feb 1964 by 'Soil Mechanics Ltd'.

[6] The design of the foundations for the 4 GeV Electron Synchrotron, Nuclear Physics Laboratory' June 1964 by Messrs Chilton and Haden of UKAEA.

[7] Report on trial boreholes at Daresbury, contract S80087, Jan 1969, by Foundation Engineering Ltd, 111 Westminster Bridge Road, London SE1.

[8] Blasting Vibrations July 1968. Report by Messrs Ball and James of ICI Ltd.

[9] UKAEA, AWRE Report No O 32/70 'Vibrations in structures' July 1970 by FH Grover.

[10] Site Vibration Measurements at DL and RAL, December 1999, AP-BU-rpt-002/AP-BLD-REP-0002, 16th February 2000.

15. Health, Safety and Environment

4GLS will be designed, procured, installed and operated in accordance with all relevant legislation and in line with CCLRC's published safety policy.

The most critical safety aspect at the Conceptual Design Report stage of the project is the estimation of the radiation hazard produced by the facility and the development of a shielding design which meets the requirements of UK legislation. The overall size and layout of the shielding will have a major influence on the 4GLS building and the total project cost. For this reason, progress on work covering radiation safety is presented in detail in this chapter.

4GLS will be a major construction project and will be carried out under the Construction, Design and Management Regulations. A full environmental impact assessment will be made at an early stage of the project lifecycle.

15.1 Safety Management

4GLS is a state-of-the-art accelerator development project which will move into a user operational phase. Its components will include:

- a very large cryogenic plant and many superconducting devices operating in a confined space;
- large numbers of high power DC and pulsed electrical power supplies;
- equipment for the production of intense RF power;
- very high field magnetic arrays;
- very high power lasers;
- extended UHV assemblies with their associated equipment.

The facility is designed to produce extremely intense beams of electromagnetic radiation from the terahertz to X-ray by accelerating electrons to high energy. In summary, the facility will require comprehensive safety management from the earliest stages to ensure that the highest standards of safety are achieved at all stages of the project including operations.

15.1.1 Legislation

The following legislative packages will strongly influence the project throughout its lifecycle:

- The Health and Safety at Work etc Act 1974, [1];
- The Management of Health and Safety at Work Regulations 1999, [2];
- The Construction Design and Management Regulations 1994, [3] as amended [4];
- The Ionising Radiations Regulations 1999 [5].

In addition to these, and in order to satisfy the requirement to take all reasonable measures to ensure safety, 4GLS will be designed to comply with the international standard for functional

safety IEC61508 [6]. This standard requires the use of formal methods to quantify both the risks associated with the project and the level of sophistication of the safety systems in place to mitigate them. Although compliance with IEC61508 is not yet a legislative requirement, the ability to demonstrate application of best practice without it is already questionable.

15.1.2 Construction Design and Management Regulations (CDMs)

CCLRC will act as Client under CDMs and be responsible for the appointment of suitably qualified staff or external organisations to take the responsibilities under CDMs of:

- the planning supervisor;
- the designers;
- the principal contractor.

Due to the specialist and state of the art nature of the 4GLS facility, it will be essential for CCLRC scientific and engineering staff to retain close control of many aspects of the design, construction and commissioning. For this reason CCLRC will attach great importance to the procurement strategy for the project and will need to modify the standard relationship between the professional partners which is common in more conventional large scale construction projects. Professional external advice from specialist high technology project management organisations will be commissioned as part of the Technical Design Report (TDR) to follow.

15.1.3 Environmental Planning

4GLS requires one of the largest liquid helium production plants in Europe and will take approximately 16 MW of electrical power from the national grid. A comprehensive environmental impact assessment will be necessary for planning permission and this will need to take place at the earliest stages of the project in order that every means possible to reduce the impact on the environment is incorporated into the design from the outset.

CCLRC will employ expert consultants to advise on environmental impact and its mitigation through the use of advanced technology.

15.2 Radiation Protection

The operation of high energy, high power electron accelerators inevitably produces significant fields of unwanted radiation as well as the co-produced user beams. Exposure to any radiation is potentially harmful so the radiation fields must be quantified and appropriate engineering solutions found to allow safe operation of the accelerators and beamlines that comprise 4GLS.

The following sections describe briefly the UK legislative position relating to accelerator operation and the estimated magnitude of unwanted stray radiation together with some simple shielding estimates. A brief comment on the environmental impact of accelerator operation is also presented. Closing comments focus on the decommissioning aspects of the project.

15.2.1 UK Legislative Position

The Ionising Radiations Regulations 1999 [5] were made under the Health and Safety at Work Act 1974 [1] and implement the Basic Safety Standards Directive 96/29/Euratom [7]. The drive behind the Regulations and supporting Approved Code of Practice [8] is to establish a framework that ensures all occupational exposures, whether internal or external, are as low as reasonably practicable (ALARP), and do not exceed the specified dose limits. The Laboratory has a legal duty to ensure all its work with ionising radiation complies with the requirements of this legislation. Separate considerations apply for environmental issues relating to the accumulation and disposal of radioactive materials such as induced activity in the accelerator structure and the discharge of short lived radioactive gases to atmosphere.

Two primary regulations relate to the employer obtaining approval from the UK's competent authority, the Health and Safety Executive, before work with radiation is undertaken and specifically authority to operate an accelerator.

15.2.1.1 Justification

New legislation on the Justification of Radiation Practices [9] designed to bring the UK into line with the European Directive [7] was introduced in 2004. CCLRC has taken advice from the Department of Trade and Industry, as the lead authority for this type of practice, and believes that 4GLS, as an accelerator based light source, does not qualify as a new radiation practice and therefore no further action in respect of these Regulations is required.

15.2.1.2 Health and Safety Executive Notification

Radiation Employers are required to notify the Health and Safety Executive of their intention to undertake work with ionising radiation at least twenty-eight days prior to the work commencing, with few exceptions. The Laboratory had previously notified the Health and Safety Executive under the Ionising Radiations Regulations 1985 [10] of its work with accelerators and providing the operation of 4GLS is not considered a material change then notification under Regulation 6 is not required.

4GLS comprises a suite of electron accelerators of comparable energy to the existing facilities at the Laboratory and their operation is not deemed to be a material change to the Laboratory's use of ionising radiation, and consequently Health and Safety Executive notification is not required.

15.2.1.3 Prior Authorisation

Separate from the required Notification, the Regulations place a clear duty on the Radiation Employer, to have permission from the Health and Safety Executive before operating any accelerator. Such permission may be granted in two ways:

- by the employer meeting all the requirements in the Generic Authorisation [11, 12], in which case authorisation is automatic; or,
- By individual application to the Health and Safety Executive in cases where these conditions cannot be met. It is for the employer to demonstrate to the Health and Safety Executive why the relevant Generic Authorisation cannot be complied with and explain why they believe an individual authorisation is needed and should be issued.

The Generic Authorisation lays down standards which any well run organisation should be able to meet. Specifically it requires accelerator facilities to be adequately shielded, be equipped with appropriate fail-safe warning signals, employ interlocks and trapped key systems to prevent access to high dose rate areas and have due regard to other hazards such as activation and adventitious radiation. CCLRC as an organisation is fully committed to ensuring that the shielding, personnel safety systems and other engineering and administrative control features specified for 4GLS meet the requirements of the Generic Authorisation and therefore individual application to the Health and Safety Executive for authorisation to run the facility will not be required.

15.2.2 Dose Limits

The statutory annual dose limit for employees over eighteen is 20 mSv whilst that for members of the public is 1 mSv. The CCLRC corporate shielding policy [13], in considering ALARP, requires employees' annual doses to be less than 1 mSv and annual doses at the site boundary i.e. the dose to members of the public to be less than 0.3 mSv. This figure of 0.3 mSv is in line with the National Radiological Protection Board (NRPB), now the Health Protection Agency, recommendation [14] for the dose constraint from a single new source.

An occupancy factor of one-third has been used in deriving working limits outside the shield wall. It is seen that the ALARP goal of 1 mSv to any employee will be met if the annual integrated dose immediately outside the shield wall is less than 3 mSv. 4GLS, as a dedicated user facility is expected to operate for 6000 hours annually resulting in a derived working limit (DWL), outside the shield wall of 0.5 $\mu Sv h^{-1}$. This DWL is used at both Diamond and ESRF.

15.2.3 Accelerator Produced Radiation

The radiation field resulting from the loss of high energy electrons (i.e. those above ~ 10 MeV) is necessarily complex and depends greatly on the target material, thickness and electron energy. Comprehensive descriptions of the physical processes have been made by Patterson and Thomas [15], Swanson [16], the NCRP [17, 18] and Sullivan [19]. A brief description of the dominant types is given in the following sections. Muon production at electron energies below a few gigaelectronvolts may be disregarded.

15.2.3.1 Direct Bremsstrahlung

High energy electrons produce bremsstrahlung photons during collisions with any absorber. These photons may go on to produce electron-positron pairs under the influence of the nuclear field and lead to the propagation of the electromagnetic shower. The angular distribution of this bremsstrahlung consists of a slowly decreasing function between 0° and 180°, superimposed onto which is a significantly more intense and forward directed core between 0° and 5°.

15.2.3.2 Indirect Gamma

As a result of high energy neutron interactions within the bulk shield there is a secondary field of gamma radiation. This field has been experimentally determined [20] to be slightly more than 25 % of the high energy neutron dose rate.

15.2.3.3 Giant Resonance Neutrons

Above the threshold of ~ 4 MeV for heavy nuclei and ~ 12 MeV for light nuclei, evaporation neutrons are produced through the giant resonance (γ,n) reaction whereby a photon interacts with a nucleus producing an excited compound which de-excites through the loss of a neutron. The spectral peak of these neutrons is ~ 1 MeV with an average energy of ~ 2 MeV and has an isotropic distribution.

15.2.3.4 Mid Energy Neutrons

Above photon energies of ~ 25 MeV the absorption of a bremsstrahlung photon takes place by a proton-neutron pair within the nucleus, the quasi-deuteron model, and produces neutrons of higher energies between 20 MeV and 100 MeV with a slightly forward peaked distribution. The cross section and therefore the neutron yield is at least an order of magnitude down on the giant resonance process.

15.2.3.5 High Energy Neutrons

These are neutrons with energies in excess of 100 MeV that are an integral part of the hadronic cascade initiated by high energy photons in the electromagnetic cascade. This is the radiation component that dominates for thick shields. Again, this group is forward peaked.

15.2.3.6 Attenuation Coefficients

The attenuation coefficients for the various radiation types are given in Table 15.1. These figures are widely used in the accelerator health physics community and have been derived from experimental and theoretical studies. They are those utilised by the SHIELD11 code [21] which has been used extensively to carry out the initial shielding estimates.

Table 15.1 Attenuation coefficients for common shielding materials

	Units	Concrete	Barytes	Lead	Steel	Polythene	Soil
Density	gcm^{-3}	2.35	3.50	11.35	7.87	1.00	1.70
Gamma – Direct	m^{-1}	5.60	7.95	47.29	23.42	1.41	4.05
Gamma – Indirect	m^{-1}	1.96	2.92	5.68	5.43	1.27	1.42
GR neutrons	m^{-1}	7.83	7.61	11.70	16.74	18.87	5.66
Mid energy neutrons	m^{-1}	4.27	6.36	5.68	5.68	1.27	3.09
High energy neutrons	m^{-1}	1.96	2.92	5.68	5.68	1.27	1.42

The attenuation coefficients for the indirect gamma component are the same as those for the high energy component, since the indirect gamma field has been shown to attenuate in direct proportion to the removal of high energy neutrons.

15.2.4 Key 4GLS Parameters

The following table details the key machine parameters that heavily influence the shielding design.

Table 15.2 Key 4GLS machine parameters

Parameter	Units	HAC Loop	XUV-FEL Branch	IR–FEL Branch
Beam energy	MeV	600	750 - 950	25 - 60
Bunch rate	MHz	1300	0.001	13
Bunch charge	pC	77	1000	200
Average current	mA	100	0.001	2.6
Average power	kW	60000	0.75 – 0.95	156

The following section describes the approach taken for estimating the shielding requirements of the HAC loop. The requirements for the XUV-FEL and the separate IR-FEL facility are not discussed here.

15.2.4.1 Beam Losses in the HAC Loop

An understanding of beam losses around the accelerator lattice is critical to designing the primary shield. Given the average power proposed for the high average current (HAC) loop this point cannot be overstated. Assuming a pessimistic 99.99 % of beam current from this loop is energy recovered, the lost beam power is 6 kW. This power loss is at least three orders of magnitude greater than that considered during the shielding calculations for Diamond [22] or ERLP [23]. Based on experience at CEBAF and on the Jefferson Laboratory IRFEL, realistic target losses would be around 1 μA. Future detailed design work will be required to confirm a current loss specification for 4GLS which is achievable, can be reliably detected and meets the requirements for machine protection.

Operational considerations will certainly impose upper limits on local beam losses, for example excessive local losses can cause quenching of the cryogenic accelerating structures, local heating and consequent damage to vacuum vessels or demagnetisation of the critical magnets of the insertion devices. Consideration must be given to the use of collimators to control losses coupled with a fast acting and sensitive beam loss monitoring system around the complete machine lattice.

The following table gives details of the first pass estimates of beam losses. These are used to derive shielding thicknesses that will aid the costing of 4GLS but will need considerable refining in the future.

Table 15.3 Proposed beam losses

Location	Constraint	Units	Power Loss
cold section – accelerator module	cryogenic cooling reserve – quench	Wm^{-1}	0.4
Warm section – elsewhere	machine damage – local heating	W	15

For comparison the cold section losses are the same as those used at TTF2 for the shield design for the VUV-FEL [24]. Warm section losses at TTF2 were assumed at 75 W whilst the LCLS at SLAC assumed 5 W [25].

15.2.5 Shielding Model

Shielding estimates have been calculated using the SLAC shielding code SHIELD11 [21]. This code has been used extensively for performing shielding analyses around high energy electron accelerators. It makes use of simple analytic expressions for the production and attenuation of photons and neutrons resulting from electron beams striking thick targets, such as dumps, stoppers, collimators, and other beam devices.

The geometry considered is that of a point source interaction of the primary electron beam with a thick iron target, Figure 15.1.

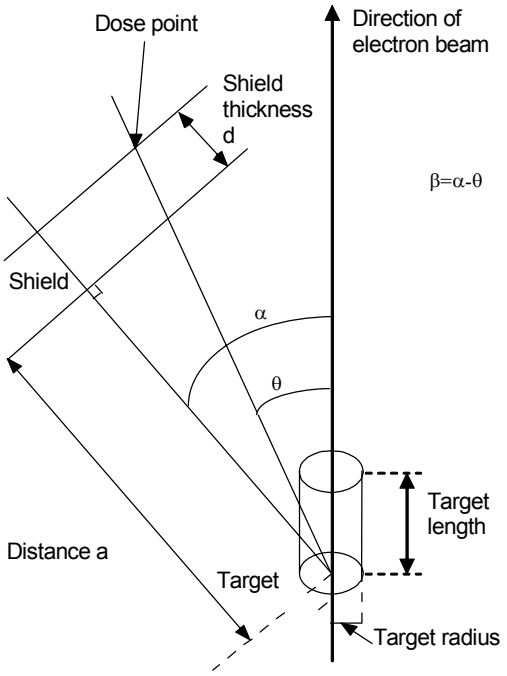

Figure 15.1 SHIELD11 target geometry

Each of the five radiation types described earlier has been fitted to an empirical model resulting in radiation yields as follows:

$$H_{GAMD} = (891.91Ee^{-0.959\sqrt{\theta}} + 207.84e^{-\theta/72.2})E \times 10^{-17} \quad (15\text{-}1)$$

$$H_{GAMI} = 0.267H_{HEN} \quad (15\text{-}2)$$

$$H_{GRN} = 4.93Z^{0.662}E \times 10^{-17} \quad (15\text{-}3)$$

$$H_{MID} = \frac{43.9A^{-0.37}}{1 - 0.75\cos\theta}E \times 10^{-17} \quad (15\text{-}4)$$

$$H_{HEN} = \frac{13.7A^{-0.65}}{(1 - 0.72\cos\theta)^2}E \times 10^{-17} \quad (15\text{-}5)$$

These yields are expressed in units of sieverts per electron at 1 m from the source (loss) point. An inverse square variation with distance is assumed. The expression for the direct gamma dose is based on the combined results from two standard target experiments performed at SLAC in the late 1960s, the standard target being a 30 cm long by 5 cm radius iron cylinder. The SHIELD11 code generalises these results for electrons interacting in thick targets of other materials and dimensions.

Point source assumptions may in certain cases overestimate the shielding requirements so the SHIELD11 code has been modified to account for a distributed loss, for example down the length of the modules in the 120 m long acceleration straight.

At this stage it is considered appropriate to use the SHIELD11 code to derive reasonable estimates of shielding thicknesses. However a weakness of the code is that it assumes a point loss in a thick target whereas, more realistically, electrons lost from the orbit interact at grazing angles in thin targets such as the vacuum chambers. To properly model this more realistic situation, a Monte Carlo code such as FLUKA [26, 27] should be used and the Technical Design Report will cover this aspect of the shielding design.

15.2.6 Proposed Shielding

The schematic shown in Figure 15.2 of the proposed layout has been used as the basis for the shielding calculations. Four areas of the main concept have been examined to determine shielding thicknesses. Combinations of ordinary concrete and soil have been used for the acceleration straight and the two main arcs whilst thicknesses of ordinary concrete or barytes have been determined for the ratchet walls.

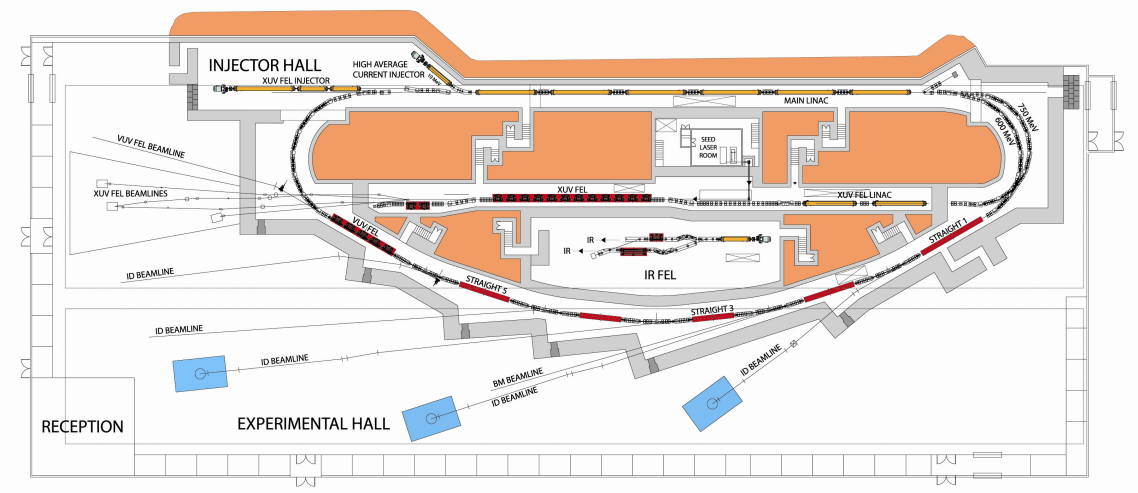

Figure 15.2 Conceptual layout of the 4GLS facility

15.2.6.1 Acceleration Straight

The acceleration straight contains the six superconducting acceleration modules. Electron loss rates down the length of this section of the lattice must be inherently low as power losses in excess of the cryogenic cooling capacity will lead to a quench and loss of acceleration. The modified version of SHIELD11 to calculate shielding requirements from distributed losses was used assuming the parameters below.

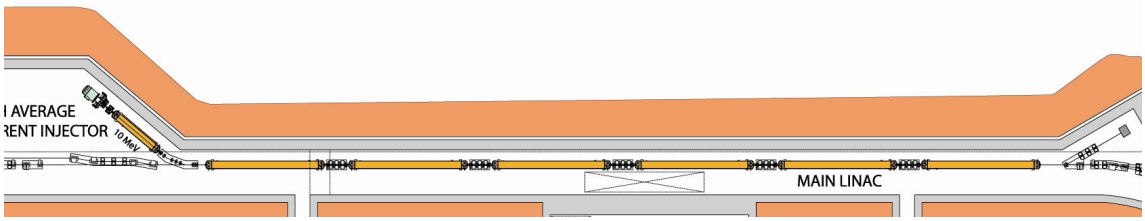

Figure 15.3 Main acceleration straight, ~ 120 m long

Length	120 m
Distance to inside of shield	1.5 m
Power loss	0.4 Wm^{-1}
Calculation point	60 m
Concrete	2.10 m
Concrete+ Soil	0.75 m + 2.25 m

15.2.6.2 Main Arc

The outward arc (see Figure 15.4) shield calculations were done using a point source loss of 15 W. Higher losses than this may lead to machine damage and will be controlled by a system of fast beam loss monitors. Only losses at 90° have been considered so far, as slant thicknesses at 0° are substantial. Of course this simplified loss geometry will need to be critically examined as the final design is settled on.

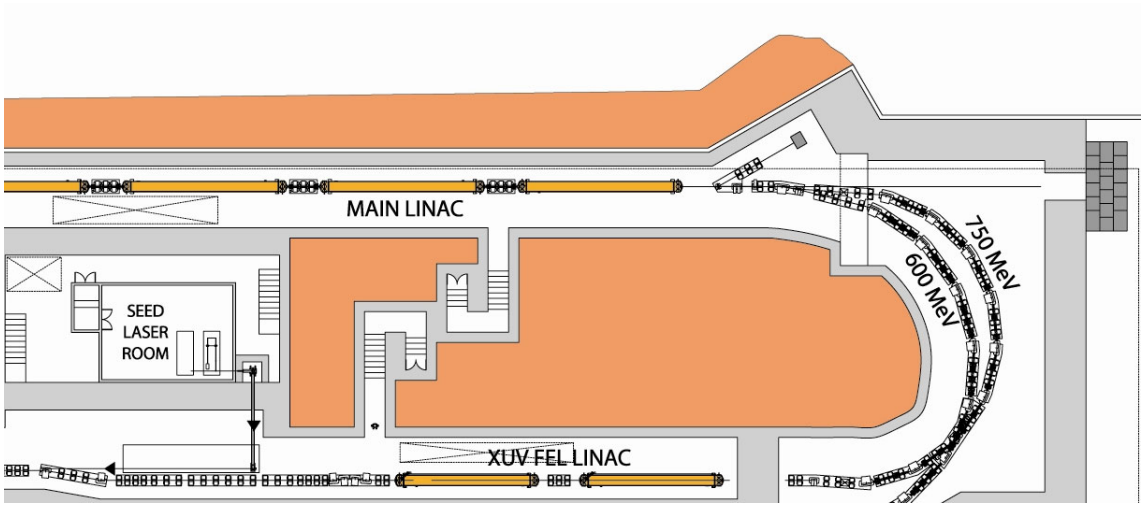

Figure 15.4 Outward arc of 4GLS lattice

Distance to inside of shield	1.5 m
Power loss	15 W
Calculation point	90° to loss point
Concrete	2.85 m
Concrete + Soil	0.75 m + 2.75 m

15.2.6.3 Ratchet Wall

The end wall thicknesses (see Figure 15.5) were calculated on the basis of point losses of 15 W at the insertion device. Side wall thicknesses were calculated on the basis of a point loss of 15 W at the centre of the arc.

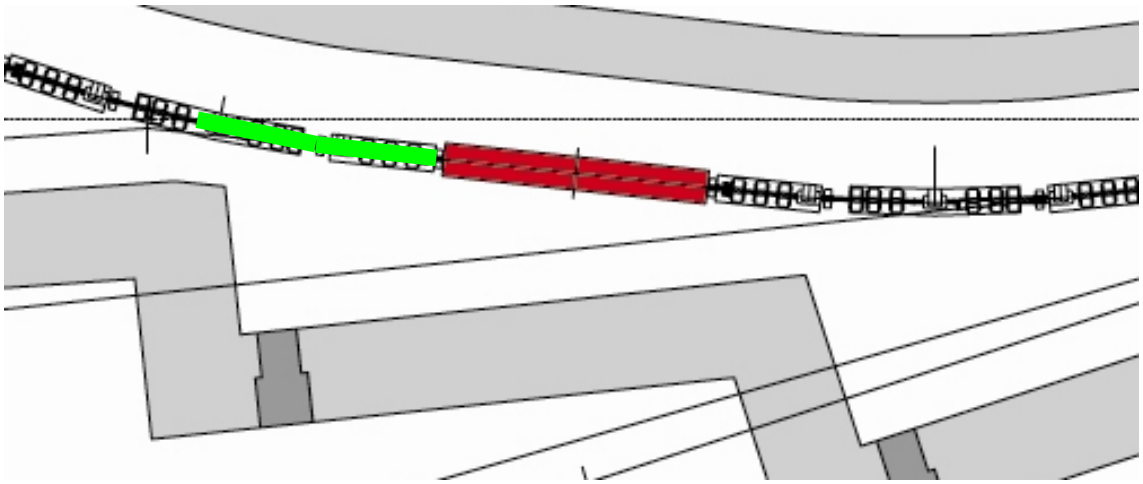

Figure 15.5 Proposed ratchet wall for photon beamlines

Side Wall		**End Wall**	
Distance to inside shield	1.5 m	Distance to inside shield	25 m
Power loss	15 W	Power loss	15 W
Calculation point	90° to loss point	Calculation point	0° to loss point
Concrete	2.85 m	Concrete	2.25 m

It is interesting to note that this simple calculation for the end wall results in a thinner shield than that for the side wall. The reason for this is predominantly distance related. The side wall calculations were done for a distance of 1.5 m as opposed to 25 m for the end wall which gives a reduction in intensity of nearly 300 based on the inverse square law.

A more realistic determination of the required end wall thickness can be made by assuming the electron losses occur in the downstream half of the arc, shaded green in Figure 15.5. Losses at 0° can now no longer target in the end wall but wider angle radiation can strike the ratchet end walls with a source point now much nearer the shield wall.

End Wall	
Distance to inside shield	7.2 m
Power loss	15 W
Concrete	3.00 m
Barytes	2.10 m

In this case the end wall thickness is now slightly thicker than the side wall which is intuitively correct. An important point to note is that for certain angles and loss points the radiation will strike the following ratchet side wall at narrow angles. This demonstrates the importance of having a clearer scheme for the insertion device arcs and ratchet end walls before a realistic shielding estimate can be made.

The shielding thicknesses given represent reasonable estimates for costing purposes only. They must not be used outside of this context. Before a radiologically optimised solution for the shield design can be completed, the following issues must be addressed:

- quantification of electron losses around the complete lattice;
- thin target, grazing incident modelling with FLUKA;
- the design of the ID arcs;
- use of collimators to localise electron losses;
- beam loss monitoring system.

15.2.7 Beamline Design

Delivering the beam to users safely is a challenging problem. Electron losses in the region of the insertion devices will lead to an intense, forward directed cone of bremsstrahlung radiation as well as a significant neutron field. If similar beamline geometries to those employed at storage rings are used, i.e. the user photon beam is brought out through the shield wall on the axis of the insertion devices, then very high gamma and neutron dose rates will be present in the experimental areas. It proves useful to contrast the power losses from an electron storage ring, such as the SRS at Daresbury, to those assumed for 4GLS in the present discussion. Electron loss rates during stable stored beam can be approximated, assuming an exponential decay of the stored beam, by the following expressions:

$$I = I_o e^{-t/\tau} \tag{15-6}$$

The electron loss rate is then given by:

$$L_{e^-} = I_0(1 - e^{-t/\tau})\frac{r}{c}\frac{6.25\times10^{15}}{t\times3600} \tag{15-7}$$

where

r	circumference of SRS	m
c	speed of light	ms^{-1}
I_o	Initial current in the SRS	mA
I	Current remaining after t hours	mA
τ	Beam lifetime	h

Assuming some typical operating parameters for the SRS, for example, an initial 200 mA beam with a 30 hour lifetime, over a period of 5 hours the average electron loss rate is $3.41\text{x}10^6$ s^{-1},

corresponding to a distributed power loss at 2 GeV of 1.09 mW. This needs to be contrasted with the assumed single point loss for the HAC loop of 4GLS of 15 W.

It is also important that it is not possible for any injected electrons to pass down an operational beamline. This issue has been explored in detail to allow top-up operation at many of today's storage ring facilities. Borland and Emery [28, 29] at the APS have carried out electron tracking simulations to demonstrate that providing a stored beam exists then it is not possible for electrons to pass down a beamline. Similar studies will be needed to carefully assess the potential for this type of accident at 4GLS. Again to bring some sort of scale to the problem, APS inject typically a few nanocoulombs over a few minutes during top-up operations with the main beamline port shutters open, whilst the gun for the HAC loop is injecting 10^8 nCs^{-1} continuously.

Given the potential for these high dose rates of bremsstrahlung and neutron radiation being produced on-axis it is essential that the required user photon beam is deflected off-axis by a primary optical element either within the main shield wall or within a heavily shielded optics enclosure immediately outside the shield wall. The latter is the approach taken for TTF2 operation at DESY [30].

15.2.7.1 Gas Bremsstrahlung

The radiative interaction of electrons with the residual gas in the chambers of electron storage rings is an important source of high energy bremsstrahlung radiation. The problem is particularly acute at today's 3rd generation facilities which utilise long straight sections and narrow gap vessels to accommodate the insertion device magnet arrays.

The power P of the gas bremsstrahlung can be expressed as:

$$P = C \frac{dE}{dx} E_c pIL \tag{15-8}$$

where dE/dx is the electron stopping power in the residual gas, E_c the electron energy, p the average pressure in the straight, I the electron beam intensity and L the length of the straight section. C is merely a proportionality factor.

The electron stopping power is proportional to the electron energy, with the vacuum pressure being approximately proportional to the circulating current and electron energy. Therefore the following may be used as a figure of merit for the gas bremsstrahlung power produced:

$$P \propto E_c^2 I^2 L \tag{15-9}$$

The following table gives such a figure of merit for a number of electron storage ring facilities and for 4GLS, normalised to the ESRF.

Table 15.4 Gas bremsstrahlung powers

	Units	ESRF	SRS	Diamond	4GLS
Energy	GeV	6	2	3	0.6
Current	mA	200	250	500	100
Straight	m	15	3.82	18.75	19
P normalised		1	0.044	1.95	0.003

It would seem that gas bremsstrahlung from the ID straights within the HAC loop should not be a serious issue. However there may not be the same vacuum constraints for 4GLS as there are for electron storage rings. Typical operating pressures in a storage ring are 10^{-9} torr, such pressures being required to achieve the long beam lifetimes of the stored beam. In contrast 4GLS is a single pass machine so pressure may not necessarily be such a rigid design goal. If vacuum pressures were only 10^{-7} torr then the figure of merit for 4GLS would be one-third that of the ESRF.

Ferrari *et al* report the results of Monte Carlo calculations using the FLUKA code [31] and derive a general expression for the dose rate due to gas bremsstrahlung. Rationalising their expression we obtain:

$$D_d = \frac{1.5 \times 10^{-11} P I E_0^{2.67} L}{d(L+d)} \tag{15-10}$$

where the symbols have the following meaning;

D_d	Absorbed dose rate	μGyh^{-1}
P	Pressure in straight	torr
I	Electron current	es^{-1}
E_o	Electron energy	MeV
L	Length of straight	m
d	Distance from end of straight	m

Assuming a straight length of 19 m as the worst case with an operating pressure of 10^{-7} torr a dose rate of 8.72×10^5 μGyh^{-1} is calculated for a distance of 25 m from the centre of the insertion device straight.

Again for the reasons given above, there are significant shielding and operational advantages in containing the gas bremsstrahlung radiation within the main machine shield wall by the use of a primary optical element to deflect the user photon beam outside the bremsstrahlung cone.

15.2.8 Beam Dump Design

The conceptual layout (Figure 15.2) shows the location of the four beam dumps (two on the IR-FEL) proposed. Table 15.5 details some of the more relevant parameters relating to the safety issues. One of the advantages of the energy recovery concept utilised in the HAC loop is that it allows the dumping of the electron beam at the injector energy of 10 MeV. This is close to the photo-neutron production threshold for a range of materials typically encountered in beam dump design, for example the thresholds for Al^{27}, Cu^{63}, Cu^{65} and C^{12} (graphite) are 13.05, 10.84, 9.91 and 18.72 MeV respectively. This means that problems from induced activity both in the dump itself and the required cooling water will be significantly reduced. Also as the photo-neutron yield is reduced the local shielding of the dump may be simplified.

Table 15.5 Beam dump parameters

	Units	HAC Loop	XUV-FEL	IR-FEL
Energy	MeV	10	950	60
Current	mA	100	0.001	2.6
Power	kW	1000	0.95	156

To provide a feel for the beam dump shielding, simple calculations have been carried out to estimate the required beam dump dimensions. The gamma yields at the dump energies of 10 MeV and 60 MeV for the HAC loop and the IR-FEL are too low to be accurately modelled by SHIELD11 so data from NCRP51 was used to estimate the photon dose rate yields in those cases. However the SHIELD11 yields for the giant resonance and mid-energy neutron groups were used in this assessment. Table 15.6 details the required shielding. The concrete thickness corresponds to the main machine shield wall in the forward direction with local lead and steel being used as necessary.

Table 15.6 Beam dump dimensions in the forward direction

	Units	HAC Loop	XUV-FEL	IR-FEL
Concrete	cm	300	300	250
Steel	cm	40	75	75
Lead	cm	-	40	-

Significant activation of both the XUV and IR-FEL dumps will occur as they are operating at high energies. Cooling of the HAC loop dump and the IR-FEL dump will need careful consideration. The Monte Carlo code FLUKA will be used both to assess the power distribution as well as the radionuclide inventory and dose rates in the dumps.

Beam losses throughout the machine lattice will also lead to induced activity issues for maintenance although the proposed losses of the order of watts will alleviate some of the problems.

15.2.9 Labyrinths and Ducts

In common with all accelerator facilities there is a requirement for penetrations through the main shield wall to permit entry not only of personnel and equipment but also electrical, RF and cryogenic services. Personnel access ways are typically rectangular in shape and 1 m by 2 m in size. Service ducts are usually much smaller and may be rectangular or circular in cross section. These ducts will usually be partially filled with cryogenic pipework, cabling and other services.

Two general rules are applicable to the design of all penetrations:

- A penetration should not be arranged so that a particle or photon beam is directed towards the primary opening. Observing this precaution ensures that the penetrations are transmitting primarily photons or neutrons resulting from large angle scattering rather than those arising from the forward peaked field or from the direct beam;

- For any labyrinth the total wall thickness between the source and region of interest should be equivalent to that required if the labyrinth were not present.

The requirements for the large personnel access labyrinths may be calculated using the formulas derived by Tesch [32, 33], from practical measurements on the scattering of gamma and neutron radiation down multi-legged labyrinths.

The Duct-III code [34] may be used to calculate the requirements of the smaller service ducts which are not amenable to the formulas derived by Tesch. The Duct-III code uses a semi-empirical formula based on an albedo analytical method. The code has been used for the design of ducts in nuclear power plants and accelerators and has been benchmarked both against Monte Carlo codes and experiment [35].

15.2.10 Environmental Issues

Two broad sources of radiation need to be taken into account when considering the environmental impact from the operation of any high power accelerator facility such as 4GLS. Prompt radiation, known as skyshine, may be measurable at significant distances from the operating accelerator. In addition induced radioactivity presents a number of potential exposure pathways to environmental pollution:

- the controlled release to atmosphere of short-lived air activation products such as N^{13} and O^{15};
- the controlled release of activated cooling water to the drains;
- the controlled release to landfill or other storage, of solid activated materials from decommissioning.

Appropriate management systems will be put in place to ensure there is no loss of control of activated materials.

15.2.10.1 Boundary Skyshine

A problem that plagued a number of early accelerators is that of neutron skyshine where high energy neutrons that "leak" through the usually thin roof shield are scattered back to ground by air atoms and may be detected at considerable distances from the accelerator. Patterson and Thomas [15] proposed the following empirical equation for distances, $r > 50$ m:

$$\phi(r) = \frac{aQ}{4\pi r^2}(1 - e^{-r/\mu}).^{-r/\lambda} \qquad (15\text{-}11)$$

$\phi(r)$ represents the fluence rate from a neutron source strength Q ns^{-1}. Here a represents an empirical buildup factor and μ is the effective buildup relaxation length and λ an effective interaction length.

The current proposal is for a thick roof over the accelerator tunnels with an experimental hall housed above. The roof will be thick enough for routine access and therefore neutron leakage leading to boundary skyshine doses will be negligible. Photon skyshine will also be negligible for the same reason.

15.2.10.2 Air Activation

The intense forward directed bremsstrahlung beams from electron loss lead directly to the formation of short-lived gaseous radionuclides. These will be discharged to atmosphere by the ventilation plant, after mixing and dilution within the accelerator vaults.

Data on the production of radioactive gases at electron accelerators has been summarised by Swanson [16] and the NCRP [18]. The reaction channel for formation of radionuclides in air is the photo-neutron, (γ,n), interaction of bremsstrahlung with air nuclei. The thresholds for the formation of N^{13} and O^{15} are 10.55 MeV and 15.67 MeV respectively. Of less significance is the formation of C^{11} via photo-spallation of both nitrogen and oxygen nuclei. The production and build-up of H^3 and Be^7 will be limited because of their smaller cross sections and their half-lives being long compared with the estimated ventilation rates. The thermal neutron activation of Ar^{40} to Ar^{41} also requires consideration.

Discharge of radioactive gases to atmosphere is regulated by the Environment Agency. Unlimited quantities of radioactive gases with half-lives less than 100 seconds may be discharged without the need for a specific authorisation under the Radioactive Substances Act 1993 [36] by virtue of the Substances of Low Activity Exemption Order [37]. The NRPB have concluded [38] that such discharges meet both the International Atomic Energy Agency [39] and the European Basic Safety Standards [7] criteria for exemption from reporting or authorisation. However many accelerator produced gaseous radionuclides, for example those considered above, have half-lives in excess of 100 seconds and are therefore subject to Environment Agency control, normally via an appropriate Authorisation made under the Radioactive Substances Act 1993.

Holbourn [40] has shown that for an assumed loss of 2.1 W and 1000 hours of operation of the ERLP facility, the dose to a member of the critical group at the site boundary is expected to be 30 nSv. Similar calculations will need to be made for 4GLS to demonstrate that boundary doses are within permitted constraints.

15.2.10.3 Water Activation

Activation of the cooling water for accelerator components, particularly the beam stops, must be considered. In a similar manner to that for air activation, Swanson [16] has compiled the results of calculations to address the production of radionuclides in water at electron accelerators, listing saturation activities normalised to beam power. At a later stage in the design process a full assessment of such activation will be made to assess the hazards to personnel working near the cooling circuits as well as doses to members of the public from discharges authorised by the Environment Agency.

Activation of the groundwater is not likely to be a significant issue as the accelerators will be built on a substantial concrete floor for stability, significantly reducing the high energy neutron field reaching the underlying bedrock.

15.2.10.4 Decommissioning

Operation of high power electron accelerator facilities such as 4GLS will inevitably lead to significant quantities of activated materials in the high energy beam dumps as well as some activity within the general machine lattice. Following closure, a planned process of decommissioning the facility will need to take place. Some useful background information on the decommissioning of accelerators is available in a EU Commission report, [41] and papers by Opelka [42] and Hofert [43].

Decommissioning is a controlled process that involves the clean up, removal, and/or securing of not only radioactive but other hazardous materials, equipment and structures. To this end there will always be a variety of options available that need to be critically evaluated with the one selected best meeting the needs of the stakeholders, i.e. the organisation, the regulators, in this case the Environment Agency, and possibly the public. The range of possible end states includes:

- continuous surveillance and maintenance with no further action;
- decontaminate and leave in place;
- isolate (seal or enclose) and leave in place;
- partial removal and disposal;
- full removal.

Disposal will need the approval of the Environment Agency if the specific activities of waste exceed the level of 0.4 Bqg^{-1} specified in the exemption order [37], made under the Radioactive Substances Act 1993 [36].

15.2.11 Radiation Monitors

A comprehensive monitoring network for the assessment of both instantaneous dose rates and integrated doses will be implemented.

15.2.11.1 Installed

Installed monitors will be located around the accelerator shield wall, experimental areas and possibly peripheral areas. These monitors will indicate instantaneous dose rates and provide audible and visual indication of the status of the monitor. It is likely that the monitors used will be based around pressurised argon and hydrogen ionisation chambers. Detectors such as these are already in use at other accelerators, for example the ERLP at Daresbury and Diamond near Oxford. Other technologies are available, the ESRF having utilised bubble detectors for neutron monitoring successfully over many years. A full scoping exercise will be undertaken to ascertain the best technological solution at the appropriate time.

The monitors will be interfaced to the Personnel Safety System to provide the necessary safety interlocks in the case of high instantaneous dose rates. The monitors will also interface with the Control System to provide full data acquisition and history information.

15.2.11.2 Integrating

In addition to the active installed monitors it is expected that a comprehensive passive network of integrating detectors will be utilised. Suitable detectors are moderated Li^6 and Li^7 thermo-luminescent detectors providing separate measurement of gamma and neutron doses. Such detectors have been used around the SRS at Daresbury for many years.

15.3 Summary

In summary, 4GLS is a complex facility requiring close safety management in accordance with current best practice and the TDR will continue to develop the necessary safety management systems.

Control of the radiation hazard is one of the more challenging safety aspects of the project with management of this hazard incorporated into the Conceptual Design. It is evident at this stage that the bulk shielding requirements are significant and that deflection of the required photon beams away from the intense on-axis bremsstrahlung fields will be required before transmission through to the experimental area.

Areas requiring significant further work include for example, more accurate modelling of the accelerator and beamline shielding requirements, electron tracking simulations to ensure electrons cannot pass down a beamline, and optimisation of the vacuum specification balancing cost and gas bremsstrahlung power. The use of collimators to control and localise electron losses together with a comprehensive beam loss and machine protection system is a further area that requires significant development.

REFERENCES

[1] 'Health and Safety at Work Act 1974', HMSO 1974, ISBN 0105437743.

[2] 'The Management of Health and Safety at Work Regulations 1999', Statutory Instrument 1999/3242, Stationery Office, 1999 ISBN 0110856252

[3] 'The Construction Design and Management Regulations 1994', Statutory Instrument 1994/3410, Stationery Office, 1994 ISBN 0110438450

[4] 'The Construction (Design and Management) (Amendment) Regulations 2000' Statutory Instrument 2000/2380, Stationery Office, 2000 ISBN 0110998049

[5] 'The Ionising Radiations Regulations 1999', SI 1999/3232 Stationery Office, 1999 ISBN 0110856147.

[6] 'Functional safety of electrical, electronic, programmable and electronic safety-related systems', IEC61508, IEC 1998,2000.

[7] 'Council Directive 96/29 Euratom of 13 May 1996 laying down basic safety standards for the protection of health of workers and the general public against the dangers arising from ionising radiation', Official Journal of the European Communities 1996 39 (L159) 1-114.

[8] 'Work with Ionising Radiation. Ionising Radiations Regulations 1999, Approved Code of Practice and Guidance L121', Stationery Office 2000, ISBN 0717617467.

[9] 'The Justification of Practices Involving Ionising Radiation Regulations 2004', Statutory Instrument 2004/1769 Stationery Office, ISBN 0110495004

[10] 'The Ionising Radiations Regulations 1985', SI 1333 Stationery Office, 1985 ISBN 0110573331.

[11] 'Authorisation under the Ionising Radiations Regulations 1999', Health and Safety Executive Information Sheet No5, 2000.

[12] 'Ionising Radiations Regulations 1999 - Prior authorisation for the use of accelerators (other than electron microscopes)', Health and Safety Executive, March 2000.

[13] P Wright and M Holbourn, 'The CCLRC Radiation Shielding Policy', May 2004.

[14] 'Occupational, Public and Medical Exposure', Documents of the NRPB Vol 4, No 2, 1993, ISBN 0859513610.

[15] H Wade Patterson and Ralph H Thomas, 'Accelerator Health Physics', Academic Press 1973. ISBN 0125471505.

REFERENCES, Continued

[16] IAEA Technical Report Series 188, 'Radiological Safety Aspects of the Operation of Electron Linear Accelerators', IAEA Vienna 1979, ISBN 9201251793.

[17] NCRP Report 51, 'Radiation Protection Design Guidelines for 0.1 to 100 MeV Particle Accelerator Facilities', NCRP 1977, ISBN 00913392332.

[18] NCRP Report 144, 'Radiation Protection for Particle Accelerator Facilities', NCRP 2003, ISBN 0929600770.

[19] AH Sullivan, 'A Guide to Radiation and Radioactivity Levels Near High Energy Particle Accelerators', Nuclear Technology Publishing 1992, ISBN 1870965183.

[20] TM Jenkins, 'Neutron and photon measurements through concrete for a 15 GeV electron beam on a target – comparison with models and calculations', NIM 159 (1979) 265.

[21] WR Nelson and TM Jenkins, 'The SHIELD11 Computer Code', SLAC-R-737 February 2005.

[22] Diamond Light Source, 'Report of the design specification', March 2002.

[23] M Holbourn, 'ERLP Radiation Safety Assessment', erlp-sfty-rpt-001, 2005.

[24] A Leuschner, 'Radiation Safety Aspects of the TESLA Test Facility Phase 2 (TTF2)', Proceedings of the 3rd International Workshop on Radiation Safety of Synchrotron Radiation Sources, SPring-8, Japan 2004.

[25] XS Mao and H Vincke, 'Gamma and Neutron Radiation Shielding for LCLS Electron Enclosure from BSY Wall to Near Hall', SLAC Radiation Physics Note R-04-10, May 2004.

[26] A Fassò, A Ferrari, PR Sala, 'Electron-photon transport in FLUKA: status', Proceedings of the Monte Carlo 2000 Conference, Lisbon, October 23-26 2000, A Kling, F Barao, M Nakagawa, L Tavora, P Vaz - eds., Springer-Verlag Berlin, p.159-164 (2001).

[27] A Fassò, A Ferrari, J Ranft, PR Sala, 'FLUKA: Status and Prospective for Hadronic Applications', Proceedings of the Monte Carlo 2000 Conference, Lisbon, October 23-26 2000, A Kling, F Barao, M Nakagawa, L Tavora, P Vaz - eds. , Springer-Verlag Berlin, p.955-960 (2001).

[28] L Emery and M Borland, 'Analytical studies of top-up safety for the Advanced Photon Source', Proceedings of the 1999 Particle Accelerator Conference, New York 1999.

[29] L Emery and M Borland, 'Tracking studies of top-up safety for the Advanced Photon Source, Proceedings of the 1999 Particle Accelerator Conference, New York 1999.

REFERENCES, Continued

[30] K Tiedtke, 'FEL beam transport into the experimental hall and radiation protection', TTF2 Review Meeting, Salzau 2002.

[31] A Ferrari, M Pellicioni and PR Sala, 'Estimation of fluence rate and absorbed dose rate due to gas bremsstrahlung from electron storage rings', NIM B 83 (1993) 518-524.

[32] K Tesch, 'The attenuation of the neutron dose equivalent in a labyrinth through an accelerator shield', Particle Accelerators 12 (1982) 169-175.

[33] K Tesch, 'Attenuation of the photon dose in labyrinths and ducts at accelerators', Radiation Protection Dosimetry 20 No. 3 (1987) 169-174.

[34] R Tayama et al, Duct-III: A simple design code for duct streaming radiations', KEK Internal Report 2001, November 2001.

[35] F Masukawa et al, 'Analyses of High Energy Neutron Streaming Experiments Using DUCT-III,' Journal of Nuclear Science and Technology Supplement 2 (2002) 1268-1271.

[36] 'Radioactive Substances Act 1993', HMSO 1993, ISBN 0105412937.

[37] 'The Radioactive Substances (Substances of Low Activity) Exemption Order 1986', No.1002 (1986), Amended 1999.

[38] SF Mobbs et al, 'Radiological Assessments of the Doses arising from Short-lived Gases and the Doses from Organic Liquids containing Tritium and Carbon-14 used and disposed under the Substances of Low Activity Exemption Order', NRPB-M1179, July 2000.

[39] International Atomic Energy Agency, 'Principles for exemption of radiation sources and practice from regulatory control', IAEA Safety Series No.89, 1988.

[40] M Holbourn, 'Radiological Assessment for the discharge of accelerator produced radioactive gases to the atmosphere', Internal Memorandum, November 2005.

[41] 'Evaluation of the radiological and economic consequences of decommissioning particle accelerators', European Commission 1999, ISBN 928287222X.

[42] JH Opelka et al, 'Reutilisation potential of accelerator components: A decommissioning perspective', IEEE Transactions on Nuclear Science 26 No.3 June 1979.

[43] M Hofert and D Forkel-Wirth, 'The Decommissioning of Accelerator Installations, A Challenge for Radiation Protection in the 21st Century', Proceedings of the IRPA10 Conference, Hiroshima May 2000.

16. Appendices

16.1 Glossary

1PPE / 2PPE	1 or 2 Photon Photo-Emission
3HC	Third Harmonic Cavity
4GLS	Fourth Generation Light Source
AC	Alternating Current
ADC	Analogue-to-Digital Converter
ALS	Advanced Light Source
APPLE	Advanced Planar Polarised Light Emitter
APT	Accelerator Production of Tritium
ASTeC	Accelerator Science and Technology Centre
ASTRA	A Space charge TRacking Algorithm
ATF	Accelerator Test Facility at BNL
BBO	Beta-Barium Borate
BBU	Beam Break-Up
BM	Bending Magnet
BNL	Berkeley National Laboratory
BNS	Balakin-Novokhatski-Smirnov (damping)
BPM	Beam Position Monitor
BTS	Beam Transport System
CBS	Compton Back-Scattering
CCD	Charge-Coupled Device
CCLRC	Council for the Central Laboratories of the Research Councils
CD	Circular Dichroism
CEA	Commissariat à l'Energie Atomique
CEBAF	Continuous Electron Beam Accelerator Facility
CESR	Cornell Electron Storage Ring
CLIC	CERN Linear Collider
CM	Collimating Mirror
CPA	Chirped Pulse Amplification

CSR	Coherent Synchrotron Radiation
CTR	Coherent Transition Radiation
CVD	Chemical Vapour Deposition
CW	Continuous Wave
DC	Direct Current
DESY	Deutsches Elektronen Synchrotron
DI	DeIonised water
DSP	Digital Signal Processor
DUVFEL	Deep Ultra-Violet Free-Electron Laser
EBIT	Electron Beam Ion Trap
ELBE	Elektronen Linearbeschleuniger für strahlen hoher Brillianz und niedriger Emittanz
ELEGANT	A particle tracking code
EM	Electro-Magnetic
EO	Electro-Optic
EOS	Electro-Optic Sensing
EP	Electro Polishing
ER	Energy Recovery
ERL	Energy Recovery Linac
ERLBBU	Energy Recovery Linac Beam Break Up
ERLP	Energy Recovery Linac Prototype
ESRF	European Synchrotron Radiation Facility
EU	European Union
EXAFS	Extended X-ray-Absorption Fine Structure
EuroFEL	European Free-Electron Laser Design Study
FEL	Free-Electron Laser
FELIX	Free-Electron Laser for Infra-red eXperiments
FM	Focussing Mirror
FODO	Focus-Drift-Defocus-Drift lattice type
FOM	Foundation for Fundamental Research on Matter (Utrecht, Netherlands)
FPGA	Field Programmable Gate Array

FROG	Frequency Resolved Optical Gating
FT	Fourier Transform
FWHM	Full Width at Half Maximum
FZR	Forschungzentrum Rossendorf
GENESIS	A particle tracking code
HACL	High Average Current Loop
HF	High Frequency
HGHG	High Gain Harmonic Generation
HH	High Harmonic
HHG	High Harmonic Generation
HOM	Higher Order Mode
HPP	High Pulse Power
HPR	High Pressure Rinsing
HVAC	Heating, Ventilation and Air-Conditioning
ICT	Integrating Current Transformer
ID	Insertion Device
ILC	International Linear Collider
INFN	Istituto Nazionale di Fiscia Nuclare
IOT	Inductive Output Tube
IR	Infra-Red
IR-FEL	Infra-Red Free-Electron Laser
IVR	Intramolecular Vibrational energy Redistribution
JAERI	Japan Atomic Energy Research Institute
JLAB	Jefferson Laboratory – See entry for TJNAF
KEK	Koh Ene Ken (Japanese national laboratory for high-energy physics)
KEK-B	An experimental facilty at KEK
LANL	Los Alamos National Laboratory
LC-ABD	Linear Collider – Accelerator and Beam Delivery
LCLS	Linac Coherent Light Source
LCR	Electrical circuit comprising inductance, capacitance and resistance
LLRF	Low-Level Radio Frequency

LMA	Large Mode Area
LOLA	Cavity providing a transverse deflection to characterise longitudinal bunch length. The abbreviation is derived from the names of the secondary beam separator designers at SLAC (c.1960)
LSC	Longitudinal Space Charge
MATLAB	Mathematical Laboratory – A mathematical software package
MCT	Mercury-Cadmium-Telluride (IR detector, also referred to as HCT)
MIT	Massachusetts Institute of Technology
ML	Multi-Layer
MLC	Mathematica Lattice Code
MPW	Multi-Pole Wiggler
NA	Numerical Aperture
NEA	Negative Electron Affinity
NIST	National Institute of Science and Technology
NOPA	Non-collinear Optical Parametric Amplifier
ODEs	Ordinary Differential Equations
OPA	Optical Parametric Amplifier
OPCPA	Optical-Parametric Chirped-Pulse Amplification
OPD	Optical Path Difference
OPG	Optical Parametric Generator
OPTI	A lattice cell simulation and matching code
OTR	Optical Transition Radiation
P-BPM	Photon Beam Position Monitors
PARMELA	Phase and Radial Motion in Electron Linear Accelerators tracking code
PEA	Positive Electron Affinity
PES	Photo-Electron Spectroscopy
PEEM	Photo-Emission Electron Microscopy
PFM	Post-Focussing Mirror
PG	Plane Grating
PHASE	A photon tracking code
PITZ	Photo Injector Test Facility at DESY, Zeuthen, Germany

PM	Plane Mirror
PPARC	Particle Physics and Astronomy Research Council
PPM	Pure Permanent Magnet
QE	Quantum Efficiency
RADIA	A software package for modelling insertion devices in mathematica
RAFEL	Regenerative-Amplifier Free-Electron Laser
RAIRS	Reflection-Absorption Infra-Red Spectroscopy
RAS	Reflection Anisotropy Spectroscopy
RF	Radio Frequency
RHIC	Relativistic Heavy-Ion Collider at BNL
RMS	Root-Mean-Squared
ROA	Raman Optical Activity
ROC	Radii Of Curvature
RP	Resolving Power
SASE	Self-Amplified Spontaneous Emission
SCRF	Super-Conducting Radio Frequency
SD	Spectral Decoding
SE	Spatial Encoding
SH	Second Harmonic
SHG	Second-Harmonic Generation
SLAC	Stanford Linear Accelerator
SLS	Swiss Light Source
SNS	Spallation Neutron Source
SPM	Self-Phase Modulation
SPPS	Sub-Picosecond Photon Source
SR	Synchrotron Radiation
SRF	Superconducting Radio Frequency
SRS	Synchrotron Radiation Source
SRW	Synchrotron Radiation Workshop
SS	Steady State
SwM	Switching Mirror

SXR	Soft X-Ray
TBA	Triple-Bend Achromat
TCSPC	Time-Correlated Single-Photon Counting
TD	Temporal Decoding
TDC	Transverse-Deflecting Cavities
TDR	Technical Design Report
TEM $_{XX}$	Transverse Electromagnetic Wave (with mode $_{XX}$)
TESLA	TeV Energy Superconducting Linear Accelerator
TTF/TTF II	TESLA Test Facility (2)
TJNAF	Thomas Jefferson National Accelerator Facility
TOF	Time-Of-Flight
UCLA	University of California, Los Angeles
UK	United Kingdom
UV	Ultra-Violet
VCO	Voltage-Controlled Oscillator
VLS	Varied Line Spacing
VUV-FEL	Vacuum Ultra-Violet Free-Electron Laser
XAS	X-ray Absorption Spectroscopy
XFEL	X-ray Free-Electron Laser
XMCD	X-ray Magnetic Circular Dichroism
XUV	eXtreme Ultra-Violet
XUV-FEL	eXtreme Ultra-Violet Free-Electron Laser
YAG	Yttrium-Aluminium-Garnet
YDFL	Ytterbium-Doped Fibre Laser

16.2 Key Tables

16.2.1 Injector Systems

Table 16.1 Beam requirements for the high average current injector, at the entrance to the main linac

Parameter	High-average current mode	Optimised for VUV-FEL	
Bunch charge	77	77	pC
Bunch repetition rate	1300	n × 4⅓	MHz
Bunches per train	continuous	1	
Energy	10	10	MeV
Normalised emittance	< 2	< 2	mm mrad
Uncorrelated energy spread	< 0.1	< 0.1	%
Bunch length (σ)	~ 2	~ 2	ps

(*where N is an integer)

Table 16.2 Beam parameters required for the XUV-FEL injector at the entrance of the main linac

Parameter	Value	
Bunch charge	1	nC
Fundamental RF frequency	1.3	GHz
Train repetition rate	1	kHz
Energy	160	MeV
Normalised emittance	< 2	mm mrad
Uncorrelated energy spread	~< 0.05	%
Bunch length (σ)	~ 2	ps

Table 16.3 Beam parameters required at the exit of the accelerating module after the IR-FEL injector

Parameter	Value	
Bunch charge	200	pC
Bunch repetition rate	13	MHz
Peak current	8 to 80	A
Energy	25 to 60	MeV
Normalised emittance	< 10	mm mrad
Energy spread (RMS)	< 0.1	%
Bunch length (σ)	1 - 10	ps

16.2.2 Superconducting Linacs

Table 16.4 Summary of 4GLS linac operating parameters

	Linac1	Linac2	Linac3	Linac4	Linac5	Linac6	Linac7
Number of Cells/Cavity	2	7	7	9	7	7	7
Number of Cavities	10	8	8	4	48	16	8
Number of Modules	2	1	1	1	6	2	1
Energy Gain (MeV)	10	95	95	-30	590	200	60
E_{acc} (MV/m)	4.3	14.7	14.7	14.5	15.2	15.5	9.3
Q_e	1×10^5	1.3×10^7	1.3×10^7	5×10^6	2.6×10^7	1.3×10^7	1.3×10^7
Total RF Power/Cavity (kW)	100	13	13	13.3	9.85*	14.9	19.5

**Includes CSR losses*

16.2.3 Electron Beam Transport

Table 16.5 XUV-FEL electron beam parameters

XUV-FEL Bunch Parameter	
Energy at XUV-FEL, E	750 to 950 MeV
Normalised Emittance at XUV-FEL, ε	2 mm mrad
RMS Projected Energy Spread at XUV-FEL	0.1%
RMS Bunch Length at XUV-FEL	<270 fs
Bunch Charge	1 nC
Bunch Repetition Rate	1 kHz
Electron Beam Average Power at XUV-FEL	1 kW
Energy at start of main linac	160 MeV

Table 16.6 HACL electron beam parameters

HACL Bunch Parameter	*100 mA Operation*	*VUV-FEL Operation*
Energy at VUV-FEL, E	600 MeV	600 MeV
Normalised Emittance at 600 MeV, ε	2 mm mrad	2 mm mrad
RMS Projected Energy Spread	0.1 %	0.1 %
RMS Bunch Length at Device	100-900 fs in six straights	100 fs
Bunch Charge	77 pC	77 pC
Bunch Repetition Rate	1.3 GHz	$n \times 4.33$ MHz
Electron Beam Average Power at 600 MeV	60 MW	$n \times 200$ kW
Injector Energy	10 MeV	10 MeV
Dump Energy	~ 10 MeV	~ 10 MeV

Table 16.7. IR-FEL electron beam parameters

IR-FEL Bunch Parameter	
Energy at IR-FELs, E	25-60 MeV
Normalised Emittance at 60 MeV, ε	10 mm mrad
RMS Projected Energy Spread at 60 MeV	0.1%
RMS Bunch Length	1 to 10 ps (variable)
Bunch Charge	200 pC
Bunch Repetition Rate	13 MHz
Electron Beam Average Power at 60 MeV	156 kW

16.2.4 FELS

Table 16.8 Summary of parameter and performance estimates for the FEL sources of 4GLS

	XUV-FEL	*VUV-FEL*	*IR-FEL*
	FEL DESCRIPTION		
FEL design	High Gain Amplifier	Regenerative Amplifier	Oscillator
Seeding type	External seeding	Self-seeding	Self-seeding
Seeding mechanism	HHG source	Low-Q cavity	High-Q cavity
	FEL PHOTON OUTPUT		
Tuning Range	8 - 100 eV	3 - 10 eV	2.5 - 200 μm
Repetition rate	1 kHz	n × 4⅓ MHz	13 MHz
Polarisation	Variable elliptical	Variable elliptical	Variable elliptical
Max Peak Power	8 GW	500 MW (3 GW*)	9 MW (>20 MW*)
Pulse length FWHM	< 50 fs	170 fs (25 fs*)	2 ps (300 fs*)
Typical $\Delta\nu\Delta t$	≈ 0.6	≈ 1.0	≈ 0.9
Max pulse energy	400 μJ	70 μJ	50 μJ
	ELECTRON BEAM PARAMETERS AT FEL		
Energy	750 - 950 MeV	600 MeV	25 - 60 MeV
Bunch Charge	1 nC	77 pC	200 pC
RMS bunch length	266 fs	100 fs	1 - 10 ps
Peak Current	1.5 kA	300 A	8 - 80 A
Normalised emittance	2 mm mrad	2 mm mrad	10 mm mrad
RMS energy spread	0.1%	0.1%	0.1%
	UNDULATOR PARAMETERS		
Undulator Type	PPM & APPLE-II	APPLE-II	APPLE-II
No of Modules	8 & 5	5	1 & 1
Module length	2 m	2.2 m	2.65 m & 5.07 m
Period	45 mm & 51 mm	60 mm	53 mm & 145 mm
Focussing	FODO	FODO	Natural
Minimum magnetic gap	10 mm	10 mm	23.5 mm & 74 mm

* indicates possible output in superradiant mode

16.2.5 Conventional SR and Laser Sources

Table 16.9 Summary of the photon output from the various sources of 4GLS

	XUV-FEL	*VUV-FEL*	*IR-FEL*	*U30*	*U60*	*Dipole CSR (HACL)*	*Wiggler*	*OPA Laser*
Harmonic	1	1	1	1 to 9	1 to 9	—	—	—
Photon Energy Range (eV)	8 to 100	3 to 10	0.006 to 0.5	33 to 600	2 to 300	0.0001 to 0.03	1 to 5000	0.1 to 6
Wavelength Range (μm)	0.15 to 0.012	0.4 to 0.12	2.5 to 200	0.04 to 0.002	0.6 to 0.004	10000 to 40	1 to 0.0002	11 to 0.2
Repetition Rate	1 kHz	n x 4.33 MHz	13 MHz	1.3 GHz	1.3 GHz	1.3 GHz	1.3 GHz	1 kHz
FWHM Photon Pulse Length (fs)	50	170	2000 to 10000	300 to 2000	300 to 2000	235	500 to 2000	130
Peak Flux (/s/0.1%)	~5 x10^{26}	~1 x10^{26}	~1 x10^{26}	~1 x10^{19}	~3 x10^{18}	~6 x10^{24}	~6 x10^{16}	~1 x10^{27}
Peak Brightness (/s/mm^2/mrad^2/0.1%)	~1 x10^{30}	~1 x10^{28}	~1 x10^{22} to ~2 x10^{25}	~2 x10^{22}	~2 x10^{21}	~1 x10^{20}	~5 x10^{17}	~1 x10^{27}
Energy per Pulse (μJ/0.1%)	~200	~60	~40	~3 x10^{-5}	~3 x10^{-6}	~1 x10^{-4}	~1 x10^{-6}	~30
Photons per Pulse (/0.1%)	~5 x10^{13}	~1 x10^{14}	~6 x10^{14} to ~2 x10^{16}	~2 x10^{6}	~1 x10^{6}	~1 x10^{12}	~4 x10^{4}	~1 x10^{14}
Average Flux (/s/0.1%)	~3 x10^{16}	~6 x10^{19}	~7 x10^{21}	~3 x10^{15}	~1 x10^{15}	~1 x10^{21}	~5 x10^{13}	~1 x10^{17}
Average Brightness (/s/mm^2/mrad^2/0.1%)	~5 x10^{19}	~5 x10^{21}	~8 x10^{17} to ~1 x10^{21}	~7 x10^{18}	~7 x10^{17}	~1 x10^{16}	~7 x10^{14}	~1 x10^{17}

16.2.6 Photon Beam Transport

Table 16.10 Comparison of two-, three- and four-mirror optical delay lines operating in the XUV energy range

	Two-mirror	Three-mirror	Four-mirror
Delay Range (ns)	1.00	1.00	1.04
Travel Required (m)	2.00	1.07	1.049
Total Length (m)	4.34	10	10
Total Width (m)	2.0	1.25	1.21
Grazing angle at min delay	12.375°	1° & 2°	1°
Grazing angle at max delay	20.25°	7° & 14°	7.5°
Total Rs at min delay @ 10 eV	0.49	0.88	0.89
Total Rs at min delay @ 100 eV	0.32	0.88	0.89
Total Rs at max delay @ 10 eV	0.42	0.45	0.43
Total Rs at max delay @ 100 eV	0.14	0.38	0.39
Total Rs/Rp at min delay @ 10 eV	5.95	1.34	1.34
Total Rs/Rp at min delay @ 100 eV	1.18	1.03	1.04
Total Rs/Rp at max delay @ 10 eV	17.36	7.72	8.84
Total Rs/Rp at max delay @ 100 eV	1.49	1.19	1.18

Table 16.11 Performance of focused direct light beamline on XUV-FEL (9 x 4μm^2 spot size)

Parameter			***Unit***
Photon Energy	10	100	eV
Peak output power of FEL	6080	1370	MW
Pulse length (rms)	22	22	fs
Beamline efficiency	75	61	%
Energy / pulse at experiment	251	46	µJ
Photons / pulse at experiment	2.10^{14}	3.10^{12}	
Image size (FWHM)	9 x 4	9 x 4	μm^2
Photon density	4.10^{12}	7.10^{10}	1 / μm^2 / pulse
Pulse energy density	6.10^{5}	1.10^{5}	mJ / cm^2 / pulse
Peak power density	$1.\ 10^{16}$	2.10^{15}	W / cm^2

Table 16.12 Properties of CSR for sources in the XUV-FEL branch and the high average current loop

	High average current loop	XUV-FEL branch
Maximum Average flux	$2*10^{21}$ phot/s/0.1%bw at 3 meV	
Maximum Average brightness	~10^{17} phot/s/0.1%bw/mrad^2/mm^2 at 7 meV	
Maximum Flux per pulse		2 x 10^{14} phot/0.1%bw at 1 meV
Energy per pulse		90 μJ mainly from 0.4 to 4 meV
Repetition rate		1 kHz

16.2.7 Technical systems

Table 16.13 Parameters of the cryogenic system

Parameter	*Value*
Operating Temperature	1.8 K
Number of Modules	14
Number of Linacs	7
Module Combined (Static + Dynamic) Heat Load	2.03 kW @ 1.8 K
Radiation Screen & RF Coupler Heat Loads (50-80K) (Static + Dynamic)	3.75 kW @ 80 K
HOM load (80K)	15.2 kW
Radiation Screen Heat Load (4 – 10K)	642 W @ 5 K
Distribution Losses	500 W @ 1.8 K
Operational Regime of RF System	Constant Wave (CW)
Operational Regime of the Cryogenic system	The 7 linacs will have different operating parameters and therefore independent control is required for each linac.
Redundancy / Factor of Safety	1.5
Flow Rate	183.7 g/s
Size of Refrigerator / Liquefier	5250 l/hr at 1.8K

Table 16.14 Losses for the cryogenic system

				1.8 K losses, W			*80 K HOM losses, W*
Linac	Modules	Cavities per module	Total Cavities	Static per module	Dynamic per cavity	Total	
LINAC 1 *10 MeV High Average Current Injector*	2	5	10	10.0	19.5	214.5	1694.0
LINAC 2 *95 MeV XUV-FEL Injector*	1	8	8	10.0	19.5	165.6	1355.2
LINAC 3 *95 MeV XUV-FEL Injector*	1	8	8	10.0	19.5	165.6	1355.2
LINAC 4 *XUV-FEL Injector 3rd Harmonic Cavity* (details to be further developed)	1	4	4	10	*	*	*
LINAC 5 *590 MeV Main Linac*	6	8	48	60.0	19.5	993.6	8131.2
LINAC 6 *200 MeV XUV-FEL*	2	8	16	20.0	19.5	331.2	2710.4
LINAC 7 *60 MeV IR-FEL*	1	8	8	10.0	19.5	165.6	1355.2
Total	**14**		**90**	**120**		**2036. 1**	**15246.0**
			Distribution Losses			500.0	W
			Total losses at 1.8K			**2536.1**	W
Total refrigeration requirement (with safety factor of 1.5)						**3499.8**	**W**
			Helium Consumption			5249.7	l/hr

16.2.8 Buildings and Engineering Services

Table 16.15 Estimated electrical power requirements

Machine		***Total load kW***
Electron gun(s)		135
RF - injectors	(200 mA – 2 MW RF power @ 40 % efficiency)	5000
RF – linacs	(cryomodules will require 80 x 25 kW IOT)	2000
Power converters (magnets)		850
Electron gun control		6
Vacuum		160
Diagnostics		20
Network/control		54
Front-end		20
Insertion devices		20
RF control		60
FELs		24
Laser room		12
Cryogenic system		5024
Beamlines (20 beamlines at 20 kW each)		400
Total machine kW		**13,785**
Ancillary plant		
Lighting		20
Climate Control	Accelerator tunnel area	300
(heating not required)	Experimental and auxiliary area	400
Chiller System	Canal raw water pumps	100
	Magnet chiller	300
	Magnet water pumps	50
	IOT water pumps - canal	75
	Cryogenics cooling water pumps - canal	100
Compressed Air		200
Offices/laboratories		50
Total ancillary load kW		**1,595**
Total 4GLS electrical load kW		**15,380**

Table 16.16 Estimated significant cooling water loads

System	***Estimated cooling load (MW)***	***Water Quality***
Radiofrequency	1	De-ionised
Cryogenics	1	Canal
Magnets	1	De-ionised
Beam dumps	1	Canal
Beamlines	0.5	De-ionised
Air conditioning (climate control)	2.5	Chilled

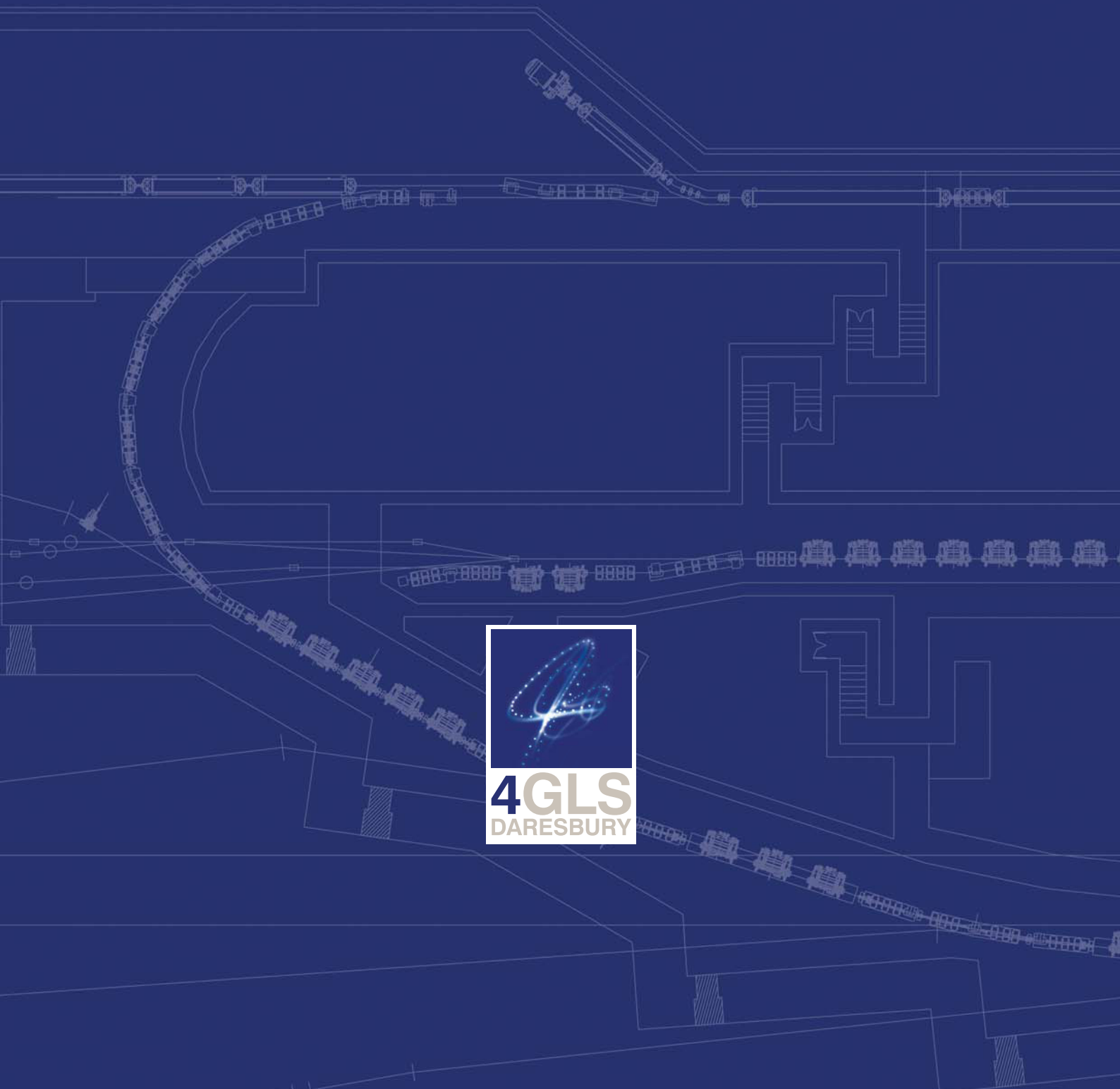

4GLS
DARESBURY

For more information call

Professor Elaine Seddon
Telephone: 01925 603245 Email: e.a.seddon@dl.ac.uk

CCLRC

4GLS is part of the
Council for the Central Laboratory of the
Research Councils

http://www.4gls.ac.uk/

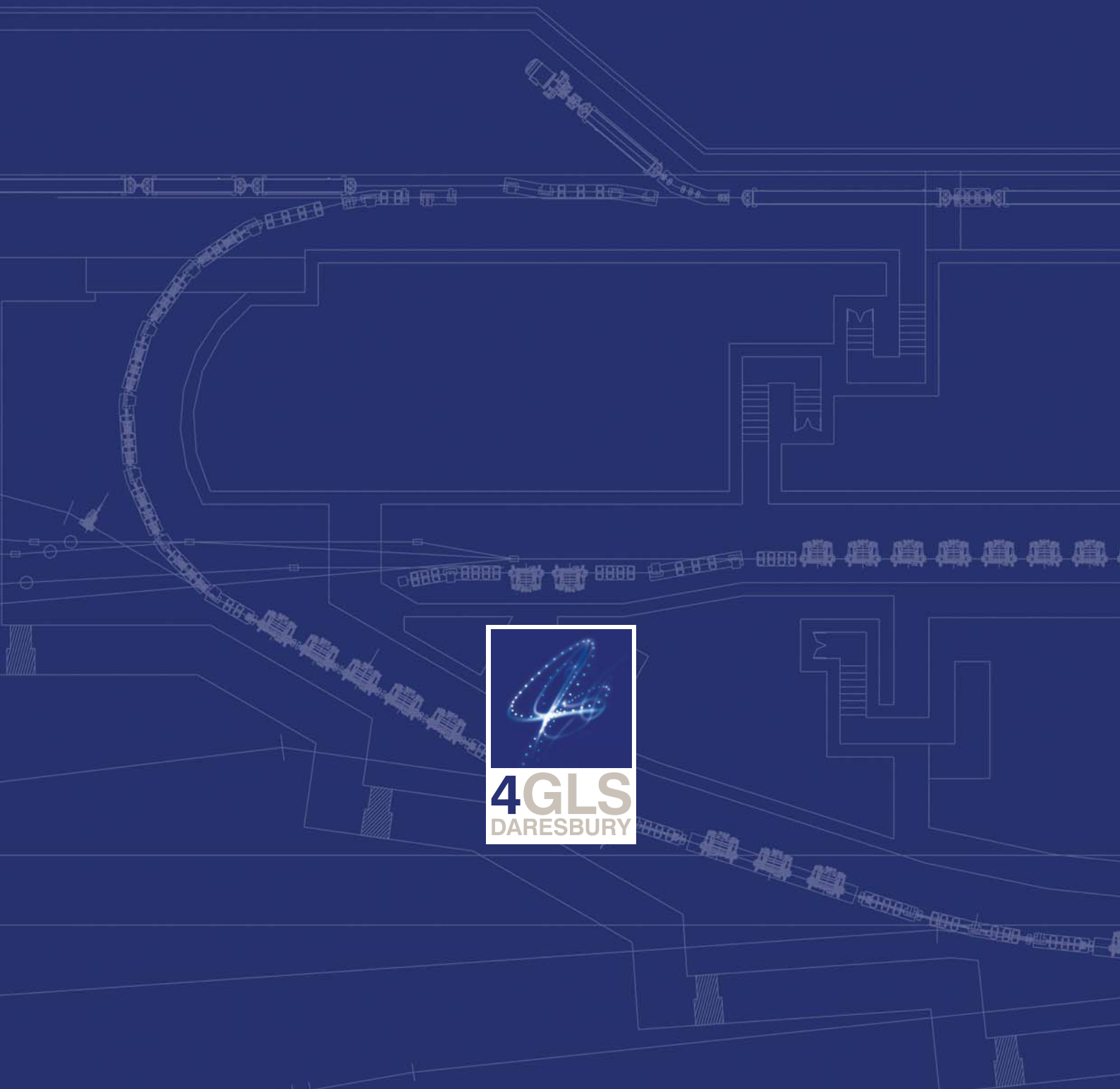

4GLS
DARESBURY

For more information call

Professor Elaine Seddon
Telephone: 01925 603245 Email: e.a.seddon@dl.ac.uk

CCLRC

4GLS is part of the
Council for the Central Laboratory of the
Research Councils

http://www.4gls.ac.uk/